NCAR/TN-486+STR
NCAR TECHNICAL NOTE
November 2012

Description of the NCAR Community Atmosphere Model (CAM 5.0)

Richard B. Neale, Chih-Chieh Chen, Andrew Gettelman, Peter H. Lauritzen, Sungsu Park, David L. Williamson

Climate And Global Dynamics Division
National Center For Atmospheric Research
Boulder, Colorado, USA

Andrew J. Conley, Rolando Garcia, Doug Kinnison, Jean-Francois Lamarque, Dan Marsh, Mike Mills, Anne K. Smith, Simone Tilmes, Francis Vitt

Atmospheric Chemistry Division
National Center For Atmospheric Research
Boulder, Colorado, USA

[1] Hugh Morrison

Mesoscale and Microscale Meteorology
National Center For Atmospheric Research
Boulder, Colorado, USA

Philip Cameron-Smith

Lawrence Livermore National Lab
Livermore, California

William D. Collins

UC Berkeley/Lawrence Berkeley National Laboratory
Berkeley, California

Michael J. Iacono

Atmospheric and Environmental Research, Inc.
Lexington, Massachusetts

Richard C. Easter, Steven J. Ghan, Xiaohong Liu, Philip J. Rasch

Pacific Northwest National Laboratory
Richland, Washington

Mark A. Taylor

Sandia National Laboratories
Albuquerque, New Mexico

[2]

NCAR TECHNICAL NOTES

The Technical Note series provides an outlet for a variety of NCAR manuscripts that contribute in specialized ways to the body of scientific knowledge but which are not suitable for journal, monograph, or book publication. Reports in this series are issued by the NCAR Scientific Divisions; copies may be obtained on request from the Publications Office of NCAR. Designation symbols for the series include:

EDD: *Engineering, Design, or Development Reports*
Equipment descriptions, test results, instrumentation, and operating and maintenance manuals.

IA: *Instructional Aids*
Instruction manuals, bibliographies, film supplements, and other research or instructional aids.

PPR: *Program Progress Reports*
Field program reports, interim and working reports, survey reports, and plans for experiments.

PROC: *Proceedings*
Documentation of symposia, colloquia, conferences, workshops, and lectures. (Distribution may be limited to attendees.)

STR: *Scientific and Technical Reports*
Data compilations, theoretical and numerical investigations, and experimental results.

The National Center for Atmospheric Research (NCAR) is operated by the University Corporation for Atmospheric Research (UCAR) and is sponsored by the National Science Foundation. Any opinions, findings, conclusions, or recommendations expressed in this publication are those of the author(s) and do not necessarily reflect the views of the National Science Foundation.

Contents

Acknowledgments **xi**

1 Introduction **1**
1.1 Brief History . . . 1
1.1.1 CCM0 and CCM1 . . . 1
1.1.2 CCM2 . . . 2
1.1.3 CCM3 . . . 3
1.1.4 CAM3 . . . 4
1.1.5 CAM4 . . . 6
1.1.6 Overview of CAM 5.0 . . . 7

2 Coupling of Dynamical Core and Parameterization Suite **11**

3 Dynamics **15**
3.1 Finite Volume Dynamical Core . . . 15
3.1.1 Overview . . . 15
3.1.2 The governing equations for the hydrostatic atmosphere . . . 15
3.1.3 Horizontal discretization of the transport process on the sphere . . . 17
3.1.4 A *vertically Lagrangian* and *horizontally Eulerian* control-volume discretization of the hy
3.1.5 Optional diffusion operators in CAM5 . . . 24
3.1.6 A mass, momentum, and total energy conserving mapping algorithm . . . 25
3.1.7 A geopotential conserving mapping algorithm . . . 28
3.1.8 Adjustment of pressure to include change in mass of water vapor . . . 28
3.1.9 Negative Tracer Fixer . . . 29
3.1.10 Global Energy Fixer . . . 30
3.1.11 Further discussion . . . 32
3.1.12 Specified Dynamics Option . . . 33
3.1.13 Further discussion . . . 33
3.2 Spectral Element Dynamical Core . . . 33
3.2.1 Continuum Formulation of the Equations . . . 34
3.2.2 Conserved Quantities . . . 36
3.2.3 Horizontal Discretization: Functional Spaces . . . 36
3.2.4 Horizontal Discretization: Differential Operators . . . 39
3.2.5 Horizontal Discretization: Discrete Inner-Product . . . 40
3.2.6 Horizontal Discretization: The Projection Operators . . . 40
3.2.7 Horizontal Discretization: Galerkin Formulation . . . 41

3.2.8 Vertical Discretization . . . 42
3.2.9 Discrete formulation: Dynamics . . . 43
3.2.10 Consistency . . . 44
3.2.11 Time Stepping . . . 44
3.2.12 Dissipation . . . 45
3.2.13 Discrete formulation: Tracer Advection . . . 46
3.2.14 Conservation and Compatibility . . . 46
3.3 Eulerian Dynamical Core . . . 47
3.3.1 Generalized terrain-following vertical coordinates . . . 48
3.3.2 Conversion to final form . . . 49
3.3.3 Continuous equations using $\partial \ln(\pi)/\partial t$ . . . 51
3.3.4 Semi-implicit formulation . . . 52
3.3.5 Energy conservation . . . 54
3.3.6 Horizontal diffusion . . . 57
3.3.7 Finite difference equations . . . 59
3.3.8 Time filter . . . 61
3.3.9 Spectral transform . . . 62
3.3.10 Spectral algorithm overview . . . 62
3.3.11 Combination of terms . . . 65
3.3.12 Transformation to spectral space . . . 66
3.3.13 Solution of semi-implicit equations . . . 67
3.3.14 Horizontal diffusion . . . 68
3.3.15 Initial divergence damping . . . 69
3.3.16 Transformation from spectral to physical space . . . 70
3.3.17 Horizontal diffusion correction . . . 71
3.3.18 Semi-Lagrangian Tracer Transport . . . 72
3.3.19 Mass fixers . . . 76
3.3.20 Energy Fixer . . . 78
3.3.21 Statistics Calculations . . . 79
3.3.22 Reduced grid . . . 79
3.4 Semi-Lagrangian Dynamical Core . . . 79
3.4.1 Introduction . . . 79
3.4.2 Vertical coordinate and hydrostatic equation . . . 80
3.4.3 Semi-implicit reference state . . . 80
3.4.4 Perturbation surface pressure prognostic variable . . . 80
3.4.5 Extrapolated variables . . . 81
3.4.6 Interpolants . . . 81
3.4.7 Continuity Equation . . . 81
3.4.8 Thermodynamic Equation . . . 83
3.4.9 Momentum equations . . . 85
3.4.10 Development of semi-implicit system equations . . . 86
3.4.11 Trajectory Calculation . . . 92
3.4.12 Mass and energy fixers and statistics calculations . . . 92

4 Model Physics **93**
4.1 Conversion to and from dry and wet mixing ratios for trace constituents in the model 95
4.2 Moist Turbulence Scheme . . . 97
4.2.1 Bulk Moist Richardson Number . . . 98
4.2.2 Identification of Convective, Stably Turbulent, and Stable Layers . . . 100
4.2.3 Turbulent Length Scale . . . 101
4.2.4 Steady-State Turbulent Kinetic Energy . . . 101
4.2.5 Stability Functions . . . 102
4.2.6 CL Extension-Merging Procedure . . . 103
4.2.7 Entrainment Rates at the CL Top and Base Interfaces . . . 104
4.2.8 Implicit Diffusion with Implicit Diffusivity . . . 104
4.2.9 Implicit Surface Stress . . . 106
4.3 Shallow Convection Scheme . . . 108
4.3.1 Reconstruction of Mean Profiles and Cloud Condensate Partitioning . . . 108
4.3.2 Source Air Properties of Convective Updraft . . . 110
4.3.3 Closures at the Cloud Base . . . 111
4.3.4 Vertical Evolution of A Single Updraft Plume . . . 112
4.3.5 Penetrative Entrainment . . . 113
4.3.6 Convective Fluxes at and below the PBL top interface . . . 114
4.3.7 Grid-Mean Tendency of Conservative Scalars . . . 115
4.3.8 Grid-Mean Tendency of Non-Conservative Scalars . . . 116
4.4 Deep Convection . . . 118
4.4.1 Updraft Ensemble . . . 118
4.4.2 Downdraft Ensemble . . . 121
4.4.3 Closure . . . 122
4.4.4 Numerical Approximations . . . 122
4.4.5 Deep Convective Momentum Transports . . . 125
4.4.6 Deep Convective Tracer Transport . . . 125
4.5 Evaporation of convective precipitation . . . 127
4.6 Cloud Microphysics . . . 128
4.6.1 Overview of the microphysics scheme . . . 128
4.6.2 Radiative Treatment of Ice . . . 133
4.6.3 Formulations for the microphysical processes . . . 133
4.7 Cloud Macrophysics . . . 141
4.7.1 Cloud Fractions . . . 141
4.7.2 Cloud Overlaps . . . 144
4.7.3 Condensation Processes . . . 146
4.8 Aerosols . . . 151
4.8.1 Emissions . . . 153
4.8.2 Chemistry . . . 154
4.8.3 Secondary Organic Aerosol . . . 154
4.8.4 Nucleation . . . 155
4.8.5 Condensation . . . 155
4.8.6 Coagulation . . . 156
4.8.7 Water Uptake . . . 156

4.8.8 Subgrid Vertical Transport and Activation/Resuspension . . . 156
4.8.9 Wet Deposition . . . 158
4.8.10 Dry Deposition . . . 159
4.9 Condensed Phase Optics . . . 161
4.9.1 Tropospheric Aerosol Optics . . . 161
4.9.2 Stratospheric Volcanic Aerosol Optics . . . 161
4.9.3 Liquid Cloud Optics . . . 163
4.9.4 Ice Cloud Optics . . . 163
4.9.5 Snow Cloud Optics . . . 165
4.10 Radiative Transfer . . . 166
4.10.1 Combination of Aerosol Radiative Properties . . . 166
4.10.2 Combination of Cloud Optics . . . 166
4.10.3 Radiative Fluxes and Heating Rates . . . 167
4.10.4 Surface Radiative Properties . . . 170
4.10.5 Time Sampling . . . 170
4.10.6 Diurnal Cycle and Earth Orbit . . . 170
4.10.7 Solar Spectral Irradiance . . . 172
4.11 Surface Exchange Formulations . . . 177
4.11.1 Land . . . 177
4.11.2 Ocean . . . 181
4.11.3 Sea Ice . . . 182
4.12 Dry Adiabatic Adjustment . . . 183
4.13 Prognostic Greenhouse Gases . . . 184

5 Extensions to CAM **185**
5.1 Introduction . . . 186
5.2 Chemistry . . . 186
5.2.1 Chemistry Schemes . . . 186
5.2.2 Emissions . . . 187
5.2.3 Boundary conditions . . . 189
5.2.4 Lightning . . . 189
5.2.5 Dry deposition . . . 190
5.2.6 Wet removal . . . 190
5.3 Photolytic Approach (Neutral Species) . . . 191
5.4 Numerical Solution Approach . . . 192
5.5 Superfast Chemistry . . . 194
5.5.1 Chemical mechanism . . . 194
5.5.2 Emissions for CAM4 superfast chemistry . . . 194
5.5.3 LINOZ . . . 194
5.5.4 Parameterized PSC ozone loss . . . 195
5.6 WACCM4.0 Physical Parameterizations . . . 196
5.6.1 WACCM4.0 Domain and Resolution . . . 196
5.6.2 Molecular Diffusion and Constituent Separation . . . 197
5.6.3 Gravity Wave Drag . . . 200
5.6.4 Turbulent Mountain Stress . . . 207

5.6.5 QBO Forcing . . . 208
5.6.6 Radiation . . . 208
5.6.7 WACCM4.0 chemistry . . . 211
5.6.8 Electric Field . . . 226
5.6.9 Boundary Conditions . . . 235

6 Initial and Boundary Data **237**
6.1 Initial Data . . . 237
6.2 Boundary Data . . . 238

Appendices

A Physical Constants **241**

B Acronyms **243**

C Resolution and dycore-dependent parameters **245**

References **246**

List of Figures

3.1 A graphical illustration of the different levels of sub-cycling in CAM5. 23
3.2 Tiling the surface of the sphere with quadrilaterals. An inscribed cube is projected to the surface
3.3 A 4×4 tensor product grid of GLL nodes used within each element, for a degree $d = 3$ discretiza
3.4 Vertical level structure of CAM 5.0 54
3.5 Pentagonal truncation parameters 63

4.1 Schematic structure of moist turbulence scheme 99
4.2 Schematic structure of shallow cumulus scheme 109
4.3 Predicted species for interstitial and cloud-borne component of each aerosol mode in MAM-7. St
4.4 Predicted species for interstitial and cloud-borne component of each aerosol mode in MAM-3. St
4.5 Kurucz spectrum. ssf in W/m^2/nm. Source Data: AER. Range from [20, 20000] nm.174
4.6 Lean spectrum. Average over 1 solar cycle, May 1, 1996 to Dec 31, 2006. Source Data: Marsh. s
4.7 Relative difference, $\frac{\texttt{Lean}-\texttt{Kurucz}}{.5(\texttt{Lean}+\texttt{Kurucz})}$ between spectra. RRTMG band boundaries are marked with ve

5.1 Global mean distribution of charged constituents during July solar minimum conditions.215
5.2 a) Global distribution of ionization rates at 7.3×10^{-5} hPa, July 1, UT0100 HRS. Contour interva

List of Tables

4.1 Size distributions of primary emissions. . . . 157
4.2 Assumed SOA (gas) yields . . . 157
4.3 Hygroscopicity of aerosol components . . . 157
4.4 Density (kg/m^3) of aerosol material. . . . 161
4.5 Hygroscopicity of aerosol components. . . . 161
4.6 RRTMG_SW spectral band boundaries and the solar irradiance in each band. . 168
4.7 RRTMG_LW spectral band boundaries. . . . 169
4.8 Band-level ratio of Solar Irradiances, based on average of one solar cycle 173

5.1 Surface fluxes for CAM4 superfast chemistry. . . . 194
5.2 WACCM4.0 Neutral Chemical Species (51 computed species + N_2) 217
5.1 (continued) WACCM4.0 Neutral Chemical Species (51 computed species + N_2) . 218
5.2 WACCM4.0 Gas-phase Reactions. . . . 219
5.2 (continued) WACCM4.0 Gas-phase Reactions. . . . 220
5.2 (continued) WACCM4.0 Gas-phase Reactions. . . . 221
5.2 (continued) WACCM4.0 Gas-phase Reactions. . . . 222
5.2 (continued) WACCM4.0 Gas-phase Reactions. . . . 223
5.3 WACCM4.0 Heterogeneous Reactions on liquid and solid aerosols. . . . 223
5.4 WACCM4.0 Photolytic Reactions. . . . 224
5.4 (continued) WACCM4.0 Photolytic Reactions. . . . 225
5.5 Ion-neutral and recombination reactions and exothermicities. . . . 226
5.6 Ionization reactions. . . . 227
5.7 EUVAC model parameters. . . . 227

C.1 Resolution-dependent parameters . . . 245

Acknowledgments

The authors wish to acknowledge members of NCAR's Atmospheric Modeling and Predictability Section (AMP), Computer Software and Engineering Group (CSEG), and Computation and Information Systems Laboratory (CISL) for their contributions to the development of CAM 5.0.

The new model would not exist without the significant input from members of the CESM Atmospheric Model Working Group (AMWG) too numerous to mention. Leo Donner (GFDL), Minghua Zhang (SUNY) and Phil Rasch (PNNL) were the co-chairs of the AMWG during the development of CAM 5.0.

We would like to acknowledge the substantial contributions to the CAM 5.0 effort from the National Science Foundation, Department of Energy, the National Oceanic and Atmospheric Administration, and the National Aeronautics and Space Administration.

Chapter 1

Introduction

This report presents the details of the governing equations, physical parameterizations, and numerical algorithms defining the version of the NCAR Community Atmosphere Model designated CAM 5.0. The material provides an overview of the major model components, and the way in which they interact as the numerical integration proceeds. Details on the coding implementation, along with in-depth information on running the CAM 5.0 code, are given in a separate technical report entitled ‘ ‘User’s Guide to Community Atmosphere ModelCAM 5.0” [Eaton, 2010]. As before, it is our objective that this model provide NCAR and the university research community with a reliable, well documented atmospheric general circulation model. This version of the CAM 5.0 incorporates a number enhancements to the physics package (*e.g.* adjustments to the deep convection algorithm including the addition of Convective Momentum Transports (CMT), a transition to the finite volume dynamical core as default and the option to run a computationally highly scaleable dynamical core). The ability to transition between CAM-standalone and fully coupled experiment frameworks is much improved in CAM 5.0. We believe that collectively these improvements provide the research community with a significantly improved atmospheric modeling capability.

1.1 Brief History

1.1.1 CCM0 and CCM1

Over the last twenty years, the NCAR Climate and Global Dynamics (CGD) Division has provided a comprehensive, three-dimensional global atmospheric model to university and NCAR scientists for use in the analysis and understanding of global climate. Because of its widespread use, the model was designated a community tool and given the name Community Climate Model (CCM). The original versions of the NCAR Community Climate Model, CCM0A [Washington, 1982] and CCM0B [Williamson, 1983], were based on the Australian spectral model [Bourke et al., 1977; McAvaney et al., 1978] and an adiabatic, inviscid version of the ECMWF spectral model [Baede et al., 1979]. The CCM0B implementation was constructed so that its simulated climate would match the earlier CCM0A model to within natural variability (*e.g.* incorporated the same set of physical parameterizations and numerical approximations), but also provided a more flexible infrastructure for conducting medium– and long–range global forecast studies. The major strength of this latter effort was that all aspects of the model were described

in a series of technical notes, which included a Users' Guide [Sato et al., 1983], a subroutine guide which provided a detailed description of the code [Williamson et al., 1983] a detailed description of the algorithms [Williamson, 1983], and a compilation of the simulated circulation statistics [Williamson and Williamson, 1984]. This development activity firmly established NCAR's commitment to provide a versatile, modular, and well–documented atmospheric general circulation model that would be suitable for climate and forecast studies by NCAR and university scientists. A more detailed discussion of the early history and philosophy of the Community Climate Model can be found in Anthes [1986].

The second generation community model, CCM1, was introduced in July of 1987, and included a number of significant changes to the model formulation which were manifested in changes to the simulated climate. Principal changes to the model included major modifications to the parameterization of radiation, a revised vertical finite-differencing technique for the dynamical core, modifications to vertical and horizontal diffusion processes, and modifications to the formulation of surface energy exchange. A number of new modeling capabilities were also introduced, including a seasonal mode in which the specified surface conditions vary with time, and an optional interactive surface hydrology that followed the formulation presented by Manabe [1969]. A detailed series of technical documentation was also made available for this version [Williamson et al., 1987; Bath et al., 1987; Williamson and Williamson, 1987; Hack et al., 1989] and more completely describe this version of the CCM.

1.1.2 CCM2

The most ambitious set of model improvements occurred with the introduction of the third generation of the Community Climate Model, CCM2, which was released in October of 1992. This version was the product of a major effort to improve the physical representation of a wide range of key climate processes, including clouds and radiation, moist convection, the planetary boundary layer, and transport. The introduction of this model also marked a new philosophy with respect to implementation. The CCM2 code was entirely restructured so as to satisfy three major objectives: much greater ease of use, which included portability across a wide range of computational platforms; conformance to a plug-compatible physics interface standard; and the incorporation of single-job multitasking capabilities.

The standard CCM2 model configuration was significantly different from its predecessor in almost every way, starting with resolution where the CCM2 employed a horizontal T42 spectral resolution (approximately 2.8 x 2.8 degree transform grid), with 18 vertical levels and a rigid lid at 2.917 mb. Principal algorithmic approaches shared with CCM1 were the use of a semi-implicit, leap frog time integration scheme; the use of the spectral transform method for treating the dry dynamics; and the use of a bi-harmonic horizontal diffusion operator. Major changes to the dynamical formalism included the use of a terrain-following hybrid vertical coordinate, and the incorporation of a shape-preserving semi-Lagrangian transport scheme [Williamson and Olson, 1994*a*] for advecting water vapor, as well as an arbitrary number of other scalar fields (*e.g.* cloud water variables, chemical constituents, etc.). Principal changes to the physics included the use of a δ-Eddington approximation to calculate solar absorption [Briegleb, 1992]; the use of a Voigt line shape to more accurately treat infrared radiative cooling in the stratosphere; the inclusion of a diurnal cycle to properly account for the interactions between the radiative effects of the diurnal cycle and the surface fluxes of sensible and latent heat; the incorporation of a finite heat

capacity soil/sea ice model; a more sophisticated cloud fraction parameterization and treatment of cloud optical properties [Kiehl et al., 1994]; the incorporation of a sophisticated non-local treatment of boundary-layer processes [Holtslag and Boville, 1993*a*]; the use of a simple mass flux representation of moist convection [Hack, 1994*a*], and the optional incorporation of the Biosphere-Atmosphere Transfer Scheme (BATS) of Dickinson et al. [1987]. As with previous versions of the model, a User's Guide [Bath et al., 1992] and model description [Hack et al., 1993] were provided to completely document the model formalism and implementation. Control simulation data sets were documented in Williamson [1993].

1.1.3 CCM3

The CCM3 was the fourth generation in the series of NCAR's Community Climate Model. Many aspects of the model formulation and implementation were identical to the CCM2, although there were a number of important changes that were incorporated into the collection of parameterized physics, along with some modest changes to the dynamical formalism. Modifications to the physical representation of specific climate processes in the CCM3 were motivated by the need to address the more serious systematic errors apparent in CCM2 simulations, as well as to make the atmospheric model more suitable for coupling to land, ocean, and sea-ice component models. Thus, an important aspect of the changes to the model atmosphere was that they address well known systematic biases in the top-of-atmosphere and surface (to the extent that they were known) energy budgets. When compared to the CCM2, changes to the model formulation fell into five major categories: modifications to the representation of radiative transfer through both clear and cloudy atmospheric columns, modifications to hydrological processes (i.e., in the form of changes to the atmospheric boundary layer, moist convection, and surface energy exchange), the incorporation of a sophisticated land surface model, the incorporation of an optional slab mixed-layer ocean/thermodynamic sea-ice component, and a collection of other changes to the formalism which did not introduce significant changes to the model climate.

Changes to the clear-sky radiation formalism included the incorporation of minor CO_2 bands trace gases (CH_4, N_2O, $CFC11$, $CFC12$) in the longwave parameterization, and the incorporation of a background aerosol (0.14 optical depth) in the shortwave parameterization. All-sky changes included improvements to the way in which cloud optical properties (effective radius and liquid water path) were diagnosed, the incorporation of the radiative properties of ice clouds, and a number of minor modifications to the diagnosis of convective and layered cloud amount. Collectively these modification substantially reduced systematic biases in the global annually averaged clear-sky and all-sky outgoing longwave radiation and absorbed solar radiation to well within observational uncertainty, while maintaining very good agreement with global observational estimates of cloud forcing. Additionally, the large warm bias in simulated July surface temperature over the Northern Hemisphere, the systematic over-prediction of precipitation over warm land areas, and a large component of the stationary-wave error in CCM2, were also reduced as a result of cloud-radiation improvements.

Modifications to hydrological processes included revisions to the major contributing parameterizations. The formulation of the atmospheric boundary layer parameterization was revised (in collaboration with Dr. A. A. M. Holtslag of KNMI), resulting in significantly improved estimates of boundary layer height, and a substantial reduction in the overall magnitude of the hydrological cycle. Parameterized convection was also modified where this process was repre-

sented using the deep moist convection formalism of Zhang and McFarlane [1995] in conjunction with the scheme developed by Hack [1994*a*] for CCM2. This change resulted in an additional reduction in the magnitude of the hydrological cycle and a smoother distribution of tropical precipitation. Surface roughness over oceans was also diagnosed as a function of surface wind speed and stability, resulting in more realistic surface flux estimates for low wind speed conditions. The combination of these changes to hydrological components resulted in a 13% reduction in the annually averaged global latent heat flux and the associated precipitation rate. It should be pointed out that the improvements in the radiative and hydrological cycle characteristics of the model climate were achieved without compromising the quality of the simulated equilibrium thermodynamic structures (one of the major strengths of the CCM2) thanks in part to the incorporation of a Sundqvist [1988] style evaporation of stratiform precipitation.

The CCM3 incorporated version 1 of the Land Surface Model (LSM) developed by Bonan [1996] which provided for the comprehensive treatment of land surface processes. This was a one-dimensional model of energy, momentum, water, and CO_2 exchange between the atmosphere and land, accounting for ecological differences among vegetation types, hydraulic and thermal differences among soil types, and allowing for multiple surface types including lakes and wetlands within a grid cell. LSM replaced the prescribed surface wetness, prescribed snow cover, and prescribed surface albedos in CCM2. It also replaced the land surface fluxes in CCM2, using instead flux parameterizations that included hydrological and ecological processes (*e.g.* soil water, phenology, stomatal physiology, interception of water by plants).

The fourth class of changes to the CCM2 included the option to run CCM3 with a simple slab ocean-thermodynamic sea ice model. The model employs a spatially and temporally prescribed ocean heat flux and mixed layer depth, which ensures replication of realistic sea surface temperatures and ice distributions for the present climate. The model allowed for the simplest interactive surface for the ocean and sea ice components of the climate system.

The final class of model modifications included a change to the form of the hydrostatic matrix which ensures consistency between ω and the discrete continuity equation, and a more generalized form of the gravity wave drag parameterization. In the latter case, the parameterization was configured to behave in the same way as the CCM2 parameterization of wave drag, but included the capability to exploit more sophisticated descriptions of this process.

One of the more significant implementation differences with the earlier model was that CCM3 included an optional message-passing configuration, allowing the model to be executed as a parallel task in distributed-memory environments. This was an example of how the Climate and Global Dynamics Division continued to invest in technical improvements to the CCM in the interest of making it easier to acquire and use in evolving computational environments. As was the case for CCM2, the code was internally documented, obviating the need for a separate technical note that describes each subroutine and common block in the model library. Thus, the Users' Guide, the land surface technical note, the CCM3 technical note [Kiehl et al., 1996], the actual code and a series of reviewed scientific publications (including a special issue of the Journal of Climate, Volume 11, Number 6) were designed to completely document CCM3.

1.1.4 CAM3

The CAM3 was the fifth generation of the NCAR atmospheric GCM. The name of the model series was changed from Community Climate Model to Community Atmosphere Model to reflect

the role of CAM3 in the fully coupled climate system. In contrast to previous generations of the atmospheric model, CAM3 had been designed through a collaborative process with users and developers in the Atmospheric Model Working Group (AMWG). The AMWG includes scientists from NCAR, the university community, and government laboratories. For CAM3, the consensus of the AMWG was to retain the spectral Eulerian dynamical core for the first official release although the code includes the option to run with semi-Lagrange dynamics or with finite-volume dynamics (FV). The addition of FV was a major extension to the model provided through a collaboration between NCAR and NASA Goddard's Data Assimilation Office (DAO). The major changes in the physics included treatment of cloud condensed water using a prognostic formulation with a bulk microphysical component following Rasch and Kristjánsson [1998*a*] and a macroscale component following Zhang et al. [2003*b*]. The Zhang and McFarlane [1995] parameterization for deep convection was retained from CCM3.

A new treatment of geometrical cloud overlap in the radiation calculations computed the shortwave and longwave fluxes and heating rates for random overlap, maximum overlap, or an arbitrary combination of maximum and random overlap. The calculation was completely separated from the radiative parameterizations. The introduction of the generalized overlap assumptions permitted more realistic treatments of cloud-radiative interactions. The methodology was designed and validated against calculations based upon the independent column approximation (ICA). A new parameterization for the longwave absorptivity and emissivity of water vapor preserved the formulation of the radiative transfer equations using the absorptivity/emissivity method. The components of the method related to water vapor were replaced with new terms calculated with the General Line-by-line Atmospheric Transmittance and Radiance Model (GENLN3). The mean absolute errors in the surface and top-of-atmosphere clear-sky longwave fluxes for standard atmospheres were reduced to less than 1 W/m^2. The near-infrared absorption by water vapor was also updated to a parameterization based upon the HITRAN2k line database [Rothman et al., 2003] that incorporated the CKD 2.4 prescription for the continuum. The magnitude of errors in flux divergences and heating rates relative to modern LBL calculations were reduced by approximately seven times compared to the previous CCM3 parameterization. The uniform background aerosol was replaced with a present-day climatology of sulfate, sea-salt, carbonaceous, and soil-dust aerosols. The climatology was obtained from a chemical transport model forced with meteorological analysis and constrained by assimilation of satellite aerosol retrievals. These aerosols affect the shortwave energy budget of the atmosphere. CAM3 also included a mechanism for treating the shortwave and longwave effects of volcanic aerosols. Evaporation of convective precipitation following Sundqvist [1988] was implemented and enhancement of atmospheric moisture through this mechanism was offset by drying introduced by changes in the longwave absorptivity and emissivity. A careful formulation of vertical diffusion of dry static energy was also implemented.

Additional capabilities included a new thermodynamic package for sea ice in order to mimic the major non-dynamical aspects of CSIM; including snow depth, brine pockets, internal shortwave radiative transfer, surface albedo, ice-atmosphere drag, and surface exchange fluxes. CAM3 also allowed for an explicit representation of fractional land and sea-ice coverage that gave a much more accurate representation of flux exchanges from coastal boundaries, island regions, and ice edges. This fractional specification provided a mechanism to account for flux differences due to sub-grid inhomogeneity of surface types. A new, extensible climatological and time-mean sea-surface temperature boundary data was made available from a blended product using the

global HadISST OI dataset prior to 1981 and the Smith/Reynolds EOF dataset post-1981. Coupling was upgraded in order to couple the dynamical core with the parameterization suite in a purely time split or process split manner. The distinction is that in the process split approximation the physics and dynamics are both calculated from the same past state, while in the time split approximations the dynamics and physics are calculated sequentially, each based on the state produced by the other.

1.1.5 CAM4

The CAM4 was the sixth generation of the NCAR atmospheric GCM and had again been developed through a collaborative process of users and developers in the Atmosphere Model Working Group (AMWG) with signficant input from the Chemistry Climate Working Group (Chem-Clim WG) and the Whole Atmosphere Model Working Group (WAMWG). The model had science enhancements from CAM3 and represented an intermediate release version as part of a staged and parallel process in atmospheric model development. In the CAM4 changes to the moist physical representations centered on enhancements to the existing Zhang and McFarlane [1995] deep convection parameterization. The calculation of Convective Available Potential Energy (CAPE) assumed an entraining plume to provide the in-cloud temperature and humidity profiles used to determine bouyancy and related cloud closure properties (chapter 4.4). The modification is based on the conservation of moist entropy and mixing methods of Raymond and Blyth [1986, 1992]. It replaced the standard undilute non-entraining plume method used in CAM3 and was employed to increase convection sensitivity to tropospheric moisture and reduce the amplitude of the diurnal cycle of precipitation over land. Sub-grid scale Convective Momentum Transports (CMT) were added to the deep convection scheme following Richter and Rasch [2008] and the methodology of Gregory et al. [1997*b*] (chapter 4.4.5). CMT affects tropospheric climate mainly through changes to the Coriolis torque. These changes resulted in improvement of the Hadley circulation during northern Winter and it reduced many of the model biases. In an annual mean, the tropical easterly bias, subtropical westerly bias, and the excessive southern hemisphere mid-latitude jet were improved.

In combination these modifications to the deep-convection lead to significant improvements in the phase, amplitude and spacial anomaly patterns of the modeled El Niño, as documented in Neale et al. [2008]. The calculation of cloud fraction in polar climates was also modified for the CAM4.0. Due to the combination of a diagnostic cloud fraction and prognostic cloud water represntation it was possible to model unphysical extensive cloud decks with near zero in-cloud water in the CAM3. This was particularly pervasize in polar climates in Winter. These calculation inconsitencies and large cloud fractions are significantly reduced with modifications to the calculation of stratiform cloud following Vavrus and Waliser [2008]. In the lower troposphere a 'freeze-drying' process is perfomed whereby cloud fractions were systematically reduced for very low water vaopr amounts. The low cloud reduction caused an Arctic-wide drop of 15 W m^{-2} in surface cloud radiative forcing (CRF) during winter and about a 50% decrease in mean annual Arctic CRF. Consequently, wintertime surface temperatures fell by up to 4 K on land and 2 K over the Arctic Ocean, thus significantly reducing the CAM3 pronounced warm bias. More generally the radiation calculation was performed using inconsistent cloud fraction and condensate quantities in the CAM3. In CAM4 this was remedied with an updated cloud fraction calculation prior to the radiation call at each physics timestep. The coupled climate performance with

the CAM4.0 physics changes was summarized in the horizontal resolution comparison study of Gent et al. [2009].

For the dynamical core component of CAM4 the finite volume (FV) scheme was made the default due to its superior transport properties [Lin and Rood, 1996]. Modifications were made that upgraded the code version to a more recent NASA Goddard supported version. Other changes provided new horizontal grid discretizations (e.g., 1.9x2.5 deg and 0.9x1.25 deg) for optimal computational processor decompostion and polar filtering changes for noise reductions and more continuous (in latitude) filtering. In addition to the existing finite volume and spectral-based dynamical core a new option was also made available that represents the first scheme released with CAM that removes the computational scalability restrictions associated with a pole convergent latitude-longitude grid and the associated polar filtering requirements.

Funded in part by the Department of Energy (DOE) Climate Change Prediction Program the scalable and efficient spectral-element-based atmospheric dynamical core uses the High Order Method Modeling Environment (HOMME) on a cubed sphere grid and was developed by members of the Computational Science Section and the Computational Numerics Group of NCAR's Computational and Information Systems Laboratory (CISL). The finite element dynamical core (commonly referred to as the HOMME core) is fully integrated into CCSM coupling architecture and is invaluable for high resolution climate integrations on existing and upcoming massively parallel computing platforms.

Model flexibility was increased significantly from the CAM3, both within CAM and the CCSM system as a whole. The method for running thermodynamic sea-ice in CAM-only mode was moved to be maintained entirely within the CICE model of the CCSM4. The single-column version of CAM was given the flexibility to be built and run using the same infrastructure as the CAM build and run mechanism. The SCAM GUI run method was no longer supported. The increased coupling flexibility also allowed the introduction of a more consistant method for performing slab-ocean model (SOM) experiments. SOM experiments were, by default, now performed using forcing data from an existing CCSM coupled run. This had the advantage of having a closed temperature budget for both the ice and the ocean mixed layer from a coupled run. The methodology was therefore configured to reproduce the fully coupled CCSM climate as opposed to a reproduction of a psuedo-observed climate available with the CAM3-specific SOM method. The CAM3-specific SOM method was no longer made available. For more information regarding updated run methods see the CAM4.0 users guide of Eaton [2010].

1.1.6 Overview of CAM 5.0

The Community Atmosphere Model

CAM has been modified substantially with a range of enhancements and improvements in the representation of physical processes since version 4 (CAM4). In particular, the combination of physical parameterization enhancements makes it possible to simulate full aerosol cloud interactions including cloud droplet activation by aerosols, precipitation processes due to particle size dependant behavior and explicit radiative interaction of cloud particles. As such the CAM 5.0represents the first version of CAM that is able to simulate the cloud-aerosol indirect radiative effects. More generally CAM 5.0forms the main atmopshere component of the COmmunity

Earth System Model, version 1 (CESM1). The entensive list of physical parameterization improvements are described below:

A new moist turbulence scheme (Section 4.2) is included that explicitly simulates stratus-radiation-turbulence interactions, making it possible to simulate full aerosol indirect effects within stratus. It is based on a diagnostic Turbulent Kinetic Energy (TKE) forumlation and uses a 1^{st} order K-diffusion scheme with entrainment [Bretherton and Park, 2009*a*] originally developed at the University of Washington.. The scheme operates in any layer of the atmopshere when the moist Ri (Richardson number) is larger than its critical value.

A new shallow convection scheme (Section 4.3) uses a realistic plume dilution equation and closure that accurately simulates the spatial distribution of shallow convective activity [Park and Bretherton, 2009]. A steady state convective updraft plume and small fractional area are assumed. An explicit computation of the convective updraft vertcial velocity and updraft fraction is performed using an updraft vertical momentum equation, and thus provides a representation of convective momentum transports. The scheme is specifically designed to interact with the new moist turbulence scheme in order to prevent double counting seen in previous CAM parameterizations. The deep convection parameterization is retained from CAM4.0 (Section 4.4).

Stratiform microphysical processes (Section 4.6) are represented by a prognostic, two-moment formulation for cloud droplet and cloud ice with mass and number concentrations following the original parameterization of Morrison and Gettelman [2008]. The implimentation in CAM 5.0[Gettelman et al., 2008] determines liquid and ice particle sizes from gamma functions and their evolution in time is subject to grid-scale advection, convective detrainment, turbulent diffusion and several microphysical processes. Activation of cloud droplets occurs on an aerosol size distribution based on aerosol chemistry, temperature and vertical velocity. A sub-grid scale vertical velocity is provided through a turbulent kinetic energy approximation. A number of mechanisms are calcuated for ice crystal nucleation [Liu et al., 2007] and combined with modifications to allow ice supersaturation [Gettelman et al., 2010*b*].

The revised cloud macrophysics scheme (Section 4.7,Park et al. [2010]) provides a more transparent treatment of cloud processes and imposes full consistency between cloud fraction and cloud condensate. Separate calculations are performed for liquid and ice stratiform cloud fractions which are assumed to be maximally overlapped. Liquid cloud fraction is based on an assumed triangular distribution of total relative humidity. Ice cloud fraction is based on Gettelman et al. [2010*a*] and allows supersaturation via a modified relative humidity over ice and the inclusion of ice condensate amount.

A new 3-mode modal aerosol scheme (MAM3, Section 4.8, Liu and Ghan [2010]) provides internally mixed representations of number concentrations and mass for Aitkin, accumulation and course aerosol modes which are merged characterizations of the more complex 7-mode version of the scheme. Anthropogenic emissions, defined as originating from industrial, domestic and agriculture activity sectors, are provided from the Lamarque et al. [2010*a*] IPCC AR5 emission data set. Emissions of black carbon and organic carbon represent an update of Bond et al. [2007] and Junker and Liousse [2008]. Emissions of sulfur dioxide are an update of Smith et al. [2001, 2004]. Injection heights, and size distribution of emissions data are not provided with the raw datasets so the protocols of [Dentener et al., 2006*a*] are followed for CAM 5.0. AEROCOM emission datastes are used for natural aeroso0l sources. All emission datasets required to run MAM for pre-industrial or 20th century scenarios are available for download. A full inventory of

observationally based aerosol emission mass and size is provided in standard available datasets. The 7-mode version of the scheme is also available.

Calculations and specifications for the condensed phase optics (aerosols, liquid cloud droplets, hydrometeors and ice crystals) are taken from the microphysics and aerosol parmeterization quantities and provided as input to the radiation scheme (Section 4.9). The radiation scheme (Section 4.10) has been updated to the Rapid Radiative Transfer Method for GCMs (RRTMG, Iacono et al. [2008]; Mlawer et al. [1997]). It employs an efficient and accurate modified correlated-k method for calculating radiative fluxes and heating rates in the clear sky and for the condensed phase species. For each short-wave band calculation extinction optical depth, single scattering albedo and asymmetry properties are specified. For each long-wave band mass-specific absorption is specified. The aerosol optical properties are defined for each mode of the MAM as described by [Ghan and Zaveri, 2007]. Hygroscopicity characteristics are specified for soluable species. For volcanic aerosols a geometric mean radius is used. Optical properties of aerosols are combined prior to the radiative calculation. Liquid-cloud optics are calculated following Wiscombe [1996] and ice-cloud optics are calculated following Mitchell [2002]. Ice-cloud size optics are extended to allow for radiatively active falling snow. Optical properties of clouds (including separate fractions and in-cloud water contents) are combined prior to the radiative calculation. RRTM separates the short-wave spectrum into 14 bands extending from 0.2 μm to 12.2 μm, and models sources of extinction for H_2O, O_3, CO_2, O_2, CH_4, N_2 and Rayleigh scattering. Solar irradiance is now specified for the short-wave bands from the Lean dataset [Wang et al., 2005]. The long-wave spectrum is separated into 16 bands extending from 3.1 μm to 1000 μm with molecular sources of absorption for the same species, in addition to CFC-11 (containing multiple CFC species) and CFC-12. RRTMG has extensive modifications from the original RRTM in order to provide significant speed-up for long climate integrations. Chief amongt these is the Monte-Carlo Independent Column Approximation (McICA, Pincus and Morcrette [2003]) that represnts sub-grid scale cloud variability. With these modifications RRTMG still retains superior offline agreement with line-by-line calculations when compared to the previous CAM radiation package (CAM-RT).

The CAM Chemistry Model (CAM-CHEM)

Chemistry in CAM is now fully interactive and implemented in CESM (Section 5.1); in particular, emissions of biogenic compounds and deposition of aerosols to snow, ice, ocean and vegetation are handled through the coupler. The released version of CAM-chem in CESM is using the recently-developed superfast chemistry (Section 5.5), in collaboration with P. Cameron-Smith from LLNL and M. Prather from UCI) to perform centennial scale simulations at a minor cost increase over the base CAM4. These simulations use the recently developed 1850-2005 emissions created in support of CMIP5.

The Whole Atmosphere Community Climate Model (WACCM)

WACCM4 (Section 5.6), incorporates several improvements and enhancements over the previous version (3.1.9). It can be run coupled to the POP2 and CICE CESM model components. The model's chemistry module (Section 5.1) has been updated according to the latest JPL-2006 recommendations; a quasi-biennial oscillation may be imposed (as an option) by relaxing the winds

to observations in the Tropics; heating from stratospheric volcanic aerosols is now computed explicitly; the effects of solar proton events are now included; the effect of unresolved orography is parameterized as a surface stress (turbulent mountain stress) leading to an improvement in the frequency of sudden stratospheric warmings; and gravity waves due to convective and frontal sources are parameterized based upon the occurrence of convection and the diagnosis of regions of frontogenesis in the model.

Chapter 2

Coupling of Dynamical Core and Parameterization Suite

The CAM 5.0 cleanly separates the parameterization suite from the dynamical core, and makes it easier to replace or modify each in isolation. The dynamical core can be coupled to the parameterization suite in a purely time split manner or in a purely process split one, as described below.

Consider the general prediction equation for a generic variable ψ,

$$\frac{\partial \psi}{\partial t} = D\left(\psi\right) + P\left(\psi\right) \ , \tag{2.1}$$

where ψ denotes a prognostic variable such as temperature or horizontal wind component. The dynamical core component is denoted D and the physical parameterization suite P.

A three-time-level notation is employed which is appropriate for the semi-implicit Eulerian spectral transform dynamical core. However, the numerical characteristics of the physical parameterizations are more like those of diffusive processes rather than advective ones. They are therefore approximated with forward or backward differences, rather than centered three-time-level forms.

The *Process Split* coupling is approximated by

$$\psi^{n+1} = \psi^{n-1} + 2\Delta t D(\psi^{n+1}, \psi^{n}, \psi^{n-1}) + 2\Delta t P(\psi^{*}, \psi^{n-1}) \ , \tag{2.2}$$

where $P(\psi^{*}, \psi^{n-1})$ is calculated first from

$$\psi^{*} = \psi^{n-1} + 2\Delta t P(\psi^{*}, \psi^{n-1}) \ . \tag{2.3}$$

The *Time Split* coupling is approximated by

$$\psi^{*} = \psi^{n-1} + 2\Delta t D(\psi^{*}, \psi^{n}, \psi^{n-1}) \ , \tag{2.4}$$

$$\psi^{n+1} = \psi^{*} + 2\Delta t P(\psi^{n+1}, \psi^{*}) \ . \tag{2.5}$$

The distinction is that in the *Process Split* approximation the calculations of D and P are both based on the same past state, ψ^{n-1}, while in the *Time Split* approximations D and P are calculated sequentially, each based on the state produced by the other.

As mentioned above, the Eulerian core employs the three-time-level notation in (2.2)-(2.5). Eqns. (2.2)-(2.5) also apply to two-time-level finite volume, semi-Lagrangian and spectral element (HOMME) cores by dropping centered n term dependencies, and replacing n-1 by n and $2\Delta t$ by Δt.

The parameterization package can be applied to produce an updated field as indicated in (2.3) and (2.5). Thus (2.5) can be written with an operator notation

$$\psi^{n+1} = \boldsymbol{P}\left(\psi^*\right) \ , \tag{2.6}$$

where only the past state is included in the operator dependency for notational convenience. The implicit predicted state dependency is understood. The *Process Split* equation (2.2) can also be written in operator notation as

$$\psi^{n+1} = \boldsymbol{D}\left(\psi^{n-1}, \frac{\boldsymbol{P}(\psi^{n-1}) - \psi^{n-1}}{2\Delta t}\right) \ , \tag{2.7}$$

where the first argument of $\boldsymbol{D}$ denotes the prognostic variable input to the dynamical core and the second denotes the forcing rate from the parameterization package, e.g. the heating rate in the thermodynamic equation. Again only the past state is included in the operator dependency, with the implicit predicted state dependency left understood. With this notation the *Time Split* system (2.5) and (2.5) can be written

$$\psi^{n+1} = \boldsymbol{P}\left(\boldsymbol{D}\left(\psi^{n-1}, 0\right)\right) \ . \tag{2.8}$$

The total parameterization package in CAM 5.0 consists of a sequence of components, indicated by

$$P = \{M, R, S, T\} \ , \tag{2.9}$$

where M denotes (Moist) precipitation processes, R denotes clouds and Radiation, S denotes the Surface model, and T denotes Turbulent mixing. Each of these in turn is subdivided into various components: M includes an optional dry adiabatic adjustment (normally applied only in the stratosphere), moist penetrative convection, shallow convection, and large-scale stable condensation; R first calculates the cloud parameterization followed by the radiation parameterization; S provides the surface fluxes obtained from land, ocean and sea ice models, or calculates them based on specified surface conditions such as sea surface temperatures and sea ice distribution. These surface fluxes provide lower flux boundary conditions for the turbulent mixing T which is comprised of the planetary boundary layer parameterization, vertical diffusion, and gravity wave drag.

Defining operators following (2.6) for each of the parameterization components, the couplings in CAM 5.0 are summarized as:
TIME SPLIT

$$\psi^{n+1} = \boldsymbol{T}\left(\boldsymbol{S}\left(\boldsymbol{R}\left(\boldsymbol{M}\left(\boldsymbol{D}\left(\psi^{n-1}, 0\right)\right)\right)\right)\right) \tag{2.10}$$

PROCESS SPLIT

$$\psi^{n+1} = \boldsymbol{D}\left(\psi^{n-1}, \frac{\boldsymbol{T}\left(\boldsymbol{S}\left(\boldsymbol{R}\left(\boldsymbol{M}\left(\psi^{n-1}\right)\right)\right)\right) - \psi^{n-1}}{2\Delta t}\right) \tag{2.11}$$

The labels *Time Split* and *Process Split* refer to the coupling of the dynamical core with the complete parameterization suite. The components within the parameterization suite are coupled via time splitting in both forms.

The *Process Split* form is convenient for spectral transform models. With *Time Split* approximations extra spectral transforms are required to convert the updated momentum variables provided by the parameterizations to vorticity and divergence for the Eulerian spectral core, or to recalculate the temperature gradient for the semi-Lagrangian spectral core. The *Time Split* form is convenient for the finite-volume core which adopts a Lagrangian vertical coordinate. Since the scheme is explicit and restricted to small time-steps by its non-advective component, it sub-steps the dynamics multiple times during a longer parameterization time step. With *Process Split* approximations the forcing terms must be interpolated to an evolving Lagrangian vertical coordinate every sub-step of the dynamical core. Besides the expense involved, it is not completely obvious how to interpolate the parameterized forcing, which can have a vertical grid scale component arising from vertical grid scale clouds, to a different vertical grid. [Williamson, 2002] compares simulations with the Eulerian spectral transform dynamical core coupled to the CCM3 parameterization suite via *Process Split* and *Time Split* approximations.

Chapter 3

Dynamics

3.1 Finite Volume Dynamical Core

3.1.1 Overview

This document describes the Finite-Volume (FV) dynamical core that was initially developed and used at the NASA Data Assimilation Office (DAO) for data assimilation, numerical weather predictions, and climate simulations. The finite-volume discretization is local and entirely in physical space. The horizontal discretization is based on a conservative "*flux-form semi-Lagrangian*" scheme described by Lin and Rood [1996] (hereafter LR96) and Lin and Rood [1997] (hereafter LR97). The vertical discretization can be best described as *Lagrangian* with a conservative re-mapping, which essentially makes it *quasi-Lagrangian*. The *quasi-Lagrangian* aspect of the vertical coordinate is transparent to model users or physical parameterization developers, and it functions exactly like the $\eta - coordinate$ (a hybrid $\sigma - p$ coordinate) used by other dynamical cores within CAM.

In the current implementation for use in CAM, the FV dynamics and physics are "time split" in the sense that all prognostic variables are updated sequentially by the "dynamics" and then the "physics". The time integration within the FV dynamics is fully explicit, with sub-cycling within the 2D Lagrangian dynamics to stabilize the fastest wave (see section 3.1.4). The transport for tracers, however, can take a much larger time step (*e.g.*, 30 minutes as for the physics).

3.1.2 The governing equations for the hydrostatic atmosphere

For reference purposes, we present the continuous differential equations for the hydrostatic 3D atmospheric flow on the sphere for a general vertical coordinate ζ (*e.g.*, Kasahara [1974]). Using standard notations, the hydrostatic balance equation is given as follows:

$$\frac{1}{\rho}\frac{\partial p}{\partial z} + g = 0, \tag{3.1}$$

where ρ is the density of the air, p the pressure, and g the gravitational constant. Introducing the "*pseudo-density*" $\pi = \frac{\partial p}{\partial \zeta}$ (*i.e.*, the vertical pressure gradient in the general coordinate), from the hydrostatic balance equation the *pseudo-density* and the true density are related as follows:

$$\pi = -\frac{\partial \Phi}{\partial \zeta}\rho, \tag{3.2}$$

where $\Phi = gz$ is the geopotential. Note that π reduces to the "true density" if $\zeta = -gz$, and the "surface pressure" P_s if $\zeta = \sigma$ ($\sigma = \frac{p}{P_s}$). The conservation of total air mass using π as the prognostic variable can be written as

$$\frac{\partial}{\partial t}\pi + \nabla \cdot \left(\vec{V}\pi\right) = 0, \tag{3.3}$$

where $\vec{V} = (u, v, \frac{d\zeta}{dt})$. Similarly, the mass conservation law for tracer species (or water vapor) can be written as

$$\frac{\partial}{\partial t}(\pi q) + \nabla \cdot \left(\vec{V}\pi q\right) = 0, \tag{3.4}$$

where q is the mass mixing ratio (or specific humidity) of the tracers (or water vapor).

Choosing the (virtual) potential temperature Θ as the thermodynamic variable, the first law of thermodynamics is written as

$$\frac{\partial}{\partial t}(\pi\Theta) + \nabla \cdot \left(\vec{V}\pi\Theta\right) = 0. \tag{3.5}$$

Letting (λ, θ) denote the (longitude, latitude) coordinate, the momentum equations can be written in the "vector-invariant form" as follows:

$$\frac{\partial}{\partial t}u = \Omega v - \frac{1}{A cos\theta}\left[\frac{\partial}{\partial \lambda}\left(\kappa + \Phi - \nu D\right) + \frac{1}{\rho}\frac{\partial}{\partial \lambda}p\right] - \frac{d\zeta}{dt}\frac{\partial u}{\partial \zeta}, \tag{3.6}$$

$$\frac{\partial}{\partial t}v = -\Omega u - \frac{1}{A}\left[\frac{\partial}{\partial \theta}\left(\kappa + \Phi - \nu D\right) + \frac{1}{\rho}\frac{\partial}{\partial \theta}p\right] - \frac{d\zeta}{dt}\frac{\partial v}{\partial \zeta}, \tag{3.7}$$

where A is the radius of the earth, ν is the coefficient for the optional divergence damping, D is the horizontal divergence

$$D = \frac{1}{A cos\theta}\left[\frac{\partial}{\partial \lambda}(u) + \frac{\partial}{\partial \theta}(v\, cos\theta)\right],$$

$$\kappa = \frac{1}{2}\left(u^2 + v^2\right),$$

and Ω, the vertical component of the absolute vorticity, is defined as follows:

$$\Omega = 2\omega\, sin\theta + \frac{1}{A\, cos\theta}\left[\frac{\partial}{\partial \lambda}v - \frac{\partial}{\partial \theta}(u\, cos\theta)\right],$$

where ω is the angular velocity of the earth. Note that the last term in (3.6) and (3.7) vanishes if the vertical coordinate ζ is a conservative quantity (*e.g.*, entropy under adiabatic conditions [Hsu and Arakawa, 1990] or an imaginary conservative tracer), and the 3D divergence operator becomes 2D along constant ζ surfaces. The discretization of the 2D horizontal transport process is described in section 3.1.3. The complete dynamical system using the Lagrangian control-volume vertical discretization is described in section 3.1.4 and section 3.1.5 describes

the explicit diffusion operators available in CAM5. A mass, momentum, and total energy conservative mapping algorithm is described in section 3.1.6 and in section 3.1.7 an alternative geopotential conserving vertical remapping method is described. Sections 3.1.8 and 3.1.9 are on the adjusctment of pressure to include the change in mass of water vapor and on the negative tracer fixer in CAM, respectively. Last the global energy fixer is described (section 3.1.10).

3.1.3 Horizontal discretization of the transport process on the sphere

Since the vertical transport term would vanish after the introduction of the vertical Lagrangian control-volume discretization (see section 3.1.4), we shall present here only the 2D (horizontal) forms of the FFSL transport algorithm for the transport of density (3.3) and mixing ratio-like quantities (3.4) on the sphere. The governing equation for the pseudo-density (3.3) becomes

$$\frac{\partial}{\partial t}\pi + \frac{1}{A cos\theta}\left[\frac{\partial}{\partial \lambda}(u\pi) + \frac{\partial}{\partial \theta}(v\pi\, cos\theta)\right] = 0. \tag{3.8}$$

The finite-volume (*integral*) representation of the continuous π field is defined as follows:

$$\widetilde{\pi}(t) \equiv \frac{1}{A^2 \Delta\theta \Delta\lambda cos\theta} \iint \pi(t;\lambda,\theta) A^2 cos\theta \, d\theta d\lambda. \tag{3.9}$$

Given the *exact* 2D wind field $\overrightarrow{V}(t;\lambda,\theta) = (U,V)$ the 2D integral representation of the conservation law for $\widetilde{\pi}$ can be obtained by integrating (3.8) in time and in space

$$\widetilde{\pi}^{n+1} = \widetilde{\pi}^{n} - \frac{1}{A^2 \Delta\theta \Delta\lambda cos\theta} \int_t^{t+\Delta t} \left[\oint \pi(t;\lambda,\theta)\overrightarrow{V} \cdot \overrightarrow{n}\, dl\right] dt. \tag{3.10}$$

The above 2D transport equation is still *exact for the finite-volume under consideration*. To carry out the contour integral, certain approximations must be made. LR96 essentially decomposed the flux integral using two orthogonal 1D flux-form transport operators. Introducing the following difference operator

$$\delta_x q = q(x + \frac{\Delta x}{2}) - q(x - \frac{\Delta x}{2}),$$

and assuming (u^*, v^*) is the time-averaged (from time t to time $t + \Delta t$) $\overrightarrow{V}$ on the C-grid (*e.g.*, Fig. 1 in LR96), the 1-D finite-volume flux-form transport operator F in the λ-direction is

$$F(u^*, \Delta t, \widetilde{\pi}) = -\frac{1}{A\Delta\lambda cos\theta}\, \delta_\lambda \left[\int_t^{t+\Delta t} \pi U \, dt\right] = -\frac{\Delta t}{A\Delta\lambda cos\theta}\, \delta_\lambda \left[\chi(u^*, \Delta t; \pi)\right], \tag{3.11}$$

where χ , the time-accumulated (from t to $t+\Delta t$) mass flux across the cell wall, is defined as follows,

$$\chi(u^*, \Delta t; \pi) = \frac{1}{\Delta t} \int_t^{t+\Delta t} \pi U \, dt \equiv u^* \pi^*(u^*, \Delta t, \widetilde{\pi}), \tag{3.12}$$

and

$$\pi^*(u^*, \Delta t; \widetilde{\pi}) \approx \frac{1}{\Delta t} \int_t^{t+\Delta t} \pi \, dt \tag{3.13}$$

can be interpreted as a time mean (from time t to time $t + \Delta t$) pseudo-density value of all material that passed through the cell edge from the upwind direction.

Note that the above *time integration* is to be carried out along the *backward-in-time* trajectory of the cell edge position from $t = t + \Delta t$ (the arrival point; (*e.g.*, point B in Fig. 3 of LR96) back to time t (the departure point; *e.g.*, point B' in Fig. 3 of LR96). The very essence of the 1D finite-volume algorithm is to construct, based on the given initial cell-mean values of $\widetilde{\pi}$, an approximated subgrid distribution of the true π field, to enable an analytic integration of (3.13). Assuming there is no error in obtaining the time-mean wind (u^*), the only error produced by the 1D transport scheme would be solely due to the approximation to the continuous distribution of π within the subgrid under consideration (this is not the case in 2D; Lauritzen et al. [2010]). From this perspective, it can be said that the 1D finite-volume transport algorithm combines the time-space discretization in the approximation of the time-mean cell-edge values π^*. The physically correct way of approximating the integral (3.13) must be "upwind", in the sense that it is integrated along the backward trajectory of the cell edges. For example, a center difference approximation to (3.13) would be physically incorrect, and consequently numerically unstable unless artificial numerical diffusion is added.

Central to the accuracy and computational efficiency of the finite-volume algorithms is the degrees of freedom that describe the subgrid distribution. The first order upwind scheme, for example, has zero degrees of freedom within the volume as it is assumed that the subgrid distribution is piecewise constant having the same value as the given volume-mean. The second order finite-volume scheme (*e.g.*, Lin et al. [1994]) assumes a piece-wise linear subgrid distribution, which allows one degree of freedom for the specification of the "slope" of the linear distribution to improve the accuracy of integrating (3.13). The Piecewise Parabolic Method (PPM, Colella and Woodward [1984]) has two degrees of freedom in the construction of the second order polynomial within the volume, and as a result, the accuracy is significantly enhanced. The PPM appears to strike a good balance between computational efficiency and accuracy. Therefore, the PPM is the basic 1D scheme we chose (see, e.g., Machenhauer [1998]). Note that the subgrid PPM distributions are compact, and do not extend beyond the volume under consideration. The accuracy is therefore significantly better than the order of the chosen polynomials implies. While the PPM scheme possesses all the desirable attributes (mass conserving, monotonicity preserving, and high-order accuracy) in 1D, it is important that a solution be found to avoid the directional splitting in the multi-dimensional problem of modeling the dynamics and transport processes of the Earth's atmosphere.

The first step for reducing the splitting error is to apply the two orthogonal 1D flux-form operators in a directionally symmetric way. After symmetry is achieved, the "inner operators" are then replaced with corresponding advective-form operators (in CAM5 the "inner operators" are based on constant cell-average values and not the PPM). A stability analysis of the consequences of using different inner and outer operators in the LR96 scheme is given in Lauritzen [2007]. A consistent advective-form operator in the $\lambda-$direction can be derived from its flux-form counterpart (F) as follows:

$$f(u^*, \Delta t, \widetilde{\pi}) = F(u^*, \Delta t, \widetilde{\pi}) + \widetilde{\rho} \, F(u^*, \Delta t, \widetilde{\pi} \equiv 1) = F(u^*, \Delta t, \widetilde{\pi}) + \widetilde{\pi} \, C^{\lambda}_{def}, \tag{3.14}$$

$$C^{\lambda}_{def} = \frac{\Delta t\, \delta_\lambda u^*}{A\Delta\lambda cos\theta}, \tag{3.15}$$

where C^{λ}_{def} is a dimensionless number indicating the degree of the flow deformation in the λ-direction. The above derivation of f is slightly different from LR96's approach, which adopted the traditional 1D advective-form semi-Lagrangian scheme. The advantage of using (3.14) is that computation of winds at cell centers (Eq. 2.25 in LR96) are avoided.

Analogously, the 1D flux-form transport operator G in the latitudinal (θ) direction is derived as follows:

$$G(v^*, \Delta t, \widetilde{\pi}) = -\frac{1}{A\Delta\theta cos\theta}\,\delta_\theta \left[\int_t^{t+\Delta t} \pi V cos\theta\, dt\right] = -\frac{\Delta t}{A\Delta\theta cos\theta}\,\delta_\theta \left[v^* cos\theta\, \pi^*\right], \tag{3.16}$$

and likewise the advective-form operator,

$$g(v^*, \Delta t, \widetilde{\pi}) = G(v^*, \Delta t, \widetilde{\pi}) + \widetilde{\pi}\, C^{\theta}_{def}, \tag{3.17}$$

where

$$C^{\theta}_{def} = \frac{\Delta t\, \delta_\theta \left[v^* cos\theta\right]}{A\Delta\theta cos\theta}. \tag{3.18}$$

To complete the construction of the 2D algorithm on the sphere, we introduce the following short hand notations:

$$(\,)^{\theta} = (\,)^n + \frac{1}{2} g\left[v^*, \Delta t, (\,)^n\right], \tag{3.19}$$

$$(\,)^{\lambda} = (\,)^n + \frac{1}{2} f\left[u^*, \Delta t, (\,)^n\right]. \tag{3.20}$$

The 2D transport algorithm (*cf*, Eq. 2.24 in LR96) can then be written as

$$\widetilde{\pi}^{n+1} = \widetilde{\pi}^n + F\left[u^*, \Delta t, \widetilde{\pi}^{\theta}\right] + G\left[v^*, \Delta t, \widetilde{\pi}^{\lambda}\right]. \tag{3.21}$$

Using explicitly the mass fluxes (χ, Y), (3.21) is rewritten as

$$\widetilde{\pi}^{n+1} = \widetilde{\pi}^n - \frac{\Delta t}{A cos\theta}\left\{\frac{1}{\Delta\lambda}\delta_\lambda\left[\chi(u^*, \Delta t; \widetilde{\pi}^{\theta})\right] + \frac{1}{\Delta\theta}\delta_\theta\left[cos\theta\, Y(v^*, \Delta t; \widetilde{\pi}^{\lambda})\right]\right\}, \tag{3.22}$$

where Y, the mass flux in the meridional direction, is defined in a similar fashion as χ (3.12). The ability of the LR96 scheme to approximate the exact geometry of the fluxes for deformational flows is discussed in Machenhauer et al. [2009] and Lauritzen et al. [2010].

It can be verified that in the special case of constant density flow ($\widetilde{\pi} = constant$) the above equation degenerates to the finite-difference representation of the *incompressibility condition* of the "time mean" wind field (u^*, v^*), *i.e.*,

$$\frac{1}{\Delta\lambda}\delta_\lambda u^* + \frac{1}{\Delta\theta}\delta_\theta\left(v^* cos\theta\right) = 0. \tag{3.23}$$

The fulfillment of the above *incompressibility condition* for constant density flows is crucial to the accuracy of the 2D flux-form formulation. For transport of volume mean mixing ratio-like quantities ($\widetilde{q}$) the mass fluxes (χ, Y) as defined previously should be used as follows

$$\widetilde{q}^{n+1} = \frac{1}{\widetilde{\pi}^{n+1}}\left[\widetilde{\pi}^n \widetilde{q}^n + F(\chi, \Delta t, \widetilde{q}^{\theta}) + G(Y, \Delta t, \widetilde{q}^{\lambda})\right]. \tag{3.24}$$

Note that the above form of the tracer transport equation consistently degenerates to (3.21) if $\widetilde{q} \equiv 1$ (*i.e.*, the tracer density equals to the background air density), which is another important condition for a flux-form transport algorithm to be able to avoid generation of noise (*e.g.*, creation of artificial gradients) and to maintain mass conservation.

3.1.4 A *vertically Lagrangian* and *horizontally Eulerian* control-volume discretization of the hydrodynamics

The very idea of using Lagrangian vertical coordinate for formulating governing equations for the atmosphere is not entirely new. Starr [1945]) is likely the first to have formulated, in the *continuous differential form*, the governing equations using a Lagrangian coordinate. Starr did not make use of the *discrete* Lagrangian control-volume concept for discretization nor did he present a solution to the problem of computing the pressure gradient forces. In the *finite-volume discretization* to be described here, the Lagrangian surfaces are treated as the bounding material surfaces of the Lagrangian control-volumes within which the finite-volume algorithms developed in LR96, LR97, and L97 will be directly applied.

To use a vertical Lagrangian coordinate system to reduce the 3D governing equations to the 2D forms, one must first address the issue of whether it is an inertial coordinate or not. For hydrostatic flows, it is. This is because both the right-hand-side and the left-hand-side of the vertical momentum equation vanish for purely hydrostatic flows.

Realizing that the earth's surface, for all practical modeling purposes, can be regarded as a non-penetrable material surface, it becomes straightforward to construct a terrain-following Lagrangian control-volume coordinate system. In fact, any commonly used terrain-following coordinates can be used as the starting reference (*i.e.*, fixed, Eulerian coordinate) of the floating Lagrangian coordinate system. To close the coordinate system, the model top (at a prescribed constant pressure) is also assumed to be a Lagrangian surface, which is the same assumption being used by practically all global hydrostatic models.

The basic idea is to start the time marching from the chosen terrain-following Eulerian coordinate (*e.g.*, pure σ or hybrid σ-p), *treating the initial coordinate surfaces as material surfaces*, the finite-volumes bounded by two coordinate surfaces, *i.e.*, the Lagrangian control-volumes, are free vertically, to float, compress, or expand with the flow as dictated by the hydrostatic dynamics.

By choosing an imaginary conservative tracer ζ that is a monotonic function of height and constant on the initial reference coordinate surfaces (*e.g.*, the value of "η" in the hybrid $\sigma - p$ coordinate used in CAM), the 3D governing equations written for the general vertical coordinate in section 1.2 can be reduced to 2D forms. After factoring out the constant $\delta\zeta$, (3.3), the conservation law for the pseudo-density ($\pi = \frac{\delta p}{\delta \zeta}$), becomes

$$\frac{\partial}{\partial t}\delta p + \frac{1}{A cos\theta}\left[\frac{\partial}{\partial \lambda}(u\delta p) + \frac{\partial}{\partial \theta}(v\delta p\, cos\theta)\right] = 0, \tag{3.25}$$

where the symbol δ represents the vertical difference between the two neighboring Lagrangian surfaces that bound the finite control-volume. From (3.1), the pressure thickness δp of that control-volume is proportional to the total mass, *i.e.*, $\delta p = -\rho g \delta z$. Therefore, it can be said that the Lagrangian control-volume vertical discretization has the hydrostatic balance built-in,

and δp can be regarded as the "pseudo-density" for the discretized Lagrangian vertical coordinate system.

Similarly, (3.4), the mass conservation law for all tracer species, is

$$\frac{\partial}{\partial t}(q\delta p) + \frac{1}{A cos\theta}\left[\frac{\partial}{\partial \lambda}(uq\delta p) + \frac{\partial}{\partial \theta}(vq\delta p\, cos\theta)\right] = 0, \tag{3.26}$$

the thermodynamic equation, (3.5), becomes

$$\frac{\partial}{\partial t}(\Theta\delta p) + \frac{1}{A cos\theta}\left[\frac{\partial}{\partial \lambda}(u\Theta\delta p) + \frac{\partial}{\partial \theta}(v\Theta\delta p\, cos\theta)\right] = 0, \tag{3.27}$$

and (3.6) and (3.7), the momentum equations, are reduced to

$$\frac{\partial}{\partial t}u = \Omega v - \frac{1}{A cos\theta}\left[\frac{\partial}{\partial \lambda}\left(\kappa + \Phi - \nu D\right) + \frac{1}{\rho}\frac{\partial}{\partial \lambda}p\right], \tag{3.28}$$

$$\frac{\partial}{\partial t}v = -\Omega u - \frac{1}{A}\left[\frac{\partial}{\partial \theta}\left(\kappa + \Phi - \nu D\right) + \frac{1}{\rho}\frac{\partial}{\partial \theta}p\right]. \tag{3.29}$$

Given the prescribed pressure at the model top P_∞, the position of each Lagrangian surface P_l (horizontal subscripts omitted) is determined in terms of the hydrostatic pressure as follows:

$$P_l = P_\infty + \sum_{k=1}^{l}\delta P_k, \quad (for\, l = 1,\, 2,\, 3,\, ...,\, N), \tag{3.30}$$

where the subscript l is the vertical index ranging from 1 at the lower bounding Lagrangian surface of the first (the highest) layer to N at the Earth's surface. There are N+1 Lagrangian surfaces to define a total number of N Lagrangian layers. The surface pressure, which is the pressure at the lowest Lagrangian surface, is easily computed as P_N using (3.30). The surface pressure is needed for the physical parameterizations and to define the reference Eulerian coordinate for the mapping procedure (to be described in section 3.1.6).

With the exception of the pressure-gradient terms and the addition of a thermodynamic equation, the above 2D Lagrangian dynamical system is the same as the shallow water system described in LR97. The conservation law for the depth of fluid h in the shallow water system of LR97 is replaced by (3.25) for the pressure thickness δp. The ideal gas law, the mass conservation law for air mass, the conservation law for the potential temperature (3.27), together with the modified momentum equations (3.28) and (3.29) close the 2D Lagrangian dynamical system, which are vertically coupled only by the hydrostatic relation (see (3.54), section 3.1.6).

The time marching procedure for the 2D Lagrangian dynamics follows closely that of the shallow water dynamics fully described in LR97. For computational efficiency, we shall take advantage of the stability of the FFSL transport algorithm by using a much larger time step (Δt) for the transport of all tracer species (including water vapor). As in the shallow water system, the Lagrangian dynamics uses a relatively small time step, $\Delta\tau = \Delta t/m$, where m is the number of the sub-cycling needed to stabilize the fastest wave in the system. We shall describe here this time-split procedure for the *prognostic variables* $[\delta p, \Theta, u, v; q]$ on the D-grid. Discretization on the C-grid for obtaining the *diagnostic variables*, the time-averaged winds (u^*, v^*), is analogous to that of the D-grid (see also LR97).

Introducing the following short hand notations (*cf*, (3.19) and (3.20)):

$$(\,)_i^{\theta} = (\,)^{n+\frac{i-1}{m}} + \frac{1}{2} g[v_i^*, \Delta\tau, (\,)^{n+\frac{i-1}{m}}],$$

$$(\,)_i^{\lambda} = (\,)^{n+\frac{i-1}{m}} + \frac{1}{2} f[u_i^*, \Delta\tau, (\,)^{n+\frac{i-1}{m}}],$$

and applying directly (3.22), the update of "pressure thickness" δp, using the fractional time step $\Delta\tau = \Delta t/m$, can be written as

$$\delta p^{n+\frac{i}{m}} = \delta p^{n+\frac{i-1}{m}} - \frac{\Delta\tau}{A cos\theta} \left\{ \frac{1}{\Delta\lambda} \delta_\lambda \left[x_i^*(u_i^*, \Delta\tau; \delta p_i^\theta) \right] + \frac{1}{\Delta\theta} \delta_\theta \left[cos\theta \, y_i^*(v_i^*, \Delta\tau; \delta p_i^\lambda) \right] \right\} \tag{3.31}$$

$$(for\, i = 1, ..., m),$$

where $[x_i^*, y_i^*]$ are the background air mass fluxes, which are then used as input to Eq. 24 for transport of the potential temperature Θ:

$$\Theta^{n+\frac{i}{m}} = \frac{1}{\delta p^{n+\frac{i}{m}}} \left[\delta p^{n+\frac{i-1}{m}} \Theta^{n+\frac{i-1}{m}} + F(x_i^*, \Delta\tau; \Theta_i^\theta) + G(y_i^*, \Delta\tau, \Theta_i^\lambda) \right]. \tag{3.32}$$

The discretized momentum equations for the shallow water system (*cf*, Eq. 16 and Eq. 17 in LR97) are modified for the pressure gradient terms as follows:

$$u^{n+\frac{i}{m}} = u^{n+\frac{i-1}{m}} + \Delta\tau \left[y_i^* \left(v_i^*, \Delta\tau; \Omega^\lambda \right) - \frac{1}{A\Delta\lambda cos\theta} \delta_\lambda (\kappa^* - \nu D^*) + \widehat{P_\lambda} \right], \tag{3.33}$$

$$v^{n+\frac{i}{m}} = v^{n+\frac{i-1}{m}} - \Delta\tau \left[x_i^* \left(u_i^*, \Delta\tau; \Omega^\theta \right) + \frac{1}{A\Delta\theta} \delta_\theta (\kappa^* - \nu D^*) - \widehat{P_\theta} \right], \tag{3.34}$$

where κ^* is the upwind-biased "kinetic energy" (as defined by Eq. 18 in LR97), and D^*, the horizontal divergence on the D-grid, is discretized as follows:

$$D^* = \frac{1}{A cos\theta} \left[\frac{1}{\Delta\lambda} \delta_\lambda u^{n+\frac{i-1}{m}} + \frac{1}{\Delta\theta} \delta_\theta \left(v^{n+\frac{i-1}{m}} cos\theta \right) \right].$$

The finite-volume mean pressure-gradient terms in (3.33) and (3.34) are computed as follows:

$$\widehat{P_\lambda} = \frac{\oint_{\Pi \rightleftharpoons \lambda} \phi d\Pi}{A cos\theta \oint_{\Pi \rightleftharpoons \lambda} \Pi d\lambda}, \tag{3.35}$$

$$\widehat{P_\theta} = \frac{\oint_{\Pi \rightleftharpoons \theta} \phi d\Pi}{A \oint_{\Pi \rightleftharpoons \theta} \Pi d\theta}, \tag{3.36}$$

where $\Pi = p^\kappa$ ($\kappa = R/C_p$), and the symbols "$\Pi \rightleftharpoons \lambda$" and "$\Pi \rightleftharpoons \theta$" indicate that the contour integrations are to be carried out, using the finite-volume algorithm described in L97, in the (Π, λ) and (Π, θ) space, respectively.

To complete one time step, equations (3.31-3.34), together with their counterparts on the C-grid are cycled m times using the fractional time step $\Delta\tau$, which are followed by the tracer transport using (3.26) with the large-time-step Δt.

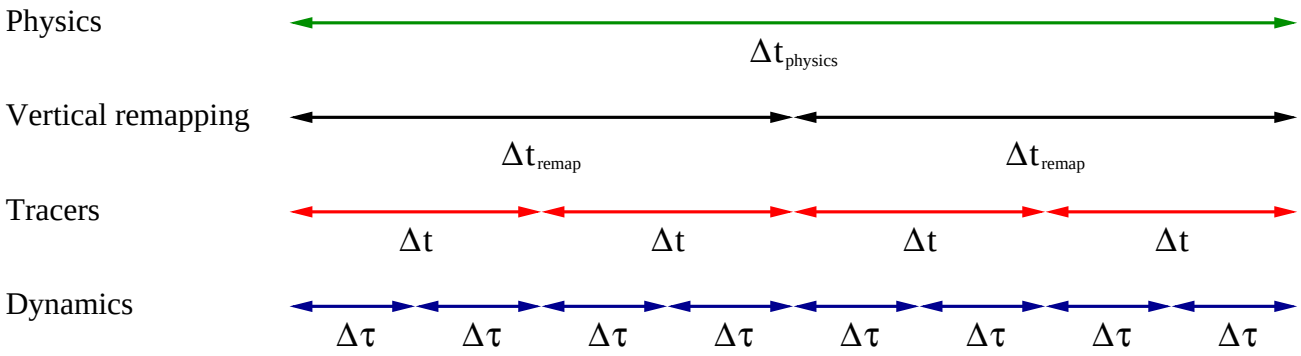

Figure 3.1: A graphical illustration of the different levels of sub-cycling in CAM5.

Mass fluxes (x^*, y^*) and the winds (u^*, v^*) on the C-grid are accumulated for the large-time-step transport of tracer species (including water vapor) q as

$$q^{n+1} = \frac{1}{\delta p^{n+1}} \left[q^n \delta p^n + F(X^*, \Delta t, q^\theta) + G(Y^*, \Delta t, q^\lambda) \right], \tag{3.37}$$

where the time-accumulated mass fluxes (X^*, Y^*) are computed as

$$X^* = \sum_{i=1}^{m} x_i^*(u_i^*,\ \Delta\tau,\ \delta p_i^\theta), \tag{3.38}$$

$$Y^* = \sum_{i=1}^{m} y_i^*(v_i^*,\ \Delta\tau,\ \delta p_i^\lambda). \tag{3.39}$$

The time-averaged winds (U^*, V^*), defined as follows, are to be used as input for the computations of q^λ and q^θ :

$$U^* = \frac{1}{m} \sum_{i=1}^{m} u_i^*, \tag{3.40}$$

$$V^* = \frac{1}{m} \sum_{i=1}^{m} v_i^*. \tag{3.41}$$

The use of the time accumulated mass fluxes and the time-averaged winds for the large-time-step tracer transport in the manner described above ensures the conservation of the tracer mass and maintains the highest degree of consistency possible given the time split integration procedure. A graphical illustration of the different levels of sub-cycling in CAM5 is given on Figure 3.1.

The algorithm described here can be readily applied to a regional model if appropriate boundary conditions are supplied. There is formally no Courant number related time step restriction associated with the transport processes. There is, however, a stability condition imposed by the gravity-wave processes. For application on the whole sphere, it is computationally advantageous to apply a polar filter to allow a dramatic increase of the size of the small time step $\Delta\tau$. The effect of the polar filter is to stabilize the short-in-wavelength (and high-in-frequency) gravity

waves that are being unnecessarily and unidirectionally resolved at very high latitudes in the zonal direction. To minimize the impact to meteorologically significant larger scale waves, the polar filter is highly scale selective and is applied only to the diagnostic variables on the auxiliary C-grid and the tendency terms in the D-grid momentum equations. No polar filter is applied directly to any of the prognostic variables.

The design of the polar filter follows closely that of Suarez and Takacs [1995] for the C-grid Arakawa type dynamical core (*e.g.*, Arakawa and Lamb [1981]). For the CAM 5.0 the fast-fourier transform component of the polar filtering has replaced the algebraic form at all filtering latitudes. Because our prognostic variables are computed on the D-grid and the fact that the FFSL transport scheme is stable for Courant number greater than one, in realistic test cases the maximum size of the time step is about two to three times larger than a model based on Arakawa and Lamb's C-grid differencing scheme. It is possible to avoid the use of the polar filter if, for example, the "Cubed grid" is chosen, instead of the current latitude-longitude grid. rewrite of the rest of the model codes including physics parameterizations, the land model, and most of the post processing packages.

The size of the small time step for the Lagrangian dynamics is only a function of the horizontal resolution. Applying the polar filter, for the 2-degree horizontal resolution, a small-time-step size of 450 seconds can be used for the Lagrangian dynamics. From the large-time-step transport perspective, the small-time-step integration of the 2D Lagrangian dynamics can be regarded as a very accurate iterative solver, with m iterations, for computing the time mean winds and the mass fluxes, analogous in functionality to a semi-implicit algorithm's elliptic solver (*e.g.*, Ringler et al. [2000]). Besides accuracy, the merit of an "explicit" versus "semi-implicit" algorithm ultimately depends on the computational efficiency of each approach. In light of the advantage of the explicit algorithm in parallelization, we do not regard the explicit algorithm for the Lagrangian dynamics as an impedance to computational efficiency, particularly on modern parallel computing platforms.

3.1.5 Optional diffusion operators in CAM5

The 'CD'-grid discretization method used in the CAM finite-volume dynamical core provides explicit control over the rotational modes at the grid scale, due to monotonicity constraint in the PPM-based advection, but there is no explicit control over the divergent modes at the grid scale [see, e.g., Skamarock, 2010]. Therefore divergence damping terms appear on the right-hand side of the momentum equations ((3.28) and (3.29)):

$$-\frac{1}{A cos\theta}\left[\frac{\partial}{\partial\lambda}\left(-\nu D\right)\right] \tag{3.42}$$

and

$$-\frac{1}{A}\left[\frac{\partial}{\partial\theta}\left(-\nu D\right)\right], \tag{3.43}$$

respectively, where the strength of the divergence damping is controlled by the coefficient ν given by

$$\nu = \frac{\nu_2\left(A^2\Delta\lambda\Delta\theta\right)}{\Delta t}, \tag{3.44}$$

where $\nu_2 = 1/128$ throughout the atmosphere except in the top model levels where it monotonically increases to approximately $4/128$ at the top of the atmosphere. The divergence damping described above is referred to as 'second-order' divergence damping as it effectively damps divergence with a ∇^2 operator.

In CAM5 optional 'fourth-order' divergence damping has been implemented where the divergence is effectively damped with a ∇^4-operator which is usually more scale selective than 'second-order' damping operators. For 'fourth-order' divergence damping the terms

$$-\frac{1}{Acos\theta}\left[\frac{\partial}{\partial\lambda}\left(-\nu_4\nabla^2 D\right)\right] \tag{3.45}$$

and

$$-\frac{1}{A}\left[\frac{\partial}{\partial\theta}\left(-\nu_4\nabla^2 D\right)\right], \tag{3.46}$$

are added to the right-hand side of (3.28) and (3.29), respectively. The horizontal Laplacian ∇^2-operator in spherical coordinates for a scalar ψ is given by

$$\nabla^2\psi = \frac{1}{A^2\cos^2\theta}\frac{\partial^2\psi}{\partial^2\lambda} + \frac{1}{A^2\cos\theta}\frac{\partial}{\partial\theta}\left(\cos\theta\frac{\partial\psi}{\partial\theta}\right). \tag{3.47}$$

The fourth-order divergence damping coefficient is given by

$$\nu_4 = 0.01\,\left(A^2\cos(\theta)\Delta\lambda\Delta\theta\right)^2/\Delta t. \tag{3.48}$$

Since divergence damping is added explicitly to the equations of motion it is unstable if the time-step is too large or the damping coefficients (ν or ν_4) are too large. To stabilize the fourth-order divergence damping the winds used to compute the divergence are filtered using the same FFT filtering which is applied to stabilize the gravity waves.

To control potentially excessive polar night jets in high-resolution configurations of CAM, Laplacian damping of the wind components has been added as an option in CAM5. That is, the terms

$$\nu_{del2}\nabla^2 u \tag{3.49}$$

and

$$\nu_{del2}\nabla^2 v \tag{3.50}$$

are added to the right-hand side of the momentum equations (3.28) and (3.29), respectively. The damping coefficient ν_{del2} is zero throughout the atmosphere except in the top layers where it increases monotonically and smoothly from zero to approximately four times a user-specified damping coefficient at the top of the atmosphere (the user-specified damping coefficient is typically on the order of 2.5×10^5 m^{2}sec^{-1}).

3.1.6 A mass, momentum, and total energy conserving mapping algorithm

The Lagrangian surfaces that bound the finite-volume will eventually deform, particularly in the presence of persistent diabatic heating/cooling, in a time scale of a few hours to a day

depending on the strength of the heating and cooling, to a degree that it will negatively impact the accuracy of the horizontal-to-Lagrangian-coordinate transport and the computation of the pressure gradient forces. Therefore, a key to the success of the Lagrangian control-volume discretization is an accurate and conservative algorithm for mapping the deformed Lagrangian coordinate back to a fixed reference Eulerian coordinate.

There are some degrees of freedom in the design of the vertical mapping algorithm. To ensure conservation, our current (and recommended) mapping algorithm is based on the reconstruction of the "mass" (pressure thickness δp), zonal and meridional "winds", "tracer mixing ratios", and "total energy" (volume integrated sum of the internal, potential, and kinetic energy), using the monotonic Piecewise Parabolic sub-grid distributions with the hydrostatic pressure (as defined by (3.30)) as the mapping coordinate. We outline the mapping procedure as follows.

Step 1: Define a suitable Eulerian reference coordinate as a target coordinate. The mass in each layer (δp) is then distributed vertically according to the chosen Eulerian coordinate. The surface pressure typically plays an "anchoring" role in defining the terrain following Eulerian vertical coordinate. The hybrid $\eta -$ *coordinate* used in the NCAR CCM3 [Kiehl et al., 1996] is adopted in the current model setup.

Step 2: Construct the piece-wise continuous vertical subgrid profiles of tracer mixing ratios (q), zonal and meridional winds (u and v), and total energy (Γ) in the Lagrangian control-volume coordinate, or the source coordinate. The total energy Γ is computed as the sum of the finite-volume integrated geopotential ϕ, internal energy ($C_v T_v$), and the kinetic energy (K) as follows:

$$\Gamma = \frac{1}{\delta p} \int \left[C_v T_v + \phi + \frac{1}{2} \left(u^2 + v^2 \right) \right] dp. \tag{3.51}$$

Applying integration by parts and the ideal gas law, the above integral can be rewritten as

$$\begin{aligned} \Gamma &= \frac{1}{\delta p} \left\{ \int \left[C_p T_v + \frac{1}{2} \left(u^2 + v^2 \right) \right] dp + \int d \left(p \phi \right) \right\} \\ &= C_p \overline{T_v} + \frac{1}{\delta p} \delta \left(p \phi \right) + K, \end{aligned} \tag{3.52}$$

where $\overline{T_v}$ is the layer mean virtual temperature, K is the layer mean kinetic energy, p is the pressure at layer edges, and C_v and C_p are the specific heat of the air at constant volume and at constant pressure, respectively. The total energy in each grid cell is calculated as

$$\begin{aligned} \Gamma_{i,j,k} &= C_p T_{v_{i,j,k}} + \frac{1}{\delta p_{i,j,k}} \left(p_{i,j,k+\frac{1}{2}} \phi_{i,j,k+\frac{1}{2}} - p_{i,j,k-\frac{1}{2}} \phi_{i,j,k-\frac{1}{2}} \right) + \\ & \frac{1}{2} \left(\frac{u^2_{i,j-\frac{1}{2},k} + u^2_{i,j+\frac{1}{2},k}}{2} + \frac{v^2_{i-\frac{1}{2},j,k} + v^2_{i+\frac{1}{2},j,k}}{2} \right) \end{aligned}$$

The method employed to create subgrid profiles is set by the flag *te_method*. For *te_method* = 0 (default), the Piece-wise Parabolic Method (PPM,

Colella and Woodward [1984]) over a pressure coordinate is used and for $te_method = 1$ a cublic spline over a logarithmic pressure coordinate is used.

Step 3: Layer mean values of q, $(u,\ v)$, and Γ in the Eulerian coordinate system are obtained by integrating analytically the sub-grid distributions, in the vertical direction, from model top to the surface, layer by layer. Since the hydrostatic pressure is chosen as the mapping coordinate, tracer mass, momentum, and total energy are locally and globally conserved. In mapping a variable from the source coordinate to the target coordinate, different limiter constraints may be used and they are controlled by two flags, iv and $kord$. For winds on D-grid, iv should be set to -1. For tracers, iv should be set to 0. For all others, $iv = 1$. $kord$ directly controls which limiter constraint is used. For $kord \geq 7$, Huynh's 2nd constraint is used. If $kord = 7$, the original quasi-monotonic constraint is used. If $kord > 7$, a full monotonic constraint is used. If $kord$ is less than 7, the variable, lmt, is determined by the following:

$$\begin{aligned} & lmt &=& \ kord - 3, \\ & lmt &=& \ \max(0, lmt), \\ \text{if}(iv = 0) \quad & lmt &=& \ \min(2, lmt). \end{aligned}$$

If $lmt = 0$, a standard PPM constraint is used. If $lmt = 1$, an improved full monotonicity constraint is used. If $lmt = 2$, a positive definite constraint is used. If $lmt = 3$, the algorithm will do nothing.

Step 4: Retrieve virtual temperature in the Eulerian (target) coordinate. Start by computing kinetic energy in the Eulerian coordinate system for each layer. Then substitute kinetic energy and the hydrostatic relationship into (3.52). The layer mean temperature $\overline{T_{vk}}$ for layer k in the Eulerian coordinate is then retrieved from the reconstructed total energy (done in Step 3) by a fully explicit integration procedure starting from the surface up to the model top as follows:

$$\overline{T_{vk}} = \frac{\Gamma_k - K_k - \phi_{k+\frac{1}{2}}}{C_p \left[1 - \kappa\, p_{k-\frac{1}{2}} \frac{ln\, p_{k+\frac{1}{2}} - ln\, p_{k-\frac{1}{2}}}{p_{k+\frac{1}{2}} - p_{k-\frac{1}{2}}}\right]}, \tag{3.53}$$

where $\kappa = R_d/C_p$ and R_d is the gas constant for dry air.

To convert the potential virtual temperature Θ_v to the layer mean temperature the conversion factor is obtained by equating the following two equivalent forms of the hydrostatic relation for Θ and $\overline{T_v}$:

$$\delta\phi = -C_p \Theta_v\, \delta\Pi, \tag{3.54}$$

$$\delta\phi = -R_d \overline{T_v}\, \delta ln\, p, \tag{3.55}$$

where $\Pi = p^\kappa$. The conversion formula between layer mean temperature and layer mean potential temperature is obtained as follows:

$$\Theta_v = \kappa \frac{\delta lnp}{\delta\Pi} \overline{T_v}. \tag{3.56}$$

The physical implication of retrieving the layer mean temperature from the total energy as described in Step 3 is that the dissipated kinetic energy, if any, is locally converted into internal energy via the vertically sub-grid mixing (dissipation) processes. Due to the monotonicity preserving nature of the sub-grid reconstruction the column-integrated kinetic energy inevitably decreases (dissipates), which leads to local frictional heating. The frictional heating is a physical process that maintains the conservation of the total energy in a closed system.

As viewed by an observer riding on the Lagrangian surfaces, the mapping procedure essentially performs the physical function of the relative-to-the-Eulerian-coordinate vertical transport, by vertically redistributing (air and tracer) mass, momentum, and total energy from the Lagrangian control-volume back to the Eulerian framework.

As described in section 3.1.4, the model time integration cycle consists of m small time steps for the 2D Lagrangian dynamics and one large time step for tracer transport. The mapping time step can be much larger than that used for the large-time-step tracer transport. In tests using the Held-Suarez forcing [Held and Suarez, 1994], a three-hour mapping time interval is found to be adequate. In the full model integration, one may choose the same time step used for the physical parameterizations so as to ensure the input state variables to physical parameterizations are in the usual "Eulerian" vertical coordinate. In CAM5, vertical remapping takes place at each physics time step.

3.1.7 A geopotential conserving mapping algorithm

An alternative vertical mapping approach is available in CAM5. Instead of retrieving temperature by remapped total energy in the Eulerian coordinate, the alternative approach maps temperature directly from the Lagrangian coordinate to the Eulerian coordinate. Since geopotential is defined as

$$\delta\phi = -C_p\Theta_v\delta\Pi = -R_dT_v\delta ln\, p,$$

mapping Θ_v over Π or T_v over $ln\, p$ preserves the geopotential at the model lid. This approach prevents the mapping procedure from generating spurious pressure gradient forces at the model lid. Unlike the energy-conserving algorithm which could produce substantial temperature fluctuations at the model lid, the geopotential conserving approach guarantees a smooth (potential) temperature profile. However, the geopotential conserving does not conserve total energy in the remapping procedure. This may be resolved by a global energy fixer already implemented in the model (see section 3.1.10).

3.1.8 Adjustment of pressure to include change in mass of water vapor

The physics parameterizations operate on a model state provided by the dynamics, and are allowed to update specific humidity. However, the surface pressure remains fixed throughout the physics updates, and since there is an explicit relationship between the surface pressure and the air mass within each layer, the total air mass must remain fixed as well throughout the physics updates. If no further correction were made, this would imply that the dry air mass changed if the water vapor mass changed in the physics updates. Therefore the pressure field is

changed to include the change in water vapor mass due to the physics updates. We impose the restrictions that dry air mass and water mass are conserved as follows:

The total pressure p is

$$p = d + e. \tag{3.57}$$

with dry pressure d, water vapor pressure e. The specific humidity is

$$q = \frac{e}{p} = \frac{e}{d+e}, \qquad d = (1-q)p. \tag{3.58}$$

We define a layer thickness as $\delta^k p \equiv p^{k+1/2} - p^{k-1/2}$, so

$$\delta^k d = (1 - q^k)\delta^k p. \tag{3.59}$$

We are concerned about 3 time levels: q_n is input to physics, q_{n*} is output from physics, q_{n+1} is the adjusted value for dynamics.

Dry mass is the same at n and $n+1$ but not at $n*$. To conserve dry mass, we require that

$$\delta^k d_n = \delta^k d_{n+1} \tag{3.60}$$

or

$$(1 - q_n^k)\delta^k p_n = (1 - q_{n+1}^k)\delta^k p_{n+1}. \tag{3.61}$$

Water mass is the same at $n*$ and $n+1$, but not at n. To conserve water mass, we require that

$$q_{n*}^k \delta^k p_n = q_{n+1}^k \delta^k p_{n+1}. \tag{3.62}$$

Substituting (3.62) into (3.61),

$$(1 - q_n^k)\delta^k p_n = \delta^k p_{n+1} - q_{n*}^k \delta^k p_n \tag{3.63}$$

$$\delta^k p_{n+1} = (1 - q_n^k + q_{n*}^k)\delta^k p_n \tag{3.64}$$

which yields a modified specific humidity for the dynamics:

$$q_{n+1}^k = q_n^k \frac{\delta^k p_n}{\delta^k p_{n+1}} = \frac{q_{n*}^k}{1 - q_n^k + q_{n*}^k}. \tag{3.65}$$

We note that this correction as implemented makes a small change to the water vapor as well. The pressure correction could be formulated to leave the water vapor unchanged.

3.1.9 Negative Tracer Fixer

In the Finite Volume dynamical core, neither the monotonic transport nor the conservative vertical remapping guarantee that tracers will remain positive definite. Thus the Finite Volume dynamical core includes a negative tracer fixer applied before the parameterizations are calculated. For negative mixing ratios produced by horizontal transport, the model will attempt to borrow mass from the east and west neighboring cells. In practice, most negative values are introduced by the vertical remapping which does not guarantee positive definiteness in the first and last layer of the vertical column.

A minimum value q_{min} is defined for each tracer. If the tracer falls below that minimum value, it is set to that minimum value. If there is enough mass of the tracer in the layer immediately above, tracer mass is removed from that layer to conserve the total mass in the column. If there is not enough mass in the layer immediately above, no compensation is applied, violating conservation. Usually such computational sources are very small.

The amount of tracer needed from the layer above to bring q_k up to q_{min} is

$$q_{fill} = (q_{min} - q_k) \frac{\Delta p_k}{\Delta p_{k-1}} \tag{3.66}$$

where k is the vertical index, increasing downward. After the filling

$$q_{k_{FILLED}} = q_{min} \tag{3.67}$$

$$q_{k-1_{FILLED}} = q_{k-1} - q_{fill} \tag{3.68}$$

Currently $q_{min} = 1.0 \times 10^{-12}$ for water vapor, $q_{min} = 0.0$ for CLDLIQ, CLDICE, NUMLIQ and NUMICE, and $q_{min} = 1.0 \times 10^{-36}$ for the remaining constituents.

3.1.10 Global Energy Fixer

The finite-volume dynamical core as implemented in CAM and described here conserves the dry air and all other tracer mass exactly without a "mass fixer". The vertical Lagrangian discretization and the associated remapping conserves the total energy exactly. The only remaining issue regarding conservation of the total energy is the horizontal discretization and the use of the "diffusive" transport scheme with monotonicity constraint. To compensate for the loss of total energy due to horizontal discretization, we apply a global fixer to add the loss in kinetic energy due to "diffusion" back to the thermodynamic equation so that the total energy is conserved. The loss in total energy (in flux unit) is found to be around 2 (W/m^2) with the 2 degrees resolution.

The energy fixer is applied following the negative tracer fixer. The fixer is applied on the unstaggered physics grid rather than on the staggered dynamics grid. The energies on these two grids are difficult to relate because of the nonlinear terms in the energy definition and the interpolation of the state variables between the grids. The energy is calculated in the parameterization suite before the state is passed to the finite volume core as described in the beginning of Chapter 4. The fixer is applied just before the parameterizations are calculated. The fixer is a simplification of the fixer in the Eulerian dynamical core described in section 3.3.20.

Let minus sign superscript $(\ )^-$ denote the values at the beginning of the dynamics time step, i.e. after the parameterizations are applied, let a plus sign superscript $(\ )^+$ denote the values after fixer is applied, and let a hat $\hat{(\ )}^+$ denote the provisional value before adjustment. The total energy over the entire computational domain after the fixer is

$$E^+ = \int_{p_t}^{p_s} \int_0^{2\pi} \int_{-\frac{\pi}{2}}^{\frac{\pi}{2}} \frac{1}{g} \left[C_p T^+ + \Phi + \frac{1}{2}\left(u^{+2} + v^{+2}\right) + \left(L_v + L_i\right) q_v^+ + L_i q_\ell^+ \right] A^2 \cos\theta \, d\theta \, d\lambda \, dp, \tag{3.69}$$

where L_v is the latent heat of vaporation, L_i is the latent heat of fusion, q_v is water vapor mixing ratio, and q_ℓ is cloud water mixing ratio. E^+ should equal the energy at the beginning of the dynamics time step

$$E^- = \int_{p_t}^{p_s} \int_0^{2\pi} \int_{-\frac{\pi}{2}}^{\frac{\pi}{2}} \frac{1}{g} \left[c_p T^- + \Phi + \frac{1}{2}\left(u^{-2} + v^{-2}\right) + \left(L_v + L_i\right) q_v^- + L_i q_\ell^- \right] A^2 \cos\theta \, d\theta \, d\lambda \, dp. \tag{3.70}$$

Let $\hat{E}^+$ denote the energy of the provisional state provided by the dynamical core before the adjustment.

$$\hat{E}^+ = \int_{p_t}^{p_s} \int_0^{2\pi} \int_{-\frac{\pi}{2}}^{\frac{\pi}{2}} \frac{1}{g} \left[c_p \hat{T}^+ + \hat{\Phi}^+ + \frac{1}{2}\left(\hat{u}^{+^2} + \hat{v}^{+^2}\right) + \left(L_v + L_i\right) \hat{q}_v^+ + L_i \hat{q}_\ell^+ \right] A^2 \cos\theta \, d\theta \, d\lambda \, dp. \tag{3.71}$$

Thus, the total energy added into the system by the dynamical core is $\hat{E}^+ - E^-$. The energy fixer then changes dry static energy ($s = C_p T + \Phi$) by a constant amount over each grid cell to conserve total energy in the entire computational domain. The dry static energy added to each grid cell may be expressed as

$$\Delta s = \frac{E^- - \hat{E}^+}{\int_{p_t}^{p_s} \int_0^{2\pi} \int_{-\frac{\pi}{2}}^{\frac{\pi}{2}} A^2 \cos\theta \, d\theta \, d\lambda \, \frac{dp}{g}}. \tag{3.72}$$

Therefore,

$$s^+ = \hat{s}^+ + \Delta s, \tag{3.73}$$

or

$$C_p T^+ + \Phi^+ = \hat{s}^+ + \Delta s. \tag{3.74}$$

This will ensure $E^+ = E^-$.

By hydrostatic approximation, the geopotential equation is

$$d\Phi = -R_d T_v d\, lnp, \tag{3.75}$$

and for any arbitrary point between $p_{k+\frac{1}{2}}$ and $p_{k-\frac{1}{2}}$ the geopotential may be written as

$$\int_{\Phi_{k+\frac{1}{2}}}^{\Phi} d\Phi' = -R_d T_v \int_{p_{k+\frac{1}{2}}}^{p} d\, lnp', \tag{3.76}$$

$$\Phi = \Phi_{k+\frac{1}{2}} + R_d T_v \left(lnp_{k+\frac{1}{2}} - lnp \right). \tag{3.77}$$

The geopotential at the mid point of a model layer between $p_{k+\frac{1}{2}}$ and $p_{k-\frac{1}{2}}$, or the layer mean,

is

$$\begin{aligned}
\Phi_k &= \frac{\int_{p_k-\frac{1}{2}}^{p_k+\frac{1}{2}} \Phi \, dp}{\int_{p_k-\frac{1}{2}}^{p_k+\frac{1}{2}} dp} \\
&= \frac{\int_{p_k-\frac{1}{2}}^{p_k+\frac{1}{2}} \left[\Phi_{k+\frac{1}{2}} + R_d T_v \left(lnp_{k+\frac{1}{2}} - lnp\right)\right] dp}{\int_{p_k-\frac{1}{2}}^{p_k+\frac{1}{2}} dp} \\
&= \Phi_{k+\frac{1}{2}} + R_d T_v lnp_{k+\frac{1}{2}} - \frac{\int_{p_k-\frac{1}{2}}^{p_k+\frac{1}{2}} lnp \, dp}{p_{k+\frac{1}{2}} - p_{k-\frac{1}{2}}} \\
&= \Phi_{k+\frac{1}{2}} + R_d T_v \left(1 - p_{k-\frac{1}{2}} \frac{lnp_{k+\frac{1}{2}} - lnp_{k-\frac{1}{2}}}{p_{k+\frac{1}{2}} - p_{k-\frac{1}{2}}}\right)
\end{aligned} \tag{3.78}$$

For layer k, the energy fixer will solve the following equation based on (3.74),

$$C_p T_k^+ + \Phi_{k+\frac{1}{2}}^+ + R_d T_k^+ \left(1 + \epsilon q_{v_k}^+\right) \left(1 - p_{k-\frac{1}{2}}^+ \frac{lnp_{k+\frac{1}{2}}^+ - lnp_{k-\frac{1}{2}}^+}{p_{k+\frac{1}{2}}^+ - p_{k-\frac{1}{2}}^+}\right) = \hat{s}^+ + \Delta s. \tag{3.79}$$

Since the energy fixer will not alter the water vapor mixing ratio and the pressure field,

$$q_v^+ = \hat{q}_v^+, \tag{3.80}$$

$$p^+ = \hat{p}^+. \tag{3.81}$$

Therefore,

$$T_k^+ = \frac{(\hat{s}^+ + \Delta s) - \Phi_{k+\frac{1}{2}}^+}{C_p + R_d \left(1 + \epsilon \hat{q}_{v_k}^+\right) \left(1 - \hat{p}_{k-\frac{1}{2}}^+ \frac{ln\hat{p}_{k+\frac{1}{2}}^+ - ln\hat{p}_{k-\frac{1}{2}}^+}{\hat{p}_{k+\frac{1}{2}}^+ - \hat{p}_{k-\frac{1}{2}}^+}\right)}. \tag{3.82}$$

The energy fixer starts from the Earth's surface and works its way up to the model top in adjusting the temperature field. At the surface layer, $\Phi_{k+\frac{1}{2}}^+ = \Phi_s$. After the temperature is adjusted in a grid cell, the geopotential at the upper interface of the cell is updated which is needed for the temperature adjustment in the grid cell above.

3.1.11 Further discussion

There are still aspects of the numerical formulation in the finite volume dynamical core that can be further improved. For example, the choice of the horizontal grid, the computational efficiency of the split-explicit time marching scheme, the choice of the various monotonicity constraints, and how the conservation of total energy is achieved.

The impact of the non-linear diffusion associated with the monotonicity constraint is difficult to assess. All discrete schemes must address the problem of subgrid-scale mixing. The finite-volume algorithm contains a non-linear diffusion that mixes strongly when monotonicity principles are locally violated. However, the effect of nonlinear diffusion due to the imposed

monotonicity constraint diminishes quickly as the resolution matches better to the spatial structure of the flow. In other numerical schemes, however, an explicit (and tunable) linear diffusion is often added to the equations to provide the subgrid-scale mixing as well as to smooth and/or stabilize the time marching.

3.1.12 Specified Dynamics Option

In CAM4 the capability included to perform simulations using specified dynamics, where offline meteorological fields are nudged to the online calculated meteorology. This procedure was originally used in the Model of Atmospheric Transport and Chemistry (MATCH) (Rasch et al., 1997). In this procedure the horizontal wind components, air temperature, surface temperature, surface pressure, sensible and latent heat flux, and wind stress are read into the model simulation from the input meteorological dataset. The nudging coefficient can be chosen to be 1 (for 100% nudging) or smaller. The desired percentage of the offline meteorology and the remaining percent from the internally calcuated meteorology is used every timestep to prescribe the meteorological parameters. In addition, the model solves the model internal advection equations for the mass flux every sub-step. In this way, some inconsistencies between the inserted and model-computed velocity and mass fields subsequently used for tracer transport are dampended. The mass flux at each sub-step is accumulated to produce the net mass flux over the entire time step. A graphical explanation of the sub-cycling is given in Lauritzen et al. (2011).

A nudging coefficent of 100 can be used to allow for more precise comparisons between measurements of atmospheric composition and model output for example using CAM-Chem (Lamarque et al., 2012). A reduced nudging coefficent is used for instant for WACCM simulations, if more of the internal transport parameters needs to be contained, while the meteorology is still close to the analysied fields (e.g., Brakebusch et al., 2012).

Currently, we recommend for input offline meteorology interpolated from 0.5x0.6 degree fields of the NASA Goddard Global Modeling and Assimilation Office (GMAO) GEOS-5 and Modern Era Retrospective-Analysis For Research And Applications (MERRA) generated meteorology. These fields are available on the Earth System Grid (http://www.earthsystemgrid.org/home.htm) for the CAM resolution of 1.9°x2.5°. These files were generated from the original resolution by using a conservative regridding procedure based on the same 1-D operators as used in the transport scheme of the finite-volume dynamical core used in GEOS-5 and CAM (S.-J. Lin, personal communication, 2009). Note that because of a difference in the sign convention of the surface wind stress (TAUX and TAUY) between CESM and GEOS5/MERRA, these fields in the interpolated datasets have been reversed from the original files supplied by GMAO. In addition, it is important for users to recognize the importance of specifying the correct surface geopotential height (PHIS) to ensure consistency with the input dynamical fields, which is important to prevent unrealistic vertical mixing.

3.1.13 Further discussion

3.2 Spectral Element Dynamical Core

The CAM includes an optional dynamical core from HOMME, NCAR's High-Order Method Modeling Environment [Dennis et al., 2005]. The stand-alone HOMME is used for re-

search in several different types of dynamical cores. The dynamical core incorporated into CAM4 uses HOMME's continuous Galerkin spectral finite element method [Taylor et al., 1997; Fournier et al., 2004; Thomas and Loft, 2005; Wang et al., 2007; Taylor and Fournier, 2010], here abbreviated to the spectral element method (SEM). This method is designed for fully unstructured quadrilateral meshes. The current configurations in the CAM are based on the cubed-sphere grid. The main motivation for the inclusion of HOMME is to improve the scalability of the CAM by introducing quasi-uniform grids which require no polar filters [Taylor et al., 2008]. HOMME is also the first dynamical core in the CAM which locally conserves energy in addition to mass and two-dimensional potential vorticity [Taylor, 2010].

HOMME represents a large change in the horizontal grid as compared to the other dynamical cores in CAM. Almost all other aspects of HOMME are based on a combination of well-tested approaches from the Eulerian and FV dynamical cores. For tracer advection, HOMME is modeled as closely as possible on the FV core. It uses the same conservation form of the transport equation and the same vertically Lagrangian discretization [Lin, 2004]. The HOMME dynamics are modeled as closely as possible on Eulerian core. They share the same vertical coordinate, vertical discretization, hyper-viscosity based horizontal diffusion, top-of-model dissipation, and solve the same moist hydrostatic equations. The main differences are that HOMME advects the surface pressure instead of its logarithm (in order to conserve mass and energy), and HOMME uses the vector-invariant form of the momentum equation instead of the vorticity-divergence formulation. Several dry dynamical cores including HOMME are evaluated in Lauritzen et al. [2010] using a grid-rotated version of the baroclinic instability test case [Jablonowski and Williamson, 2006].

The timestepping in HOMME is a form of dynamics/tracer/physics subcycling, achieved through the use of multi-stage 2nd order accurate Runge-Kutta methods. The tracers and dynamics use the same timestep which is controlled by the maximum anticipated wind speed, but the dynamics uses more stages than the tracers in order to maintain stability in the presence of gravity waves. The forcing is applied using a time-split approach. The optimal forcing strategy in HOMME has not yet been determined, so HOMME supports several options. The first option is modeled after the FV dynamical core and the forcing is applied as an adjustment at each physics timestep. The second option is to convert all forcings into tendencies which are applied at the end of each dynamics/tracer timestep. If the physics timestep is larger than the tracer timestep, then the tendencies are held fixed and only updated at each physics timestep. Finally, a hybrid approach can be used where the tracer tendencies are applied as in the first option and the dynamics tendencies are applied as in the second option.

3.2.1 Continuum Formulation of the Equations

HOMME uses a conventional vector-invariant form of the moist primitive equations. For the vertical discretization it uses the hybrid η pressure vertical coordinate system modeled after 3.3.1 The formulation here differs only in that surface pressure is used as a prognostic variable as opposed to its logarithm.

In the η-coordinate system, the pressure is given by

$$p(\eta) = A(\eta)p_0 + B(\eta)p_s.$$

The hydrostatic approximation $\partial p/\partial z = -g\rho$ is used to replace the mass density ρ by an η-coordinate pseudo-density $\partial p/\partial \eta$. The material derivative in η-coordinates can be written (e.g.

Satoh [2004], Sec.3.3),

$$\frac{DX}{Dt} = \frac{\partial X}{\partial t} + \vec{u} \cdot \nabla X + \dot{\eta}\frac{\partial X}{\partial \eta}$$

where the $\nabla()$ operator (as well as $\nabla \cdot ()$ and $\nabla \times ()$ below) is the two-dimensional gradient on constant η-surfaces, $\partial/\partial\eta$ is the vertical derivative, $\dot{\eta} = D\eta/Dt$ is a vertical flow velocity and $\vec{u}$ is the horizontal velocity component (tangent to constant z-surfaces, not η-surfaces).

The η-coordinate atmospheric primitive equations, neglecting dissipation and forcing terms can then be written as

$$\frac{\partial \vec{u}}{\partial t} + (\zeta + f)\,\hat{k}\times\vec{u} + \nabla\left(\frac{1}{2}\vec{u}^2 + \Phi\right) + \dot{\eta}\frac{\partial \vec{u}}{\partial \eta} + \frac{RT_v}{p}\nabla p = 0 \tag{3.83}$$

$$\frac{\partial T}{\partial t} + \vec{u} \cdot \nabla T + \dot{\eta}\frac{\partial T}{\partial \eta} - \frac{RT_v}{c_p^* p}\omega = 0 \tag{3.84}$$

$$\frac{\partial}{\partial t}\left(\frac{\partial p}{\partial \eta}\right) + \nabla \cdot \left(\frac{\partial p}{\partial \eta}\vec{u}\right) + \frac{\partial}{\partial \eta}\left(\dot{\eta}\frac{\partial p}{\partial \eta}\right) = 0 \tag{3.85}$$

$$\frac{\partial}{\partial t}\left(\frac{\partial p}{\partial \eta}q\right) + \nabla \cdot \left(\frac{\partial p}{\partial \eta}q\vec{u}\right) + \frac{\partial}{\partial \eta}\left(\dot{\eta}\frac{\partial p}{\partial \eta}q\right) = 0. \tag{3.86}$$

These are prognostic equations for $\vec{u}$, the temperature T, density $\frac{\partial p}{\partial \eta}$, and $\frac{\partial p}{\partial \eta}q$ where q is the specific humidity. The prognostic variables are functions of time t, vertical coordinate η and two coordinates describing the surface of the sphere. The unit vector normal to the surface of the sphere is denoted by $\hat{k}$. This formulation has already incorporated the hydrostatic equation and the ideal gas law, $p = \rho R T_v$. There is a no-flux ($\dot{\eta} = 0$) boundary condition at $\eta = 1$ and $\eta = \eta_{\text{top}}$. The vorticity is denoted by $\zeta = \hat{k} \cdot \nabla \times \vec{u}$, f is a Coriolis term and $\omega = Dp/Dt$ is the pressure vertical velocity. The virtual temperature T_v and variable-of-convenience c_p^* are defined as in 3.3.1.

The diagnostic equations for the geopotential height field Φ is

$$\Phi = \Phi_s + \int_\eta^1 \frac{RT_v}{p}\frac{\partial p}{\partial \eta}\,d\eta \tag{3.87}$$

where Φ_s is the prescribed surface geopotential height (given at $\eta = 1$). To complete the system, we need diagnostic equations for $\dot{\eta}$ and ω, which come from integrating (3.85) with respect to η. In fact, (3.85) can be replaced by a diagnostic equation for $\dot{\eta}\frac{\partial p}{\partial \eta}$ and a prognostic equation for surface pressure p_s

$$\frac{\partial}{\partial t}p_s + \int_{\eta_{\text{top}}}^1 \nabla \cdot \left(\frac{\partial p}{\partial \eta}\vec{u}\right)\,d\eta = 0 \tag{3.88}$$

$$\dot{\eta}\frac{\partial p}{\partial \eta} = -\frac{\partial p}{\partial t} - \int_{\eta_{\text{top}}}^\eta \nabla \cdot \left(\frac{\partial p}{\partial \eta'}\vec{u}\right)\,d\eta', \tag{3.89}$$

where (3.88) is (3.89) evaluated at the model bottom ($\eta = 1$) after using that $\partial p/\partial t = B(\eta)\partial p_s/\partial t$ and $\dot{\eta}(1) = 0, B(1) = 1$. Using Eq 3.89, we can derive a diagnostic equation for the pressure vertical velocity $\omega = Dp/Dt$,

$$\omega = \frac{\partial p}{\partial t} + \vec{u} \cdot \nabla p + \dot{\eta}\frac{\partial p}{\partial \eta} = \vec{u} \cdot \nabla p - \int_{\eta_{\text{top}}}^\eta \nabla \cdot \left(\frac{\partial p}{\partial \eta}\vec{u}\right)\,d\eta'$$

Finally, we rewrite (3.89) as

$$\dot{\eta}\frac{\partial p}{\partial \eta} = B(\eta)\int_{\eta_{\text{top}}}^{1} \nabla\cdot\left(\frac{\partial p}{\partial \eta}\vec{u}\right)\,d\eta - \int_{\eta_{\text{top}}}^{\eta} \nabla\cdot\left(\frac{\partial p}{\partial \eta'}\vec{u}\right)\,d\eta', \tag{3.90}$$

3.2.2 Conserved Quantities

The equations have infinitely many conserved quantities, including mass, tracer mass, potential temperature defined by

$$M_X = \iint \frac{\partial p}{\partial \eta} X\, d\eta d\mathcal{A}$$

with ($X = 1, q$ or $(p/p_0)^{-\kappa}T$) and the total moist energy E defined by

$$E = \iint \frac{\partial p}{\partial \eta}\left(\frac{1}{2}\vec{u}^2 + c_p^* T\right)\,d\eta d\mathcal{A} + \int p_s \Phi_s\, d\mathcal{A} \tag{3.91}$$

where $d\mathcal{A}$ is the spherical area measure. To compute these quantities in their traditional units they should be divided by the constant of gravity g. We have omitted this scaling since g has also been scaled out from (3.83)–(3.86). We note that in this formulation of the primitive equations, the pressure p is a moist pressure, representing the effects of both dry air and water vapor. The unforced equations conserve both the moist air mass ($X = 1$ above) and the dry air mass ($X = 1 - q$). However, in the presence of a forcing term in (3.86) (representing sources and sinks of water vapor as would be present in a full model) a corresponding forcing term must be added to (3.85) to ensure that dry air mass is conserved.

The energy (3.91) is specific to the hydrostatic equations. We have omitted terms from the physical total energy which are constant under the evolution of the unforced hydrostatic equations [Staniforth et al., 2003]. It can be converted into a more universal form involving $\frac{1}{2}\vec{u}^2 + c_v^* T + \Phi$, with c_v^* defined similarly to c_p^*, so that $c_v^* = c_v + (c_{vv} - c_v)q$ where c_v and c_{vv} are the specific heats of dry air and water vapor defined at constant volume. We note that $c_p = R + c_v$ and $c_{pv} = R_v + c_{vv}$ so that $c_p^* T = c_v^* T + R T_v$. Expanding $c_p^* T$ with this expression, integrating by parts with respect to η and making use of the fact that the model top is at a constant pressure

$$\int \frac{\partial p}{\partial \eta} R T_v\, d\eta = -\int p\frac{\partial \Phi}{\partial \eta}\, d\eta = \int \frac{\partial p}{\partial \eta}\Phi\, d\eta - (p\Phi)\Big|_{\eta=\eta_{\text{top}}}^{\eta=1}$$

and thus

$$E = \iint \frac{\partial p}{\partial \eta}\left(\frac{1}{2}\vec{u}^2 + c_v^* T + \Phi\right)\,d\eta d\mathcal{A} + \int p_{\text{top}}\Phi(\eta_{\text{top}})\, d\mathcal{A}. \tag{3.92}$$

The model top boundary term in (3.92) vanishes if $p_{\text{top}} = 0$. Otherwise it must be included to be consistent with the hydrostatic equations. It is present due to the fact that the hydrostatic momentum equation (3.83) neglects the vertical pressure gradient.

3.2.3 Horizontal Discretization: Functional Spaces

In the finite element method, instead of constructing discrete approximations to derivative operators, one constructs a discrete functional space, and then finds the function in this space

which solves the equations of interest in a minimum residual sense. As compared to finite volume methods, there is less choice in how one constructs the discrete derivative operators in this setting, since functions in the discrete space are represented in terms of known basis functions whose derivatives are known, often analytically.

Let x^α and $\vec{x} = x^1\vec{e}_1 + x^2\vec{e}_2$ be the Cartesian coordinates and position vector of a point in the reference square $[-1,1]^2$ and let r^α and $\vec{r}$ be the coordinates and position vector of a point on the surface of the sphere, denoted by Ω. We mesh Ω using the cubed-sphere grid (Fig. 3.2) first used in Sadourny [1972]. Each cube face is mapped to the surface of the sphere with the equal-angle gnomonic projection [Rančić et al., 1996]. The map from the reference element $[-1,1]^2$ to the cube face is a translation and scaling. The composition of these two maps defines a $\mathcal{C}^1$ map from the spherical elements to the reference element $[-1,1]^2$. We denote this map and its inverse by

$$\vec{r} = \vec{r}(\vec{x}; m), \qquad \vec{x} = \vec{x}(\vec{r}; m). \tag{3.93}$$

Figure 3.2: Tiling the surface of the sphere with quadrilaterals. An inscribed cube is projected to the surface of the sphere. The faces of the cubed sphere are further subdivided to form a quadrilateral grid of the desired resolution. Coordinate lines from the gnomonic equal-angle projection are shown.

We now define the discrete space used by the SEM. First we denote the space of polynomials up to degree d in $[-1,1]^2$ by

$$\mathcal{P}_d = \operatorname*{span}_{i,j=0}^{d} (x^1)^i (x^2)^j = \operatorname*{span}_{\vec{\imath}\in\mathbb{I}} \phi_{\vec{\imath}}(\vec{x}),$$

where $\mathbb{I} = \{0,\ldots,d\}^2$ contains all the degrees and $\phi_{\vec{\imath}}(\vec{x}) = \varphi_{i^1}(x^1)\varphi_{i^2}(x^2)$, $i^\alpha = 0,\ldots,d$, are the cardinal functions, namely polynomials that interpolate the tensor-product of degree-d Gauss-Lobatto-Legendre (GLL) nodes $\vec{\xi}_{\vec{\imath}} = \xi_{i^1}\vec{e}_1 + \xi_{i^2}\vec{e}_2$. The GLL nodes used within an element for $d = 3$ are shown in Fig. 3.3. The cardinal-function expansion coefficients of a function g are its GLL nodal values, so we have

$$g(\vec{x}) = \sum_{\vec{\imath}\in\mathbb{I}} g(\vec{\xi}_{\vec{\imath}})\phi_{\vec{\imath}}(\vec{x}). \tag{3.94}$$

We can now define the piecewise-polynomial SEM spaces $\mathcal{V}^0$ and $\mathcal{V}^1$ as

$$\mathcal{V}^0 = \{f \in \mathcal{L}^2(\Omega) : f(\vec{r}(\cdot; m)) \in \mathcal{P}_d, \forall m\} = \operatorname*{span}_{m=1}^{M} \{\phi_{\vec{\imath}}(\vec{x}(\cdot; m))\}_{\vec{\imath}\in\mathbb{I}} \tag{3.95}$$

$$\text{and} \qquad \mathcal{V}^1 = \mathcal{C}^0(\Omega) \cap \mathcal{V}^0.$$

Functions in $\mathcal{V}^0$ are polynomial within each element but may be discontinuous at element boundaries and $\mathcal{V}^1$ is the subspace of continuous function in $\mathcal{V}^0$. We take $M_d = \dim \mathcal{V}^0 = (d+1)^3 M$, and $L = \dim \mathcal{V}^1 < M_d$. We then construct a set of L unique points by

$$\{\vec{r}_\ell\}_{\ell=1}^{L} = \bigcup_{m=1}^{M} \vec{r}(\{\vec{\xi}_{\vec{\imath}}\}_{\vec{\imath}\in\mathbb{I}}; m), \tag{3.96}$$

For every point $\vec{r}_\ell$, there exists at least one element Ω_m and at least one GLL node $\vec{\xi}_{\vec{\imath}} = \vec{x}(\vec{r}_\ell; m)$. In 2D, if $\vec{r}_\ell$ belongs to exactly one Ω_m it is an element-interior node. If it belongs to exactly two Ω_ms, it is an element-edge interior node. Otherwise it is a vertex node.

Figure 3.3: A 4×4 tensor product grid of GLL nodes used within each element, for a degree $d = 3$ discretization. Nodes on the boundary are shared by neighboring elements.

We also define similar spaces for 2D vectors. We introduce two families of spaces, with a subscript of either *con* or *cov*, denoting if the contravariant or covariant components of the vectors are piecewise polynomial, respectively.

$$\begin{aligned} & \mathcal{V}^0_{\text{con}} = \{\vec{u} \in \mathcal{L}^2(\Omega)^2 : u^\alpha \in \mathcal{V}^0,\ \alpha = 1,2\} \\ \text{and} \quad & \mathcal{V}^1_{\text{con}} = \mathcal{C}^0(\Omega)^2 \cap \mathcal{V}^0_{\text{con}}, \end{aligned}$$

where u^1, u^2 are the contravariant components of $\vec{u}$ defined below. Vectors in $\mathcal{V}^1_{\text{con}}$ are globally continuous and their contravariant components are polynomials in each element. Similarly,

$$\begin{aligned} & \mathcal{V}^0_{\text{cov}} = \{\vec{u} \in \mathcal{L}^2(\Omega)^2 : u_\beta \in \mathcal{V}^0,\ \beta = 1,2\} \\ \text{and} \quad & \mathcal{V}^1_{\text{cov}} = \mathcal{C}^0(\Omega)^2 \cap \mathcal{V}^0_{\text{cov}}. \end{aligned}$$

The SEM is a Galerkin method with respect to the $\mathcal{V}^1$ subspace and it can be formulated solely in terms of functions in $\mathcal{V}^1$. In CAM-HOMME, the typical configuration is to run with $d = 3$ which achieves a 4th order accurate horizontal discretization [Taylor and Fournier, 2010]. All variables in the CAM-HOMME initial condition and history files as well as variables passed to the physics routines are represented by their grid point values at the points $\{\vec{r}_\ell\}_{\ell=1}^{L}$. However, for some intermediate quantities and internally in the dynamical core it is useful to consider the larger $\mathcal{V}^0$ space, where variables are represented by their grid point values at the M_d mapped GLL nodes. This later representation can also be considered as the cardinal-function (3.94) expansion of a function f local to each element,

$$f(\vec{r}) = \sum_{\vec{\imath}\in\mathbb{I}} f(\vec{r}(\vec{\xi}_{\vec{\imath}}; m))\phi_{\vec{\imath}}(\vec{x}(\vec{r}; m)) \tag{3.97}$$

since the expansion coefficients are the function values at the mapped GLL nodes. Functions f in $\mathcal{V}^0$ can be multiple-valued at GLL nodes that are *redundant* (i.e., shared by more than one element), while for $f \in \mathcal{V}^1$, the values at any redundant points must all be the same.

3.2.4 Horizontal Discretization: Differential Operators

We use the standard curvilinear coordinate formulas for vector operators following Heinbockel [2001]. Given the 2×2 Jacobian of the the mapping (3.93) from $[-1,1]^2$ to Ω_m, we denote its determinant-magnitude by

$$J = \left| \frac{\partial \vec{r}}{\partial \vec{x}} \right|. \tag{3.98}$$

A vector $\vec{v}$ may be written in terms of physical or covariant or contravariant components, $v[\gamma]$ or v_β or v^α,

$$\vec{v} = \sum_{\gamma=1}^{3} v[\gamma] \frac{\partial \vec{r}}{\partial r^\gamma} = \sum_{\beta=1}^{3} v_\beta \vec{g}^\beta = \sum_{\alpha=1}^{3} v^\alpha \vec{g}_\alpha, \tag{3.99}$$

that are related by $v_\beta = \vec{v} \cdot \vec{g}_\beta$ and $v^\alpha = \vec{v} \cdot \vec{g}^\alpha$, where $\vec{g}^\alpha = \nabla x^\alpha$ is a contravariant basis vector and $\vec{g}_\beta = \frac{\partial \vec{r}}{\partial x^\beta}$ is a covariant basis vector.

The dot product and contravariant components of the cross product are Heinbockel [2001, Table 1]

$$\vec{u} \cdot \vec{v} = \sum_{\alpha=1}^{3} u_\alpha v^\alpha \qquad \text{and} \qquad (\vec{u} \times \vec{v})^\alpha = \frac{1}{J} \sum_{\beta,\gamma=1}^{3} \epsilon^{\alpha\beta\gamma} u_\beta v_\gamma \tag{3.100}$$

where $\epsilon^{\alpha\beta\gamma} \in \{0, \pm 1\}$ is the Levi-Civita symbol. The divergence, covariant coordinates of the gradient and contravariant coordinates of the curl are Heinbockel [2001, eqs. 2.1.1, 2.1.4 & 2.1.6]

$$\nabla \cdot \vec{v} = \frac{1}{J} \sum_{\alpha} \frac{\partial}{\partial x^\alpha} (J v^\alpha), \quad (\nabla f)_\alpha = \frac{\partial f}{\partial x^\alpha} \quad \text{and} \quad (\nabla \times \vec{v})^\alpha = \frac{1}{J} \sum_{\beta,\gamma} \epsilon^{\alpha\beta\gamma} \frac{\partial v_\gamma}{\partial x^\beta}. \tag{3.101}$$

In the SEM, these operators are all computed in terms of the derivatives with respect to $\vec{x}$ in the reference element, computed exactly (to machine precision) by differentiating the local element expansion (3.97). For the gradient, the covariant coordinates of $\nabla f, f \in \mathcal{V}^0$ are thus computed exactly within each element. Note that $\nabla f \in \mathcal{V}^0_{\text{cov}}$, but may not be in $\mathcal{V}^1_{\text{cov}}$ even for $f \in \mathcal{V}^1$ due to the fact that its components will be multi-valued at element boundaries because ∇f computed in adjacent elements will not necessarily agree along their shared boundary. In the case where J is constant within each element, the SEM curl of $\vec{v} \in \mathcal{V}^0_{\text{cov}}$ and the divergence of $\vec{u} \in \mathcal{V}^0_{\text{con}}$ will also be exact, but as with the gradient, multiple-valued at element boundaries.

For non-constant J, these operators may not be computed exactly by the SEM due to the Jacobian factors in the operators and the Jacobian factors that appear when converting between covariant and contravariant coordinates. We follow Thomas and Loft [2000] and evaluate these operators in the form shown in (3.101). The quadratic terms that appear are first projected into $\mathcal{V}^0$ via interpolation at the GLL nodes and then this interpolant is differentiated exactly using (3.97). For example, to compute the divergence of $\vec{v} \in \mathcal{V}^0_{\text{con}}$, we first compute the interpolant $\mathcal{I}(J v^\alpha) \in \mathcal{V}^0$ of $J v^\alpha$, where the GLL interpolant of a product fg derives simply from the product of the GLL nodal values of f and g. This operation is just a reinterpretation of the nodal values and is essentially free in the SEM. The derivatives of this interpolant are then computed exactly from (3.97). The sum of partial derivatives are then divided by J at the GLL nodal values and thus the SEM divergence operator $\nabla_{\text{h}} \cdot ()$ is given by

$$\nabla \cdot \vec{v} \approx \nabla_{\text{h}} \cdot \vec{v} = \mathcal{I} \left(\frac{1}{J} \sum_{\alpha} \frac{\partial \mathcal{I}(J v^\alpha)}{\partial x^\alpha} \right) \in \mathcal{V}^0. \tag{3.102}$$

Similarly, the gradient and curl are approximated by

$$(\nabla f)_\alpha \approx (\nabla_{\mathrm{h}} f)_\alpha = \frac{\partial f}{\partial x^\alpha} \tag{3.103}$$

$$\text{and} \qquad (\nabla \times \vec{v})^\alpha \approx (\nabla_{\mathrm{h}} \times \vec{v})^\alpha = \sum_{\beta,\gamma} \epsilon^{\alpha\beta\gamma} \mathcal{I}\left(\frac{1}{J}\frac{\partial v_\gamma}{\partial x^\beta}\right) \tag{3.104}$$

with $\nabla_{\mathrm{h}} f \in \mathcal{V}^0_{\mathrm{cov}}$ and $\nabla_{\mathrm{h}} \times \vec{v} \in \mathcal{V}^0_{\mathrm{con}}$. The SEM is well known for being quite efficient in computing these types of operations. The SEM divergence, gradient and curl can all be evaluated at the $(d+1)^3$ GLL nodes within each element in $\mathcal{O}(d)$ operations per node using the tensor-product property of these points [Deville et al., 2002; Karniadakis and Sherwin, 2005].

3.2.5 Horizontal Discretization: Discrete Inner-Product

Instead of using exact integration of the basis functions as in a traditional finite-element method, the SEM uses a GLL quadrature approximation for the integral over Ω, that we denote by $\langle\cdot\rangle$. We can write this integral as a sum of area-weighted integrals over the set of elements $\{\Omega_m\}_{m=1}^M$ used to decompose the domain,

$$\int f g \, d\mathcal{A} = \sum_{m=1}^{M} \int_{\Omega_m} f g \, d\mathcal{A}.$$

The integral over a single element Ω_m is written as an integral over $[-1,1]^2$ by

$$\int_{\Omega_m} f g \, d\mathcal{A} = \iint_{[-1,1]^2} f(\vec{r}(\cdot;m)) g(\vec{r}(\cdot;m)) J_m \, dx^1 \, dx^2 \approx \langle fg \rangle_{\Omega_m},$$

where we approximate the integral over $[-1,1]^2$ by GLL quadrature,

$$\langle fg \rangle_{\Omega_m} = \sum_{\vec{i} \in \mathbb{I}} w_{i^1} w_{i^2} J_m(\vec{\xi}_{\vec{i}}) f(\vec{r}(\vec{\xi}_{\vec{i}};m)) g(\vec{r}(\vec{\xi}_{\vec{i}};m)) \tag{3.105}$$

The SEM approximation to the global integral is then naturally defined as

$$\int f g \, d\mathcal{A} \approx \sum_{m=1}^{M} \langle fg \rangle_{\Omega_m} = \langle fg \rangle \tag{3.106}$$

When applied to the product of functions $f, g \in \mathcal{V}^0$, the quadrature approximation $\langle fg \rangle$ defines a discrete inner-product in the usual manner.

3.2.6 Horizontal Discretization: The Projection Operators

Let $P : \mathcal{V}^0 \to \mathcal{V}^1$ be the unique orthogonal (self-adjoint) projection operator from $\mathcal{V}^0$ onto $\mathcal{V}^1$ w.r.t. the SEM discrete inner product (3.106). The operation P is essentially the same as the common procedure in the SEM described as *assembly* [Karniadakis and Sherwin, 2005, p. 7], or *direct stiffness summation* [Deville et al., 2002, eq. 4.5.8]. Thus the SEM assembly procedure

is not an ad-hoc way to remove the redundant degrees of freedom in $\mathcal{V}^0$, but is in fact the natural projection operator P. Applying the projection operator in a finite element method requires inverting the finite element mass matrix. A remarkable fact about the SEM is that with the GLL based discrete inner product and the careful choice of global basis functions, the mass matrix is diagonal [Maday and Patera, 1987]. The resulting projection operator then has a very simple form: at element interior points, it leaves the nodal values unchanged, while at element boundary points shared by multiple elements it is a Jacobian-weighted average over all redundant values [Taylor and Fournier, 2010].

To apply the projection $P : \mathcal{V}^0_{\text{cov}} \to \mathcal{V}^1_{\text{cov}}$ to vectors $\vec{u}$, one cannot project the covariant components since the corresponding basis vectors $\vec{g}_\beta$ and $\vec{g}^\alpha$ do not necessarily agree along element faces. Instead we must define the projection as acting on the components using a globally continuous basis such as the latitude-longitude unit vectors $\hat{\theta}$ and $\hat{\lambda}$,

$$P(\vec{u}) = P(\vec{u} \cdot \hat{\lambda})\hat{\lambda} + P(\vec{u} \cdot \hat{\theta})\hat{\theta}.$$

3.2.7 Horizontal Discretization: Galerkin Formulation

The SEM solves a Galerkin formulation of the equations of interest. Given the discrete differential operators described above, the primitive equations can be written as an ODE for a generic prognostic variable U and right-hand-side (RHS) terms

$$\frac{\partial U}{\partial t} = \text{RHS}.$$

The SEM solves this equation in integral form with respect to the SEM inner product. That is, for a RHS $\in \mathcal{V}^0$, the SEM finds the unique $\frac{\partial U}{\partial t} \in \mathcal{V}^1$ such that

$$\left\langle \phi \frac{\partial U}{\partial t} \right\rangle = \langle \phi \, \text{RHS} \rangle \qquad \forall \phi \in \mathcal{V}^1.$$

As the prognostic variable is assumed to belong to $\mathcal{V}^1$, the RHS will in general belong to $\mathcal{V}^0$ since it contains derivatives of the prognostic variables, resulting in the loss of continuity at the element boundaries. If one picks a suitable basis for $\mathcal{V}^1$, this discrete integral equation results in a system of L equations for the L expansion coefficients of $\frac{\partial U}{\partial t}$. The SEM solves these equations exactly, and the solution can be written in terms of the SEM projection operator as

$$\frac{\partial U}{\partial t} = P\left(\text{RHS}\right).$$

The projection operator commutes with any time-stepping scheme, so the equations can be solved in a two step process, illustrated here for simplicity with the forward Euler method

- Step 1:
$$U^* = U^t + \Delta t \, \text{RHS} \qquad U^* \in \mathcal{V}^0$$
- Step 2:
$$U^{t+1} = P\left(U^*\right) \qquad U^{t+1} \in \mathcal{V}^1$$

For compactness of notation, we will denote this two step procedure in what follows by

$$P^{-1}\frac{\partial U}{\partial t} = \text{RHS}.$$

Note that P maps a M_d dimensional space $\mathcal{V}^0$ into a L dimensional space $\mathcal{V}^1$, so here P^{-1} denotes the left inverse of P. This inverse will never be computed, it is only applied as in step 2 above.

This two step Galerkin solution process represents a natural separation between computation and communication for the implementation of the SEM on a parallel computer. The computations in step 1 are all local to the data contained in a single element. Assuming an element-based decomposition so that each processor contains at least one element, no inter-processor communication is required in step 1. All inter-processor communication in HOMME is isolated to the projection operator step, in which element boundary data must be exchanged between adjacent elements.

3.2.8 Vertical Discretization

The vertical coordinate system uses a Lorenz staggering of the variables as shown in 3.4. Let K be the total number of layers, with variables $\vec{u}, T, q, \omega, \Phi$ at layer mid points denoted by $k = 1, 2, \ldots, K$. We denote layer interfaces by $k + \frac{1}{2}, k = 0, 1, \ldots, K$, so that $\eta_{1/2} = \eta_{\text{top}}$ and $\eta_{K+1/2} = 1$. The η-integrals will be replaced by sums. We will use δ_η to denote the discrete $\partial/\partial\eta$ operator. The δ_η operator uses centered differences to compute derivatives with respect to η at layer mid point from layer interface values, $\delta_\eta(X)_k = (X_{k+1/2} - X_{k-1/2})/(\eta_{k+1/2} - \eta_{k-1/2})$. We will use the over-bar notation for vertical averaging, $\overline{q}_{k+1/2} = (q_{k+1} + q_k)/2$. We also introduce the symbol π to denote the discrete pseudo-density $\frac{\partial p}{\partial \eta}$ given by

$$\pi_k = \delta_\eta(p)_k$$

.

We will use $\overline{\dot{\eta}\delta_\eta}$ to denote the discrete form of the $\dot{\eta}\partial/\partial\eta$ operator. We use the discretization given in 3.3.5. This operator acts on quantities defined at layer mid-points and returns a result also at layer mid-points,

$$\overline{\dot{\eta}\delta_\eta}(X)_k = \frac{1}{2\pi_k\Delta\eta_k}\left[(\dot{\eta}\pi)_{k+1/2}\,(X_{k+1} - X_k) + (\dot{\eta}\pi)_{k-1/2}(X_k - X_{k-1})\right] \tag{3.107}$$

where $\Delta\eta_k = \eta_{k+1/2} - \eta_{k-1/2}$. We use the over-bar notation since the formula can be seen as a π-weighted average of a layer interface centered difference approximation to $\dot{\eta}\partial/\partial\eta$. This formulation was constructed in Simmons and Burridge [1981] in order to ensure mass and energy conservation. Here we will use an equivalent expression that can be written in terms of δ_η,

$$\overline{\dot{\eta}\delta_\eta}(X)_k = \frac{1}{\pi_k}\Big[\,\delta_\eta\left(\dot{\eta}\pi\overline{X}\right)_k - X\,\delta_\eta\left(\dot{\eta}\pi\right)_k\Big]. \tag{3.108}$$

3.2.9 Discrete formulation: Dynamics

We discretize the equations exactly in the form shown in (3.83), (3.84), (3.88) and (3.90), obtaining

$$P^{-1}\frac{\partial \vec{u}}{\partial t} = -\left(\zeta + f\right)\hat{k}\times\vec{u} + \nabla_{\mathrm{h}}\left(\frac{1}{2}\vec{u}^2 + \Phi\right) - \overline{\dot{\eta}\delta_\eta}(\vec{u}) - \frac{RT_v}{p}\nabla_{\mathrm{h}}(p) \tag{3.109}$$

$$P^{-1}\frac{\partial T}{\partial t} = -\vec{u}\cdot\nabla_{\mathrm{h}}(T) - \overline{\dot{\eta}\delta_\eta}(T) + \frac{RT_v}{c_p^* p}\omega \tag{3.110}$$

$$P^{-1}\frac{\partial p_s}{\partial t} = -\sum_{j=1}^{K}\nabla_{\mathrm{h}}\cdot\left(\pi\vec{u}\right)_j \Delta\eta_j \tag{3.111}$$

$$\left(\dot{\eta}\pi\right)_{i+1/2} = B(\eta_{i+1/2})\sum_{j=1}^{K}\nabla_{\mathrm{h}}\cdot\left(\pi\vec{u}\right)_j \Delta\eta_j - \sum_{j=1}^{i}\nabla_{\mathrm{h}}\cdot\left(\pi\vec{u}\right)_j \Delta\eta_j. \tag{3.112}$$

We consider $(\dot{\eta}\pi)$ a single quantity given at layer interfaces and defined by (3.112). The no-flux boundary condition is $(\dot{\eta}\pi)_{1/2} = (\dot{\eta}\pi)_{K+1/2} = 0$. In (3.112), we used a midpoint quadrature rule to evaluate the indefinite integral from (3.90). In practice $\Delta\eta$ can be eliminated from the discrete equations by scaling π, but here we retain them so as to have a direct correspondence with the continuum form of the equations written in terms of $\frac{\partial p}{\partial \eta}$.

Finally we give the approximations for the diagnostic equations. We first integrate to layer interface $i-\frac{1}{2}$ using the same mid-point rule as used to derive (3.112), and then add an additional term representing the integral from $i-\frac{1}{2}$ to i:

$$\omega_i = \left(\vec{u}\cdot\nabla_{\mathrm{h}}p\right)_i - \sum_{j=1}^{i-1}\nabla_{\mathrm{h}}\cdot\left(\pi\vec{u}\right)_j \Delta\eta_j + \nabla_{\mathrm{h}}\cdot\left(\pi\vec{u}\right)_i \frac{\Delta\eta_i}{2} \tag{3.113}$$

$$= \left(\vec{u}\cdot\nabla_{\mathrm{h}}p\right)_i - \sum_{j=1}^{K} C_{ij}\nabla_{\mathrm{h}}\cdot\left(\pi\vec{u}\right)_j \tag{3.114}$$

where

$$C_{ij} = \begin{cases} \Delta\eta_j & i > j \\ \Delta\eta_j/2 & i = j \\ 0 & i < j \end{cases}$$

and similar for Φ,

$$\left(\Phi - \Phi_s\right)_i = \left(\frac{RT_v}{p}\pi\right)_i \frac{\Delta\eta_i}{2} + \sum_{j=i+1}^{K}\left(\frac{RT_v}{p}\pi\right)_j \Delta\eta_j \tag{3.115}$$

$$= \sum_{j=1}^{K} H_{ij}\left(\frac{RT_v}{p}\pi\right)_j \tag{3.116}$$

where

$$H_{ij} = \begin{cases} \Delta\eta_j & i < j \\ \Delta\eta_j/2 & i = j \\ 0 & i > j \end{cases}$$

Similar to 3.3.5, we note that

$$\Delta\eta_i \, C_{ij} = \Delta\eta_j \, H_{ji} \tag{3.117}$$

which ensures energy conservation [Taylor, 2010].

3.2.10 Consistency

It is important that the discrete equations be as consistent as possible. In particular, we need a discrete version of (3.85), the non-vertically averaged continuity equation. Equation (3.112) implicitly implies such an equation. To see this, apply δ_η to (3.112) and using that $\partial p/\partial t = B(\eta)\partial p_s/\partial t$ then we can derive, at layer mid-points,

$$P^{-1}\frac{\partial \pi}{\partial t} = -\nabla_{\rm h} \cdot (\pi \vec{u}) - \delta_\eta \left(\dot{\eta}\pi\right). \tag{3.118}$$

A second type of consistency that has been identified as important is that (3.113), the discrete equation for ω, be consistent with (3.112), the discrete continuity equation [Williamson and Olson, 1994*b*]. The two discrete equations should imply a reasonable discretization of $\omega = Dp/Dt$. To show this, we take the average of (3.112) at layers $i-1/2$ and $i+1/2$ and combine this with (3.113) (at layer mid-points i) and assuming that $B(\eta_i) = B(\eta_{i-1/2}) + B(\eta_{i+1/2})$ we obtain

$$P^{-1}\frac{\partial p}{\partial t} = \omega_i - (\vec{u} \cdot \nabla_{\rm h} p)_i - \frac{1}{2}\left((\dot{\eta}\,\delta_\eta)_{i-1/2} + (\dot{\eta}\,\delta_\eta)_{i+1/2}\right).$$

which, since $\vec{u}\cdot\nabla_{\rm h}p$ is given at layer mid-points and $\dot{\eta}\pi$ at layer interfaces, is the SEM discretization of $w = \partial p/\partial t + \vec{u}\cdot\nabla_{\rm h}p + \dot{\eta}\pi$.

3.2.11 Time Stepping

Applying the SEM discretization to (3.109)-(3.112) results in a system of ODEs. These are solved with an N-stage Runge-Kutta method. This method allows for a gravity-wave based CFL number close to $N-1$, (normalized so that the largest stable timestep of the Robert filtered Leapfrog method has a CFL number of 1.0). The value of N is chosen large enough so that the dynamics will be stable at the same timestep used by the tracer advection scheme. To determine N, we first note that the tracer advection scheme uses a less efficient (in terms of maximum CFL) strong stability preserving Runge-Kutta method described below. It is stable at an advective CFL number of 1.4. Let u_0 be a maximum wind speed and c_0 be the maximum gravity wave speed. The gravity wave and advective CFL conditions are

$$\Delta t \leq (N-1)\Delta x/c_0, \qquad \Delta t \leq 1.4\Delta x/u_0.$$

In the case where Δt is chosen as the largest stable timestep for advection, then we require $N \geq 1 + 1.4c_0/u_0$ for a stable dynamics timestep. Using a typical values $u_0 = 120$ m/s and $c_0 = 340$m/s gives $N = 5$. CAM places additional restrictions on the timestep (such as that the physics timestep must be an integer multiple of Δt) which also influence the choice of Δt and N.

3.2.12 Dissipation

A horizontal hyper-viscosity operator, modeled after 3.3.6 is applied to the momentum and temperature equations. It is applied in a time-split manor after each dynamics timestep. The hyper-viscosity step for vectors can be written as

$$\frac{\partial \vec{u}}{\partial t} = -\nu \Delta^2 \vec{u}.$$

An integral form of this equation suitable for the SEM is obtained using a mixed finite element formulation (following Giraldo [1999]) which writes the equation as a system of equations involving only first derivatives. We start by introduced an auxiliary vector $\vec{f}$ and using the identity $\Delta\vec{u} = \nabla(\nabla\cdot\vec{u}) - \nabla\times(\nabla\times\vec{u})$,

$$\frac{\partial \vec{u}}{\partial t} = -\nu \left(\nabla(\nabla\cdot\vec{f}) - \nabla\times\hat{k}(\nabla\times\vec{f}) \right) \tag{3.119}$$

$$\vec{f} = \nabla(\nabla\cdot\vec{u}) - \nabla\times(\nabla\times\vec{u})\hat{k}. \tag{3.120}$$

Integrating the gradient and curl operators by parts gives

$$\iint \vec{\phi}\cdot\frac{\partial \vec{u}}{\partial t}\, d\mathcal{A} = \nu \iint \left[(\nabla\cdot\vec{\phi})(\nabla\cdot\vec{f}) + (\nabla\times\vec{\phi})\cdot\hat{k}(\nabla\times\vec{f}) \right] d\mathcal{A} \tag{3.121}$$

$$\iint \vec{\phi}\cdot\vec{f}\, d\mathcal{A} = -\iint \left[(\nabla\cdot\vec{\phi})(\nabla\cdot\vec{u}) + (\nabla\times\vec{\phi})\cdot\hat{k}(\nabla\times\vec{u}) \right] d\mathcal{A}. \tag{3.122}$$

$$\tag{3.123}$$

The SEM Galerkin solution of this integral equation is most naturally written in terms of an inverse mass matrix instead of the projection operator. It can be written in terms of the SEM projection operator by first testing with the product of the element cardinal functions and the contravariant basis vector $\vec{\phi} = \phi_{\vec{i}}\vec{g}_\alpha$. With this type of test function, the RHS of (3.122) can be defined as a weak Laplacian operator $\vec{f} = D(\vec{u}) \in \mathcal{V}^0_{\text{cov}}$. The covariant components of $\vec{f}$ given by $f_\alpha = \vec{f}\cdot\vec{g}_\alpha$ are then

$$f_\alpha(\vec{r}(\vec{\xi}_{\vec{i}}; m)) = \frac{-1}{w_{i^1} w_{i^2} J_m(\vec{\xi}_{\vec{i}})} \left\langle (\nabla_{\text{h}}\cdot\phi_{\vec{i}}\vec{g}_\alpha)(\nabla_{\text{h}}\cdot\vec{u}) + (\nabla_{\text{h}}\times\phi_{\vec{i}}\vec{g}_\alpha)\cdot\hat{k}(\nabla_{\text{h}}\times\vec{u}). \right\rangle$$

Then the SEM solution to (3.121) and (3.122) is given by

$$\vec{u}(t+\Delta t) = \vec{u}(t) - \nu\Delta t P\left(D\Big(P\big(D(\vec{u})\big)\Big)\right).$$

Because of the SEM tensor product decomposition, the expression for D can be evaluated in only $O(d)$ operations per grid point, and in CAM-HOMME typically $d = 3$.

Following 3.3.6, a correction term is added so the hyper-viscosity does not damp rigid rotation. The hyper-viscosity formulation used for scalars such as T is much simpler, since instead of the vector Laplacian identity we use $\Delta T = \nabla\cdot\nabla T$. Otherwise the approach is identical to that used above so we omit the details. The correction for terrain following coordinates given in 3.3.6 is not yet implemented in CAM-HOMME.

3.2.13 Discrete formulation: Tracer Advection

All tracers, including specific humidity, are advected with a discretized version of (3.86). HOMME uses the vertically Lagrangian approach (see 3.1.4) from Lin [2004]. At the beginning of each timestep, the tracers are assumed to be given on the η-coordinate layer mid points. The tracers are advanced in time on a moving vertical coordinate system η' defined so that $\dot{\eta}' = 0$. At the end of the timestep, the tracers are remapped back to the η-coordinate layer mid points using the monotone remap algorithm from Zerroukat et al. [2005].

The horizontal advection step consists of using the SEM to solve

$$\frac{\partial}{\partial t}(\pi q) = -\nabla_{\mathrm{h}} \cdot \left(\overline{(\pi \vec{u})} q\right) \tag{3.124}$$

on the surfaces defined by the η' layer mid points. The quantity $\overline{(\pi \vec{u})}$ is the mean flux computed during the dynamics update. The mean flux used in (3.124), combined with a suitable mean vertical flux used in the remap stage allows HOMME to preserve mass/tracer-mass consistency: The tracer advection of πq with $q = 1$ will be identical to the advection of π implied from (3.118). The mass/tracer-mass consistency capability is not in the version of HOMME included in CAM 4.0, but should be in all later versions.

The equation is discretized in time using the optimal 3 stage strong stability preserving (SSP) second order Runge-Kutta method from Spiteri and Ruuth [2002]. The RK-SSP method is chosen because it will preserve the monotonicity properties of the horizontal discretization. RK-SSP methods are convex combinations of forward-Euler timesteps, so each stage s of the RK-SSP timestep looks like

$$(\pi q)^{s+1} = (\pi q)^{s} - \Delta t \nabla_{\mathrm{h}} \cdot \left(\overline{(\pi \vec{u})} q^{s}\right) \tag{3.125}$$

Simply discretizing this equation with the SEM will result in locally conservative, high-order accurate but oscillatory transport scheme. A limiter is added to reduce or eliminate these oscillations [Taylor et al., 2009]. HOMME supports both monotone and sign-preserving limiters, but the most effective limiter for HOMME has not yet been determined. The default configuration in CAM4 is to use the sign-preserving limiter to prevent negative values of q coupled with a sign-preserving hyper-viscosity operator which dissipates q^2.

3.2.14 Conservation and Compatibility

The SEM is compatible, meaning it has a discrete version of the divergence theorem, Stokes theorem and curl/gradient annihilator properties Taylor and Fournier [2010]. The divergence theorem is the key property of the horizontal discretization that is needed to show conservation. For an arbitrary scalar h and vector $\vec{u}$ at layer mid-points, the divergence theorem (or the divergence/gradient adjoint relation) can be written

$$\int h \nabla \cdot \vec{u} \, d\mathcal{A} + \int \vec{u} \nabla h \, d\mathcal{A} = 0.$$

The discrete version obeyed by the SEM discretization, using (3.106), is given by

$$\langle h \nabla_{\mathrm{h}} \cdot \vec{u} \rangle + \langle \vec{u} \cdot \nabla_{\mathrm{h}} h \rangle = 0. \tag{3.126}$$

The discrete divergence and Stokes theorem apply locally at the element with the addition of an element boundary integral. The local form is used to show local conservation of mass and that the horizontal advection operator locally conserves the two-dimensional potential vorticity [Taylor and Fournier, 2010].

In the vertical, Simmons and Burridge [1981] showed that the δ_η and $\overline{\dot{\eta}\delta_\eta}$ operators needed to satisfy two integral identities to ensure conservation. For any $\dot{\eta}$ layer interface velocity which satisfies $\dot{\eta}_{1/2} = \dot{\eta}_{K+1/2} = 0$ and f, g arbitrary functions of layer mid points. The first identity is the adjoint property (compatibility) for δ_η and π,

$$\sum_{i=1}^{K} \Delta\eta_i \, \pi_i \, \overline{\dot{\eta}\delta_\eta}(f) + \sum_{i=1}^{K} \Delta\eta_i \, f_i \, \delta_\eta(\dot{\eta}\pi) = 0 \tag{3.127}$$

which follows directly from the definition of the $\overline{\dot{\eta}\delta_\eta}$ difference operator given in (3.108). The second identity we write in terms of δ_η,

$$\sum_{i=1}^{K} \Delta\eta_i \, fg \, \delta_\eta(\dot{\eta}\pi) = \sum_{i=1}^{K} \Delta\eta_i \, f \, \delta_\eta(\dot{\eta}\pi\overline{g}) + \sum_{i=1}^{K} \Delta\eta_i \, g \, \delta_\eta(\dot{\eta}\pi\overline{f}) \tag{3.128}$$

which is a discrete integrated-by-parts analog of $\partial(fg) = f\partial g + g\partial f$. Construction of methods with both properties on a staggered unequally spaced grid is the reason behind the complex definition for $\overline{\dot{\eta}\delta_\eta}$ in (3.108).

The energy conservation properties of CAM-HOMME were studied in Taylor [2010] using the aqua planet test case [Neale and Hoskins, 2001*a*,*b*]. CAM-HOMME uses

$$E = \left\langle \sum_{i=1}^{K} \Delta\eta_i \pi_i \left(\frac{1}{2}\vec{u}^2 + c_p^* T \right)_i \right\rangle + \langle p_s \Phi_s \rangle$$

as the discretization of the total moist energy (3.91). The conservation of E is *semi-discrete*, meaning that the only error in conservation is the time truncation error. In the adiabatic case (with no hyper-viscosity and no limiters), running from a fully spun up initial condition, the error in conservation decreases to machine precision at a second-order rate with decreasing timestep. In the full non-adiabatic case with a realistic timestep, $dE/dt \sim 0.013\text{W/m}^2$.

The CAM physics conserve a dry energy E_{dry} from Boville and Bretherton [2003*a*] which is not conserved by the moist primitive equations. Although $E - E_{dry}$ is small, adiabatic processes in the primitive equations result in a net heating $dE_{dry}/dt \sim 0.5\text{W/m}^2$ [Taylor, 2010]. If it is desired that the dynamical core conserve E_{dry} instead of E, HOMME uses the energy fixer from 3.3.20.

3.3 Eulerian Dynamical Core

The hybrid vertical coordinate that has been implemented in CAM 5.0 is described in this section. The hybrid coordinate was developed by Simmons and Strüfing [1981] in order to provide a general framework for a vertical coordinate which is terrain following at the Earth's surface, but reduces to a pressure coordinate at some point above the surface. The hybrid

coordinate is more general in concept than the modified σ scheme of Sangster [1960], which is used in the GFDL SKYHI model. However, the hybrid coordinate is normally specified in such a way that the two coordinates are identical.

The following description uses the same general development as Simmons and Strüfing [1981], who based their development on the generalized vertical coordinate of Kasahara [1974]. A specific form of the coordinate (the hybrid coordinate) is introduced at the latest possible point. The description here differs from Simmons and Strüfing [1981] in allowing for an upper boundary at finite height (nonzero pressure), as in the original development by Kasahara. Such an upper boundary may be required when the equations are solved using vertical finite differences.

3.3.1 Generalized terrain-following vertical coordinates

Deriving the primitive equations in a generalized terrain-following vertical coordinate requires only that certain basic properties of the coordinate be specified. If the surface pressure is π, then we require the generalized coordinate $\eta(p, \pi)$ to satisfy:

1. $\eta(p, \pi)$ is a monotonic function of p.
2. $\eta(\pi, \pi) = 1$
3. $\eta(0, \pi) = 0$
4. $\eta(p_t, \pi) = \eta_t$ where p_t is the top of the model.

The latter requirement provides that the top of the model will be a pressure surface, simplifying the specification of boundary conditions. In the case that $p_t = 0$, the last two requirements are identical and the system reduces to that described in Simmons and Strüfing [1981]. The boundary conditions that are required to close the system are:

$$\dot{\eta}(\pi, \pi) = 0, \tag{3.129}$$
$$\dot{\eta}(p_t, \pi) = \omega(p_t) = 0. \tag{3.130}$$

Given the above description of the coordinate, the continuous system of equations can be written following Kasahara [1974] and Simmons and Strüfing [1981]. The prognostic equations are:

$$\frac{\partial \zeta}{\partial t} = \boldsymbol{k} \cdot \nabla \times (\boldsymbol{n}/\cos\phi) + F_{\zeta_H}, \tag{3.131}$$
$$\frac{\partial \delta}{\partial t} = \nabla \cdot (\boldsymbol{n}/\cos\phi) - \nabla^2 (E + \Phi) + F_{\delta_H}, \tag{3.132}$$
$$\frac{\partial T}{\partial t} = \frac{-1}{a\cos^2\phi}\left[\frac{\partial}{\partial\lambda}(UT) + \cos\phi\frac{\partial}{\partial\phi}(VT)\right] + T\delta - \dot{\eta}\frac{\partial T}{\partial \eta} + \frac{R}{c_p^*}T_v\frac{\omega}{p} + Q + F_{T_H} + F_{F_H}, \tag{3.133}$$
$$\frac{\partial q}{\partial t} = \frac{-1}{a\cos^2\phi}\left[\frac{\partial}{\partial\lambda}(Uq) + \cos\phi\frac{\partial}{\partial\phi}(Vq)\right] + q\delta - \dot{\eta}\frac{\partial q}{\partial \eta} + S, \tag{3.134}$$
$$\frac{\partial \pi}{\partial t} = \int_1^{\eta_t} \boldsymbol{\nabla}\cdot\left(\frac{\partial p}{\partial \eta}\boldsymbol{V}\right) d\eta. \tag{3.135}$$

The notation follows standard conventions, and the following terms have been introduced with $\boldsymbol{n} = (n_U, n_V)$:

$$n_U = +(\zeta + f)V - \dot{\eta}\frac{\partial U}{\partial \eta} R\frac{T_v}{p}\frac{1}{a} - \frac{\partial p}{\partial \lambda} + F_U\,, \tag{3.136}$$

$$n_V = -(\zeta + f)U - \dot{\eta}\frac{\partial V}{\partial \eta} - R\frac{T_v}{p}\frac{\cos\phi}{a}\frac{\partial p}{\partial \phi} + F_V\,, \tag{3.137}$$

$$E = \frac{U^2 + V^2}{2\cos^2\phi}\,, \tag{3.138}$$

$$(U, V) = (u, v)\cos\phi\,, \tag{3.139}$$

$$T_v = \left[1 + \left(\frac{R_v}{R} - 1\right) q\right] T\,, \tag{3.140}$$

$$c_p^* = \left[1 + \left(\frac{c_{p_v}}{c_p} - 1\right) q\right] c_p\,. \tag{3.141}$$

The terms F_U, F_V, Q, and S represent the sources and sinks from the parameterizations for momentum (in terms of U and V), temperature, and moisture, respectively. The terms F_{ζ_H} and F_{δ_H} represent sources due to horizontal diffusion of momentum, while F_{T_H} and F_{F_H} represent sources attributable to horizontal diffusion of temperature and a contribution from frictional heating (see sections on horizontal diffusion and horizontal diffusion correction).

In addition to the prognostic equations, three diagnostic equations are required:

$$\Phi = \Phi_s + R\int_{p(\eta)}^{p(1)} T_v d\ln p, \tag{3.142}$$

$$\dot{\eta}\frac{\partial p}{\partial \eta} = -\frac{\partial p}{\partial t} - \int_{\eta_t}^{\eta} \boldsymbol{\nabla}\cdot\left(\frac{\partial p}{\partial \eta}\boldsymbol{V}\right) d\eta, \tag{3.143}$$

$$\omega = \boldsymbol{V}\cdot\nabla p - \int_{\eta_t}^{\eta} \boldsymbol{\nabla}\cdot\left(\frac{\partial p}{\partial \eta}\boldsymbol{V}\right) d\eta. \tag{3.144}$$

Note that the bounds on the vertical integrals are specified as values of η (*e.g.* η_t, 1) or as functions of p (*e.g.* p (1), which is the pressure at $\eta = 1$).

3.3.2 Conversion to final form

Equations (3.129)-(3.144) are the complete set which must be solved by a GCM. However, in order to solve them, the function $\eta(p, \pi)$ must be specified. In advance of actually specifying $\eta(p, \pi)$, the equations will be cast in a more convenient form. Most of the changes to the equations involve simple applications of the chain rule for derivatives, in order to obtain terms that will be easy to evaluate using the predicted variables in the model. For example, terms involving horizontal derivatives of p must be converted to terms involving only $\partial p/\partial\pi$ and horizontal derivatives of π. The former can be evaluated once the function $\eta(p, \pi)$ is specified.

The vertical advection terms in (3.133), (3.134), (3.136), and (3.137) may be rewritten as:

$$\dot{\eta}\frac{\partial \psi}{\partial \eta} = \dot{\eta}\frac{\partial p}{\partial \eta}\frac{\partial \psi}{\partial p}\,, \tag{3.145}$$

since $\dot{\eta}\partial p/\partial\eta$ is given by (3.143). Similarly, the first term on the right-hand side of (3.143) can be expanded as

$$\frac{\partial p}{\partial t} = \frac{\partial p}{\partial \pi}\frac{\partial \pi}{\partial t}, \tag{3.146}$$

and (3.135) invoked to specify $\partial\pi/\partial t$.

The integrals which appear in (3.135), (3.143), and (3.144) can be written more conveniently by expanding the kernel as

$$\boldsymbol{\nabla}\cdot\left(\frac{\partial p}{\partial \eta}\boldsymbol{V}\right) = \boldsymbol{V}\cdot\nabla\left(\frac{\partial p}{\partial \eta}\right) + \frac{\partial p}{\partial \eta}\boldsymbol{\nabla}\cdot\boldsymbol{V}\ . \tag{3.147}$$

The second term in (3.147) is easily treated in vertical integrals, since it reduces to an integral in pressure. The first term is expanded to:

$$\begin{aligned}\boldsymbol{V}\cdot\nabla\left(\frac{\partial p}{\partial \eta}\right) &= \boldsymbol{V}\cdot\frac{\partial}{\partial\eta}\left(\nabla p\right)\\ &= \boldsymbol{V}\cdot\frac{\partial}{\partial\eta}\left(\frac{\partial p}{\partial\pi}\nabla\pi\right)\\ &= \boldsymbol{V}\cdot\frac{\partial}{\partial\eta}\left(\frac{\partial p}{\partial\pi}\right)\nabla\pi + \boldsymbol{V}\cdot\frac{\partial p}{\partial\pi}\nabla\left(\frac{\partial\pi}{\partial\eta}\right)\ .\end{aligned} \tag{3.148}$$

The second term in (3.148) vanishes because $\partial\pi/\partial\eta = 0$, while the first term is easily treated once $\eta(p,\pi)$ is specified. Substituting (3.148) into (3.147), one obtains:

$$\boldsymbol{\nabla}\cdot\left(\frac{\partial p}{\partial \eta}\boldsymbol{V}\right) = \frac{\partial}{\partial\eta}\left(\frac{\partial p}{\partial\pi}\right)\boldsymbol{V}\cdot\nabla\pi + \frac{\partial p}{\partial\eta}\boldsymbol{\nabla}\cdot V\,. \tag{3.149}$$

Using (3.149) as the kernel of the integral in (3.135), (3.143), and (3.144), one obtains integrals of the form

$$\begin{aligned}\int\boldsymbol{\nabla}\cdot\left(\frac{\partial p}{\partial \eta}\boldsymbol{V}\right)d\eta &= \int\left[\frac{\partial}{\partial\eta}\left(\frac{\partial p}{\partial\pi}\right)\boldsymbol{V}\cdot\nabla\pi + \frac{\partial p}{\partial\eta}\boldsymbol{\nabla}\cdot V\right]d\eta\\ &= \int\boldsymbol{V}\cdot\nabla\pi d\left(\frac{\partial p}{\partial\pi}\right) + \int\delta dp.\end{aligned} \tag{3.150}$$

The original primitive equations (3.131)-(3.135), together with (3.136), (3.137), and (3.142)-

(3.144) can now be rewritten with the aid of (3.145), (3.146), and (3.150).

$$\frac{\partial \zeta}{\partial t} = \boldsymbol{k} \cdot \nabla \times (\boldsymbol{n}/\cos\phi) + F_{\zeta_H} \ , \tag{3.151}$$

$$\frac{\partial \delta}{\partial t} = \boldsymbol{\nabla} \cdot (\boldsymbol{n}/\cos\phi) - \nabla^2 (E + \Phi) + F_{\delta_H} \ , \tag{3.152}$$

$$\frac{\partial T}{\partial t} = \frac{-1}{a\cos^2\phi}\left[\frac{\partial}{\partial\lambda}(UT) + \cos\phi\frac{\partial}{\partial\phi}(VT)\right] + T\delta - \dot{\eta}\frac{\partial p}{\partial \eta}\frac{\partial T}{\partial p} + \frac{R}{c_p^*}T_v\frac{\omega}{p} + Q + F_{T_H} + F_{F_H} \tag{3.153}$$

$$\frac{\partial q}{\partial t} = \frac{-1}{a\cos^2\phi}\left[\frac{\partial}{\partial\lambda}(Uq) + \cos\phi\frac{\partial}{\partial\phi}(Vq)\right] + q\delta - \dot{\eta}\frac{\partial p}{\partial \eta}\frac{\partial q}{\partial p} + S, \tag{3.154}$$

$$\frac{\partial \pi}{\partial t} = -\int_{(\eta_t)}^{(1)} \boldsymbol{V} \cdot \nabla\pi d\left(\frac{\partial p}{\partial \pi}\right) - \int_{p(\eta_t)}^{p(1)} \delta dp, \tag{3.155}$$

$$n_U = +(\zeta + f)V - \dot{\eta}\frac{\partial p}{\partial \eta}\frac{\partial - U}{\partial p} - R\frac{T_v}{a}\frac{1}{p}\frac{\partial p}{\partial \pi}\frac{\partial \pi}{\partial \lambda} + F_U, \tag{3.156}$$

$$n_V = -(\zeta + f)U - \dot{\eta}\frac{\partial p}{\partial \eta}\frac{\partial - V}{\partial p}R\frac{T_v\cos\phi}{a}\frac{1}{p}\frac{\partial p}{\partial \pi}\frac{\partial \pi}{\partial \phi} + F_V, \tag{3.157}$$

$$\Phi = \Phi_s + R\int_{p(\eta)}^{p(1)} T_v d\ln p, \tag{3.158}$$

$$\dot{\eta}\frac{\partial p}{\partial \eta} = \frac{\partial p}{\partial \pi}\left[\int_{(\eta_t)}^{(1)} \boldsymbol{V} \cdot \nabla\pi d\left(\frac{\partial p}{\partial \pi}\right) + \int_{p(\eta_t)}^{p(1)} \delta dp\right] - \int_{(\eta_t)}^{(\eta)} \boldsymbol{V} \cdot \nabla\pi d\left(\frac{\partial p}{\partial \pi}\right) - \int_{p(\eta_t)}^{p(\eta)} \delta dp, \tag{3.159}$$

$$\omega = \frac{\partial p}{\partial \pi}\boldsymbol{V} \cdot \nabla\pi - \int_{(\eta_t)}^{(\eta)} \boldsymbol{V} \cdot \nabla\pi d\left(\frac{\partial p}{\partial \pi}\right) - \int_{p(\eta_t)}^{p(\eta)} \delta dp. \tag{3.160}$$

Once $\eta(p,\pi)$ is specified, then $\partial p/\partial\pi$ can be determined and (3.151)-(3.160) can be solved in a GCM.

In the actual definition of the hybrid coordinate, it is not necessary to specify $\eta(p,\pi)$ explicitly, since (3.151)-(3.160) only requires that p and $\partial p/\partial\pi$ be determined. It is sufficient to specify $p(\eta,\pi)$ and to let η be defined implicitly. This will be done in section 3.3.7. In the case that $p(\eta,\pi) = \sigma\pi$ and $\eta_t = 0$, (3.151)-(3.160) can be reduced to the set of equations solved by CCM1.

3.3.3 Continuous equations using $\partial \ln(\pi)/\partial t$

In practice, the solutions generated by solving the above equations are excessively noisy. This problem appears to arise from aliasing problems in the hydrostatic equation (3.158). The $\ln p$ integral introduces a high order nonlinearity which enters directly into the divergence equation (3.152). Large gravity waves are generated in the vicinity of steep orography, such as in the Pacific Ocean west of the Andes.

The noise problem is solved by converting the equations given above, which use π as a prognostic variable, to equations using $\Pi = \ln(\pi)$. This results in the hydrostatic equation

becoming only quadratically nonlinear except for moisture contributions to virtual temperature. Since the spectral transform method will be used to solve the equations, gradients will be obtained during the transform from wave to grid space. Outside of the prognostic equation for Π, all terms involving $\nabla\pi$ will then appear as $\pi\nabla\Pi$.

Equations (3.151)-(3.160) become:

$$\frac{\partial\zeta}{\partial t} = \boldsymbol{k}\cdot\nabla\times(\boldsymbol{n}/\cos\phi) + F_{\zeta_H}, \tag{3.161}$$

$$\frac{\partial\delta}{\partial t} = \boldsymbol{\nabla}\cdot(\boldsymbol{n}/\cos\phi) - \nabla^2(E+\Phi) + F_{\delta_H}, \tag{3.162}$$

$$\frac{\partial T}{\partial t} = \frac{-1}{a\cos^2\phi}\left[\frac{\partial}{\partial\lambda}(UT) + \cos\phi\frac{\partial}{\partial\phi}(VT)\right] + T\delta - \dot\eta\frac{\partial p}{\partial\eta}\frac{\partial T}{\partial p} + \frac{R}{c_p^*}T_v\frac{\omega}{p} + Q + F_{T_H} + F_{F_H}, \tag{3.163}$$

$$\frac{\partial q}{\partial t} = \frac{-1}{a\cos^2\phi}\left[\frac{\partial}{\partial\lambda}(Uq) + \cos\phi\frac{\partial}{\partial\phi}(Vq)\right] + q\delta - \dot\eta\frac{\partial p}{\partial\eta}\frac{\partial q}{\partial p} + S, \tag{3.164}$$

$$\frac{\partial\Pi}{\partial t} = -\int_{(\eta_t)}^{(1)}\boldsymbol{V}\cdot\nabla\Pi d\left(\frac{\partial p}{\partial\pi}\right) - \frac{1}{\pi}\int_{p(\eta_t)}^{p(1)}\delta dp, \tag{3.165}$$

$$n_U = +(\zeta+f)V - \dot\eta\frac{\partial p}{\partial\eta}\frac{\partial - U}{\partial p}R\frac{T_v}{a}\frac{\pi}{p}\frac{\partial p}{\partial\pi}\frac{\partial\Pi}{\partial\lambda} + F_U, \tag{3.166}$$

$$n_V = -(\zeta+f)U - \dot\eta\frac{\partial p}{\partial\eta}\frac{\partial - V}{\partial p}R\frac{T_v\cos\phi}{a}\frac{\pi}{p}\frac{\partial p}{\partial\pi}\frac{\partial\Pi}{\partial\phi} + F_V, \tag{3.167}$$

$$\Phi = \Phi_s + R\int_{p(\eta)}^{p(1)}T_v d\ln p, \tag{3.168}$$

$$\dot\eta\frac{\partial p}{\partial\eta} = \frac{\partial p}{\partial\pi}\left[\int_{(\eta_t)}^{(1)}\pi\boldsymbol{V}\cdot\nabla\Pi d\left(\frac{\partial p}{\partial\pi}\right) + \int_{p(\eta_t)}^{p(1)}\delta dp\right] - \int_{(\eta_t)}^{(\eta)}\pi\boldsymbol{V}\cdot\nabla\Pi d\left(\frac{\partial p}{\partial\pi}\right) - \int_{p(\eta_t)}^{p(\eta)}\delta dp, \tag{3.169}$$

$$\omega = \frac{\partial p}{\partial\pi}\pi\boldsymbol{V}\cdot\nabla\Pi - \int_{(\eta_t)}^{(\eta)}\pi\boldsymbol{V}\cdot\nabla\Pi d\left(\frac{\partial p}{\partial\pi}\right) - \int_{p(\eta_t)}^{p(\eta)}\delta dp. \tag{3.170}$$

The above equations reduce to the standard σ equations used in CCM1 if $\eta=\sigma$ and $\eta_t=0$. (Note that in this case $\partial p/\partial\pi = p/\pi = \sigma$.)

3.3.4 Semi-implicit formulation

The model described by (3.161)-(3.170), without the horizontal diffusion terms, together with boundary conditions (3.129) and (3.130), is integrated in time using the semi-implicit leapfrog scheme described below. The semi-implicit form of the time differencing will be applied to (3.162) and (3.164) without the horizontal diffusion sources, and to (3.165). In order to derive the semi-implicit form, one must linearize these equations about a reference state. Isolating the terms that will have their linear parts treated implicitly, the prognostic equations (3.161),

(3.162), and (3.165) may be rewritten as:

$$\frac{\partial \delta}{\partial t} = -RT_v \nabla^2 \ln p - \nabla^2 \Phi + X_1, \tag{3.171}$$

$$\frac{\partial T}{\partial t} = +\frac{R}{c_p^*} T_v \frac{\omega}{p} - \dot{\eta} \frac{\partial p}{\partial \eta} \frac{\partial T}{\partial p} + Y_1, \tag{3.172}$$

$$\frac{\partial \Pi}{\partial t} = -\frac{1}{\pi} \int_{p(\eta_t)}^{p(1)} \delta dp + Z_1, \tag{3.173}$$

where X_1, Y_1, Z_1 are the remaining nonlinear terms not explicitly written in (3.171)-(3.173). The terms involving Φ and ω may be expanded into vertical integrals using (3.168) and (3.170), while the $\nabla^2 \ln p$ term can be converted to $\nabla^2 \Pi$, giving:

$$\frac{\partial \delta}{\partial t} = -RT \frac{\pi}{p} \frac{\partial p}{\partial \pi} \nabla^2 \Pi - R \nabla^2 \int_{p(\eta)}^{p(1)} T d \ln p \ + X_2, \tag{3.174}$$

$$\frac{\partial T}{\partial t} = -\frac{R}{c_p} \frac{T}{p} \int_{p(\eta_t)}^{p(\eta)} \delta dp - \left[\frac{\partial p}{\partial \pi} \int_{p(\eta_t)}^{p(1)} \delta dp - \int_{p(\eta_t)}^{p(\eta)} \delta dp \right] \frac{\partial T}{\partial p} + Y_2, \tag{3.175}$$

$$\frac{\partial \Pi}{\partial t} = -\frac{1}{pi} \int_{p(\eta_t)}^{p(1)} \delta dp + Z_2. \tag{3.176}$$

Once again, only terms that will be linearized have been explicitly represented in (3.174)-(3.176), and the remaining terms are included in X_2, Y_2, and Z_2. Anticipating the linearization, T_v and c_p^* have been replaced by T and c_p in (3.174) and (3.175). Furthermore, the virtual temperature corrections are included with the other nonlinear terms.

In order to linearize (3.174)-(3.176), one specifies a reference state for temperature and pressure, then expands the equations about the reference state:

$$T = T^r + T', \tag{3.177}$$

$$\pi = \pi^r + \pi', \tag{3.178}$$

$$p = p^r(\eta, \pi^r) + p'. \tag{3.179}$$

In the special case that $p(\eta, \pi) = \sigma \pi$, (3.174)-(3.176) can be converted into equations involving only $\Pi = \ln \pi$ instead of p, and (3.178) and (3.179) are not required. This is a major difference between the hybrid coordinate scheme being developed here and the σ coordinate scheme in CCM1.

Expanding (3.174)-(3.176) about the reference state (3.177)-(3.179) and retaining only the linear terms explicitly, one obtains:

$$\frac{\partial \delta}{\partial t} = -R \nabla^2 \left[T^r \frac{\pi^r}{p^r} \left(\frac{\partial p}{\partial \pi} \right)^r \Pi + \int_{p^r(\eta)}^{p^r(1)} T' d \ln p^r + \int_{p'(\eta)}^{p'(1)} \frac{T^r}{p^r} dp' \right] + X_3, \tag{3.180}$$

$$\frac{\partial T}{\partial t} = -\frac{R}{c_p} \frac{T^r}{p^r} \int_{p^r(\eta_t)}^{p^r(\eta)} \delta dp^r - \left[\left(\frac{\partial p}{\partial \pi} \right)^r \int_{p^r(\eta_t)}^{p^r(1)} \delta dp^r - \int_{p^r(\eta_t)}^{p^r(\eta)} \delta dp^r \right] \frac{\partial T^r}{\partial p^r} + Y_3, \tag{3.181}$$

$$\frac{\partial \Pi}{\partial t} = -\frac{1}{\pi^r} \int_{p^r(\eta_t)}^{p^r(1)} \delta dp^r + Z_3. \tag{3.182}$$

Figure 3.4: Vertical level structure of CAM 5.0

The semi-implicit time differencing scheme treats the linear terms in (3.180)-(3.182) by averaging in time. The last integral in (3.180) is reduced to purely linear form by the relation

$$dp' = \pi' d \left(\frac{\partial p}{\partial \pi} \right)^r + x \,. \tag{3.183}$$

In the hybrid coordinate described below, p is a linear function of π, so x above is zero.

We will assume that centered differences are to be used for the nonlinear terms, and the linear terms are to be treated implicitly by averaging the previous and next time steps. Finite differences are used in the vertical, and are described in the following sections. At this stage only some very general properties of the finite difference representation must be specified. A layering structure is assumed in which field values are predicted on K layer midpoints denoted by an integer index, η_k (see Figure 3.4). The interface between η_k and η_{k+1} is denoted by a half-integer index, $\eta_{k+1/2}$. The model top is at $\eta_{1/2} = \eta_t$, and the Earth's surface is at $\eta_{K+1/2} = 1$. It is further assumed that vertical integrals may be written as a matrix (of order K) times a column vector representing the values of a field at the η_k grid points in the vertical. The column vectors representing a vertical column of grid points will be denoted by underbars, the matrices will be denoted by bold-faced capital letters, and superscript T will denote the vector transpose. The finite difference forms of (3.180)-(3.182) may then be written down as:

$$\begin{aligned}
\underline{\delta}^{n+1} &= \underline{\delta}^{n-1} + 2\Delta t \underline{X}^n \\
&\quad -2\Delta t R \underline{b}^r \nabla^2 \left(\frac{\Pi^{n-1} + \Pi^{n+1}}{2} - \Pi^n \right) \\
&\quad -2\Delta t R \boldsymbol{H}^r \nabla^2 \left(\frac{(\underline{T}')^{n-1} + (\underline{T}')^{n+1}}{2} - (\underline{T}')^n \right) \\
&\quad -2\Delta t R \underline{h}^r \nabla^2 \left(\frac{\Pi^{n-1} + \Pi^{n+1}}{2} - \Pi^n \right), \qquad (3.184) \\
\underline{T}^{n+1} &= \underline{T}^{n-1} + 2\Delta t \underline{Y}^n - 2\Delta t \boldsymbol{D}^r \left(\frac{\underline{\delta}^{n-1} + \underline{\delta}^{n+1}}{2} - \underline{\delta}^n \right), \qquad (3.185) \\
\Pi^{n+1} &= \Pi^{n-1} + 2\Delta t Z^n - 2\Delta t \left(\frac{\underline{\delta}^{n-1} + \underline{\delta}^{n+1}}{2} - \underline{\delta}^n \right)^T \frac{1}{\Pi^r} \underline{\Delta p}^r, \qquad (3.186)
\end{aligned}$$

where $()^n$ denotes a time varying value at time step n. The quantities $\underline{X}^n, \underline{Y}^n$, and Z^n are defined so as to complete the right-hand sides of (3.171)-(3.173). The components of $\underline{\Delta p}^r$ are given by $\Delta p^r_k = p^r_{k+\frac{1}{2}} - p^r_{k-\frac{1}{2}}$. This definition of the vertical difference operator Δ will be used in subsequent equations. The reference matrices $\boldsymbol{H}^r$ and $\boldsymbol{D}^r$, and the reference column vectors $\underline{b}^r$ and $\underline{h}^r$, depend on the precise specification of the vertical coordinate and will be defined later.

3.3.5 Energy conservation

We shall impose a requirement on the vertical finite differences of the model that they conserve the global integral of total energy *in the absence of sources and sinks*. We need to derive

equations for kinetic and internal energy in order to impose this constraint. The momentum equations (more painfully, the vorticity and divergence equations) without the F_U, F_V, F_{ζ_H} and F_{δ_H} contributions, can be combined with the continuity equation

$$\frac{\partial}{\partial t}\left(\frac{\partial p}{\partial \eta}\right) + \nabla \cdot \left(\frac{\partial p}{\partial \eta}\boldsymbol{V}\right) + \frac{\partial}{\partial \eta}\left(\frac{\partial p}{\partial \eta}\dot{\eta}\right) = 0 \tag{3.187}$$

to give an equation for the rate of change of kinetic energy:

$$\begin{aligned}\frac{\partial}{\partial t}\left(\frac{\partial p}{\partial \eta}E\right) &= -\nabla \cdot \left(\frac{\partial p}{\partial \eta}E\boldsymbol{V}\right) - \frac{\partial}{\partial \eta}\left(\frac{\partial p}{\partial \eta}E\dot{\eta}\right) \\ &\quad -\frac{RT_v}{p}\frac{\partial p}{\partial \eta}\boldsymbol{V}\cdot\nabla p - \frac{\partial p}{\partial \eta}\boldsymbol{V}\cdot\nabla\Phi \; - \; .\end{aligned} \tag{3.188}$$

The first two terms on the right-hand side of (3.188) are transport terms. The horizontal integral of the first (horizontal) transport term should be zero, and it is relatively straightforward to construct horizontal finite difference schemes that ensure this. For spectral models, the integral of the horizontal transport term will not vanish in general, but we shall ignore this problem.

The vertical integral of the second (vertical) transport term on the right-hand side of (3.188) should vanish. Since this term is obtained from the vertical advection terms for momentum, which will be finite differenced, we can construct a finite difference operator that will ensure that the vertical integral vanishes.

The vertical advection terms are the product of a vertical velocity ($\dot{\eta}\partial p/\partial\eta$) and the vertical derivative of a field ($\partial\psi/\partial p$). The vertical velocity is defined in terms of vertical integrals of fields (3.170), which are naturally taken to interfaces. The vertical derivatives are also naturally taken to interfaces, so the product is formed there, and then adjacent interface values of the products are averaged to give a midpoint value. It is the definition of the average that must be correct in order to conserve kinetic energy under vertical advection in (3.188). The derivation will be omitted here, the resulting vertical advection terms are of the form:

$$\left(\dot{\eta}\frac{\partial p}{\partial \eta}\frac{\partial \psi}{\partial p}\right)_k = \frac{1}{2\Delta p_k}\left[\left(\dot{\eta}\frac{\partial p}{\partial \eta}\right)_{k+1/2}(\psi_{k+1}-\psi_k) + \left(\dot{\eta}\frac{\partial p}{\partial \eta}\right)_{k-1/2}(\psi_k - \psi_{k-1})\right], \tag{3.189}$$

$$\Delta p_k = p_{k+1/2} - p_{k-1/2}. \tag{3.190}$$

The choice of definitions for the vertical velocity at interfaces is not crucial to the energy conservation (although not completely arbitrary), and we shall defer its definition until later. The vertical advection of temperature is not required to use (3.189) in order to conserve mass or energy. Other constraints can be imposed that result in different forms for temperature advection, but we will simply use (3.189) in the system described below.

The last two terms in (3.188) contain the conversion between kinetic and internal (potential) energy and the form drag. Neglecting the transport terms, under assumption that global integrals will be taken, noting that $\nabla p/p = \frac{\pi}{p}\frac{\partial p}{\partial \pi}\nabla\Pi$, and substituting for the geopotential using (3.168), (3.188) can be written as:

$$\begin{aligned}\frac{\partial}{\partial t}\left(\frac{\partial p}{\partial \eta}E\right) &= -RT_v\frac{\partial p}{\partial \eta}\boldsymbol{V}\cdot\left(\frac{\pi}{p}\frac{\partial p}{\partial \pi}\nabla\Pi\right) \\ &\quad -\frac{\partial p}{\partial \eta}\boldsymbol{V}\cdot\nabla\Phi_s - \frac{\partial p}{\partial \eta}\boldsymbol{V}\cdot\nabla\int_{p(\eta)}^{p(1)} RT_v d\ln p + \; \ldots\end{aligned} \tag{3.191}$$

The second term on the right-hand side of (3.192) is a source (form drag) term that can be neglected as we are only interested in internal conservation properties. The last term on the right-hand side of (3.192) can be rewritten as

$$\frac{\partial p}{\partial \eta}\boldsymbol{V}\cdot\nabla\int_{p(\eta)}^{p(1)} RT_v d\ln p = \nabla\cdot\left\{\frac{\partial p}{\partial \eta}\boldsymbol{V}\int_{p(\eta)}^{p(1)} RT_v d\ln p\right\} - \nabla\cdot\left(\frac{\partial p}{\partial \eta}\boldsymbol{V}\right)\int_{p(\eta)}^{p(1)} RT_v d\ln p\,. \quad (3.192)$$

The global integral of the first term on the right-hand side of (3.192) is obviously zero, so that (3.192) can now be written as:

$$\frac{\partial}{\partial t}\left(\frac{\partial p}{\partial \eta}E\right) = -RT_v\frac{\partial p}{\partial \eta}\boldsymbol{V}\cdot\left(\frac{\pi}{p}\frac{\partial p}{\partial \pi}\nabla\Pi\right) + \nabla\cdot\left(\frac{\partial p}{\partial \eta}\boldsymbol{V}\right)\int_{p(\eta)}^{p(1)} RT_v d\ln p + ... \quad (3.193)$$

We now turn to the internal energy equation, obtained by combining the thermodynamic equation (3.164), without the Q, F_{T_H}, and F_{F_H} terms, and the continuity equation (3.187):

$$\frac{\partial}{\partial t}\left(\frac{\partial p}{\partial \eta}c_p^* T\right) = -\nabla\cdot\left(\frac{\partial p}{\partial \eta}c_p^* T\boldsymbol{V}\right) - \frac{\partial}{\partial \eta}\left(\frac{\partial p}{\partial \eta}c_p^* T\dot{\eta}\right) + RT_v\frac{\partial p}{\partial \eta}\frac{\omega}{p}\,. \quad (3.194)$$

As in (3.188), the first two terms on the right-hand side are advection terms that can be neglected under global integrals. Using (3.144), (3.194) can be written as:

$$\frac{\partial}{\partial t}\left(\frac{\partial p}{\partial \eta}c_p^* T\right) = RT_v\frac{\partial p}{\partial \eta}\boldsymbol{V}\cdot\left(\frac{\pi}{p}\frac{\partial p}{\partial \pi}\nabla\Pi\right) - RT_v\frac{\partial p}{\partial \eta}\frac{1}{p}\int_{\eta_t}^{\eta}\nabla\cdot\left(\frac{\partial p}{\partial \eta}\boldsymbol{V}\right)d\eta + ... \quad (3.195)$$

The rate of change of total energy due to internal processes is obtained by adding (3.193) and (3.195) and must vanish. The first terms on the right-hand side of (3.193) and (3.195) obviously cancel in the continuous form. When the equations are discretized in the vertical, the terms will still cancel, providing that the same definition is used for $(1/p\;\partial p/\partial\pi)_k$ in the nonlinear terms of the vorticity and divergence equations (3.166) and (3.167), and in the ω term of (3.164) and (3.170).

The second terms on the right-hand side of (3.193) and (3.195) must also cancel in the global mean. This cancellation is enforced locally in the horizontal on the column integrals of (3.193) and (3.195), so that we require:

$$\int_{\eta_t}^{1}\left\{\nabla\cdot\left(\frac{\partial p}{\partial \eta}\boldsymbol{V}\right)\int_{p(\eta)}^{p(1)} RT_v d\ln p\right\}d\eta = \int_{\eta_t}^{1}\left\{RT_v\frac{\partial p}{\partial \eta}\frac{1}{p}\int_{\eta_t}^{\eta}\nabla\cdot\left(\frac{\partial p}{\partial \eta'}\boldsymbol{V}\right)d\eta'\right\}d\eta. \quad (3.196)$$

The inner integral on the left-hand side of (3.196) is derived from the hydrostatic equation (3.168), which we shall approximate as

$$\begin{aligned}\Phi_k &= \Phi_s + R\sum_{\ell=k}^{K} H_{k\ell}T_{v\ell},\\ &= \Phi_s + R\sum_{\ell=1}^{K} H_{k\ell}T_{v\ell}, \quad (3.197)\\ \underline{\Phi} &= \Phi_s\underline{1} + R\boldsymbol{H}\underline{T_v}, \quad (3.198)\end{aligned}$$

where $H_{k\ell} = 0$ for $\ell < k$. The quantity $\underline{1}$ is defined to be the unit vector. The inner integral on the right-hand side of (3.196) is derived from the vertical velocity equation (3.170), which we shall approximate as

$$\left(\frac{\omega}{p}\right)_k = \left(\frac{\pi}{p}\frac{\partial p}{\partial \pi}\right)_k \boldsymbol{V}_k \cdot \nabla\Pi - \sum_{\ell=1}^{K} C_{k\ell}\left[\delta_\ell \Delta p_\ell + \pi\left(\boldsymbol{V}_\ell \cdot \nabla\Pi\right)\Delta\left(\frac{\partial p}{\partial \pi}\right)_\ell\right], \tag{3.199}$$

where $C_{k\ell} = 0$ for $\ell > k$, and $C_{k\ell}$ is included as an approximation to $1/p_k$ for $\ell \leq k$ and the symbol Δ is similarly defined as in (3.190). $C_{k\ell}$ will be determined so that ω is consistent with the discrete continuity equation following Williamson and Olson [1994*a*]. Using (3.197) and (3.199), the finite difference analog of (3.196) is

$$\begin{aligned}\sum_{k=1}^{K}\left\{\frac{1}{\Delta\eta_k}\left[\delta_k \Delta p_k + \pi\left(\boldsymbol{V}_k \cdot \nabla\Pi\right)\Delta\left(\frac{\partial p}{\partial \pi}\right)_k\right] R\sum_{\ell=1}^{K} H_{k\ell}T_{v\ell}\right\}\Delta\eta_k \\ = \sum_{k=1}^{K}\left\{RT_{vk}\frac{\Delta p_k}{\Delta\eta_k}\sum_{\ell=1}^{K} C_{k\ell}\left[\delta_\ell \Delta p_\ell + \pi\left(\boldsymbol{V}_\ell \cdot \nabla\Pi\right)\Delta\left(\frac{\partial p}{\partial \pi}\right)_\ell\right]\right\}\Delta\eta_k,\end{aligned} \tag{3.200}$$

where we have used the relation

$$\nabla \cdot \boldsymbol{V}(\partial p/\partial\eta)_k = \left[\delta_k \Delta p_k + \pi\left(\boldsymbol{V}_k \cdot \nabla\Pi\right)\Delta\left(\partial p/\partial\pi\right)_k\right]/\Delta\eta_k \tag{3.201}$$

(see 3.150). We can now combine the sums in (3.200) and simplify to give

$$\begin{aligned}\sum_{k=1}^{K}\sum_{\ell=1}^{K}\left\{\left[\delta_k \Delta p_k + \pi\left(\boldsymbol{V}_k \cdot \nabla\Pi\right)\Delta\left(\frac{\partial p}{\partial \pi}\right)_k\right] H_{k\ell}T_{v\ell}\right\} \\ = \sum_{k=1}^{K}\sum_{\ell=1}^{K}\left\{\left[\delta_\ell \Delta p_\ell + \pi\left(\boldsymbol{V}_\ell \cdot \nabla\Pi\right)\Delta\left(\frac{\partial p}{\partial \pi}\right)_\ell\right]\Delta p_k C_{k\ell}T_{vk}\right\}.\end{aligned} \tag{3.202}$$

Interchanging the indexes on the left-hand side of (3.202) will obviously result in identical expressions if we require that

$$H_{k\ell} = C_{\ell k}\Delta p_\ell. \tag{3.203}$$

Given the definitions of vertical integrals in (3.198) and (3.199) and of vertical advection in (3.189) and (3.190) the model will conserve energy as long as we require that $\boldsymbol{C}$ and $\boldsymbol{H}$ satisfy (3.203). We are, of course, still neglecting lack of conservation due to the truncation of the horizontal spherical harmonic expansions.

3.3.6 Horizontal diffusion

CAM 5.0 contains a horizontal diffusion term for T, ζ, and δ to prevent spectral blocking and to provide reasonable kinetic energy spectra. The horizontal diffusion operator in CAM 5.0 is also used to ensure that the CFL condition is not violated in the upper layers of the model. The horizontal diffusion is a linear ∇^2 form on η surfaces in the top three levels of the model and a linear ∇^4 form with a partial correction to pressure surfaces for temperature elsewhere.

The ∇^2 diffusion near the model top is used as a simple sponge to absorb vertically propagating planetary wave energy and also to control the strength of the stratospheric winter jets. The ∇^2 diffusion coefficient has a vertical variation which has been tuned to give reasonable Northern and Southern Hemisphere polar night jets.

In the top three model levels, the ∇^2 form of the horizontal diffusion is given by

$$F_{\zeta_H} = K^{(2)} \left[\nabla^2 (\zeta + f) + 2 (\zeta + f) / a^2\right], \tag{3.204}$$

$$F_{\delta_H} = K^{(2)} \left[\nabla^2 \delta + 2(\delta/a^2)\right], \tag{3.205}$$

$$F_{T_H} = K^{(2)} \nabla^2 T. \tag{3.206}$$

Since these terms are linear, they are easily calculated in spectral space. The undifferentiated correction term is added to the vorticity and divergence diffusion operators to prevent damping of uniform ($n = 1$) rotations [Orszag, 1974; Bourke et al., 1977]. The ∇^2 form of the horizontal diffusion is applied *only* to pressure surfaces in the standard model configuration.

The horizontal diffusion operator is better applied to pressure surfaces than to terrain-following surfaces (applying the operator on isentropic surfaces would be still better). Although the governing system of equations derived above is designed to reduce to pressure surfaces above some level, problems can still occur from diffusion along the lower surfaces. Partial correction to pressure surfaces of harmonic horizontal diffusion ($\partial\xi/\partial t = K\nabla^2\xi$) can be included using the relations:

$$\begin{aligned} \nabla_p \xi &= \nabla_\eta \xi - p \frac{\partial \xi}{\partial p} \nabla_\eta \ln p \\ \nabla_p^2 \xi &= \nabla_\eta^2 \xi - p \frac{\partial \xi}{\partial p} \nabla_\eta^2 \ln p - 2 \nabla_\eta \left(\frac{\partial \xi}{\partial p}\right) \cdot \nabla_\eta p + \frac{\partial^2 \xi}{\partial^2 p} \nabla_\eta^2 p \,. \end{aligned} \tag{3.207}$$

Retaining only the first two terms above gives a correction to the η surface diffusion which involves only a vertical derivative and the Laplacian of log surface pressure,

$$\nabla_p^2 \xi = \nabla_\eta^2 \xi - \pi \frac{\partial \xi}{\partial p} \frac{\partial p}{\partial \pi} \nabla^2 \Pi + \ldots \tag{3.208}$$

Similarly, biharmonic diffusion can be partially corrected to pressure surfaces as:

$$\nabla_p^4 \xi = \nabla_\eta^4 \xi - \pi \frac{\partial \xi}{\partial p} \frac{\partial p}{\partial \pi} \nabla^4 \Pi + \ldots \tag{3.209}$$

The bi-harmonic ∇^4 form of the diffusion operator is applied at all other levels (generally throughout the troposphere) as

$$F_{\zeta_H} = -K^{(4)} \left[\nabla^4 (\zeta + f) - (\zeta + f) \left(2/a^2\right)^2\right], \tag{3.210}$$

$$F_{\delta_H} = -K^{(4)} \left[\nabla^4 \delta - \delta (2/a^2)^2\right], \tag{3.211}$$

$$F_{T_H} = -K^{(4)} \left[\nabla^4 T - \pi \frac{\partial T}{\partial p} \frac{\partial p}{\partial \pi} \nabla^4 \Pi\right]. \tag{3.212}$$

The second term in F_{T_H} consists of the leading term in the transformation of the ∇^4 operator to pressure surfaces. It is included to offset partially a spurious diffusion of T over mountains.

As with the ∇^2 form, the ∇^4 operator can be conveniently calculated in spectral space. The correction term is then completed after transformation of T and $\nabla^4\Pi$ back to grid–point space. As with the ∇^2 form, an undifferentiated term is added to the vorticity and divergence diffusion operators to prevent damping of uniform rotations.

3.3.7 Finite difference equations

The governing equations are solved using the spectral method in the horizontal, so that only the vertical and time differences are presented here. The dynamics includes horizontal diffusion of $T, (\zeta + f)$, and δ. Only T has the leading term correction to pressure surfaces. Thus, equations that include the terms in this time split sub-step are of the form

$$\frac{\partial \psi}{\partial t} = \mathrm{Dyn}\,(\psi) - (-1)^i K^{(2i)} \nabla_\eta^{2i} \psi\,, \tag{3.213}$$

for $(\zeta + f)$ and δ, and

$$\frac{\partial T}{\partial t} = \mathrm{Dyn}\,(T) - (-1)^i K^{(2i)} \left\{ \nabla_\eta^{2i} T - \pi \frac{\partial T}{\partial p} \frac{\partial p}{\partial \pi} \nabla^{2i} \Pi \right\}\,, \tag{3.214}$$

where $i = 1$ in the top few model levels and $i = 2$ elsewhere (generally within the troposphere). These equations are further subdivided into time split components:

$$\psi^{n+1} = \psi^{n-1} + 2\Delta t\ \mathrm{Dyn}\left(\psi^{n+1}, \psi^n, \psi^{n-1}\right)\,, \tag{3.215}$$

$$\psi^* = \psi^{n+1} - 2\Delta t\ (-1)^i K^{(2i)} \nabla_\eta^{2i} \left(\psi^{*n+1}\right)\,, \tag{3.216}$$

$$\hat{\psi}^{n+1} = \psi^*\,, \tag{3.217}$$

for $(\zeta + f)$ and δ, and

$$T^{n+1} = T^{n-1} + 2\Delta t\ \mathrm{Dyn}\left(T^{n+1}, T^n, T^{n-1}\right) \tag{3.218}$$

$$T^* = T^{n+1} - 2\Delta t\ \ (-1)^i\, K^{(2i)} \nabla^{2i} \eta\,(T^*)\,, \tag{3.219}$$

$$\hat{T}^{n+1} = T^* + 2\Delta t\ \ (-1)^i\, K^{(2i)} \pi \frac{\partial T^*}{\partial p} \frac{\partial p}{\partial \pi} \nabla^{2i}\,\Pi\,, \tag{3.220}$$

for T, where in the standard model i only takes the value 2 in (3.220). The first step from $(\ )^{n-1}$ to $(\ )^{n+1}$ includes the transformation to spectral coefficients. The second step from $(\ )^{n+1}$ to $(\hat{\ })^{n+1}$ for δ and ζ, or $(\ )^{n+1}$ to $(\ )^*$ for T, is done on the spectral coefficients, and the final step from $(\ )^*$ to $(\hat{\ })^{n+1}$ for T is done after the inverse transform to the grid point representation.

The following finite-difference description details only the forecast given by (3.215) and (3.218). The finite-difference form of the forecast equation for water vapor will be presented later in Section 3c. The general structure of the complete finite difference equations is determined by the semi-implicit time differencing and the energy conservation properties described above. In order to complete the specification of the finite differencing, we require a definition of the vertical coordinate. The actual specification of the generalized vertical coordinate takes advantage of the structure of the equations (3.161)-(3.170). The equations can be finite-differenced in the vertical and, in time, without having to know the value of η anywhere. The quantities that must

be known are p and $\partial p/\partial\pi$ at the grid points. Therefore the coordinate is defined implicitly through the relation:

$$p(\eta,\pi) = A(\eta)p_0 + B(\eta)\pi\,, \tag{3.221}$$

which gives

$$\frac{\partial p}{\partial \pi} = B(\eta)\,. \tag{3.222}$$

A set of levels η_k may be specified by specifying A_k and B_k, such that $\eta_k \equiv A_k + B_k$, and difference forms of (3.161)-(3.170) may be derived.

The finite difference forms of the Dyn operator (3.161)-(3.170), including semi-implicit time integration are:

$$\underline{\zeta}^{n+1} = \underline{\zeta}^{n-1} + 2\Delta t \boldsymbol{k}\cdot\nabla\times(\underline{\boldsymbol{n}}^n/\cos\phi)\,, \tag{3.223}$$

$$\begin{aligned}\underline{\delta}^{n+1} &= \underline{\delta}^{n-1} + 2\Delta t\left[\nabla\cdot(\underline{\boldsymbol{n}}^n/\cos\phi) - \nabla^2\left(\underline{E}^n + \Phi_s\underline{1} + R\boldsymbol{H}^n(\underline{T_v}')^n\right)\right]\\ &\quad -2\Delta t R\boldsymbol{H}^r\nabla^2\left(\frac{(\underline{T}')^{n-1}+(\underline{T}')^{n+1}}{2} - (\underline{T}')^n\right)\\ &\quad -2\Delta t R\left(\underline{b}^r + \underline{h}^r\right)\nabla^2\left(\frac{\Pi^{n-1}+\Pi^{n+1}}{2} - \Pi^n\right),\end{aligned} \tag{3.224}$$

$$\begin{aligned}(\underline{T}')^{n+1} &= (\underline{T}')^{n-1} - 2\Delta t\left[\frac{1}{a\cos^2\phi}\frac{\partial}{\partial\lambda}(\underline{UT}')^n + \frac{1}{a\cos\phi}\frac{\partial}{\partial\phi}(\underline{VT}')^n - \underline{\Gamma}^n\right]\\ &\quad -2\Delta t\boldsymbol{D}^r\left(\frac{\underline{\delta}^{n-1}+\underline{\delta}^{n+1}}{2} - \underline{\delta}^n\right)\end{aligned} \tag{3.225}$$

$$\begin{aligned}\Pi^{n+1} &= \Pi^{n-1} - 2\Delta t\frac{1}{\pi^n}\left((\underline{\delta}^n)^T\,\underline{\Delta p}^n + (\underline{\boldsymbol{V}}^n)^T\cdot\nabla\Pi^n\pi^n\underline{\Delta B}\right)\\ &\quad -2\Delta t\left(\frac{\underline{\delta}^{n-1}+\underline{\delta}^{n+1}}{2} - \underline{\delta}^n\right)^T\frac{1}{\pi^r}\underline{\Delta p}^r,\end{aligned} \tag{3.226}$$

$$\begin{aligned}(n_U)_k &= (\zeta_k + f)\,V_k - RT_{vk}\left(\frac{1}{p}\frac{\partial p}{\partial\pi}\right)_k\pi\frac{1}{a}\frac{\partial\Pi}{\partial\lambda}\\ &\quad -\frac{1}{2\Delta p_k}\left[\left(\dot\eta\frac{\partial p}{\partial\eta}\right)_{k+1/2}(U_{k+1}-U_k) + \left(\dot\eta\frac{\partial p}{\partial\eta}\right)_{k-1/2}(U_k - U_{k-1})\right]\\ &\quad +(F_U)_k\ ,\end{aligned} \tag{3.227}$$

$$\begin{aligned}(n_V)_k &= -(\zeta_k + f)\,U_k - RT_{vk}\left(\frac{1}{p}\frac{\partial p}{\partial\pi}\right)_k\pi\frac{\cos\phi}{a}\frac{\partial\Pi}{\partial\phi}\\ &\quad -\frac{1}{2\Delta p_k}\left[\left(\dot\eta\frac{\partial p}{\partial\eta}\right)_{k+1/2}(V_{k+1}-V_k) + \left(\dot\eta\frac{\partial p}{\partial\eta}\right)_{k-1/2}(V_k - V_{k-1})\right]\\ &\quad +(F_V)_k\ ,\end{aligned} \tag{3.228}$$

$$\begin{aligned}\Gamma_k &= T'_k\delta_k + \frac{RT_{vk}}{(c_p^*)_k}\left(\frac{\omega}{p}\right)_k - Q\\ &\quad -\frac{1}{2\Delta p_k}\left[\left(\dot\eta\frac{\partial p}{\partial\eta}\right)_{k+1/2}(T_{k+1}-T_k) + \left(\dot\eta\frac{\partial p}{\partial\eta}\right)_{k-1/2}(T_k - T_{k-1})\right],\end{aligned} \tag{3.229}$$

$$E_k = (u_k)^2 + (v_k)^2, \tag{3.230}$$

$$\frac{RT_{vk}}{(c_p^*)_k} = \frac{R}{c_p}\left(\frac{T_k^r + T_{vk}'}{1+\left(\frac{c_{pv}}{c_p}-1\right)q_k}\right), \tag{3.231}$$

$$\begin{aligned}\left(\dot{\eta}\frac{\partial p}{\partial \eta}\right)_{k+1/2} &= B_{k+1/2}\sum_{\ell=1}^{K}\left[\delta_\ell \Delta p_\ell + \boldsymbol{V}_\ell \cdot \pi\nabla\Pi\Delta B_\ell\right] \\ &\quad -\sum_{\ell=1}^{k}\left[\delta_\ell \Delta p_\ell + \boldsymbol{V}_\ell \cdot \pi\nabla\Pi\Delta B_\ell\right],\end{aligned} \tag{3.232}$$

$$\left(\frac{\omega}{p}\right)_k = \left(\frac{1}{p}\frac{\partial p}{\partial \pi}\right)_k \boldsymbol{V}_k \cdot \pi\nabla\Pi - \sum_{\ell=1}^{k} C_{k\ell}\left[\delta_\ell \Delta p_\ell + \boldsymbol{V}_\ell \cdot \pi\nabla\Pi\Delta B_\ell\right], \tag{3.233}$$

$$C_{k\ell} = \begin{cases} \frac{1}{p_k}, & \ell < k \\ \frac{1}{2p_k}, & \ell = k, \end{cases} \tag{3.234}$$

$$H_{k\ell} = C_{\ell k}\Delta p_\ell, \tag{3.235}$$

$$\begin{aligned}D_{k\ell}^r &= \Delta p_\ell^r \frac{R}{c_p} T_k^r C_{\ell k}^r + \frac{\Delta p_\ell^r}{2\Delta p_k^r}\left(T_k^r - T_{k-1}^r\right)\left(\epsilon_{k\ell+1} - B_{k-1/2}\right) \\ &\quad + \frac{\Delta p_\ell^r}{2\Delta p_k^r}\left(T_{k+1}^r - T_k^r\right)\left(\epsilon_{k\ell} - B_{k+1/2}\right),\end{aligned} \tag{3.236}$$

$$\frac{\epsilon_{k\ell}}{R} = \begin{cases} 1, & \ell \le k \\ 0, & \ell > k, \end{cases} \tag{3.237}$$

where notation such as $(\underline{UT}')^n$ denotes a column vector with components $(U_k T_k')^n$. In order to complete the system, it remains to specify the reference vector $\underline{h}^r$, together with the term $(1/p\,\partial p/\partial\pi)$, which results from the pressure gradient terms and also appears in the semi-implicit reference vector $\underline{b}^r$:

$$\left(\frac{1}{p}\frac{\partial p}{\partial \pi}\right)_k = \left(\frac{1}{p}\right)_k \left(\frac{\partial p}{\partial \pi}\right)_k = \frac{B_k}{p_k}, \tag{3.238}$$

$$\underline{b}^r = \underline{T}^r, \tag{3.239}$$

$$\underline{h}^r = 0. \tag{3.240}$$

The matrices $\boldsymbol{C}^n$ and $\boldsymbol{H}^n$ (*i.e.* with components $C_{k\ell}$ and $H_{k\ell}$) must be evaluated at each time step and each point in the horizontal. It is more efficient computationally to substitute the definitions of these matrices into (3.224) and (3.233) at the cost of some loss of generality in the code. The finite difference equations have been written in the form (3.223)-(3.240) because this form is quite general. For example, the equations solved by Simmons and Strüfing [1981] at ECMWF can be obtained by changing only the vectors and hydrostatic matrix defined by (3.237)-(3.240).

3.3.8 Time filter

The time step is completed by applying a recursive time filter originally designed by [Robert, 1966] and later studied by [Asselin, 1972].

$$\overline{\psi}^n = \psi^n + \alpha\left(\overline{\psi}^{n-1} - 2\psi^n + \psi^{n+1}\right) \tag{3.241}$$

3.3.9 Spectral transform

The spectral transform method is used in the horizontal exactly as in CCM1. As shown earlier, the vertical and temporal aspects of the model are represented by finite–difference approximations. The horizontal aspects are treated by the spectral–transform method, which is described in this section. Thus, at certain points in the integration, the prognostic variables $(\zeta + f), \delta, T,$ and Π are represented in terms of coefficients of a truncated series of spherical harmonic functions, while at other points they are given by grid–point values on a corresponding Gaussian grid. In general, physical parameterizations and nonlinear operations are carried out in grid–point space. Horizontal derivatives and linear operations are performed in spectral space. Externally, the model appears to the user to be a grid–point model, as far as data required and produced by it. Similarly, since all nonlinear parameterizations are developed and carried out in grid–point space, the model also appears as a grid–point model for the incorporation of physical parameterizations, and the user need not be too concerned with the spectral aspects. For users interested in diagnosing the balance of terms in the evolution equations, however, the details are important and care must be taken to understand which terms have been spectrally truncated and which have not. The algebra involved in the spectral transformations has been presented in several publications [Daley et al., 1976; Bourke et al., 1977; Machenhauer, 1979]. In this report, we present only the details relevant to the model code; for more details and general philosophy, the reader is referred to these earlier papers.

3.3.10 Spectral algorithm overview

The horizontal representation of an arbitrary variable ψ consists of a truncated series of spherical harmonic functions,

$$\psi(\lambda, \mu) = \sum_{m=-M}^{M} \sum_{n=|m|}^{\mathcal{N}(m)} \psi_n^m P_n^m(\mu) e^{im\lambda}, \tag{3.242}$$

where $\mu = \sin\phi$, M is the highest Fourier wavenumber included in the east–west representation, and $\mathcal{N}(m)$ is the highest degree of the associated Legendre polynomials for longitudinal wavenumber m. The properties of the spherical harmonic functions used in the representation can be found in the review by Machenhauer [1979]. The model is coded for a general pentagonal truncation, illustrated in Figure 3.5, defined by three parameters: $M, K,$ and N, where M is defined above, K is the highest degree of the associated Legendre polynomials, and N is the highest degree of the Legendre polynomials for $m = 0$. The common truncations are subsets of this pentagonal case:

$$\begin{aligned} \text{Triangular}: &\quad M = N = K, \\ \text{Rhomboidal}: &\quad K = N + M, \\ \text{Trapezoidal}: &\quad N = K > M. \end{aligned} \tag{3.243}$$

The quantity $\mathcal{N}(m)$ in (3.242) represents an arbitrary limit on the two-dimensional wavenumber n, and for the pentagonal truncation described above is simply given by $\mathcal{N}(m) = \min(N + |m|, K)$.

Figure 3.5: Pentagonal truncation parameters

The associated Legendre polynomials used in the model are normalized such that

$$\int_{-1}^{1} \left[P_n^m(\mu)\right]^2 d\mu = 1. \tag{3.244}$$

With this normalization, the Coriolis parameter f is

$$f = \frac{\Omega}{\sqrt{0.375}} P_1^o, \tag{3.245}$$

1498 which is required for the absolute vorticity.

The coefficients of the spectral representation (3.242) are given by

$$\psi_n^m = \int_{-1}^{1} \frac{1}{2\pi} \int_0^{2\pi} \psi(\lambda,\mu) e^{-im\lambda} d\lambda P_n^m(\mu) d\mu. \tag{3.246}$$

The inner integral represents a Fourier transform,

$$\psi^m(\mu) = \frac{1}{2\pi} \int_0^{2\pi} \psi(\lambda,\mu) e^{-im\lambda} d\lambda, \tag{3.247}$$

which is performed by a Fast Fourier Transform (FFT) subroutine. The outer integral is performed via Gaussian quadrature,

$$\psi_n^m = \sum_{j=1}^{J} \psi^m(\mu_j) P_n^m(\mu_j) w_j, \tag{3.248}$$

where μ_j denotes the Gaussian grid points in the meridional direction, w_j the Gaussian weight at point μ_j, and J the number of Gaussian grid points from pole to pole. The Gaussian grid points (μ_j) are given by the roots of the Legendre polynomial $P_J(\mu)$, and the corresponding weights are given by

$$w_j = \frac{2(1-\mu_j^2)}{\left[J\ P_{J-1}(\mu_j)\right]^2}. \tag{3.249}$$

The weights themselves satisfy

$$\sum_{j=1}^{J} w_j = 2.0\ . \tag{3.250}$$

The Gaussian grid used for the north–south transformation is generally chosen to allow unaliased computations of quadratic terms only. In this case, the number of Gaussian latitudes J must satisfy

$$J \geq (2N + K + M + 1)/2 \quad \text{for } M \leq 2(K-N)\,, \tag{3.251}$$

$$J \geq (3K+1)/2 \quad \text{for } M \geq 2(K-N)\,. \tag{3.252}$$

For the common truncations, these become

$$J \geq (3K+1)/2 \qquad \text{for triangular and trapezoidal,} \tag{3.253}$$

$$J \geq (3N+2M+1)/2 \qquad \text{for rhomboidal.} \tag{3.254}$$

In order to allow exact Fourier transform of quadratic terms, the number of points P in the east–west direction must satisfy

$$P \geq 3M+1 \ . \tag{3.255}$$

The actual values of J and P are often not set equal to the lower limit in order to allow use of more efficient transform programs.

Although in the next section of this model description, we continue to indicate the Gaussian quadrature as a sum from pole to pole, the code actually deals with the symmetric and antisymmetric components of variables and accumulates the sums from equator to pole only. The model requires an even number of latitudes to easily use the symmetry conditions. This may be slightly inefficient for some spectral resolutions. We define a new index, which goes from $-I$ at the point next to the south pole to $+I$ at the point next to the north pole and not including 0 (there are no points at the equator or pole in the Gaussian grid), *i.e.,* let $I = J/2$ and $i = j - J/2$ for $j \geq J/2+1$ and $i = j - J/2 - 1$ for $j \leq J/2$; then the summation in (3.248) can be rewritten as

$$\psi_n^m = \sum_{i=-I,\, i\neq 0}^{I} \psi^m(\mu_i) P_n^m(\mu_i) w_i. \tag{3.256}$$

The symmetric (even) and antisymmetric (odd) components of ψ^m are defined by

$$(\psi_E)_i^m = \frac{1}{2}\left(\psi_i^m + \psi_{-i}^m\right),$$

$$(\psi_O)_i^m = \frac{1}{2}\left(\psi_i^m - \psi_{-i}^m\right). \tag{3.257}$$

Since w_i is symmetric about the equator, (3.256) can be rewritten to give formulas for the coefficients of even and odd spherical harmonics:

$$\psi_n^m = \begin{cases} \sum_{i=1}^{I} (\psi_E)_i^m (\mu_i) P_n^m(\mu_i) 2w_i & \text{for } n-m \text{ even,} \\ \sum_{i=1}^{I} (\psi_O)_i^m (\mu_i) P_n^m(\mu_i) 2w_i & \text{for } n-m \text{ odd.} \end{cases} \tag{3.258}$$

The model uses the spectral transform method [Machenhauer, 1979] for all nonlinear terms. However, the model can be thought of as starting from grid–point values at time t (consistent with the spectral representation) and producing a forecast of the grid–point values at time $t+\Delta t$ (again, consistent with the spectral resolution). The forecast procedure involves computation of the nonlinear terms including physical parameterizations at grid points; transformation via Gaussian quadrature of the nonlinear terms from grid–point space to spectral space; computation of the spectral coefficients of the prognostic variables at time $t+\Delta t$ (with the implied spectral truncation to the model resolution); and transformation back to grid–point space. The details of the equations involved in the various transformations are given in the next section.

3.3.11 Combination of terms

In order to describe the transformation to spectral space, for each equation we first group together all undifferentiated explicit terms, all explicit terms with longitudinal derivatives, and all explicit terms with meridional derivatives appearing in the Dyn operator. Thus, the vorticity equation (3.223) is rewritten

$$\underline{(\zeta+f)}^{n+1} = \underline{V} + \frac{1}{a(1-\mu^2)}\left[\frac{\partial}{\partial\lambda}(\underline{V}_\lambda) - (1-\mu^2)\frac{\partial}{\partial\mu}(\underline{V}_\mu)\right], \tag{3.259}$$

where the explicit forms of the vectors $\underline{V}, \underline{V}_\lambda$, and $\underline{V}_\mu$ are given as

$$\begin{aligned} \underline{V} &= \underline{(\zeta+f)}^{n-1}, & (3.260)\\ \underline{V}_\lambda &= 2\Delta t\, \underline{n}_V^n, & (3.261)\\ \underline{V}_\mu &= 2\Delta t\, \underline{n}_U^n. & (3.262) \end{aligned}$$

The divergence equation (3.224) is

$$\begin{aligned} \underline{\delta}^{n+1} &= \underline{D} + \frac{1}{a(1-\mu^2)}\left[\frac{\partial}{\partial\lambda}(\underline{D}_\lambda) + (1-\mu^2)\frac{\partial}{\partial\mu}(\underline{D}_\mu)\right] - \nabla^2\underline{D}_\nabla \\ &\quad -\Delta t\nabla^2(R\boldsymbol{H}^r\underline{T}'^{n+1} + R\,(\underline{b}^r + \underline{h}^r)\,\Pi^{n+1}). \end{aligned} \tag{3.263}$$

The mean component of the temperature is not included in the next–to–last term since the Laplacian of it is zero. The thermodynamic equation (3.226) is

$$\underline{T}'^{n+1} = \underline{T} - \frac{1}{a(1-\mu^2)}\left[\frac{\partial}{\partial\lambda}(\underline{T}_\lambda) + (1-\mu^2)\frac{\partial}{\partial\mu}(\underline{T}_\mu) -\right] - \Delta t\boldsymbol{D}^r\,\underline{\delta}^{n+1}. \tag{3.264}$$

The surface–pressure tendency (3.226) is

$$\Pi^{n+1} = PS - \frac{\Delta t}{\pi^r}\left(\underline{\Delta p}^r\right)^T\underline{\delta}^{n+1}. \tag{3.265}$$

The grouped explicit terms in (3.263)–(3.265) are given as follows. The terms of (3.263) are

$$\begin{aligned} \underline{D} &= \underline{\delta}^{n-1}, & (3.266)\\ \underline{D}_\lambda &= 2\Delta t\, \underline{n}_U^n, & (3.267)\\ \underline{D}_\mu &= 2\Delta t\, \underline{n}_V^n, & (3.268) \end{aligned}$$

$$\begin{aligned} \underline{D}_\nabla &= 2\Delta t\left[\underline{E}^n + \Phi_s\underline{1} + R\boldsymbol{H}^r\underline{T}'^n\right] \\ &\quad + \Delta t\left[R\boldsymbol{H}^r\left(\left(\underline{T}'\right)^{n-1} - 2(\underline{T}')^n\right) + R\,(\underline{b}^r + \underline{h}^r)\left(\Pi^{n-1} - 2\Pi^n\right)\right]. \end{aligned} \tag{3.269}$$

The terms of (3.264) are

$$\begin{aligned} \underline{T} &= (\underline{T}')^{n-1} + 2\Delta t\,\underline{\Gamma}^n - \Delta t\boldsymbol{D}^r\left[\underline{\delta}^{n-1} - 2\underline{\delta}^n\right], & (3.270)\\ \underline{T}_\lambda &= 2\Delta t\underline{(UT')}^n, & (3.271)\\ \underline{T}_\mu &= 2\Delta t\underline{(VT')}^n. & (3.272) \end{aligned}$$

The nonlinear term in (3.265) is

$$PS = \Pi^{n-1} - 2\Delta t \frac{1}{\pi^n}\left[\left(\underline{\delta}^n\right)^T\left(\underline{\Delta p}^n\right) + \left(\underline{\boldsymbol{V}}^n\right)^T \nabla\Pi^n \pi^n \underline{\Delta B}\right]$$
$$- \Delta t\left[\left(\underline{\Delta p}^r\right)^T \frac{1}{\pi^r}\right]\left[\underline{\delta}^{n-1} - 2\underline{\delta}^n\right] \ . \tag{3.273}$$

3.3.12 Transformation to spectral space

Formally, Equations (3.259)-(3.265) are transformed to spectral space by performing the operations indicated in (3.274) to each term. We see that the equations basically contain three types of terms, for example, in the vorticity equation the undifferentiated term $\underline{V}$, the longitudinally differentiated term $\underline{V}_\lambda$, and the meridionally differentiated term $\underline{V}_\mu$. All terms in the original equations were grouped into one of these terms on the Gaussian grid so that they could be transformed at once.

Transformation of the undifferentiated term is obtained by straightforward application of (3.246)-(3.248),

$$\{\underline{V}\}_n^m = \sum_{j=1}^{J} \underline{V}^m(\mu_j) P_n^m(\mu_j) w_j, \tag{3.274}$$

where $\underline{V}^m(\mu_j)$ is the Fourier coefficient of $\underline{V}$ with wavenumber m at the Gaussian grid line μ_j. The longitudinally differentiated term is handled by integration by parts, using the cyclic boundary conditions,

$$\left\{\frac{\partial}{\partial\lambda}(\underline{V}_\lambda)\right\}^m = \frac{1}{2\pi}\int_o^{2\pi} \frac{\partial \underline{V}_\lambda}{\partial\lambda} e^{-im\lambda} d\lambda, \tag{3.275}$$

$$= im\frac{1}{2\pi}\int_o^{2\pi} \underline{V}_\lambda e^{-im\lambda} d\lambda, \tag{3.276}$$

$$\tag{3.277}$$

so that the Fourier transform is performed first, then the differentiation is carried out in spectral space. The transformation to spherical harmonic space then follows (3.280):

$$\left\{\frac{1}{a(1-\mu^2)}\frac{\partial}{\partial\lambda}(\underline{V}_\lambda)\right\}_n^m = im\sum_{j=1}^{J} \underline{V}_\lambda^m(\mu_j)\frac{P_n^m(\mu_j)}{a(1-\mu_j^2)} w_j, \tag{3.278}$$

where $\underline{V}_\lambda^m(\mu_j)$ is the Fourier coefficient of $\underline{V}_\lambda$ with wavenumber m at the Gaussian grid line μ_j.

The latitudinally differentiated term is handled by integration by parts using zero boundary conditions at the poles:

$$\left\{\frac{1}{a(1-\mu^2)}(1-\mu^2)\frac{\partial}{\partial\mu}(\underline{V}_\mu)\right\}_n^m = \int_{-1}^{1} \frac{1}{a(1-\mu^2)}(1-\mu^2)\frac{\partial}{\partial\mu}(\underline{V}_\mu)^m P_n^m d\mu, \tag{3.279}$$

$$= -\int_{-1}^{1} \frac{1}{a(1-\mu^2)}(\underline{V}_\mu)^m (1-\mu^2)\frac{dP_n^m}{d\mu} d\mu. \tag{3.280}$$

Defining the derivative of the associated Legendre polynomial by

$$H_n^m = (1-\mu^2)\frac{dP_n^m}{d\mu}, \tag{3.281}$$

(3.283) can be written

$$\left\{\frac{1}{a(1-\mu^2)}(1-\mu^2)\frac{\partial}{\partial\mu}(\underline{V}_\mu)\right\}_n^m = -\sum_{j=1}^{J}(\underline{V}_\mu)^m\frac{H_n^m(\mu_j)}{a(1-\mu_j^2)}w_j. \tag{3.282}$$

Similarly, the ∇^2 operator in the divergence equation can be converted to spectral space by sequential integration by parts and then application of the relationship

$$\nabla^2 P_n^m(\mu)e^{im\lambda} = \frac{-n(n+1)}{a^2}P_n^m(\mu)e^{im\lambda}, \tag{3.283}$$

to each spherical harmonic function individually so that

$$\left\{\nabla^2\underline{D}_\nabla\right\}_n^m = \frac{-n(n+1)}{a^2}\sum_{j=1}^{J}\underline{D}_\nabla^m(\mu_j)P_n^m(\mu_j)w_j, \tag{3.284}$$

where $\underline{D}_\nabla^m(\mu)$ is the Fourier coefficient of the original grid variable $\underline{D}_\nabla$.

3.3.13 Solution of semi-implicit equations

The prognostic equations can be converted to spectral form by summation over the Gaussian grid using (3.274), (3.278), and (3.282). The resulting equation for absolute vorticity is

$$\underline{(\zeta+f)}_n^m = \underline{VS}_n^m, \tag{3.285}$$

where $\underline{(\zeta+f)}_n^m$ denotes a spherical harmonic coefficient of $\underline{(\zeta+f)}^{n+1}$, and the form of $\underline{VS}_n^m$, as a summation over the Gaussian grid, is given as

$$\underline{VS}_n^m = \sum_{j=1}^{J}\left[\underline{V}^m(\mu_j)P_n^m(\mu_j) + im\underline{V}_\lambda^m(\mu_j)\frac{P_n^m(\mu_j)}{a(1-\mu_j^2)} + \underline{V}_\mu^m(\mu_j)\frac{H_n^m(\mu_j)}{a(1-\mu_j^2)}\right]w_j. \tag{3.286}$$

The spectral form of the divergence equation (3.263) becomes

$$\underline{\delta}_n^m = \underline{DS}_n^m + \Delta t\frac{n(n+1)}{a^2}\left[R\boldsymbol{H}^r\underline{T}_n'^m + R\left(\underline{b}^r + \underline{h}^r\right)\Pi_n^m\right], \tag{3.287}$$

where $\underline{\delta}_n^m$, $\underline{T}_n'^m$, and Π_n^m are spectral coefficients of $\underline{\delta}^{n+1}$, $\underline{T}'^{n+1}$, and Π^{n+1}. The Laplacian of the total temperature in (3.263) is replaced by the equivalent Laplacian of the perturbation temperature in (3.287). $\underline{DS}_n^m$ is given by

$$\begin{aligned}\underline{DS}_n^m = \sum_{j=1}^{J}\Bigg\{&\left[\underline{D}^m(\mu_j) + \frac{n(n+1)}{a^2}\underline{D}_\nabla^m(\mu_j)\right]P_n^m(\mu_j)\\ &+im\underline{D}_\lambda^m(\mu_j)\frac{P_n^m(\mu_j)}{a(1-\mu_j^2)} - \underline{D}_\mu^m(\mu_j)\frac{H_n^m(\mu_j)}{a(1-\mu_j^2)}\Bigg\}w_j.\end{aligned} \tag{3.288}$$

The spectral thermodynamic equation is

$$\underline{T}_n'^m = \underline{TS}_n^m - \Delta t \boldsymbol{D}^r \underline{\delta}_n^m, \tag{3.289}$$

with $\underline{TS}_n^m$ defined as

$$\underline{TS}_n^m = \sum_{j=1}^{J} \left[\underline{T}^m(\mu_j) P_n^m(\mu_j) - im \underline{T}_\lambda^m(\mu_j) \frac{P_n^m(\mu_j)}{a(1-\mu_j^2)} + \underline{T}_\mu^m(\mu_j) \frac{H_n^m(\mu_j)}{a(1-\mu_j^2)} \right] w_j, \tag{3.290}$$

while the surface pressure equation is

$$\Pi_n^m = PS_n^m - \underline{\delta}_n^m \left(\underline{\Delta p}^r\right)^T \frac{\Delta t}{\pi^r}, \tag{3.291}$$

where PS_n^m is given by

$$PS_n^m = \sum_{j=1}^{J} PS^m(\mu_j) P_n^m(\mu_j) w_j. \tag{3.292}$$

Equation (3.285) for vorticity is explicit and complete at this point. However, the remaining equations (3.287)–(3.291) are coupled. They are solved by eliminating all variables except $\underline{\delta}_n^m$:

$$\boldsymbol{A}_n \underline{\delta}_n^m = \underline{DS}_n^m + \Delta t \frac{n(n+1)}{a^2} \left[R \boldsymbol{H}^r (\underline{TS})_n^m + R \left(\underline{b}^r + \underline{h}^r\right) (PS)_n^m \right], \tag{3.293}$$

where

$$\boldsymbol{A}_n = \boldsymbol{I} + \Delta t^2 \frac{n(n+1)}{a^2} \left[R \boldsymbol{H}^r \boldsymbol{D}^r + R \left(\underline{b}^r + \underline{h}^r\right) \left(\left(\underline{\Delta p}^r\right)^T \frac{1}{\pi^r} \right) \right], \tag{3.294}$$

which is simply a set of K simultaneous equations for the coefficients with given wavenumbers (m,n) at each level and is solved by inverting $\boldsymbol{A}_n$. In order to prevent the accumulation of round–off error in the global mean divergence (which if exactly zero initially, should remain exactly zero) $(\boldsymbol{A}_o)^{-1}$ is set to the null matrix rather than the identity, and the formal application of (3.293) then always guarantees $\underline{\delta}_o^o = 0$. Once δ_n^m is known, $\underline{T}_n'^m$ and Π_n^m can be computed from (3.289) and (3.291), respectively, and all prognostic variables are known at time $n+1$ as spherical harmonic coefficients. Note that the mean component $\underline{T}_o'^o$ is not necessarily zero since the perturbations are taken with respect to a specified $\underline{T}^r$.

3.3.14 Horizontal diffusion

As mentioned earlier, the horizontal diffusion in (3.216) and (3.219) is computed implicitly via time splitting after the transformations into spectral space and solution of the semi-implicit equations. In the following, the ζ and δ equations have a similar form, so we write only the δ equation:

$$(\delta^*)_n^m = \left(\delta^{n+1}\right)_n^m - (-1)^i 2\Delta t K^{(2i)} \left[\nabla^{2i} (\delta^*)_n^m - (-1)^i (\delta^*)_n^m \left(2/a^2\right)^i \right], \tag{3.295}$$

$$(T^*)_n^m = \left(T^{n+1}\right)_n^m - (-1)^i 2\Delta t K^{(2i)} \left[\nabla^{2i} (T^*)_n^m \right] . \tag{3.296}$$

The extra term is present in (3.295), (3.299) and (3.301) to prevent damping of uniform rotations. The solutions are just

$$\left(\delta^*\right)_n^m = K_n^{(2i)}\left(\delta\right)\left(\delta^{n+1}\right)_n^m, \tag{3.297}$$

$$\left(T^*\right)_n^m = K_n^{(2i)}\left(T\right)\left(T^{n+1}\right)_n^m, \tag{3.298}$$

$$K_n^{(2)}\left(\delta\right) = \left\{1 + 2\Delta t D_n K^{(2)}\left[\left(\frac{n(n+1)}{a^2}\right) - \frac{2}{a^2}\right]\right\}^{-1}, \tag{3.299}$$

$$K_n^{(2)}\left(T\right) = \left\{1 + 2\Delta t D_n K^{(2)}\left(\frac{n(n+1)}{a^2}\right)\right\}^{-1}, \tag{3.300}$$

$$K_n^{(4)}\left(\delta\right) = \left\{1 + 2\Delta t D_n K^{(4)}\left[\left(\frac{n(n+1)}{a^2}\right)^2 - \frac{4}{a^4}\right]\right\}^{-1}, \tag{3.301}$$

$$K_n^{(4)}\left(T\right) = \left\{1 + 2\Delta t D_n K^{(4)}\left(\frac{n(n+1)}{a^2}\right)^2\right\}^{-1}. \tag{3.302}$$

$K_n^{(2)}\left(\delta\right)$ and $K_n^{(4)}\left(\delta\right)$ are both set to 1 for $n = 0$. The quantity D_n represents the "Courant number limiter", normally set to 1. However, D_n is modified to ensure that the CFL criterion is not violated in selected upper levels of the model. If the maximum wind speed in any of these upper levels is sufficiently large, then $D_n = 1000$ in that level for all $n > n_c$, where $n_c = a\Delta t / \max|\boldsymbol{V}|$. This condition is applied whenever the wind speed is large enough that $n_c < K$, the truncation parameter in (3.243), and temporarily reduces the effective resolution of the model in the affected levels. The number of levels at which this "Courant number limiter" may be applied is user-selectable, but it is only used in the top level of the 26 level CAM 5.0 control runs.

The diffusion of T is not complete at this stage. In order to make the partial correction from η to p in (3.210) local, it is not included until grid–point values are available. This requires that $\nabla^4\Pi$ also be transformed from spectral to grid–point space. The values of the coefficients $K^{(2)}$ and $K^{(4)}$ for the standard T42 resolution are $2.5 \times 10^5 \mathrm{m}^2\mathrm{sec}^{-1}$ and $1.0 \times 10^{16}\mathrm{m}^4\mathrm{sec}^{-1}$, respectively.

3.3.15 Initial divergence damping

Occasionally, with poorly balanced initial conditions, the model exhibits numerical instability during the beginning of an integration because of excessive noise in the solution. Therefore, an optional divergence damping is included in the model to be applied over the first few days. The damping has an initial e-folding time of Δt and linearly decreases to 0 over a specified number of days, t_D, usually set to be 2. The damping is computed implicitly via time splitting after the horizontal diffusion.

$$r = \max\left[\frac{1}{\Delta t}(t_D - t)/t_D,\ 0\right] \tag{3.303}$$

$$\left(\delta^*\right)_n^m = \frac{1}{1 + 2\Delta t r}\left(\delta^*\right)_n^m \tag{3.304}$$

3.3.16 Transformation from spectral to physical space

After the prognostic variables are completed at time $n+1$ in spectral space $\left(\underline{(\zeta+f)^*}\right)_n^m$, $(\underline{\delta^*})_n^m$, $(\underline{T^*})_n^m$, $(\Pi^{n+1})_n^m$ they are transformed to grid space. For a variable ψ, the transformation is given by

$$\psi(\lambda,\mu) = \sum_{m=-M}^{M} \left[\sum_{n=|m|}^{\mathcal{N}(m)} \psi_n^m P_n^m(\mu) \right] e^{im\lambda}. \tag{3.305}$$

The inner sum is done essentially as a vector product over n, and the outer is again performed by an FFT subroutine. The term needed for the remainder of the diffusion terms, $\nabla^4\Pi$, is calculated from

$$\nabla^4\Pi^{n+1} = \sum_{m=-M}^{M} \left[\sum_{n=|m|}^{\mathcal{N}(m)} \left(\frac{n(n+1)}{a^2} \right)^2 \left(\Pi^{n+1}\right)_n^m P_n^m(\mu) \right] e^{im\lambda}. \tag{3.306}$$

In addition, the derivatives of Π are needed on the grid for the terms involving $\nabla\Pi$ and $\boldsymbol{V}\cdot\nabla\Pi$,

$$\boldsymbol{V}\cdot\nabla\Pi = \frac{U}{a(1-\mu^2)}\frac{\partial\Pi}{\partial\lambda} + \frac{V}{a(1-\mu^2)}(1-\mu^2)\frac{\partial\Pi}{\partial\mu}. \tag{3.307}$$

These required derivatives are given by

$$\frac{\partial\Pi}{\partial\lambda} = \sum_{m=-M}^{M} im \left[\sum_{n=|m|}^{\mathcal{N}(m)} \Pi_n^m P_n^m(\mu) \right] e^{im\lambda}, \tag{3.308}$$

and using (3.281),

$$(1-\mu^2)\frac{\partial\Pi}{\partial\mu} = \sum_{m=-M}^{M} \left[\sum_{n=|m|}^{\mathcal{N}(m)} \Pi_n^m H_n^m(\mu) \right] e^{im\lambda}, \tag{3.309}$$

which involve basically the same operations as (3.306). The other variables needed on the grid are U and V. These can be computed directly from the absolute vorticity and divergence coefficients using the relations

$$(\zeta+f)_n^m = -\frac{n(n+1)}{a^2}\psi_n^m + f_n^m, \tag{3.310}$$

$$\delta_n^m = -\frac{n(n+1)}{a^2}\chi_n^m, \tag{3.311}$$

in which the only nonzero f_n^m is $f_1^o = \Omega/\sqrt{.375}$, and

$$U = \frac{1}{a}\frac{\partial\chi}{\partial\lambda} - \frac{(1-\mu^2)}{a}\frac{\partial\psi}{\partial\mu}, \tag{3.312}$$

$$V = \frac{1}{a}\frac{\partial\psi}{\partial\lambda} + \frac{(1-\mu^2)}{a}\frac{\partial\chi}{\partial\mu}. \tag{3.313}$$

Thus, the direct transformation is

$$U = -\sum_{m=-M}^{M} a \sum_{n=|m|}^{\mathcal{N}(m)} \left[\frac{im}{n(n+1)} \delta_n^m P_n^m(\mu) - \frac{1}{n(n+1)} (\zeta + f)_n^m H_n^m(\mu) \right] e^{im\lambda} - \frac{a}{2} \frac{\Omega}{\sqrt{0.375}} H_1^o, \tag{3.314}$$

$$V = -\sum_{m=-M}^{M} a \sum_{n=|m|}^{\mathcal{N}(m)} \left[\frac{im}{n(n+1)} (\zeta + f)_n^m P_n^m(\mu) + \frac{1}{n(n+1)} \delta_n^m H_n^m(\mu) \right] e^{im\lambda}. \tag{3.315}$$

The horizontal diffusion tendencies are also transformed back to grid space. The spectral coefficients for the horizontal diffusion tendencies follow from (3.295) and (3.296):

$$F_{T_H} (T^*)_n^m = (-1)^{i+1} K^{2i} \left[\nabla^{2i} (T^*) \right]_n^m, \tag{3.316}$$

$$F_{\zeta_H} ((\zeta + f)^*)_n^m = (-1)^{i+1} K^{2i} \left\{ \nabla^{2i} (\zeta + f)^* - (-1)^i (\zeta + f)^* \left(2/a^2 \right)^i \right\}, \tag{3.317}$$

$$F_{\delta_H} (\delta^*)_n^m = (-1) K^{2i} \left\{ \nabla^{2i} (\delta^*) - (-1)^i \delta^* \left(2/a^2 \right)^i \right\}, \tag{3.318}$$

using $i = 1$ or 2 as appropriate for the ∇^2 or ∇^4 forms. These coefficients are transformed to grid space following (3.242) for the T term and (3.314) and (3.315) for vorticity and divergence. Thus, the vorticity and divergence diffusion tendencies are converted to equivalent U and V diffusion tendencies.

3.3.17 Horizontal diffusion correction

After grid–point values are calculated, frictional heating rates are determined from the momentum diffusion tendencies and are added to the temperature, and the partial correction of the ∇^4 diffusion from η to p surfaces is applied to T. The frictional heating rate is calculated from the kinetic energy tendency produced by the momentum diffusion

$$F_{F_H} = -u^{n-1} F_{u_H}(u^*)/c_p^* - v^{n-1} F_{v_H}(v^*)/c_p^*, \tag{3.319}$$

where F_{u_H}, and F_{v_H} are the momentum equivalent diffusion tendencies, determined from F_{ζ_H} and F_{δ_H} just as U and V are determined from ζ and δ, and

$$c_p^* = c_p \left[1 + \left(\frac{c_{p_v}}{c_p} - 1 \right) q^{n+1} \right]. \tag{3.320}$$

These heating rates are then combined with the correction,

$$\hat{T}_k^{n+1} = T_k^* + (2\Delta t F_{F_H})_k + 2\Delta t \left(\pi B \frac{\partial T^*}{\partial p} \right)_k K^{(4)} \nabla^4 \Pi^{n+1}. \tag{3.321}$$

The vertical derivatives of T^* (where the * notation is dropped for convenience) are defined by

$$\left(\pi B\frac{\partial T}{\partial p}\right)_1 = \frac{\pi}{2\Delta p_1}\left[B_{1+\frac{1}{2}}\left(T_2 - T_1\right)\right] \ , \tag{3.322}$$

$$\left(\pi B\frac{\partial T}{\partial p}\right)_k = \frac{\pi}{2\Delta p_k}\left[B_{k+\frac{1}{2}}\left(T_{k+1} - T_k\right) + B_{k-\frac{1}{2}}\left(T_k - T_{k-1}\right)\right] \ , \tag{3.323}$$

$$\left(\pi B\frac{\partial T}{\partial p}\right)_K = \frac{\pi}{2\Delta p_K}\left[B_{K-\frac{1}{2}}\left(T_K - T_{K-1}\right)\right] . \tag{3.324}$$

The corrections are added to the diffusion tendencies calculated earlier (3.316) to give the total temperature tendency for diagnostic purposes:

$$\hat{F}_{T_H}(T^*)_k = F_{T_H}(T^*)_k + \left(2\Delta t F_{F_H}\right)_k + 2\Delta t B_k\left(\pi\frac{\partial T^*}{\partial p}\right)_k K^{(4)}\nabla^4\Pi^{n+1}. \tag{3.325}$$

3.3.18 Semi-Lagrangian Tracer Transport

The forecast equation for water vapor specific humidity and constituent mixing ratio in the η system is from (3.164) excluding sources and sinks.

$$\frac{dq}{dt} = \frac{\partial q}{\partial t} + \boldsymbol{V}\cdot\nabla q + \dot{\eta}\frac{\partial p}{\partial \eta}\frac{\partial q}{\partial p} = 0 \tag{3.326}$$

or

$$\frac{dq}{dt} = \frac{\partial q}{\partial t} + \boldsymbol{V}\cdot\nabla q + \dot{\eta}\frac{\partial q}{\partial \eta} = 0. \tag{3.327}$$

Equation (3.327) is more economical for the semi-Lagrangian vertical advection, as $\Delta\eta$ does not vary in the horizontal, while Δp does. Written in this form, the η advection equations look exactly like the σ equations.

The parameterizations are time-split in the moisture equation. The tendency sources have already been added to the time level $(n-1)$. The semi-Lagrangian advection step is subdivided into horizontal and vertical advection sub-steps, which, in an Eulerian form, would be written

$$q^* = q^{n-1} + 2\Delta t\left(\boldsymbol{V}\cdot\nabla q\right)^n \tag{3.328}$$

and

$$q^{n+1} = q^* + 2\Delta t\left(\dot{\eta}\frac{\partial q}{\partial n}\right)^n . \tag{3.329}$$

In the semi-Lagrangian form used here, the general form is

$$q^* = \mathrm{L}_{\lambda\varphi}\left(q^{n-1}\right), \tag{3.330}$$

$$q^{n+1} = \mathrm{L}_{\eta}\left(q^*\right). \tag{3.331}$$

Equation (3.330) represents the horizontal interpolation of q^{n-1} at the departure point calculated assuming $\dot{\eta} = 0$. Equation (3.331) represents the vertical interpolation of q^* at the departure point, assuming $\boldsymbol{V} = 0$.

The horizontal departure points are found by first iterating for the mid-point of the trajectory, using winds at time n, and a first guess as the location of the mid-point of the previous time step

$$\lambda_M^{k+1} = \lambda_A - \Delta t u^n \left(\lambda_M^k, \varphi_M^k\right) / a \cos \varphi_M^k, \tag{3.332}$$

$$\varphi_M^{k+1} = \varphi_A - \Delta t v^n \left(\lambda_M^k, \varphi_M^k\right) / a, \tag{3.333}$$

where subscript A denotes the arrival (Gaussian grid) point and subscript M the midpoint of the trajectory. The velocity components at $\left(\lambda_M^k, \varphi_M^k\right)$ are determined by Lagrange cubic interpolation. For economic reasons, the equivalent Hermite cubic interpolant with cubic derivative estimates is used at some places in this code. The equations will be presented later.

Once the iteration of (3.332) and (3.333) is complete, the departure point is given by

$$\lambda_D = \lambda_A - 2\Delta t u^n \left(\lambda_M, \varphi_M\right) / a \cos \varphi_M, \tag{3.334}$$

$$\varphi_D = \lambda_A - 2\Delta t v^n \left(\lambda_M, \varphi_M\right) / a, \tag{3.335}$$

where the subscript D denotes the departure point.

The form given by (3.332)-(3.335) is inaccurate near the poles and thus is only used for arrival points equatorward of 70° latitude. Poleward of 70° we transform to a local geodesic coordinate for the calculation at each arrival point. The local geodesic coordinate is essentially a rotated spherical coordinate system whose equator goes through the arrival point. Details are provided in Williamson and Rasch [1989]. The transformed system is rotated about the axis through $\left(\lambda_A - \frac{\pi}{2}, 0\right)$ and $\left(\lambda_A + \frac{\pi}{2}, 0\right)$, by an angle φ_A so the equator goes through (λ_A, φ_A). The longitude of the transformed system is chosen to be zero at the arrival point. If the local geodesic system is denoted by (λ', φ'), with velocities (u', v'), the two systems are related by

$$\sin \phi' = \sin \phi \cos \phi_A - \cos \phi \sin \phi_A \cos \left(\lambda_A - \lambda\right), \tag{3.336}$$

$$\sin \phi = \sin \phi' \cos \phi_A + \cos \phi' \sin \prime_A \cos \lambda' , \tag{3.337}$$

$$\sin \lambda' \cos \phi' = -\sin \left(\lambda_A - \lambda\right) \cos \phi , \tag{3.338}$$

$$v' \cos \phi' = v \left[\cos \phi \cos \phi_A + \sin \phi \sin \phi_A \cos \left(\lambda_A - \lambda\right)\right] - u \sin \phi_A \sin \left(\lambda_A - \lambda\right), \tag{3.339}$$

$$u' \cos \lambda' - v' \sin \lambda' \sin \phi' = u \cos \left(\lambda_A - \lambda\right) + v \sin \phi \sin \left(\lambda_A - \lambda\right) . \tag{3.340}$$

The calculation of the departure point in the local geodesic system is identical to (3.332)-(3.335) with all variables carrying a prime. The equations can be simplified by noting that $\left(\lambda'_A, \varphi'_A\right) = (0, 0)$ by design and $u'\left(\lambda'_A, \varphi'_A\right) = u\left(\lambda_A, \varphi_A\right)$ and $v'\left(\lambda'_A, \varphi'_A\right) = v\left(\lambda_A, \varphi_A\right)$. The interpolations are always done in global spherical coordinates.

The interpolants are most easily defined on the interval $0 \le \theta \le 1$. Define

$$\theta = \left(x_D - x_i\right) / \left(x_{i+1} - x_i\right), \tag{3.341}$$

where x is either λ or φ and the departure point x_D falls within the interval (x_i, x_{i+1}). Following (23) of [Rasch and Williamson, 1990] with $r_i = 3$ the Hermite cubic interpolant is given by

$$q_D = q_{i+1}\left[3 - 2\theta\right]\theta^2 - d_{i+1}\left[h_i \theta^2 \left(1 - \theta\right)\right] + q_i\left[3 - 2\left(1 - \theta\right)\right]\left(1 - \theta\right)^2 + d_i\left[h_i \theta \left(1 - \theta\right)^2\right] \tag{3.342}$$

where q_i is the value at the grid point x_i, d_i is the derivative estimate given below, and $h_i = x_{i+1} - x_i$.

Following (3.2.12) and (3.2.13) of Hildebrand [1956], the Lagrangian cubic polynomial interpolant used for the velocity interpolation, is given by

$$f_D = \sum_{j=-1}^{2} \ell_j(x_D)\, f_{i+j} \tag{3.343}$$

where

$$\ell_j(x_D) = \frac{(x_D - x_{i-1})\ldots(x_D - x_{i+j-1})(x_D - x_{i+j+1})\ldots(x_D - x_{i+2})}{(x_{i+j} - x_{i-1})\ldots(x_{i+j} - x_{i+j-1})(x_{i+j} - x_{i+j+1})\ldots(x_{i+j} - x_{i+2})} \tag{3.344}$$

where f can represent either u or v, or their counterparts in the geodesic coordinate system.

The derivative approximations used in (3.342) for q are obtained by differentiating (3.343) with respect to x_D, replacing f by q and evaluating the result at x_D equal x_i and x_{i+1}. With these derivative estimates, the Hermite cubic interpolant (3.342) is equivalent to the Lagrangian (3.343). If we denote the four point stencil $(x_{i-1}, x_i, x_{i+1}, x_{i+2})$ by $(x_1, x_2, x_3, x_4,)$ the cubic derivative estimates are

$$d_2 = \left[\frac{(x_2 - x_3)(x_2 - x_4)}{(x_1 - x_2)(x_1 - x_3)(x_1 - x_4)}\right] q_1 \tag{3.345}$$

$$- \left[\frac{1}{(x_1 - x_2)} - \frac{1}{(x_2 - x_3)} - \frac{1}{(x_2 - x_4)}\right] q_2 \tag{3.346}$$

$$+ \left[\frac{(x_2 - x_1)(x_2 - x_4)}{(x_1 - x_3)(x_2 - x_3)(x_3 - x_4)}\right] q_3 \tag{3.347}$$

$$- \left[\frac{(x_2 - x_1)(x_2 - x_3)}{(x_1 - x_4)(x_2 - x_4)(x_3 - x_4)}\right] q_4 \tag{3.348}$$

and

$$d_3 = \left[\frac{(x_3 - x_2)(x_3 - x_4)}{(x_1 - x_2)(x_1 - x_3)(x_1 - x_4)}\right] q_1 \tag{3.349}$$

$$- \left[\frac{(x_3 - x_1)(x_3 - x_4)}{(x_1 - x_2)(x_2 - x_3)(x_2 - x_4)}\right] q_2 \tag{3.350}$$

$$- \left[\frac{1}{(x_1 - x_3)} + \frac{1}{(x_2 - x_3)} - \frac{1}{(x_3 - x_4)}\right] q_3 \tag{3.351}$$

$$- \left[\frac{(x_3 - x_1)(x_3 - x_2)}{(x_1 - x_4)(x_2 - x_4)(x_3 - x_4)}\right] q_4 \tag{3.352}$$

The two dimensional (λ, φ) interpolant is obtained as a tensor product application of the one-dimensional interpolants, with λ interpolations done first. Assume the departure point falls in the grid box $(\lambda_i, \lambda_{i+1})$ and $(\varphi_i, \varphi_{i+1})$. Four λ interpolations are performed to find q values at $(\lambda_D, \varphi_{j-1})$, (λ_D, φ_j), $(\lambda_D, \varphi_{j+1})$, and $(\lambda_D, \varphi_{j+2})$. This is followed by one interpolation in φ using these four values to obtain the value at (λ_D, φ_D). Cyclic continuity is used in longitude. In latitude, the grid is extended to include a pole point (row) and one row across the pole. The

pole row is set equal to the average of the row next to the pole for q and to wavenumber 1 components for u and v. The row across the pole is filled with the values from the first row below the pole shifted π in longitude for q and minus the value shifted by π in longitude for u and v.

Once the departure point is known, the constituent value of $q^* = q_D^{n-1}$ is obtained as indicated in (3.330) by Hermite cubic interpolation (3.342), with cubic derivative estimates (3.343) and (3.344) modified to satisfy the Sufficient Condition for Monotonicity with C° continuity (SCMO) described below. Define $\Delta_i q$ by

$$\Delta_i q = \frac{q_{i+1} - q_i}{x_{i+1} - x_i} \ . \tag{3.353}$$

First, if $\Delta_i q = 0$ then

$$d_i = d_{i+1} = 0 \ . \tag{3.354}$$

Then, if either

$$0 \le \frac{d_i}{\Delta_i q} \le 3 \tag{3.355}$$

or

$$0 \le \frac{d_{i+1}}{\Delta_i q} \le 3 \tag{3.356}$$

is violated, d_i or d_{i+1} is brought to the appropriate bound of the relationship. These conditions ensure that the Hermite cubic interpolant is monotonic in the interval $[x_i, x_{i+1}]$.

The horizontal semi-Lagrangian sub-step (3.330) is followed by the vertical step (3.331). The vertical velocity $\dot\eta$ is obtained from that diagnosed in the dynamical calculations (3.222) by

$$(\dot\eta)_{k+\frac{1}{2}} = \left(\dot\eta \frac{\partial p}{\partial \eta}\right)_{k+\frac{1}{2}} \Bigg/ \left(\frac{p_{k+1} - p_k}{\eta_{k+1} - \eta_k}\right), \tag{3.357}$$

with $\eta_k = A_k + B_k$. Note, this is the only place that the model actually requires an explicit specification of η. The mid-point of the vertical trajectory is found by iteration

$$\eta_M^{k+1} = \eta_A - \Delta t \dot\eta^n \left(\eta_M^k\right). \tag{3.358}$$

Note, the arrival point η_A is a mid-level point where q is carried, while the $\dot\eta$ used for the interpolation to mid-points is at interfaces. We restrict η_M by

$$\eta_1 \le \eta_M \le \eta_K, \tag{3.359}$$

which is equivalent to assuming that q is constant from the surface to the first model level and above the top q level. Once the mid-point is determined, the departure point is calculated from

$$\eta_D = \eta_A - 2\Delta t \dot\eta^n \left(\eta_M\right), \tag{3.360}$$

with the restriction

$$\eta_1 \le \eta_D \le \eta_K. \tag{3.361}$$

The appropriate values of $\dot\eta$ and q are determined by interpolation (3.342), with the derivative estimates given by (3.343) and (3.344) for $i = 2$ to $K - 1$. At the top and bottom we assume a zero derivative (which is consistent with (3.359) and (3.361)), $d_i = 0$ for the interval $k = 1$,

and $\delta_{i+1} = 0$ for the interval $k = K - 1$. The estimate at the interior end of the first and last grid intervals is determined from an uncentered cubic approximation; that is d_{i+1} at the $k = 1$ interval is equal to d_i from the $k = 2$ interval, and d_i at the $k = K - 1$ interval is equal to d_{i+1} at the $k = K - 2$ interval. The monotonic conditions (3.355) to (3.356) are applied to the q derivative estimates.

3.3.19 Mass fixers

This section describes original and modified fixers used for the Eulerian and semi-Lagrangian dynamical cores.

Let π^0, Δp^0 and q^0 denote the values of air mass, pressure intervals, and water vapor specific humidity at the beginning of the time step (which are the same as the values at the end of the previous time step.)

π^+, Δp^+ and q^+ are the values after fixers are applied at the end of the time step.

π^-, Δp^- and q^- are the values after the parameterizations have updated the moisture field and tracers.

Since the physics parameterizations do not change the surface pressure, π^- and Δp^- are also the values at the beginning of the time step.

The fixers which ensure conservation are applied to the dry atmospheric mass, water vapor specific humidity and constituent mixing ratios. For water vapor and atmospheric mass the desired discrete relations, following Williamson and Olson [1994*a*] are

$$\int_2 \pi^+ - \int_3 q^+ \Delta p^+ = \boldsymbol{P}, \tag{3.362}$$

$$\int_3 q^+ \Delta p^+ = \int_3 q^- \Delta p^-, \tag{3.363}$$

where $\boldsymbol{P}$ is the dry mass of the atmosphere. From the definition of the vertical coordinate,

$$\Delta p = p_0 \Delta A + \pi \Delta B, \tag{3.364}$$

and the integral $\int_2$ denotes the normal Gaussian quadrature while $\int_3$ includes a vertical sum followed by Gaussian quadrature. The actual fixers are chosen to have the form

$$\pi^+(\lambda, \varphi) = \boldsymbol{M} \hat{\pi}^+(\lambda, \varphi), \tag{3.365}$$

preserving the horizontal gradient of Π, which was calculated earlier during the inverse spectral transform, and

$$q^+(\lambda, \varphi, \eta) = \hat{q}^+ + \alpha \eta \hat{q}^+ |\hat{q}^+ - q^-|. \tag{3.366}$$

In (3.365) and (3.366) the $\hat{\ }$ denotes the provisional value before adjustment. The form (3.366) forces the arbitrary corrections to be small when the mixing ratio is small and when the change made to the mixing ratio by the advection is small. In addition, the η factor is included to make the changes approximately proportional to mass per unit volume [Rasch et al., 1995]. Satisfying

(3.362) and (3.363) gives

$$\alpha = \frac{\int\limits_3 q^- \Delta p^- - \int\limits_3 \hat{q}^+ p_0 \Delta A - M \int\limits_3 \hat{q}^+ \hat{\pi}^+ \Delta B}{\int\limits_3 \eta \hat{q}^+ |\hat{q}^+ - q^-| \, p_0 \Delta A + M \int\limits_3 \eta \hat{q}^+ |\hat{q}^+ - q^-| \hat{\pi}^+ \Delta B} \tag{3.367}$$

and

$$\boldsymbol{M} = \left(\boldsymbol{P} + \int\limits_3 q^- \Delta p^- \right) \Big/ \int\limits_2 \hat{\pi}^+ \ . \tag{3.368}$$

Note that water vapor and dry mass are corrected simultaneously. Additional advected constituents are treated as mixing ratios normalized by the mass of dry air. This choice was made so that as the water vapor of a parcel changed, the constituent mixing ratios would not change. Thus the fixers which ensure conservation involve the dry mass of the atmosphere rather than the moist mass as in the case of the specific humidity above. Let χ denote the mixing ratio of constituents. Historically we have used the following relationship for conservation:

$$\int\limits_3 \chi^+ (1 - q^+) \Delta p^+ = \int\limits_3 \chi^- (1 - q^-) \Delta p^- \ . \tag{3.369}$$

The term $(1-q)\Delta p$ defines the dry air mass in a layer. Following Rasch et al. [1995] the change made by the fixer has the same form as (3.366)

$$\chi^+ (\lambda, \varphi, \eta) = \hat{\chi}^+ + \alpha_\chi \eta \hat{\chi}^+ |\hat{\chi}^+ - \chi^-| \ . \tag{3.370}$$

Substituting (3.370) into (3.369) and using (3.365) through (3.368) gives

$$\alpha_\chi = \frac{\int\limits_3 \chi^- (1 - q^-) \Delta p^- - \int\limits_{A,B} \hat{\chi}^+ (1 - \hat{q}^+) \Delta \hat{p}^+ + \alpha \int\limits_{A,B} \hat{\chi}^+ \eta \hat{q}^+ |\hat{q}^+ - q^-| \Delta p}{\int\limits_{A,B} \eta \hat{\chi}^+ |\hat{\chi}^+ - \chi^-| (1 - \hat{q}^+) \Delta p - \alpha \int\limits_{A,B} \eta \hat{\chi}^+ |\hat{\chi}^+ - \chi^-| \eta \hat{q}^+ |\hat{q}^+ - q^-| \Delta p} \ , \tag{3.371}$$

where the following shorthand notation is adopted:

$$\int\limits_{A,B} (\ \ ) \Delta p = \int\limits_3 (\ \ ) p_0 \Delta A + M \int\limits_3 (\ \ ) p_s \Delta B \ . \tag{3.372}$$

We note that there is a small error in (3.369). Consider a situation in which moisture is transported by a physical parameterization, but there is no source or sink of moisture. Under this circumstance $q^- \neq q^0$, but the surface pressure is not allowed to change. Since $(1 - q^-)\Delta p^- \neq (1 - q^0)\Delta p^0$, there is an implied change of dry mass of dry air in the layer, and even in circumstances where there is no change of dry mixing ratio χ there would be an implied change in mass of the tracer. The solution to this inconsistency is to define a dry air mass *only once* within the model time step, and use it consistently throughout the model. In this revision, we have chosen to fix the dry air mass in the model time step where the surface pressure is updated, e.g. at the end of the model time step. Therefore, we now replace (3.369) with

$$\int\limits_3 \chi^+ (1 - q^+) \Delta p^+ = \int\limits_3 \chi^- (1 - q^0) \Delta p^0 \ . \tag{3.373}$$

There is a corresponding change in the first term of the numerator of (3.371) in which q^- is replace by q^0. CAM 5.0uses (3.371) for water substances and constituents affecting the temperature field to prevent changes to the IPCC simulations. In the future, constituent fields may use a *corrected* version of (3.371).

3.3.20 Energy Fixer

Following notation in section 3.3.19, the total energy integrals are

$$\int_3 \frac{1}{g}\left[c_p T^+ + \Phi_s + \frac{1}{2}\left(u^{+2} + v^{+2}\right)\right]\Delta p^+ = \boldsymbol{E} \tag{3.374}$$

$$\boldsymbol{E} = \int_3 \frac{1}{g}\left[c_p T^- + \Phi_s + \frac{1}{2}\left(u^{-2} + v^{-2}\right)\right]\Delta p^- + \boldsymbol{S} \tag{3.375}$$

$$\boldsymbol{S} = \int_2 \left[(FSNT - FLNT) - (FSNS - FLNS - SHFLX - \rho_{H_2O} L_v PRECT) -\right]\Delta t \tag{3.376}$$

$$\begin{aligned} \boldsymbol{S} &= \int_2 \left[(FSNT - FLNT) - (FSNS - FLNS - SHFLX)\right]\Delta t & (3.377)\\ &+ \int_2 \left[\rho_{H_2O} L_v \left(PRECL + PRECC\right) + \rho_{H_2O} L_i \left(PRESL + PRESC\right)\right]\Delta t & (3.378) \end{aligned}$$

where $\boldsymbol{S}$ is the net source of energy from the parameterizations. $FSNT$ is the net downward solar flux at the model top, $FLNT$ is the net upward longwave flux at the model top, $FSNS$ is the net downward solar flux at the surface, $FLNS$ is the net upward longwave flux at the surface, $SHFLX$ is the surface sensible heat flux, and $PRECT$ is the total precipitation during the time step. From equation (3.365)

$$\pi^+(\lambda,\varphi) = \boldsymbol{M}\hat{\pi}^+(\lambda,\varphi) \tag{3.379}$$

and from (3.364)

$$\Delta p = p_0 \Delta A + \pi \Delta B \tag{3.380}$$

The energy fixer is chosen to have the form

$$\begin{aligned} T^+(\lambda,\varphi,\eta) &= \hat{T}^+ + \beta & (3.381)\\ u^+(\lambda,\varphi,\eta) &= \hat{u}^+ & (3.382)\\ v^+(\lambda,\varphi,\eta) &= \hat{v}^+ & (3.383) \end{aligned}$$

Then

$$\beta = \frac{g\boldsymbol{E} - \int_3 \left[c_p \hat{T}^+ + \Phi_s + \frac{1}{2}\left(\hat{u}^{+2} + \hat{v}^{+2}\right)\right] p_0 \Delta A - \boldsymbol{M}\int_3 \left[c_p \hat{T}^+ + \Phi_s + \frac{1}{2}\left(\hat{u}^{+2} + \hat{v}^{+2}\right)\right]\hat{\pi}^+ \Delta B}{\int_3 c_p\, p_0 \Delta A + \boldsymbol{M}\int_3 c_p \hat{\pi}^+ \Delta B} \tag{3.384}$$

3.3.21 Statistics Calculations

At each time step, selected global average statistics are computed for diagnostic purposes when the model is integrated with the Eulerian and semi-Lagrangian dynamical cores. Let $\int_3$ denote a global and vertical average and $\int_2$ a horizontal global average. For an arbitrary variable ψ, these are defined by

$$\int_3 \psi dV = \sum_{k=1}^{K} \sum_{j=1}^{J} \sum_{i=1}^{I} \psi_{ijk} w_j \left(\frac{\Delta p_k}{\pi} \right) \Big/ 2I, \tag{3.385}$$

and

$$\int_2 \psi dA = \sum_{j=1}^{J} \sum_{i=1}^{I} \psi_{ijk} w_j / 2I, \tag{3.386}$$

where recall that

$$\sum_{j=1}^{J} w_j = 2. \tag{3.387}$$

The quantities monitored are:

$$\text{global rms } (\zeta + f)(\text{s}^{-1}) = \left[\int_3 (\zeta^n + f)^2 dV \right]^{1/2}, \tag{3.388}$$

$$\text{global rms } \delta(\text{s}^{-1}) = \left[\int_3 (\delta^n)^2 dV \right]^{1/2}, \tag{3.389}$$

$$\text{global rms } T \text{ (K)} = \left[\int_3 (T^r + T'^n)^2 dV \right]^{1/2}, \tag{3.390}$$

$$\text{global average mass times } g \text{ (Pa)} = \int_2 \pi^n dA, \tag{3.391}$$

$$\text{global average mass of moisture (kg m}^{-2}) = \int_3 \pi^n q^n / g dV. \tag{3.392}$$

3.3.22 Reduced grid

The Eulerian core and semi-Lagrangian tracer transport can be run on reduced grids. The term reduced grid generally refers to a grid based on latitude and longitude circles in which the longitudinal grid increment increases at latitudes approaching the poles so that the longitudinal distance between grid points is reasonably constant. Details are provided in [Williamson and Rosinski, 2000]. This option provides a saving of computer time of up to 25%.

3.4 Semi-Lagrangian Dynamical Core

3.4.1 Introduction

The two-time-level semi-implicit semi-Lagrangian spectral transform dynamical core in CAM 5.0 evolved from the three-time-level CCM2 semi-Lagrangian version detailed in

Williamson and Olson [1994*a*] hereafter referred to as W&O94. As a first approximation, to convert from a three-time-level scheme to a two-time-level scheme, the time level index n-1 becomes n, the time level index n becomes n+$\frac{1}{2}$, and $2\Delta t$ becomes Δt. Terms needed at n+$\frac{1}{2}$ are extrapolated in time using time n and n-1 terms, except the Coriolis term which is implicit as the average of time n and n+1. This leads to a more complex semi-implicit equation to solve. Additional changes have been made in the scheme to incorporate advances in semi-Lagrangian methods developed since W&O94. In the following, reference is made to changes from the scheme developed in W&O94. The reader is referred to that paper for additional details of the derivation of basic aspects of the semi-Lagrangian approximations. Only the details of the two-time-level approximations are provided here.

3.4.2 Vertical coordinate and hydrostatic equation

The semi-Lagrangian dynamical core adopts the same hybrid vertical coordinate (η) as the Eulerian core defined by

$$p(\eta, p_s) = A(\eta)p_o + B(\eta)p_s \ , \tag{3.393}$$

where p is pressure, p_s is surface pressure, and p_o is a specified constant reference pressure. The coefficients A and B specify the actual coordinate used. As mentioned by Simmons and Burridge [1981] and implemented by Simmons and Strüfing [1981] and Simmons and Strüfing [1983], the coefficients A and B are defined only at the discrete model levels. This has implications in the continuity equation development which follows.

In the η system the hydrostatic equation is approximated in a general way by

$$\Phi_k = \Phi_s + R\sum_{l=k}^{K} H_{kl}\,(p)\,T_{vl} \tag{3.394}$$

where k is the vertical grid index running from 1 at the top of the model to K at the first model level above the surface, Φ_k is the geopotential at level k, Φ_s is the surface geopotential, T_v is the virtual temperature, and R is the gas constant. The matrix H, referred to as the hydrostatic matrix, represents the discrete approximation to the hydrostatic integral and is left unspecified for now. It depends on pressure, which varies from horizontal point to point.

3.4.3 Semi-implicit reference state

The semi-implicit equations are linearized about a reference state with constant T^r and p_s^r. We choose

$$T^r = 350\text{K}, \qquad p_s^r = 10^5\text{Pa} \tag{3.395}$$

3.4.4 Perturbation surface pressure prognostic variable

To ameliorate the mountain resonance problem, Ritchie and Tanguay [1996] introduce a perturbation $\ln p_s$ surface pressure prognostic variable

$$\ln p_s' = \ln p_s - \ln p_s^* \tag{3.396}$$

$$\ln p_s^* = -\frac{\Phi_s}{RT^r} \tag{3.397}$$

The perturbation surface pressure, $\ln p'_s$, is never actually used as a grid point variable in the CAM 5.0 code. It is only used for the semi-implicit development and solution. The total $\ln p_s$ is reclaimed in spectral space from the spectral coefficients of Φ_s immediately after the semi-implicit equations are solved, and transformed back to spectral space along with its derivatives. This is in part because $\nabla^4 \ln p_s$ is needed for the horizontal diffusion correction to pressure surfaces. However the semi-Lagrangian CAM 5.0 default is to run with no horizontal diffusion.

3.4.5 Extrapolated variables

Variables needed at time $(n+\frac{1}{2})$ are obtained by extrapolation

$$(\quad)^{n+\frac{1}{2}} = \frac{3}{2}(\quad)^{n} - \frac{1}{2}(\quad)^{n-1} \tag{3.398}$$

3.4.6 Interpolants

Lagrangian polynomial quasi-cubic interpolation is used in the prognostic equations for the dynamical core. Monotonic Hermite quasi-cubic interpolation is used for tracers. Details are provided in the Eulerian Dynamical Core description. The trajectory calculation uses tri-linear interpolation of the wind field.

3.4.7 Continuity Equation

The discrete semi-Lagrangian, semi-implicit continuity equation is obtained from (16) of W&O94 modified to be spatially uncentered by a fraction ϵ, and to predict $\ln p'_s$

$$\begin{aligned}
\Delta B_l \left\{ \left(\ln p'_{s_l}\right)_A^{n+1} - \left[(\ln p_{s_l})^n + \frac{\Phi_s}{RT^r}\right]_{D_2} \right\} \Big/ \Delta t = \\
- \frac{1}{2}\Bigg\{ \left[(1+\epsilon)\,\Delta\left(\frac{1}{p_s}\dot{\eta}\frac{\partial p}{\partial \eta}\right)_l\right]_A^{n+1} + \left[(1-\epsilon)\,\Delta\left(\frac{1}{p_s}\dot{\eta}\frac{\partial p}{\partial \eta}\right)_l\right]_{D_2}^{n} \Bigg\} \\
- \left(\frac{1}{p_s}\delta_l \Delta p_l\right)_{M_2}^{n+\frac{1}{2}} + \frac{\Delta B_l}{RT^r}\left(\boldsymbol{V}_l \cdot \nabla\, \Phi_s\right)_{M_2}^{n+\frac{1}{2}} \\
- \left\{ \frac{1}{2}\left[(1+\epsilon)\left(\frac{1}{p_s^r}\delta_l \Delta p_l^r\right)_A^{n+1} + (1-\epsilon)\left(\frac{1}{p_s^r}\delta_l \Delta p_l^r\right)_{D_2}^{n}\right] - \left(\frac{1}{p_s^r}\delta_l \Delta p_l^r\right)_{M_2}^{n+\frac{1}{2}} \right\}
\end{aligned} \tag{3.399}$$

where

$$\Delta(\quad)_l = (\quad)_{l+\frac{1}{2}} - (\quad)_{l-\frac{1}{2}} \tag{3.400}$$

and

$$(\quad)_{M_2}^{n+\frac{1}{2}} = \frac{1}{2}\left[(1+\epsilon)(\quad)_A^{n+\frac{1}{2}} + (1-\epsilon)(\quad)_{D_2}^{n+\frac{1}{2}}\right] \tag{3.401}$$

$\Delta(\quad)_l$ denotes a vertical difference, l denotes the vertical level, A denotes the arrival point, D_2 the departure point from horizontal (two-dimensional) advection, and M_2 the midpoint of that trajectory.

The surface pressure forecast equation is obtained by summing over all levels and is related to (18) of W&O94 but is spatially uncentered and uses $\ln p'_s$

$$\begin{aligned}
\left(\ln p'_s\right)_A^{n+1} &= \sum_{l=1}^{K} \Delta B_l \left[\left(\ln p_{s_l}\right)^n + \frac{\Phi_s}{RT^r}\right]_{D_2} - \frac{1}{2}\Delta t \sum_{l=1}^{K} \left[\left(1-\epsilon\right)\Delta\left(\frac{1}{p_s}\dot{\eta}\frac{\partial p}{\partial \eta}\right)_l\right]_{D_2}^n \\
&\quad -\Delta t \sum_{l=1}^{K}\left(\frac{1}{p_s}\delta_l \Delta p_l\right)_{M_2}^{n+\frac{1}{2}} + \Delta t \sum_{l=1}^{K} \frac{\Delta B_l}{RT^r}\left(\boldsymbol{V}_l \cdot \nabla\, \Phi_s\right)_{M_2}^{n+\frac{1}{2}} \\
&\quad -\Delta t \sum_{l=1}^{K} \frac{1}{p_s^r}\left\{\frac{1}{2}\left[\left(1+\epsilon\right)\left(\delta_l\right)_A^{n+1} + \left(1-\epsilon\right)\left(\delta_l\right)_{D_2}^{n}\right] - \left(\delta_l\right)_{M_2}^{n+\frac{1}{2}}\right\}\Delta p_l^r
\end{aligned} \tag{3.402}$$

The corresponding $\left(\frac{1}{p_s}\dot{\eta}\frac{\partial p}{\partial \eta}\right)$ equation for the semi-implicit development follows and is related to (19) of W&O94, again spatially uncentered and using $ln\, p'_s$.

$$\begin{aligned}
\left(1+\epsilon\right)\left(\frac{1}{p_s}\dot{\eta}\frac{\partial p}{\partial \eta}\right)_{k+\frac{1}{2}}^{n+1} &= -\frac{2}{\Delta t}\left\{B_{k+\frac{1}{2}}\left(\ln p'_s\right)_A^{n+1} - \sum_{l=1}^{k}\Delta B_l\left[\left(\ln p_{s_l}\right)^n + \frac{\Phi_s}{RT^r}\right]_{D_2}\right\} \\
&\quad - \sum_{l=1}^{k}\left[\left(1-\epsilon\right)\Delta\left(\frac{1}{p_s}\dot{\eta}\frac{\partial p}{\partial \eta}\right)_l\right]_{D_2}^n \\
&\quad - 2\sum_{l=1}^{k}\left(\frac{1}{p_s}\delta_l \Delta p_l\right)_{M_2}^{n+\frac{1}{2}} + 2\sum_{l=1}^{k}\frac{\Delta B_l}{RT^r}\left(\boldsymbol{V}_l \cdot \nabla\, \Phi_s\right)_{M_2}^{n+\frac{1}{2}} \\
&\quad - 2\sum_{l=1}^{k}\frac{1}{p_s^r}\left\{\frac{1}{2}\left[\left(1+\epsilon\right)\left(\delta_l\right)_A^{n+1} + \left(1-\epsilon\right)\left(\delta_l\right)_{D_2}^{n}\right] - \left(\delta_l\right)_{M_2}^{n+\frac{1}{2}}\right\}\Delta p_l^r
\end{aligned} \tag{3.403}$$

This is not the actual equation used to determine $\left(\frac{1}{p_s}\dot{\eta}\frac{\partial p}{\partial \eta}\right)$ in the code. The equation actually used in the code to calculate $\left(\frac{1}{p_s}\dot{\eta}\frac{\partial p}{\partial \eta}\right)$ involves only the divergence at time $(n+1)$ with $\left(\ln p'_s\right)^{n+1}$ eliminated.

$$
\begin{aligned}
(1+\epsilon)\left(\frac{1}{p_s}\dot{\eta}\frac{\partial p}{\partial \eta}\right)^{n+1}_{k+\frac{1}{2}} = \\
\frac{2}{\Delta t}\left[\sum_{l=1}^{k} - B_{k+\frac{1}{2}}\sum_{l=1}^{K}\right]\Delta B_l\left[(\ln p_{s_l})^n + \frac{\Phi_s}{RT^r}\right]_{D_2} \\
-\left[\sum_{l=1}^{k} - B_{k+\frac{1}{2}}\sum_{l=1}^{K}\right]\left[(1-\epsilon)\,\Delta\left(\frac{1}{p_s}\dot{\eta}\frac{\partial p}{\partial \eta}\right)_l\right]^n_{D_2} \\
-2\left[\sum_{l=1}^{k} - B_{k+\frac{1}{2}}\sum_{l=1}^{K}\right]\left(\frac{1}{p_s}\delta_l \Delta p_l\right)^{n+\frac{1}{2}}_{M_2} \\
+2\left[\sum_{l=1}^{k} - B_{k+\frac{1}{2}}\sum_{l=1}^{K}\right]\frac{\Delta B_l}{RT^r}\left(\boldsymbol{V}_l \cdot \nabla\,\Phi_s\right)^{n+\frac{1}{2}}_{M_2} \\
-2\left[\sum_{l=1}^{k} - B_{k+\frac{1}{2}}\sum_{l=1}^{K}\right]\frac{1}{p_s^r}\left\{\frac{1}{2}\left[(1+\epsilon)\,(\delta_l)^{n+1}_{A} + (1-\epsilon)\,(\delta_l)^{n}_{D_2}\right] - (\delta_l)^{n+\frac{1}{2}}_{M_2}\right\}\Delta p_l^r
\end{aligned}
\tag{3.404}
$$

The combination $\left[(\ln p_{s_l})^n + \frac{\Phi_s}{RT^r} + \frac{1}{2}\frac{\Delta t}{RT^r}\left(\boldsymbol{V}\cdot\nabla\,\Phi_s\right)^{n+\frac{1}{2}}\right]_{D_2}$ is treated as a unit, and follows from (3.401).

3.4.8 Thermodynamic Equation

The thermodynamic equation is obtained from (25) of W&O94 modified to be spatially uncentered and to use $\ln p_s'$. In addition Hortal's modification [Temperton et al., 2001] is included, in which

$$
\frac{d}{dt}\left[-\left(p_s B\frac{\partial T}{\partial p}\right)_{ref}\frac{\Phi_s}{RT^r}\right] \tag{3.405}
$$

is subtracted from both sides of the temperature equation. This is akin to horizontal diffusion which includes the first order term converting horizontal derivatives from eta to pressure coordinates, with $(\ln p_s)$ replaced by $-\frac{\Phi_s}{RT^r}$, and $\left(p_s B\frac{\partial T}{\partial p}\right)_{ref}$ taken as a global average so it is invariant with time and can commute with the differential operators.

$$
\begin{aligned}
\frac{T_A^{n+1} - T_D^n}{\Delta t} &= \left\{ \left\{ \left[-\left(p_s B(\eta) \frac{\partial T}{\partial p} \right)_{ref} \frac{\Phi_s}{RT^r} \right]_A^{n+1} - \left[-\left(p_s B(\eta) \frac{\partial T}{\partial p} \right)_{ref} \frac{\Phi_s}{RT^r} \right]_D^{n} \right\} \Big/ \Delta t \right. \\
&\quad \left. + \frac{1}{RT^r} \left[\left(p_s B(\eta) \frac{\partial T}{\partial p} \right)_{ref} \boldsymbol{V} \cdot \nabla \, \Phi_s + \Phi_s \dot{\eta} \frac{\partial}{\partial \eta} \left(p_s B(\eta) \frac{\partial T}{\partial p} \right)_{ref} \right]_M^{n+\frac{1}{2}} \right\} \\
&\quad + \left(\frac{RT_v}{c_p^*} \frac{\omega}{p} \right)_M^{n+\frac{1}{2}} + Q_M^n \\
&\quad + \frac{RT^r}{c_p} \frac{p_s^r}{p^r} \left[B(\eta) \frac{d_2 \ln p_s'}{dt} + \overline{\left(\frac{1}{p_s} \dot{\eta} \frac{\partial p}{\partial \eta} \right)}^t \right] \\
&\quad - \frac{RT^r}{c_p} \frac{p_s^r}{p^r} \left[\left(\frac{p}{p_s} \right) \left(\frac{\omega}{p} \right) \right]_M^{n+\frac{1}{2}} \\
&\quad - \frac{RT^r}{c_p} \frac{p_s^r}{p^r} B(\eta) \left[\frac{1}{RT^r} \boldsymbol{V} \cdot \nabla \, \Phi_s \right]_{M_2}^{n+\frac{1}{2}}
\end{aligned} \tag{3.406}
$$

Note that Q^n represents the heating calculated to advance from time n to time $n+1$ and is valid over the interval.

The calculation of $\left(p_s B \frac{\partial T}{\partial p} \right)_{ref}$ follows that of the ECMWF (Research Manual 3, ECMWF Forecast Model, Adiabatic Part, ECMWF Research Department, 2nd edition, 1/88, pp 2.25-2.26) Consider a constant lapse rate atmosphere

$$T = T_0 \left(\frac{p}{p_0}\right)^{R\gamma/g} \tag{3.407}$$

$$\frac{\partial T}{\partial p} = \frac{1}{p}\frac{R\gamma}{g} T_0 \left(\frac{p}{p_0}\right)^{R\gamma/g} \tag{3.408}$$

$$p_s B \frac{\partial T}{\partial p} = B \frac{p_s}{p} \frac{R\gamma}{g} T \tag{3.409}$$

$$\left(p_s B \frac{\partial T}{\partial p}\right)_{ref} = B_k \frac{(p_s)_{ref}}{(p_k)_{ref}} \frac{R\gamma}{g} (T_k)_{ref} \quad \text{for} \quad (T_k)_{ref} > T_C \tag{3.410}$$

$$\left(p_s B \frac{\partial T}{\partial p}\right)_{ref} = 0 \quad for \quad (T_k)_{ref} \leq T_C \tag{3.411}$$

$$(p_k)_{ref} = A_k p_0 + B_k (p_s)_{ref} \tag{3.412}$$

$$(T_k)_{ref} = T_0 \left(\frac{(p_k)_{ref}}{(p_s)_{ref}}\right)^{R\gamma/g} \tag{3.413}$$

$$(p_s)_{ref} = 1013.25\text{mb} \tag{3.414}$$

$$T_0 = 288\text{K} \tag{3.415}$$

$$p_0 = 1000\text{mb} \tag{3.416}$$

$$\gamma = 6.5\text{K/km} \tag{3.417}$$

$$T_C = 216.5\text{K} \tag{3.418}$$

3.4.9 Momentum equations

The momentum equations follow from (3) of W&O94 modified to be spatially uncentered, to use $\ln p'_s$, and with the Coriolis term implicit following Côté and Staniforth [1988] and Temperton [1997]. The semi-implicit, semi-Lagrangian momentum equation at level k (but with the level subscript k suppressed) is

$$
\begin{aligned}
\frac{\boldsymbol{V}_A^{n+1} - \boldsymbol{V}_D^{n}}{\Delta t} \;=\; & -\frac{1}{2}\Big\{ (1+\epsilon)\left[f\hat{\boldsymbol{k}}\times\boldsymbol{V}\right]_A^{n+1} + (1-\epsilon)\left[f\hat{\boldsymbol{k}}\times\boldsymbol{V}\right]_D^{n} \Big\} + \boldsymbol{F}_M^n \\
& -\frac{1}{2}\Big\{ (1+\epsilon)\left[\nabla\left(\Phi_s + R\boldsymbol{H}_k\cdot\boldsymbol{T}_v\right) + RT_v\frac{B}{p}p_s\nabla\ln p_s\right]_A^{n+\frac{1}{2}} \\
& \quad + (1-\epsilon)\left[\nabla\left(\Phi_s + R\boldsymbol{H}_k\cdot\boldsymbol{T}_v\right) + RT_v\frac{B}{p}p_s\nabla\ln p_s\right]_D^{n+\frac{1}{2}} \Big\} \\
& -\frac{1}{2}\Big\{ (1+\epsilon)\nabla\left[R\boldsymbol{H}_k^r\cdot\boldsymbol{T} + RT^r\ln p_s'\right]_A^{n+1} \\
& \quad - (1+\epsilon)\nabla\left[\Phi_s + R\boldsymbol{H}_k^r\cdot\boldsymbol{T} + RT^r\ln p_s\right]_A^{n+\frac{1}{2}} \\
& \quad + (1-\epsilon)\nabla\left[\Phi_s + R\boldsymbol{H}_k^r\cdot\boldsymbol{T} + RT^r\ln p_s\right]_D^{n} \\
& \quad - (1-\epsilon)\nabla\left[\Phi_s + R\boldsymbol{H}_k^r\cdot\boldsymbol{T} + RT^r\ln p_s\right]_D^{n+\frac{1}{2}} \Big\}
\end{aligned}
\tag{3.419}
$$

The gradient of the geopotential is more complex than in the σ system because the hydrostatic matrix $\boldsymbol{H}$ depends on the local pressure:

$$
\nabla\left(\boldsymbol{H}_k\cdot\boldsymbol{T}_v\right) = \boldsymbol{H}_k\cdot\left[\left(1+\epsilon_v\boldsymbol{q}\right)\nabla\boldsymbol{T} + \epsilon_v\boldsymbol{T}\nabla\boldsymbol{q}\right] + \boldsymbol{T}_v\cdot\nabla\boldsymbol{H}_k \tag{3.420}
$$

where ϵ_v is $(R_v/R - 1)$ and R_v is the gas constant for water vapor. The gradient of T is calculated from the spectral representation and that of q from a discrete cubic approximation that is consistent with the interpolation used in the semi-Lagrangian water vapor advection. In general, the elements of $\boldsymbol{H}$ are functions of pressure at adjacent discrete model levels

$$
H_{kl} = f_{kl}(p_{l+1/2}, p_l, p_{l-1/2}) \tag{3.421}
$$

The gradient is then a function of pressure and the pressure gradient

$$
\nabla H_{kl} = g_{kl}(p_{l+1/2},\ p_l,\ p_{l-1/2}, \nabla p_{l+1/2}, \nabla p_l, \nabla p_{l-1/2}) \tag{3.422}
$$

The pressure gradient is available from (3.393) and the surface pressure gradient calculated from the spectral representation

$$
\nabla p_l = B_l\nabla p_s = B_l p_s\nabla\ln p_s \tag{3.423}
$$

3.4.10 Development of semi-implicit system equations

The momentum equation can be written as

$$
\begin{aligned}
\frac{\boldsymbol{V}_A^{n+1} - \boldsymbol{V}_D^{n}}{\Delta t} = & -\frac{1}{2}\Big\{ (1+\epsilon)\left[f\hat{\boldsymbol{k}}\times\boldsymbol{V}\right]_A^{n+1} + (1-\epsilon)\left[f\hat{\boldsymbol{k}}\times\boldsymbol{V}\right]_D^{n} \Big\} \\
& -\frac{1}{2}\Big\{ (1+\epsilon)\nabla\left[R\boldsymbol{H}_k^r\cdot\boldsymbol{T} + RT^r\ln p_s'\right]_A^{n+1} \Big\} + RHS_{\boldsymbol{V}}\ ,
\end{aligned}
\tag{3.424}
$$

where $RHS_{\boldsymbol{V}}$ contains known terms at times $(n+\frac{1}{2})$ and (n).

By combining terms, 3.424 can be written in general as

$$\mathcal{U}_{A}^{n+1}\hat{\mathbf{i}}_{A}+\mathcal{V}_{A}^{n+1}\hat{\mathbf{j}}_{A}=\mathcal{U}_{A}\hat{\mathbf{i}}_{A}+\mathcal{V}_{A}\hat{\mathbf{j}}_{A}+\mathcal{U}_{D}\hat{\mathbf{i}}_{D}+\mathcal{V}_{D}\hat{\mathbf{j}}_{D}\ , \tag{3.425}$$

where $\hat{\mathbf{i}}$ and $\hat{\mathbf{j}}$ denote the spherical unit vectors in the longitudinal and latitudinal directions, respectively, at the points indicated by the subscripts, and $\mathcal{U}$ and $\mathcal{V}$ denote the appropriate combinations of terms in 3.424. Note that $\mathcal{U}_{A}^{n+1}$ is distinct from the $\mathcal{U}_{A}$. Following Bates et al. [1990], equations for the individual components are obtained by relating the unit vectors at the departure points ($\hat{\mathbf{i}}_{D}$,$\hat{\mathbf{j}}_{D}$) to those at the arrival points ($\hat{\mathbf{i}}_{A}$,$\hat{\mathbf{j}}_{A}$):

$$\hat{\mathbf{i}}_{D}=\alpha_{A}^{u}\hat{\mathbf{i}}_{A}+\beta_{A}^{u}\hat{\mathbf{j}}_{A} \tag{3.426}$$

$$\hat{\mathbf{j}}_{D}=\alpha_{A}^{v}\hat{\mathbf{i}}_{A}+\beta_{A}^{v}\hat{\mathbf{j}}_{A}\ , \tag{3.427}$$

in which the vertical components ($\hat{\mathbf{k}}$) are ignored. The dependence of α's and β's on the latitudes and longitudes of the arrival and departure points is given in the Appendix of Bates et al. [1990].

W&O94 followed Bates et al. [1990] which ignored rotating the vector to remain parallel to the earth's surface during translation. We include that factor by keeping the length of the vector written in terms of $\left(\hat{\boldsymbol{i}}_{A},\hat{\boldsymbol{j}}_{A}\right)$ the same as the length of the vector written in terms of $\left(\hat{\boldsymbol{i}}_{D},\hat{\boldsymbol{j}}_{D}\right)$. Thus, (10) of W&O94 becomes

$$\begin{aligned}\mathcal{U}_{A}^{n+1}&=\mathcal{U}_{A}+\gamma\alpha_{A}^{u}\mathcal{U}_{D}+\gamma\alpha_{A}^{v}\mathcal{V}_{D}\\ \mathcal{V}_{A}^{n+1}&=\mathcal{V}_{A}+\gamma\beta_{A}^{u}\mathcal{U}_{D}+\gamma\beta_{A}^{v}\mathcal{V}_{D}\end{aligned} \tag{3.428}$$

where

$$\gamma=\left[\frac{\mathcal{U}_{D}^{2}+\mathcal{V}_{D}^{2}}{\left(\mathcal{U}_{D}\alpha_{A}^{u}+\mathcal{V}_{D}\alpha_{A}^{v}\right)^{2}+\left(\mathcal{U}_{D}\beta_{A}^{u}+\mathcal{V}_{D}\beta_{A}^{v}\right)^{2}}\right]^{\frac{1}{2}} \tag{3.429}$$

After the momentum equation is written in a common set of unit vectors

$$\boldsymbol{V}_{A}^{n+1}+\left(\frac{1+\epsilon}{2}\right)\Delta t\left[f\hat{\boldsymbol{k}}\times\boldsymbol{V}\right]_{A}^{n+1}+\left(\frac{1+\epsilon}{2}\right)\Delta t\nabla\left[R\boldsymbol{H}_{k}^{r}\cdot\boldsymbol{T}+RT^{r}\ln p_{s}^{\prime}\right]_{A}^{n+1}=\mathcal{R}_{\boldsymbol{V}}^{*} \tag{3.430}$$

Drop the $(\quad)_{A}^{n+1}$ from the notation, define

$$\alpha=(1+\epsilon)\,\Delta t\Omega \tag{3.431}$$

and transform to vorticity and divergence

$$\zeta+\alpha\sin\varphi\delta+\frac{\alpha}{a}v\cos\varphi=\frac{1}{a\cos\varphi}\left[\frac{\partial\mathcal{R}_{v}^{*}}{\partial\lambda}-\frac{\partial}{\partial\varphi}\left(\mathcal{R}_{u}^{*}\cos\varphi\right)\right] \tag{3.432}$$

$$\begin{aligned}\delta-\alpha\sin\varphi\zeta+\frac{\alpha}{a}u\cos\varphi&+\left(\frac{1+\epsilon}{2}\right)\Delta t\nabla^{2}\left[R\boldsymbol{H}_{k}^{r}\cdot\boldsymbol{T}+RT^{r}\ln p_{s}^{\prime}\right]_{A}^{n+1}\\&=\frac{1}{a\cos\varphi}\left[\frac{\partial\mathcal{R}_{u}^{*}}{\partial\lambda}+\frac{\partial}{\partial\varphi}\left(\mathcal{R}_{v}^{*}\cos\varphi\right)\right]\end{aligned} \tag{3.433}$$

Note that

$$u\cos\varphi = \frac{1}{a}\frac{\partial}{\partial\lambda}\left(\nabla^{-2}\delta\right) - \frac{\cos\varphi}{a}\frac{\partial}{\partial\varphi}\left(\nabla^{-2}\zeta\right) \tag{3.434}$$

$$v\cos\varphi = \frac{1}{a}\frac{\partial}{\partial\lambda}\left(\nabla^{-2}\zeta\right) + \frac{\cos\varphi}{a}\frac{\partial}{\partial\varphi}\left(\nabla^{-2}\delta\right) \tag{3.435}$$

Then the vorticity and divergence equations become

$$\begin{aligned}\zeta + \alpha\sin\varphi\delta + \frac{\alpha}{a^2}\frac{\partial}{\partial\lambda}\left(\nabla^{-2}\zeta\right) &+ \frac{\alpha\cos\varphi}{a^2}\frac{\partial}{\partial\varphi}\left(\nabla^{-2}\delta\right) \\ &= \frac{1}{a\cos\varphi}\left[\frac{\partial\mathcal{R}_v^*}{\partial\lambda} - \frac{\partial}{\partial\varphi}\left(\mathcal{R}_u^*\cos\varphi\right)\right] = \mathcal{L}\end{aligned} \tag{3.436}$$

$$\begin{aligned}\delta - \alpha\sin\varphi\zeta + \frac{\alpha}{a^2}\frac{\partial}{\partial\lambda}\left(\nabla^{-2}\delta\right) &- \frac{\alpha\cos\varphi}{a^2}\frac{\partial}{\partial\varphi}\left(\nabla^{-2}\zeta\right) + \left(\frac{1+\epsilon}{2}\right)\Delta t\nabla^2\left[R\boldsymbol{H}_k^r\cdot\boldsymbol{T} + RT^r\ln p_s'\right]_A^{n+1} \\ &= \frac{1}{a\cos\varphi}\left[\frac{\partial\mathcal{R}_u^*}{\partial\lambda} + \frac{\partial}{\partial\varphi}\left(\mathcal{R}_v^*\cos\varphi\right)\right] = \mathcal{M}\end{aligned} \tag{3.437}$$

Transform to spectral space as described in the description of the Eulerian spectral transform dynamical core. Note, from (4.5b) and (4.6) on page 177 of Machenhauer [1979]

$$\mu P_n^m = D_{n+1}^m P_{n+1}^m + D_n^m P_{n-1}^m \tag{3.438}$$

$$D_n^m = \left(\frac{n^2-m^2}{4n^2-1}\right)^{\frac{1}{2}} \tag{3.439}$$

and from (4.5a) on page 177 of Machenhauer [1979]

$$\left(1-\mu^2\right)\frac{\partial}{\partial\mu}P_n^m = -nD_{n+1}^m P_{n+1}^m + (n+1)\,D_n^m P_{n-1}^m \tag{3.440}$$

Then the equations for the spectral coefficients at time $n+1$ at each vertical level are

$$\zeta_n^m\left(1 - \frac{im\alpha}{n\,(n+1)}\right) + \delta_{n+1}^m\alpha\left(\frac{n}{n+1}\right)D_{n+1}^m + \delta_{n-1}^m\alpha\left(\frac{n+1}{n}\right)D_n^m = \mathcal{L}_n^m \tag{3.441}$$

$$\begin{aligned}\delta_n^m\left(1 - \frac{im\alpha}{n\,(n+1)}\right) - \zeta_{n+1}^m\alpha\left(\frac{n}{n+1}\right)D_{n+1}^m - \zeta_{n-1}^m\alpha\left(\frac{n+1}{n}\right)D_n^m & \\ - \left(\frac{1+\epsilon}{2}\right)\Delta t\frac{n\,(n+1)}{a^2}\left[R\boldsymbol{H}_k^r\cdot\boldsymbol{T}_n^m + RT^r\ln p_{sn}'^m\right] &= \mathcal{M}_n^m\end{aligned} \tag{3.442}$$

$$\ln p_{sn}'^m = \mathrm{PS}_n^m - \left(\frac{1+\epsilon}{2}\right)\frac{\Delta t}{p_s^r}\left(\underline{\Delta p}^r\right)^T\underline{\delta}_n^m \tag{3.443}$$

$$\underline{T}_n^m = \underline{\mathrm{TS}}_n^m - \left(\frac{1+\epsilon}{2}\right)\Delta t\boldsymbol{D}^r\underline{\delta}_n^m \tag{3.444}$$

The underbar denotes a vector over vertical levels. Rewrite the vorticity and divergence equations in terms of vectors over vertical levels.

$$\underline{\delta}_n^m \left(1 - \frac{im\alpha}{n\,(n+1)}\right) - \underline{\zeta}_{n+1}^m \alpha \left(\frac{n}{n+1}\right) - D_{n+1}^m \underline{\zeta}_{n-1}^m \alpha \left(\frac{n+1}{-n}\right) D_n^m \tag{3.445}$$
$$- \left(\frac{1+\epsilon}{2}\right) \Delta t \frac{n\,(n+1)}{a^2} \left[R\boldsymbol{H}^r \underline{T}_n^m + R\underline{T}^r \ln p'^{\,m}_{sn}\right] = \underline{DS}_n^m$$

$$\underline{\zeta}_n^m \left(1 - \frac{im\alpha}{n\,(n+1)}\right) + \underline{\delta}_{n+1}^m \alpha \left(\frac{n}{n+1}\right) D_{n+1}^m + \underline{\delta}_{n-1}^m \alpha \left(\frac{n+1}{n}\right) D_n^m = \underline{VS}_n^m \tag{3.446}$$

Define $\underline{h}_n^m$ by

$$g\underline{h}_n^m = R\boldsymbol{H}^r T_n^m + R\underline{T}^r \ln p'^{\,m}_{sn} \tag{3.447}$$

and

$$\mathcal{A}_n^m = 1 - \frac{im\alpha}{n\,(n+1)} \tag{3.448}$$

$$\mathcal{B}^{+m}_{\ n} = \alpha \left(\frac{n}{n+1}\right) D_{n+1}^m \tag{3.449}$$

$$\mathcal{B}^{-m}_{\ n} = \alpha \left(\frac{n+1}{n}\right) D_n^m \tag{3.450}$$

Then the vorticity and divergence equations are

$$\mathcal{A}_n^m \underline{\zeta}_n^m + \mathcal{B}^{+m}_{\ n} \underline{\delta}_{n+1}^m + \mathcal{B}^{-m}_{\ n} \underline{\delta}_{n-1}^m = \underline{VS}_n^m \tag{3.451}$$

$$\mathcal{A}_n^m \underline{\delta}_n^m - \mathcal{B}^{+m}_{\ n} \underline{\zeta}_{n+1}^m \mathcal{B}^{-m}_{\ n} - \underline{\zeta}_{n-1}^m - \left(\frac{1+\epsilon}{2}\right) \Delta t \frac{n\,(n+1)}{a^2} g\underline{h}_n^m = \underline{DS}_n^m \tag{3.452}$$

Note that these equations are uncoupled in the vertical, i.e. each vertical level involves variables at that level only. The equation for $\underline{h}_n^m$ however couples all levels.

$$g\underline{h}_n^m = -\left(\frac{1+\epsilon}{2}\right) \Delta t \left[R\boldsymbol{H}^r \boldsymbol{D}^r + R\underline{T}^r \frac{\left(\Delta \underline{p}^r\right)^T}{p_s^r}\right] \underline{\delta}_n^m + R\boldsymbol{H}^r \underline{TS}_n^m + R\underline{T}^r \mathrm{PS}_n^m \tag{3.453}$$

Define $\boldsymbol{C}^r$ and $\underline{HS}_n^m$ so that

$$g\underline{h}_n^m = -\left(\frac{1+\epsilon}{2}\right) \Delta t\, C^r \underline{\delta}_n^m + \underline{HS}_n^m \tag{3.454}$$

Let $g\mathrm{D}_\ell$ denote the eigenvalues of $\boldsymbol{C}^r$ with corresponding eigenvectors $\underline{\Phi}_\ell$ and $\boldsymbol{\Phi}$ is the matrix with columns $\underline{\Phi}_\ell$

$$\boldsymbol{\Phi} = \left(\underline{\Phi}_1\, \underline{\Phi}_2 \ldots \underline{\Phi}_L \right) \tag{3.455}$$

and $g\boldsymbol{D}$ the diagonal matrix of corresponding eigenvalues

$$g\boldsymbol{D} = g\begin{pmatrix} \mathrm{D}_1 & 0 & \cdots & 0 \\ 0 & \mathrm{D}_2 & \cdots & 0 \\ \vdots & \vdots & \ddots & \vdots \\ 0 & 0 & \cdots & \mathrm{D}_L \end{pmatrix} \tag{3.456}$$

$$\boldsymbol{C}^r\boldsymbol{\Phi} = \boldsymbol{\Phi} g\boldsymbol{D} \tag{3.457}$$

$$\boldsymbol{\Phi}^{-1}\boldsymbol{C}^r\boldsymbol{\Phi} = g\boldsymbol{D} \tag{3.458}$$

Then transform

$$\tilde{\underline{\zeta}}_n^m = \boldsymbol{\Phi}^{-1}\underline{\zeta}_n^m \quad , \quad \widetilde{\underline{VS}}_n^m = \boldsymbol{\Phi}^{-1}\underline{VS}_n^m \tag{3.459}$$

$$\tilde{\underline{\delta}}_n^m = \boldsymbol{\Phi}^{-1}\underline{\delta}_n^m \quad , \quad \widetilde{\underline{DS}}_n^m = \boldsymbol{\Phi}^{-1}\underline{DS}_n^m \tag{3.460}$$

$$\tilde{\underline{h}}_n^m = \boldsymbol{\Phi}^{-1}\underline{h}_n^m \quad , \quad \widetilde{\underline{HS}}_n^m = \boldsymbol{\Phi}^{-1}\underline{HS}_n^m \tag{3.461}$$

$$\mathcal{A}_n^m\tilde{\underline{\zeta}}_n^m + \mathcal{B}^+{}_n^m\tilde{\underline{\delta}}_{n+1}^m + \mathcal{B}^-{}_n^m\tilde{\underline{\delta}}_{n-1}^m = \widetilde{\underline{VS}}_n^m \tag{3.462}$$

$$\mathcal{A}_n^m\tilde{\underline{\delta}}_n^m - \mathcal{B}^+{}_n^m\tilde{\underline{\zeta}}_{n+1}^m\mathcal{B}^-{}_n^m - \tilde{\underline{\zeta}}_{n-1}^m - \left(\frac{1+\epsilon}{2}\right)\Delta t\frac{n\,(n+1)}{a^2}g\tilde{\underline{h}}_n^m = \widetilde{\underline{DS}}_n^m \tag{3.463}$$

$$g\tilde{\underline{h}}_n^m + \left(\frac{1+\epsilon}{2}\right)\Delta t\boldsymbol{\Phi}^{-1}\boldsymbol{C}^r\boldsymbol{\Phi}\boldsymbol{\Phi}^{-1}\underline{\delta}_n^m = \widetilde{\underline{HS}}_n^m \tag{3.464}$$

$$\tilde{\underline{h}}_n^m + \left(\frac{1+\epsilon}{2}\right)\Delta t\boldsymbol{D}\tilde{\underline{\delta}}_n^m = \frac{1}{g}\widetilde{\underline{HS}}_n^m \tag{3.465}$$

Since $\boldsymbol{D}$ is diagonal, all equations are now uncoupled in the vertical.

For each vertical mode, i.e. element of $(\tilde{\ \underline{\ }})_n^m$, and for each Fourier wavenumber m we have a system of equations in n to solve. In following we drop the Fourier index m and the modal element index $(\ \ )_\ell$ from the notation.

$$\mathcal{A}_n\tilde{\zeta}_n + \mathcal{B}^+{}_n\tilde{\delta}_{n+1} + \mathcal{B}^-{}_n\tilde{\delta}_{n-1} = \widetilde{VS}_n \tag{3.466}$$

$$\mathcal{A}_n\tilde{\delta}_n - \mathcal{B}^+{}_n\tilde{\zeta}_{n+1}\mathcal{B}^-{}_n\tilde{\zeta}_{n-1} - \left(\frac{1+\epsilon}{2}\right)\Delta t\frac{n\,(n+1)}{a^2}g\tilde{h}_n = \widetilde{DS}_n \tag{3.467}$$

$$\tilde{h}_n + \left(\frac{1+\epsilon}{2}\right)\Delta t\mathrm{D}_\ell\tilde{\delta}_n = \frac{1}{g}\widetilde{HS}_n \tag{3.468}$$

The modal index $(\ \ )_\ell$ was included in the above equation on D only as a reminder, but will also be dropped in the following.

Substitute $\tilde{\zeta}$ and $\tilde{h}$ into the $\tilde{\delta}$ equation.

$$\begin{aligned}\left[\mathcal{A}_n + \left(\frac{1+\epsilon}{2}\right)^2(\Delta t)^2\,\frac{n\,(n+1)}{a^2}g\mathrm{D} + \mathcal{B}^+{}_n\mathcal{A}_{n+1}^{-1}\mathcal{B}^-{}_{n+1} + \mathcal{B}^-{}_n\mathcal{A}_{n-1}^{-1}\mathcal{B}^+{}_{n-1}\right]\tilde{\delta}_n \\ + \left(\mathcal{B}^+{}_n\mathcal{A}_{n+1}^{-1}\mathcal{B}^+{}_{n+1}\right)\tilde{\delta}_{n+2} \quad + \quad \left(\mathcal{B}^-{}_n\mathcal{A}_{n-1}^{-1}\mathcal{B}^-{}_{n-1}\right)\tilde{\delta}_{n-2} \\ = \widetilde{DS}_n + \left(\frac{1+\epsilon}{2}\right)\Delta t\frac{n\,(n+1)}{a^2}\widetilde{HS}_n + \mathcal{B}^+{}_n\mathcal{A}_{n+1}^{-1}\widetilde{VS}_{n+1} + \mathcal{B}^-{}_n\mathcal{A}_{n-1}^{-1}\widetilde{VS}_{n-1}\end{aligned} \tag{3.469}$$

which is just two tri-diagonal systems of equations, one for the even and one for the odd n's, and $m \leq n \leq N$

At the end of the system, the boundary conditions are

$$\begin{aligned} n = m, \qquad & \mathcal{B}^{-}{}_{n} = \mathcal{B}^{-m}{}_{m} = 0 \\ n = m+1, \quad & \mathcal{B}^{-}{}_{n-1} = \mathcal{B}^{-m}{}_{m} = \mathcal{B}^{-m}{}_{(m+1)-1} = 0 \end{aligned} \tag{3.470}$$

the $\tilde{\delta}_{n-2}$ term is not present, and from the underlying truncation

$$\tilde{\delta}^{m}_{N+1} = \tilde{\delta}^{m}_{N+2} = 0 \tag{3.471}$$

For each m and ℓ we have the general systems of equations

$$-A_n\tilde{\delta}_{n+2} + B_n\tilde{\delta}_n - C_n - \tilde{\delta}_{n-2} = D_n \, , \begin{cases} n = m, m+2, ..., \begin{cases} N+1 \\ \text{or} \\ N+2 \end{cases} \\ n = m+1, m+3, ..., \begin{cases} N+1 \\ \text{or} \\ N+2 \end{cases} \end{cases} \tag{3.472}$$

$$C_m = C_{m+1} = 0 \tag{3.473}$$

$$\tilde{\delta}_{N+1} = \tilde{\delta}_{N+2} = 0 \tag{3.474}$$

Assume solutions of the form

$$\tilde{\delta}_n = E_n\tilde{\delta}_{n+2} + F_n \tag{3.475}$$

then

$$E_m = \frac{A_m}{B_m} \tag{3.476}$$

$$F_M = \frac{D_m}{B_m} \tag{3.477}$$

$$E_n = \frac{A_n}{B_n - C_nE_{n-2}} \quad , \quad n = m+2, m+4, ..., \begin{cases} N-2 \\ \text{or} \\ N-3 \end{cases} \tag{3.478}$$

$$F_n = \frac{D_n + C_nF_{n-2}}{B_n - C_nE_{n-2}} \quad , \quad n = m+2, m+4, ..., \begin{cases} N \\ \text{or} \\ N-1 \end{cases} \tag{3.479}$$

$$\tilde{\delta}_N = F_N \quad \text{or} \quad \tilde{\delta}_{N-1} = F_{N-1} \, , \tag{3.480}$$

$$\tilde{\delta}_n = E_n\tilde{\delta}_{n+2} + F_n \, , \quad \begin{cases} n = N-2, N-4, ..., \begin{cases} m \\ \text{or} \\ m+1 \end{cases} \\ n = N-3, N-5, ..., \begin{cases} m+1 \\ \text{or} \\ m \end{cases} \end{cases} \tag{3.481}$$

Divergence in physical space is obtained from the vertical mode coefficients by

$$\underline{\delta}_n^m = \mathbf{\Phi}\underline{\tilde{\delta}}_n^m \tag{3.482}$$

The remaining variables are obtained in physical space by

$$\zeta_n^m\left(1-\frac{im\alpha}{n\left(n+1\right)}\right) = \mathcal{L}_n^m - \delta_{n+1}^m\alpha\left(\frac{n}{n+1}\right)D_{n+1}^m - \delta_{n-1}^m\alpha\left(\frac{n+1}{n}\right)D_n^m \tag{3.483}$$

$$\underline{T}_n^m = \underline{\mathrm{TS}}_n^m - \left(\frac{1+\epsilon}{2}\right)\Delta t\boldsymbol{D}^r\underline{\delta}_n^m \tag{3.484}$$

$$\ln p'^m_{sn} = \mathrm{PS}_n^m - \left(\frac{1+\epsilon}{2}\right)\frac{\Delta t}{p_s^r}\left(\underline{\Delta p^r}\right)^T\underline{\delta}_n^m \tag{3.485}$$

3.4.11 Trajectory Calculation

The trajectory calculation follows Hortal [1999] Let $\boldsymbol{R}$ denote the position vector of the parcel,

$$\frac{d\boldsymbol{R}}{dt} = \boldsymbol{V} \tag{3.486}$$

which can be approximated in general by

$$\boldsymbol{R}_D^n = \boldsymbol{R}_A^{n+1} - \Delta t\boldsymbol{V}_M^{n+\frac{1}{2}} \tag{3.487}$$

Hortal's method is based on a Taylor's series expansion

$$\boldsymbol{R}_A^{n+1} = \boldsymbol{R}_D^n + \Delta t\left(\frac{d\boldsymbol{R}}{dt}\right)_D^n + \frac{\Delta t^2}{2}\left(\frac{d^2\boldsymbol{R}}{dt^2}\right)_D^n + \ldots \tag{3.488}$$

or substituting for $d\boldsymbol{R}/dt$

$$\boldsymbol{R}_A^{n+1} = \boldsymbol{R}_D^n + \Delta t\boldsymbol{V}_D^n + \frac{\Delta t^2}{2}\left(\frac{d\boldsymbol{V}}{dt}\right)_D^n + \ldots \tag{3.489}$$

Approximate

$$\left(\frac{d\boldsymbol{V}}{dt}\right)_D^n \approx \frac{\boldsymbol{V}_A^n - \boldsymbol{V}_D^{n-1}}{\Delta t} \tag{3.490}$$

giving

$$\boldsymbol{V}_M^{n+\frac{1}{2}} = \frac{1}{2}\left[\left(2\boldsymbol{V}^n - \boldsymbol{V}^{n-1}\right)_D + \boldsymbol{V}_A^n\right] \tag{3.491}$$

for the trajectory equation.

3.4.12 Mass and energy fixers and statistics calculations

The semi-Lagrangian dynamical core applies the same mass and energy fixers and statistical calculations as the Eulerian dynamical core. These are described in sections 3.3.19, 3.3.20, and 3.3.21.

Chapter 4

Model Physics

As stated in chapter 2, the total parameterization package in CAM 5.0 consists of a sequence of components, indicated by

$$P = \{M, R, S, T\} \ , \tag{4.1}$$

where M denotes (Moist) precipitation processes, R denotes clouds and Radiation, S denotes the Surface model, and T denotes Turbulent mixing. Each of these in turn is subdivided into various components: M includes an optional dry adiabatic adjustment normally applied only in the stratosphere, moist penetrative convection, shallow convection, and large-scale stable condensation; R first calculates the cloud parameterization followed by the radiation parameterization; S provides the surface fluxes obtained from land, ocean and sea ice models, or calculates them based on specified surface conditions such as sea surface temperatures and sea ice distribution. These surface fluxes provide lower flux boundary conditions for the turbulent mixing T which is comprised of the planetary boundary layer parameterization, vertical diffusion, and gravity wave drag.

The updating described in the preceding paragraph of all variable except temperature is straightforward. Temperature, however, is a little more complicated and follows the general procedure described by Boville and Bretherton [2003*a*] involving dry static energy. The state variable updated after each time-split parameterization component is the dry static energy s_i. Let i be the index in a sequence of I time-split processes. The dry static energy at the end of the ith process is s_i. The dry static energy is updated using the heating rate Q calculated by the ith process:

$$s_i = s_{i-1} + (\Delta t)\, Q_i(s_{i-1}, T_{i-1}, \Phi_{i-1}, q_{i-1}, ...) \tag{4.2}$$

In processes not formulated in terms of dry static energy but rather in terms of a temperature tendency, the heating rate is given by $Q_i = (T_i - T_{i-1}) \,/\, (C_p \Delta t)$.

The temperature, T_i, and geopotential, Φ_i, are calculated from s_i by inverting the equation for s

$$s = C_p T + gz = C_p T + \Phi \tag{4.3}$$

with the hydrostatic equation

$$\Phi_k = \Phi_s + R \sum_{l=k}^{K} H_{kl} T_{vl} \tag{4.4}$$

substituted for Φ.

The temperature tendencies for each process are also accumulated over the processes. For processes formulated in terms of dry static energy the temperature tendencies are calculated from the dry static energy tendency. Let $\Delta T_i/\Delta t$ denote the total accumulation at the end of the ith process. Then

$$\frac{\Delta T_i}{\Delta t} = \frac{\Delta T_{i-1}}{\Delta t} + \frac{\Delta s_i}{\Delta t}/C_p \tag{4.5}$$

$$\frac{\Delta s_i}{\Delta t}/C_p = \frac{(s_i - s_{i-1})}{\Delta t}/C_p \tag{4.6}$$

which assumes Φ is unchanged. Note that the inversion of s for T and Φ changes T and Φ. This is not included in the $\Delta T_i/\Delta t$ above for processes formulated to give dry static energy tendencies.. In processes not formulated in terms of dry static energy but rather in terms of a temperature tendency, that tendency is simply accumulated.

After the last parameterization is completed, the dry static energy of the last update is saved. This final column energy is saved and used at the beginning of the next physics calculation following the Finite Volume dynamical update to calculate the global energy fixer associated with the dynamical core. The implication is that the energy inconsistency introduced by sending the T described above to the FV rather than the T returned by inverting the dry static energy is included in the fixer attributed to the dynamics. The accumulated physics temperature tendency is also available after the last parameterization is completed, $\Delta T_I/\Delta t$. An updated temperature is calculated from it by adding it to the temperature at the beginning of the physics.

$$T_I = T_0 + \frac{\Delta T_I}{\Delta t} * \Delta t \tag{4.7}$$

This temperature is converted to virtual potential temperature and passed to the Finite Volume dynamical core. The temperature tendency itself is passed to the spectral transform Eulerian and semi-Lagrangian dynamical cores. The inconsistency in the use of temperature and dry static energy apparent in the description above should be eliminated in future versions of the model.

4.1 Conversion to and from dry and wet mixing ratios for trace constituents in the model

There are trade offs in the various options for the representation of trace constituents χ in any general circulation model:

1. When the air mass in a model layer is defined to include the water vapor, it is frequently convenient to represent the quantity of trace constituent as a "moist" mixing ratio χ^m, that is, the mass of tracer per mass of moist air in the layer. The advantage of the representation is that one need only multiply the moist mixing ratio by the moist air mass to determine the tracer air mass. It has the disadvantage of implicitly requiring a change in χ^m whenever the water vapor q changes within the layer, even if the mass of the trace constituent does not.

2. One can also utilize a "dry" mixing ratio χ^d to define the amount of constituent in a volume of air. This variable does not have the implicit dependence on water vapor, but does require that the mass of water vapor be factored out of the air mass itself in order to calculate the mass of tracer in a cell.

NCAR atmospheric models have historically used a combination of dry and moist mixing ratios. Physical parameterizations (including convective transport) have utilized moist mixing ratios. The resolved scale transport performed in the Eulerian (spectral), and semi-Lagrangian dynamics use dry mixing ratios, specifically to prevent oscillations associated with variations in water vapor requiring changes in tracer mixing ratios. The finite volume dynamics module utilizes moist mixing ratios, with an attempt to maintain internal consistency between transport of water vapor and other constituents.

There is no "right" way to resolve the requirements associated with the simultaneous treatment of water vapor, air mass in a layer and tracer mixing ratios. But the historical treatment significantly complicates the interpretation of model simulations, and in the latest version of CAM we have also provided an "alternate" representation. That is, we allow the user to specify whether any given trace constituent is interpreted as a "dry" or "wet" mixing ratio through the specification of an "attribute" to the constituent in the physics state structure. The details of the specification are described in the users manual, but we do identify the interaction between state quantities here.

At the end of the dynamics update to the model state, the surface pressure, specific humidity, and tracer mixing ratios are returned to the model. The physics update then is allowed to update specific humidity and tracer mixing ratios through a sequence of operator splitting updates *but the surface pressure is not allowed to evolve*. Because there is an explicit relationship between the surface pressure and the air mass within each layer we assume that water mass can change within the layer by physical parameterizations *but dry air mass cannot*. We have chosen to define the dry air mass in each layer at the beginning of the physics update as

$$\delta p^d_{i,k} = (1 - q^0_{i,k})\delta^m_{i,k}$$

for column i, level k. Note that the specific humidity used is the value defined at the beginning of the physics update. We define the transformation between dry and wet mixing ratios to be

$$\chi^d_{i,k} = (\delta p^d_{i,k}/\delta p^m_{i,k})\chi^m_{i,k}$$

We note that the various physical parameterizations that operate on tracers on the model (convection, turbulent transport, scavenging, chemistry) will require a specification of the air mass within each cell as well as the value of the mixing ratio in the cell. We have modified the model so that it will use the correct value of δp depending on the attribute of the tracer, that is, we use couplets of $(\chi^m, \delta p^m)$ or $(\chi^d, \delta p^d)$ in order to assure that the process conserves mass appropriately.

We note further that there are a number of parameterizations (*e.g.* convection, vertical diffusion) that transport species using a continuity equation in a flux form that can be written generically as

$$\frac{\partial \chi}{\partial t} = \frac{\partial F(\chi)}{\partial p} \tag{4.8}$$

where F indicates a flux of χ. For example, in convective transports $F(\chi)$ might correspond to $M_u \chi$ where M_u is an updraft mass flux. In principle one should adjust M_u to reflect the fact that it may be moving a mass of dry air or a mass of moist air. We assume these differences are small, and well below the errors required to produce equation 4.8 in the first place. The same is true for the diffusion coefficients involved in turbulent transport. All processes using equations of such a form still satisfy a conservation relationship

$$\frac{\partial}{\partial t} \sum_k \chi_k \delta p_k = F_{kbot} - F_{ktop}$$

provided the appropriate δp is used in the summation.

4.2 Moist Turbulence Scheme

Moist turbulence scheme in CAM5 is from Bretherton and Park [2009*a*] that is a replacement of dry turbulence scheme of Holtslag and Boville [1993*b*] in CAM3 and CAM4. The role of moist turbulence scheme is to vertically transport heat (dry static energy $s \equiv C_p \cdot T + g \cdot z$), moistures (q_v, q_l, q_i, n_l, n_i where n_l, n_i are number concentrations of cloud liquid droplets and ice crystals), horizontal momentum (u, v), and tracers (mass and number concentrations of aerosol and chemical species) by symmetric turbulences. In the symmetric turbulence, updraft and downdraft have similar vertical velocities, fractional areas, and degrees of saturation.

Compared to the dry PBL (Planetary Boundary Layer) scheme in CAM3 and CAM4, moist turbulence scheme in CAM5 has the following unique characteristics: (1) it is a diagnostic TKE-based (Turbulent Kinetic Energy, e) 1^{st} order K-diffusion scheme with entrainment parameterization but without counter-gradient transport, (2) it simulates $cloud - radiation - turbulence$ interactions in an explicit way, which makes it possible to simulate full aerosol indirect effects with direct interactions with cloud macro-microphysics and radiation schemes, (3) using a single set of consistent physical formula, it is operating in any layers above as well as within PBL as long as moist Ri (Richardson number) is larger than a critical value Ri_c=0.19. Thanks to explicit simulation of moist turbulences driven by LW (Longwave) radiative cooling at the cloud top, CAM5 does not need a separate formula for stability-based stratus fraction - stratus fraction is computed only using mean relative humidity. It performs much better in the cloud-topped PBL than CAM3/4's dry PBL scheme with similar or superior performance in dry stable and convective PBLs.

In order to illucidate conceptual background behind the CAM5's moist turbulence scheme, let's imagine a single symmetric turbulence being perturbed by a static vertical distance l from its equilibrium height. This symmetric turbulence is assumed to be imbedded in the environment without vertical discontinuity such as sharp inversion. If l is sufficiently smaller than the vertical length scale over which vertical gradient of environmental scalar ($\gamma_{\bar{\phi}} \equiv \partial\bar{\phi}/\partial z$) changes and if turbulent vertical velocity (w') is approximated to $\sqrt{e}$, we can easily derive that turbulent flux of any conservative scalar (ϕ) becomes $\overline{w'\phi'} = -l \cdot \sqrt{e} \cdot \gamma_{\bar{\phi}}$. In reality, however, atmospheric stability controls turbulent vertical velocity (i.e., w' will be a product of $\sqrt{e}$ and an anisotropic factor of TKE, which is a function of atmospheric stability) and actual vertical perturbation distance of turbulent updraft and downdraft (i.e., turbulent *mixing* length will be a product of a *static* perturbation distance l and a certain atmospheric stability parameter). In addition, during vertical displacement, turbulent properties may be changed due to diabatic forcings or mixing with environment. All of these anomalous effects associated with atmospheric stability, diabatic forcings, and mixing are incorporated into a single stability function, S. As a result, turbulent flux of conservative scalar by symmetric turbulences embedded in the vertially-smooth-transitioning environment becomes

$$\overline{w'\phi'} = -l \cdot \sqrt{e} \cdot S \cdot \gamma_{\bar{\phi}} = -K \cdot \gamma_{\bar{\phi}} \tag{4.9}$$

Thus, computation of turbulent fluxes by symmetric turbulence is reduced to the computations of static turbulence length scale (l), turbulent kinetic energy (e), and stability function (S). The product of these 3 terms is so called eddy diffusivity, $K = l \cdot \sqrt{e} \cdot S$. Due to diabatic adjustment of turbulent horizontal momentum to the environment during vertical displacement,

S for horizontal momentum (S_m) is likely to be smaller than the S for heat and moisture (S_h). This means that K_ϕ is a function of scalar, ϕ.

If turbulence is embedded in the environment with a sharp vertical transition of stability such as inversion layer at the top of convective PBL, Eqn.(4.9) is inappropriate since turbulent motion will be suppressed in the stable portion of the discontinuous interface. In this case, we use the following entrainment parameterization.

$$\overline{w'\phi'} = -w_e \cdot \Delta\bar{\phi} = -\Delta z_e \cdot w_e \cdot \gamma_{\bar{\phi}} = -K_e \cdot \gamma_{\bar{\phi}} \tag{4.10}$$

where w_e is entrainment rate and Δz_e is the thickness of the entrainment interfacial layer. Above entrainment parameterization is applied at the top and base interfaces of Convective Layer (CL. See Fig.1) after finishing CL extension-merging procedures that will be explained later. In this case, eddy diffusivity is simply a product of Δz_e and w_e, identical for all scalars.

CAM5's moist turbulence scheme consists of 9 main processes: (1) Bulk Moist Richardson number, (2) Initial identification of Convective (CL), Stably Turbulent (STL), and Stable (SL) Layers, (3) Turbulence Length Scale (l), (4) Steady-State TKE (e), (5) Stability Functions (S_ϕ), (6) CL Extension-Merging Procedures, (7) Entrainment Rates at the CL Top and Base Interfaces (w_e), (8) Implicit Diffusion with Implicit Eddy Diffusivity, and (9) Implicit Surface Stress. Since many symmetric turbulences exist with different vertical length and velocity scales at any interface, the quantities we are trying to parameterize (l, e, S_ϕ, w_e) should be understood as the ensemble of all symmetric turbulences.

4.2.1 Bulk Moist Richardson Number

Richardson number (Ri) is used to diagnose the existence of turbulences. It is defined as the ratio of buoyancy production ($P_b \equiv \overline{w'b'} = (g/\theta_v) \cdot \overline{w'\theta_v'}$) to shear production ($P_s \equiv -\overline{w'u'} \cdot \partial\bar{u}/\partial z - \overline{w'v'} \cdot \partial\bar{v}/\partial z$) at the model interface. P_b represents energy conversion from mean available potential energy (APE) to TKE, while P_s is converison from mean kinetic energy to TKE. If Ri is negative, turbulence is absolutely generated but if it is positive, turbulence can be either generated or dissipated depending on the relative magnitude of $|P_b|$ and $|P_s|$.

Special treatment is necessary for saturated turbulences. If turbulence keeps its unsaturated state during vertical diaplacement, θ_v is a conserved quantity and Eqn.(4.9) can be directly used for computing $\overline{w'\theta_v'}$. However, if it is saturated, θ_v decreases within downdraft due to evaporative cooling of cloud droplet, while increases within updraft due to condensation heating of water vapor. The resulting $\overline{w'b'}$ including the effects of condensation and evaporation can be represented by the linear combinations of $\overline{w's_c'}$ and $\overline{w'q_t'}$ where $s_c \equiv C_p \cdot T + g \cdot z - L_v \cdot q_l - L_s \cdot q_i$ is *condensate static energy* and $q_t \equiv q_v + q_l + q_i$ is *total specific humidity*. Both s_c and q_t are conserved during vertical displacement and phase change. If we know saturated fractional area at the model interface (e.g., stratus fraction), we can write

$$\overline{w'b'} = c_h \cdot \overline{w's_c'} + c_q \cdot \overline{w'q_t'} \tag{4.11}$$

$$c_h = c_{h,s} \cdot a + c_{h,u} \cdot (1-a), \qquad c_q = c_{q,s} \cdot a + c_{q,u} \cdot (1-a) \tag{4.12}$$

where c_h, c_m are buoyancy coefficients for heat (s_c) and moisture (q_t) which are complex functions of temperature and pressure (Schubert et al. [1979], Bretherton and Park [2009*a*]),

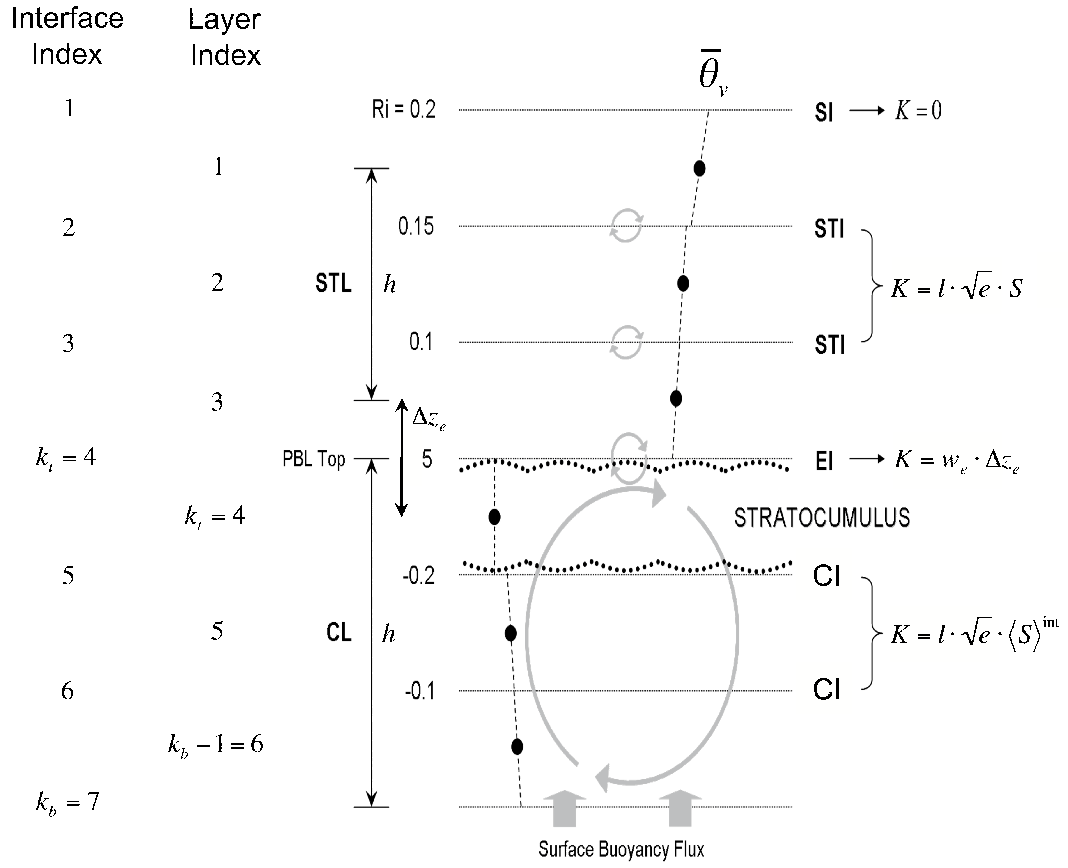

Figure 4.1: The indexing and example of turbulent layer structure in the bottom part of a typical column in the CAM5's moist turbulence scheme. Layer indexing used in CAM5 is shown at left. The bulk Richardson number Ri is used to locate a stable interface (SI) with $Ri > Ri_c$, stably turbulent interfaces (STI) with $0 < Ri < Ri_c$ comprising an STL, and unstable convective interfaces (CI) with $Ri < 0$ comprising a CL core. The CL is extended up to an entrainment interfaces (EI), at which the turbulent eddy diffusivity is computed from an explicitly predicted entrainment rate w_e. In the interior interfaces of the turbulent layers, the turbulent diffusivity K is conventionally using a length scale, diagnosed TKE, and stability function computed from local Ri in an STL and from layer-mean RI in a CL. Thickness of STL and CL are denoted by h, and the thickness of entrainment interface is denoted by Δz_e. See text for further details.

subscrits s, u denotes saturated and unsaturated turbulences, and a is stratus fraction. Applying Eqn.(4.9) to each term on the R.H.S. of Eqn.(4.11) and assuming $K_h \approx K_m$, Ri can be written solely in terms of grid mean variables as follows.

$$Ri \equiv -\mathcal{C}P_b P_s = \mathcal{C}K_h \cdot N^2 K_m \cdot S^2 \approx \mathcal{C}N^2 S^2 \tag{4.13}$$

$$N^2 \equiv c_h \cdot \mathcal{C}\partial\bar{s}_c \partial z + c_q \cdot \mathcal{C}\partial\bar{q}_t \partial z, \quad S^2 \equiv (\mathcal{C}\partial\bar{u}\partial z)^2 + (\mathcal{C}\partial\bar{v}\partial z)^2 \tag{4.14}$$

In the code, $c_{h,s}, c_{h,u}, c_{q,s}, c_{q,u}$ and a are given at the layer mid-points. By averaging two adjacent layers' mid-point values, these are converted into model interface values. However, if a in the adjacent upper layer is smaller than the average value, we took the smaller value, which is a necessary procedure to identify stably stratified interface at the top of stratocumulus-capped PBL.

4.2.2 Identification of Convective, Stably Turbulent, and Stable Layers

Using Ri defined at the interfaces, all model interfaces are grouped into *Convective Interface* (CI with $Ri \leq 0$), *Stably Turbulent Interface* (STI with $0 \leq Ri \leq Ri_c$), and *Stable Interface* (SI with $Ri > Ri_c$). Here, $Ri_c = 0.19$ is a critical Richardson number and turbulence can exist only when $Ri < Ri_c$ (see Fig.4.1). If several CIs are adjacent (or even when one CI exists), they form a single *Convective Layer*, CL. If several STIs are adjacent (or even when one STI exists), they form a single *Stably Turbulent Layer*, STL. The remaining SIs form *Stable Layer*, SL where no turbulence exists. After finishing CL extension-merging which will be explained later, the external interfaces surrounding CL will be named as *Entrainment Interface* (EI with $Ri > 0$) and the remaining CL interfaces as CL internal interfaces.

In CL and STL, we neglect TKE storage. In STL, we further neglect TKE transport. In CL, turbulence can exist from the base to the top interfaces of CL, but in the STL, turbulence can exist from the layer mid-point just below the lowest STI to the layer mid-point just above the highest STI. This defines turbulent layer thickness, h in a slightly different way between CL and STL (see Fig.4.1). After CL extension-merging, a single stability function $\langle S \rangle^{int}$ is assigned to all CL internal interfaces.

We use Eqn.(4.9) to compute eddy diffusivity at all interfaces except the top entrainment interface of CL where Eqn.(4.10) is used. If CL is elevated from the surface, Eqn.(4.10) is also applied to the CL base entrainment interface. If any interface is a double entraining interface from above and below, final eddy diffusivity is a simple sum of the two eddy diffusivities obtained from above CL and below CL. If surface buoyancy flux is positive (negative), surface is considered as a CL internal (external) interface and contributes (does not contribute) to the computation of internal energetics of CL.

Several CLs and STLs can exist in a single grid column. The same physical equation set is used for all CLs and STLs regardless of whether they are based at the surface or elevated. Our moist turbulence scheme, thus, is not a PBL scheme - it is operating in all layers above as well as within the PBL. The conventional PBL is simply a surface-based CL or surface-based STL in our scheme. PBL top height is defined as the top external interface of surface-based CL. If

STL is based at the surface instead, PBL top height is defined as the layer mid-point height just above the STL top interface. We don't impose any minimum value on the PBL height.

We also define additional *Single Radiatively Driven Convective Layer* (SRCL) if any single layer satisfies the following 5 conditions: it has (1) grid-mean LWC larger than 10^{-2} $[g \cdot kg^{-1}]$ but no LWC in the layer just above it, (2) LW radiative cooling, (3) $Ri > Ri_c$ at the top interface, (4) positive buoyancy production in the upper half-layer, and (5) it is not within the previously identified CLs. Similar to other CLs, entrainment parameterization is applied at the top and base interfaces of SRCL. Several SRCLs can exist in a single column.

4.2.3 Turbulent Length Scale

Following Blackadar [1962] and Grenier and Bretherton [2001], turbulent length scale is computed as

$$(\mathcal{C}1l)^{\alpha} = (\mathcal{C}1k \cdot z)^{\alpha} + (\mathcal{C}1l_{\infty})^{\alpha} \tag{4.15}$$

$$l_{\infty} = \eta \cdot h \tag{4.16}$$

$$\eta = \begin{cases} 0.085 & \text{at STI} \\ 0.085 \cdot [\ 2 - exp(min(0, \langle Ri \rangle^{int}))\ ] & \text{at CI} \end{cases} \tag{4.17}$$

where $k = 0.4$ is a von Karman constant, l_{∞} is asymptotic length scale, h is turbulent layer thickness, and $\langle Ri \rangle^{int} = \langle l^2 \cdot N^2 \rangle^{int} / \langle l^2 \cdot S^2 \rangle^{int}$ is the mean Ri averaged over CL internal interfaces ($\langle\ \ \rangle^{int}$ denotes vertical average over the CL internal interfaces). We chose $\alpha = 3$.

As explained in the previous section and Fig.4.1, h for CL is defined as the depth between two external interfaces, while h for STL is defined as the distance between the two outmost layers' mid-points. When CL is based at surface but surface buoyancy flux is negative, h is defined down to the mid-point of the lowest model layer instead of down to the surface.

Our formulation approximates l to l_{∞} except near the ground, where it asymptotes $k \cdot z$ to match surface layer similarity theory. As explained before, the actual turbulent *mixing* length should be understood as the product of l and stability function S.

4.2.4 Steady-State Turbulent Kinetic Energy

We assume steady-state TKE, that is, at each model interface, $P_b + P_s + T_e - D = 0$ where dissipation (D) and TKE transport (T_e) are parameterized as

$$D = \left[\mathcal{C}e^{3/2} b_1 \cdot l\right] \tag{4.18}$$

$$T_e = \left[a_e \cdot \mathcal{C}\sqrt{e} \cdot (\langle e \rangle - e) l\right] \tag{4.19}$$

where $b_1 = 5.8$ and $\langle e \rangle$ denotes TKE averaged over the whole CL. In case of STL, $a_e = 0$ (no TKE transport) while in CL, $a_e = 1$. Ideally, $\langle T_e \rangle$ should be zero but Eqn.(4.19) only satisfies this condition approximately. Combining with P_b and P_s, steady-state TKE at any model interface becomes

$$e = b_1 \cdot \left[\mathcal{C}l\sqrt{e} \cdot (P_b + P_s) + a_e \cdot (\langle e \rangle - e)\right] \tag{4.20}$$

At the internal interfaces of CL, $P_b = -K_h \cdot N^2$ and $P_s = K_m \cdot S^2$ with $K_h = l \cdot \sqrt{e} \cdot \langle S_h \rangle^{int}$ and $K_m = l \cdot \sqrt{e} \cdot \langle S_m \rangle^{int}$ where $\langle S_h \rangle^{int}$ and $\langle S_m \rangle^{int}$ are mean stability functions averaged over internal interfaces of CL computed by using $\langle Ri \rangle^{int}$ and Eqn.(4.23) and (4.24).

At entrainment interfaces, $P_b = -K_e \cdot N^2 + f_R \cdot c_{h,s} \cdot \Delta \bar{F}_R / \rho$ and $P_s = K_e \cdot S^2$ with $K_e = w_e \cdot \Delta z_e$ where Δz_e is the thickness of entrainment interface. In computing P_b at the entrainment interfaces, N^2 is redefined using the cloud fraction in the half-layer just below (above) the CL top (base) entrainment interface. This redefinition of N^2 is necessary in order to correctly take into account of buoyancy production associated with the evaporative cooling of entrained airs. $\Delta \bar{F}_R$ is grid-mean radiative flux divergence across the CL top layer in unit of $[W \cdot m^{-2}]$ given from the radiation scheme and $0 \leq f_R \leq 1$ is the fraction of radiative flux divergence confined in the thin transition zone near the top entrainment interface of CL among $\Delta \bar{F}_R$. Following Bretherton and Park [2009*a*], f_R is parameterized as

$$f_R = [\mathcal{C}\tau \cdot (4 + \tau) 24 + \tau \cdot (6 + \tau)] \tag{4.21}$$

$$\tau = 156 \cdot \ \bar{q}_l^{top} \cdot \Delta p^{top} / g \tag{4.22}$$

where τ is the grid-mean cloud optical depth of CL top layer that has grid-mean LWC of $\bar{q}_l^{top}$ and a thickness of Δp^{top}. As PBL deepens, cloud can be formed in the layer just above the PBL top (i.e., *ambiguous layer*). In this case, most of radiative flux divergence will be confined at the top of the ambiguous layer. In order to take into account of this case, we simply added $f_R \cdot \Delta \bar{F}_R / \rho$ both in the CL top and ambiguous layers.

At the surface interface, $P_{b,sfc} = c_h \cdot (F_h^* / \rho) + c_m \cdot \left(F_q^* / \rho \right)$ where F_h^* is sensible heat flux $[J \cdot s^{-1} \cdot m^{-2}]$ and F_q^* is water vapor flux $[kg \cdot s^{-1} \cdot m^{-2}]$ at surface given from the surface flux computation scheme to the moist turbulence scheme, and $P_{s,sfc} = u_*^3 / (k \cdot z_0)$ where z_0 is the mid-point height of the lowest model layer and u_* is frictional velocity at surface defined as $u_*^2 = \sqrt{\tau_x^2 + \tau_y^2} / \rho$ where τ_x, τ_y is surface momentum flux $[kg \cdot m \cdot s^{-1} \cdot s^{-1} \cdot m^{-2}]$. Assuming no TKE transport and turbulent length scale $l = k \cdot z_0$, we compute TKE at surface half-layer, e_{sfc} using Eqn.(4.20). In order to prevent negative e_s, we impose a minimum positive value on e_{sfc}.

By integrating Eqn.(4.20) over the whole CL with an approximation of $e \approx \langle e \rangle$ at the entrainment interfaces, we can compute $\langle e \rangle$ by solving a cubic equation of $\langle e \rangle^{1/2}$. Once $\langle e \rangle$ is computed, we can compute e at each internal interfaces of CL using Eqn.(4.20) again.

Our moist turbulence scheme computes characteristic excesses (or standard deviations) of turbulent updraft vertical velocity (σ_w), temperature (σ_T), and water vapor (σ_q) within PBL or near surface. If PBL is CL (STL), we estimate $\sigma_w = \sqrt{\langle e \rangle}$ ($\sigma_w = u_* / 8.5$) and then $\sigma_T = (F_h^* / \rho / C_p) / \sigma_w$ and $\sigma_q = (F_q^* / \rho) / \sigma_w$. These characteristic convective excesses when PBL is CL are used to define cumulus source air properties within deep convection scheme.

4.2.5 Stability Functions

Following Galperin et al. [1988], stability functions are parameterized as

$$S_h = [\mathcal{C}\alpha_5 1 + \alpha_3 \cdot G_h] \tag{4.23}$$

$$S_m = [\mathcal{C}\alpha_1 + \alpha_2 \cdot G_h (1 + \alpha_3 \cdot G_h) \cdot (1 + \alpha_4 \cdot G_h)] \tag{4.24}$$

where $\alpha_1 = 0.5562$, $\alpha_2 = -4.3643$, $\alpha_3 = -34.6764$, $\alpha_4 = -6.1272$, $\alpha_5 = 0.6986$ and $G_h \equiv -N^2 \cdot l^2/(2 \cdot e)$ is a nondimensional stability ratio restricted by $-3.5334 < G_h < 0.0233$. In case of STL, G_h is obtained by combining Eqn.(4.20),(4.23),(4.24) as follows.

$$Ri \cdot (1 + \alpha_3 \cdot G_h) \cdot (1 + \alpha_4 \cdot G_h) = 2 \cdot b_1 \cdot G_h \cdot [Ri \cdot \alpha_5 \cdot (1 + \alpha_4 \cdot G_h) - (\alpha_1 + \alpha_2 \cdot G_h)] \quad (4.25)$$

For $Ri > Ri_c = 0.19$, there is no physically realizable solution G_h and the interface is assumed to be non-turbulent. For $Ri < Ri_c$, this polynormial has two real roots, but only the larger one is realizable. In case of internal CL, we use the same Eqn.(4.25) but with $\langle Ri \rangle^{int} = \langle l^2 \cdot N^2 \rangle^{int} / \langle l^2 \cdot S^2 \rangle^{int}$ to compute $\langle G_h \rangle^{int}$, $\langle S_h \rangle^{int}$ and $\langle S_m \rangle^{int}$. For $\langle Ri \rangle^{int} < -44.5$, the allowable upper bound $\langle G_h \rangle^{int} = 0.0233$ is exceeded and stability functions assume their maximum values $S_h^{max} = 3.64$ and $S_m^{max} = 2.76$.

4.2.6 CL Extension-Merging Procedure

Several CLs can be identified in a single grid column. A contiguous set of interfaces with negative Ri is initially identified as a CL core. Starting from the lowest CL, each CL is extended first upward as far as possible, then downward as far as possible from the CL core into any adjacent layers of sufficiently weak stable stratification. Any external interface of CL is incorporated into the CL if the following criterion is satisfied.

$$(\Delta z \cdot l^2 \cdot N^2)^E < \left[\mathcal{C} r_{inc} 1 - r_{inc} \right] \cdot \int_{CL_{int}} l^2 \cdot N^2 \cdot dz \quad (4.26)$$

where superscript E denotes CL external interface being tested for incorporation into CL, Δz is the thickness of external interface, and the R.H.S. denotes vertical integration over the CL internal interfaces. We chose $r_{inc} = -0.04$ to be consistent with a dry convective boundary layer in which the entrainment buoyancy flux is -0.2 of the surface buoyancy flux. Strictly speaking, Eqn.(4.26) compares buoyancy production during TKE dissipation time scale by assuming that S_h of the external interface being tested for merging is the same as the $\langle S_h \rangle^{int}$. The first interface above (below) CL that fails this criterion will be the top (bottom) entrainment interface for that CL. No extension-merging is performed for SRCL since SRCL does not have internal interfaces.

Above criteria ensures that as long as the initial CL internal core (CL_{int}) has net positive buoyancy production, the internal CL after incorporating external interface will also have positive buoyancy production. Our incorporation test also guarantees that if any external interface is unstably stratified, it will be incorporated. Thus, if we incorporate any of the interior of a CL, we will incorporate or merge all of it.

If CL is based at surface and surface buoyancy flux is positive, the contribution of surface half-layer is also incorporated into the above integration of CL_{int}. In the surface half-layer, we use $G_h = (k \cdot z_0 \cdot P_{b,sfc})/(2 \cdot S_h \cdot e_{sfc}^{3/2})$ and by combining with Eqn.(4.23), S_h can be computed. Finally, $(l^2 \cdot N^2)_{sfc} = -k \cdot z_0 \cdot P_{b,sfc}/(S_h \cdot \sqrt{e_{sfc}})$.

In computing turbulent length scale from Eqns.(4.15)-(4.17) during CL extension-merging procedure, we simply assume $\eta = 0.5 \cdot (0.085 + 0.170) = 0.1275$ for all merging and merged interfaces and turbulent layer thickness h is fixed by the initial value before CL extension-merging. After finishing all the extension-merging procedure, $\langle S_h \rangle^{int}$ and $\langle S_m \rangle^{int}$ are computed using $\langle Ri \rangle^{int} = \langle l^2 \cdot N^2 \rangle^{int} / \langle l^2 \cdot S^2 \rangle^{int}$ and the updated h.

4.2.7 Entrainment Rates at the CL Top and Base Interfaces

At entrainment interfaces, eddy diffusivity is computed using Eqn.(4.10). Entrainment rate w_e is computed as

$$w_e = A \cdot (\mathcal{C}\bar{s}_{vl} g) \cdot \left[\mathcal{C} w_*^3 \Delta^E \bar{s}_{vl} \cdot h\right] \tag{4.27}$$

where $h = z_t - z_b$ is the thickness of CL, $\Delta^E \bar{s}_{vl}$ is the jump of mean liquid virtual static energy $s_{vl} \equiv s_l \cdot (1 + 0.61 \cdot q_t)$ across the entrainment interfaces at the top ($\Delta^E \bar{s}_{vl} = \bar{s}_{vl}(k_t - 1) - \bar{s}_{vl}(k_t)$) and base ($\Delta^E \bar{s}_{vl} = \bar{s}_{vl}(k_b - 1) - \bar{s}_{vl}(k_b)$) of the CL. w_* is convective velocity defined as

$$w_* = \left[2.5 \cdot \int_{z_b}^{z_t} P_b \cdot dz\right]^{1/3} \tag{4.28}$$

and A is an entrainment coefficient defined as

$$A = \begin{cases} 0.2 \cdot \left[1 + a_2 \cdot 0.8 \cdot \left(\mathcal{C} L_v \cdot \bar{q}_l^{top} \Delta^E \bar{s}_{vl}\right)\right] & \text{at CL top} \\ 0.2 & \text{at CL base} \end{cases} \tag{4.29}$$

where a_2 is a tuning parameter being allowed to be changed between 10 and 60, and we chose $a_2 = 30$. As PBL deepens, cloud can be formed in the ambiguous layer. In order to fully take into account of all possible mixtures between PBL air and free air above inversion, $\Delta^E \bar{s}_{vl}$ in *computing* A in Eqn.(4.29) is obtained by using the layer-value just above the ambiguous layer, not the value in the ambiguous layer (i.e., $\Delta^E \bar{s}_{vl} = \bar{s}_{vl}(k_t - 2) - \bar{s}_{vl}(k_t)$ in Eqn.(4.29)). In the similar context, we take $\bar{q}_l^{top} = max[\bar{q}_l(k_t), \bar{q}_l(k_t - 1)]$.

Due to the way how the model is structured, we don't have information on K_h when entrainment rate is computed. Thus, in computing $P_b = -K_h \cdot N^2$ at CL internal interfaces for entrainment parameterization, we use K_h of previous iteration or previous time step. Since we are using a predictor-corrector iteration method, K_h is likely to converge as iteration is proceeded.

If eddy diffusivity at the entrainment interface is smaller than the value obtained by assuming entrainment interface is STI, the final eddy diffusivity is set to be that of STI.

4.2.8 Implicit Diffusion with Implicit Diffusivity

CAM5 is using process splitting. At each time step, successive parameterizations operate on the updated state resulting from the previous parameterizations. The parameterizations in CAM5 are called in the following order at each time step: **deep convection** $\rightarrow$ **shallow convection** (computes (1) cumulus fraction and condensate, (2) vertical transport of heat, moisture, momentum, and tracers by asymmetric turbulences) $\rightarrow$ **stratiform macrophysics** (stratus fractions and stratiform net condensation-deposition rates) $\rightarrow$ **stratiform microphysics** ((1) activation of cloud liquid droplets and ice crystals, (2) conversions among cloud liquid droplets, ice crystals, rain, and snow, (3) evaporations of precipitation and sedimented cloud condensates) $\rightarrow$ **wet deposition of aerosols** $\rightarrow$ **radiation** $\rightarrow$ **surface fluxes** (upward fluxes of heat, water vapor, momentum, and tracers at surface) $\rightarrow$ **aerosol and chemical conversion processes** (conversions among various aerosol and chemical species) $\rightarrow$ **turbulent diffusion** (vertical transport of heat, moisture, momentum, and

tracers by symmetric turbulences) → **gravity wave drag → dry deposition of aerosols → dynamics** (large scale advection of grid mean heat, moisture, momentum, and tracers).

Given a diffusivity profile $K(z)$ and an input state $\bar{\phi}^*(z)$ updated to include all physical and dynamic processes (including explicit deposition of surface fluxes into the lowest model layer except horizontal momentum), our moist turbulence scheme diffuses $\bar{\phi}^*$ using the following implicit backward Euler scheme.

$$\left[\mathcal{C}\bar{\phi}(t+\Delta t) - \bar{\phi}^*\Delta t\right] = \mathcal{C}\partial\partial z\left[K(z)\cdot\mathcal{C}\partial\partial z\bar{\phi}(t+\Delta t)\right] \tag{4.30}$$

subject to specified upward surface fluxes of horizontal momentums ($\tau_{x,tot} = \tau_x^* - k_{tms}\cdot\bar{u}_{s,i}$, $\tau_{y,tot} = \tau_y^* - k_{tms}\cdot\bar{v}_{s,i}$ in unit of $[kg\cdot m\cdot s^{-1}\cdot s^{-1}\cdot m^{-2}]$ where the second term on the R.H.S. is turbulent mountain stress obtained by using updated surface wind $\bar{u}_{s,i}, \bar{v}_{s,i}$ after i^{th} iteration), sensible heat (F_h^* in unit of $[J\cdot s^{-1}\cdot m^{-2}]$), and water vapor (F_q^* in unit of $[kg\cdot s^{-1}\cdot m^{-2}]$) where superscript $*$ denotes the input value given to the moist turbulence scheme. The eddy diffusivity profile $K(z)$ may be computed using the input state variable $\bar{\phi}^*$. However, when a long time step $\Delta t = 1800$ $[s]$ is used as in CAM5, this is not a desirable approach since the physical processes proceeding turbulent diffusion scheme (e.g., radiation) can dramatically destabilize the input profile $\bar{\phi}^*(z)$, resulting in unreasonable $K(z)$. To address this problem, we use an iterative predictor-corrector approach to recalculate eddy diffusivities based on an better approximation to the post-diffusion state.

Let's assume that K_i is diffusivity profile obtained from $\bar{\phi}_i$. When $i = 0$, $\bar{\phi}_0 \equiv \bar{\phi}^*$ and $K_0 \equiv K^*$. Using $\bar{\phi}_0$, we compute K_0 and obtain the first diffused profile $\bar{\phi}_1$ by solving Eqn.(4.30) applied to the initial state $\bar{\phi}^*$. Using $\bar{\phi}_1$, we compute K_1 and the predictor-corrector averaged $K_{0:1} \equiv \lambda\cdot K_1 + (1-\lambda)\cdot K_0$. Using this $K_{0:1}$, we diffuse the *input state* $\bar{\phi}^*$ again and obtain the second diffused profile $\bar{\phi}_2$ from which K_2 and $K_{0:2} \equiv \lambda\cdot K_2 + (1-\lambda)\cdot K_{0:1}$ are computed. By repeating this process, the predictor-corrector averaged K profile after N iteration becomes

$$K_{0:N} \equiv \lambda\cdot K_N + (1-\lambda)\cdot K_{0:N-1} \tag{4.31}$$

$$K_{0:0} \equiv K^* \tag{4.32}$$

We chose $N = 4$ and $\lambda = 0.5$ to compute the final eddy diffusivity $K = K_{0:N}$ from the eddy diffusion scheme. During individual iterative diffusion processes of $\bar{\phi}^*$ by $K = K_{0:n}$ $(1 \le n \le N)$, we diffused conservative scalars $\bar{\phi}^* = \bar{s}_l^*, \bar{q}_t^*, \bar{u}^*, \bar{v}^*$ and reconstructed the diffused non-conservative scalars $\bar{T}, \bar{q}_v, \bar{q}_l, \bar{q}_i$ profiles by assuming that (1) $\bar{q}_i$ is not diffused and (2) the layer has homogeneous distribution of cloud condensate across the grid at saturation equilibrium state.

Since the initial profiles $\bar{\phi}^*$ are continuously updated within each iteration, we should also update surface fluxes ($\tau_x^*, \tau_y^*, F_h^*, F_q^*$) and the profiles of stratus fraction and radiative heating rate within each iteration. However, this will hugely increase computation time and make the CAM5 structure much more complex. Thus, we simply ignore the variations of surface fluxes, stratus fraction and radiative heating rate during iteration. This simplification can inevitably cause K_i ($i \ge 1$) to be computed on the $\bar{\phi}_i$ that has inconsistency among various state variables. Finally, because of the flipping of layer structures and corresponding eddy diffusivities between the iterations, our predictor-corrector method may not produce fully convergent K regardless of the iteration number. By choosing $\lambda = 0.5$, however, we address this issue to our best. Once the

final K is obtained from Eqn.(4.31), we diffuse the input grid mean scalars ($\bar{s}, \bar{q}_v, \bar{q}_l, \bar{q}_i, \bar{n}_i, \bar{u}, \bar{v}$).

Vertical transport of horizontal momentum by symmetric turbulence conserves column-mean horizontal momentum. However, it will change column-mean kinetic energy (KE) of the mean wind. In reality, this KE change will be converted into TKE and eventually internal heat energy (or potential energy, PE). In CAM5, however, we don't store TKE between time steps because of steady-state TKE assumption and yet require conservation of column-mean total energy, PE+KE. In order to conserve total energy in each column, we computed KE dissipation heating rate in each layer following Boville and Bretherton [2003*b*] after diffusing horizontal momentum, and explicitly added KE dissipation heating into $\bar{s}$ before diffusing $\bar{s}$.

Since air parcel temperature changes during vertical displacement due to adiabatic compression-expansion, moist turbulence scheme should also handle associated condensation-evaporation of cloud droplets during vertical transport. The same should be true for convection and large-scale advection schemes. However, this evaporation-condensation associated with vertical diaplacement of air parcels will be treated in the following stratiform cloud macrophysics. Thus, diffusing non-conservative scalars with a phase change ($\bar{s}, \bar{q}_v, \bar{q}_l, \bar{q}_i, \bar{n}_l, \bar{n}_i$) is not a problem if we admit that reasonable profiles of cloud condensates can be restored only after stratiform macro-microphysics.

When turbulence transports non-saturated airs into the overlying saturated airs, new cloud droplets can be formed without the change of cloud condensate mass (so called, cloud droplet activation). In order to handle adiabatic turbulent vertical transport and concurrent diabatic sources of cloud droplet number in a consistent way, turbulent diffusions of $\bar{n}_l$, aerosol mass and numbers are separately treated by the cloud droplet activation routine within the stratiform microphysics.

4.2.9 Implicit Surface Stress

In CAM5, surface fluxes of various scalars ($s, q_v, q_l, q_i, n_l, n_i$ and tracers) are explicitly deposited into the lowest model layer (this forms the input $\bar{\phi}^*$ to Eqn.(4.30)) and then implicit vertical diffusion is performed using Eqn.(4.30). In case of surface momentum fluxes (τ_x^*, τ_y^*), however, such explicit adding can flip the direction of the lowest model layer wind ($\bar{u}_s^*, \bar{v}_s^*$). This is not a physically realizable situation since as wind speed decreases by surface drag, surface drag itself decreases too, preventing flipping of wind in nature. This flipping of the wind in the model can be a source of numerical instability especially when the lowest model layer is thin. Thus, τ_x^*, τ_y^* should be added into the lowest model layer in an implicit way. This implicit adding, however, will cause discrepancy between the horizontal momentum that the Earth surface lost (which are explicit surface momentum flux τ_x^*, τ_y^* given to the turbulent diffusion scheme) and the momentum that the atmosphere receives (which are implicit surface momentum flux). To conserve horizontal momentum of the whole coupled system, they should be identical. In order to address both the numerical stability and momentum conservation issues, we partitioned the residual surface momentum flux (= explicit surface momentum flux - implicit surface momentum flux) over a certain time interval, e.g., 2 hr. This process is called implicit surface stress being detailed below.

First, in order to compute implicit surface stress, we compute total surface drag coefficient (

k_{tot}) by summing the *normal* drag coefficient (k_{nor}) obtained from the lowest model layer wind and the *turbulent mountain stress* drag coefficient (k_{tms}) triggered by sub-grid distribution of surface topography. This k_{tms} is computed by separate turbulent mountain stress module.

$$k_{nor} = max\left[\mathcal{C}\sqrt{(\tau_x^*)^2 + (\tau_y^*)^2} max(\sqrt{(\bar{u}_s^*)^2 + (\bar{v}_s^*)^2}, 1), 10^{-4}\right] \tag{4.33}$$

$$k_{tot} = k_{nor} + k_{tms} \tag{4.34}$$

Second, a certain fraction of residual stress accumulated upto the current time step from the first time step is added into the lowest model layer. This changes the wind in the lowest model layer.

$$\bar{u}_s^+(t) = \bar{u}_s^*(t) + \tau_{x,res}(t) \cdot \Lambda\left(\mathcal{C}g\Delta p\right) \cdot \Delta t, \quad \bar{v}_s^+(t) = \bar{v}_s^*(t) + \tau_{y,res}(t) \cdot \Lambda\left(\mathcal{C}g\Delta p\right) \cdot \Delta t, \tag{4.35}$$

$$\Lambda = \left[\mathcal{C}\Delta t \Delta t_{res}\right], \quad \Delta t \leq \Delta t_{res} = 7200\ [sec] \tag{4.36}$$

where $\tau_{x,res}(t), \tau_{y,res}(t)$ are residual stress accumulated upto the current time step from the first time step, and Δt_{res} is a time interval over which residual stress is deposited into the atmosphere. With $K(z)$, k_{tot}, and given input wind profiles of $\bar{u}^*(t)$ and $\bar{v}^*(t)$ but with the lowest model layer winds of $\bar{u}_s^+(t)$ and $\bar{v}_s^+(t)$ instead of $\bar{u}_s^*(t)$ and $\bar{v}_s^*(t)$, we can solve Eqn.(4.30) to obtain implicitly time-marched wind profiles, $\bar{u}(t + \Delta t)$ and $\bar{v}(t + \Delta t)$.

Finally, the net residual stress accumulated upto the end of current time step which will be used at the next time step becomes

$$\tau_{x,res}(t + \Delta t) = \tau_{x,res}(t) \cdot (1 - \Lambda) + \tau_x^* + k_{nor} \cdot \bar{u}_s(t + \Delta t) \tag{4.37}$$

$$\tau_{y,res}(t + \Delta t) = \tau_{y,res}(t) \cdot (1 - \Lambda) + \tau_y^* + k_{nor} \cdot \bar{v}_s(t + \Delta t) \tag{4.38}$$

where $\bar{u}_s(t + \Delta t)$ and $\bar{v}_s(t + \Delta t)$ are implicitly marched winds of the lowest model layer at the end of turbulent diffusion scheme at the current time step. At the first time step, it is $\tau_{x,res}(t) = \tau_{y,res}(t) = 0$. Our formulation assumes that turbulent mountain stress is fully implicitly added into the atmosphere without generating any residual stress. This assumption causes no conservation problem since turbulent mountain stress is used only within the atmospheric model not in the ocean, sea ice, and land models.

One complexity arises because $K(z)$ is iteratively computed at each time step. We assume that all of $\tau_{x,res}(t)$, k_{tms} and k_{nor} are not changed within the iteration loop : k_{tms} and k_{nor} are obtained from the initial wind profile $\bar{u}_s^*(t), \bar{v}_s^*(t)$ given to the moist turbulence scheme. In computing eddy diffusivity K_i within each iteration loop, however, we used $\tau_{x,tot} = \tau_x^* - k_{tms} \cdot \bar{u}_{s,i}(t)$, $\tau_{y,tot} = \tau_y^* - k_{tms} \cdot \bar{v}_{s,i}(t)$ where $\bar{u}_{s,i}(t), \bar{v}_{s,i}(t)$ are iteratively updated wind in the lowest model layer after i^{th} iteration at the current time step. Here, we included turbulent mountain stress in computing eddy diffusivity since it is a source of shear production and TKE in the lowest model layer, too.

4.3 Shallow Convection Scheme

Shallow convection scheme in CAM5 is from Park and Bretherton [2009] that is a replacement of Hack [1994*b*] shallow convection scheme in CAM3 and CAM4. Similar to its precedents, CAM5 performs shallow convection scheme just after deep convection scheme. In general, distinctions between deep and shallow convections are made by the differences in cloud top height, the existence of convective precipitation and convective downdraft. While named as shallow convection, CAM5's shallow convection scheme does not have any limitation on its cloud top height and convective precipitation. However, because the proceeding deep convection scheme consumes most of Convective Available Potential Energy (CAPE) and stabilizes the atmosphere, cloud top height simulated by shallow convection scheme is naturally limited in the tropical regions. In contrast to deep convection scheme, shallow convection scheme does not have a separate formulation for convective downdraft, but have an explicit parameterization of penetrative entrainment in the overshooting zone near cumulus top. Future implementation of convective downdraft as well as refinements of other aspects (e.g., updraft mixing rate and cloud microphysics) can make shallow convection scheme work for deep convective case, too.

The role of shallow convection scheme is to vertically transport heat, moisture, momentum, and tracers by asymmetric turbulences. On the other hands, vertical transport by symmetric turbulences are performed by separate moist turbulence scheme. CAM5's shallow convection scheme is carefully designed to optimally operate with CAM5's moist turbulence scheme without missing or double-counting processes. Similar to the other convection schemes, CAM5 shallow convection scheme assumes (1) steady state convective updraft plume, and (2) small updraft fractional area, so that compensating subsidence entirely exists within the same grid box as convective updraft. One of the unique aspects of CAM5 shallow convection scheme is its ability to compute convective updraft vertical velocity and updraft fractional area by using updraft vertical momentum equation. Computation of updraft vertical velocity enables to compute more refined fractional entrainment-detrainment rates, cloud top height, and penetrative entrainment. While not implemented in the current CAM5's shallow convection scheme, updraft vertical velocity will make it possible to compute activated fraction of aerosol masses and numbers at the cumulus base, more elegant cumulus microphysics, and aerosol-cumulus interactions.

CAM5's shallow convection scheme consists of 8 main processes: (1) Reconstruction of mean profiles and cloud condensate partitioning, (2) Computation of source air properties of a single ensemble-mean updraft plume at the PBL (Planetary Boundary Layer) top, (3) Cloud base mass flux and updraft vertical velocity closures using Convective Inhibition (CIN) and TKE (Turbulent Kinetic Energy), (4) Vertical evolution of a single entraining-detraining buoyancy sorting plume from the PBL top to the cumulus top, (5) Penetrative entrainment in the overshooting zone near cumulus top, (6) Computation of convective fluxes within the PBL, (7) Computation of grid-mean tendencies of conservative scalars, and (8) Computation of grid-mean tendencies of non-conservative scalars. The following sections describe each of these processes in detail.

4.3.1 Reconstruction of Mean Profiles and Cloud Condensate Partitioning

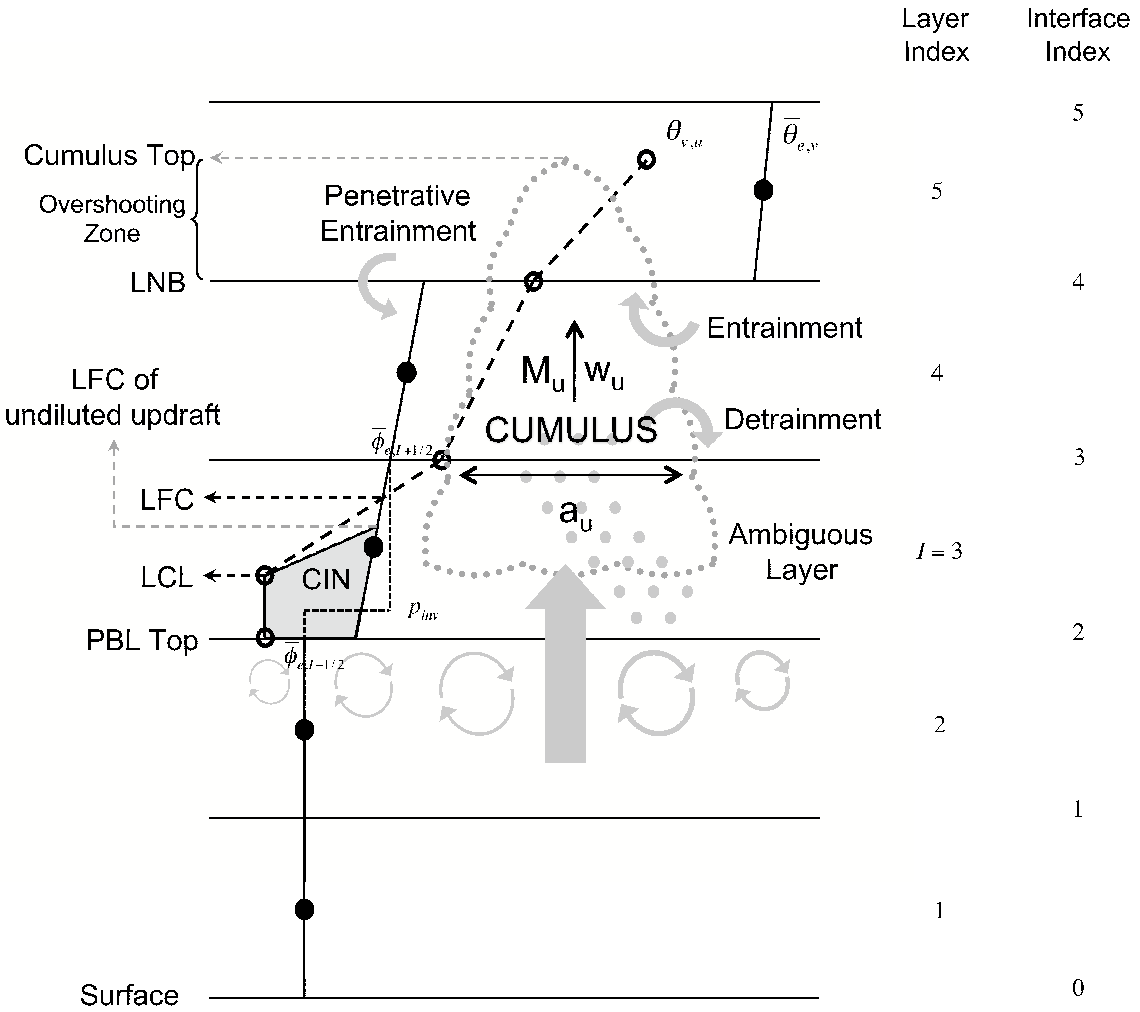

Figure 4.2: Schematic structure of shallow cumulus scheme describing vertical evolution of a bulk cumulus updraft and its interaction with environment and the subcloud layer. Black dots denote environmental mean virtual potential temperature $\bar{\theta}_{e,v}$, from which a $\bar{\theta}_{e,v}$ profile (solid line) is reconstructed. The horizontal solid lines are flux interfaces, where the updraft virtual potential temperature $\theta_{v,u}$ (open circles) is computed, from which a cumulus updraft $\theta_{v,u}$ profile (dashed) is reconstructed. The model layer and interface indices used in CAM5 are denoted on the right axis. The layer index I indicates the ambiguous layer, and p_{inv} is the reconstructed PBL capping inversion within this layer. Environmental conservative variables reconstructed just above and below the ambiguous layer are denoted by $\bar{\phi}_{e,I+1/2}$ and $\bar{\phi}_{e,I-1/2}$, respectively. See the text for details.

The input state variables to shallow convection scheme are environmental mean $\bar{q}_v, \bar{q}_l, \bar{q}_i, \bar{T}, \bar{u}, \bar{v}$, and mass and number of aerosols, $\bar{\zeta}$. While stratus condensate should reside only within cloudy portion, shallow convection scheme assumes uniform distribution of stratus condensate across the grid except when evaporation of precipitation is computed. From the given inputs, we compute *condensate potential temperature* $\bar{\theta}_c = \bar{\theta} - (L_v/C_p/\pi)\cdot\bar{q}_l - (L_s/C_p/\pi)\cdot\bar{q}_i$ and *total specific humidity* $\bar{q}_t = \bar{q}_v + \bar{q}_l + \bar{q}_i$. With respect to vertical displacement involving phase change but without precipitation formation and evaporation of precipitation, θ_c is nearly conserved and q_t is completely conserved.

Instead of assuming zero slope, we assign a certain slope of $\bar{\theta}_c$ and $\bar{q}_t$ within each layer. In each layer, upward [$(\bar{\theta}_c(k+1) - \bar{\theta}_c(k))/(p(k+1) - p(k))$] and downward [$(\bar{\theta}_c(k) - \bar{\theta}_c(k-1))/(p(k) - p(k-1))$] slopes are computed. If they have different signs or either of two has zero slope, internal slope is set to zero. If they have the same sign, we take the one with minimum absolute slope. In the lowest model layer, internal slope is set to the upward slope, and in the top model layer, it is set to the slope of the layer below. This profile reconstruction is performed indepently to each of $\bar{\theta}_c, \bar{q}_t, \bar{u}, \bar{v}$ and $\bar{\zeta}$. The reconstructed profiles conserve mean quantity in each layer but have discontinuity across the model interfaces. Similar profile reconstruction is performed in the moist turbulence scheme.

From the reconstructed $\bar{\theta}_c$ and $\bar{q}_t$, we compute *virtual potential temperature* $\bar{\theta}_v = \bar{\theta} \cdot (1 + 0.61 \cdot \bar{q}_v - \bar{q}_l - \bar{q}_i)$ at just below and above each model interface by assuming that ice fraction among cloud condensate is a raming function of temperature between 248 K and 268 K, and saturation specific humidity is a weighting average of two values defined over water and ice. The same temperature pertitioning is applied to cloud condensate within convective updraft. In case of detrained convective condensate, we use 238.15 K and 268.15 K as the two end points of temperature in the cloud condensate ramping function. For computation of radiative properties of cumulus updraft, we repartition in-cumulus condensate into liquid and ice following the partitioning of pre-existing of stratus clouds.

4.3.2 Source Air Properties of Convective Updraft

At the PBL top, we define source air properties of a single updraft plume. In CAM5, PBL top is located at the top most interface of convective boundary layer, which is diagnosed by the separate moist turbulence scheme. Here, we define $\hat{q}_{t,src}$, $\hat{\theta}_{c,src}$, $\hat{u}_{src}$, $\hat{v}_{src}$, $\hat{\zeta}_{src}$ where the *hat* denotes convective updraft properties and the subscript *src* denotes the values of convective updraft source air at the PBL top interface. $\hat{q}_{t,src}$ is defined as the environmental-mean value in the lowest model layer (In the below equations, (1) denotes the lowest model layer value). $\hat{\zeta}_{src}$ is defined in the same way as $\hat{q}_{t,src}$. We first define condensate virtual potential temperature of source air ($\theta_{vc} = \theta_c \cdot (1 + 0.61 \cdot q_t)$) using the profile-reconstructed minimum value within the PBL ($\bar{\theta}_{vc,min}$), and from $\hat{q}_{t,src}$ and $\hat{\theta}_{vc,src}$, $\hat{\theta}_{c,src}$ is computed. $\hat{u}_{src}$ and $\hat{v}_{src}$ are defined as the profile-reconstructed values just below the PBL top interface.

$$\hat{q}_{t,src} = \bar{q}_t(1) \tag{4.39}$$

$$\hat{\theta}_{c,src} = \left[\mathcal{C}\bar{\theta}_{vc,min}(1 + 0.61 \cdot \hat{q}_{t,src})\right] \tag{4.40}$$

$$\hat{u}_{src} = \bar{u}_{top} \tag{4.41}$$

$$\hat{v}_{src} = \bar{v}_{top} \tag{4.42}$$

$$\hat{\zeta}_{src} = \bar{\zeta}(1) \tag{4.43}$$

ζ includes the mass of individual aerosol species and aerosol numbers in each mode (Aitken, Accumulation, Coarse). ζ also contains the numbers of cloud liquid droplets and ice crystals. Since CAM5's cumulus microphysics is the first moment scheme and the size of in-cumulus and detrained shallow convective condensate are independently specified, vertical convective transport of cloud droplet numbers do not influence climate simulation in the current CAM5. But we retain this functionality to transport cloud droplet number for future development of higher order cumulus microphysics and aerosol-cumulus interactions.

The only unknown source air properties at this stage are updraft mass flux ($\hat{M}_{src}$) and updraft vertical velocity ($\hat{w}_{src}$) which are computed in the next section. $\hat{M}_{src}$ and $\hat{w}_{src}$ allows us to compute updraft fractional area, A_{src}.

4.3.3 Closures at the Cloud Base

We assume that turbulent updraft vertical velocity w at the PBL top follows a symmetric Gaussian distribution. The width of the distribution σ_w is determined by the mean TKE within the PBL ($\bar{e}_{PBL}$) given from the moist turbulence scheme, $\sigma_w = \sqrt{k \cdot \bar{e}_{PBL} + e_m}$ where $k = 1$ and $e_m = 5 \cdot 10^{-4}$ $[m^2 \cdot s^{-2}]$ is a background minimum TKE. P(w), PDF of w at the PBL top is given as

$$P(w) = \mathcal{C}1\sigma_w \cdot \sqrt{2 \cdot \pi} \cdot exp\left[-\mathcal{C}w^2 2 \cdot \sigma_w^2\right] \tag{4.44}$$

Among these, only strong updrafts enough to reach to their undiluted Level of Free Convection (LFC) are assumed to form *a single ensemble mean convective updraft* being simulated by shallow convection scheme. The effects of remaining weak updrafts that eventually sink back to the PBL by negative buoyancy are implicitly simulated by the separate moist turbulence scheme through entrainment parameterization. We define CIN as the strength of potential energy barrier of the undiluted ensemble-mean plume from the PBL top to the undiluted LFC (see Fig.4.2). Then, the minimum vertical velocity of the deflatable convective updrafts, or critical vertical velocity becomes $w_c = \sqrt{2 \cdot a \cdot CIN}$ where buoyancy coefficient $a = 1$. In order to reduce the on-and-off behavior of convection between the long model time step $\Delta t = 1800$ $[s]$, CIN is computed using thermodynamic profiles at the end of convection time step (so called, implicit CIN) as described in Park and Bretherton [2009].

Then, mass flux ($\hat{M}_{src}$), updraft fractional area ($\hat{A}_{src}$), and area-weighted updraft vertical velocity ($\hat{w}_{src}$) of a single ensemble-mean convective updraft at the PBL top can be computed as follows by integrating all deflatable plumes with $w > w_c$.

$$\hat{M}_{src} = \rho \cdot \int_{w_c}^{\infty} w \cdot P(w) \cdot dw = \rho \cdot \mathcal{C}\sigma_w \sqrt{2 \cdot \pi} \cdot exp\left[-\mathcal{C}a \cdot CIN\sigma_w^2\right] \tag{4.45}$$

$$\hat{A}_{src} = \int_{w_c}^{\infty} P(w) \cdot dw = \mathcal{C}12 \cdot erf\left[\mathcal{C}\sqrt{a \cdot CIN}\sigma_w\right] \tag{4.46}$$

$$\hat{w}_{src} = \left[\mathcal{C} \int_{w_c}^{\infty} w \cdot P(w) \cdot dw \int_{w_c}^{\infty} P(w) \cdot dw \right] = \left[\mathcal{C} \hat{M}_{src} \rho \cdot \hat{A}_{src} \right] \tag{4.47}$$

Here, we impose additional constraints that (1) $\hat{M}_{src}$ should be smaller than 0.9 of the mass in the layer just below the PBL top, that is, $\hat{M}_{src} < 0.9 \cdot \Delta p(I-1)/g/\Delta t$ where $\Delta p(I-1)$ is the pressure thickness of the layer just below the PBL top, and (2) $\hat{A}_{src}$ and $\hat{A}_{LCL}$ (updraft core fractional area at the LCL) are smaller than 0.1, assuming no lateral mixing from the PBL top to the LCL. From the constrained $\hat{M}_{src}$ and $\hat{A}_{src}$, we compute the constrained $\hat{w}_{src}$. As of this, we finished the convective closure at the PBL top.

4.3.4 Vertical Evolution of A Single Updraft Plume

Assuming steady-state updraft plume (or updraft plume with very small fractional area), vertical variations of updraft mass flux and conservative scalars can be written as

$$\mathcal{C}1\hat{M} \cdot \mathcal{C}\partial\hat{M}\partial p = \epsilon - \delta \tag{4.48}$$

$$\mathcal{C}\partial\hat{\phi}\partial p = -\epsilon \cdot (\hat{\phi} - \bar{\phi}_e) + \hat{S}_\phi + \hat{C}_\phi \tag{4.49}$$

where pressure coordinate p is defined increasing upward, (ϵ, δ) are fractional entrainment and detrainment rates, respectively, $\phi = q_t, \theta_c, u, v, \zeta$ is scalar being transported, $\hat{\phi}$ is updraft value, $\bar{\phi}_e$ is environmental mean value (note that this is different from the grid-mean $\bar{\phi} = \hat{A} \cdot \hat{\phi} + (1 - \hat{A}) \cdot \bar{\phi}_e$ unless $\hat{A} = 0$), $\hat{S}_\phi$ is net diabatic source within cumulus updraft, and $\hat{C}_\phi$ is a direct conversion term from environmental to updraft without lateral mass exchange. In case of steady state updraft plume, $\hat{S}_\phi$ changes the column mean total energy, while $\hat{C}_\phi$ conserves the column mean total energy. $\hat{S}_\phi$ and $\hat{C}_\phi$ for each component are parameterized as follows. Otherwise, they are set to zero.

$$\hat{S}_{q_t} \cdot \Delta p = -max(\hat{q}_l + \hat{q}_i - \hat{q}_{c,crit}, 0) \tag{4.50}$$

$$\hat{S}_{\theta_c} \cdot \Delta p = max\left[(\mathcal{C}L_v \cdot \hat{q}_l + L_s \cdot \hat{q}_i C_p \cdot \pi \cdot (\hat{q}_l + \hat{q}_i)) \cdot (\hat{q}_l + \hat{q}_i - \hat{q}_{c,crit}), 0 \right] \tag{4.51}$$

$$\hat{C}_u = PGFc \cdot (\mathcal{C}\partial\bar{u}_e\partial p)\,, \quad \hat{C}_v = PGFc \cdot (\mathcal{C}\partial\bar{v}_e\partial p) \tag{4.52}$$

where $\hat{q}_{c,crit} = 0.7\ [g \cdot kg^{-1}]$ is maximum cloud condensate amount that cumulus updraft can hold, and $PGFc = 0.7$ measures the degree to which cumulus updraft adjusts to environment by large-scale horizontal pressure gradient force during vertical motion. Above $\hat{S}_{q_t}$ and $\hat{S}_{\theta_c}$ assume that if in-cumulus cloud condensate is larger than $\hat{q}_{c,crit}$, the excessive condensate is simply precipitated out. This simple cumulus microphysics can be refined using updraft vertical velocity and cloud drop size distribution in future. Following Gregory et al. [1997*a*], $\hat{C}_u$ and $\hat{C}_v$ assume that when cumulus updraft rises across the layer with vertical shear of environmental horizontal wind, updraft gains horizontal momentum increment directly from the environment without lateral mass exchange. We neglect radiative effect and evaporation of convective precipitation within convective updraft.

One unique aspect of our shallow convection scheme is to compute updraft vertical velocity for computing (1) updraft fractional area, (2) lateral entrainment and detrainment rates, and

(3) cumulus top height and penetrative entrainment rates. Steady state vertical momentum equation is

$$\mathcal{C}12 \cdot \mathcal{C}\partial\hat{w}^2\partial p = a \cdot B - b \cdot \epsilon \cdot \hat{w}^2 \tag{4.53}$$

where B is updraft buoyancy ($B = (g/\bar{\theta}_v) \cdot (\hat{\theta}_v - \bar{\theta}_v)$), and non-dimentional coefficients a, b include the partition of perturbation vertical PGF into buoyancy and entrainment drag forces. Without perturbation vertical PGF, $a = b = 1$ but we use $a = 1$, $b = 2$ assuming that perturbation vertical PGF is entirely incorporated into entrainment drag force.

Instead of directly parameterizing (ϵ, δ), we assume that a certain amount of updraft airs ($\epsilon_o \cdot \hat{M} \cdot \delta p$) is mixed with the same amount of environmental airs during incremental vertical displacement δp, producing a spectrum of mixtures with the same mixing probability $P(\chi) = 1$ where $0 \leq \chi \leq 1$ ($\chi = 0$ is cumulus updraft, $\chi = 1$ is environmental air). Among these mixtures, we entrain (1) positively buoyant mixtures and (2) negatively buoyany mixtures with vertical velocity strong enough to reach 0.1 of cumulus top height. This process is so called *inertial buoyancy sorting* (Kain and Fritsch [1990], Bretherton et al. [2004]). This allows us to compute a single critical mixing fraction χ_c: mixtures with $\chi \leq \chi_c$ are entrained while the others are detrained. Then, we can derive (ϵ, δ) as follows.

$$\epsilon = \epsilon_o \cdot \chi_c^2 \tag{4.54}$$

$$\delta = \epsilon_o \cdot (1 - \chi_c)^2 \tag{4.55}$$

where fractional mixing rate ϵ_o is parameterized as an inverse function of geometric height,

$$\epsilon_o = \left[\mathcal{C}c\rho \cdot g \cdot z\right] \tag{4.56}$$

where non-dimensional coefficient $c = 8$ and z is geometric height above the surface. In order to simulate deep convection, we can use a smaller value, e.g., $c = 4$. Cumulus top height necessary to compute χ_c is initially set to the previous time step's value and then recomputed using an iteration loop.

Now, we can compute vertical evolution of $\hat{M}, \hat{\phi}, \hat{w}$. Instead of solving discrete numerical equation, we used the explicit analytical solution by solving the first order differential equation to obtain the cumulus updraft properties at the top interface of each layer from the value at the base interface. In solving Eqn.(4.53), we assume a linear profile of B in each layer. At the top interface, we computed updraft fractional area $\hat{A}$ from $\hat{M}$ and $\hat{w}$, and if $\hat{A} > 0.1$, detrainment rate δ is enhanced such that $\hat{A}$ is always less than 0.1. Note that this enhancement of detrainment only changes $\hat{M}$ not $\hat{w}$ at the top interface.

4.3.5 Penetrative Entrainment

When convective updraft rises into the stably stratified layers (i.e., Overshooting Zone. See Fig.4.2) above the Level of Neutral Buoyancy (LNB), some air masses within the overshooting zone are entrained into the layers below. This process is so called *penetrative entrainment*. We assume that the amount of penetratively entrained airs (M_{pen}) is proportional to the mass involved in the lateral mixing in the overshooting zone and the properties of penetratively

entrained airs (ϕ_{pen}) are identical to the mean environmental values from LNB to LNB + Δp_{pen}:

$$M_{pen} = r_{pen} \cdot \hat{M} \cdot \epsilon_o \cdot \Delta p_{pen} \tag{4.57}$$

$$\phi_{pen} = \bar{\phi}_e \tag{4.58}$$

where Δp_{pen} is vertical overshooting distance of cumulus updraft above LNB and $1 \leq r_{pen} \leq 10$ is a tunable non-dimensional penetrative entrainment coefficient. In CAM5, we chose $r_{pen} = 10$. The thickness of overshooting zone above LNB, or the cumulus top height is diagnosed as the level where convective updraft vertical velocity $\hat{w}$ becomes zero.

When convective updraft penetrates into several layers above LNB, Eqn.(4.57) and (4.58) are computed for each layers within penetrative overshooting zone, and all the penetratively entrained mass is deposited into a single layer just below LNB. We neglect convective updraft fluxes at the interfaces at and above LNB since most of updraft mass fluxes crossing over the LNB are likely to sink down below LNB due to negative updraft buoyancy in the overshooting zone. The thickness of overshooting zone above LNB, or the cumulus top height is diagnosed as the level where convective updraft vertical velocity $\hat{w}$ becomes zero.

4.3.6 Convective Fluxes at and below the PBL top interface

We view the layer just above the PBL top (*ambiguous layer*, I. See Fig.4.2) as the accumulation of partial grid layer of PBL air and another partial grid layer of above-PBL air. The interface between these two partial layers, the reconstructed PBL top height p_{inv}, is computed using a simple conservation principle for individual scalar component $\phi = q_t, \theta_c, u, v, \zeta$ as follows.

$$p_{inv} = pi_{I-1} - r \cdot |\Delta p_I|, \quad r = \left[\mathcal{C}\bar{\phi}_{e,I} - \bar{\phi}_{e,I+1/2}\bar{\phi}_{e,I-1/2} - \bar{\phi}_{e,I+1/2} \right] \tag{4.59}$$

where $|p_I|$ is the pressure thickness of the ambiguous layer, pi is the pressure at the model interface, $\bar{\phi}_{e,I-1/2}$ and $\bar{\phi}_{e,I+1/2}$ are the profile-reconstructed environmental values just below the PBL top interface and just above the ambiguous layer, respectively (See Fig.4.2).

Convective updraft mass flux $\hat{M}_{src}$ is assumed to be deflated from the p_{inv} with $\hat{\phi}_{src}$, which enables us to compute convective flux at the p_{inv}. To avoid over stabilizing or destabilizing the ambiguous layer and PBL through cumulus ventilation, this flux is uniformly extracted throughout the whole PBL, which results in the following linear profile of convective flux at model interfaces below p_{inv}.

$$(\overline{\omega'\phi'})(k) = g \cdot \hat{M}_{src} \cdot (\hat{\phi}_{src} - \bar{\phi}_{e,I-1/2}) \cdot \left[\mathcal{C}pi_0 - pi_k pi_0 - p_{inv} \right], \quad for \;\; 0 \leq k \leq I-1 \tag{4.60}$$

where ω is pressure vertical velocity, $k = 0$ is surface, $k = I - 1$ is PBL top interface index.

It is possible for compensating subsidence associated with cumulus updraft mass flux to lower the p_{inv} below the bottom of the ambiguous layer, in which case compensating subsidence will also warm and dry the grid layer below. To diagnose whether compensating subsidence would lower p_{inv} below pi_{I-1} during Δt, we compare the normalized cumulus updraft mass flux, $r_c = (g \cdot \hat{M}_{src} \cdot \Delta t)/|\Delta p_I|$ to r. If $r_c \geq r$, p_{inv} will be lowered down into the layer $I-1$, replacing

PBL-top air with $\phi = \bar{\phi}_{e,I-1/2}$ with above-PBL air with $\phi = \bar{\phi}_{e,I+1/2}$. This effect is included by adding the below compensating subsidence flux

$$(\overline{\omega'\phi'})(k = I-1) = -g \cdot \hat{M}_{src} \cdot (\bar{\phi}_{e,I+1/2} - \bar{\phi}_{e,I-1/2}) \cdot \left[1 - \mathcal{C}rr_c\right], \quad for \;\; r_c > r \tag{4.61}$$

where we assumed that cumulus mass flux is not strong enough to lower down p_{inv} below pi_{I-2}, that is, $g \cdot \hat{M}_{src} \cdot \Delta t < r \cdot |\Delta p_I| + |\Delta p_{I-1}|$. In order to ensure this condition, we impose an upper bound on the convective base mass flux of $g \cdot \hat{M}_{src} \cdot \Delta t < 0.9 \cdot |\Delta p_{I-1}|$.

4.3.7 Grid-Mean Tendency of Conservative Scalars

In case of steady state updraft plume approximation with a finite updraft fractional area but compensating subsidence entirely within the same grid box as convective updraft, the budget equation of grid mean conservative scalar represented in flux convergence form becomes

$$\mathcal{C}\partial\bar{\phi}\partial t = \mathcal{C}\partial\partial t\left(A_e \cdot \bar{\phi}_e\right) = -g{\cdot}\mathcal{C}\partial\partial p\left[\hat{M} \cdot (\hat{\phi} - \bar{\phi}_e) + M_{pen} \cdot (\phi_{pen} - \bar{\phi}_e)\right] + g{\cdot}\hat{M}{\cdot}\hat{S}_\phi + \mathcal{C}\partial\partial t\left(A_e \cdot \bar{\phi}_e\right)_S \tag{4.62}$$

where $A_e = 1 - \hat{A}$ is environmental fractional area and on the R.H.S. the first and second terms are convergence of convective updraft and penetrative entrainment fluxes, respectively, and the third and fourth terms are diabatic sources within convective updraft and environment, respectively. We use the above flux convergence form to compute tendencies of conservative scalars in order to ensure conservation of column-integrated energy during vertical redistribution of air masses by convective updraft. $\hat{M}$ in the third term of the R.H.S. is obtained by averaging updraft mass fluxes at the top and base interfaces of each layer. In contrast to $\hat{\phi}$, $\bar{\phi}_e$ is discontinuous across the model interface due to profile reconstruction. In order to take into account of the effects of compensating subsidence (upwelling) in this flux form, $\bar{\phi}_e$ in the first (second) term on the R.H.S is taken as the reconstructed environmental value just above the top interface (below the base interface) of each layer. If downdraft is also considered in future, we should add $-g \cdot \partial/\partial p[\hat{M}_d \cdot (\hat{\phi}_d - \bar{\phi}_e)] + g \cdot \hat{M}_d \cdot \hat{S}_{d,\phi}$ on the R.H.S.

If $\phi = u, v$, diabatic sources both within convective updraft ($\hat{S}_\phi$) and environment are zero. Note that a direct conversion term from environment to updraft without lateral mass exchange ($\hat{C}_\phi$) should not be included in this tendency equation in order to conserve column-integrated horizontal momentum. If $\phi = q_t, \theta_c$, these diabatic sources are precipitation production within convective updraft (Eqn.(4.50),(4.51)) and evaporation of precipitation within environment. Following the formulation in CAM3 and CAM4, we assume that whenever convective precipitation flux exists, it is spread all over the grid. The resulting formulation of evaporation of convective precipitation within environment is

$$\mathcal{C}\partial\partial t\left(A_e \cdot \bar{q}_{t,e}\right)_S = A_e \cdot k_e \cdot (1 - \bar{U}_e) \cdot (\sqrt{\bar{F}_R} + \sqrt{\bar{F}_S}) \tag{4.63}$$

where $\bar{F}_R$ and $\bar{F}_S$ are grid-mean rain and snow fluxes respectively in unit of $[kg \cdot m^{-2} \cdot s^{-1}]$ falling into the model layer from the top interface, and $\bar{U}_e$ is mean relative humidity within environment obtained using a mean saturation specific humidity that is a weighting average over water and ice, $k_e = 2 \cdot 10^{-6}$ $[(kg \cdot m^{-2} \cdot s^{-1})^{-1/2} \cdot s^{-1}]$ is evaporation efficiency. We also consider snow

melting during fall and corresponding changes of θ_c. This is a very simple formula bypassing the detailed vertical overlap structure of cumulus and stratus clouds. More refined treatment considering vertical cloud overlap will be done in future.

Vertical transport of horizontal momentum by convective updraft does not change column-mean horizontal momentum. However, it will change column-mean kinetic energy (KE) of the mean wind. In reality, this KE change will be eventually converted into internal heat energy (or potential energy, PE). In CAM5, we require conservation of column-mean total energy, PE+KE. In order to satisfy this constraint, we add kinetic energy dissipation heating into $\bar{\theta}_c$ following Boville and Bretherton [2003*b*]. Similar treatment was made in the moist turbulence scheme.

In CAM5, input state variables passed into individual physical schemes is *not* the grid-mean value including cumulus updraft contribution ($\bar{\phi} = \hat{A} \cdot \hat{\phi} + (1 - \hat{A}) \cdot \bar{\phi}_e$) *but* the environmental mean value without cumulus portion ($\bar{\phi}_e$). In order to conserve column-integrated grid-mean energy, we print out $\partial \left(A_e \cdot \bar{\phi}_e \right) / \partial t$ instead of $\partial \left(\bar{\phi}_e \right) / \partial t$ from our shallow convection scheme. Under the approximation of very small updraft fractional area ($\hat{A} \approx 0$ and $A_e \approx 1$), it is $\partial \left(A_e \cdot \bar{\phi}_e \right) / \partial t \approx \partial \left(\bar{\phi}_e \right) / \partial t$. In Eqn.(4.63), we also approximate $A_e \approx 1$.

4.3.8 Grid-Mean Tendency of Non-Conservative Scalars

In contrast to the conservative scalars, we use the following explicit *detrainmnet* and *compensating subsidence* tendency form to compute the tendency of non-conservative scalars. We first compute the tendencies of cloud condensates, and then the tendencies of water vapor ($\bar{q}_v$) and dry static energy ($\bar{s}$) are extracted from them.

$$\mathcal{C}\partial\partial t \left(A_e \cdot \bar{q}_{l,e} \right) = -g \cdot (\hat{M} - M_{pen}) \cdot \mathcal{C}\partial \bar{q}_{l,e} \partial p + g \cdot \hat{M} \cdot \delta \cdot (\hat{q}_l - \bar{q}_{l,e}) + g \cdot M_{pen} \cdot (q_{l,pen} - \bar{q}_{l,e}) \quad (4.64)$$

$$\mathcal{C}\partial\partial t \left(A_e \cdot \bar{q}_{i,e} \right) = -g \cdot (\hat{M} - M_{pen}) \cdot \mathcal{C}\partial \bar{q}_{i,e} \partial p + g \cdot \hat{M} \cdot \delta \cdot (\hat{q}_i - \bar{q}_{i,e}) + g \cdot M_{pen} \cdot (q_{i,pen} - \bar{q}_{i,e}) \quad (4.65)$$

$$\mathcal{C}\partial\partial t \left(A_e \cdot \bar{q}_{v,e} \right) = \mathcal{C}\partial\partial t \left(A_e \cdot \bar{q}_{t,e} \right) - \mathcal{C}\partial\partial t \left(A_e \cdot \bar{q}_{l,e} \right) - \mathcal{C}\partial\partial t \left(A_e \cdot \bar{q}_{i,e} \right) \quad (4.66)$$

$$\mathcal{C}\partial\partial t \left(A_e \cdot \bar{s}_e \right) = \mathcal{C}\partial\partial t \left(A_e \cdot \bar{s}_{c,e} \right) + L_v \cdot \mathcal{C}\partial\partial t \left(A_e \cdot \bar{q}_{l,e} \right) + L_s \cdot \mathcal{C}\partial\partial t \left(A_e \cdot \bar{q}_{i,e} \right) \quad (4.67)$$

where *condensate static energy* $s_c = C_p \cdot \pi \cdot \theta_c + g \cdot z$ and the first term on the R.H.S in Eqn.(4.64) and (4.65) is tendency associated with compensating subsidence and upwelling of environmental condensate, and the second and third terms are tendencies due to condensate detrainment from convective updraft and penetrative entrainment masses. If $\hat{M} - M_{pen} > 0$ ($\hat{M} - M_{pen} < 0$), downward (upward) diffencing between upper (lower) and current layers is used in computing compensating subsidence (upwelling) tendency. Any convective updraft condensate detrained into the layers above the LNB are assumed to move down into the layer just below LNB by negative buoyancy and be detrained there. That is, the second term on the R.H.S. in Eqn.(4.64) and (4.65) is zero in the overshooting zone. Similarly, all the penetratively entrained condensate are detrained into the layer just below LNB. That is, the third term on the R.H.S. in Eqn.(4.64) and (4.65) is non-zero only in the layer just below LNB.

If environmental condensate is displaced vertically by compensating subsidence/upwelling, phase change should occur due to compression heating/expansion cooling. Ideally, this phase

change should be treated within convection scheme but our current scheme does not. However, this phase change of displaced condensate will be treated by separate stratiform macro-microphysics schemes later.

The tendencies of cloud droplet number concentration ($\bar{n}_{l,e}, \bar{n}_{i,e}$) by compensationg subsidence/upwelling are treated in a similar way as the tendencies of cloud condensate mass. However, because CAM5's cumulus microphysics is the 1^{st} moment scheme, we don't have any information on the droplet number concentration within cumulus updraft ($\hat{n}_l, \hat{n}_i$). We assume that the effective droplet radius of detrained shallow (deep) convective condensate is 8 (10) and 25 (50) $[\mu m]$ for liquid and ice respectively.

4.4 Deep Convection

The process of deep convection is treated with a parameterization scheme developed by Zhang and McFarlane [1995] and modified with the addition of convective momentum transports by Richter and Rasch [2008] and a modified dilute plume calculation following Raymond and Blyth [1986, 1992]. The scheme is based on a plume ensemble approach where it is assumed that an ensemble of convective scale updrafts (and the associated saturated downdrafts) may exist whenever the atmosphere is conditionally unstable in the lower troposphere. The updraft ensemble is comprised of plumes sufficiently buoyant so as to penetrate the unstable layer, where all plumes have the same upward mass flux at the bottom of the convective layer. Moist convection occurs only when there is convective available potential energy (CAPE) for which parcel ascent from the sub-cloud layer acts to destroy the CAPE at an exponential rate using a specified adjustment time scale. For the convenience of the reader we will review some aspects of the formulation, but refer the interested reader to Zhang and McFarlane [1995] for additional detail, including behavioral characteristics of the parameterization scheme. Evaporation of convective precipitation is computed following the procedure described in section 4.5.

The large-scale budget equations distinguish between a cloud and sub-cloud layer where temperature and moisture response to convection in the cloud layer is written in terms of bulk convective fluxes as

$$c_p \left(\frac{\partial T}{\partial t}\right)_{cu} = -\frac{1}{\rho}\frac{\partial}{\partial z}\left(M_u S_u + M_d S_d - M_c S\right) + L(C - E) \tag{4.68}$$

$$\left(\frac{\partial q}{\partial t}\right)_{cu} = -\frac{1}{\rho}\frac{\partial}{\partial z}\left(M_u q_u + M_d q_d - M_c q\right) + E - C \ , \tag{4.69}$$

for $z \geq z_b$, where z_b is the height of the cloud base. For $z_s < z < z_b$, where z_s is the surface height, the sub-cloud layer response is written as

$$c_p \left(\rho \frac{\partial T}{\partial t}\right)_m = -\frac{1}{z_b - z_s}\left(M_b[S(z_b) - S_u(z_b)] + M_d[S(z_b) - S_d(z_b)]\right) \tag{4.70}$$

$$\left(\rho \frac{\partial q}{\partial t}\right)_m = -\frac{1}{z_b - z_s}\left(M_b[q(z_b) - q_u(z_b)] + M_d[q(z_b) - q_d(z_b)]\right) \ , \tag{4.71}$$

where the net vertical mass flux in the convective region, M_c, is comprised of upward, M_u, and downward, M_d, components, C and E are the large-scale condensation and evaporation rates, S, S_u, S_d, q, q_u, q_d, are the corresponding values of the dry static energy and specific humidity, and M_b is the cloud base mass flux.

4.4.1 Updraft Ensemble

The updraft ensemble is represented as a collection of entraining plumes, each with a characteristic fractional entrainment rate λ. The moist static energy in each plume h_c is given by

$$\frac{\partial h_c}{\partial z} = \lambda(h - h_c), \quad z_b < z < z_D \ . \tag{4.72}$$

Mass carried upward by the plumes is detrained into the environment in a thin layer at the top of the plume, z_D, where the detrained air is assumed to have the same thermal properties as in the environment ($S_c = S$). Plumes with smaller λ penetrate to larger z_D. The entrainment rate λ_D for the plume which detrains at height z is then determined by solving (4.72), with lower boundary condition $h_c(z_b) = h_b$:

$$\frac{\partial h_c}{\partial(z - z_b)} = \lambda_D(h - h_b) - \lambda_D(h_c - h_b) \tag{4.73}$$

$$\frac{\partial(h_c - h_b)}{\partial(z - z_b)} - \lambda_D(h_c - h_b) = \lambda_D(h - h_b) \tag{4.74}$$

$$\frac{\partial(h_c - h_b)e^{\lambda_D(z-z_b)}}{\partial(z - z_b)} = \lambda_D(h - h_b)e^{\lambda_D(z-z_b)} \tag{4.75}$$

$$(h_c - h_b)e^{\lambda_D(z-z_b)} = \int_{z_b}^{z} \lambda_D(h - h_b)e^{\lambda_D(z'-z_b)}dz' \tag{4.76}$$

$$(h_c - h_b) = \lambda_D \int_{z_b}^{z} (h - h_b)e^{\lambda_D(z'-z)}dz' \ . \tag{4.77}$$

Since the plume is saturated, the detraining air must have $h_c = h^*$, so that

$$(h_b - h^*) = \lambda_D \int_{z_b}^{z} (h_b - h)e^{\lambda_D(z'-z)}dz' \ . \tag{4.78}$$

Then, λ_D is determined by solving (4.78) iteratively at each z.

The top of the shallowest of the convective plumes, z_0 is assumed to be no lower than the mid-tropospheric minimum in saturated moist static energy, h^*, ensuring that the cloud top detrainment is confined to the conditionally stable portion of the atmospheric column. All condensation is assumed to occur within the updraft plumes, so that $C = C_u$. Each plume is assumed to have the same value for the cloud base mass flux M_b, which is specified below. The vertical distribution of the cloud updraft mass flux is given by

$$M_u = M_b \int_0^{\lambda_D} \frac{1}{\lambda_0} e^{\lambda(z-z_b)}d\lambda = M_b \frac{e^{\lambda_D(z-z_b)} - 1}{\lambda_0(z - z_b)} \ , \tag{4.79}$$

where λ_0 is the maximum detrainment rate, which occurs for the plume detraining at height z_0, and λ_D is the entrainment rate for the updraft that detrains at height z. Detrainment is confined to regions where λ_D decreases with height, so that the total detrainment $D_u = 0$ for $z < z_0$. Above z_0,

$$D_u = -\frac{M_b}{\lambda_0}\frac{\partial \lambda_D}{\partial z} \ . \tag{4.80}$$

The total entrainment rate is then just given by the change in mass flux and the total detrainment,

$$E_u = \frac{\partial M_u}{\partial z} - D_u \ . \tag{4.81}$$

The updraft budget equations for dry static energy, water vapor mixing ratio, moist static

energy, and cloud liquid water, ℓ, are:

$$\frac{\partial}{\partial z}\left(M_u S_u\right) = \left(E_u - D_u\right) S + \rho L C_u \tag{4.82}$$

$$\frac{\partial}{\partial z}\left(M_u q_u\right) = E_u q - D_u q^* + \rho C_u \tag{4.83}$$

$$\frac{\partial}{\partial z}\left(M_u h_u\right) = E_u h - D_u h^* \tag{4.84}$$

$$\frac{\partial}{\partial z}\left(M_u \ell\right) = -D_u \ell_d + \rho C_u - \rho R_u \ , \tag{4.85}$$

where (4.84) is formed from (4.82) and (4.83) and detraining air has been assumed to be saturated ($q = q^*$ and $h = h^*$). It is also assumed that the liquid content of the detrained air is the same as the ensemble mean cloud water ($\ell_d = \ell$). The conversion from cloud water to rain water is given by

$$\rho R_u = c_0 M_u \ell \ , \tag{4.86}$$

following Lord et al. [1982], with $c_0 = 2 \times 10^{-3}$ m^{-1}.

Since M_u, E_u and D_u are given by (4.79-4.81), and h and h^* are environmental profiles, (4.84) can be solved for h_u, given a lower boundary condition. The lower boundary condition is obtained by adding a 0.5 K temperature perturbation to the dry (and moist) static energy at cloud base, or $h_u = h + c_p \times 0.5$ at $z = z_b$. Below the lifting condensation level (LCL), S_u and q_u are given by (4.82) and (4.83). Above the LCL, q_u is reduced by condensation and S_u is increased by the latent heat of vaporization. In order to obtain to obtain a saturated updraft at the temperature implied by S_u, we define ΔT as the temperature perturbation in the updraft, then:

$$h_u = S_u + L q_u \tag{4.87}$$

$$S_u = S + c_p \Delta T \tag{4.88}$$

$$q_u = q^* + \frac{dq^*}{dT} \Delta T \ . \tag{4.89}$$

Substituting (4.88) and (4.89) into (4.87),

$$h_u = S + L q^* + c_p \left(1 + \frac{L}{c_p} \frac{dq^*}{dT}\right) \Delta T \tag{4.90}$$

$$= h^* + c_p \left(1 + \gamma\right) \Delta T \tag{4.91}$$

$$\gamma \equiv \frac{L}{c_p} \frac{dq^*}{dT} \tag{4.92}$$

$$\Delta T = \frac{1}{c_p} \frac{h_u - h^*}{1 + \gamma} \ . \tag{4.93}$$

The required updraft quantities are then

$$S_u = S + \frac{h_u - h^*}{1 + \gamma} \tag{4.94}$$

$$q_u = q^* + \frac{\gamma}{L} \frac{h_u - h^*}{1 + \gamma} \ . \tag{4.95}$$

With S_u given by (4.94), (4.82) can be solved for C_u, then (4.85) and (4.86) can be solved for ℓ and R_u.

The expressions above require both the saturation specific humidity to be

$$q^* = \frac{\epsilon e^*}{p - e^*}, \qquad e^* < p \ , \tag{4.96}$$

where e^* is the saturation vapor pressure, and its dependence on temperature (in order to maintain saturation as the temperature varies) to be

$$\begin{aligned} \frac{dq^*}{dT} &= \frac{\epsilon}{p-e^*}\frac{de^*}{dT} - \frac{\epsilon e^*}{(p-e^*)^2}\frac{d(p-e^*)}{dT} && (4.97)\\ &= \frac{\epsilon}{p-e^*}\left(1 + \frac{1}{p-e^*}\right)\frac{de^*}{dT} && (4.98)\\ &= \frac{\epsilon}{p-e^*}\left(1 + \frac{q^*}{\epsilon e^*}\right)\frac{de^*}{dT} \ . && (4.99) \end{aligned}$$

The deep convection scheme does not use the same approximation for the saturation vapor pressure e^* as is used in the rest of the model. Instead,

$$e^* = c_1 \exp\left[\frac{c_2(T - T_f)}{(T - T_f + c_3)}\right] \ , \tag{4.100}$$

where $c_1 = 6.112$, $c_2 = 17.67$, $c_3 = 243.5$ K and $T_f = 273.16$ K is the freezing point. For this approximation,

$$\begin{aligned} \frac{de^*}{dT} &= e^*\frac{d}{dT}\left[\frac{c_2(T - T_f)}{(T - T_f + c_3)}\right] && (4.101)\\ &= e^*\left[\frac{c_2}{(T - T_f + c_3)} - \frac{c_2(T - T_f)}{(T - T_f + c_3)^2}\right] && (4.102)\\ &= e^*\frac{c_2 c_3}{(T - T_f + c_3)^2} && (4.103)\\ \frac{dq^*}{dT} &= q^*\left(1 + \frac{q^*}{\epsilon e^*}\right)\frac{c_2 c_3}{(T - T_f + c_3)^2} \ . && (4.104) \end{aligned}$$

We note that the expression for γ in the code gives

$$\frac{dq^*}{dT} = \frac{c_p}{L}\gamma = q^*\left(1 + \frac{q^*}{\epsilon}\right)\frac{\epsilon L}{RT^2} \ . \tag{4.105}$$

The expressions for dq^*/dT in (4.104) and (4.105) are not identical. Also, $T - T_f + c_3 \neq T$ and $c_2 c_3 \neq \epsilon L/R$.

4.4.2 Downdraft Ensemble

Downdrafts are assumed to exist whenever there is precipitation production in the updraft ensemble where the downdrafts start at or below the bottom of the updraft detrainment layer.

Detrainment from the downdrafts is confined to the sub-cloud layer, where all downdrafts have the same mass flux at the top of the downdraft region. Accordingly, the ensemble downdraft mass flux takes a similar form to (4.79) but includes a "proportionality factor" to ensure that the downdraft strength is physically consistent with precipitation availability. This coefficient takes the form

$$\alpha = \mu \left[\frac{P}{P + E_d} \right] , \tag{4.106}$$

where P is the total precipitation in the convective layer and E_d is the rain water evaporation required to maintain the downdraft in a saturated state. This formalism ensures that the downdraft mass flux vanishes in the absence of precipitation, and that evaporation cannot exceed some fraction, μ, of the precipitation, where $\mu = 0.2$.

4.4.3 Closure

The parameterization is closed, i.e., the cloud base mass fluxes are determined, as a function of the rate at which the cumulus consume convective available potential energy (CAPE). Since the large-scale temperature and moisture changes in both the cloud and sub-cloud layer are linearly proportional to the cloud base updraft mass flux (*e.g.* see eq. 4.68 – 4.71), the CAPE change due to convective activity can be written as

$$\left(\frac{\partial A}{\partial t} \right)_{cu} = -M_b F , \tag{4.107}$$

where F is the CAPE consumption rate per unit cloud base mass flux. The closure condition is that the CAPE is consumed at an exponential rate by cumulus convection with characteristic adjustment time scale $\tau = 7200$ s:

$$M_b = \frac{A}{\tau F} . \tag{4.108}$$

4.4.4 Numerical Approximations

The quantities $M_{u,d}$, ℓ, $S_{u,d}$, $q_{u,d}$, $h_{u,d}$ are defined on layer interfaces, while D_u, C_u, R_u are defined on layer midpoints. S, q, h, γ are required on both midpoints and interfaces and the interface values $\psi^{k\pm}$ are determined from the midpoint values ψ^k as

$$\psi^{k-} = \log \left(\frac{\psi^{k-1}}{\psi^k} \right) \frac{\psi^{k-1}\psi^k}{\psi^{k-1} - \psi^k} . \tag{4.109}$$

All of the differencing within the deep convection is in height coordinates. The differences are naturally taken as

$$\frac{\partial \psi}{\partial z} = \frac{\psi^{k-} - \psi^{k+}}{z^{k-} - z^{k+}} , \tag{4.110}$$

where ψ^{k-} and ψ^{k+} represent values on the upper and lower interfaces, respectively for layer k. The convention elsewhere in this note (and elsewhere in the code) is $\delta^k \psi = \psi^{k+} - \psi^{k-}$. Therefore, we avoid using the compact δ^k notation, except for height, and define

$$d^k z \equiv z^{k-} - z^{k+} = -\delta^k z , \tag{4.111}$$

so that $d^k z$ corresponds to the variable dz(k) in the deep convection code.

Although differences are in height coordinates, the equations are cast in flux form and the tendencies are computed in units kg m^{-3} s^{-1}. The expected units are recovered at the end by multiplying by $g\delta z/\delta p$.

The environmental profiles at midpoints are

$$\begin{aligned} S^k &= c_p T^k + g z^k && (4.112)\\ h^k &= S^k + L q^k && (4.113)\\ h^{*k} &= S^k + L q^{*k} && (4.114)\\ q^{*k} &= \epsilon e^{*k}/(p^k - e^{*k}) && (4.115)\\ e^{*k} &= c_1 \exp\left[\frac{c_2(T^k - T_f)}{(T^k - T_f + c_3)}\right] && (4.116)\\ \gamma^k &= q^{*k}\left(1 + \frac{q^{*k}}{\epsilon}\right)\frac{\epsilon L^2}{c_p R T^{k2}} \ . && (4.117) \end{aligned}$$

The environmental profiles at interfaces of S, q, q^*, and γ are determined using (4.109) if $|\psi^{k-1} - \psi^k|$ is large enough. **However, there are inconsistencies in what happens if $|\psi^{k-1} - \psi^k|$ is not large enough**. For S and q the condition is

$$\psi^{k-} = (\psi^{k-1} + \psi^k)/2, \quad \frac{|\psi^{k-1} - \psi^k|}{\max(\psi^{k-1} - \psi^k)} \le 10^{-6} \ . \tag{4.118}$$

For q^* and γ the condition is

$$\psi^{k-} = \psi^k, \quad |\psi^{k-1} - \psi^k| \le 10^{-6} \ . \tag{4.119}$$

Interface values of h are not needed and interface values of h^* are given by

$$h^{*k-} = S^{k-} + L q^{*k-} \ . \tag{4.120}$$

The unitless updraft mass flux (scaled by the inverse of the cloud base mass flux) is given by differencing (4.79) as

$$M_u^{k-} = \frac{1}{\lambda_0(z^{k-} - z_b)}\left(e^{\lambda_D^k (z^{k-} - z_b)} - 1\right) \ , \tag{4.121}$$

with the boundary condition that $M_u^{M+} = 1$. The entrainment and detrainment are calculated using

$$\begin{aligned} m_u^{k-} &= \frac{1}{\lambda_0(z^{k-} - z_b)}\left(e^{\lambda_D^{k+1} (z^{k-} - z_b)} - 1\right) && (4.122)\\ E_u^k &= \frac{m_u^{k-} - M_u^{k+}}{d^k z} && (4.123)\\ D_u^k &= \frac{m_u^{k-} - M_u^{k-}}{d^k z} \ . && (4.124) \end{aligned}$$

Note that M_u^{k-} and m_u^{k-} differ only by the value of λ_D.

The updraft moist static energy is determined by differencing (4.84)

$$\frac{M_u^{k-}h_u^{k-} - M_u^{k+}h_u^{k+}}{d^k z} = E_u^k h^k - D_u^k h^{*k} \tag{4.125}$$

$$h_u^{k-} = \frac{1}{M_u^{k-}}\left[M_u^{k+}h_u^{k+} + d^k z\left(E_u^k h^k - D_u^k h^{*k}\right)\right] \ , \tag{4.126}$$

with $h_u^{M-} = h^M + c_p/2$, where M is the layer of maximum h.

Once h_u is determined, the lifting condensation level is found by differencing (4.82) and (4.83) similarly to (4.84):

$$S_u^{k-} = \frac{1}{M_u^{k-}}\left[M_u^{k+}S_u^{k+} + d^k z\left(E_u^k S^k - D_u^k S^k\right)\right] \tag{4.127}$$

$$q_u^{k-} = \frac{1}{M_u^{k-}}\left[M_u^{k+}q_u^{k+} + d^k z\left(E_u^k q^k - D_u^k q^{*k}\right)\right] \ . \tag{4.128}$$

The detrainment of S_u is given by $D_u^k S^k$ not by $D_u^k S_u^k$, since detrainment occurs at the environmental value of S. The detrainment of q_u is given by $D_u^k q^{*k}$, even though the updraft is not yet saturated. The LCL will usually occur below z_0, the level at which detrainment begins, but this is not guaranteed.

The lower boundary conditions, $S_u^{M-} = S^M + c_p/2$ and $q_u^{M-} = q^M$, are determined from the first midpoint values in the plume, rather than from the interface values of S and q. The solution of (4.127) and (4.128) continues upward until the updraft is saturated according to the condition

$$q_u^{k-} > q^*(T_u^{k-}), \tag{4.129}$$

$$T_u^{k-} = \frac{1}{c_p}\left(S_u^{k-} - gz^{k-}\right) \ . \tag{4.130}$$

The condensation (in units of m^{-1}) is determined by a centered differencing of (4.82):

$$\frac{M_u^{k-}S_u^{k-} - M_u^{k+}S_u^{k+}}{d^k z} = (E_u^k - D_u^k)S^k + LC_u^k \tag{4.131}$$

$$C_u^k = \frac{1}{L}\left[\frac{M_u^{k-}S_u^{k-} - M_u^{k+}S_u^{k+}}{d^k z} - (E_u^k - D_u^k)S^k\right] \ . \tag{4.132}$$

The rain production (in units of m^{-1}) and condensed liquid are then determined by differencing (4.85) as

$$\frac{M_u^{k-}\ell^{k-} - M_u^{k+}\ell^{k+}}{d^k z} = -D_u^k \ell^{k+} + C_u^k - R_u^k \ , \tag{4.133}$$

and (4.86) as

$$R_u^k = c_0 M_u^{k-}\ell^{k-} \ . \tag{4.134}$$

Then

$$M_u^{k-}\ell^{k-} = M_u^{k+}\ell^{k+} - d^k z\left(D_u^k \ell^{k+} - C_u^k + c_0 M_u^{k-}\ell^{k-}\right) \tag{4.135}$$

$$M_u^{k-}\ell^{k-}\left(1 + c_0 d^k z\right) = M_u^{k+}\ell^{k+} + d^k z\left(D_u^k \ell^{k+} - C_u^k\right) \tag{4.136}$$

$$\ell^{k-} = \frac{1}{M_u^{k-}\left(1 + c_0 d^k z\right)}\left[M_u^{k+}\ell^{k+} - d^k z\left(D_u^k \ell^{k+} - C_u^k\right)\right] \ . \tag{4.137}$$

4.4.5 Deep Convective Momentum Transports

Sub-grid scale Convective Momentum Transports (CMT) have ben added to the existing deep convection parameterization following Richter and Rasch [2008] and the methodology of Gregory et al. [1997*b*]. The sub-grid scale transport of momentum can be cast in the same manner as (4.69). Expressing the grid mean horizontal velocity vector, $\boldsymbol{V}$, tendency due to deep convection transport following Kershaw and Gregory [1997] gives

$$\left(\frac{\partial \boldsymbol{V}}{\partial t}\right)_{cu} = -\frac{1}{\rho}\frac{\partial}{\partial z}\left(M_u \boldsymbol{V}_u + M_d \boldsymbol{V}_d - M_c \boldsymbol{V}\right) \ , \tag{4.138}$$

and neglecting the contribution from the environment the updraft and downdraft budget equation can similarly be written as

$$-\frac{\partial}{\partial z}\left(M_u \boldsymbol{V}_u\right) = E_u \boldsymbol{V} - D_u \boldsymbol{V}_u + \boldsymbol{P}_G^u \tag{4.139}$$

$$-\frac{\partial}{\partial z}\left(M_d \boldsymbol{V}_d\right) = E_d \boldsymbol{V} + \boldsymbol{P}_G^d \ , \tag{4.140}$$

where $\boldsymbol{P}_G^u$ and $\boldsymbol{P}_G^d$ the updraft and downdraft pressure gradient sink terms parameterized from Gregory et al. [1997*b*] as

$$\boldsymbol{P}_G^u = -C_u M_u \frac{\partial \boldsymbol{V}}{\partial z} \tag{4.141}$$

$$\boldsymbol{P}_G^d = -C_d M_d \frac{\partial \boldsymbol{V}}{\partial z}. \tag{4.142}$$

C_u and C_d are tunable parameters. In the CAM 5.0 implementation we use $C_u = C_d = 0.4$. The value of C_u and C_d control the strength of convective momentum transport. As these coefiicients increase so do the pressure gradient terms, and convective momentum transport decreases.

4.4.6 Deep Convective Tracer Transport

The CAM 5.0 provides the ability to transport constituents via convection. The method used for constituent transport by deep convection is a modification of the formulation described in Zhang and McFarlane [1995].

We assume the updrafts and downdrafts are described by a steady state mass continuity equation for a "bulk" updraft or downdraft

$$\frac{\partial (M_x q_x)}{\partial p} = E_x q_e - D_x q_x \ . \tag{4.143}$$

The subscript x is used to denote the updraft (u) or downdraft (d) quantity. M_x here is the mass flux in units of Pa/s defined at the layer interfaces, q_x is the mixing ratio of the updraft or downdraft. q_e is the mixing ratio of the quantity in the environment (that part of the grid volume not occupied by the up and downdrafts). E_x and D_x are the entrainment and detrainment rates (units of s^{-1}) for the up- and down-drafts. Updrafts are allowed to entrain or detrain in any layer. Downdrafts are assumed to entrain only, and all of the mass is assumed to be deposited into the surface layer.

Equation 4.143 is first solved for up and downdraft mixing ratios q_u and q_d, assuming the environmental mixing ratio q_e is the same as the gridbox averaged mixing ratio $\bar{q}$.

Given the up- and down-draft mixing ratios, the mass continuity equation used to solve for the gridbox averaged mixing ratio $\bar{q}$ is

$$\frac{\partial \bar{q}}{\partial t} = \frac{\partial}{\partial p}(M_u(q_u - \bar{q}) + M_d(q_d - \bar{q})) \ . \tag{4.144}$$

These equations are solved for in subroutine `CONVTRAN`. There are a few numerical details employed in `CONVTRAN` that are worth mentioning here as well.

- mixing quantities needed at interfaces are calculated using the geometric mean of the layer mean values.
- simple first order upstream biased finite differences are used to solve 4.143 and 4.144.
- fluxes calculated at the interfaces are constrained so that the resulting mixing ratios are positive definite. *This means that this parameterization is not suitable for moving mixing ratios of quantities meant to represent perturbations of a trace constituent about a mean value* (in which case the quantity can meaningfully take on positive and negative mixing ratios). The algorithm can be modified in a straightforward fashion to remove this constraint, and provide meaningful transport of perturbation quantities if necessary. *the reader is warned however that there are other places in the model code where similar modifications are required because the model assumes that all mixing ratios should be positive definite quantities.*

4.5 Evaporation of convective precipitation

The CAM 5.0 employs a Sundqvist [1988] style evaporation of the convective precipitation as it makes its way to the surface. This scheme relates the rate at which raindrops evaporate to the local large-scale subsaturation, and the rate at which convective rainwater is made available to the subsaturated model layer

$$E_{r_k} = K_E \, (1 - \mathrm{RH}_k) \, (\hat{R}_{r_k})^{1/2} \ . \tag{4.145}$$

where RH_k is the relative humidity at level k, $\hat{R}_{r_k}$ denotes the total rainwater flux at level k (which can be different from the locally diagnosed rainwater flux from the convective parameterization, as will be shown below), the coefficient K_E takes the value $0.2 \cdot 10^{-5}$ (kg m^{-2} s^{-1})$^{-1/2}$s^{-1}, and the variable E_{r_k} has units of s^{-1}. The evaporation rate E_{r_k} is used to determine a local change in q_k and T_k, associated with an evaporative reduction of $\hat{R}_{r_k}$. Conceptually, the evaporation process is invoked after a vertical profile of R_{r_k} has been evaluated. An evaporation rate is then computed for the uppermost level of the model for which $R_{r_k} \neq 0$ using (4.145), where in this case $R_{r_k} \equiv \hat{R}_{r_k}$. This rate is used to evaluate an evaporative reduction in R_{r_k} which is then accumulated with the previously diagnosed rainwater flux in the layer below,

$$\hat{R}_{r_{k+1}} = \hat{R}_{r_k} - \left(\frac{\Delta p_k}{g} \right) \, E_{r_k} + R_{r_{k+1}} \ . \tag{4.146}$$

A local increase in the specific humidity q_k and a local reduction of T_k are also calculated in accordance with the net evaporation

$$q_k = q_k + E_{r_k} \, 2\Delta t \ \ , \tag{4.147}$$

and

$$T_k = T_k - \left(\frac{L}{c_p} \right) E_{r_k} \, 2\Delta t \ \ . \tag{4.148}$$

The procedure, (4.145)-(4.148), is then successively repeated for each model level in a downward direction where the final convective precipitation rate is that portion of the condensed rainwater in the column to survive the evaporation process

$$P_s = \left(\hat{R}_{r_K} - \left(\frac{\Delta p_K}{g} \right) \, E_{r_K} \right) / \rho_{H_2 0} \ . \tag{4.149}$$

In global annually averaged terms, this evaporation procedure produces a very small reduction in the convective precipitation rate where the evaporated condensate acts to moisten the middle and lower troposphere.

4.6 Cloud Microphysics

The base parameterization of stratiform cloud microphysics is described by Morrison and Gettelman [2008]. Details of the CAM implementation are described by Gettelman et al. [2008]. Modifications to handle ice nucleation and ice supersaturation are described by Gettelman et al. [2010*b*].

The scheme seeks the following:

- A more flexible, self-consistent, physically-based treatment of cloud physics.
- A reasonable level of simplicity and computational efficiency.
- Treatment of both number concentration and mixing ratio of cloud particles to address indirect aerosol effects and cloud-aerosol interaction.
- Representation of precipitation number concentration, mass, and phase to better treat wet deposition and scavenging of aerosol and chemical species.
- The achievement of equivalent or better results relative to the CAM3 microphysics parameterization when compared to observations.

The novel aspects of the scheme are an explicit representation of sub-grid cloud water distribution for calculation of the various microphysical process rates, and the diagnostic two-moment treatment of rain and snow.

4.6.1 Overview of the microphysics scheme

The two-moment scheme is based loosely on the approach of Morrison et al. [2005]. This scheme predicts the number concentrations (Nc, Ni) and mixing ratios (qc, qi) of cloud droplets (subscript c) and cloud ice (subscript i). Hereafter, unless stated otherwise, the cloud variables Nc, Ni, qc, and qi represent grid-averaged values; prime variables represent mean in-cloud quantities (e.g., such that Nc = Fcld Nc, where Fcld is cloud fraction); and double prime variables represent local in-cloud quantities. The treatment of sub-grid cloud variability is detailed in section 2.1.

The cloud droplet and ice size distributions ϕ are represented by gamma functions:

$$\phi(D) = N_0 D^{\mu} \exp^{-\lambda D} \tag{4.150}$$

where $D$is diameter, N_0 is the intercept parameter, λ is the slope parameter, and $\mu = 1/\eta^2 - 1$ is the spectra shape parameter; η is the relative radius dispersion of the size distribution. The parameter η for droplets is specified following Martin et al. [1994]. Their observations of maritime versus continental warm stratocumulus have been approximated by the following $\eta - N_c''$ relationship:

$$\eta = 0.0005714 N_c'' + 0.2714 \tag{4.151}$$

where N_c'' has units of cm^{-3}. The upper limit for η is 0.577, corresponding with aN_c'' of 535 cm^{-3}. Note that this expression is uncertain, especially when applied to cloud types other than those observed by Martin et al. [1994]. In the current version of the scheme, μ= 0 for cloud ice.

The spectral parameters N_0 and λ are derived from the predicted N'' and q'' and specified μ:

$$\lambda = \left[\frac{\pi \rho N'' \Gamma(\mu+4)}{6 q'' \Gamma(\mu+1)}\right]^{(1/3)} \tag{4.152}$$

$$N_0 = \frac{N'' \lambda^{\mu+1}}{\Gamma(\mu+1)} \tag{4.153}$$

where Γ is the Euler gamma function. Note that 4.152 and 4.153 assume spherical cloud particles with bulk density $\rho = 1000$ kg m^{-3} for droplets and ρ= 500 kg m^{-3} for cloud ice following Reisner et al. [1998].

The effective size for cloud ice needed by the radiative transfer scheme is obtained directly by dividing the third and second moments of the size distribution given by 4.150 and accounting for differenceds in cloud ice density and that of pure ice. After rearranging terms, this yields

$$d_e i = \frac{3\rho}{\lambda \rho_i} \tag{4.154}$$

where $\rho_i = 917$ kg m-2 is the bulk density of pure ice. Note that optical properties for cloud droplets are calculated using a lookup table from the N_0 and λ parameters. The droplet effective radius, which is used for output purposes only, is given by

$$r_e c = \frac{\Gamma(\mu+4)}{2\lambda\Gamma(\mu+3)} \tag{4.155}$$

The time evolution of q and N is determined by grid-scale advection, convective detrainment, turbulent diffusion, and several microphysical processes:

$$\frac{\partial N}{\partial t} + \frac{1}{\rho}\nabla\cdot[\rho \mathbf{u} N] = \left(\frac{\partial N}{\partial t}\right)_{nuc} + \left(\frac{\partial N}{\partial t}\right)_{evap} + \left(\frac{\partial N}{\partial t}\right)_{auto} + \left(\frac{\partial N}{\partial t}\right)_{acer} + \left(\frac{\partial N}{\partial t}\right)_{accs} + \left(\frac{\partial N}{\partial t}\right)_{het} + \left(\frac{\partial N}{\partial t}\right)_{hom} + \left(\tag{4.156}$$

$$\frac{\partial q}{\partial t} + \frac{1}{\rho}\nabla\cdot[\rho \mathbf{u} q] = \left(\frac{\partial q}{\partial t}\right)_{cond} + \left(\frac{\partial q}{\partial t}\right)_{evap} + \left(\frac{\partial q}{\partial t}\right)_{auto} + \left(\frac{\partial q}{\partial t}\right)_{acer} + \left(\frac{\partial q}{\partial t}\right)_{accs} + \left(\frac{\partial q}{\partial t}\right)_{het} + \left(\frac{\partial q}{\partial t}\right)_{hom} + \left(\frac{\partial q}{\partial t}\right)_{mlt} \tag{4.157}$$

where t is time, $\mathbf{u}$ is the 3D wind vector, ρ is the air density, and D is the turbulent diffusion operator. The symbolic terms on the right hand side of 4.156 and 4.157 represent the grid-average microphysical source/sink terms for N and q. Note that the source/sink terms for q and N are considered separately for cloud water and ice (giving a total of four rate equations), but are generalized here using 4.156 and 4.157 for conciseness. These terms include activation of cloud condensation nuclei or deposition/condensation-freezing nucleation on ice nuclei to form droplets or cloud ice (subscript nuc; N only); ice multiplication via rime-splintering on snow (subscript mult); condensation/deposition (subscript cond; q only), evaporation/sublimation (subscript evap), autoconversion of cloud droplets and ice to form rain and snow (subscript auto), accretion of cloud droplets and ice by rain (subscript accr), accretion of cloud droplets and ice by snow (subscript accs), heterogeneous freezing of droplets to form ice (subscript het),

homogeneous freezing of cloud droplets (subscript hom), melting (subscript mlt), ice multiplication (subsrcipt mult), sedimentation (subscript sed), and convective detrainment (subscript det). The formulations for these processes are detailed in section 3. Numerical aspects in solving 4.156 and 4.157 are detailed in section 4.

Sub-grid cloud variability

Sub-grid variability is considered for cloud water but neglected for cloud ice and precipitation at present; furthermore, we neglect sub-grid variability of droplet number concentration for simplicity. We assume that the PDF of in-cloud cloud water, $P(q_c'')$, follows a gamma distribution function based on observations of optical depth in marine boundary layer clouds [Barker, 1996; Barker et al., 1996; McFarlane and Klein, 1999]:

$$P(q_c'') = \frac{q_c''^{\nu-1}\alpha^{\nu}}{\Gamma(\nu)} \exp^{-\alpha q_c''} \tag{4.158}$$

where $\nu = 1/\sigma^2$;σ^2 is the relative variance (i.e., variance divided by $q_c'^2$); and $\alpha = \nu/q_c'$ (q_c' is the mean in-cloud cloud water mixing ratio). Note that this PDF is applied to all cloud types treated by the stratiform cloud scheme; the appropriateness of such a PDF for stratiform cloud types other than marine boundary layer clouds (e.g., deep frontal clouds) is uncertain given a lack of observations.

Satellite retrievals described by Barker et al. [1996] suggest that $\nu > 1$ in overcast conditions and $\nu \sim 1$ (corresponding to an exponential distribution) in broken stratocumulus. The model assumes a constant $\nu = 1$ for simplicity.

A major advantage of using gamma functions to represent sub-grid variability of cloud water is that the grid-average microphysical process rates can be derived in a straightforward manner as follows. For any generic local microphysical process rate $M_p = xq_c''^y$, replacing q_c'' with $P(q_c'')$ from 4.158 and integrating over the PDF yields a mean in-cloud process rate

$$M_p' = x\frac{\Gamma(\nu+y)}{\Gamma(\nu)\nu^y}q_c'^y \tag{4.159}$$

Thus, each cloud water microphysical process rate in 4.156 and 4.157 is multiplied by a factor

$$E = \frac{\Gamma(\nu+y)}{\Gamma(\nu)\nu^y} \tag{4.160}$$

Diagnostic treatment of precipitation

As described by Ghan and Easter [1992], diagnostic treatment of precipitation allows for a longer time step, since prognostic precipitation is constrained by the Courant criterion for sedimentation. Furthermore, the neglect of horizontal advection of precipitation in the diagnostic approach is reasonable given the large grid spacing ($\sim$ 100 km) and long time step ($\sim$15-40 min) of GCMs. A unique aspect of this scheme is the diagnostic treatment of both precipitation mixing ratio q_p and number concentration N_p. Considering only the vertical dimension, the grid-scale time rates of change of q_p and N_p are:

$$\frac{\partial q_p}{\partial t} = \frac{1}{\rho}\frac{\partial (V_q \rho q_p)}{\partial z} + S_q \tag{4.161}$$

$$\frac{\partial N_p}{\partial t} = \frac{1}{\rho}\frac{\partial (V_N \rho N_p)}{\partial z} + S_N \tag{4.162}$$

where z is height, V_q and V_N are the mass- and number-weighted terminal fallspeeds, respectively, and S_q and S_N are the grid-mean source/sink terms for q_p and N_p, respectively:

$$S_q = \left(\frac{\partial q_p}{\partial t}\right)_{auto} + \left(\frac{\partial q_p}{\partial t}\right)_{accw} + \left(\frac{\partial q_p}{\partial t}\right)_{acci} + \left(\frac{\partial q_p}{\partial t}\right)_{het} + \left(\frac{\partial q_p}{\partial t}\right)_{hom} + \left(\frac{\partial q_p}{\partial t}\right)_{mlt} + \left(\frac{\partial q_p}{\partial t}\right)_{mult} + \left(\frac{\partial q_p}{\partial t}\right)_{evap} + \left(\frac{\partial$$
(4.163)

$$S_N = \left(\frac{\partial N_p}{\partial t}\right)_{auto} + \left(\frac{\partial N_p}{\partial t}\right)_{het} + \left(\frac{\partial N_p}{\partial t}\right)_{hom} + \left(\frac{\partial N_p}{\partial t}\right)_{mlt} + \left(\frac{\partial N_p}{\partial t}\right)_{evap} + \left(\frac{\partial N_p}{\partial t}\right)_{self} + \left(\frac{\partial N_p}{\partial t}\right)_{coll} \tag{4.164}$$

The symbolic terms on the right-hand sides of 4.163 and 4.164 are autoconversion (subscript auto), accretion of cloud water (subscript accw), accretion of cloud ice (subscript acci), heterogeneous freezing (subscript het), homogeneous freezing (subscript hom), melting (subscript mlt), ice multiplication via rime splintering (subsrcipt mult; qp only), evaporation (subscript evap), and self-collection (subscript self; collection of rain drops by other rain drops, or snow crystals by other snow crystals; Np only), and collection of rain by snow (subscript coll). Formulations for these processes are described in section 3.

In the diagnostic treatment , $(\partial q_p/\partial t)$ =0 and $(\partial N_p/\partial t)$ =0 . This allows 4.161 and 4.162 to be expressed as a function of z only. The q_p and N_p are therefore determined by discretizing and numerically integrating 4.161 and 4.162 downward from the top of the model atmosphere following Ghan and Easter [1992]:

$$\rho_{a,k} V_{q,k} q_{p,k} = \rho_{a,k+1} V_{q,k+1} q_{p,k+1} + \frac{1}{2}[\rho_{a,k} S_{q,k} \delta Z_k + \rho_{a,k+1} S_{q,k+1} \delta Z_{k+1}] \tag{4.165}$$

$$\rho_{a,k} V_{N,k} N_{p,k} = \rho_{a,k+1} V_{N,k+1} N_{p,k+1} + \frac{1}{2}[\rho_{a,k} S_{N,k} \delta Z_k + \rho_{a,k+1} S_{N,k+1} \delta Z_{k+1}] \tag{4.166}$$

where k is the vertical level (increasing with height, i.e., $k+1$ is the next vertical level above k). Since $V_{q,k}$, $S_{q,k}$, $V_{N,k}$, and $S_{N,k}$ depend on $q_{p,k}$ and $N_{p,k}$, 4.165 and 4.166 must be solved by iteration or some other method. The approach of Ghan and Easter [1992] uses values of $q_{p,k}$ and $N_{p,k}$ from the previous time step as provisional estimates in order to calculate $V_{q,k}$, $V_{N,k}$, $S_{p,k}$, and $S_{N,k}$. "Final" values of $q_{p,k}$ and $N_{p,k}$ are calculated from these values of $V_{q,k}$, $V_{N,k}$, $S_{q,k}$ and $S_{N,k}$ using 4.165 and 4.166. Here we employ another method that obtains provisional values of $q_{p,k}$ and $N_{p,k}$ from 4.165 and 4.166 assuming $V_{q,k} \sim V_{q,k+1}$ and $V_{N,k} \sim V_{N,k+1}$. It is also assumed that all source/sink terms in $S_{q,k}$ and $S_{N,q}$ can be approximated by the values at $k+1$, except for the autoconversion, which can be obtained directly at the k level since it does not depend on $q_{p,k}$ or $N_{p,k}$. If there is no precipitation flux from the level above, then the provisional $q_{p.k}$ and $N_{p,k}$ are calculated using autoconversion at the k level in $S_{q,k}$ and $S_{N,k}$; $V_{q,k}$ and $V_{N,k}$ are

estimated assuming newly-formed rain and snow particles have fallspeeds of 0.45 m/s for rain and 0.36 m/s for snow.

Rain and snow are considered separately, and both may occur simultaneously in supercooled conditions (hereafter subscript p for precipitation is replaced by subscripts r for rain and s for snow). The rain/snow particle size distributions are given by 4.150, with the shape parameter $\mu = 0$, resulting in Marshall-Palmer (exponential) size distributions. The size distribution parameters λ and N_0 are similarly given by 4.152 and 4.153 with $\mu = 0$. The bulk particle density (parameter ρ in 4.152) is $\rho = 1000$ kg m^{-3} for rain and $\rho = 100$ kg m^{-3} for snow following Reisner et al. [1998].

Cloud and precipitation particle terminal fallspeeds

The mass- and number-weighted terminal fallspeeds for all cloud and precipitation species are obtained by integration over the particle size distributions with appropriate weighting by number concentration or mixing ratio:

$$V_N = \frac{\int_0^\infty \left(\frac{\rho_a}{\rho_{a0}}\right)^{0.54} aD^b \phi(D) \mathrm{d}D}{\int_0^\infty \phi(D) \mathrm{d}D} = \frac{\left(\frac{\rho_a}{\rho_{a0}}\right)^{0.54} a\Gamma(1+b+\mu)}{\lambda^b \Gamma(\mu+1)} \tag{4.167}$$

$$V_q = \frac{\int_0^\infty \frac{\pi\rho}{6} \left(\frac{\rho_a}{\rho_{a0}}\right)^{0.54} aD^{b+3} \phi(D) \mathrm{d}D}{\int_0^\infty \frac{\pi\rho}{6} D^3 \phi(D) \mathrm{d}D} = \frac{\left(\frac{\rho_a}{\rho_{a0}}\right)^{0.54} a\Gamma(4+b+\mu)}{\lambda^b \Gamma(\mu+4)} \tag{4.168}$$

where ρ^{a0} is the reference air density at 850 mb and 0 C, a and b are empirical coefficients in the diameter-fallspeed relationship $V = aD^b$, where V is terminal fallspeed for an individual particle with diameter D. The air density correction factor is from Heymsfield and Banseemer (2007). V_N and V_q are limited to maximum values of 9.1 m/s for rain and 1.2 m/s for snow. The a and b coefficients for each hydrometeor species are given in Table 2. Note that for cloud water fallspeeds, sub-grid variability of q is considered by appropriately multiplying the V_N and V_q by the factor E given by 4.160.

Ice Cloud Fraction

Several modifications have been made to the determination of diagnostic fractional cloudiness in the simulations. The ice and liquid cloud fractions are now calculated separately. Ice and liquid cloud can exist in the same grid box. Total cloud fraction, used for radiative transfer, is determined assuming maximum overlap between the two.

The diagnostic ice cloud fraction closure is constructed using a total water formulation of the Slingo [1987*a*] scheme. There is an indirect dependence of prognostic cloud ice on the ice cloud fraction since the in-cloud ice content is used for all microphysical processes involving ice. The new formulation of ice cloud fraction (CF_i) is calculated using relative humidity (RH) based on total ice water mixing ratio, including the ice mass mixing ratio (q_i) and the vapor mixing ratio (q_v). The RH based on total ice water (RH_{ti}) is then $RH_{ti} = (q_v + q_i)/q_{sat}$ where q_{sat} is the saturation vapor mixing ratio over ice. Because this is for ice clouds only, we do not include q_l (liquid mixing ratio). We have tested that the inclusion of q_l does not substantially impact the scheme (since there is little liquid present in this regime).

Ice cloud fraction is then given by $CF_i = min(1, RH_d^2)$ where

$$RH_d = max\left(0, \frac{RH_{ti} - RHi_{min}}{RHi_{max} - RHi_{min}}\right) \tag{4.169}$$

RHi_{max} and RHi_{min} are prescribed maximum and minimum threshold humidities with respect to ice, set at RHi_{max}=1.1 and RHi_{min}=0.8. These are adjustable parameters that reflect assumptions about the variance of humidity in a grid box. The scheme is not very sensitive to RHi_{min}. RHi_{max} affects the total ice supersaturation and ice cloud fraction.

With $RHi_{max} = 1$ and $q_i = 0$ the scheme reduces to the Slingo [1987*a*] scheme. RH_{ti} is preferred over RH in RH_d because when q_i increases due to vapor deposition, it reduces q_v, and without any precipitation or sedimentation the decrease in RH would change diagnostic cloud fraction, whereas RH_{ti} is constant.

4.6.2 Radiative Treatment of Ice

The simulations use a self consistent treatment of ice in the radiation code. The radiation code uses as input the prognostic effective diameter of ice from the cloud microphysics (give eq. # from above). Ice cloud optical properties are calculated based on the modified anomalous diffraction approximation (MADA), described in Mitchell [2000, 2002] and Mitchell et al. [2006*a*]. The mass-weighted extinction (volume extinction coefficient/ice water content) and the single scattering albedo, ω_0, are evaluated using a look-up table. For solar wavelengths, the asymmetry parameter g is determined as a function of wavelength and ice particle size and shape as described in Mitchell et al. [1996*a*] and Nousiainen and McFarquhar [2004] for quasi-spherical ice crystals. For terrestrial wavelengths, g was determined following Yang et al. [2005]. An ice particle shape recipe was assumed when calculating these optical properties. The recipe is described in Mitchell et al. [2006*b*] based on mid-latitude cirrus cloud data from Lawson et al. [2006] and consists of 50% quasi-spherical and 30% irregular ice particles, and 20% bullet rosettes for the cloud ice (i.e. small crystal) component of the ice particle size distribution (PSD). Snow is also included in the radiation code, using the diagnosed mass and effective diameter of falling snow crystals (MG2008). For the snow component, the ice particle shape recipe was based on the crystal shape observations reported in Lawson et al. [2006] at -45°C: 7% hexagonal columns, 50% bullet rosettes and 43% irregular ice particles.

4.6.3 Formulations for the microphysical processes

Activation of cloud droplets

Activation of cloud droplets, occurs on a multi-modal lognormal aerosol size distribution based on the scheme of Abdul-Razzak and Ghan [2000*a*]. Activation of cloud droplets occurs if N_c decreases below the number of active cloud condensation nuclei diagnosed as a function of aerosol chemical and physical parameters, temperature, and vertical velocity (see Abdul-Razzak and Ghan [2000*a*]), and if liquid condensate is present. We use the existing Nc as a proxy for the number of aerosols previously activated as droplets since the actual number of activated aerosols is not tracked as a prognostic variable from time step to time step (for

coupling with prescribed aerosol scheme). This approach is similar to that of Lohmann et al. [1999].

Since local rather than grid-scale vertical velocity is needed for calculating droplet activation, a sub-grid vertical velocity w_{sub} is derived from the square root of the Turbulent Kinetic Energy (TKE) following Morrison and Pinto [2005]:

$$w_{sub} = \sqrt{\frac{2}{3} TKE} \tag{4.170}$$

where TKE is defined using a steady state energy balance (eqn [17] and [28] in Bretherton and Park [2009*b*])

In regions with weak turbulent diffusion, a minimum sub-grid vertical velocity of 10 cm/s is assumed. Some models use the value of w at cloud base to determine droplet activation in the cloud layer (e.g., Lohmann et al. [1999]); however, because of coarse vertical and horizontal resolution and difficulty in defining the cloud base height in GCMs, we apply the w_{sub} calculated for a given layer to the droplet activation for that layer. Note that the droplet number may locally exceed the number activated for a given level due to advection of Nc. Some models implicitly assume that the timescale for droplet activation over a cloud layer is equal to the model time step (e.g., Lohmann et al. [1999]), which could enhance sensitivity to the time step. This timescale can be thought of as the timescale for recirculation of air parcels to regions of droplet activation (i.e., cloud base), similar to the timescale for large eddy turnover; here, we assume an activation timescale of 20 min.

Primary ice nucleation

Ice crystal nucleation is based on Liu et al. [2007], which includes homogeneous freezing of sulfate competing with heterogeneous immersion freezing on mineral dust in ice clouds (with temperatures below -37°C) [Liu and Penner, 2005]. Because mineral dust at cirrus levels is very likely coated [Wiacek and Peter, 2009], deposition nucleation is not explicitly included in this work for pure ice clouds. Immersion freezing is treated for cirrus (pure ice), but not for mixed phase clouds. The relative efficiency of immersion versus deposition nucleation in mixed phase clouds is an unsettled problem, and the omission of immersion freezing in mixed phase clouds may not be appropriate (but is implicitly included in the deposition/condensation nucleation: see below). Deposition nucleation may act at temperatures lower than immersion nucleation (i.e. T<-25°C) [Field et al., 2006], and immersion nucleation has been inferred to dominate in mixed phase clouds [Ansmann et al., 2008, 2009; Hoose and Kristjansson, 2010]. We have not treated immersion freezing on soot because while Liu and Penner [2005] assumed it was an efficient mechanism for ice nucleation, more recent studies [Kärcher et al., 2007] indicate it is still highly uncertain.

In the mixed phase cloud regime (-37<T<0°C), deposition/condensation nucleation is considered based on Meyers et al. [1992], with a constant nucleation rate for T<-20°C. The Meyers et al. [1992] parameterization is assumed to treat deposition/condensation on dust in the mixed phase. Since it is based on observations taken at water saturation, it should include all important ice nucleation mechanisms (such as the immersion and deposition nucleation discussed above) except contact nucleation, though we cannot distinguish all the specific processes. Meyers et al. [1992] has been shown to produce too many ice nuclei during the Mixed Phase

Arctic Clouds Experiment (MPACE) by Prenni et al. [2007]. Contact nucleation by mineral dust is included based on Young [1974] and related to the coarse mode dust number. It acts in the mixed phase where liquid droplets are present and and includes Brownian diffusion as well as phoretic forces. Hallet-Mossop secondary ice production due to accretion of drops by snow is included following Cotton et al. [1986].

In the Liu and Penner [2005] scheme, the number of ice crystals nucleated is a function of temperature, humidity, sulfate, dust and updraft velocity, derived from fitting the results from cloud parcel model experiments. A threshold RH_w for homogeneous nucleation was fitted as a function of temperature and updraft velocity (see Liu et al. [2007], equation 6). For driving the parameterization, the sub-grid velocity for ice (w_{sub}) is derived following ewuation 4.170. A minimum of 0.2 m s^{-1} is set for ice nucleation.

It is also implicitly assumed that there is some variation in humidity over the grid box. For purposes of ice nucleation, nucleation rates for a grid box are estimated based on the 'most humid portion' of the grid-box. This is assumed to be the grid box average humidity plus a fixed value (20% RH). This implies that the 'local' threshold supersaturation for ice nucleation will be reached at a grid box mean value 20% lower than the RH process threshold value. This represents another gross assumption about the RH variability in a model grid box and is an adjustable parameter in the scheme. In the baseline case, sulfate for homogeneous freezing is taken as the portion of the Aitken mode particles with radii greater than 0.1 microns, and was chosen to better reproduce observations (this too can be adjusted to alter the balance of homogeneous freezing). The size represents the large tail of the Aitken mode. In the upper troposphere there is little sulfate in the accumulation mode (it falls out), and almost all sulfate is in the Aitken mode.

Deposition/sublimation of ice

Several cases are treated below that involve ice deposition in ice-only clouds or mixed-phase clouds in which all liquid water is depleted within the time step. Case [1] Ice only clouds in which $q_v > q_{vi}*$ where q_v is the grid mean water vapor mixing ratio and $q_{vi}*$ is the local vapor mixing ratio at ice saturation (q_{sat}). Case [2] is the same as case [1] ($q_v > q_{vi}*$) but there is existing liquid water depleted by the Bergeron-Findeisen process (ber). Case [3], liquid water is depleted by the Bergeron-Findeisen process and the local liquid is less than local ice saturation ($q_v* \leq q_{vi}*$). In Case [4] $q_v < q_{vi}*$ so sublimation of ice occurs.

Case [1]: If the ice cloud fraction is larger than the liquid cloud fraction (including grid cells with ice but no liquid water), or if all new and existing liquid water in mixed-phase clouds is depleted via the Bergeron-Findeisen process within the time step, then vapor depositional ice growth occurs at the expense of water vapor. In the case of a grid cell where ice cloud fraction exceeds liquid cloud fraction, vapor deposition in the pure ice cloud portion of the cell is calculated similarly to eq. [21] in MG08:

$$\left(\frac{\partial q_i}{\partial t}\right)_{dep} = \frac{(q_v - q_{vi}*)}{\Gamma_p \tau}, q_v > q_{vi}* \tag{4.171}$$

where $\Gamma_p = 1 + \frac{L_s}{c_p}\frac{dq_{vi}}{dT}$ is the psychrometric correction to account for the release of latent heat, L_s is the latent heat of sublimation, c_p is the specific heat at constant pressure, $\frac{dq_{vi}}{dT}$ is the change of ice saturation vapor pressure with temperature, and τ is the supersaturation relaxation

timescale associated with ice deposition given by eq. [22] in MG08 (a function of ice crystal surface area and the diffusivity of water vapor in air). The assumption for pure ice clouds is that the in-cloud vapor mixing ratio for deposition is equal to the grid-mean value. The same assumption is used in Liu et al. [2007], and while it is uncertain, it is the most straightforward. Thus we do not consider sub-grid variability of water vapor for calculating vapor deposition in pure ice-clouds.

The form of the deposition rate in equation 4.171 differs from that used by Rotstayn et al. [2000] and Liu et al. [2007] because they considered the increase in ice mixing ratio q_i due to vapor deposition during the time step, and formulated an implicit solution based on this consideration (see eq. [6] in Rotstayn et al. [2000]). However, these studies did not consider sinks for the ice due to processes such as sedimentation and conversion to precipitation when formulating their implicit solution; these sink terms may partially (or completely) balance the source for the ice due to vapor deposition. Thus, we use a simple explicit forward-in-time solution that does not consider changes of q_i within the microphysics time step.

Case [2]: When all new and existing liquid water is depleted via the Bergeron-Findeisen process (ber) within the time step, the vapor deposition rate is given by a weighted average of the values for growth in mixed phase conditions prior to the depletion of liquid water (first term on the right hand side) and in pure ice clouds after depletion (second term on the right hand side):

$$\left(\frac{\partial q_i}{\partial t}\right)_{dep} = \frac{q_c*}{\Delta t} + \left(1 - \frac{q_c*}{\Delta t}\left(\frac{\partial q_i}{\partial t}\right)_{ber}^{-1}\right)\left(\frac{(q_v * - q_{vi}*)}{\Gamma_p \tau}\right), q_v > q_{vi}* \tag{4.172}$$

where q_c* is the sum of existing and new liquid condensate mixing ratio, Δt is the model time step, $\left(\frac{\partial q_i}{\partial t}\right)_{ber}$ is the ice deposition rate in the presence of liquid water (i.e., assuming vapor mixing ratio is equal to the value at liquid saturation) as described above, and q_v* is an average of the grid-mean vapor mixing ratio and the value at liquid saturation.

Case [3]: If $q_v* \leq q_{vi}*$ then it is assumed that no additional ice deposition occurs after depletion of the liquid water. The deposition rate in this instance is given by:

$$\left(\frac{\partial q_i}{\partial t}\right)_{dep} = \left(\frac{q_c*}{\Delta t}\right), q_v* \leq q_{vi}* \tag{4.173}$$

Case [4]: Sublimation of pure ice cloud occurs when the grid-mean water vapor mixing ratio is less than value at ice saturation. In this case the sublimation rate of ice is given by:

$$\left(\frac{\partial q_i}{\partial t}\right)_{sub} = \frac{(q_v - q_{vi}*)}{\Gamma_p \tau}, q_v < q_{vi}* \tag{4.174}$$

Again, the use of grid-mean vapor mixing ratio in equation 4.174 follows the assumption of Liu et al. [2007] that the in-cloud q_v is equal to the grid box mean in pure ice clouds. Grid-mean deposition and sublimation rates are given by the in-cloud values for pure ice or mixed-phase clouds described above, multiplied by the appropriate ice or mixed-phase cloud fraction. Finally, ice deposition and sublimation are limited to prevent the grid-mean mixing ratio from falling below the value for ice saturation in the case of deposition and above this value in the case of sublimation.

Cloud water condensation and evaporation are given by the bulk closure scheme within the cloud macrophysics scheme, and therefore not described here.

Conversion of cloud water to rain

Autoconversion of cloud droplets and accretion of cloud droplets by rain is given by a version of the Khairoutdinov and Kogan [2000] scheme that is modified here to account for sub-grid variability of cloud water within the cloudy part of the grid cell as described previously in section 2.1. Note that the Khairoutdinov and Kogan scheme was originally developed for boundary layer stratocumulus, but is applied here to all stratiform cloud types.

The grid-mean autoconversion and accretion rates are found by replacing the qc in Eqs. (29) and (33) of Khairoutdinov and Kogan [2000] with $P(q_c'')$ given by equation 4.158 here, integrating the resulting expressions over the cloud water PDF, and multiplying by the cloud fraction. This yields

$$\left(\frac{\partial q_c}{\partial t}\right)_{auto} = -F_{cld}\frac{\Gamma(\nu+2.47)}{\Gamma(\nu)\nu^{2.47}}1350 q_c'^{2.47} N_c'^{-1.79} \tag{4.175}$$

$$\left(\frac{\partial q_c}{\partial t}\right)_{accr} = -F_{cld}\frac{\Gamma(\nu+1.15)}{\Gamma(\nu)\nu^{1.15}}67(q_c' q_r')^{1.15} \tag{4.176}$$

The changes in qr due to autoconversion and accretion are given by $(\partial q_r/\partial t)_{auto} = -(\partial q_c/\partial t)_{auto}$ and $(\partial q_r/\partial t)_{accr} = -(\partial q_c/\partial t)_{accr}$. The changes in N_c and N_r due to autoconversion and accretion $(\partial N_c/\partial t)_{auto}$, $(\partial N_r/\partial t)_{auto}$, $(\partial N_c/\partial t)_{accr}$, are derived from Eqs. (32) and (35) in Khairoutdinov and Kogan [2000]. Since accretion is nearly linear with respect to q_c, sub-grid variability of cloud water is much less important for accretion than it is for autoconversion.

Note that in the presence of a precipitation flux into the layer from above, new drizzle drops formed by cloud droplet autoconversion would be accreted rapidly by existing precipitation particles (rain or snow) given collection efficiencies near unity for collision of drizzle with rain or snow (e.g., Pruppacher and Klett [1997]). This may be especially important in models with low vertical resolution, since they cannot resolve the rapid growth of precipitation that occurs over distances much less than the vertical grid spacing. Thus, if the rain or snow mixing ratio in the next level above is greater than 10-6 g kg-1, we assume that autoconversion produces an increase in rain mixing ratio but not number concentration (since the newly-formed drops are assumed to be rapidly accreted by the existing precipitation). Otherwise, autoconversion results in a source of both rain mixing ratio and number concentration.

Conversion of cloud ice to snow

The autoconversion of cloud ice to form snow is calculated by integration of the cloud ice mass- and number-weighted size distributions greater than some specified threshold size, and transferring the resulting mixing ratio and number into the snow category over some specified timescale, similar to Ferrier [1994]. The grid-scale changes in qi and Ni due to autoconversion are

$$\left(\frac{\partial q_i}{\partial t}\right)_{auto} = -F\frac{\pi\rho_i N_{0i}}{6\tau_{auto}}\left[\frac{D_{cs}^3}{\lambda_i} + \frac{3D_{cs}^2}{\lambda_i^2} + \frac{6D_{cs}}{\lambda_i^3} + \frac{6D}{\lambda_i^4}\right]\exp^{-\lambda_i D_{cs}} \tag{4.177}$$

$$\left(\frac{\partial N_i}{\partial t}\right)_{auto} = -F\frac{N_{0i}}{\lambda_i\tau_{auto}}\exp^{-\lambda_i D_{cs}} \tag{4.178}$$

where $D_{cs} = 200$ μm is the threshold size separating cloud ice from snow, ρ_i is the bulk density of cloud ice, and $\tau_{auto} = 3$ min is the assumed autoconversion timescale. Note that this formulation assumes the shape parameter $\mu = 0$ for the cloud ice size distribution; different formulation must be used for other values of μ. The changes in q_s and N_s due to autoconversion are given by $(\partial q_s/\partial t)_{auto} = -(\partial q_i/\partial t)_{auto}$ and $(\partial N_s/\partial t)_{auto} = -(\partial N_i/\partial t)_{auto}$.

Accretion of q_i and N_i by snow $(\partial q_i/\partial t)_{accs}$, $(\partial N_i/\partial t)_{accs}$, $(\partial q_s/\partial t)_{acci}$, and $(\partial q_s/\partial t)_{acci} = -(\partial q_i/\partial t)_{accs}$, are given by the continuous collection equation following Lin et al. [1983], which assumes that the fallspeed of snow $\gg$ cloud ice fallspeed. The collection efficiency for collisions between cloud ice and snow is 0.1 following Reisner et al. [1998]. Newly- formed snow particles formed by cloud ice autoconversion are not assumed to be rapidly accreted by existing snowflakes, given aggregation efficiencies typically much less than unity (e.g., Field et al. [2007]).

Other collection processes

The accretion of q_c and N_c by snow $(\partial q_c/\partial t)_{accs}$, $(\partial N_c/\partial t)_{accs}$, and $(\partial q_s/\partial t)_{accw} = -(\partial q_c/\partial t)_{accs}$ are given by the continuous collection equation. The collection efficiency for droplet-snow collisions is a function of the Stokes number following Thompson et al. [2004] and thus depends on droplet size. Self-collection of snow, $(\partial N_s/\partial t)_{self}$ follows Reisner et al. [1998] using an assumed collection efficiency of 0.1. Self-collection of rain$(\partial N_r/\partial t)_{self}$ follows Beheng [1994]. Collisions between rain and cloud ice, cloud droplets and cloud ice, and self-collection of cloud ice are neglected for simplicity. Collection of q_r and N_r by snow in subfreezing conditions, $(\partial q_r/\partial t)_{coll} = -(\partial q_s/\partial t)_{coll}$ and $(\partial N_r/\partial t)_{coll}$, is given by Ikawa and Saito [1990] assuming collection efficiency of unity.

Freezing of cloud droplets and rain and ice multiplication

Heterogeneous freezing of cloud droplets and rain to form cloud ice and snow, respectively, occurs by immersion freezing following Bigg [1953], which has been utilized in previous microphysics schemes (e.g., Reisner et al. [1998], see Eq. A.22, A.55, A.56; Morrison et al. [2005]; Thompson et al. [2008]). Here the freezing rates are integrated over the mass- and number-weighted cloud droplet and rain size distributions and the impact of sub-grid cloud water variability is included as described previously. Homogeneous freezing of cloud droplets to form cloud ice occurs instantaneously at -40°C. All rain is assumed to freeze instantaneously at -5°C.

Contact freezing of cloud droplets by mineral dust is included based on Young [1974] and related to the coarse mode dust number. It acts in the mixed phase where liquid droplets are present and includes Brownian diffusion as well as phoretic forces. Hallet-Mossop ice multiplication (secondary ice production) due to accretion of drops by snow is included following Cotton et al. [1986]. This represents a sink term for snow mixing ratio and source term for cloud ice mixing ratio and number concentration.

Melting of cloud ice and snow

For simplicity, detailed formulations for heat transfer during melting of ice and snow are not included. Melting of cloud ice occurs instantaneously at 0°C. Melting of snow occurs instantaneously at +2°C. We have tested the sensitivity of both single- column and global results

to changing the specified snow melting temperature from +2° to 0°C and found no significant changes.

Evaporation/sublimation of precipitation

Evaporation of rain and sublimation of snow, $(\partial q_s/\partial t)_{evap}$ and $(\partial q_r/\partial t)_{evap}$, are given by diffusional mass balance in subsaturated conditions Lin et al. [1983], including ventilation effects. Evaporation of precipitation occurs within the region of the grid cell containing precipitation but outside of the cloudy region. The fraction of the grid cell with evaporation of precipitation is therefore , where F_{pre} is the precipitation fraction. F_{pre} is calculated assuming maximum cloud overlap between vertical levels, and neglecting tilting of precipitation shafts due to wind shear ($F_{pre} = F_{cld}$ at cloud top). The out-of-cloud water vapor mixing ratio is given by

$$q_{clr} = \frac{q_v - F_{cld} q_s(T)}{1 - F_{cld}}, F_{cld} < 1 \tag{4.179}$$

where $q_s(T)$ is the in-cloud water vapor mixing ratio after bulk condensation/evaporation of cloud water and ice as described previously. As in the older CAM3 microphysics parameterization, condensation/deposition onto rain/snow is neglected. Following Morrison et al. [2005], the evaporation/sublimation of N_r and N_s, $(\partial N_r/\partial t)_{evap}$ and $(\partial N_s/\partial t)_{evap}$, is proportional to the reduction of q_r and q_s during evaporation/sublimation.

Sedimentation of cloud water and ice

The time rates of change of q and N for cloud water and cloud ice due to sedimentation, $(\partial q_c/\partial t)_{sed}$, $(\partial q_i/\partial t)_{sed}$, $(\partial N_c/\partial t)_{sed}$, and $(\partial N_i/\partial t)_{sed}$, are calculated with a first-order forward-in-time-backward-in-space scheme. Numerical stability for cloud water and ice sedimentation is ensured by sub-stepping the time step, although these numerical stability issues are insignificant for cloud water and ice because of the low terminal fallspeeds ($\ll$ 1 m/s). We assume that the sedimentation of cloud water and ice results in evaporation/sublimation when the cloud fraction at the level above is larger than the cloud fraction at the given level (i.e., a sedimentation flux from cloudy into clear regions), with the evaporation/condensate rate proportional to the difference in cloud fraction between the levels.

Convective detrainment of cloud water and ice

The ratio of ice to total cloud condensate detrained from the convective parameterizations, Fdet, is a linear function of temperature between -40° C and -10° C; $F_{det} = 1$ at T < -40° C, and Fdet = 0 at T > -10° C. Detrainment of number concentration is calculated by assuming a mean volume radius of 8 and 32 micron for droplets and cloud ice, respectively.

Numerical considerations

To ensure conservation of both q and N for each species, the magnitudes of the various sink terms are reduced if the provisional q and N are negative after stepping forward in time. This approach ensures critical water and energy balances in the model, and is similar to the approach employed in other bulk microphysics schemes (e.g., Reisner et al. [1998]. Inconsistencies are possible

because of the separate treatments for N and q, potentially leading to unrealistic mean cloud and precipitation particle sizes. For consistency, N is adjusted if necessary so that mean (number-weighted) particle diameter ( ) remains within a specified range of values for each species. Limiting to a maximum mean diameter can be thought of as an implicit parameterization of particle breakup.

For the diagnostic precipitation, the source terms for q and N at a given vertical level are adjusted if necessary to ensure that the vertical integrals of the source terms (from that level to the model top) are positive. In other words, we ensure that at any given level, there isnt more precipitation removed (both in terms of mixing ratio and number concentration) than is available falling from above (this is also the case in the absence of any sources/sinks at that level). This check and possible adjustment of the precipitation and cloud water also ensures conservation of the total water and energy. Our simple adjustment procedure to ensure conservation could potentially result in sensitivity to time step, although as described in section 3, time truncation errors are minimized with appropriate sub-stepping.

Melting rates of cloud ice and snow are limited so that the temperature of the layer does not decrease below the melting point (i.e., in this instance an amount of cloud ice or snow is melted so that the temperature after melting is equal to the melting point). A similar approach is applied to ensure that homogeneous freezing does increase the temperature above homogeneous freezing threshold.

4.7 Cloud Macrophysics

Cloud macrophysics is a suite of physical processes that computes (1) cloud fractions in each layer, (2) horizontal and vertical overlapping structures of clouds, (3) net conversion rates of water vapor into cloud condensates. Cloud macrophysics is a process unique for GCM that handles partial cloud fraction. In case of cloud resolving model, for example, cloud fraction in each layer is either 0 or 1, and so there is no need to use special treatment for cloud overlap and partial condensation. Along with convection scheme, correct setting of cloud macrophysics is essential for developing a seamless GCM across the various sizes of horizontal GCM grid.

Cloud macrophysics sets a stage for cloud droplet activation and nucleation, cloud microphysics (i.e., processes controlling conversion from sustained to falling hydrometeors), wet scavenging of aerosols, radiative transfer, and moist turbulent processes. Cloud macrophysics in CAM3/CAM4 (cloud macrophysics in CAM3 is nearly identical to the cloud macrophysics in CAM4) was constructed to be compatible with and to some degrees to compensate for the incomplete CAM3/CAM4 physics package. For example, (1) without a need to do explicit droplet nucleation and activation processes due to the prescribed cloud droplet radius, CAM3/CAM4 simply assume zero supersaturation within ice stratus, (2) without the information of realistic in-cumulus condensate from shallow and deep convection schemes, CAM3/CAM4 assumes that in-cumulus condensate is identical to in-stratus condensate, and (3) without cloud-radiation-turbulence interaction in the dry PBL scheme, CAM3/CAM4 uses additional stability-based stratus fraction as well as RH-based stratus fraction to simulate marine stratocumulus over the subtropical, mid-latitude and Arctic oceans. With the new CAM5 physics addressing these limitations in the CAM3/CAM4 physics, cloud macrophysics should also be revised for consistency among various model physics. Here, we document the revised cloud macrophysics in CAM5. Additional details on CAM5's cloud macrophysics are discussed in Park et al. [2010].

In the following sections, we will document how CAM5 computes (1) cloud fractions - deep cumulus fraction, shallow cumulus fraction, and stratus (liquid and ice separately) fractions, (2) horizontal and vertical overlapping structures of clouds, and (3) net condensation rates of water vapor into cloud liquid and ice.

4.7.1 Cloud Fractions

Cloud fraction is a volume containing hydrometeors sustained in the atmosphere. In CAM5, two types of clouds exist: *stratus* and *cumulus*. In nature, these two clouds can be identified by their shapes and turbulent properties. Stratus is horizontally extended with symmetric turbulence properties: fractional area, strength of vertical velocity, vertical extent, and degree of saturation within updraft are similar to those within downdraft. On the other hand, cumulus is vertically stretched with asymmetric turbulence properties: updraft is narrow, strong, and usually saturared while compensating subsidence is broad, weak, and unsaturated. In CAM5, moist turbulence scheme is designed to simulate symmetric turbulences while convection schemes are for simulating asymmetric turbulences. While there is an attempt to treat these two distinct turbulences in a unified way, we stick to the more convectional approach.

Deep Cumulus Fraction

Similar to CAM3/CAM4, CAM5 computes deep cumulus fraction $a_{dp,cu}$ using the following empirical formula.

$$a_{dp,cu} = k_{1,dp} \cdot \log_e(1 + \cdot k_2 M_{dp,cu}), \quad a_{dp,cu} = max(0, min(a_{dp,cu}, 0.6)) \tag{4.180}$$

where $k_{1,dp}$ is an adjustable parameter given in Appendix C, $k_2 = 675$ and $M_{dp,cu}$ is convective updraft mass flux $[kg \cdot m^{-2} \cdot s^{-1}]$ from deep convection scheme. When identified to be active, $M_{dp,cu}$ is non-zero from the lowest model layer to the cumulus top. With no further attempt to separate dry and moist deep convection, Eqn.(4.180) can generate *empty* (without in-cumulus condensate) deep convective cloud fraction in the layers below the Lifting Condensation Level (LCL). In contrast to stratus fraction that will be discussed later, we compute a single deep cumulus fraction not the separate liquid and ice deep cumulus fractions. We impose a constraint that $a_{dp,cu}$ is always smaller than 0.6.

Originally, this empirical formula was obtained by including not only cumulus but also stratus generated by detrained cumulus condensate, which by construction results in overestimated cumulus fraction. Thus, we are using a freedom to change the two coefficients 0.04 and 675 to simulate convective updraft fractional area only. Currently these coefficients are also used as tuning parameters to obtain reasonable regional/global radiation budget and grid-mean LWC/IWC.

Shallow Cumulus Fraction

In contrast to CAM3/CAM4, CAM5's new shallow convection scheme (Park and Bretherton, 2009) computes vertical velocity as well as mass flux within cumulus updraft. Thus, shallow cumulus fraction $a_{sh,cu}$ in CAM5 is directly computed using the definition of convective updraft mass flux:

$$a_{sh,cu} = 2 \cdot \left[\mathcal{C} M_{sh,cu} \rho \cdot w_{u,cu} \right], \quad a_{sh,cu} = max(0, min(a_{sh,cu}, 0.2)) \tag{4.181}$$

where $M_{sh,cu}$ is shallow convective mass flux within cumulus updraft $[kg \cdot m^{-2} \cdot s^{-1}]$, ρ is density $[kg \cdot m^{-3}]$ and $w_{u,cu}$ is vertical velocity within cumulus updraft $[m \cdot s^{-1}]$. Note that a factor 2 is multiplied by considering the difference between *core* (e.g., positively buoyant saturated portions) updraft fractional area and saturated updraft fractional area estimated from the LES. The details on how to compute $M_{sh,cu}$ and $w_{u,cu}$ are described in Park and Bretherton [2009]. This $a_{sh,cu}$ is computed from the LCL of cumulus updraft (or PBL top if LCL is within the PBL) to the cumulus top where updraft vertical velocity is zero. So, $a_{sh,cu}$ always contains positive cumulus condensate, that is, there is no empty shallow cumulus clouds. Similar to deep cumulus fraction, we compute a single shallow cumulus fraction not the separate liquid and ice shallow cumulus fractions. We impose a constraint that $a_{sh,cu}$ is always smaller than 0.2.

Liquid Stratus Fraction

In CAM3/CAM4, stratus fraction was parameterized as a sum of $RH-based$ and $Stability-based$ cloud fractions. The latter was necessary because the dry PBL scheme in CAM3/CAM4 cannot moisten upper portion of stratocumulus-topped PBL due to its inability to simulate cloud-radiation-turbulence interactions.

The RH-based stratus fraction in CAM3/CAM4 is a quadratic function of grid-mean RH (Slingo [1987*b*], Rasch and Kristjansson [1998*b*]).

$$a_{st} = \left[\mathcal{C}U - U_c 1 - U_c\right]^2 \tag{4.182}$$

where U is grid-mean RH defined using saturation specific humidity over a mixture of cloud water and ice where mixing fraction is a function of temperature, and U_c is a critical RH. Stratus is formed only when U is larger than U_c. Note that CAM3/CAM4 diagnoses a single stratus fraction not the separate liquid and ice stratus fractions in contrast to CAM5. While simple to use, above Eqn.(4.182) has two shortcomings. First, at the limit of $a_{st}\rightarrow 1$, we expect that RH in the clear portion (U_r) approaches to 1 in nature. However, Eqn.(4.182) does not satisfy this condition unless $U_c\rightarrow 1$ as shown below:

$$lim_{a_{st}\rightarrow 1} U_r = lim_{a_{st}\rightarrow 1}\left[\mathcal{C}(1-U_c)\sqrt{a_{st}} + U_c - a_{st}1 - a_{st}\right] = 0.5\cdot(1+U_c) \tag{4.183}$$

Second, Eqn.(4.182) is not derived from the explicit subgrid scale distributions of total specific humidity, making it hard to impose internal consistency between stratus fraction and in-stratus condensate. Following Smith [1990], liquid stratus fraction in CAM5 is derived from the assumed triangular distribution of total relative humidity, $v = q_{t,l}/q_{s,w}$ where $q_{t,l}$ is total liquid specific humidity ($=q_v + q_l$) and $q_{s,w}$ is saturation specific humidity over water. Then liquid stratus fraction $a_{l,st}$ becomes a function of grid-mean RH over water, U_l (Park et al. [2010]).

$$a_{l,st} = \begin{cases} 1 & \text{if } U_l \geq \hat{U}_l, \\ 1 - \left[\mathcal{C}3\sqrt{2}\cdot\left(\mathcal{C}\hat{U}_l - U_l\hat{U}_l - U_{cl}\right)\right]^{2/3} & \text{if } \mathcal{C}16\cdot(5+U_{cl}) \leq U_l \leq \hat{U}_l, \\ 4\cdot cos\left[\mathcal{C}13\cdot\left\{acos\left(\mathcal{C}32\cdot\sqrt{2}\cdot\left(\mathcal{C}U_l - U_{cl}\hat{U}_l - U_{cl}\right)\right) - 2\cdot\pi\right\}\right] & \text{if } U_{cl} \leq U_l \leq \mathcal{C}16\cdot(5+U_{cl}), \\ 0 & \text{if } U_l \leq U_{cl}, \end{cases} \tag{4.184}$$

where $\hat{U}_l$ is RH within liquid stratus (=1) and U_{cl} is critical RH that liquid stratus is formed when U_l is larger than U_{cl}. We can easily check $lim_{a_{l,st}\rightarrow 1} RH_r = 1$. For a given $U_l \geq U_{cl}$, CAM5 (Eqn.(4.184)) produces less stratus fraction than CAM3/CAM4 (Eqn.(4.182)). In addition, the sensitivity of liquid stratus fraction to the changes of grid-mean RH differs between the two models.

Note that $U_{cl} = 1 - \Delta v$ where Δv is the half-width of the triangular distribution. Ideally, subgrid-scale variability Δv should be internally computed by considering all sources of subgrid-scale motions from individual physical processes - moist turbulence, detrainment of convective condensate, meso-scale organizations, gravity waves induced by convection or surface inhomogeneity, and etc. In CAM5, however, U_{cl} is externally specified as a function of height and surface properties and being used as a tuning parameter. We chose $U_{cl} = 0.89$ in the layers

below 700 hPa (Low-Level Stratus) but $U_{cl} = 0.79$ over lands when a water-equivalent snow depth is less than 10^{-6} $[m]$, $U_{cl} = 0.80$ in the layers above 400 hPa (High-Level Stratus), and a linearly-interpolated U_{cl} between 700 hPa and 400 hPa (Mid-Level Stratus).

In principle, LWC within the liquid stratus can be diagnosed from the assumed triangular PDF (Smith [1990], Park et al. [2010]). However, CAM5 uses a separate prognostic condensation scheme for liquid stratus condensation similar to CAM3/CAM4. This (diagnostic cloud fraction but separate prognostic condensation for liquid stratus) can cause inconsistency between stratus fraction and in-stratus cloud condensate. We perform additional pseudo condensation-evaporation process to remove this inconsistency as will be discussed later.

Ice Stratus Fraction

In CAM3/CAM4, a single stratus fraction a_{st} was diagnosed using a mean saturation specific humidity $q_s = \alpha \cdot q_{s,w} + (1 - \alpha) \cdot q_{s,i}$ where $q_{s,w}$ and $q_{s,i}$ are saturation specific humidities over water and ice, respectively, and $0 \leq \alpha \leq 1$ is a function of temperature. In CAM5, however, we separately diagnose ice stratus fraction $a_{i,st}$ using a modified Slingo's formula as below (Gettelman et al. [2010*a*]).

$$a_{i,st} = \left[\mathcal{C} U_i - U_{ci} \hat{U}_i - U_{ci} \right]^2 \tag{4.185}$$

$$U_i = \left[\mathcal{C} q_v + q_i q_{s,i} \right]$$

where U_i is grid-mean total RH *including ice condensate* defined over ice, and $\hat{U}_i$ is RH within ice stratus. In contrast to liquid condensation that always occurs whenever $q_v > q_{s,w}$, ice nucleation and ice growth processes are not spontaneous and very slow. Thus, the linkage between ice saturation excess $s = q_v - q_{s,i}$ and the amount of ice condensate is weak. Eqn.(4.185) is an attempt to address these properties of ice processes: supersaturation within ice stratus is taken into account by using $\hat{U}_i > 1$, and by including ice condensate in the definition of U_i, ice condensate as well as ice saturation excess contributes to ice stratus fraction. In CAM5, we chose $\hat{U}_i = 1.1$ and $U_{ci} = 0.80$ regardless of heights and the properties of the Earth surface.

4.7.2 Cloud Overlaps

We have computed 4 independent cloud fractions ($0 \leq a_{l,st}, a_{i,st} \leq 1$, $0 \leq a_{sh,cu} \leq 0.2$, $0 \leq a_{dp,cu} \leq 0.6$) in each layer. The performance of individual physical processes is sensitive how these clouds are distributed in the horizontal plane and vertical column. For example, if $a_{l,st}$ and $a_{i,st}$ are maximally-overlapped (non-overlapped) in the horizontal, Bergeron-Findeisen conversion process from cloud liquid droplet to ice crystal will be active (inactive). If cumulus prefentially grows into the pre-existing stratus (clear portions), cumulus will detrain convective condensate into the pre-existing stratus (clear portions) without (with) evaporation. We can also easily expect that the vertical profiles of grid-mean radiative flux, evaporation of precipitation, activation and wet deposition of aerosols are sensitive to the vertical overlapping structures of various clouds. Given the 2-moment stratiform microphysics in CAM5, correct simulations

of activation and wet deposition of aerosols become even more important. So, parameterization of cloud overlapping structures is as important as the parameterization of individual cloud fractions. Ideally, all physics schemes should use a single consistent cloud overlapping structure. In this section, we describe the horizontal and vertical overlapping structures of clouds in CAM5.

Horizontal Overlap

In CAM5, we assume that (1) shallow and deep cumulus fractions are non-overlapped with each other, (2) liquid and ice stratus fractions are maximally overlapped, i.e., $a_{st} = max(a_{l,st}, a_{i,st})$, and (3) stratus only fills the non-cumulus areas, i.e., a higher occupancy priority is given to the cumulus over stratus in each layer. Stratiform microphysics in CAM5 assumes that stratus LWC/IWC is uniformly distributed over the single stratus fraction a_{st} even though further elaboration is possible. The third assumption above comes from distinct turbulent properties in each clouds: cumulus updraft is strong and grows vertically, and so, if there are any pre-existing stratus on its path, cumulus updraft will push out the pre-existing stratus and occupy the original portion. The assumed horizontal overlapping structure between cumulus and stratus determines the *physical* stratus fractions. If a is each of 4 cloud fractions computed in the previous section, the physical cloud fraction A of each cloud fraction a becomes

$$A_{sh,cu} = a_{sh,cu} \leq 0.2 \tag{4.186}$$

$$A_{dp,cu} = a_{dp,cu} \leq 0.6$$
$$A_{cu} = A_{sh,cu} + A_{dp,cu} \leq 0.8$$
$$A_{l,st} = (1 - A_{cu}) \cdot a_{l,st} \leq 1$$
$$A_{i,st} = (1 - A_{cu}) \cdot a_{i,st} \leq 1$$
$$A_{st} = max(A_{l,st}, A_{i,st}) \leq 1$$
$$A_{net} = A_{st} + A_{cu} \leq 1$$

where U_l and U_i in Eqs.(4.184) and (4.185) are now changed to the mean RH averaged over the non-cumulus areas in each layer. In CAM5, state variables saved into the standard physical state arrays are the mean values averaged over the non-cumulus areas, that is, environmental mean not the grid mean. These physical cloud fractions A are passed into various physics schemes following the cloud macrophysics.

Vertical Overlap

In CAM5, the following physical processes make use of vertical overlap assumption of clouds: (a) deep and shallow convection schemes to compute evaporation of convective precipitations, (b) stratiform microphysics to compute production and evaporation of stratiform precipitation, (c) activation and wet scavenging of aerosols by convective and stratiform precipitations, and (d) radiation scheme. While computations of cloud fractions and horizontal cloud overlaps are substantially revised, CAM5's vertical cloud overlap is similar to CAM3/CAM4, which is summarized below.

(a) CAM5's deep and shallow convection schemes assume that convective precipitation area is always 1 if convective precipitation flux is positive. In reality, however, if vertical shear of horizontal winds is neglected, most of the convective precipitation is likely to fall into the saturated cumulus updraft not into clear portions. Thus, CAM5's vertical cumulus overlap may overestimate evaporation of convective precipitation, leading to excessive water vapor in the atmosphere.

(b) CAM5's stratiform microphysics assumes that stratus fraction a_{st} is maximally overlapped in vertical regardless of vertical separation distance, and stratiform precipitation area is the same as maximum stratus fraction in the layers above the current layer as long as precipitation flux is positive. In reality, however, precipitation falling into clear portion can be completely evaporated, so that precipitation area can be smaller than the maximum stratus fraction in the layers above.

(c) CAM5's cloud droplet activation routine assumes maximum overlap of stratus fraction between any adjacent layers. CAM5 computes wet scavenging of aerosols by two processes. The first is the scavenging of activated aerosols within cloud droplets by the production of precipitation. The second is the scavenging of the remaining non-activated aerosols by the precipitation flux. These two processes are separately applied for each convective and stratiform precipitations. For the purpose of wet scavenging of aerosols, CAM5 assumes that (1) convective (stratiform) precipitation area at any height is a sum of cumulus (stratus) fractions in the layers above weighted by the ratio of net production rate of convective (stratiform) precipitation in each layer to the vertically integrated net production rate of convective (stratiform) precipitation from the top layer to the layer just above the current layer, and (2) in computing wet scavenging of non-activated aerosols, precipitation flux area at the top interface of each layer is randomly overlapped with the cloud fraction. The second assumption allows CAM5 to bypass the computation of complex overlapping areas between precipitation flux and cloud fractions.

(d) CAM5's radiation scheme computes one single cloud fraction and in-cloud LWC/IWC in each layer by combining deep and shallow cumulus and stratus cloud properties through a simple cloud area weighting. Then, it assumes a maximum vertical overlap in each of the 3 regimes representing lower (p > 700 hPa), middle (400 hPa < p < 700 hPa), and upper (p < 400 hPa) atmospheres, and a random vertical overlap between these 3 regimes. This generates a set of sub-columns in which cloud fraction is either 1 or 0 in each layer. By averaging each sub-column's radiative heating rate, it computes grid-mean radiative heating rate.

In principle, all the above 4 processes should use the identical vertical cloud overlapping structure. Due to the contrasting natures of turbulences, cumulus and stratus are likely to have different vertical cloud overlap. If vertical shear of horizontal winds is neglected, cumulus fractions are likely to be maximally overlapped over the entire depth of convective updrafts. On the other hand, vertical distance over which stratus is maximally overlapped is likely to be much smaller than the cumulus. Simultaneous treatment of different vertical overlapping structures of cumulus and stratus and implementation of the single unified vertical cloud overlap into the CAM is one of the future development plans.

4.7.3 Condensation Processes

This section describes how much water vapor is converted into cloud condensates. This

process differs from the conversion of cloud droplet into precipitation, which is treated by the cloud microphysics.

Stratus Liquid

Similar to CAM3/4 (Zhang et al. [2003*a*]), CAM5 uses prognostic condensation scheme for liquid stratus condensate. The fundamental assumption used for computing grid-mean net condensation rate of water vapor into liquid stratus droplet (Q) is that (1) RH over the water within the liquid stratus is always 1, and (2) no liquid stratus droplet exists in the clear portion outside of the liquid stratus fraction. These two conditions will be called *saturation equilibrium* of liquid stratus. Whenever any GCM grid is perturbed by external forcings, the system always tries to restore the saturation equilibrium state. This allows us to compute the grid-mean net condensation rate of water vapor into liquid stratus condensate for a given set of external forcings. The details of liquid stratus condensation is described in Park et al. [2010].

Let's assume that one GCM grid layer is in saturation equilibrium state at a certain moment. During the model time step Δt, the layer is perturbed by external forcings (e.g., stratiform microphysics, radiation, moist turbulence, large-scale advection, and convections). In order to restore saturation equilibrium, Q should be initiated within the layer. The changes of grid-mean liquid stratus condensate $\bar{q}_{l,st} = A_{l,st} \cdot \hat{q}_{l,st}$ during Δt is the sum of grid-mean net condensate rate Q and the grid-mean external forcings of liquid condensates $\bar{F}_l$:

$$Q = \dot{\bar{q}}_{l,st} - \bar{F}_l = \; A_{l,st} \cdot \dot{\hat{q}}_{l,st} + \; c \cdot \hat{q}_{l,st} \cdot \dot{A}_{l,st} - \bar{F}_l \tag{4.187}$$

where $0 \leq c \leq 1$ is the ratio of in-cloud condensate of newly formed or dissipated stratus to the in-cloud condensate of pre-existing stratus. The $\dot{\phi}$ denotes time-tendency of ϕ. If liquid stratus has homogeneous condensate, it will be $c = 1$, but it is likely that $c < 1$ in nature since stratus has non-homogeneous condensate in general. In CAM5, we use $c = 0.1$.

From the two assumptions for saturation equilibrium of liquid stratus, we can derive the following simultaneous linear equations (Park et al. [2010]).

$$a_{11} \cdot \dot{\hat{q}}_{l,st} + \; a_{12} \cdot \dot{A}_{l,st} = b_1 \tag{4.188}$$

$$a_{21} \cdot \dot{\hat{q}}_{l,st} + \; a_{22} \cdot \dot{A}_{l,st} = b_2$$

where individual coefficients a_{ij} and b_i are

$$a_{11} = \gamma \cdot A_{l,st} \tag{4.189}$$

$$a_{12} = G + \gamma \cdot c \cdot \hat{q}_{l,st}$$

$$a_{21} = \alpha + (\mathcal{C} L_v C_p) \cdot \hat{\beta} \cdot A_{l,st}$$

$$a_{22} = (\mathcal{C} L_v C_p) \cdot \hat{\beta} \cdot c \cdot \hat{q}_{l,st}$$

$$b_1 = \alpha \cdot \dot{\bar{q}}_{t,all} - \beta \cdot \dot{\bar{T}}_{l,all} - G \cdot a_{l,st} \cdot \dot{a}_{cu}$$

$$b_2 = \alpha \cdot \dot{\hat{q}}_{t,all} - \beta \cdot \dot{\bar{T}}_{l,all}$$

with

$$\alpha = [\mathcal{C}1q_{s,w}] \tag{4.190}$$
$$\beta = \mathcal{C}\bar{q}_v q_{s,w}^2 \cdot (\mathcal{C}\partial q_{s,w}\partial T)$$
$$\hat{\beta} = \alpha \cdot (\mathcal{C}\partial q_{s,w}\partial T)$$
$$\gamma = \alpha + \mathcal{C}L_v C_p \cdot \beta$$
$$G = \mathcal{C}11 - a_{cu} \cdot \left(\mathcal{C}\partial a_{l,st}\partial \bar{U}_e\right)^{-1}$$

and

$$\dot{\bar{q}}_{t,all} = \dot{\bar{q}}_{v,adv} + \dot{\bar{q}}_{l,adv} + \dot{\bar{q}}_{v,mic} + \dot{\bar{q}}_{l,mic} \tag{4.191}$$
$$\dot{\bar{T}}_{l,all} = \dot{\bar{T}}_{adv} + \dot{\bar{T}}_{mic} - \mathcal{C}L_v C_p \cdot (\dot{\bar{q}}_{l,adv} + \dot{\bar{q}}_{l,mic}) \tag{4.192}$$
$$\dot{\hat{q}}_{t,all} = \dot{\bar{q}}_{v,adv} + \dot{\bar{q}}_{l,adv} + \dot{\hat{q}}_{l,mic} \tag{4.193}$$
$$\dot{\hat{q}}_{l,mic} = [\mathcal{C}\dot{\bar{q}}_{l,mic} max(A_{l,st}, A_{i,st})] \tag{4.194}$$

where $\dot{\phi}$ denotes local time-tendency, subscript *all* denotes all the processes except cloud macrophysics, which is the sum of cloud microphysics (subscript *mic*) and the other processes denoted by subscript *adv*. In Eqn.(4.194), we used $max(A_{l,st}, A_{i,st})$ instead of $A_{l,st}$ since stratiform microphysics is formulated based on a single stratus fraction, $max(A_{l,st}, A_{i,st})$. Above formulation was derived assuming that temperature is uniform within the grid, and stratiform microphysics does not change water vapor within the liquid stratus, and all forcings except stratiform microphysics are uniformly applied into the grid. Using $A_{l,st}$ from Eqn.(4.184) and (4.186), we can compute Q if $\bar{F}_l$ is given.

Although the computation of Q explicitly makes use of $A_{l,st}$, the updated $\bar{q}_{l,st}(t+\Delta t)$ is not necessarily consistent with the updated $A_{l,st}(t+\Delta t)$. For example, it can be $\bar{q}_{l,st}(t+\Delta t) = 0$ but $A_{l,st}(t+\Delta t) > 0$ (so called *empty cloud*) or $\bar{q}_{l,st}(t+\Delta t) > 0$ but $A_{l,st}(t+\Delta t) = 0$ (so called *infinitely dense cloud*). This inconsistency between stratus fraction and in-stratus condensate comes from the combined use of prognostic stratiform condensation and diagnostic stratus fraction schemes with a finite model intergation time step Δt. In order to prevent these unreasonable situations, we additionally condensate water vapor or evaporate stratus liquid droplets until the *in-stratus LWC*, $\hat{q}_{l,st}(t+\Delta t)$ falls within the externally specified ranges, $0.02 \leq \hat{q}_{l,st}(t+\Delta t)\ [g \cdot kg^{-1}] \leq 3$. Note that this *pseudo condensation − evaporation* process does not change the grid-mean liquid stratus condensate and is not performed if $\bar{q}_{l,st}(t+\Delta t) = 0$ and $A_{l,st}(t+\Delta t) = 0$ at the beginning.

CAM5 is using two moment stratiform microphysics and so prognoses not only the mass but also the number concentration of cloud droplets. When net condensation occurs ($Q > 0$), cloud macrophysics does not change droplet number concentration, but when net evaporation occurs ($Q < 0$), droplet number concentration is reduced in proportion to the decrease of the mass of stratus liquid droplets. Regardless of the sign of Q, however, droplet activation process within stratus is additionally performed at the beginning of cloud microphysics at each time step. Thus, cloud droplet number is consistently generated when $Q > 0$ in the initially clear layer.

Stratus Ice

In contrast to liquid stratus, we cannot assume a certain equilibrium state for ice stratus because ice process is much slower than the liquid process. Thus, deposition-sublimation rate between water vapor and ice crystals are computed using an explicit process algorithm.

In CAM5, deposition of water vapor into ice crystals (this is a separate process from the Bergeron-Findeisen conversion of cloud liquid droplets into ice crystals) only occurs when ice stratus exists at temperature lower than 273.15K. In case of pure ice stratus, in-cloud water vapor is set to the grid-mean water vapor. If in-cloud water vapor is larger than the saturation water vapor over ice, water vapor is deposited into ice crystals. In case of mixed-phase stratus, in-cloud water vapor is set to the equal weighting average of grid-mean water vapor and saturation water vapor over water. In this case, however, direct deposition of water vapor into ice crystals occurs only after pre-existing cloud liquid droplets are completly depleted into ice crystals by Bergeron-Findeisen process. That is, if Bergeron-Findeisen process is not strong enough to deplete pre-existing cloud liquid droplets, no direct deposition occurs from the water vapor into ice crystals. Sublimation of ice crystals into water vapor occurs regardless of temperature as long as water vapor within the ice stratus is smaller than the saturation water vapor over the pre-existing ice crystals.

A constraint is imposed such that direct deposition of water vapor into ice crystals does not reduce grid-mean RH over ice below 1. Additional constraint is imposed such that sublimation should not exceed the available ice crystals and not increase grid-mean RH over ice above 1. See Gettelman et al. [2010*a*] and the chapter for cloud microphysics for additional details.

Condensation within Shallow Cumulus Updraft

Condensation within shallow cumulus updraft is described in Park and Bretherton [2009]. Shallow convective updraft rises from the PBL top but condensation occurs from the LCL. If LCL is lower than PBL top, condensation is assumed to occur from the PBL top. During ascent, convective updraft experiences adiabatic cooling, mixing with environmental airs, and precipitation fallout. Vertical evolutions of two conservative scalars $q_t = q_v + q_l + q_i$, $\theta_c = \theta - (L_v/C_p/\pi) \cdot q_l - (L_s/C_p/\pi) \cdot q_i$ within convective updraft are explicitly computed using the parameterized entrainment mixing and precipitation processes. From the computed q_t, θ_c and saturation specific humidity q_s defined as a weighting average of the values over water $q_{s,w}$ and ice $q_{s,i}$ (the weighting factor is a function of temperature), we compute condensate amount within convective updraft. Since shallow convective cloud fraction $a_{sh,cu}$ is non-zero from the LCL (or PBL top if LCL is below the PBL) to the cumulus top, shallow cumulus does not have any empty clouds.

Within shallow convection scheme, condensate is partitioned into liquid and ice as a ramping function of temperature between 248K and 268K. However, a separate re-partitioning is performed for convective detrainment (as a ramping function of temperature between 238.15K and 268.15K) and for radiative treatment of in-cumulus condensate (in this case, the repartitioning function is the same as that of stratiform condensate). When shallow convective condensate is detrained into the environment, we assume a fixed droplet radius of 8 and 25 $[\mu \cdot m]$ for liquid and ice condensates, respectively.

Condensation within Deep Cumulus Updraft

Condensates within deep convective updraft is computed in a similar way as shallow convective updraft. When deep convective condensate is detrained into the environment, we assume a fixed droplet radius of 10 and 50 $[\mu \cdot m]$ for liquid and ice condensates, respectively. See the chapter for deep convection for additional details.

4.8 Aerosols

Two different modal representations of the aerosol were implemented in CAM5. A 7-mode version of the modal aerosol model (MAM-7) serves as a benchmark for the further simplification. It includes Aitken, accumulation, primary carbon, fine dust and sea salt and coarse dust and sea salt modes (4.3). Within a single mode, for example the accumulation mode, the mass mixing ratios of internally-mixed sulfate, ammonium, secondary organic aerosol (SOA), primary organic matter (POM) aged from the primary carbon mode, black carbon (BC) aged from the primary carbon mode, sea salt, and the number mixing ratio of accumulation mode particles are predicted. Primary carbon (OM and BC) particles are emitted to the primary carbon mode and aged to the accumulation mode due to condensation of H_2SO_4, NH_3 and SOA (gas) and coagulation with Aitken and accumulation mode (see section below).

Aerosol particles exist in different attachment states. We mostly think of aerosol particles that are suspended in air (either clear or cloudy air), and these are referred to as interstitial aerosol particles. Aerosol particles can also be attached to (or contained within) different hydrometeors, such as cloud droplets. In CAM5, the interstitial aerosol particles and the aerosol particles in stratiform cloud droplets[1] (referred to as cloud-borne aerosol particles) are both explicitly predicted, as in Easter et al. [2004]. The interstitial aerosol particle species are stored in the q array of the state variable and are transported in 3 dimensions. The cloud-borne aerosol particle species are stored in the *qqcw* array of the physics buffer and are not transported (except for vertical turbulent mixing), which saves computer time but has little impact on their predicted values Ghan and Easter [2006].

Aerosol water mixing ratio associated with interstitial aerosol for each mode is diagnosed following Kohler theory (see water uptake below), assuming equilibrium with the ambient relative humidity. It also is not transported in 3 dimensions, and is held in the *qaerwat* array of the physics buffer.

The size distributions of each mode are assumed to be log-normal, with the mode dry or wet radius varying as number and total dry or wet volume change, and standard deviation prescribed as given in 4.3. The total number of transported aerosol species is 31 for MAM-7. The transported gas species are SO_2, H_2O_2, DMS, H_2SO_4, NH_3, and SOA (gas).

For long-term (multiple century) climate simulations a 3-mode version of MAM (MAM-3) is also developed which has only Aitken, accumulation and coarse modes (4.4). For MAM-3 the following assumptions are made: (1) primary carbon is internally mixed with secondary aerosol by merging the primary carbon mode with the accumulation mode; (2) the coarse dust and sea salt modes are merged into a single coarse mode based on the assumption that the dust and sea salt are geographically separated. This assumption will impact dust loading over the central Atlantic transported from Sahara desert because the assumed internal mixing between dust and sea salt there will increase dust hygroscopicity and thus wet removal; (3) the fine dust and sea salt modes are similarly merged with the accumulation mode; and (4) sulfate is partially neutralized by ammonium in the form of NH_4HSO_4, so ammonium is effectively prescribed and NH_3 is not simulated. We note that in MAM-3 we predict the mass mixing ratio of sulfate

[1]Note that the explicitly-predicted cloud-borne aerosol particles are for stratiform clouds only, and thus are stratiform-cloud-borne aerosol particles. The convective-cloud-borne aerosol particles in deep and shallow convective clouds are not treated explicitly, and are prescribed as a fraction of the interstitial aerosol particles when calculating wet removal.

aerosol in the form of NH_4HSO_4 while in MAM-7 it is in the form of SO_4. The total number of transported aerosol tracers in MAM-3 is 15.

The time evolution of the interstitial aerosol mass ($M^a_{i,j}$) and number (N^a_j) for the i-th species and j-th mode is described in the following equations:

$$\begin{aligned}\frac{\partial M^a_{i,j}}{\partial t} + \frac{1}{\rho}\nabla\cdot[\rho\mathbf{u}M^a_{i,j}] = &\left(\frac{\partial M^a_{i,j}}{\partial t}\right)_{conv} + \left(\frac{\partial M^a_{i,j}}{\partial t}\right)_{diffus} \\ &+ \left(\frac{\partial M^a_{i,j}}{\partial t}\right)_{nuc} + \left(\frac{\partial M^a_{i,j}}{\partial t}\right)_{cond} + \left(\frac{\partial M^a_{i,j}}{\partial t}\right)_{activ} + \left(\frac{\partial M^a_{i,j}}{\partial t}\right)_{resus} \\ &+ \left(\frac{\partial M^a_{i,j}}{\partial t}\right)_{emis} + \left(\frac{\partial M^a_{i,j}}{\partial t}\right)_{sedime} + \left(\frac{\partial M^a_{i,j}}{\partial t}\right)_{drydep} + \left(\frac{\partial M^a_{i,j}}{\partial t}\right)_{imp_scav}\end{aligned} \tag{4.195}$$

$$\begin{aligned}\frac{\partial N^a_j}{\partial t} + \frac{1}{\rho}\nabla\cdot[\rho\mathbf{u}N^a_j] = &\left(\frac{\partial N^a_j}{\partial t}\right)_{conv} + \left(\frac{\partial N^a_j}{\partial t}\right)_{diffus} \\ &+ \left(\frac{\partial N^a_j}{\partial t}\right)_{nuc} + \left(\frac{\partial N^a_j}{\partial t}\right)_{coag} + \left(\frac{\partial N^a_j}{\partial t}\right)_{activ} + \left(\frac{\partial N^a_j}{\partial t}\right)_{resus} \\ &+ \left(\frac{\partial N^a_j}{\partial t}\right)_{emis} + \left(\frac{\partial N^a_{i,j}}{\partial t}\right)_{sedime} + \left(\frac{\partial N^a_j}{\partial t}\right)_{drydep} + \left(\frac{\partial N^a_j}{\partial t}\right)_{imp_scav}\end{aligned} \tag{4.196}$$

Similarly, the time evolution for the cloud-borne aerosol mass ($M^c_{i,j}$) and number (N^c_j) is described as:

$$\begin{aligned}\frac{\partial M^c_{i,j}}{\partial t} = &\left(\frac{\partial M^c_{i,j}}{\partial t}\right)_{conv} + \left(\frac{\partial M^c_{i,j}}{\partial t}\right)_{diffus} \\ &+ \left(\frac{\partial M^c_{i,j}}{\partial t}\right)_{chem} + \left(\frac{\partial M^c_{i,j}}{\partial t}\right)_{activ} + \left(\frac{\partial M^c_{i,j}}{\partial t}\right)_{resus} \\ &+ \left(\frac{\partial M^c_{i,j}}{\partial t}\right)_{sedime} + \left(\frac{\partial M^c_{i,j}}{\partial t}\right)_{drydep} + \left(\frac{\partial M^c_{i,j}}{\partial t}\right)_{nuc_scav}\end{aligned} \tag{4.197}$$

$$\begin{aligned}\frac{\partial N^c_j}{\partial t} = &\left(\frac{\partial N^c_j}{\partial t}\right)_{conv} + \left(\frac{\partial N^c_j}{\partial t}\right)_{diffus} \\ &+ \left(\frac{\partial N^c_j}{\partial t}\right)_{activ} + \left(\frac{\partial N^c_j}{\partial t}\right)_{resus} \\ &+ \left(\frac{\partial N^c_j}{\partial t}\right)_{sedime} + \left(\frac{\partial N^c_j}{\partial t}\right)_{drydep} + \left(\frac{\partial N^c_j}{\partial t}\right)_{nuc_scav}\end{aligned} \tag{4.198}$$

where t is time, $\mathbf{u}$ is the 3D wind vector, and ρ is the air density. The symbolic terms on the right hand side represent the source/sink terms for $M_{i,j}$ and N_j [**?**].

4.8.1 Emissions

Anthropogenic (defined here as originating from industrial, domestic and agriculture activity sectors) emissions are from the Lamarque et al. [2010*a*] IPCC AR5 emission data set. Emissions of black carbon (BC) and organic carbon (OC) represent an update of Bond et al. [2007] and Junker and Liousse [2008]. Emissions of sulfur dioxide are an update of Smith et al. [2001, 2004].

The IPCC AR5 emission data set includes emissions for anthropogenic aerosols and precursor gases: SO_2, primary OM (POM), and BC. However, it does not provide injection heights and size distributions of primary emitted particles and precursor gases for which we have followed the AEROCOM protocols [Dentener et al., 2006*a*]. We assumed that 2.5% by molar of sulfur emissions are emitted directly as primary sulfate aerosols and the rest as SO_2 [Dentener et al., 2006*a*]. Sulfur from agriculture, domestic, transportation, waste, and shipping sectors is emitted at the surface while sulfur from energy and industry sectors is emitted at 100-300 m above the surface, and sulfur from forest fire and grass fire is emitted at higher elevations (0-6 km). Sulfate particles from agriculture, waste, and shipping (surface sources), and from energy, industry, forest fire and grass fire (elevated sources) are put in the accumulation mode, and those from domestic and transportation are put in the Aitken mode. POM and BC from forest fire and grass fire are emitted at 0-6 km, while those from other sources (domestic, energy, industry, transportation, waste, and shipping) are emitted at surface. Injection height profiles for fire emissions are derived from the corresponding AEROCOM profiles, which vary spatially and temporally. Mass emission fluxes for sulfate, POM and BC are converted to number emission fluxes for Aitken and accumulation mode at surface or at higher elevations based on AEROCOM prescribed lognormal size distributions as summarized in Table 4.1.

The IPCC AR5 data set also does not provide emissions of natural aerosols and precursor gases: volcanic sulfur, DMS, NH_3, and biogenic volatile organic compounds (VOCs). Thus AEROCOM emission fluxes, injection heights and size distributions for volcanic SO_2 and sulfate and for DMS flux at surface are used. The emission flux for NH_3 is prescribed from the MOZART-4 data set [Emmons, 2010]. Emission fluxes for isoprene, monoterpenes, toluene, big alkenes, and big alkanes, which are used to derive SOA (gas) emissions (see below), are prescribed from the MOZART-2 data set [Horowitz, 2003]. These emissions represent late 1990's conditions. For years prior to 2000, we use anthropogenic non-methane volatile organic compound (NMVOC) emissions from IPCC AR5 data set and scale the MOZART toluene, bigene, and big alkane emissions by the ratio of year-of-interest NMVOC emissions to year 2000 NMVOC emissions.

The emission of sea salt aerosols from the ocean follows the parameterization by Martensson et al. [2003] for aerosols with geometric diameter < 2.8 μm. The total particle flux F_0 is described by

$$\frac{dF_0}{dlogD_p} = \Phi W = (A_k T_w + B_k)W \tag{4.199}$$

where D_p is the particle diameter, T_w is the water temperature and A_k and B_k are coefficients dependent on the size interval. W is the white cap area:

$$W = 3.84 \times 10^{-4} U_{10}^{3.41} \tag{4.200}$$

where U_{10} is the wind speed at 10 m. For aerosols with a geometric diameter > 2.8 μm, sea salt emissions follow the parameterization by Monahan et al. [1986]

$$\frac{dF_0}{dlogr} = 1.373 U_{10}^{3.41} r^{-3} (1 + 0.0057 r^{1.05}) \times 10^{1.19 e^{-B^2}} \quad (4.201)$$

where r is the radius of the aerosol at a relative humidity of 80% and B=(0.380-log$r$)/0.650. All sea salt emissions fluxes are calculated for a size interval of $d\log D_p$=0.1 and then summed up for each modal size bin. The cut-off size range for sea salt emissions in MAM-7 is 0.02-0.08 (Aitken), 0.08-0.3 (accumulation), 0.3-1.0 (fine sea salt), and 1.0-10 μm (coarse sea salt); for MAM-3 the range is 0.02-0.08 (Aitken), 0.08-1.0 (accumulation), and 1.0-10 μm (coarse).

Dry, unvegetated soils, in regions of strong winds generate soil particles small enough to be entrained into the atmosphere, and these are referred to here at desert dust particles. The generation of desert dust particles is calculated based on the Dust Entrainment and Deposition Model, and the implementation in the Community Climate System Model has been described and compared to observations [Mahowald et al., 2006*b*,*d*; Yoshioka et al., 2007]. The only change to the CAM5 source scheme from the previous studies is the increase in the threshold for leaf area index for the generation of dust from 0.1 to 0.3 m^2/m^2, to be more consistent with observations of dust generation in more productive regions [Okin, 2008]. The cut-off size range for dust emissions is 0.1-2.0 μm (fine dust) and 2.0-10 μm (coarse dust) for MAM-7; and 0.1-1.0 μm (accumulation), and 1.0-10 μm (coarse) for MAM-3.

4.8.2 Chemistry

Simple gas-phase chemistry is included for sulfate aerosol. This includes (1) DMS oxidation with OH and NO_3 to form SO_2; (2) SO_2 oxidation with OH to form H_2SO_4 (gas); (3) H_2O_2 production (HO_2+HO_2); and (4) H_2O_2 loss (H_2O_2 photolysis and H_2O_2+OH). The rate coefficients for these reactions are provided from the MOZART model [Emmons, 2010]. Oxidant concentrations (O_3, OH, HO_2, and NO_3) are temporally interpolated from monthly averages taken from MOZART simulations [Lamarque et al., 2010*a*].

SO_2 oxidation in bulk cloud water by H_2O_2 and O_3 is based on the MOZART treatment [Tie et al., 2001]. The pH value in the bulk cloud water is calculated from the electroneutrality equation between the bulk cloud-borne SO_4 and NH_4 ion concentrations (summation over modes), and ion concentrations from the dissolution and dissociation of trace gases based on the Henry's law equilibrium. Irreversible uptake of H_2SO_4 (gas) to cloud droplets is also calculated [Seinfeld and Pandis, 1998]. The sulfate produced by SO_2 aqueous oxidation and H_2SO_4 (gas) uptake is partitioned to the cloud-borne sulfate mixing ratio in each mode in proportion to the cloud-borne aerosol number of the mode (i.e., the cloud droplet number associated with each aerosol mode), by assuming droplets associated with each mode have the same size. For MAM-7, changes to aqueous NH_4 ion from dissolution of NH_3 (g) are similarly partitioned among modes. SO_2 and H_2O_2 mixing ratios are at the same time reduced due to aqueous phase consumption.

4.8.3 Secondary Organic Aerosol

The simplest treatment of secondary organic aerosol (SOA), which is used in many global models, is to assume fixed mass yields for anthropogenic and biogenic precursor VOC's, then directly emit this mass as primary aerosol particles. MAM adds one additional step of complexity by simulating a single lumped gas-phase SOA (gas) species. Fixed mass yields for five VOC categories of the MOZART-4 gas-phase chemical mechanism are assumed, as shown in Table

4.2. These yields have been increased by an additional 50% for the purpose of reducing aerosol indirect forcing by increasing natural aerosols. The total yielded mass is emitted as the SOA (gas) species. MAM then calculates condensation/evaporation of the SOA (gas) to/from several aerosol modes. The condensation/evaporation is treated dynamically, as described later. The equilibrium partial pressure of SOA (gas), over each aerosol mode m is expressed in terms of Raoult's Law as:

$$P_m^* = (\frac{A_m^{SOA}}{A_m^{SOA} + 0.1A_m^{POA}})P^0 \tag{4.202}$$

where A_m^{SOA} is SOA mass concentration in mode m, A_m^{POA} is the primary organic aerosol (POA) mass concentration in mode m (10% of which is assumed to be oxygenated), and P^0 is the mean saturation vapor pressure of SOA whose temperature dependence is expressed as:

$$P^0(T) = P^0(298K) \times exp[\frac{-\Delta H_{vap}}{R}(\frac{1}{T} - \frac{1}{298})] \tag{4.203}$$

where P^0 (298 K) is assumed at 1×10^{-10} atm and the mean enthalpy of vaporization ΔH_{vap} is assumed at 156 kJ mol^{-1}.

Treatment of the gaseous SOA and explicit condensation/evaporation provides (1) a realistic method for calculating the distribution of SOA among different modes and (2) a minimal treatment of the temperature dependence of the gas/aerosol partitioning.

4.8.4 Nucleation

New particle formation is calculated using parameterizations of binary H_2SO_4-H_2O homogeneous nucleation, ternary H_2SO_4-NH_3-H_2O homogeneous nucleation, and boundary layer nucleation. A binary parameterization [Vehkamaki et al., 2002] is used in MAM-3, which does not predict NH_3, while a ternary parameterization [Merikanto et al., 2007] is used in MAM-7. The boundary layer parameterization, which is used in both versions, uses the empirical 1st order nucleation rate in H_2SO_4 from Sihto et al. [2006], with a first order rate coefficient of $1.0 \times 10^{-6}s^{-1}$ as in Wang et al. [2009]. The new particles are added to the Aitken mode, and we use the parameterization of Kerminen and Kulmala [2002] to account for loss of the new particles by coagulation as they grow from critical cluster size to Aitken mode size.

4.8.5 Condensation

Condensation of H_2SO_4 vapor, NH_3 (MAM-7 only), and the SOA (gas) to various modes is treated dynamically, using standard mass transfer expressions [Seinfeld and Pandis, 1998] that are integrated over the size distribution of each mode [Binkowski and Shankar, 1995]. An accommodation coefficient of 0.65 is used for H_2SO_4 [Poschl et al., 1998], and currently, for the other species too. H_2SO_4 and NH_3 condensation are treated as irreversible. NH_3 uptake stops when the NH_4/SO_4 molar ratio of a mode reaches 2. SOA (gas) condensation is reversible, with the equilibrium vapor pressure over particles given by Eq. (4.296).

In MAM-7, condensation onto the primary carbon mode produces aging of the particles in this mode. Various treatments of the aging process have been used in other models [Cooke and Wilson, 1996; Wilson et al., 2001; Liu et al., 2005; Riemer et al., 2003]. In CAM5

a criterion of 3 mono-layers of sulfate is used to convert a fresh POM/BC particle to the aged accumulation mode. Using this criterion, the mass of sulfate required to age all the particles in the primary carbon mode, $M_{SO4,age-all}$, is computed. If $M_{SO4,cond}$ condenses on the mode during a time step, we assume that a fraction $f_{age} = M_{SO4,cond} \ / \ M_{SO4,age-all}$ has been aged. This fraction of the POM, BC, and number in the mode is transferred to the accumulation mode, along with the condensed soluble species. SOA is included in the aging process. The SOA that condenses in a time step is scaled by its lower hygroscopicity to give a condensed SO_4 equivalent.

The two continuous growth processes (condensation and aqueous chemistry) can result in Aitken mode particles growing to a size that is nominally within the accumulation mode size range. Most modal aerosol treatments thus transfer part of the Aitken mode number and mass (those particles on the upper tail of the distribution) to the accumulation mode after calculating continuous growth [Easter et al., 2004].

4.8.6 Coagulation

Coagulation of the Aitken, accumulation, and primary carbon modes is treated. Coagulation within each of these modes reduces number but leaves mass unchanged. For coagulation of Aitken with accumulation mode and of primary-carbon with accumulation mode, mass is transferred from Aitken or primary-carbon mode to the accumulation mode. For coagulation of Aitken with primary-carbon mode in MAM-7, Aitken mass is first transferred to the primary-carbon mode. This ages some of the primary-carbon particles. An aging fraction is calculated as with condensation, then the Aitken mass and the aged fraction of the primary-carbon mass and number are transferred to the accumulation mode. Coagulation rates are calculated using the fast/approximate algorithms of the Community Multiscale Air Quality (CMAQ) model, version 4.6 [Binkowski and Roselle, 2003].

4.8.7 Water Uptake

Water uptake is based on the equilibrium Kohler theory [Ghan and Zaveri, 2007] using the relative humidity and the volume mean hygroscopicity for each mode to diagnose the wet volume mean radius of the mode from the dry volume mean radius. The hygroscopity of each component is listed in Table 4.3. The hygroscopicities here are equivalent to the κ parameters of Petters and Kreidenweis [2007]. Note that the measured solubility of dust varies widely, from 0.03 to 0.26 [Koehler et al., 2009*a*].

4.8.8 Subgrid Vertical Transport and Activation/Resuspension

The vertical transport of interstitial aerosols and trace gases by deep convective clouds, using updraft and downdraft mass fluxes from the Zhang-McFarlane parameterization, is described in Collins et al. [2004*a*]. Currently this vertical transport is calculated separately from wet removal, but a more integrated treatment is planned. Cloud-borne aerosols, which are associated with large-scale stratiform cloud, are assumed to not interact with the convective clouds. Vertical transport by shallow convective clouds is treated similarly, using mass fluxes from the shallow convection parameterization. Turbulent transport of the aerosol is given a special treatment with

Table 4.1: Size distributions of primary emissions.

Emission Source	Geometric standard deviation, s_g	Number mode diameter, $D_{gn}(\mu\text{m})$	D_{emit} (μm)[1]
BC/OM			
Forest fire/grass fire	1.8	0.080	0.134
Domestic/energy/industry/ transportation/shipping/waste	See note [2]	See note [2]	0.134
SO_4			
Forest fire/grass fire/waste	1.8	0.080	0.134
Energy/industry/shipping	See note [3]	See note [3]	0.261
Domestic/transportation	1.8	0.030	0.0504
Continuous volcano, 50% in Aitken mode	1.8	0.030	0.0504
Continuous volcano, 50% in accum. mode	1.8	0.080	0.134

[1]Demit is volume-mean diameter = $D_{gn}exp(1.5\times ln(s_g)^2)$ used in number emissions as $E_{number} = E_{mass}/(\pi/6\times\rho D^3_{emit})$

[2]This value is intermediate between the Dentener et al. [2006*a*] $D_{emit} = 0.0504m$ and Liu et al. [2005] $D_{emit} = 0.206m$.

[3]Adapted from Stier et al. [2005] where 50% of mass goes to accumulation mode with Demit = 0.207 m, and 50% goes to coarse mode with $D_{emit} = 3.08m$. We put all mass in accumulation mode, and $D_{emit} = 0.261m$ gives same number emissions as Stier et al. [2005]. [Dentener et al. [2006*a*] put all in coarse mode with Demit = 2.06 m]

Table 4.2: Assumed SOA (gas) yields

Species	Mass yield	Reference
Big Alkanes	5%	Lim and Ziemann [2005]
Big Alkenes	5%	assumed
Toluene	15%	Odum et al. [1997*a*]
Isoprene	4%	Kroll et al. [2006]
Monoterpenes	25%	Ng et al. [2007*a*]

Table 4.3: Hygroscopicity of aerosol components

Seasalt	sulfate	nitrate	ammonium	SOA	POM	BC	dust
1.16	0.507	0.507	0.507	0.14	0.10	10^{-10}	0.068

respect to other tracers. To strengthen the coupling between turbulent transport and aerosol activation in stratiform clouds, the implicit time integration scheme used for turbulent transport of heat, energy, and momentum is replaced by an explicit scheme for droplets and aerosol. A sub-timestep is calculated for each column based on the minimum turbulent transport time in the column. Turbulent transport is integrated over the sub-time steps using a forward time integration scheme.

Aerosol activation converts particles from the interstitial attachment state to the cloud-borne state. In stratiform cloud, activation is treated consistently with droplet nucleation, so that the total number of particles activated and transferred to the cloud-borne state equals to the number of droplets nucleated. Activation is parameterized in terms of updraft velocity and the properties of all of the aerosol modes [Abdul-Razzak and Ghan, 2000*b*], with both mass and number transferred to the cloud-borne state. The updraft velocity is approximated by the square root of the turbulence kinetic energy, with a minimum value of 0.2 m s^{-1}. Activation is assumed to occur as updrafts carry air into the base of the cloud [Ghan et al., 1997] and as cloud fraction increases [Ovtchinnikov and Ghan, 2005]. In addition, activation is assumed to occur as air is continuously cycled through clouds, assuming a cloud regeneration time scale of one hour. Consider a model time step of 20 minutes, so that 1/3 of the cloud is regenerated in a time step. We essentially dissipate then reform 1/3 of cloud each time step. During dissipation, grid-cell mean cloud droplet number is reduced by 1/3, and 1/3 of the cloud-borne aerosols are resuspended and converted to the interstitial state. During regeneration, interstitial aerosols are activated in the "new" cloud, and cloud droplet number is increased accordingly. The regeneration has small impact on shallow boundary layer clouds, but it noticeably increases droplet number in deeper free-tropospheric clouds where vertical turbulence mixing is slow. Particles are resuspended as aerosol when droplets evaporate. This process is assumed to occur as droplets are transferred below or above cloud and as clouds dissipate.

4.8.9 Wet Deposition

Aerosol wet removal is calculated using the CAM3.5 wet removal routine [Rasch et al., 2000; Barth et al., 2000] with modifications for the consistency with cloud macro- and microphysics. The routine treats in-cloud scavenging (the removal of cloud-borne aerosol particles) and below-cloud scavenging (the removal of interstitial aerosol particles by precipitation particles through impaction and Brownian diffusion).

For in-cloud scavenging, the stratiform and convective cloud fraction, cloud water, and precipitation production profiles are used to calculate first-order loss rate profiles for cloud-water. These cloud-water first-order loss rates are multiplied by "solubility factors" to obtain aerosol first-order loss rates, which are applied to the aerosol profiles. The solubility factors can be interpreted as (the fraction of aerosols that are in cloud drops) × (an additional tuning factor). In CAM3.5, where the cloud-borne aerosol is not explicitly calculated, a value of 0.3 is used for solubility factors for all aerosol types and sizes. Different values are used for the MAM. The stratiform in-cloud scavenging only affects the stratiform-cloud-borne aerosol particles, and these have solubility factors of 1.0. It does not affect the interstitial aerosol particles, and these have solubility factors of 0.0.

For convective in-cloud scavenging of MAM aerosols, both a solubility factor and a within-convective-cloud activation fraction are passed to the wet removal routine. For the stratiform-

cloud-borne aerosol particles, there is no wet removal by convective clouds, and these factors are zero. For interstitial (with respect to stratiform cloud) aerosol, the solubility factor is 0.5, and the activation fractions are 0.0 for the primary carbon mode, 0.4 for the fine and coarse dust modes, and 0.8 for other modes. The lower values reflect lower hygroscopity. These factors are applied to both number and mass species within each mode, with one exception. In MAM-3, different activation fractions are applied to the dust and sea salt of the coarse mode (0.4 and 0.8 respectively), and a weighted average is applied to the coarse mode sulfate and number.

For below-cloud scavenging, the first-order removal rate is equal to [(solubility factor) $\times$ (scavenging coefficient) $\times$ (precipitation rate)]. Again, the solubility factor can be viewed as a tuning factor. In CAM3.5, a solubility factor of 0.3 and a scavenging coefficient of 0.1 mm^{-1} are used for all aerosols. In MAM, the scavenging coefficient for interstitial aerosol is explicitly calculated as in Easter et al. [2004] and thus varies strongly with particle size, with lowest values for the accumulation mode; and the solubility factor is 0.1. For stratiform-cloud-borne aerosol, there is no below-cloud scavenging, and the solubility factor is 0.0.

Aerosol that is scavenged at one altitude can be resuspended at a lower altitude if precipitation evaporates. In CAM5, as in CAM3.5, this process is treated for aerosol removed by stratiform in-cloud scavenging. A fraction of the in-cloud scavenged aerosol is resuspended, and the resuspended fraction is equal to the fraction of precipitation that evaporates below cloud.

4.8.10 Dry Deposition

Aerosol dry deposition velocities are calculated using the [Zhang et al., 2001] parameterization with the CAM5 land-use and surface layer information. Gravitational settling velocities are calculated at layers above the surface [Seinfeld and Pandis, 1998]. Both velocities depend on particle wet size and are different for mass and number and between modes. The velocities for cloud-borne aerosols are calculated based on droplet sizes. Aerosol mixing ratio changes and fluxes from dry deposition and sedimentation throughout a vertical column are then calculated using the CAM5 dust deposition/sedimentation routine.

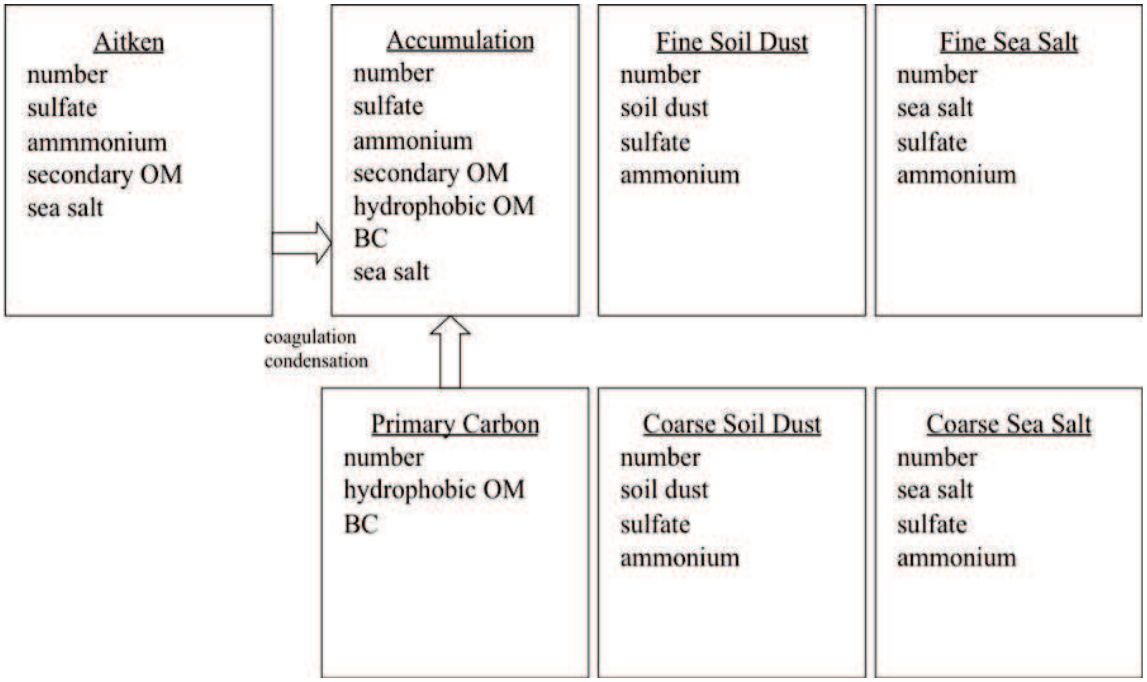

Figure 4.3: Predicted species for interstitial and cloud-borne component of each aerosol mode in MAM-7. Standard deviation for each mode is 1.6 (Aitken), 1.8 (accumulation), 1.6 (primary carbon), 1.8 (fine and coarse soil dust), and 2.0 (fine and coarse sea salt)

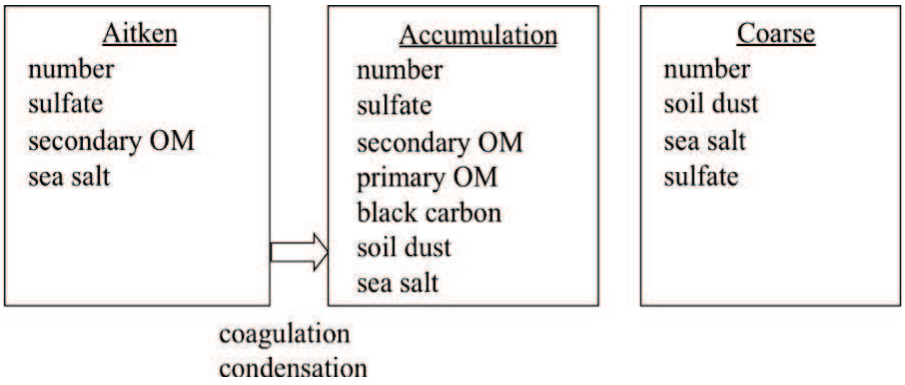

Figure 4.4: Predicted species for interstitial and cloud-borne component of each aerosol mode in MAM-3. Standard deviation for each mode is 1.6 (Aitken), 1.8 (accumulation) and 1.8 (coarse mode)

Table 4.4: Density (kg/m^3) of aerosol material.

Sea salt	Sulfate	Nitrate	Ammonium	SOA	POA	BC	Dust
1900	1770	1770	1770	1000	1000	1700	2600

Table 4.5: Hygroscopicity of aerosol components.

Sea salt	Sulfate	Nitrate	Ammonium	SOA	POA	BC	Dust
1.16	0.507	0.507	0.507	0.14	1.e-10	1.e-10	0.068

4.9 Condensed Phase Optics

Condensed phase (aerosols, liquid cloud droplets, hydrometeors, and ice crystal) optics are provided as a mass-specific quantities in m^2/kg. These optics are specified for each band of the shortwave and longwave radiation code. For the shortwave, unscaled extinction, single-scattering albedo, and asymmetry parameter are specified. For the longwave, the mass-specific absorption is specified. Vertical optical depths are computed by multiplying by the mass-specific quantities by the vertical mass path of the corresponding material.

For clouds, the in-cloud values of the mixing ratios are used to compute the in-cloud values of cloud optical depths. The radiation does not use grid-cell average optical depths of clouds.

4.9.1 Tropospheric Aerosol Optics

While the radiation code supports a range of possible aerosol packages, the modal aerosol package is the default configuration, and we will discuss the optics treatment used in that package. Aerosol optical properties for each mode are parameterized in terms of wet refractive index and wet surface mode radius of the mode, as described by [Ghan and Zaveri, 2007], except that volume mixing rather than the Maxwell-Garnett mixing rule is used to calculate the wet refractive index for mixtures of insoluble and soluble particles (We found little difference between the volume mixing treatment and the Maxwell-Garnett mixing rule.) Refractive indices for water and for most aerosol components are taken from OPAC [Koepke and Schult, 1998], but for black carbon the value (1.95,0.79i) from [Bond and Bergstrom, 2006] is used for solar wavelengths. Densities for each component are listed in Table 4.4.

The wet volume mean radius for each mode is calculated from the dry volume mean radius using equilibrium Kohler theory [Ghan and Zaveri, 2007], the relative humidity and the volume mean hygroscopicity. The hygroscopicity of each component is listed in Table 4.5. Note that the measured solubility of dust varies widely, from 0.03 to 0.26 [Koehler et al., 2009*b*]. The wet surface mode radius is calculated from the wet volume mean radius assuming a wet lognormal size distribution with the same geometric standard deviation as the dry size distribution. The geometric standard deviation is assumed to be constant for each mode.

4.9.2 Stratospheric Volcanic Aerosol Optics

CAM 5.0 specifies the volcanic aerosol as a mass mixing ratio q_V of wet volcanic aerosol to dry air as a function of height, latitude, longitude and time. CAM 5.0 also specifies a geometric

mean radius r_g of the volcanic aerosol. The volcanic optics are stored as a lookup table as a function of geometric mean radius.

The size distribution is defined by a log-normal size distribution with a geometric mean radius r_g and geometric standard deviation σ_g. For the standard version of the optics,

$$\begin{aligned}
\sigma_g &= 1.8 && (4.204)\\
\mu &= \ln(r_g) && (4.205)\\
\mu &\in [\mu_{\min}, \mu_{\max}] && (4.206)\\
\mu_{\min} &= \ln(0.01 * 10^{-6} \exp(-5/2 * (\ln \sigma_g)^2)) && (4.207)\\
\mu_{\max} &= \ln(2.00 * 10^{-6} \exp(-5/2 * (\ln \sigma_g)^2)) && (4.208)
\end{aligned}$$

In other words, r_{eff} spans the range [0.01,2.0] μm. The density of the sulfuric acid / water mixture at 75% / 25% at 215K is

$$\rho = 1.75 * 10^3 \text{ kg/m}^3 \tag{4.209}$$

The index of refraction is that specified by Biermann [Biermann et al., 2000] and is available from the HITRAN [Rothman et al., 2009] database. The index at 75%/25% weight percent (sulfuric acid to water) and at 215K is used.

The incomplete gamma weight,

$$L(r) = \int_0^r r^{*2} n(r^*) dr^* / \int_0^\infty r^{*2} n(r^*) dr^* \tag{4.210}$$

can be used to define the mass-specific aerosol extinction, scattering, and asymmetric scattering,

$$\begin{aligned}
b_{\text{ext}} &= \frac{3}{4\rho\, r_{\text{eff}}} \int_0^\infty q_{\text{ext}}(r) dL(r) && (4.211)\\
b_{\text{sca}} &= \frac{3}{4\rho\, r_{\text{eff}}} \int_0^\infty q_{\text{sca}}(r) dL(r) && (4.212)\\
b_{\text{asm}} &= \frac{3}{4\rho\, r_{\text{eff}}} \int_0^\infty q_{\text{gqsc}}(r) dL(r) && (4.213)\\
b_{\text{abs}} &= \frac{3}{4\rho\, r_{\text{eff}}} \int_0^\infty (q_{\text{ext}}(r) - q_{\text{sca}}(r)) dL(r) && (4.214)
\end{aligned}$$

where $q_{\text{ext}}(r), q_{\text{sca}}(r), q_{\text{gqsc}}(r)$ are efficiencies obtained from the MIEV0 program of Wiscombe [Wiscombe, 1996].

These mass-specific properties are averaged over each frequency band of RRTMG and parameterized in a lookup table with $\mu = \ln(r_g)$ as the dependent variable.

The vertical optical depths are derived as the product of vertical mass path with mass-specific aerosol properties at runtime.

$$\tau_{\text{ext}} = q_V * \frac{\Delta P_{\text{dry}}}{g} * b_{\text{ext}}(\mu) \tag{4.215}$$

where q_V is the mixing ratio of volcanic aerosol. The corresponding scattering optical depth, asymmetric scattering optical depth, and absorption optical depth are derived similarly.

4.9.3 Liquid Cloud Optics

For liquid clouds CAM 5.0 specifies the fraction of each grid cell occupied by liquid cloud droplets $C_{\rm liq}$, the ratio of mass of condensed water to wet air in the cloud $q_{\rm liq}$, and the number-size distribution in terms of the 2 parameters, μ and λ of the gamma distribution,

$$n(D) = \frac{dN}{dD} = \frac{\lambda^{\mu+1}}{\Gamma(\mu+1)} D^{\mu} e^{-\lambda D} \tag{4.216}$$

where D is the diameter of the droplets.

Both the parameters, μ and λ have limited ranges:

$$2. < \mu < 15. \tag{4.217}$$

$$\frac{\mu+1}{50 * 10^{-6}\text{m}} < \lambda < \frac{\mu+1}{2 * 10^{-6}\text{m}} \tag{4.218}$$

The liquid cloud optics are specified in terms of a lookup table in μ and $1/\lambda$. These optics are computed as size-distribution and spectral-band averages of the quantities (e.g., $Q_{\rm ext}$) computed by the MIEV0 program [Wiscombe, 1996].

The size-integrated mass-specific extinction coefficient, $k_{\rm ext}$, (units m^2/kg) is given by:

$$k_{\rm ext}(\nu) = \frac{\frac{\pi}{4} \int_0^{\infty} D^2 \, Q_{\rm ext}(D;\nu,m) \, n(D) \, dD}{\frac{\pi}{6} \rho_w \int_0^{\infty} D^3 \, n(D) \, dD} \tag{4.219}$$

The corresponding quantities are used to compute mass-specific absorption in the longwave as well as single-scattering albedo and asymmetry parameter.

The in-cloud optical depth is then given by:

$$\tau_{\rm liq}(\nu) = k_{\rm ext}(\nu) \, q_{\rm liq} \, \frac{\Delta P}{g} \tag{4.220}$$

where $q_{\rm liq}$ is the ratio of droplet mass to dry air mass.

For RRTMG, the wavenumber average values of $\tau_{\rm liq}$, $\tau_{\rm liq}\omega_{\rm liq}$, $\tau_{\rm liq}\omega_{\rm liq}g_{\rm liq}$ on each SW band, and the wavenumber average value of the absorption optical depth, $\tau_{\rm liq}(1-\omega_{\rm liq})$, on each longwave band.

In-cloud water path variability is not treated by the optics.

4.9.4 Ice Cloud Optics

CAM 5.0 specifies an in-cloud ice water path, an ice cloud fraction, and an effective diameter for ice particles in the cloud. The optics for ice clouds are constructed as a lookup table as a function of effective diameter for each of the shortwave and longwave bands in the radiation code.

Ice cloud optical properties have been derived using two approaches: (1) calculations of single ice crystal scattering properties based on electrodynamic theory, followed by their application to assumed ice particle size distributions (PSD) and the representation of PSD optical properties through the effective diameter (D_e) of the PSD, and (2) parameterization of scattering/absorption processes in terms of ice particle shape and size, and integrating these expressions

over the PSD to produce analytical expressions of PSD optical properties in terms of ice crystal and PSD parameters. In the latter case, the PSD extinction and absorption coefficients can be expressed as explicit functions of the ice particle projected area- and mass-dimension power laws and the PSD parameters of the gamma form. The modified anomalous diffraction approximation (MADA) uses this second approach to calculate ice cloud optical properties. The development of MADA was motivated by a desire to explicitly represent ice optical properties in terms of the ice PSD and ice crystal shape parameters, given that the ice PSD optical properties cannot be uniquely defined by D_e[Mitchell, 2002].

MADA was developed from van de Hulst's anomalous diffraction theory or ADT [van de Hulst, 1957] through a series of physical insights, which are:

1. The effective photon path through a particle by which its scattering properties can be predicted is given by the ratio of particle projected area/particle volume [Bryant and Latimer, 1969; Mitchell and Arnott, 1994], where volume is defined as particle mass/bulk density of ice (0.917 g/cm^3).

2. The processes of internal reflection and refraction can be viewed as extending the photon path and can be parameterized using a MADA framework [Mitchell et al., 1996*b*].

3. The maximum contribution of wave resonance or photon tunneling to absorption and extinction can be estimated as a linear function of the real part of the refractive index for ice, n_r. Photon tunneling can then be parameterized in terms of n_r, size parameter x and the other MADA parameters described above [Mitchell, 2000].

4. Edge effects as surface wave phenomena pertain only to extinction and can be represented in terms of the size parameter x as described by [Wu, 1956] and modified by [Mitchell, 2000]. Based on a laboratory ice cloud study [Mitchell et al., 2001], edge effects for non-spherical ice crystals do not appear significant.

The first insight greatly simplified van de Hulst's ADT, resulting in analytic and integrable expressions for the PSD extinction and absorption coefficients as shown in [Mitchell and Arnott, 1994]. This simplified ADT may be more accurate than the original ADT [Mitchell et al., 2006*a*]. This simplified ADT provided an analytical framework on which the other three insights or processes were expressed. These processes were represented analytically for a single ice particle, and then integrated over the PSD to produce extinction and absorption coefficients that account for these processes. These coefficients were formulated in terms of ice particle shape (i.e. the ice particle area- and mass-dimension power laws) and the three gamma PSD parameters. The basic MADA equations formulated for ice clouds are given in the appendix of [Mitchell, 2002]. Details regarding their derivation and their physical basis are described in [Mitchell, 2000] and [Mitchell et al., 1996*b*].

The asymmetry parameter g is not treated by MADA, but was parameterized for solar wavelengths as a function of wavelength and ice particle shape and size, based on ray-tracing calculations by Andreas Macke, as described in [Mitchell et al., 1996*b*]. The g parameterization for quasi-spherical ice particles is based on the phase function calculations of [Nousiainen and McFarquhar, 2004]. These parameterizations relate g for a PSD to the ice particle size that divides the PSD into equal projected areas (since scattering depends on projected area). For terrestrial radiation, CAM 5.0 g values for ice are based on the g parameterization described in [Yang et al., 2005].

Tests of MADA

While this treatment of ice optical properties began and evolved through van de Hulst's original insights formulated in ADT, optical properties predicted by MADA closely agree with those predicted by other ice optics schemes based on electrodynamic theory. As described in [Mitchell et al., 2001, 2006*a*], MADA has been tested in a laboratory ice cloud experiment where the MADA extinction error was 3% on average relative to the FTIR measured extinction efficiency over the 2-14 μm wavelength range. These same laboratory PSD were used to calculate the absorption efficiencies using MADA and T-matrix, which differed by 6% on average over the wavelength range 2-18 μm (size parameter range 2-22). In corresponding T-matrix calculations of the single-scattering albedo, the mean MADA error was 2.5%. In another test, MADA absorption errors relative to the Finite Difference Time Domain (FDTD) method (i.e. [Yang et al., 2005] over the wavelength range 3-100 μm were no greater than 15% for six ice particle shapes. Finally, the absorption coefficients predicted by MADA and the [Fu et al., 1998] and the [Yang et al., 2005] ice optics schemes generally agreed within 5%.

Application to CAM 5.0

The MADA-based ice optics scheme described above is not used explicitly in CAM 5.0, but was used to generate a look-up table of optical properties as a function of effective diameter, D_e. The PSD optical properties consist of the mass-normalized extinction coefficient (volume extinction coefficient / ice water content), the single-scattering albedo and the asymmetry parameter for bands covering all solar and terrestrial wavelengths. The radiation bands coincide with those used in RRTMG. The ice refractive index values used are from [Warren and Brandt, 2008]. Since MADA is formulated to accept any ice particle shape recipe, a shape recipe corresponding to that observed for mid-latitude cirrus clouds at $-45\,^{\circ}$C (see [Lawson et al., 2006]) was assumed for ice particles larger than 60 μm: 7% hexagonal columns, 50% bullet rosettes and 43% irregular ice particles. At smaller sizes, the shape recipe consists of 50% quasi-spherical, 30% irregular and 20% bullet rosette ice crystals, based on in-situ measurements in tropical cirrus [P. Lawson, 2005, personal communication].

The effective diameter is defined in a way that is universal for both ice and water clouds, which is essentially the photon path characterizing the PSD [Mitchell, 2002]:

$$De = \frac{3}{2}\frac{\mathrm{IWC}}{\rho_i A} \tag{4.221}$$

where IWC is the ice water content (g/cm^3), ρ_i is the bulk ice density (0.917 g/cm^3) and A is the total projected area of the PSD (cm^2/cm^3).

4.9.5 Snow Cloud Optics

CAM 5.0 specifies snow as a cloud fraction of snow, an effective diameter of snow, and an in-cloud mass mixing ratio of snow. The snow optics are identical to the optics for ice clouds.

4.10 Radiative Transfer

Radiative transfer calculations in the longwave and shortwave are provided by the radiation code RRTMG [Iacono et al., 2008; Mlawer et al., 1997]. This is an accelerated and modified version of the correlated k-distribution model, RRTM. The condensed phase radiative parameterizations are external to the radiation package, however the gas optics and radiative transfer solver are provided within RRTMG.

4.10.1 Combination of Aerosol Radiative Properties

The number N_a of aerosol species is arbitrary; however in the standard configuration there are 3 modes. The radiative properties are combined before being passed to the radiative transfer solver. If the extinction optical depth of species i in band b is τ_{ib} and the single-scattering albedo is ω_{ib} and the asymmetry parameter is g_{ib} then the aerosol optics are combined as follows:

$$\tau_b = \sum_{i=1}^{N_a} \tau_{ib} \tag{4.222}$$

$$\omega_b = \sum_{i=1}^{N_a} \tau_{ib}\omega_{ib}/\tau_b \tag{4.223}$$

$$g_b = \sum_{i=1}^{N_a} \tau_{ib}\omega_{ib}g_{ib}/(\tau_b\omega_b) \tag{4.224}$$

where τ_b is the total aerosol extinction optical depth in band b, ω_b is the total single-scattering albedo in band b, and g_b is the asymmetry parameter in band b.

4.10.2 Combination of Cloud Optics

CAM 5.0 are specifies three different types of clouds: ice clouds, liquid clouds, and snow clouds. Each of these clouds has a separate cloud fraction $C_{\rm liq}, C_{\rm ice}, C_{\rm snow}$, as well as an in-cloud radiative characterization in terms of optical depths τ_i, single-scattering albedo ω_i and asymmetry parameter g_i. The optics are smeared together into a total cloud fraction C as follows:

$$C = \max\{C_{\rm liq}, C_{\rm ice}, C_{\rm snow}\} \tag{4.225}$$

$$\tau_c = \sum_{\rm t\in type} \tau_t * C_t/C \tag{4.226}$$

$$\omega_c = \sum_{\rm t\in type} \tau_{tb}\omega_{tb}C_t/(\tau_c C) \tag{4.227}$$

$$g_c = \sum_{\rm t\in type} \tau_{tb}\omega_{tb}g_{tb}C_t/(\tau_c\omega_c C) \tag{4.228}$$

where C, τ_c, ω_c, g_c are the combined cloud radiative parameters.

4.10.3 Radiative Fluxes and Heating Rates

Radiative fluxes and heating rates in CAM 5.0 are calculated using RRTMG[Iacono et al., 2008].

This model utilizes the correlated k-distribution technique to calculate irradiance and heating rate efficiently in broad spectral intervals, while realizing the objective of retaining a high level of accuracy relative to measurements and high-resolution line-by-line models. Sub-grid cloud characterization in RRTMG is treated in both the longwave and shortwave spectral regions with McICA, the Monte-Carlo Independent Column Approximation [Pincus and Morcrette, 2003], using the maximum-random cloud overlap assumption.

The thermodynamic state, gas concentrations, cloud fraction, condensed phase optics, and aerosol properties are specified elsewhere. The CAM 5.0 surface model provides both the surface albedo, area-averaged for each atmospheric column, and the upward longwave surface flux, which incorporates the surface emissivity, for input to the radiation. The bulk aerosol package of CAM4 continues to be supported by this radiation code as an option, however a description of this optional configuration is not provided in this document.

To provide fluxes at the top of the atmosphere, RRTMG uses with an additional layer above the CAM 5.0 model top in both the longwave and shortwave. This extra layer is specified by replicating the composition of the highest CAM 5.0 layer into a layer that extends from the top of the model to 10^{-4} hPa. RRTMG does not treat non-LTE (local thermodynamic equilibrium) effects in the upper atmosphere. It provides accurate fluxes and heating rates up to about 0.1 hPa, above which non-LTE effects become more significant.

Shortwave Radiative Transfer

RRTMG divides the solar spectrum into 14 shortwave bands that extend over the spectral range from 0.2 μm to 12.2 μm (820 to 50000 cm^{-1}). Modeled sources of extinction (absorption and scattering) are H2O, O3, CO2, O2, CH4, N2, clouds, aerosols, and Rayleigh scattering. The model uses a two-stream δ-Eddington approximation assuming homogeneously mixed layers, while accounting for both absorption and scattering in the calculation of reflectance and transmittance. The model distinguishes the direct solar beam from scattered (diffuse) radiation. The scattering phase function is parameterized using the Henyey-Greenstein approximation to represent the forward scattering fraction as a function of the asymmetry parameter. This delta-scaling is applied to the total irradiance as well as to the direct and diffuse components. The latter are consistent with the direct and diffuse components of the surface albedo, which are applied to the calculation of surface reflectance.

The shortwave version of RRTMG used in CAM5 is derived from RRTM_SW [Clough et al., 2005]. It utilizes a reduced complement of 112 quadrature points (g-points) to calculate radiative transfer across the 14 spectral bands, which is half of the 224 g-points used in RRTM_SW, to enhance computational performance with little impact on accuracy. The number of g-points needed within each band varies depending on the strength and complexity of the absorption in each spectral interval. Total fluxes are accurate to within 1-2 W/m^2 relative to the standard RRTM_SW (using DISORT with 16 streams) in clear sky and in the presence of aerosols and within 6 W/m^2 in overcast sky. RRTM_SW with DISORT is itself accurate to within 2 W/m^2 of the data-validated multiple scattering model, CHARTS [Moncet and Clough, 1997]. Input absorption coefficient data for the k-distributions used by RRTMG are obtained directly from the line-by-line radiation model LBLRTM [Clough et al., 2005].

Table 4.6: RRTMG_SW spectral band boundaries and the solar irradiance in each band.

Band Index	Band Min (μm)	Band Max (μm)	Band Min (cm^{-1})	Band Max (cm^{-1})	Solar Irradiance (W/m^2)
1	3.077	3.846	2600	3250	12.11
2	2.500	3.077	3250	4000	20.36
3	2.150	2.500	4000	4650	23.73
4	1.942	2.150	4650	5150	22.43
5	1.626	1.942	5150	6150	55.63
6	1.299	1.626	6150	7700	102.93
7	1.242	1.299	7700	8050	24.29
8	0.778	1.242	8050	12850	345.74
9	0.625	0.778	12850	16000	218.19
10	0.442	0.625	16000	22650	347.20
11	0.345	0.442	22650	29000	129.49
12	0.263	0.345	29000	38000	50.15
13	0.200	0.263	38000	50000	3.08
14	3.846	12.195	820	2600	12.89

RRTMG shortwave utilizes McICA, the Monte-Carlo Independent Column Approximation, to represent sub-grid scale cloud variability such as cloud fraction and cloud overlap. An external sub-column generator is used to define the stochastic cloud arrays used by the McICA technique.

The Kurucz solar source function is used in the shortwave model, which assumes a total solar irradiance (TSI) at the top of the atmosphere of 1368.22 W/m^2. However, this value is scaled in each spectral band through the specification of a time-varying solar spectral irradiance as discussed below. The TSI assumed in each RRTMG shortwave band is listed in the table below, along with the spectral band boundaries in μm and wavenumbers.

Shortwave radiation is only calculated by RRTMG when the cosine of the zenith angle is larger than zero, that is, when the sun is above the horizon.

Longwave Radiative Transfer

The infrared spectrum in RRTMG is divided into 16 longwave bands that extend over the spectral range from 3.1 μm to 1000.0 μm (10 to 3250 cm^{-1}). The band boundaries are listed in the table below. The model calculates molecular, cloud and aerosol absorption and emission. Scattering effects are not presently included. Molecular sources of absorption are H2O, CO2, O3, N2O, CH4, O2, N2 and the halocarbons CFC-11 and CFC-12. CFC-11 is specified by CAM5 as a weighed sum of multiple CFCs (other than CFC-12). The water vapor continuum is treated with the CKD_v2.4 continuum model. For completeness, band 16 includes a small adjustment to add the infrared contribution from the spectral interval below 3.1 μm.

The longwave version of RRTMG [Iacono et al., 2008, 2003, 2000] used in CAM5 has been modified from RRTM_LW [Mlawer et al., 1997] to enhance its computational efficiency with minimal effect on the accuracy. This includes a reduction in the total number of g-points from 256 to 140. The number of g-points used within each band varies depending on the strength

Table 4.7: RRTMG_LW spectral band boundaries.

Band Index	Band Min (μm)	Band Max (μm)	Band Min (cm^{-1})	Band Max (cm^{-1})
1	28.57	1000.0	10	350
2	20.00	28.57	350	500
3	15.87	20.00	500	630
4	14.29	15.87	630	700
5	12.20	14.29	700	820
6	10.20	12.20	820	980
7	9.26	10.20	980	1080
8	8.47	9.26	1080	1180
9	7.19	8.47	1180	1390
10	6.76	7.19	1390	1480
11	5.56	6.76	1480	1800
12	4.81	5.56	1800	2080
13	4.44	4.81	2080	2250
14	4.20	4.44	2250	2380
15	3.85	4.20	2380	2600
16	3.08	3.85	2600	3250

and complexity of the absorption in each band. Fluxes are accurate to within 1.0 W/m^2 at all levels, and cooling rate generally agrees within 0.1 K/day in the troposphere and 0.3 K/day the stratosphere relative to the line-by-line radiative transfer model, LBLRTM [Clough et al., 2005; Clough and Iacono, 1995]. Input absorption coefficient data for the k-distributions used by RRTMG are obtained directly from LBLRTM.

This model also utilizes McICA, the Monte-Carlo Independent Column Approximation [Pincus and Morcrette, 2003], to represent sub-grid scale cloud variability such as cloud fraction and cloud overlap. An external sub-column generator is used to define the stochastic cloud arrays needed by the McICA technique.

Within the longwave radiation model, the surface emissivity is assumed to be 1.0. However, the radiative surface temperature used in the longwave calculation is derived with the Stefan-Boltzmann relation from the upward longwave surface flux that is input from the land model. Therefore, this value may include some representation of surface emissivity less than 1.0 if this condition exists in the land model. RRTMG longwave also provides the capability of varying the surface emissivity within each spectral band, though this feature is not presently utilized.

Longwave radiative transfer is performed over a single (diffusivity) angle (secant =1.66) for one upward and one downward calculation. RRTMG includes an accuracy adjustment in profiles with very high water vapor that slightly varies the diffusivity angle in some bands as a function of total column water vapor.

4.10.4 Surface Radiative Properties

For the shortwave, the surface albedoes are specified at every grid point at every time step. The albedoes are partitioned for the spectral ranges [2.0, 0.7]μm and [0.7,12.0]μm. In addition they are partitioned between the direct and diffuse beam.

In the longwave, the surface is assumed to have an emissivity of 1.0 within the radiation model. However, the radiative surface temperature used in the longwave calculation is derived with the Stefan-Boltzmann relation from the upward longwave surface flux that is input from the surface models. Therefore, this value may include some representation of surface emissivity less than 1.0, if this condition exists in surface models (e.g. the land model).

4.10.5 Time Sampling

Both the shortwave and longwave radiation is computed at hourly intervals by default. The heating rates and fluxes are assumed to be constant between time steps.

4.10.6 Diurnal Cycle and Earth Orbit

In CAM 5.0, the diurnal cycle and earth orbit is computed using the method of [Berger, 1978]. Using this formulation, the insolation can be determined for any time within 10^6 years of 1950 AD. The insolation at the top of the model atmosphere is given by

$$S_I = S_0 \, \rho^{-2} \, \cos \mu, \tag{4.229}$$

where S_0 is the solar constant, μ is the solar zenith angle, and ρ^{-2} is the distance factor (square of the ratio of mean to actual distance that depends on the time of year). A time series of the solar spectral irradiance at 1 a.u. for 1870-2100 based upon [Wang et al., 2005] is included with the standard model and is in section 4.10.7.

We represent the annual and diurnal cycle of solar insolation with a repeatable solar year of exactly 365 days and with a mean solar day of exactly 24 hours, respectively. The repeatable solar year does not allow for leap years. The expressions defining the annual and diurnal variation of solar insolation are:

$$\cos \mu = \sin \phi \sin \delta - \cos \phi \cos \delta \cos(H) \tag{4.230}$$

$$\delta = \arcsin(\sin \epsilon \sin \lambda) \tag{4.231}$$

$$\rho = \frac{1 - e^2}{1 + e \, \cos(\lambda - \tilde{\omega})} \tag{4.232}$$

$$\tilde{\omega} = \Pi + \psi \tag{4.233}$$

where

$$\begin{aligned}
\phi &= \text{latitude in radians} \\
\delta &= \text{solar declination in radians} \\
H &= \text{hour angle of sun during the day} \\
\epsilon &= \text{obliquity} \\
\lambda &= \text{true longitude of the earth relative to vernal equinox} \\
e &= \text{eccentricity factor} \\
\tilde{\omega} &= \text{longitude of the perihelion} + 180^\circ \\
\Pi &= \text{longitude of perihelion based on the fixed equinox} \\
\psi &= \text{general precession}
\end{aligned} \tag{4.234}$$

The hour angle H in the expression for $\cos\mu$ depends on the calendar day d as well as model longitude:

$$H = 2\,\pi\left(d + \frac{\theta}{360^\circ}\right), \tag{4.235}$$

where θ = model longitude in degrees starting from Greenwich running eastward. Note that the calendar day d varies continuously throughout the repeatable year and is updated every model time step. The values of d at 0 GMT for January 1 and December 31 are 0 and 364, respectively. This would mean, for example, that a model calendar day d having no fraction (such as 182.00) would refer to local midnight at Greenwich, and to local noon at the date line (180° longitude).

The obliquity ϵ may be approximated by an empirical series expansion of solutions for the Earth's orbit

$$\epsilon = \epsilon^* + \sum_{j=1}^{47} A_j\,\cos\left(f_j\,t + \delta_j\right) \tag{4.236}$$

where A_j, f_j, and δ_j are determined by numerical fitting. The term $\epsilon^* = 23.320556^\circ$, and t is the time (in years) relative to 1950 AD.

Since the series expansion for the eccentricity e is slowly convergent, it is computed using

$$e = \sqrt{\left(e\cos\Pi\right)^2 + \left(e\sin\Pi\right)^2} \tag{4.237}$$

The terms on the right-hand side may also be written as empirical series expansions:

$$e\left\{\begin{array}{c}\cos\\ \sin\end{array}\right\}\Pi = \sum_{j=1}^{19} M_j\,\left\{\begin{array}{c}\cos\\ \sin\end{array}\right\}\left(g_j\,t + \beta_j\right) \tag{4.238}$$

where M_j, g_j, and β_j are estimated from numerical fitting. Once these series have been computed, the longitude of perihelion Π is calculated using

$$\Pi = \arctan\left(\frac{e\,\sin\Pi}{e\,\cos\Pi}\right) \tag{4.239}$$

The general precession is given by another empirical series expansion

$$\psi = \tilde{\psi}\,t + \zeta + \sum_{j=1}^{78} F_j\,\sin\left(f'_j\,t + \delta'_j\right) \tag{4.240}$$

where $\tilde{\psi} = 50.439273''$, $\zeta = 3.392506°$, and F_j, f'_j, and δ'_j are estimated from the numerical solution for the Earth's orbit.

The calculation of λ requires first determining two mean longitudes for the orbit. The mean longitude λ_{m0} at the time of the vernal equinox is :

$$\begin{aligned} \lambda_{m0} &= 2\left\{\left(\frac{e}{2}+\frac{e^3}{8}\right)(1+\beta)\sin(\tilde{\omega})\right. \\ &\quad -\frac{e^2}{4}\left(\frac{1}{2}+\beta\right)\sin(2\,\tilde{\omega}) \\ &\quad \left.+\frac{e^3}{8}\left(\frac{1}{3}+\beta\right)\sin(3\,\tilde{\omega})\right\} \end{aligned} \tag{4.241}$$

where $\beta = \sqrt{1-e^2}$. The mean longitude is

$$\lambda_m = \lambda_{m0} + \frac{2\,\pi\,(d-d_{ve})}{365} \tag{4.242}$$

where $d_{ve} = 80.5$ is the calendar day for the vernal equinox at noon on March 21. The true longitude λ is then given by:

$$\begin{aligned} \lambda = \lambda_m &+ \left(2\,e-\frac{e^3}{4}\right)\sin(\lambda_m-\tilde{\omega}) \\ &+ \frac{5\,e^2}{4}\sin\left[2(\lambda_m-\tilde{\omega})\right] \\ &+ \frac{13\,e^3}{12}\sin\left[3(\lambda_m-\tilde{\omega})\right] \end{aligned} \tag{4.243}$$

The orbital state used to calculate the insolation is held fixed over the length of the model integration. This state may be specified in one of two ways. The first method is to specify a year for computing t. The value of the year is held constant for the entire length of the integration. The year must fall within the range of 1950 ± 10^6. The second method is to specify the eccentricity factor e, longitude of perihelion $\tilde{\omega} - 180°$, and obliquity ϵ. This set of values is sufficient to specify the complete orbital state. Settings for AMIP II style integrations under 1995 AD conditions are $\epsilon = 23.4441$, $e = 0.016715$, and $\tilde{\omega} - 180 = 102.7$.

4.10.7 Solar Spectral Irradiance

The reference spectrum assumed by RRTMG is the Kurucz spectrum. CAM 5.0 specifies the solar spectral irradiance in a file, based on the work of Lean [Wang et al., 2005]. The Kurucz spectrum can be seen in figure 4.5. The Lean data seen in figure 4.6 is time-varying and the graphed values are an average over one solar cycle. These two spectra postulate different values of the total solar irradiance. A graph of the relative difference between them can be seen in figure 4.7.

Solar Irradiance	Kurucz	Lean
Total	1368.60	1366.96
In RRTMG bands	1368.14	1366.39
> 12195 nm	0.46	0.46
$[120, 200]$ nm	0	0.11
EUV	0	0.0047

RRTMG Band Index	λ_{high}, nm	λ_{low}, nm	Kurucz W/m^2	Lean W/m^2	Lean - Kurucz	Relative %	Lean(t) Max % Variation	Lean(t) Max ΔFlux
14	12195	3846	12.79	12.78	-0.01	-0.08	0.16	0.020
1	3846	3077	12.11	11.99	-0.12	-1.00	0.02	0.003
2	3077	2500	20.36	20.22	-0.14	-0.69	0.03	0.007
3	2500	2151	23.73	23.49	-0.24	-1.02	0.02	0.005
4	2151	1942	22.43	22.17	-0.26	-1.17	0.01	0.003
5	1942	1626	55.63	55.61	-0.02	-0.04	0.02	0.011
6	1626	1299	102.9	102.9	0.0	0.	0.02	0.019
7	1299	1242	24.29	24.79	0.50	2.06	0.04	0.011
8	1242	778	345.7	348.9	3.2	0.93	0.06	0.226
9	778	625	218.1	218.2	0.1	0.05	0.11	0.238
10	625	441	347.2	344.9	-2.3	-0.67	0.13	0.463
11	441	345	129.5	130.0	0.5	0.39	0.26	0.340
12	345	263	50.15	47.41	-2.74	-5.78	0.45	0.226
13	263	200	3.120	3.129	0.009	0.29	4.51	0.141

Table 4.8: Band-level ratio of Solar Irradiances, based on average of one solar cycle

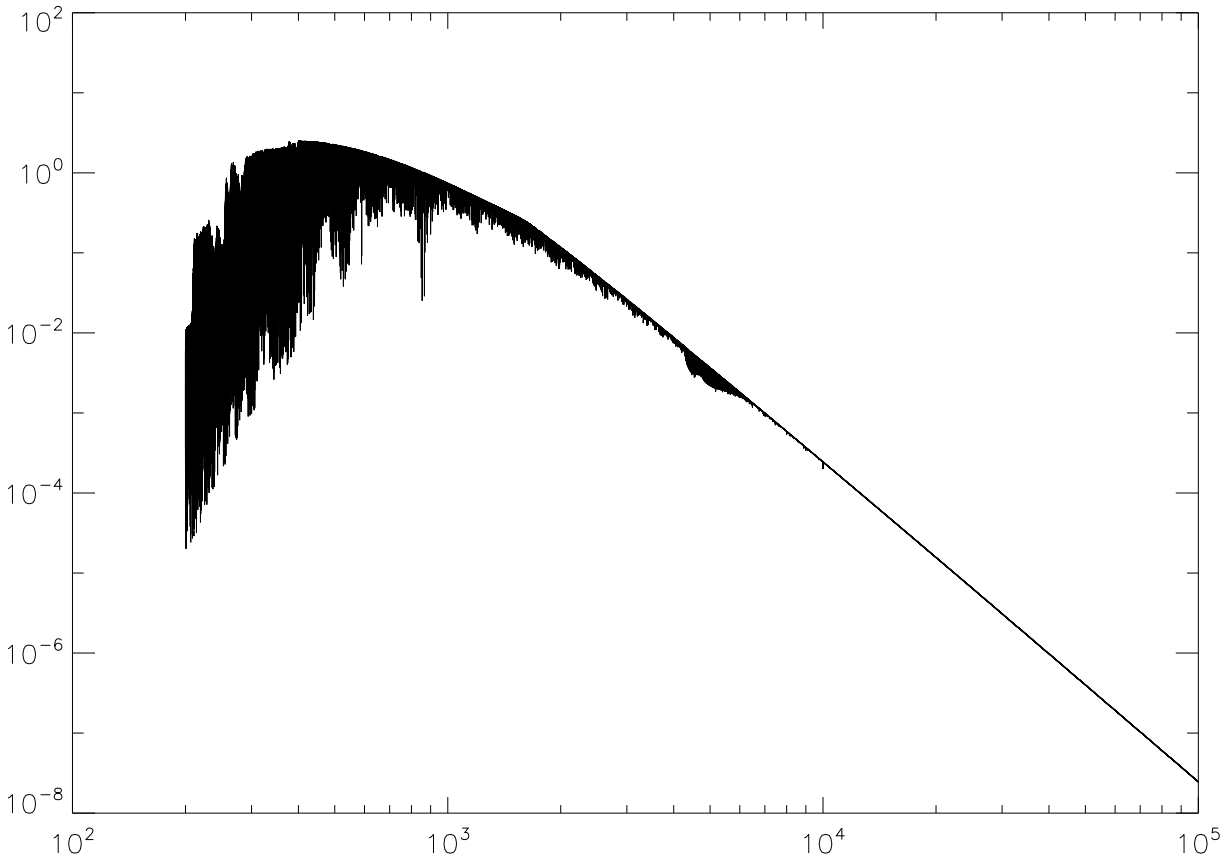

Figure 4.5: Kurucz spectrum. ssf in W/m^2/nm. Source Data: AER. Range from [20, 20000] nm.

The heating in each band b is scaled by the ratio, $\frac{\texttt{Lean}(t)_b}{\texttt{Kurucz}_b}$, where $\texttt{Kurucz}_b$ is assumed by RRTMG as specified in table 4.8 , and $\texttt{Lean}(t)_b$ is the solar irradiance specified by the time-dependent solar spectral irradiance file. $\texttt{Lean}(t)_{14}$ includes the Lean irradiance longward of 12195 nm to capture irradiance in the very far infrared.

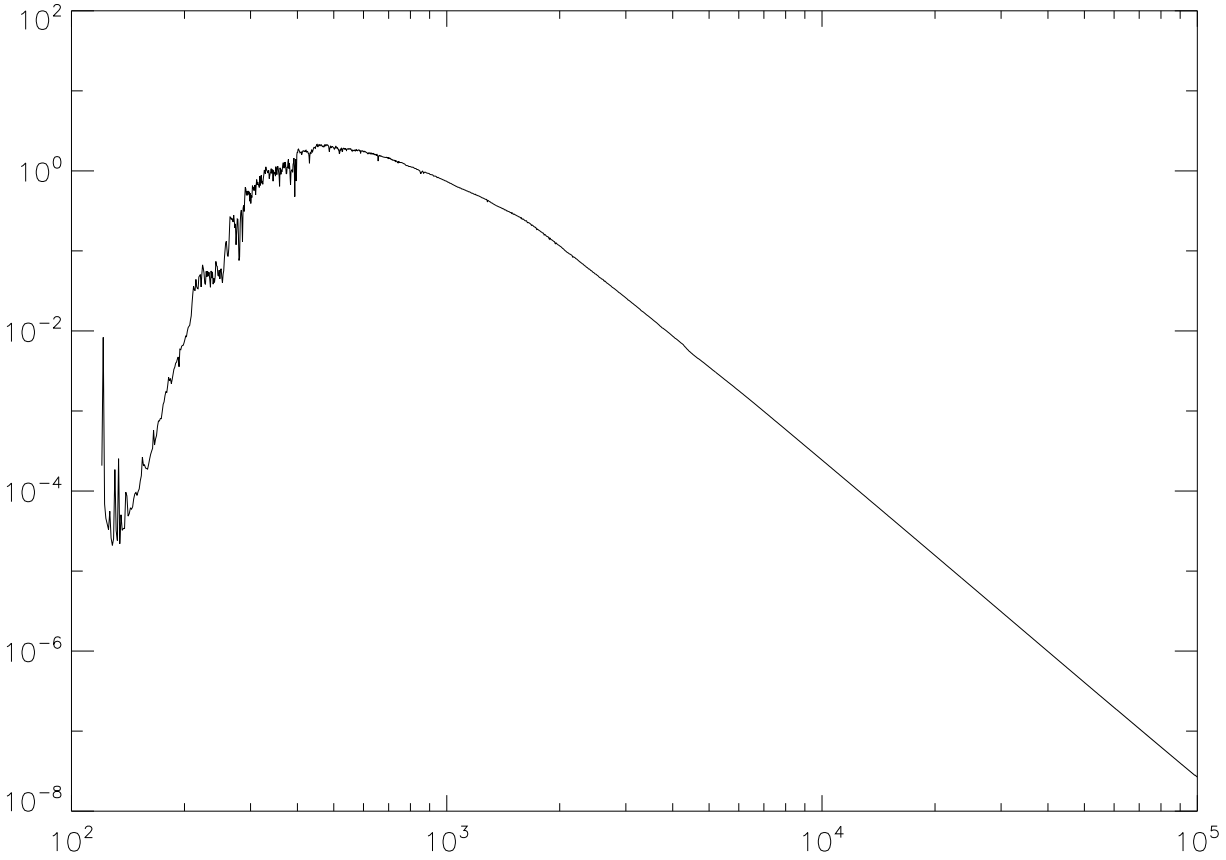

Figure 4.6: Lean spectrum. Average over 1 solar cycle, May 1, 1996 to Dec 31, 2006. Source Data: Marsh. ssf in W/m^2/nm. Range from [120, 99975] nm.

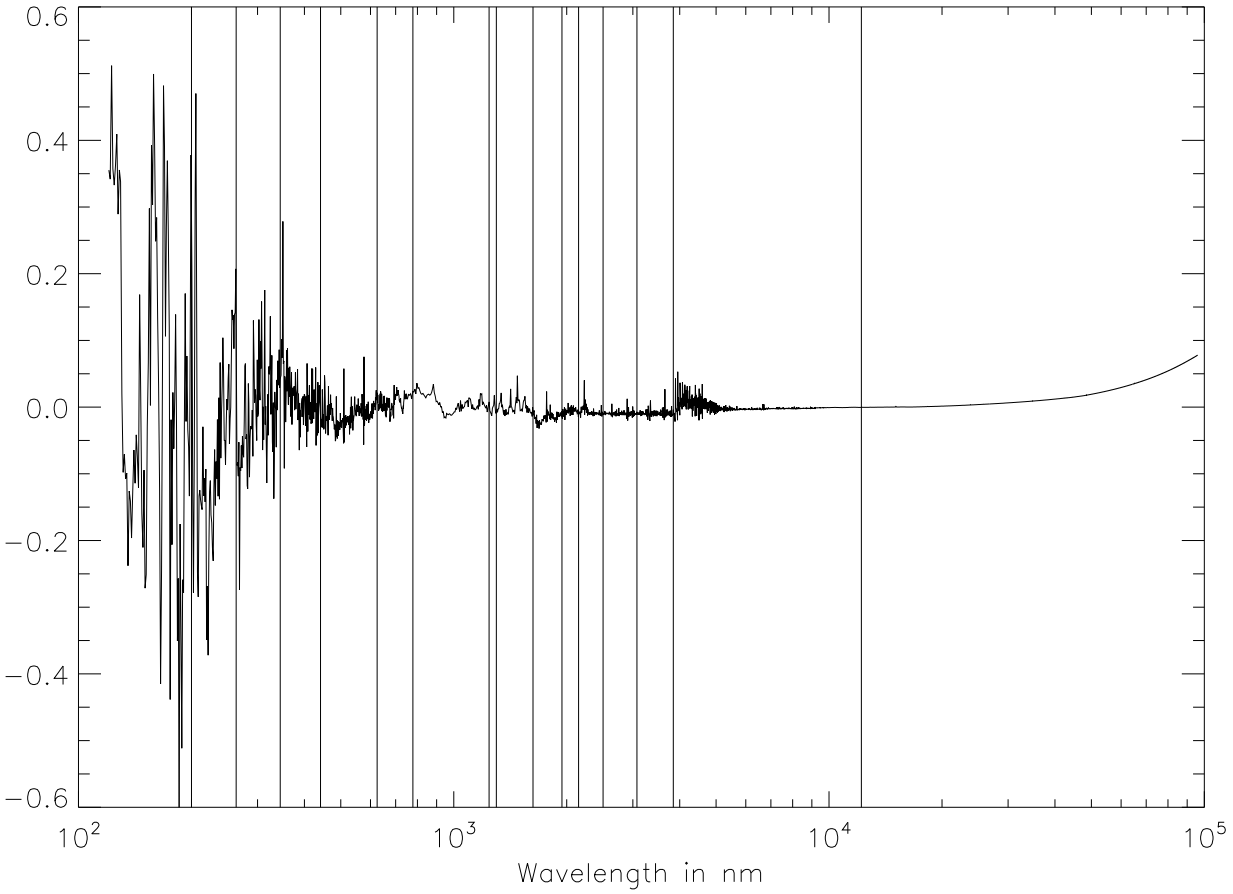

Figure 4.7: Relative difference, $\frac{\texttt{Lean}-\texttt{Kurucz}}{.5(\texttt{Lean}+\texttt{Kurucz})}$ between spectra. RRTMG band boundaries are marked with vertical lines.

4.11 Surface Exchange Formulations

The surface exchange of heat, moisture and momentum between the atmosphere and land, ocean or ice surfaces are treated with a bulk exchange formulation. We present a description of each surface exchange separately. Although the functional forms of the exchange relations are identical, we present the descriptions of these components as developed and represented in the various subroutines in CAM 5.0. The differences in the exchange expressions are predominantly in the definition of roughness lengths and exchange coefficients. The description of surface exchange over ocean follows from Bryan et al. [1996], and the surface exchange over sea ice is discussed in the sea-ice model documentation. Over lakes, exchanges are computed by a lake model embedded in the land surface model described in the following section.

4.11.1 Land

In CAM 5.0, the NCAR Land Surface Model (LSM) [Bonan, 1996] has been replaced by the Community Land Model CLM2 [Bonan et al., 2002]. This new model includes components treating hydrological and biogeochemical processes, dynamic vegetation, and biogeophysics. Because of the increased complexity of this new model and since a complete description is available online, users of CAM 5.0 interested in CLM should consult this documentation at `http://www.cgd.ucar.edu/tss/clm/`. A discussion is provided here only of the component of CLM which controls surface exchange processes.

Land surface fluxes of momentum, sensible heat, and latent heat are calculated from Monin-Obukhov similarity theory applied to the surface (i.e. constant flux) layer. The zonal τ_x and meridional τ_y momentum fluxes (kg m^{-1}s^{-2}), sensible heat H (W m^{-2}) and water vapor E (kg m^{-2}s^{-1}) fluxes between the surface and the lowest model level z_1 are:

$$\tau_x = -\rho_1 \overline{(u'w')} = -\rho_1 u_*^2 (u_1/V_a) = \rho_1 \frac{u_s - u_1}{r_{am}} \tag{4.244}$$

$$\tau_y = -\rho_1 \overline{(v'w')} = -\rho_1 u_*^2 (v_1/V_a) = \rho_1 \frac{v_s - v_1}{r_{am}} \tag{4.245}$$

$$H = \rho_1 c_p (\overline{w'\theta'}) = -\rho_1 c_p u_* \theta_* = \rho_1 c_p \frac{\theta_s - \theta_1}{r_{ah}} \tag{4.246}$$

$$E = \rho_1 (\overline{w'q'}) = -\rho_1 u_* q_* = \rho_1 \frac{q_s - q_1}{r_{aw}} \tag{4.247}$$

$$r_{am} = V_a/u_*^2 \tag{4.248}$$

$$r_{ah} = (\theta_1 - \theta_s)/u_*\theta_* \tag{4.249}$$

$$r_{aw} = (q_1 - q_s)/u_* q_* \tag{4.250}$$

where ρ_1, u_1, v_1, θ_1 and q_1 are the density (kg m^{-3}), zonal wind (m s^{-1}), meridional wind (m s^{-1}), air potential temperature (K), and specific humidity (kg kg^{-1}) at the lowest model level. By definition, the surface winds u_s and v_s equal zero. The symbol θ_1 represents temperature, and q_1 is specific humidity at surface. The terms r_{am}, r_{ah}, and r_{aw} are the aerodynamic resistances (s m^{-1}) for momentum, sensible heat, and water vapor between the lowest model level at height

z_1 and the surface at height $z_{0m} + d$ [$z_{0h} + d$]. Here z_{0m} [z_{0h}] is the roughness length (m) for momentum [scalar] fluxes, and d is the displacement height (m).

For the vegetated fraction of the grid, $\theta_s = T_{af}$ and $q_s = q_{af}$, where T_{af} and q_{af} are the air temperature and specific humidity within canopy space. For the non-vegetated fraction, $\theta_s = T_g$ and $q_s = q_g$, where T_g and q_g are the air temperature and specific humidity at ground surface. These terms are described by Dai et al. [2001].

Roughness lengths and zero-plane displacement

The aerodynamic roughness z_{0m} is used for wind, while the thermal roughness z_{0h} is used for heat and water vapor. In general, z_{0m} is different from z_{0h}, because the transfer of momentum is affected by pressure fluctuations in the turbulent waves behind the roughness elements, while for heat and water vapor transfer no such dynamical mechanism exists. Rather, heat and water vapor must ultimately be transferred by molecular diffusion across the interfacial sublayer. Over bare soil and snow cover, the simple relation from Zilitinkevich [1970] can be used [Zeng and Dickinson, 1998]:

$$\ln \frac{z_{0m}}{z_{0h}} = a \left(\frac{u_* z_{0m}}{\nu} \right)^{0.45} \tag{4.251}$$

$$a = 0.13 \tag{4.252}$$

$$\nu = 1.5 \times 10^{-5} \mathrm{m^2 s^{-1}} \tag{4.253}$$

Over canopy, the application of energy balance

$$R_n - H - L_v E = 0 \tag{4.254}$$

(where R_n is the net radiation absorbed by the canopy) is equivalent to the use of different z_{0m} versus z_{0h} over bare soil, and hence thermal roughness is not needed over canopy [Zeng et al., 1998].

The roughness z_{0m} is proportional to canopy height, and is also affected by fractional vegetation cover, leaf area index, and leaf shapes. The roughness is derived from the simple relationship $z_{0m} = 0.07\, h_c$, where h_c is the canopy height. Similarly, the zero-plane displacement height d is proportional to canopy height, and is also affected by fractional vegetation cover, leaf area index, and leaf shapes. The simple relationship $d/h_c = 2/3$ is used to obtain the height.

Monin-Obukhov similarity theory

(1) Turbulence scaling parameters

A length scale (the Monin-Obukhov length) L is defined by

$$L = \frac{\theta_v u_*^2}{kg\theta_{v*}} \tag{4.255}$$

where k is the von Kàrman constant, and g is the gravitational acceleration. $L > 0$ indicates stable conditions, $L < 0$ indicates unstable conditions, and $L = \infty$ applies to neutral conditions. The virtual potential temperature θ_v is defined by

$$\theta_v = \theta_1(1 + 0.61 q_1) = T_a \left(\frac{p_s}{p_l} \right)^{R/c_p} (1 + 0.61 q_1) \tag{4.256}$$

where T_1 and q_1 are the air temperature and specific humidity at height z_1 respectively, θ_1 is the atmospheric potential temperature, p_l is the atmospheric pressure, and p_s is the surface pressure. The surface friction velocity u_* is defined by

$$u_*^2 = [\overline{u'w'}^2 + \overline{v'w'}^2]^{1/2} \tag{4.257}$$

The temperature scale θ_* and θ_{*v} and a humidity scale q_* are defined by

$$\theta_* = -\overline{w'\theta'}/u_* \tag{4.258}$$

$$q_* = -\overline{w'q'}/u_* \tag{4.259}$$

$$\begin{aligned} \theta_{v*} &= -\overline{w'\theta'_v}/u_* \\ &\approx -(\overline{w'\theta'} + 0.61\overline{\theta}\overline{w'q'})/u_* \\ &= \theta_* + 0.61\overline{\theta}q_* \end{aligned} \tag{4.260}$$

(where the mean temperature $\overline{\theta}$ serves as a reference temperature in this linearized form of θ_v).

The stability parameter is defined as

$$\varsigma = \frac{z_1 - d}{L} \quad , \tag{4.261}$$

with the restriction that $-100 \leqslant \varsigma \leqslant 2$. The scalar wind speed is defined as

$$V_a^2 = u_1^2 + v_1^2 + U_c^2 \tag{4.262}$$

$$U_c = \begin{cases} 0.1 \text{ ms}^{-1} & \text{, if } \varsigma \geqslant 0 \text{ (stable)} \\ \beta w_* = \beta \left(z_i \frac{g}{\overline{\theta}_v} \theta_{v*} u_* \right)^{1/3} & \text{, if } \varsigma < 0 \text{ (unstable)} . \end{cases} \tag{4.263}$$

Here w_* is the convective velocity scale, z_i is the convective boundary layer height, and $\beta = 1$. The value of z_i is taken as 1000 m

(2) Flux-gradient relations [Zeng et al., 1998]

The flux-gradient relations are given by:

$$\frac{k(z_1 - d)}{\theta_*} \frac{\partial \theta}{\partial z} = \phi_h(\varsigma) \tag{4.264}$$

$$\frac{k(z_1 - d)}{q_*} \frac{\partial q}{\partial z} = \phi_q(\varsigma) \tag{4.265}$$

$$\phi_h = \phi_q \tag{4.266}$$

$$\phi_m(\varsigma) = \begin{cases} (1 - 16\varsigma)^{-1/4} & \text{for } \varsigma < 0 \\ 1 + 5\varsigma & \text{for } 0 < \varsigma < 1 \end{cases} \tag{4.267}$$

$$\phi_h(\varsigma) = \begin{cases} (1 - 16\varsigma)^{-1/2} & \text{for } \varsigma < 0 \\ 1 + 5\varsigma & \text{for } 0 < \varsigma < 1 \end{cases} \tag{4.268}$$

Under very unstable conditions, the flux-gradient relations are taken from Kader and Yaglom [1990]:

$$\phi_m = 0.7k^{2/3}(-\varsigma)^{1/3} \tag{4.269}$$

$$\phi_h = 0.9k^{4/3}(-\varsigma)^{-1/3} \tag{4.270}$$

To ensure the functions $\phi_m(\varsigma)$ and $\phi_h(\varsigma)$ are continuous, the simplest approach (i.e., without considering any transition regions) is to match the above equations at $\varsigma_m = -1.574$ for $\phi_m(\varsigma)$ and $\varsigma_h = -0.465$ for $\phi_h(\varsigma)$.

Under very stable conditions (i.e., $\varsigma > 1$), the relations are taken from Holtslag et al. [1990]:

$$\phi_m = \phi_h = 5 + \varsigma \tag{4.271}$$

(3) Integral forms of the flux-gradient relations

Integration of the wind profile yields:

$$V_a = \frac{u_*}{k} f_M(\varsigma) \tag{4.272}$$

$$f_M(\varsigma) = \left\{ \left[\ln\left(\frac{\varsigma_m L}{z_{0m}}\right) - \psi_m(\varsigma_m) \right] + 1.14[(-\varsigma)^{1/3} - (-\varsigma_m)^{1/3}] \right\}, \quad \varsigma < \varsigma_m = -1.574 \tag{4.272a}$$

$$f_M(\varsigma) = \left[\ln\left(\frac{z_1 - d}{z_{0m}}\right) - \psi_m(\varsigma) + \psi_m\left(\frac{z_{0m}}{L}\right) \right], \quad \varsigma_m < \varsigma < 0 \tag{4.272b}$$

$$f_M(\varsigma) = \left[\ln\left(\frac{z_1 - d}{z_{0m}}\right) + 5\varsigma \right], \quad 0 < \varsigma < 1 \tag{4.272c}$$

$$f_M(\varsigma) = \left\{ \left[\ln\left(\frac{L}{z_{0m}}\right) + 5 \right] + [5\ln(\varsigma) + \varsigma - 1] \right\}, \quad \varsigma > 1 \tag{4.272d}$$

Integration of the potential temperature profile yields:

$$\theta_1 - \theta_s = \frac{\theta_*}{k} f_T(\varsigma) \tag{4.273}$$

$$f_T(\varsigma) = \left\{ \left[\ln\left(\frac{\varsigma_h L}{z_{0h}}\right) - \psi_h(\varsigma_h) \right] + 0.8[(-\varsigma_h)^{-1/3} - (-\varsigma)^{-1/3}] \right\}, \quad \varsigma < \varsigma_h = -0.465 \tag{4.273a}$$

$$f_T(\varsigma) = \left[\ln\left(\frac{z_1 - d}{z_{0h}}\right) - \psi_h(\varsigma) + \psi_h\left(\frac{z_{0h}}{L}\right) \right], \quad \varsigma_h < \varsigma < 0 \tag{4.273b}$$

$$f_T(\varsigma) = \left[\ln\left(\frac{z_1 - d}{z_{0h}}\right) + 5\varsigma \right], \quad 0 < \varsigma < 1 \tag{4.273c}$$

$$f_T(\varsigma) = \left\{ \left[\ln\left(\frac{L}{z_{0h}}\right) + 5 \right] + [5\ln(\varsigma) + \varsigma - 1] \right\}, \quad \varsigma > 1 \tag{4.273d}$$

The expressions for the specific humidity profiles are the same as those for potential temperature except that $(\theta_1 - \theta_s)$, θ_* and z_{0h} are replaced by $(q_1 - q_s)$, q_* and z_{0q} respectively. The stability functions for $\varsigma < 0$ are

$$\psi_m = 2\ln\left(\frac{1+\chi}{2}\right) + \ln\left(\frac{1+\chi^2}{2}\right) - 2\tan^{-1}\chi + \frac{\pi}{2} \tag{4.274}$$

$$\psi_h = \psi_q = 2\ln\left(\frac{1+\chi^2}{2}\right) \tag{4.275}$$

where

$$\chi = (1 - 16\varsigma)^{1/4} \tag{4.276}$$

Note that the CLM code contains extra terms involving z_{0m}/ς, z_{0h}/ς, and z_{0q}/ς for completeness. These terms are very small most of the time and hence are omitted in Eqs. 4.272 and 4.273.

In addition to the momentum, sensible heat, and latent heat fluxes, land surface albedos and upward longwave radiation are needed for the atmospheric radiation calculations. Surface albedos depend on the solar zenith angle, the amount of leaf and stem material present, their optical properties, and the optical properties of snow and soil. The upward longwave radiation is the difference between the incident and absorbed fluxes. These and other aspects of the land surface fluxes have been described by Dai et al. [2001].

4.11.2 Ocean

The bulk formulas used to determine the turbulent fluxes of momentum (stress), water (evaporation, or latent heat), and sensible heat into the atmosphere over ocean surfaces are

$$(\boldsymbol{\tau}, E, H) = \rho_A \, |\Delta \, \boldsymbol{v}| \, (C_D \Delta \, \boldsymbol{v}, C_E \Delta \, q, C_p C_H \Delta\theta), \tag{4.277}$$

where ρ_A is atmospheric surface density and C_p is the specific heat. Since CAM 5.0 does not allow for motion of the ocean surface, the velocity difference between surface and atmosphere is $\Delta \, \boldsymbol{v} = \boldsymbol{v}_A$, the velocity of the lowest model level. The potential temperature difference is $\Delta\theta = \theta_A - T_s$, where T_s is the surface temperature. The specific humidity difference is $\Delta \, q = q_A - q_s(T_s)$, where $q_s(T_s)$ is the saturation specific humidity at the sea-surface temperature.

In (4.277), the transfer coefficients between the ocean surface and the atmosphere are computed at a height Z_A and are functions of the stability, ζ:

$$C_{(D,E,H)} = \kappa^2 \left[\ln\left(\frac{Z_A}{Z_{0m}}\right) - \psi_m \right]^{-1} \left[\ln\left(\frac{Z_A}{Z_{0(m,e,h)}}\right) - \psi_{(m,s,s)} \right]^{-1} \tag{4.278}$$

where $\kappa = 0.4$ is von Kármán's constant and $Z_{0(m,e,h)}$ is the roughness length for momentum, evaporation, or heat, respectively. The integrated flux profiles, ψ_m for momentum and ψ_s for scalars, under stable conditions ($\zeta > 0$) are

$$\psi_m(\zeta) = \psi_s(\zeta) = -5\zeta. \tag{4.279}$$

For unstable conditions ($\zeta < 0$), the flux profiles are

$$\begin{aligned} \psi_m(\zeta) =& 2\ln[0.5(1+X)] + \ln[0.5(1+X^2)] \\ & - 2\tan^{-1} X + 0.5\pi, && (4.280) \\ \psi_s(\zeta) =& 2\ln[0.5(1+X^2)], && (4.281) \\ X =& (1-16\zeta)^{1/4}. && (4.282) \end{aligned}$$

The stability parameter used in (4.279)–(4.282) is

$$\zeta = \frac{\kappa \, g \, Z_A}{u^{*2}} \left(\frac{\theta^*}{\theta_v} + \frac{Q^*}{(\epsilon^{-1} + q_A)} \right), \tag{4.283}$$

where the virtual potential temperature is $\theta_v = \theta_A(1 + \epsilon q_A)$; q_A and θ_A are the lowest level atmospheric humidity and potential temperature, respectively; and $\epsilon = 0.606$. The turbulent velocity scales in (4.283) are

$$\begin{aligned} u^* =& C_D^{1/2} |\Delta \boldsymbol{v}|, \\ (Q^*, \theta^*) =& C_{(E,H)} \frac{|\Delta \boldsymbol{v}|}{u^*} (\Delta q, \Delta\theta). \end{aligned} \tag{4.284}$$

Over oceans, $Z_{0e} = 9.5 \times 10^{-5}$ m under all conditions and $Z_{0h} = 2.2 \times 10^{-9}$ m for $\zeta > 0$, $Z_{0h} = 4.9 \times 10^{-5}$ m for $\zeta \leq 0$, which are given in Large and Pond [1982]. The momentum roughness length depends on the wind speed evaluated at 10 m as

$$\begin{aligned} Z_{om} &= 10 \exp\left[-\kappa \left(\frac{c_4}{U_{10}} + c_5 + c_6 U_{10}\right)^{-1}\right], \\ U_{10} &= U_A \left[1 + \frac{\sqrt{C_{10}^N}}{\kappa} \ln\left(\frac{Z_A}{10} - \psi_m\right)\right]^{-1}, \end{aligned} \tag{4.285}$$

where $c_4 = 0.0027$ m s^{-1}, $c_5 = 0.000142$, $c_6 = 0.0000764$ m^{-1} s, and the required drag coefficient at 10-m height and neutral stability is $C_{10}^N = c_4 U_{10}^{-1} + c_5 + c_6 U_{10}$ as given by Large et al. [1994].

The transfer coefficients in (4.277) and (4.278) depend on the stability following (4.279)–(4.282), which itself depends on the surface fluxes (4.283) and (4.284). The transfer coefficients also depend on the momentum roughness, which itself varies with the surface fluxes over oceans (4.285). The above system of equations is solved by iteration.

4.11.3 Sea Ice

The fluxes between the atmosphere and sea ice are described in detail in the sea-ice model documentation.

4.12 Dry Adiabatic Adjustment

If a layer is unstable with respect to the dry adiabatic lapse rate, dry adiabatic adjustment is performed. The layer is stable if

$$\frac{\partial T}{\partial p} < \frac{\kappa T}{p}. \tag{4.286}$$

In finite–difference form, this becomes

$$T_{k+1} - T_k < C1_{k+1}(T_{k+1} + T_k) + \delta, \tag{4.287}$$

where

$$C1_{k+1} = \frac{\kappa(p_{k+1} - p_k)}{2p_{k+1/2}} \ . \tag{4.288}$$

If there are any unstable layers in the top three model layers, the temperature is adjusted so that (4.287) is satisfied everywhere in the column. The variable δ represents a convergence criterion. The adjustment is done so that sensible heat is conserved,

$$c_p(\hat{T}_k \Delta p_k + \hat{T}_{k+1}\Delta p_{k+1}) = c_p(T_k \Delta p_k + T_{k+1}\Delta p_{k+1}), \tag{4.289}$$

and so that the layer has neutral stability:

$$\hat{T}_{k+1} - \hat{T}_k = C1_{k+1}(\hat{T}_{k+1} + \hat{T}_k)\,. \tag{4.290}$$

As mentioned above, the hats denote the variables after adjustment. Thus, the adjusted temperatures are given by

$$\hat{T}_{k+1} = \frac{\Delta p_k}{\Delta p_{k+1} + \Delta p_k C2_{k+1}} T_k + \frac{\Delta p_{k+1}}{\Delta p_{k+1} + \Delta p_k C2_{k+1}} T_{k+1}, \tag{4.291}$$

and

$$\hat{T}_k = C2_{k+1}\hat{T}_{k+1}, \tag{4.292}$$

where

$$C2_{k+1} = \frac{1 - C1_{k+1}}{1 + C1_{k+1}} \ . \tag{4.293}$$

Whenever the two layers undergo dry adjustment, the moisture is assumed to be completely mixed by the process as well. Thus, the specific humidity is changed in the two layers in a conserving manner to be the average value of the original values,

$$\hat{q}_{k+1} = \hat{q}_k = (q_{k+1}\Delta p_{k+1} + q_k \Delta p_k)/(\Delta p_{k+1} + \Delta p_k). \tag{4.294}$$

The layers are adjusted iteratively. Initially, $\delta = 0.01$ in the stability check (4.287). The column is passed through from $k = 1$ to a user-specifiable lower level (set to 3 in the standard model configuration) up to 15 times; each time unstable layers are adjusted until the entire column is stable. If convergence is not reached by the 15th pass, the convergence criterion is doubled, a message is printed, and the entire process is repeated. If δ exceeds 0.1 and the column is still not stable, the model stops.

As indicated above, the dry convective adjustment is only applied to the top three levels of the standard model. The vertical diffusion provides the stabilizing vertical mixing at other levels. Thus, in practice, momentum is mixed as well as moisture and potential temperature in the unstable case.

4.13 Prognostic Greenhouse Gases

The principal greenhouse gases whose longwave radiative effects are included in CAM 5.0 are H_2O, CO_2, O_3, CH_4, N_2O, CFC11, and CFC12. The prediction of water vapor is described elsewhere in this chapter, and CO_2 is assumed to be well mixed. Monthly O_3 fields are specified as input, as described in chapter 6. The radiative effects of the other four greenhouse gases (CH_4, N_2O, CFC11, and CFC12) may be included in CAM 5.0 through specified concentration distributions [Kiehl et al., 1998] or prognostic concentrations [Boville et al., 2001].

The specified distributions are globally uniform in the troposphere. Above a latitudinally and seasonally specified tropopause height, the distributions are zonally symmetric and decrease upward, with a separate latitude-dependent scale height for each gas.

Prognostic distributions are computed following Boville et al. [2001]. Transport equations for the four gases are included, and losses have been parameterized by specified zonally symmetric loss frequencies: $\partial q/\partial t = -\alpha(y, z, t)q$. Monthly averaged loss frequencies, α, are obtained from the two-dimensional model of Garcia and Solomon [1994].

We have chosen to specify globally uniform surface concentrations of the four gases, rather than their surface fluxes. The surface sources are imperfectly known, particularly for CH_4 and N_2O in preindustrial times. Even given constant sources and reasonable initial conditions, obtaining equilibrium values for the loading of these gases in the atmosphere can take many years. CAM 5.0 was designed for tropospheric simulation with relatively coarse vertical resolution in the upper troposphere and lower stratosphere. It is likely that the rate of transport into the stratosphere will be misrepresented, leading to erroneous loading and radiative forcing if surface fluxes are specified. Specifying surface concentrations has the advantage that we do not need to worry much about the atmospheric lifetime. However, we cannot examine observed features such as the interhemispheric gradient of the trace gases. For climate change experiments, the specified surface concentrations are varied but the stratospheric loss frequencies are not.

Oxidation of CH_4 is an important source of water vapor in the stratosphere, contributing about half of the ambient mixing ratio over much of the stratosphere. Although CH_4 is not generally oxidized directly into water vapor, this is not a bad approximation, as shown by Le Texier et al. [1988]. In CAM 5.0, it is assumed that the water vapor (volume mixing ratio) source is twice the CH_4 sink. This approach was also taken by Mote et al. [1993] for middle atmosphere studies with an earlier version of the CCM. This part of the water budget is of some importance in climate change studies, because the atmospheric CH_4 concentrations have increased rapidly with time and this increase is projected to continue into the next century (e.g., Alcamo et al. [1995]) The representation of stratospheric water vapor in CAM 5.0 is necessarily crude, since there are few levels above the tropopause. However, the model is capable of capturing the main features of the CH_4 and water distributions.

Chapter 5

Extensions to CAM

5.1 Introduction

This section contains a description of the neutral constituent chemical options available CAM and WACCM4.0, including different chemical schemes, emissions, boundary conditions, lightning, dry depositions and wet removal; 2) the photolysis approach; 3) numerical algorithms used to solve the corresponding set of ordinary differential equations.; 4) additions to superfast chemistry.

5.2 Chemistry

5.2.1 Chemistry Schemes

For CAM-Chem, an extensive tropospheric chemistry option is available (trop mozart), as well as an extensive tropospheric and stratospheric chemistry (trop-strat mozart) as discussed in detail in Lamarque et al. [2012], including a list of all species and reactions. Furthermore, a superfast chemistry option is available for CAM, as discussed in Section 5.5. For each chemical scheme, CAM-chem uses the same chemical preprocessor as MOZART-4. This preprocessor generates Fortran code for each specific chemical mechanism, allowing for an easy update and modification of existing chemical mechanisms. In particular, the generated code provides two chemical solvers, one explicit and one semi-implicit, which the user specifies based on the chemical lifetime of each species. For all supported compsets, this generated code is available in a sub-directory of atm/src/chemistry.

The Bulk Aerosol Model

CAM4-chem uses the bulk aerosol model discussed in Lamarque et al. [2005] and Emmons et al. [2010]. This model has a representation of aerosols based on the work by Tie et al. [2002] and Tie et al. [2005*a*], i.e. sulfate aerosol is formed by the oxidation of SO_2 in the gas phase (by reaction with the hydroxyl radical) and in the aqueous phase (by reaction with ozone and hydrogen peroxide). Furthermore, the model includes a representation of ammonium nitrate that is dependent on the amount of sulfate present in the air mass following the parameterization of gas/aerosol partitioning by [Metzger et al., 2002]. Because only the bulk mass is calculated, a lognormal distribution is assumed for all aerosols using different mean radius and geometric standard deviation [Liao et al., 2003]. The conversion of carbonaceous aerosols (organic and black) from hydrophobic to hydrophilic is assumed to occur within a fixed 1.6 days [Tie et al., 2005*a*]. Natural aerosols (desert dust and sea salt) are implemented following Mahowald et al. [2006*a*] and Mahowald et al. [2006*c*] and the sources of these aerosols are derived based on the model calculated wind speed and surface conditions. In addition, secondary-organic aerosols (SOA) are linked to the gas-phase chemistry through the oxidation of atmospheric non-methane hydrocarbons (NMHCs), as in Lack et al. [2004].

CAM-Chem using the Modal Aerosol Model

CAM-Chem has the ability to run with two modal aerosols models, the MAM3 and MAM7 [Liu et al., 2012]. The Modal Aerosols Model, is described in Section 4.8.2. In CAM5-Chem,

the gase-phase chemistry is coupled to Modal Aerosol Model in chemical species O_3, OH, HO_2 and NO_3, as derived from the chemical mechanism and not from a climatoloty. The tropospheric gas-phase and heterogeneous reactions as discribed in Section 4.8.2. are added to the standard MAM chemical mechanism.

Trop MOZART Chemistry

The extensive tropospheric chemistry scheme represents a minor update to the MOZART-4 mechanism, fully described in Emmons et al. [2010]. In particular, we have included C_2H_2, HCOOH, HCN and CH_3CN. Reaction rates have been updated to JPL-2006 [Sander, S. P., et al., 2006]. A minor update has been made to the isoprene oxidation scheme, including an increase in the production of glyoxal. This mechanism is mainly of relevance in the troposphere and is intended for simulations for which long-term trends in the stratospheric composition are not crucial. Therefore, in this configuration, the stratospheric distributions of long-lived species (see discussion below) are specified from previously performed WACCM simulations [Garcia et al., 2007]; see Section 5.2.3).

Trop-Strat MOZART Chemistry

The extensive tropospheric and stratospheric chemistry includes the full stratospheric chemistry from WACCM4.0, with an updated enforcement of the conservation of total chlorine and total bromine under advection to improve the performance of the model in simulating the ozone hole. In addition, we have updated the heterogeneous chemistry module to reflect that the model was underestimating the supercooled ternary solution (STS) surface area density (SAD), see more detail in Section 5.6; [Lamarque et al., 2012], Kinnison et al, 2012, (in prepareation).

SOA calculation in CAM-Chem

An SOA simulation of intermediate complexity is also available in CAM-Chem. This is based on the 2-product model scheme of Odum et al. [1997*b*], as implemented in CAM-Chem by Heald et al. [2008]. This treats the products of VOC oxidation as semi-volatile species, which re-partition every time step based on the temperature (enthalpy of vaporization of 42 kJmol-1) and organic aerosol mass available for condensation of vapours [Pankow, 1994]. In CAM-Chem we treat secondary organic aerosol formation from the products of isoprene, monoterpene and aromatic (benzene, toluene and xylene) oxidation by OH, O_3 and NO_3. The yields and partitioning coefficients are based on smog chamber studies [Griffin et al., 1999; Henze et al., 2008; Ng et al., 2007*b*]. The SOA calculation is setup to run with biogenic emissions calucated by the MEGAN2.1 model (see Section 5.2.2).

5.2.2 Emissions

Surface emissions are used in as a flux boundary condition for the diffusion equation of all applicable tracers in the planetary boundary-layer scheme. The surface flux files used in the released version are discussed in Lamarque et al. [2010*b*] and conservatively remapped from their original resolution (monthly data available every decade at 0.5x0.5) to (monthly data every year at 1.9x2.5). The remapping is made offline to avoid the internal remapping, which consists

of a simple linear interpolation and therefore does not ensure exact conservation of emissions between resolutions.

Emissions of Trace Gases

Emissions for historic and future model simulations are based on ACCMIP (Lamarque et al. [2010*b*]) and different RCP scenarios, which are available for the years 1850-2000, and 2000-2100.

Additional emissions are available for a short period covering 1992-2010, as discussed in Emmons et al. [2010]. More specifically, for 1992-1996, which is prior to satellite-based fire inventories, monthly mean averages of the fire emissions for 1997-2008 from GFED2 [van der Werf et al., 2006, and updates] are used for each year. For 2009-2010, fire emissions are from FINN (Fire INventory from NCAR) [Wiedinmyer et al., 2011]. If running with FINN fire emissions, additional species are availabel: NO_2, BIGALD, CH_3COCHO, CH_3COOH, CRESOL, GLYALD, HYAC, MACR, MVK. Most of the anthropogenic emissions come from the POET (Precursors of Ozone and their Effects in the Troposphere) database for 2000 [Granier et al., 2005]. The anthropogenic emissions (from fossil fuel and biofuel combustion) of black and organic carbon determined for 1996 are from Bond et al. [2004]. For SO_2 and NH_3, anthropogenic emissions are from the EDGAR-FT2000 and EDGAR-2 databases, respectively (http://www.mnp.nl/edgar/).

For Asia, these inventories have been replaced by the Regional Emission inventory for Asia (REAS) with the corresponding annual inventory for each year simulated [Ohara et al., 2007]. Only the Asian emissions from REAS vary each year, all other emissions are repeated annually for each year of simulation. The DMS emissions are monthly means from the marine biogeochemistry model HAMOCC5, representative of the year 2000 [Kloster et al., 2006].

Additional emissions (volcanoes and aircraft) are included as three-dimensional arrays, conservatively-remapped to the CAM-chem grid. The volcanic emission are from Dentener et al. [2006*b*] and the aircraft (NO_2) emissions are from Lamarque et al. [2010*b*]. In the case of volcanic emissions (SO_2 and SO_2), an assumed 2% of the total sulfur mass is directly released as SO_2. SO_2 emissions from continuously outgassing volcanoes are from the GEIAv1 inventory (Andres and Kasgnoc, 1998). Totals for each year and emitted species are listed in Lamarque et al. [2012], Table 7. Aerosol Emissions available to be used in CAM5-Chem are described above (Section 4.8.1.).

Biogenic emissions

Biogenic emissions can be calculated by the Model of Emissions of Gases and Aerosols from Nature version 2.1 (MEGAN2.1) [Guenther et al., 2012]. In this case, MEGAN2.1 is coupled to the CESM atmosphere and land model. Biogenic emissions of volatile organic compounds (i.e. isoprene and monoterpenes) are calculated based upon emission factors, land cover (LAI and PFT), and driving meteorological variables. CO_2 effect on isoprene emission is also included [Heald et al., 2009]. Emission factors of different MEGAN compounds can be specified from mapped files or based on PFTs. These are made available for atmospheric chemistry, unless the user decides to explicitly set those emissions using pre-defined (i.e. contained in a file) gridded values. Details of this implementation in the CLM3 are discussed in Heald et al. [2008] and

Guenther et al. [2012]: Vegetation in the CLM model is described by 17 plant function types (PFTs, see Lamarque et al. [2012, Table 1]). Present-day land cover data such as leaf area index are consistent with MODIS land surface data sets [Lawrence and Chase, 2007]. Alternate land cover and density can be either specified or interactively simulated with the dynamic vegetation model (CLMCNDV) or the carbon nitrogen model (CLMCN) of the CLM for any time period of interest. Additional namelist parameters have been included to facilitate the mapping between the emissions in MEGAN2.1 (147 species) and the chemical mechanism. Surface emissions without biogenic emissions have to be used if the MEGAN2.1 model produces biogenic emissions to prevent double counting.

5.2.3 Boundary conditions

Lower boundary conditions

For all long-lived species (methane and longer lifetimes, in addition to hydrogen and methyl bromide) [Lamarque et al., 2012, see Table 3], the surface concentrations are specified using the historical reconstruction from Meinshausen et al. [2011]. In addition, for CO_2 and CH_4, an observationally-based seasonal cycle and latitudinal gradient are imposed on the annual average values provided by Meinshausen et al. [2011]. These values are used in the model by overwriting at each time step the corresponding model mixing ratio in the lowest model level with the time (and latitude, if applicable) interpolated specified mixing ratio.

Specified stratospheric distributions

For the trop-mozart chemistry, no stratospheric chemistry is explicitly represented in the model. Therefore, it is necessary to ensure a proper distribution of some chemically-active stratospheric (namely O_3, NO, NO_2, HNO_3, CO, CH_4, N_2O, and N_2O_5) species, as is the case for MOZART-4. This monthly-mean climatological distribution is obtained from WACCM simulations covering 1950-2005 [Garcia et al., 2007]. Because of the vast changes that occur over that time period, our data distribution provides files for three separate periods: 1950-1959, 1980-1989 and 1996-2005. This ensure that users can perform simulations with a stratospheric climatology representative of the pre-CFC era, as well as during the high CFC and post-Pinatubo era. Additional datasets for different RCP runs are also available or can easily be constructed if necessary.

Upper boundary condition

The model top at about 40km is considered a rigid lid (no flux across that boundary) for all chemical species. For trop-mozart

5.2.4 Lightning

The emissions of NO from lightning are included as in Emmons et al. [2010], i.e. using the Price parameterization ([Price and Rind, 1992; Price et al., 1997*a*], scaled to provide a global annual emission of 3-4 Tg(N)/year. The vertical distribution follows DeCaria et al. [2006] as in Emmons et al. [2010]. In addition, the strength of intra-cloud (IC) lightning strikes is assumed to be equal to cloud-to-ground strikes, as recommended by Ridley et al. [2005].

Lightning NOx can be modifid in the namelist. For CAM5-Chem, lightning NOx is increased by a factor of 3 to reach the same emissions of 3-4 Tg(N)/year.

5.2.5 Dry deposition

Dry deposition is represented following the resistance approach originally described in Wesely [1989], as discussed in Emmons et al. [2010], this earlier paper was subsequently updated and we have included all updates [Walmsley and Wesely, 1996; Wesely and Hicks, 2000]. Following this approach, all deposited chemical species (the specific list of deposited species is defined along with the chemical mechanisms, see section 4) are mapped to a weighted-combination of ozone and sulfur dioxide depositions; this combination represents a definition of the ability of each considered species to oxidize or to be taken up by water. In particular, the latter is dependent on the effective Henry's law coefficient. While this weighting is applicable to many species, we have included specific representations for CO/H_2 [Yonemura et al., 2000; Sanderson et al., 2003] and peroxyacetylnitrate (PAN) [Sparks et al., 2003]. Furthermore, it is assumed that the surface resistance for SO_2 can be neglected [Walcek et al., 1986]. Finally, following Cooke et al. [1999], the deposition velocities of black and organic carbonaceous aerosols are specified to be 0.1 cm/s over all surfaces. Dust and sea-salt are represented following Mahowald et al. [2006*a*] and Mahowald et al. [2006*c*].

The computation of deposition velocities in CAM-chem takes advantage of its coupling to the Community Land Model (CLM; http://www.cesm.ucar.edu/ models/cesm1.0/ clm/index.shtml). In particular, the computation of surface resistances in CLM leads to a representation at the level of each plant functional type (Table 1) of the various drivers for deposition velocities. The grid-averaged velocity is computed as the weighted-mean over all land cover types available at each grid point. This ensures that the impact on deposition velocities from changes in land cover, land use or climate is taken into account. All species in the mechanism are per default affected by dry deposition if depostion velocities are defined in the model.

5.2.6 Wet removal

Wet removal of soluble gas-phase species is the combination of two processes: in-cloud, or nucleation scavenging (rainout), which is the local uptake of soluble gases and aerosols by the formation of initial cloud droplets and their conversion to precipitation, and below-cloud, or impaction scavenging (washout), which is the collection of soluble species from the interstitial air by falling droplets or from the liquid phase via accretion processes [e.g. Rotstayn and Lohmann, 2002].

Removal is modeled as a simple first-order loss process $X_{iscav} = X_i \cdot F \cdot (1 - exp(-\lambda\ \Delta t))$. In this formula, X_{iscav} is the species mass (in kg) and X_i scavenged in time step Δt , F is the fraction of the grid box from which tracer is being removed, and λ is the loss rate. In-cloud scavenging is proportional to the amount of condensate converted to precipitation, and the loss rate depends on the amount of cloud water, the rate of precipitation formation, and the rate of tracer uptake by the liquid phase. Below-cloud scavenging is proportional to the precipitation flux in each layer and the loss rate depends on the precipitation rate and either the rate of tracer

uptake by the liquid phase (for accretion processes), the mass-transfer rate (for highly soluble gases and small aerosols), or the collision rate (for larger aerosols).

In CAM-chem two separate parameterizations are available: Horowitz et al. [2003] from MOZART-2 and Neu and Prather [2012]. The distinguishing features of the Neu and Prather scheme are related to three aspects of the parameterization: 1) the partitioning between in-cloud and below cloud scavenging, 2) the treatment of soluble gas uptake by ice and 3) the Neu and Prather scheme uniquely accounts for the spatial distribution of clouds in a column and the overlap of condensate and precipitation. Given a cloud fraction and precipitation rate in each layer, the scheme determines the fraction of the gridbox exposed to precipitation from above and that exposed to new precipitation formation under the assumption of maximum overlap of the precipitating fraction. Each model level is partitioned into as many as four sections, each with a gridbox fraction, precipitation rate, and precipitation diameter: 1) Cloudy with precipitation falling through from above; 2) Cloudy with no precipitation falling through from above; 3) Clear sky with precipitation falling through from above; 4) Clear sky with no precipitation falling from above. Any new precipitation formation is spread evenly between the cloudy fractions (1 and 2). In region 3, we assume a constant rate of evaporation that reduces both the precipitation area and amount so that the rain rate remains constant. Between levels, we average the properties of the precipitation and retain only two categories, precipitation falling into cloud and precipitation falling into ambient air, at the top boundary of each level. If the precipitation rate drops to zero, we assume full evaporation and random overlap with any precipitating levels below. Our partitioning of each level and overlap assumptions are in many ways similar to those used for the moist physics in the ECMWF model [Jakob and Klein, 2000].

The transfer of soluble gases into liquid condensate is calculated using Henry's Law, assuming equilibrium between the gas and liquid phase. Nucleation scavenging by ice, however, is treated as a burial process in which trace gas species deposit on the surface along with water vapor and are buried as the ice crystal grows. Kärcher and Voigt [2006] have found that the burial model successfully reproduces the molar ratio of HNO_3 to H_2O on ice crystals as a function of temperature for a large number of aircraft campaigns spanning a wide variety of meteorological conditions. We use the empirical relationship between the HNO_3:H_2O molar ratio and temperature given by Kärcher and Voigt [2006] to determine in-cloud scavenging during ice particle formation, which is applied to nitric acid only. Below-cloud scavenging by ice is calculated using a rough representation of the riming process modeled as a collision-limited first order loss process. Neu and Prather [2012] provide a full description of the scavenging algorithm.

On the other hand, the Horowitz approach uses the rain generation diagnostics from the large-scale and convection precipitation parameterizations in CAM; equilibrium between gas-phase and liquid phase is then assumed based on the effective Henry's law.

5.3 Photolytic Approach (Neutral Species)

The calculation of the photolysis coefficients is divided into two regions: (1) 120 nm to 200 nm (33 wavelength intervals); (2) 200 nm to 750 nm (67 wavelength intervals). The total photolytic rate constant (J) for each absorbing species is derived during model execution by integrating the product of the wavelength dependent exo-atmospheric flux (F_{exo}); the atmospheric transmission function (or normalized actinic flux) (N_A), which is unity at the top of atmosphere in most

wavelength regions; the molecular absorption cross-section (σ); and the quantum yield (ϕ). The exo-atmospheric flux over these wavelength intervals can be specified from observations and varied over the 11-year solar sunspot cycle (see section 5.6.6).

The wavelength-dependent transmission function is derived as a function of the model abundance of ozone and molecular oxygen. For wavelengths greater than 200 nm a normalized flux lookup table (LUT) approach is used, based on the 4-stream version of the Stratosphere, Troposphere, Ultraviolet (STUV) radiative transfer model (S. Madronich, personal communication), [Kinnison et al., 2007]. The transmission function is interpolated from the LUT as a function of altitude, column ozone, surface albedo, and zenith angle. The temperature and pressure dependences of the molecular cross sections and quantum yields for each photolytic process are also represented by a LUT in this wavelength region. At wavelengths less than 200 nm, the wavelength-dependent cross section and quantum yields for each species are specified and the transmission function is calculated explicitly for each wavelength interval. There are two exceptions to this approach. In the case of J(NO) and J(O_2), detailed photolysis parameterizations are included inline. In the Schumann-Runge Band region (SRBs), the parameterization of NO photolysis in the δ-bands is based on Minschwaner and Siskind [1993]. This parameterization includes the effect of self-absorption and subsequent attenuation of atmospheric transmission by the model-derived NO concentration. For J(O_2), the SRB and Lyman-alpha parameterizations are based on Koppers and Murtagh [1996] and Chabrillat and Kockarts [1997], respectively.

While the lookup table provides explicit quantum yields and cross-sections for a large number of photolysis rate determinations, additional ones are available by scaling of any of the explicitly defined rates. This process is available in the definition of the chemical preprocessor input files (see Lamarque et al. [2012, Table 3] for a complete list of the photolysis rates available). The impact of clouds on photolysis rates is parameterized following Madronich [1987]. However, because we use a lookup table approach, the impact of aerosols (tropospheric or stratospheric) on photolysis rates cannot be represented.

As an extension of MOZART-4 and to provide the ability to seamlessly perform tropospheric and stratospheric chemistry simulations, the calculation of photolysis rates for wavelengths shorter than 200 nm is included; this was shown to be important for ozone chemistry in the tropical upper troposphere [Prather, 2009]. In addition, because the standard configuration of CAM only extends into the lower stratosphere (model top is usually around 40 km), an additional layer of ozone and oxygen above the model top is included to provide a very accurate representation of photolysis rates in the upper portion of the model as compared to the equivalent calculation using a fully-resolved stratospheric distribution.

In addition, tropospheric photolysis rates can be computed interactively. Users interested in using this capability have to contact the Chemistry-CLimate Working Group Liaison as this is an unsupported option.

5.4 Numerical Solution Approach

Chemical and photochemical processes are expressed by a system of time-dependent ordinary differential equations at each point in the spatial grid, of the following form:

$$\frac{d\vec{y}}{dt} = \vec{P}(\vec{y},t) - \vec{L}(\vec{y},t)\cdot\vec{y} \tag{5.1}$$

$$\vec{y}(t) = \{y_i(t)\} \quad i = 1, 2, \ldots, N$$

where $\vec{y}$ is the vector of all solution variables (chemical species), N is the number of variables in the system, and y_i represents the i^{th} variable. $\vec{P}$ and $\vec{L}$ represent the production and loss rates, which are, in general, non-linear functions of the y_i. This system of equations is solved via two algorithms: an explicit forward Euler method:

$$y_i^{n+1} = y_i^n + \Delta t \cdot f_i(t_n, y^n) \tag{5.2}$$

in the case of species with long lifetimes and weak forcing terms (e.g., N_2O), and a more robust implicit backward Euler method:

$$y_i^{n+1} = y_i^n + \Delta t \cdot f_i(t_{n+1}, y^{n+1}) \tag{5.3}$$

for species that comprise a"stiff system" with short lifetimes and strong forcings (e.g., OH). Here n represents the time step index. Each method is first order accurate in time and conservative. The overall chemistry time step, $\Delta t = t_{n+1} - t_n$, is fixed at 30 minutes. Preprocessing software requires the user to assign each solution variable, y_i, to one of the solution schemes. The discrete analogue for methods (5.2) and (5.3) above results in two systems of algebraic equations at each grid point. The solution to these algebraic systems for equation (5.2) is straightforward (i.e., explicit). The algebraic system from the implicit method (5.3) is quadratically non-linear. This system can be written as:

$$\vec{G}(\vec{y}^{\,n+1}) = \vec{y}^{\,n+1} - \vec{y}^{\,n} - \Delta t \cdot \vec{f}(t_{n+1}, \vec{y}^{\,n+1}) = 0 \tag{5.4}$$

Here G is an N-valued, non-linear vector function, where N equals the number of species solved via the implicit method. The solution to equation (5.4) is solved with a Newton- Raphson iteration approach as shown below:

$$\vec{y}_{m+1}^{\,n+1} = \vec{y}_m^{\,n+1} - \vec{J} \cdot \vec{G}(\vec{y}_m^{\,n+1}); \; m = 0, 1, \ldots, M \tag{5.5}$$

Where m is the iteration index and has a maximum value of ten. The elements of the Jacobian matrix $\vec{J}$ are given by:

$$J_{ij} = \frac{\partial G_i}{\partial y_j}$$

The iteration and solution of equation (5.5) is carried out with a sparse matrix solution algorithm. This process is terminated when the given solution variable changes in a relative measure by less than a prescribed fractional amount. This relative error criterion is set on a species by species basis, and is typically 0.001; however, for some species (e.g., O_3), where a tighter error criterion is desired, it is set to 0.0001. If the iteration maximum is reached (for any species) before the error criterion is met, the time step is cut in half and the solution to equation (5.5) is iterated again. The time step can be reduced five times before the solution is accepted. This approach is based on the work of Sandu et al. [1996] and Sandu et al. [1997]; see also Brasseur et al. [1999].

5.5 Superfast Chemistry

5.5.1 Chemical mechanism

The super-fast mechanism was developed for long coupled chemistry-climate simulations, and is based on an updated version of the full non-methane hydrocarbon effects (NMHC) chemical mechanism for the troposphere and stratosphere used in the Lawrence Livermore National Laboratory off-line 3D global chemistry-transport model (IMPACT) citep[]rotman:04. The super-fast mechanism includes 15 photochemically active trace species (O_3, OH, HO_2, H_2O_2, NO, NO_2, HNO_3, CO, CH_2O, CH_3O_2, CH_3OOH, DMS, SO_2, SO_4, and C_5H_8) that allow us to calculate the major terms by which global change operates in tropospheric ozone and sulfate photochemistry. The families selected are Ox, HOx, NOy, the CH_4 oxidation suite plus isoprene (to capture the main NMHC effects), and a group of sulfur species to simulate natural and anthropogenic sources leading to sulfate aerosol. Sulfate aerosols is handled following Tie et al. [2005*b*]. In this scheme, CH4 concentrations are read in from a file and uses CAM3.5 simulations Lamarque et al. [2010*b*]. The super-fast mechanism was validated by comparing the super-fast and full mechanisms in side-by-side simulations.

5.5.2 Emissions for CAM4 superfast chemistry

	Anthro.	Natural	Interactive
CH_2O	x	x	
CO	x	x	
DMS		x	
ISOP			x
NO	x		
SO_2	x		

Table 5.1: Surface fluxes for CAM4 superfast chemistry.

5.5.3 LINOZ

Linoz is linearized ozone chemistry for stratospheric modeling [McLinden et al., 2000]. It calculates the net production of ozone (i.e., production minus loss) as a function of only three independent variables: local ozone concentration, temperature, and overhead column ozone). A zonal mean climatology for these three variables as well as the other key chemical variables such a total odd-nitrogen methane abundance is developed from satellite and other in situ observations. A relatively complete photochemical box model Prather [1992] is used to integrate the radicals to a steady state balance and then compute the net production of ozone. Small perturbations about the chemical climatology are used to calculate the coefficients of the first-order Taylor series expansion of the net production in terms of local ozone mixing ratio (f), temperature (T), and overhead column ozone (c).

$$\frac{df}{df} = (P-L)^o + \left.\frac{\delta(P-L)}{\delta f}\right|_o (f-f^o) + \left.\frac{\delta(P-L)}{\delta T}\right|_o (T-T^o) + \left.\frac{\delta(P-L)}{\delta c}\right|_o (c-c^o) \quad (5.6)$$

The photochemical tendency for the climatology is denoted by $(P-L)_o$, and the climatology values for the independent variables are denoted by f_o, c_o, and T_o, respectively. Including these four climatology values and the three partial derivatives, Linoz is defined by seven tables. Each table is specified by 216 atmospheric profiles: 12 months by 18 latitudes (85^oS to 85^oN). For each profile, quantities are evaluated at every 2 km in pressure altitude from $z^* = 10$ to 58 km ($z^* = 16$ km $\log_10$ (1000/p)). These tables (calculated for each decade, 1850-2000 to take into account changes in CH4 and N2O) are automatically remapped onto the CAM-chem grid with the mean vertical properties for each CAM-chem level calculated as the mass-weighted average of the interpolated Linoz profiles. Equation (1) is implemented for the chemical tendency of ozone in CAM-chem.

5.5.4 Parameterized PSC ozone loss

In the superfast chemistry, we incorporate the PSCs parameterization scheme of Cariolle et al. [1990] when the temperature falls below 195 K and the sun is above the horizon at stratospheric altitudes. The O_3 loss scales as the squared stratospheric chlorine loading (normalized by the 1980 level threshold). In this formulation PSC activation invokes a rapid e-fold of O_3 based on a photochemical model, but only when t he temperature stays below the PSC threshold. The stratospheric chlorine loading (1850-2005) is input in the model using equivalent effective stratospheric chlorine (EESC) [Newman et al., 2007] table based on observed mixing ratios at the surface.

This can be used instead of the more explicit representation available from WACCM in the strat-trop configuration.

5.6 WACCM4.0 Physical Parameterizations

In WACCM4.0, we extend the physical parameterizations used in CAM4 by adding constituent separation velocities to the molecular (vertical) diffusion and modifying the gravity spectrum parameterization. Both of these parameterizations are present, but not used, in CAM4. In addition, we replace the CAM4 parameterizations for both solar and longwave radiation above ~ 65 km, and add neutral and ion chemistry models.

5.6.1 WACCM4.0 Domain and Resolution

WACCM4.0 has 66 vertical levels from the ground to 5.1×10^{-6} hPa, as in the previous WACCM versions. As in CAM4, the vertical coordinate is purely isobaric above 100 hPa, but is terrain following below that level. At any model grid point, the local pressure p is determined by

$$p(i, j, k) = A(k)\, p_0 + B(k)\, p_s(i, j) \tag{5.7}$$

where A and B are functions of model level, k, only; $p_0 = 10^3$ hPa is a reference surface pressure; and p_s is the predicted surface pressure, which is a function of model longitude and latitude (indexed by i and j). The finite volume dynamical core uses locally material surfaces for its internal vertical coordinate and remaps (conservatively interpolates) to the hybrid surfaces after each time step.

Within the physical and chemical parameterizations, a local pressure coordinate is used, as described by (5.7). However, in the remainder of this note we refer to the vertical coordinate in terms of log-pressure altitude

$$Z = H \log\left(\frac{p_0}{p}\right). \tag{5.8}$$

The value adopted for the scale height, $H = 7$ km, is representative of the real atmosphere up to ~ 100 km, above that altitude temperature increases very rapidly and the typical scale height becomes correspondingly larger. It is important to distinguish Z from the *geopotential* height z, which is obtained from integration of the hydrostatic equation.

In terms of log-pressure altitude, the model top level is found at $Z = 140$ km ($z \simeq 150$ km). It should be noted that the solution in the top 15-20 km of the model is undoubtedly affected by the presence of the top boundary. However, it should not be thought of as a *sponge layer*, since molecular diffusion is a real process and is the primary damping on upward propagating waves near the model top. Indeed, this was a major consideration in moving the model top well above the turbopause. Considerable effort has been expended in formulating the upper boundary conditions to obtain realistic solutions near the model top and all of the important physical and chemical processes for that region have been included.

The standard vertical resolution is variable; it is 3.5 km above about 65 km, 1.75 km around the stratopause (50 km), 1.1-1.4 km in the lower stratosphere (below 30 km), and 1.1 km in the troposphere (except near the ground where much higher vertical resolution is used in the planetary boundary layer).

Two standard horizontal resolutions are supported in WACCM4.0: the $4 \times 5^\circ$ (latitude $\times$ longitude) low resolution version has 72 longitude and 46 latitude points; the $1.9 \times 2.5^\circ$ medium resolution version has 96 longitude and 144 latitude points. A $0.9 \times 1.25^\circ$ high resolution

version of WACCM4.0 has had limited testing, and is not yet supported, due to computational cost constraints. The $4 \times 5^\circ$ version has been used extensively for MLT studies, where it gives very similar results to the $1.9 \times 2.5^\circ$ version. However, caution should be exercised in using $4 \times 5^\circ$ results below the stratopause, since the meridional resolution may not be sufficient to represent adequately the dynamics of either the polar vortex or synoptic and planetary waves.

At all resolutions, the time step is 1800 s for the physical parameterizations. Within the finite volume dynamical core, this time step is subdivided as necessary for computational stability.

5.6.2 Molecular Diffusion and Constituent Separation

The vertical diffusion parameterization in CAM4 provides the interface to the turbulence parameterization, computes the molecular diffusivities (if necessary) and finally computes the tendencies of the input variables. The diffusion equations are actually solved implicitly, so the tendencies are computed from the difference between the final and initial profiles. In WACCM4.0, we extend this parameterization to include the terms required for the gravitational separation of constituents of differing molecular weights. The formulation for molecular diffusion follows Banks and Kockarts [1973]

A general vertical diffusion parameterization can be written in terms of the divergence of diffusive fluxes:

$$\frac{\partial}{\partial t}(u, v, q) = -\frac{1}{\rho}\frac{\partial}{\partial z}(F_u, F_v, F_q) \tag{5.9}$$

$$\frac{\partial}{\partial t}s = -\frac{1}{\rho}\frac{\partial}{\partial z}F_H + D \tag{5.10}$$

where $s = c_p T + gz$ is the dry static energy, z is the geopotential height above the local surface (does not include the surface elevation) and D is the heating rate due to the dissipation of resolved kinetic energy in the diffusion process. The diffusive fluxes are defined as:

$$F_{u,v} = -\rho K_m \frac{\partial}{\partial z}(u, v), \tag{5.11}$$

$$F_H = -\rho K_H \frac{\partial s}{\partial z} + \rho K_H^t \gamma_H, \tag{5.12}$$

$$F_q = -\rho K_q \frac{\partial q}{\partial z} + \rho K_q^t \gamma_q + \text{sep} - \text{flux}. \tag{5.13}$$

The viscosity K_m and diffusivities $K_{q,H}$ are the sums of: turbulent components $K^t_{m,q,H}$, which dominate below the mesopause; and molecular components $K^m_{m,q,H}$, which dominate above 120 km. The non-local transport terms $\gamma_{q,H}$ are given by the ABL parameterization and and the kinetic energy dissipation is

$$D \equiv -\frac{1}{\rho}\left(F_u \frac{\partial u}{\partial z} + F_v \frac{\partial v}{\partial z}\right). \tag{5.14}$$

The treatment of the turbulent diffusivities $K^t_{m,q,H}$, the energy dissipation D and the nonlocal transport terms $\gamma_{H,q}$ is described in the CAM 5.0 Technical Description and will be omitted here.

Molecular viscosity and diffusivity

The empirical formula for the molecular kinematic viscosity is

$$K_m^m = 3.55 \times 10^{-7} T^{2/3}/\rho, \tag{5.15}$$

and the molecular diffusivity for heat is

$$K_H^m = P_r K_m^m, \tag{5.16}$$

where P_r is the Prandtl number and we assume $P_r = 1$ in WACCM4.0. The constituent diffusivities are

$$K_q^m = T^{1/2} M_w/\rho, \tag{5.17}$$

where M_w is the molecular weight.

Diffusive separation velocities

As the mean free path increases, constituents of different molecular weights begin to separate in the vertical. In WACCM4.0, this separation is represented by a separation velocity for each constituent with respect mean air. Since WACCM4.0 extends only into the lower thermosphere, we avoid the full complexity of the separation problem and represent mean air by the usual dry air mixture used in the lower atmosphere ($M_w = 28.966$) Banks and Kockarts [1973].

Discretization of the vertical diffusion equations

In CAM4, as in previous version of the CCM, (5.9–5.12) are cast in pressure coordinates, using

$$dp = -\rho g dz, \tag{5.18}$$

and discretized in a time-split form using an Euler backward time step. Before describing the numerical solution of the diffusion equations, we define a compact notation for the discrete equations. For an arbitrary variable ψ, let a subscript denote a discrete time level, with current step ψ_n and next step ψ_{n+1}. The model has L layers in the vertical, with indexes running from top to bottom. Let ψ^k denote a layer midpoint quantity and let $\psi^{k\pm}$ denote the value at the interface above (below) k. The relevant quantities, used below, are then:

$$\begin{aligned}
\psi^{k+} &= (\psi^k + \psi^{k+1})/2, \quad k \in (1, 2, 3, ..., L-1) \\
\psi^{k-} &= (\psi^{k-1} + \psi^k)/2, \quad k \in (2, 3, 4..., L) \\
\delta^k \psi &= \psi^{k+} - \psi^{k-}, \\
\delta^{k+} \psi &= \psi^{k+1} - \psi^k, \\
\delta^{k-} \psi &= \psi^k - \psi^{k-1}, \\
\psi_{n+} &= (\psi_n + \psi_{n+1})/2, \\
\delta_n \psi &= \psi_{n+1} - \psi_n, \\
\delta t &= t_{n+1} - t_n, \\
\Delta^{k,l} &= 1, \; k = l, \\
&= 0, \; k \neq l.
\end{aligned}$$

Like the continuous equations, the discrete equations are required to conserve momentum, total energy and constituents. Neglecting the nonlocal transport terms, the discrete forms of (5.9–5.10) are:

$$\frac{\delta_n(u,v,q)^k}{\delta t} = g\frac{\delta^k F_{u,v,q}}{\delta^k p} \tag{5.19}$$

$$\frac{\delta_n s^k}{\delta t} = g\frac{\delta^k F_H}{\delta^k p} + D^k. \tag{5.20}$$

For interior interfaces, $1 \le k \le L-1$,

$$F^{k+}_{u,v} = \left(g\rho^2 K_m\right)^{k+}_n \frac{\delta^{k+}(u,v)_{n+1}}{\delta^{k+}p} \tag{5.21}$$

$$F^{k+}_{q,H} = \left(g\rho^2 K_{q,H}\right)^{k+}_n \frac{\delta^{k+}(u,v)_{n+1}}{\delta^{k+}p}. \tag{5.22}$$

Surface fluxes $F^{L+}_{u,v,q,H}$ are provided explicitly at time n by separate surface models for land, ocean, and sea ice while the top boundary fluxes are usually $F^{1-}_{u,v,q,H} = 0$. The turbulent diffusion coefficients $K^t_{m,q,H}$ and non-local transport terms $\gamma_{q,H}$ are calculated for time n by the turbulence model (identical to CAM4). The molecular diffusion coefficients, given by (5.15–5.17) are also evaluated at time n.

Solution of the vertical diffusion equations

Neglecting the discretization of $K^t_{m,q,H}$, D and $\gamma_{q,H}$, a series of time-split operators is defined by (5.19–5.22). Once the diffusivities ($K_{m,q,H}$) and the non-local transport terms ($\gamma_{q,H}$) have been determined, the solution of (5.19–5.22), proceeds in several steps.

1. update the bottom level values of u, v, q and s using the surface fluxes;
2. invert (5.19) and (5.21) for u, v_{n+1};
3. compute D and use to update the s profile;
4. invert (5.19,5.20) and (5.22) for s_{n+1} and q_{n+1}

Note that since all parameterizations in CAM4 return tendencies rather modified profiles, the actual quantities returned by the vertical diffusion are $\delta_n(u,v,s,q)/\delta t$.

Equations (5.19–5.22) constitute a set of four tridiagonal systems of the form

$$-A^k\psi^{k+1}_{n+1} + B^k\psi^k_{n+1} - C^k\psi^{k-1}_{n+1} = \psi^k_{n\prime}, \tag{5.23}$$

where $\psi_{n\prime}$ indicates u, v, q, or s after updating from time n values with the nonlocal and boundary fluxes. The super-diagonal (A^k), diagonal (B^k) and sub-diagonal (C^k) elements of (5.23) are:

$$A^k = \frac{1}{\delta^k p}\frac{\delta t}{\delta^{k+}p}\left(g^2\rho^2 K\right)^{k+}_n, \tag{5.24}$$

$$B^k = 1 + A^k + C^k, \tag{5.25}$$

$$C^k = \frac{1}{\delta^k p}\frac{\delta t}{\delta^{k-}p}\left(g^2\rho^2 K\right)^{k-}_n. \tag{5.26}$$

The solution of (5.23) has the form

$$\psi_{n+1}^k = E^k \psi_{n+1}^{k-1} + F^k, \tag{5.27}$$

or,

$$\psi_{n+1}^{k+1} = E^{k+1} \psi_{n+1}^k + F^{k+1}. \tag{5.28}$$

Substituting (5.28) into (5.23),

$$\psi_{n+1}^k = \frac{C^k}{B^k - A^k E^{k+1}} \psi_{n+1}^{k-1} + \frac{\psi_{n\prime}^k + A^k F^{k+1}}{B^k - A^k E^{k+1}}. \tag{5.29}$$

Comparing (5.27) and (5.29), we find

$$E^k = \frac{C^k}{B^k - A^k E^{k+1}}, \quad L > k > 1, \tag{5.30}$$

$$F^k = \frac{\psi_{n\prime}^k + A^k F^{k+1}}{B^k - A^k E^{k+1}}, \quad L > k > 1. \tag{5.31}$$

The terms E^k and F^k can be determined upward from $k = L$, using the boundary conditions

$$E^{L+1} = F^{L+1} = A^L = 0. \tag{5.32}$$

Finally, (5.29) can be solved downward for ψ_{n+1}^k, using the boundary condition

$$C^1 = 0 \Rightarrow E^1 = 0. \tag{5.33}$$

CCM1-3 used the same solution method, but with the order of the solution reversed, which merely requires writing (5.28) for ψ_{n+1}^{k-1} instead of ψ_{n+1}^{k+1}. The order used here is particularly convenient because the turbulent diffusivities for heat and all constituents are the same but their molecular diffusivities are not. Since the terms in (5.30-5.31) are determined from the bottom upward, it is only necessary to recalculate A^k, C^k, E^k and $1/(B^k - A^k E^{k+1})$ for each constituent within the region where molecular diffusion is important.

5.6.3 Gravity Wave Drag

Vertically propagating gravity waves can be excited in the atmosphere where stably stratified air flows over an irregular lower boundary and by internal heating and shear. These waves are capable of transporting significant quantities of horizontal momentum between their source regions and regions where they are absorbed or dissipated. Previous GCM results have shown that the large-scale momentum sinks resulting from breaking gravity waves play an important role in determining the structure of the large-scale flow. CAM4 incorporates a parameterization for a spectrum of vertically propagating internal gravity waves based on the work of Lindzen [1981], Holton [1982], Garcia and Solomon [1985] and McFarlane [1987]. The parameterization solves separately for a general spectrum of monochromatic waves and for a single stationary wave generated by flow over orography, following McFarlane [1987]. The spectrum is omitted in the standard tropospheric version of CAM4, as in previous versions of the CCM. Here we describe the modified version of the gravity wave spectrum parameterization used in WACCM4.0.

Adiabatic inviscid formulation

Following Lindzen [1981], the continuous equations for the gravity wave parameterization are obtained from the two-dimensional hydrostatic momentum, continuity and thermodynamic equations in a vertical plane:

$$\left(\frac{\partial}{\partial t} + u\frac{\partial}{\partial x}\right) u = -\frac{\partial \Phi}{\partial x}\,, \tag{5.34}$$

$$\frac{\partial u}{\partial x} + \frac{\partial W}{\partial Z} = 0\,, \tag{5.35}$$

$$\left(\frac{\partial}{\partial t} + u\frac{\partial}{\partial x}\right) \frac{\partial \Phi}{\partial Z} + N^2 w = 0\,. \tag{5.36}$$

Where N is the local Brunt-Väisällä frequency, and W is the vertical velocity in log pressure height (Z) coordinates. Eqs. (5.34)–(5.36) are linearized about a large scale background wind $\overline{u}$, with perturbations u', w', and combined to obtain:

$$\left(\frac{\partial}{\partial t} + \overline{u}\frac{\partial}{\partial x}\right)^2 \frac{\partial^2 w'}{\partial Z^2} + N^2 \frac{\partial^2 w'}{\partial x^2} = 0\,. \tag{5.37}$$

Solutions to (5.37) are assumed to be of the form:

$$w' = \hat{w}\, e^{ik(x-ct)}\, e^{Z/2H}\,, \tag{5.38}$$

where H is the scale height, k is the horizontal wavenumber and c is the phase speed of the wave. Substituting (5.38) into (5.37), one obtains:

$$-k^2(\overline{u}-c)^2 \left(\frac{\partial}{\partial Z} + \frac{1}{2H}\right)^2 \hat{w} - k^2 N^2 \hat{w} = 0\,. \tag{5.39}$$

Neglecting $\frac{1}{2H}$ compared to $\frac{\partial}{\partial Z}$ in (5.39), one obtains the final form of the two dimensional wave equation:

$$\frac{d^2\hat{w}}{dZ^2} + \lambda^2 \hat{w} = 0\,, \tag{5.40}$$

with the coefficient defined as:

$$\lambda = \frac{N}{(\overline{u}-c)}\,. \tag{5.41}$$

The WKB solution of (5.40) is:

$$\hat{w} = A\lambda^{-1/2} \exp\left(i\int_0^Z \lambda dz'\right)\,, \tag{5.42}$$

and the full solution, from (5.38), is:

$$w'(Z,t) = A\lambda^{-1/2} \exp\left(i\int_0^Z \lambda dz'\right)\, e^{ik(x-ct)}\, e^{Z/2H}\,. \tag{5.43}$$

The constant A is determined from the wave amplitude at the source ($z = 0$), The Reynolds stress associated with (5.43) is:

$$\tau(Z) = \tau(0) = \rho\overline{u'w'} = -\frac{2}{k}|A|^2\rho_0 \mathrm{sgn}(\lambda)\,, \tag{5.44}$$

and is conserved, while the momentum flux $\overline{u'w'} = -(m/k)\ \overline{w'w'}$ grows exponentially with altitude as $\exp(Z/H)$, per (5.43). We note that the vertical flux of wave energy is $c_{gz}\ E' = (U - c)\ \tau$ (Andrews et al. [1987]), where c_{gz} is the vertical group velocity, so that deposition of wave momentum into the mean flow will be accompanied by a transfer of energy to the background state.

Saturation condition

The wave amplitude in (5.43) grows as $e^{Z/2H}$ until the wave becomes unstable to convective overturning, Kelvin-Helmholtz instability, or other nonlinear processes. At that point, the wave amplitude is assumed to be limited to the amplitude that would trigger the instability and the wave is "saturated". The saturation condition used in CAM4 is from McFarlane [1987], based on a maximum Froude number (F_c), or streamline slope.

$$|\rho\overline{u'w'}| \leq \tau^* = F_c^2\frac{k}{2}\rho\frac{|\overline{u} - c|^3}{N}\,, \tag{5.45}$$

where τ^* is the saturation stress and $F_c^2 = 0.5$. In WACCM4.0, $F_c^2 = 1$ and is omitted hereafter. Following Lindzen [1981], within a saturated region the momentum tendency can be determined analytically from the divergence of τ^*:

$$\begin{aligned}\frac{\partial\overline{u}}{\partial t} &= -\frac{e}{\rho}\frac{\partial}{\partial Z}\rho\overline{u'w'}\,,\\ &\simeq -e\frac{k}{2}\frac{(\overline{u} - c)^3}{N}\frac{1}{\rho}\frac{\partial\rho}{\partial Z}\,,\\ &\simeq -e\frac{k}{2}\frac{(\overline{u} - c)^3}{NH},\end{aligned} \tag{5.46}$$

where e is an "efficiency" factor. For a background wave spectrum, e represents the temporal and spatial intermittency in the wave sources. The analytic solution (5.46) is not used in WACCM4.0; it is shown here to illustrate how the acceleration due to breaking gravity waves depends on the intrinsic phase speed. In the model, the stress profile is computed at interfaces and differenced to get the specific force at layer midpoints.

Diffusive damping

In addition to breaking as a result of instability, vertically propagating waves can also be damped by molecular diffusion (both thermal and momentum) or by radiative cooling. Because the intrinsic periods of mesoscale gravity waves are short compared to IR relaxation time scales throughout the atmosphere, we ignore radiative damping. We take into account the molecular viscosity, K_m^m, such that the stress profile is given by:

$$\tau(Z) = \tau(Z_t)\exp\left(-\frac{2}{H}\int_0^Z \lambda_i dz'\right)\,, \tag{5.47}$$

where Z_t denotes the top of the region, below Z, not affected by thermal dissipation or molecular diffusion. The imaginary part of the local vertical wavenumber, λ_i is then:

$$\lambda_i = \frac{N^3 \; K_m^m}{2k(\overline{u} - c)^4} \, . \tag{5.48}$$

In WACCM4.0, (5.47–5.48) are only used within the domain where molecular diffusion is important (above $\sim$ 75 km). At lower altitudes, molecular diffusion is negligible, $\lambda_i \to 0$, and τ is conserved outside of saturation regions.

Transport due to dissipating waves

When the wave is dissipated, either through saturation or diffusive damping, there is a transfer of wave momentum and energy to the background state. In addition, a phase shift is introduced between the wave's vertical velocity field and its temperature and constituent perturbations so that fluxes of heat and constituents are nonzero within the dissipation region. The nature of the phase shift and the resulting transport depends on the dissipation mechanism; in WACCM4.0, we assume that the dissipation can be represented by a linear damping on the potential temperature and constituent perturbations. For potential temperature, θ, this leads to:

$$\left(\frac{\partial}{\partial t} + \overline{u} \frac{\partial}{\partial x} \right) \theta' + w' \frac{\partial \overline{\theta}}{\partial z} = -\delta \theta' \, , \tag{5.49}$$

where δ is the dissipation rate implied by wave breaking, which depends on the wave's group velocity, c_{gz} (see Garcia [2001]):

$$\delta = \frac{c_{gz}}{2H} = k \, \frac{(\overline{u} - c)^2}{2HN} \, . \tag{5.50}$$

Substitution of (5.50) into (5.49) then yields the eddy heat flux:

$$\overline{w'\theta'} = - \left[\frac{\delta \; \overline{w'w'}}{k^2(\overline{u} - c)^2 + \delta^2} \right] \frac{\partial \overline{\theta}}{\partial z} \, . \tag{5.51}$$

Similar expressions can be derived for the flux of chemical constituents, with mixing ratio substituted in place of potential temperature in (5.51). We note that these wave fluxes are always downgradient and that, for convenience of solution, they may be represented as vertical diffusion, with coefficient K_{zz} equal to the term in brackets in (5.51), but they do not represent turbulent diffusive fluxes but rather eddy fluxes. Any additional turbulent fluxes due to wave breaking are ignored. To take into account the effect of localization of turbulence (e.g., Fritts and Dunkerton [1985]; McIntyre [1989]), (5.51) is multiplied times an inverse Prandtl number, Pr^{-1}; in WACCM4.0 we use $Pr^{-1} = 0.25$.

Heating due to wave dissipation

The vertical flux of wave energy density, E', is related to the stress according to:

$$c_{gz} \; E' = (\overline{u} - c) \; \tau \; , \tag{5.52}$$

where c_{gz} is the vertical group velocity [Andrews et al., 1987]. Therefore, the stress divergence $\partial\tau/\partial Z$ that accompanies wave breaking implies a loss of wave energy. The rate of dissipation of wave energy density is:

$$\frac{\partial E'}{\partial t} \simeq (\overline{u} - c)\frac{1}{c_{gz}}\frac{\partial \tau}{\partial t} = (\overline{u} - c)\frac{\partial \tau}{\partial Z} \; . \tag{5.53}$$

For a saturated wave, the stress divergence is given by (5.46), so that:

$$\frac{\partial E'}{\partial t} = (\overline{u} - c)\; \frac{\partial\, \tau^*}{\partial Z} = -e \cdot \rho\; \frac{k\,(U-c)^4}{2NH} \; . \tag{5.54}$$

This energy loss by the wave represents a heat source for the background state, as does the change in the background kinetic energy density implied by wave drag on the background flow:

$$\frac{\partial \overline{K}}{\partial t} \equiv \frac{\rho}{2}\frac{\partial \overline{u}^2}{\partial t} = \overline{u}\; \frac{\partial\, \tau^*}{\partial Z} = -e \cdot \rho\; \frac{k\,\overline{u}\,(\overline{u}-c)^3}{2NH} \; , \tag{5.55}$$

which follows directly from (5.46). The background heating rate, in K sec^{-1}, is then:

$$Q_{gw} = -\frac{1}{\rho\, c_p}\left[\frac{\partial \overline{K}}{\partial t} + \frac{\partial E'}{\partial t}\right] . \tag{5.56}$$

Using (5.54) – (5.55), this heating rate may be expressed as:

$$Q_{gw} = \frac{1}{\rho\, c_p}\; c\; \frac{\partial\, \tau^*}{\partial Z} = \frac{1}{c_p}\left[\; e \cdot \frac{k\, c\,(c-\overline{u})^3}{2NH}\right] , \tag{5.57}$$

where c_p is the specific heat at constant pressure. In WACCM4.0, Q_{gw} is calculated for each component of the gravity wave spectrum using the first equality in (5.57), i.e., the product of the phase velocity times the stress divergence.

Orographic source function

For orographically generated waves, the source is taken from McFarlane [1987]:

$$\tau_g = |\rho\overline{u'w'}|_0 = \frac{k}{2}h_0^2\rho_0 N_0 \overline{u}_0 \, , \tag{5.58}$$

where h_0 is the streamline displacement at the source level, and ρ_0, N_0, and $\overline{u}_0$ are also defined at the source level. For orographic waves, the subgrid-scale standard deviation of the orography σ is used to estimate the average mountain height, determining the typical streamline displacement. An upper bound is used on the displacement (equivalent to defining a "separation streamline") which corresponds to requiring that the wave not be supersaturated at the source level:

$$h_0 = \min(2\sigma, \frac{\overline{u}_0}{N_0}) \, . \tag{5.59}$$

The source level quantities ρ_0, N_0, and $\overline{u}_0$ are defined by vertical averages over the source region, taken to be 2σ, the depth to which the average mountain penetrates into the domain:

$$\psi_0 = \int_0^{2\sigma} \psi\rho dz, \qquad \psi \in \{\rho, N, u, v\} \, . \tag{5.60}$$

The source level wind vector (u_0, v_0) determines the orientation of the coordinate system in (5.34)–(5.36) and the magnitude of the source wind $\overline{u}_0$.

Non-orographic source functions

The source spectrum for non-orographic gravity waves is no longer assumed to be a specified function of location and season, as was the case with the earlier version of the model described by Garcia et al. [2007]. Instead, gravity waves are launched according to trigger functions that depend on the atmospheric state computed in WACCM4 at any given time and location, as discussed by Richter et al. [2010]. Two trigger functions are used: convective heat release (which is a calculated model field) and a "frontogenesis function", Hoskins [1982], which diagnoses regions of strong wind field deformation and temperature gradient using the horizontal wind components and potential temperature field calculated by the model.

In the case of convective excitation, the method of Beres et al. [2005] is used to determine a phase speed spectrum based upon the properties of the convective heating field. A spectrum is launched whenever the deep convection parameterization in WACCM4 is active, and the vertical profile of the convective heating, together with the mean wind field in the heating region, are used to determine the phase speed spectrum of the momentum flux. Convectively generated waves are launched at the top of the convective region (which varies according to the depth of the convective heating calculated in the model).

Waves excited by frontal systems are launched whenever the frontogenesis trigger function exceeds a critical value (see Richter et al. [2010]). The waves are launched from a constant source level, which is specified to be 600 mb. The momentum flux phase speed spectrum is given by a Gaussian function in phase speed:

$$\tau_s(c) = \tau_b \exp\left[-\left(\frac{c - V_s}{c_w}\right)^2\right], \tag{5.61}$$

centered on the source wind, $V_s = |\mathbf{V}_s|$, with width $c_w = 30$ m/s. A range of phase speeds with specified width and resolution is used:

$$c \in V_s + [\pm d_c, \pm 2d_c, ... \pm c_{max}], \tag{5.62}$$

with $d_c = 2.5$ m s^{-1} and $c_{max} = 80$ m s^{-1}, giving 64 phase speeds. Note that $c = V_s$ is retained in the code for simplicity, but has a critical level at the source and, therefore, $\tau_s(c = V_s) = 0$. Note also that τ_b is a tunable parameter; in practice this is set such that the height of the polar mesopause, which is very sensitive to gravity wave driving, is consistent with observations. In WACCM4, $\tau_b = 1.5$ x 10^{-3} Pa.

Above the source region, the saturation condition is enforced separately for each phase speed, c_i, in the momentum flux spectrum:

$$\tau(c_i) \leq \tau_i^* = F_c^2 \frac{k}{2} \rho \frac{|\overline{u} - c_i|^3}{N}. \tag{5.63}$$

Numerical approximations

The gravity wave drag parameterization is applied immediately after the nonlinear vertical diffusion. The interface Brunt-Väisällä frequency is

$$\left(N^{k+}\right)^2 = \frac{g^2}{T^{k+}} \left(\frac{1}{c_p} - \rho^{k+} \frac{\delta^{k+} T}{\delta^{k+} p}\right), \tag{5.64}$$

Where the interface density is:

$$\rho^{k+} = \frac{RT^{k+}}{p^{k+}}. \tag{5.65}$$

The midpoint Brunt-Väisällä frequencies are $N^k = (N^{k+} + N^{k-})/2$.

The level for the orographic source is an interface determined from an estimate of the vertical penetration of the subgrid mountains within the grid box. The subgrid scale standard deviation of the orography, σ_h, gives the variation of the mountains about the mean elevation, which defines the Earth's surface in the model. Therefore the source level is defined as the interface, $k_s - 1/2$, for which $z^{k_s+} < 2\sigma_h < z^{k_s-}$, where the interface heights are defined from the midpoint heights by $z^{k+} = \sqrt{(}z^k z^{k+1})$.

The source level wind vector, density and Brunt-Väisällä frequency are determined by vertical integration over the region from the surface to interface $k_s + 1/2$:

$$\psi_0 = \sum_{k=k_s}^{K} \psi^k \delta^k p\,, \qquad \psi \in \{\rho, N, u, v\}\,. \tag{5.66}$$

The source level background wind is $\overline{u}_0 = \sqrt{(}u_0^2 + v_0^2)$, the unit vector for the source wind is

$$(x_0, y_0) = (u_0, v_0)/\overline{u}_0\,, \tag{5.67}$$

and the projection of the midpoint winds onto the source wind is

$$\overline{u}^k = u^k x_0 + v^k y_0\,. \tag{5.68}$$

Assuming that $\overline{u}_0 > 2$ m s^{-1} and $2\sigma^h > 10$ m, then the orographic source term, τ_g is given by (5.58) and (5.59), with F_c^2 =1 and $k = 2\pi/10^5$ m^{-1}. Although the code contains a provision for a linear stress profile within a "low level deposition region", this part of the code is not used in the standard model.

The stress profiles are determined by scanning up from the bottom of the model to the top. The stress at the source level is determined by (5.58). The saturation stress, τ_ℓ^* at each interface is determined by (5.63), and $\tau_\ell^* = 0$ if a critical level is passed. A critical level is contained within a layer if $(\overline{u}^{k+} - c_\ell)/(\overline{u}^{k-} - c_\ell) < 0$.

Within the molecular diffusion domain, the imaginary part of the vertical wavenumber is given by (5.48). The interface stress is then determined from the stress on the interface below by:

$$\tau^{k-} = \min\left[(\tau^*)^{k-}\,, \tau^{k+} \exp\left(-2\lambda_i \frac{R}{g} T^k \delta^k \ln p\right)\right]\,. \tag{5.69}$$

Below the molecular diffusion domain, the exponential term in (5.69) is omitted.

Once the complete stress profile has been obtained, the forcing of the background wind is determined by differentiating the profile during a downward scan:

$$\frac{\partial \overline{u}_\ell^k}{\partial t} = g\frac{\delta^k \tau_\ell}{\delta^k p} < \left(\frac{\partial \overline{u}_\ell^k}{\partial t}\right)^{\max}\,. \tag{5.70}$$

$$\left(\frac{\partial \overline{u}_\ell^k}{\partial t}\right)^{\max} = \min\left[\frac{|c_\ell - \overline{u}_\ell^k|}{2\delta t}\,, 500 \text{ m s}^{-1} \text{ day}^{-1}\right]\,. \tag{5.71}$$

The first bound on the forcing comes from requiring that the forcing not be large enough to push the wind more than half way towards a critical level within a time step and takes the place of an implicit solution. This bound is present for numerical stability, it comes into play when the time step is too large for the forcing. It is not feasible to change the time step, or to write an implicit solver, so an *a priori* bound is used instead. The second bound is used to constrain the forcing to lie within a physically plausible range (although the value used is extremely large) and is rarely invoked.

When any of the bounds in (5.70) are invoked, conservation of stress is violated. In this case, stress conservation is ensured by decreasing the stress on the lower interface to match the actual stress divergence in the layer:

$$\tau_\ell^{k+} = \tau_\ell^{k-} + \frac{\partial \overline{u}^k}{\partial t} \frac{\delta^k p}{g} \,. \tag{5.72}$$

This has the effect of pushing some of the stress divergence into the layer below, a reasonable choice since the waves are propagating up from below.

Finally, the vector momentum forcing by the gravity waves is determined by projecting the background wind forcing with the unit vectors of the source wind:

$$\frac{\partial \mathbf{V}^k}{\partial t} = (x_0, y_0) \times E \sum_\ell \frac{\partial \overline{u}_\ell^k}{\partial t} \,. \tag{5.73}$$

In addition, the frictional heating implied by the momentum tendencies, $\frac{1}{c_p}\mathbf{V}^k \cdot \partial \mathbf{V}^k / \partial t$, is added to the thermodynamic equation. This is the correct heating for orographic ($c_\ell = 0$) waves, but not for waves with $c_\ell \neq 0$, since it does not account for the wave energy flux. This flux is accounted for in some middle and upper atmosphere versions of CAM4, but also requires accounting for the energy flux at the source.

5.6.4 Turbulent Mountain Stress

An important difference between WACCM4 and earlier versions is the addition of surface stress due to unresolved orography. A numerical model can compute explicitly only surface stresses due to resolved orography. At the standard 1.9° x 2.5° (longitude x latitude) resolution used by WACCM4 only the gross outlines of major mountain ranges are resolved. To address this problem, unresolved orography is parameterized as turbulent surface drag, using the concept of effective roughness length developed by Fiedler and Panofsky [1972]. Fiedler and Panofsky defined the roughness length for heterogeneous terrain as the roughness length that homogenous terrain would have to give the correct surface stress over a given area. The concept of effective roughness has been used in several Numerical Weather Prediction models (e.g., Wilson [2002]; Webster et al. [2003]).

In WACCM4 the effective roughness stress is expressed as:

$$\tau = \rho \, C_d \, |\mathbf{V}| \mathbf{V} \,, \tag{5.74}$$

where ρ is the density and C_d is a turbulent drag coefficient,

$$C_d = \frac{f(R_i)\, k^2}{\ln^2 \left[\frac{z+z_0}{z_0} \right]} \,, \tag{5.75}$$

k is von Kármán's constant; z is the height above the surface; z_0 is an effective roughness length, defined in terms of the standard deviation of unresolved orography; and $f(R_i)$ is a function of the Richardson number (see Richter et al. [2010] for details).

The stress calculated by (5.74) is used the model's nonlocal PBL scheme to evaluate the PBL height and nonlocal transport, per Eqs. (3.10)(3.12) of Holstlag and Boville [1993]. This calculation is carried out only over land, and only in grid cells where the height of topography above sea level, z, is nonzero.

5.6.5 QBO Forcing

WACCM4 has several options for forcing a quasi-biennial oscillation (QBO) by applying a momentum forcing in the tropical stratosphere. The parameterization relaxes the simulated winds to a specified wind field that is either fixed or varies with time. The parameterization can also be turned off completely. The namelist variables and input files can be selected to choose one of the following options:

- Idealized QBO East winds, used for perpetual fixed-phase of the QBO, as described by Matthes et al. [2010].
- Idealized QBO West winds, as above but for the west phase.
- Repeating idealized 28-month QBO, also described by Matthes et al. [2010].
- QBO for the years 1953-2004 based on the climatology of Giorgetta [see: http://www.pa.op.dlr.de/CCMVal/Forcings/qbo_data_ccmval/u_profile_195301-200412.html, 2004].
- QBO with a 51-year repetition, based on the 1953-2004 climatology of Giorgetta, which can be used for any calendar year, past or future.

The relaxation of the zonal wind is based on Balachandran and Rind [1995] and is described in Matthes et al. [2010]. The input winds are specified at the equator and the parameterization extends latitudinally from 22°N to 22°S, as a Gaussian function with a half width of 10° centered at the equator. Full vertical relaxation extends from 86 to 4 hPa with a time constant of 10 days. One model level below and above this altitude range, the relaxation is half as strong and is zero for all other levels. This procedure constrains the equatorial winds to more realistic values while allowing resolved and parameterized waves to continue to propagate.

The fixed or idealized QBO winds (first 3 options) can be applied for any calendar period. The observed input (Giorgetta climatology) can be used only for the model years 1953-2004. The winds in the final option were determined from the Giorgetta climatology for 1954-2004 via filtered spectral decomposition of that climatology. This gives a set of Fourier coefficients that can be expanded for any day and year. The expanded wind fields match the climatology during the years 1954-2004.

5.6.6 Radiation

The radiation parameterizations in CAM4 are quite accurate up to $\sim$ 65 km, but deteriorate rapidly above that altitude. Because 65 km is near a local minimum in both shortwave heating

and longwave cooling, it is a particularly convenient height to merge the heating rates from parameterizations for the lower and upper atmosphere. Therefore, we retain the CAM4 parameterizations below ~ 65 km and use new parameterizations above.

The merged shortwave and longwave radiative heatings are determined from

$$Q = w_1 \, Q_{CAM3} + w_2 \, Q_{MLT}, \tag{5.76}$$

where $w_1(z^* < z_b^*) = 1$, $w_2(z^* > z_t^*) = 1$ and $z^* = \log(10^5/p)$ is the pressure scale height. The CAM4 radiation parameterizations are used below z_b^* and the MLT parameterizations are used above z_t^*. For $z_b^* < z < z_t^*$, $w_2 = 1 - w_1$ and

$$w_1 = 1 - \tanh\left(\frac{z^* - z_b^*}{z_w*}\right), \tag{5.77}$$

where z_w* is the transition width.

The merging was developed and tested separately for shortwave and longwave radiation and the constants are slightly different. For longwave radiation, the constants are $z_b^* = 8.57$, $z_t^* = 10$ and $z_w^* = 0.71$. For shortwave radiation, the constants are $z_b^* = 9$, $z_t^* = 10$ and $z_w^* = 0.75$. These constants give smooth heating profiles. Note that a typical atmospheric scale height of $H = 7$ km places the transition zones between 60 and 70 km.

Longwave radiation

WACCM4.0 retains the longwave (LW) formulation used in CAM4 [Kiehl and Briegleb, 1991]. However, in the MLT longwave radiation uses the parameterization of Fomichev et al. [1998] for CO_2 and O_3 cooling and the parameterization of Kockarts [1980] for NO cooling at 5.3 μm. As noted above, the LW heating/cooling rates produced by these parameterizations are merged smoothly at 65 km with those produced by the standard CAM4 LW code, as recently revised by Collins et al. [2002]. In the interactive chemistry case all of the gases (O, O_2, O_3, N_2, NO, and CO_2) that are required by these parameterizations, are predicted within WACCM4.0.

Shortwave radiation

WACCM4.0 uses a combination of solar parameterizations to specify spectral irradiances over two spectral intervals. The first spectral interval covers soft x-ray and extreme ultraviolet irradiances (wavelengths between 0.05 nm to Lyman-α (121.6 nm)) and is calculated using the parameterization of Solomon and Qiang [2005]. The parameterizations take as input the 10.7 cm solar radio flux ($f10.7$) and its 81-day average ($f10.7a$). Daily values of $f10.7$ are obtained from NOAA's Space Environment Center (www.sec.noaa.gov).

The irradiance of the jth spectral interval is:

$$F_j = F_j^0 * \left\{1 + R_j * \left[\frac{(f10.7 + f10.7a)}{2} - F_{min}\right]\right\} \tag{5.78}$$

where $F_{min} = 80$. F_j^0 and R_j are taken from Table A1 of Solomon and Qiang [2005].

Fluxes for the second interval between Lyman-α (121.6 nm) and 100 μm. are specified using an empirical model of the wavelength-dependent sunspot and facular influences [Lean, 2000;

Wang et al., 2005]. Spectral resolution is 1 nm between 121.6 nm and 750nm, 5 nm between 750nm and 5μm, 10 nm between 5μm and 10μm, and 50 nm between 10μm and 100 μm.

In the troposphere, stratosphere and lower mesosphere (z < 65km) WACCM4.0 retains the CAM4 shortwave heating (200 nm to 4.55 μm) which is calculated from the net shortwave spectral flux into each layer Collins et al. [2004*b*]. The solar spectrum for the CAM4 heating calculation is divided into 19 intervals [Collins, 1998]. The heating in these intervals must be adjusted to match the irradiances calculated for the upper part of the model, and those used in the photolysis calculations. This is achieved by applying a scaling (S_j) to the solar heating in the jth CAM4 spectral interval using the spectrum from Lean [2000] and Wang et al. [2005]:

$$S_j = \frac{F_j}{F_j^{ref}}, \tag{5.79}$$

where F_j is the spectral irradiance (W/m^2/nm) integrated over the jth band, and F_j^{ref} is the same integral taken over a reference spectrum calculated from annual mean fluxes over a 3-solar-cycle period from XX to YY.

In the MLT region, shortwave heating is the sum of the heating due to absorption of photons and subsequent exothermic chemical reactions that are initiated by photolysis. The majority of energy deposited by an absorbed photon goes into breaking molecular bonds, rather than into translational energy of the absorbing molecule (heat). Chemical heating results when constituents react to form products of lower total chemical potential energy. This heating can take place months after the original photon absorption and thousands of kilometers away. Heating rates range from 1 K/day near 75 km to 100-300 K/day near the top of the model domain. It is clear that quenching of $O(^1D)$ is a large source of heating throughout the MLT. Above 100 km ion reactions and reactions involving atomic nitrogen are significant sources of heat, while below that level O_X (= O + O_3) and HO_X (= H + OH + HO_2) reactions are the dominant producers of chemical heating.

Heating within the MLT from the absorption of radiation that *is* directly thermalized is calculated over the wavelength range of 0.05 nm to 350 nm. For wavelengths less than Lyman-α, it is assumed that 5% of the energy of each absorbed photon is directly thermalized:

$$Q_{EUV} = (\rho c_p)^{-1} \sum_k n_k \sum_j \epsilon J_k(\lambda_j) \frac{hc}{\lambda_j}, \tag{5.80}$$

where $\epsilon = 0.05$. Here ρ is mass density, c_p is the specific heat of dry air, n is the number density of the absorbing species, and J is the photolysis/photoionization rate. The total heating is the sum of k photolysis reactions and j wavelengths intervals. At these wavelengths absorption of a photon typically leads to photoionization, with the resulting photoelectron having sufficient energy to ionize further molecules. Calculation of J_{ij} and ionization rates from photoelectrons is calculated based on the parameterization of Solomon and Qiang [2005]. In a similar manner, the heating rate within the aurora (Q_{AUR}) is calculated as the product of the total ionization rate, 35 eV per ion pair, and the same heating efficiency of 5%.

Between Lyman-α and 350 nm the energy required to break molecular bonds is explicitly accounted for. The heating rate is thus defined as:

$$Q_{UV} = (\rho c_p)^{-1} \sum_k n_k \sum_j J_k(\lambda_j) \{ \frac{hc}{\lambda_j} - BDE_k \}, \tag{5.81}$$

where BDE is the bond dissociation energy.

In addition to these sources of heat, WACCM4.0 calculates heating by absorption in the near-infrared by CO_2 (between 1.05 to 4.3 μm), which has its largest contribution near 70km and can exceed 1 K/day [Fomichev et al., 2004]. Heating from this process is calculated using the parameterization of Ogibalov and Fomichev [2003]. Finally, the heating produced by collisions of electrons and neutrals (Joule heating) is also calculated using the predicted ion and electron concentrations. This is described in section 5.6.8. Local heating rates from joule heating can be very large in the auroral regions, reaching over 10^3K/day in the upper levels of the model.

Airglow, radiation produced when excited atoms or molecules spontaneously emit, is accounted for in WACCM4.0 for emissions of $O_2(^1\Delta)$, $O_2(^1\Sigma)$, and vibrationally excited OH. Airglow from the excited molecular oxygen species are handled explicitly; radiative lifetimes for $O_2(^1\Delta)$ and $O_2(^1\Sigma)$ are 2.58×10^{-4} s^{-1} and 0.085 s^{-1} respectively. However, modeling of the many possible vibrational transitions of OH is impractical in a model as large as WACCM4.0. Energy losses from the emission of vibrationally excited OH are therefore accounted for by applying an efficiency factor to the exothermicity of the reaction that produces vibrationally excited OH; the reaction of hydrogen and ozone. In other words, the reaction H + O_3 produces ground state OH only, but the chemical heating from the reaction has been reduced to take into consideration that some of the chemical potential energy has been lost in airglow. This approach is the same one used by Mlynczak and Solomon [1993] and we use their recommended efficiency factor of 60%. Any energy lost through airglow is assumed to be lost to space, and so represents an energy pathway that does not generate heat.

Volcanic Heating

The sulfate aerosol heating is a function of a prescribed aerosol distribution varying in space and time that has a size distribution similar to that seen after a volcanic eruption [Tilmes et al., 2009]. The H_2SO_4 mass distribution is calculated from the prescribed sulfate surface area density (SAD) assuming a lognormal size distribution, number of particles per cm-3, and distribution width (see section 3.6.2). The H2SO4 mass distribution is then passed to the radiative transfer code (CAMRT), which in turn calculates heating and cooling rates.

5.6.7 WACCM4.0 chemistry

Chemical Mechanism (Neutral Species)

WACCM4.0 includes a detailed neutral chemistry model for the middle atmosphere based on the Model for Ozone and Related Chemical Tracers, Version 3 [Kinnison et al., 2007]. The mechanism represents chemical and physical processes in the troposphere through the lower thermosphere. The species included within this mechanism are contained within the O_X, NO_X, HO_X, ClO_X, and BrO_X chemical families, along with CH_4 and its degradation products. This mechanism contains 52 neutral species, one invariant (N_2), 127 neutral gas-phase reactions, 48 neutral photolytic reactions, and 17 heterogeneous reactions on three aerosol types (see below). Lists of the chemical species are given in Table 1. The first column lists the symbolic name (as used in the mechanism); the second column lists the species atomic composition; the third column designates which numerical solution approach is used (i.e., explicit or implicit); the fourth column lists any deposition processes (wet or dry) for that species; and the fifth column

indicates whether the surface (or upper) boundary condition is fixed vmr or flux, or if a species has an in-situ flux (from lightning or aircraft emissions).

The gas-phase reactions included in the WACCM4.0 middle atmosphere chemical mechanism are listed in Table 2. In most all cases the chemical rate constants are taken from JPL06-2 [Sander, S. P., et al., 2006]. Exceptions to this condition are described in the comment section for any given reaction.

Heterogeneous reactions on four different aerosols types are also represented in the WACCM4.0 chemical mechanism (see Table 3): 1) liquid binary sulfate (LBS); 2) Supercooled ternary solution (STS); 3) Nitric acid trihydrate (NAT); and 4) water-ice. There are 17 reactions, six reactions on liquid sulfate aerosols (LBS or STS), five reactions on solid NAT aerosols, and six reactions on solid water-ice aerosols. The rate constants for these 17 heterogeneous reactions can be divided up into two types: 1) first order; and 2) pseudo second order. For first order hydrolysis reactions (Table 3, reactions 1-3, 7-8, 11, and 12-14), the heterogeneous rate constant is derived in the following manner:

$$k = \frac{1}{4} V \cdot SAD \cdot \gamma \tag{5.82}$$

Where V = mean velocity; SAD = surface area density of LBS, STS, NAT, or water-ice, and γ = reaction probability for each reaction. The units for this rate constant are s^{-1}. Here the H_2O abundance is in excess and assumed not change relative to the other reactant trace constituents. The mean velocity is dependent on the molecular weight of the non-H_2O reactant (i.e., N_2O_5, $ClONO_2$, or $BrONO_2$). The SAD for each aerosol type is described in section 7. The reaction probability is dependent on both composition and temperature for sulfate aerosol (see JPL06-2). The reaction probability is a fixed quantity for NAT and water-ice aerosols and is listed in Table 3. Multiplying the rate constant times the concentration gives a loss rate in units of molecules cm^{-3} sec^{-1} for the reactants and is used in the implicit solution approach. The non-hydrolysis reaction (Table 3, reactions 4-6, 9-10, and 15-17) are second order reactions. Here, the first order rate constant (equation 6) is divided by the HCl concentration, giving it the typical bimolecular rate constant unit value of cm^3 $molecule^{-1}$ sec^{-1}. This approach assumes that all the HCl is in the aerosol particle.

Stratospheric Aerosols

Heterogeneous processes on liquid sulfate aerosols and solid polar stratospheric clouds (Type 1a, 1b, and 2) are included following the approach of Considine et al. [2000]. This approach assumes that the condensed phase mass follows a lognormal size distribution taken from Considine et al. [2000],

$$N(r) = \frac{N_0}{r\sigma\sqrt{2\pi}} \exp\left[\frac{-\ln(r/r_0)^2}{2\sigma^2}\right] \tag{5.83}$$

where N is the aerosol number density (particles cm^{-3}); r and r_0 are the particle radius and median radius respectively; and σ is the standard deviation of the lognormal distribution. N_0 and r_0 are supplied for each aerosol type. The aerosol surface area density (SAD) is the second moment of this distribution.

At model temperatures (T_{model}) greater than 200 K, liquid binary sulfate (LBS) is the only aerosol present. The surface area density (SAD) for LBS is derived from observations from SAGE, SAGE-II and SAMS [Thomason et al., 1997] as updated by Considine

[World Meteorological Organization, 2003]. As the model atmosphere cools, the LBS aerosol swells, taking up both HNO_3 and H_2O to give STS aerosol. The Aerosol Physical Chemistry Model (ACPM) is used to derive STS composition Tabazadeh et al. [1994]. The STS aerosol median radius and surface area density is derived following the approach of Considine et al. [2000]. The width of the STS size distribution ($\sigma = 1.6$) and number density (10 particles cm^{-3}) are prescribed according to measurements from Dye et al. [1992]. The STS aerosol median radius can swell from approximately 0.1 μm to approximately 0.5 μm. There is no aerosol settling assumed for this type of aerosol. The median radius is used in derivation of sulfate aerosol reaction probability coefficients. Both the LBS and STS surface area densities are used for the calculation of the rate constants as listed in Table 3; reactions (1)-(6).

Solid nitric acid containing aerosol formation is allowed when the model temperature reaches a prescribed super saturation ratio of HNO_3 over NAT [Hansen and Mauersberger, 1988]. This ratio is set to 10 in WACCM4.0 [Peter et al., 1991]. There are three methods available to handle the HNO_3 uptake on solid aerosol. The first method directly follows Considine et al. [2000, 2004]. Here, after the supersaturation ratio assumption is met, the available condensed phase HNO_3 is assumed to reside in the solid NAT aerosol. The derivation of the NAT median radius and surface area density follows the same approach as the STS aerosol, by assuming: a lognormal size distribution, a width of a distribution ($\sigma = 1.6$; Dye et al. [1992]), and a number density (0.01 particles cm^{-3}; Tabazadeh et al. [2000]). The NAT radius settles with a value of r_0 ranging between 2 and 5 μm; this value depends on the model temperature and subsequent amount of condensed phase HNO_3 formed. This NAT median radius r_0 is also used to derive the terminal velocity for settling of NAT (section 8) and the eventual irreversible denitrification. The NAT surface area density is used to calculate the rate constants for heterogeneous reactions 7-11 (Table 3). Since the available HNO_3 is included inside the NAT aerosol, there is no STS aerosol present. However, there are still heterogeneous reactions occurring on the surface of LBS aerosols.

If the calculated atmospheric temperature, T, becomes less than or equal to the saturation temperature (T_{sat}) for water vapor over ice (e.g., Marti and Mauersberger [1993]), water-ice aerosols can form. In WACCM4.0 the condensed phase H_2O is derived in the prognotic water routines of CAM and passed into the chemistry module. Using this condensed phase H_2O, the median radius and the surface area density for water-ice are again derived following the approach of Considine et al. [2000]. The water-ice median radius and surface area density assumes a lognormal size distribution, a width of a distribution = 1.6 [Dye et al., 1992], and a number density of 0.001 particles cm^{-3} [Dye et al., 1992]. The value of r_0 is typically 10μm. The water-ice surface area density is used for the calculation of the rate constants for reactions 12-17 (Table 3).

Sedimentation of Stratospheric Aerosols

The sedimentation of HNO_3 in stratospheric aerosols follows the approach described in Considine et al. [2000]. The following equation is used to derive the flux (F) of HNO_3, as NAT aerosol, across model levels in units of molecules cm^{-2} sec^{-1}.

$$F_i = V_i \cdot C_i \exp(8 \ln^2 \sigma_i), \tag{5.84}$$

where $i = 1$ for NAT; V_i is the terminal velocity of the aerosol particles (cm s^{-1}); C is the condensed-phase concentration of HNO_3 (molecules cm^{-3}); σ is the width of the lognormal size distribution for NAT (see discussion above). The terminal velocity is dependent on the given aerosol: 1) mass density; 2) median radius; 3) shape; 4) dynamic viscosity; and 5) Cunningham correction factor for spherical particles (see Fuch [1964] and Kasten [1968] for the theory behind the derivation of terminal velocity). For each aerosol type the terminal velocity could be calculated, however, in WACCM4.0 this quantity is only derived for NAT. Settling of HNO_3 contain in STS is not derived based on the assumption that the median radius is too small to cause any significant denitrification and settling of condensed phase H_2O is handled in the CAM4 prognostic water routines.

Ion Chemistry

WACCM4.0 includes a six constituent ion chemistry model (O^+, O_2^+, N^+, N_2^+, NO^+, and electrons) that represents the the E-region ionosphere. The global mean ion and electron distributions simulated by WACCM4.0 for solar minimum conditions are shown in Figure 5.1, which clearly shows that the dominant ions in this region are NO^+ and O_2^+. Ion-neutral and recombination reactions included in WACCM4.0 are listed in Table 5.6.7. The reaction rate constants for these reactions are taken from R.G.Roble [1995].

Ionization sources include not only the aforementioned absorption of extreme ultraviolet and soft x-ray photons, and photoelectron impact, but also energetic particles precipitation in the auroral regions. The latter is calculated by a parameterization based on code from the NCAR TIME-GCM model [Roble and Ridley, 1987] that rapidly calculates ion-pair production rates, including production in the polar cusp and polar cap. The parameterization takes as input hemispheric power (HP), the estimated power in gigawatts deposited in the polar regions by energetic particles.

Currently WACCM4.0 uses a parameterization of HP (in GW) based on an empirical relationships between HP and the K_p planetary geomagnetic index. For $K_p \leq 7$, WACCM4.0 uses the relationship obtained by Zhang and Paxton [2008] from TIMED/GUVI observations:

$$\mathrm{HP} = 16.82 * K_p * \exp(0.32) - 4.86 \tag{5.85}$$

For $K_p > 7$, WACCM4.0 linearly interpolates HP, assuming HP equals to 300 when K_p is 9, based on NOAA satellite measurements:

$$\mathrm{HP} = 153.13 + \frac{K_p - 7}{9 - 7} * (300 - 153.13) \tag{5.86}$$

K_p is also available from NOAA's Space Environment Center and covers the period from 1933 to the present, making it ideal for long-term retrospective simulations.

Total ionization rates at 110km during July for solar maximum conditions are shown in Figure 5.2a. The broad region of ionization centered in the tropics is a result of EUV ionization, and has a peak value of almost 10^3 at 22°N. Ionization rates from particle precipitation can exceed this rate by 40% but are limited to the high-latitudes, as can been seen by the two bands that are approximately aligned around the magnetic poles. The global mean ionization rate (Figure 5.2b)

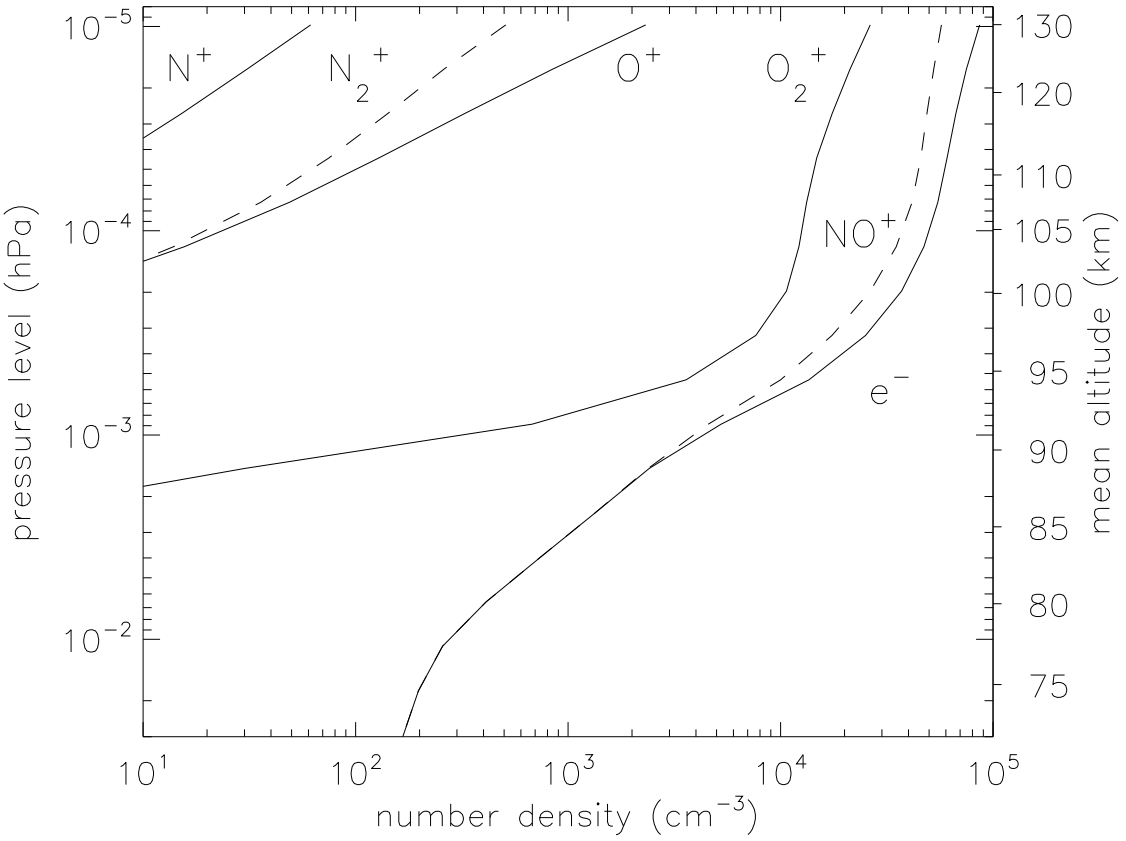

Figure 5.1: Global mean distribution of charged constituents during July solar minimum conditions.

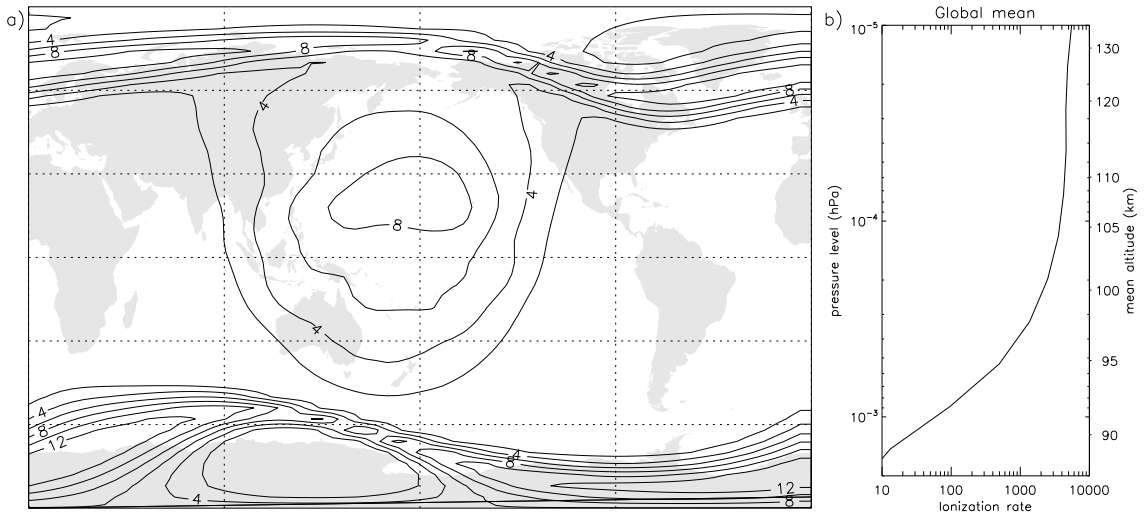

Figure 5.2: a) Global distribution of ionization rates at 7.3×10^{-5} hPa, July 1, UT0100 HRS. Contour interval is 2×10^{3} cm^{-3} s^{-1}. b) Simultaneous global mean ionization rates (cm^{-3} s^{-1}) versus pressure.

An important aspect of including ionization processes (both in the aurora and by energetic photons and photoelectrons), is that it leads to a more accurate representation of thermospheric nitric oxide. Not only does nitric oxide play an important role in the energy balance of the lower thermosphere through emission at 5.3 μm, it might also be transported to the upper stratosphere, where it can affect ozone concentrations. Nitric oxide is produced through quenching of N(^2D):

$$N(^2D) + O_2 \rightarrow NO + O(^1D) + 1.84eV \tag{5.87}$$

N(^2D) is produced either via recombination of NO^+ (see Table 5.6.7) or directly by ionization of molecular nitrogen. The branching ratio between N(^2D) and ground-state atomic nitrogen for the photoionization process is critical in determining the effectiveness of NO production. If ground-state atomic nitrogen is produced then it can react with NO to produce molecular nitrogen and effectively remove to members of the NOx family. In WACCM4.0 60% of the atomic nitrogen produced is in the excited state, which implies absorption of EUV results in a net source of NO. Also shown are maxima at high latitudes due to auroral ionization. WACCM4.0 reproduces many of the features of the Nitric Oxide Empirical Model (NOEM) distribution [Marsh et al., 2004], which is based on data from the Student Nitric Oxide Explorer satellite [Barth et al., 2003] In particular, larger NO in the winter hemisphere (a result of less photolytic loss), and a more localized NO maximum in the Northern Hemisphere (related to the lesser offset of geographic and magnetic poles, and so less spread when viewed as a geographic zonal mean).

Table 5.2: WACCM4.0 Neutral Chemical Species (51 computed species + N_2)

no.	Symbolic Name	Chemical Formula	Numerics	Deposition	Boundary Condition
1	O	$O(^3P)$	Implicit		ubvmr
2	O1D	$O(^1D)$	Implicit		
3	O3	O_3	Implicit	dry	
4	O2	O_2	Implicit		ubvmr
5	O2_1S	$O_2(^1\Sigma)$	Implicit		
6	O2_1D	$O_2(^1\Delta)$	Implicit		
7	H	H	Implicit		ubvmr
8	OH	OH	Implicit		
9	HO2	HO_2	Implicit		
10	H2	H_2	Implicit		vmr, ubvmr
11	H2O2	H_2O_2	Implicit	dry, wet	
12	N	N	Implicit		ubvmr
13	N2D	$N(^2D)$	Implicit		from TIME-GCM
14	N2	N_2	Invariant		
15	NO	NO	Implicit		flux, ubvmr, lflux, airflux
16	NO2	NO_2	Implicit	dry	
17	NO3	NO_3	Implicit		
18	N2O5	N_2O_5	Implicit		
19	HNO3	HNO_3	Implicit	dry, wet	
20	HO2NO2	HO_2NO_2	Implicit	dry, wet	
21	CL	Cl	Implicit		
22	CLO	ClO	Implicit		
23	CL2	Cl_2	Implicit		
24	OCLO	OClO	Implicit		
25	CL2O2	Cl_2O_2	Implicit		
26	HCL	HCl	Implicit	wet	
27	HOCL	HOCl	Implicit	wet	
28	ClONO2	$ClONO_2$	Implicit	wet	
29	BR	Br	Implicit		
30	BRO	BrO	Implicit		
31	HOBR	HOBr	Implicit	wet	
32	HBR	HBr	Implicit	wet	
33	BrONO 2	$BrONO_2$	Implicit	wet	
34	BRCL	BrCl	Implicit		

Table 5.1: (continued) WACCM4.0 Neutral Chemical Species (51 computed species + N_2)

no.	Symbolic Name	Chemical Formula	Numerics	Deposition	Boundary Condition
35	CH4	CH_4	Implicit		vmr, airflux
36	CH3O2	CH_3O_2	Implicit		
37	CH3OOH	CH_3OOH	Implicit	dry, wet	
38	CH2O	CH_2O	Implicit	dry, wet	flux
39	CO	CO	Explicit	dry	flux, ubvmr, airflux
40	CH3CL	CH_3Cl	Explicit		vmr
41	CH3BR	CH_3Br	Explicit		vmr
42	CFC11	$CFCl_3$	Explicit		vmr
43	CFC12	CF_2Cl_2	Explicit		vmr
44	CFC113	CCl_2FCClF_2	Explicit		vmr
45	HCFC22	$CHClF_2$	Explicit		vmr
46	CCL4	CCl_4	Explicit		vmr
47	CH3CCL3	CH_3CCl_3	Explicit		vmr
48	CF2CLBR	CBr_2F_2 (Halon-1211)	Explicit		vmr
49	CF3BR	$CBrF_3$ (Halon-1301)	Explicit		vmr
50	H2O	H_2O	Explicit		flux
51	N2O	N_2O	Explicit		vmr
52	CO2	CO_2	Explicit		vmr, ubvmr

Deposition:
wet = wet deposition included
dry = surface dry deposition included
If there is no designation in the deposition column, this species is not operated on by wet or dry deposition algorthims.

Boundary Condition:
flux = flux lower boundary conditions
vmr = fixed volume mixing ratio (vmr) lower boundary condition
ubvmr = fixed vmr upper boundary condition
lflux = lightning emission included for this species
airflux= aircraft emissions included for this species
If there is no designation in the Boundary Conditions column, this species has a zero flux boundary condition for the top and bottom of the model domain.

Table 5.2: WACCM4.0 Gas-phase Reactions.

no.	Reactions	Comments
	Oxygen Reactions	
1	$O + O_2 + M \rightarrow O_3 + M$	JPL-06
2	$O + O_3 \rightarrow 2\ O_2$	JPL-06
3	$O + O + M \rightarrow O_2 + M$	Smith and Robertson (2008)
4	$O_2(^1\Sigma) + O \rightarrow O_2(^1\Delta) + O$	JPL-06
5	$O_2\ 1S + O_2 \rightarrow O_2(^1\Delta) + O_2$	JPL-06
6	$O_2(^1\Sigma) + N_2 \rightarrow O_2(^1\Delta) + N_2$	JPL-06
7	$O_2(^1\Sigma) + O_3 \rightarrow O_2(^1\Delta) + O_3$	JPL-06
8	$O_2(^1\Sigma) + CO_2 \rightarrow O_2(^1\Delta) + CO_2$	JPL-06
9	$O_2(^1\Sigma) \rightarrow O_2$	JPL-06
10	$O_2(^1\Delta) + O \rightarrow O_2 + O$	JPL-06
11	$O_2(^1\Delta) + O_2 \rightarrow 2\ O_2$	JPL-06
12	$O_2(^1\Delta) + N_2 \rightarrow O_2 + N_2$	JPL-06
13	$O_2(^1\Delta) \rightarrow O_2$	JPL-06
14	$O(^1D) + N_2 \rightarrow O + N_2$	JPL-06
15	$O(^1D) + O_2 \rightarrow O + O_2(^1\Sigma)$	JPL-06
16	$O(^1D) + O_2 \rightarrow O + O_2$	JPL-06
17	$O(^1D) + H_2O \rightarrow 2\ OH$	JPL-06
18	$O(^1D) + N_2O \rightarrow 2\ NO$	JPL-06
19	$O(^1D) + N_2O \rightarrow N_2 + O_2$	JPL-06
20	$O(^1D) + O_3 \rightarrow 2\ O_2$	JPL-06
21	$O(^1D) + CFC11 \rightarrow 3\ Cl$	JPL-06; Bloomfield [1994] for quenching of $O(^1D)$
22	$O(^1D) + CFC12 \rightarrow 2\ Cl$	JPL-06; Bloomfield [1994]
23	$O(^1D) + CFC113 \rightarrow 3\ Cl$	JPL-06; Bloomfield [1994]
24	$O(^1D) + HCFC22 \rightarrow Cl$	JPL-06; Bloomfield [1994]
25	$O(^1D) + CCl_4 \rightarrow 4\ Cl$	JPL-06
26	$O(^1D) + CH_3Br \rightarrow Br$	JPL-06
27	$O(^1D) + CF_2ClBr \rightarrow Cl + Br$	JPL-06
28	$O(^1D) + CF_3Br \rightarrow Br$	JPL-06
29	$O(^1D) + CH_4 \rightarrow CH_3O_2 + OH$	JPL-06
30	$O(^1D) + CH_4 \rightarrow CH_2O + H + HO_2$	JPL-06
31	$O(^1D) + CH_4 \rightarrow CH_2O + H_2$	JPL-06
32	$O(^1D) + H_2 \rightarrow H + OH$	JPL-06
33	$O(^1D) + HCl \rightarrow Cl + OH$	JPL-06
34	$O(^1D) + HBr \rightarrow Br + OH$	JPL-06

Table 5.2: (continued) WACCM4.0 Gas-phase Reactions.

no.	Reactions	Comments
	Nitrogen Radicals	
35	$N(^2D) + O_2 \rightarrow NO + O(^1D)$	JPL-06
36	$N(^2D) + O \rightarrow N + O$	JPL-06
37	$N + O_2 \rightarrow NO + O$	JPL-06
38	$N + NO \rightarrow N_2 + O$	JPL-06
39	$N + NO_2 \rightarrow N_2O + O$	JPL-06
40	$NO + O + M \rightarrow NO_2 + M$	JPL-06
41	$NO + HO_2 \rightarrow NO_2 + OH$	JPL-06
42	$NO + O_3 \rightarrow NO_2 + O_2$	JPL-06
43	$NO_2 + O \rightarrow NO + O_2$	JPL-06
44	$NO_2 + O + M \rightarrow NO_3 + M$	JPL-06
45	$NO_2 + O_3 \rightarrow NO_3 + O_2$	JPL-06
46	$NO_2 + NO_3 + M \rightarrow N_2O5 + M$	JPL-06
47	$N_2O_5 + M \rightarrow NO_2 + NO_3 + M$	JPL-06
48	$NO_2 + OH + M \rightarrow HNO_3 + M$	JPL-06
49	$HNO_3 + OH \rightarrow NO_3 + H_2O$	JPL-06
50	$NO_2 + HO_2 + M \rightarrow HO_2NO_2 + M$	JPL-06
51	$NO_3 + NO \rightarrow 2\ NO_2$	JPL-06
52	$NO_3 + O \rightarrow NO_2 + O_2$	JPL-06
53	$NO_3 + OH \rightarrow NO_2 + HO_2$	JPL-06
54	$NO_3 + HO_2 \rightarrow NO_2 + OH + O_2$	JPL-06
55	$HO_2NO_2 + OH \rightarrow NO_2 + H_2O + O_2$	JPL-06
56	$HO_2NO_2 + M \rightarrow HO_2 + NO_2 + M$	JPL-06

Table 5.2: (continued) WACCM4.0 Gas-phase Reactions.

no.	Reactions	Comments
	Hydrogen Radicals	
57	$H + O_2 + M \rightarrow HO_2 + M$	JPL-06
58	$H + O_3 + M \rightarrow OH + O_2$	JPL-06
59	$H + HO_2 \rightarrow 2\ OH$	JPL-06
60	$H + HO_2 \rightarrow H_2 + O_2$	JPL-06
61	$H + HO_2 \rightarrow H_2O + O$	JPL-06
62	$OH + O \rightarrow H + O_2$	JPL-06
63	$OH + O_3 \rightarrow HO_2 + O_2$	JPL-06
64	$OH + HO_2 \rightarrow H_2O + O_2$	JPL-06
65	$OH + OH \rightarrow H_2O + O$	JPL-06
66	$OH + OH + M \rightarrow H_2O_2 + M$	JPL-06
67	$OH + H_2 \rightarrow H_2O + H$	JPL-06
68	$OH + H_2O_2 \rightarrow H_2O + HO_2$	JPL-06
69	$HO_2 + O \rightarrow OH + O_2$	JPL-06
70	$HO_2 + O_3 \rightarrow OH + 2O_2$	JPL-06
71	$HO_2 + HO_2 \rightarrow H_2O_2 + O_2$	JPL-06
72	$H_2O_2 + O \rightarrow OH + HO_2$	JPL-06
	Chlorine Radicals	
73	$Cl + O_3 \rightarrow ClO + O_2$	JPL-06
74	$Cl + H_2 \rightarrow HCl + H$	JPL-06
75	$Cl + H_2O_2 \rightarrow HCl + HO_2$	JPL-06
76	$Cl + HO_2 \rightarrow HCl + O_2$	JPL-06
77	$Cl + HO_2 \rightarrow ClO + OH$	JPL-06
78	$Cl + CH_2O \rightarrow HCl + HO_2 + CO$	JPL-06
79	$Cl + CH_4 \rightarrow CH_3O_2 + HCl$	JPL-06
80	$ClO + O \rightarrow Cl + O_2$	JPL-06
81	$ClO + OH \rightarrow Cl + HO_2$	JPL-06
82	$ClO + OH \rightarrow HCl + O_2$	JPL-06
83	$ClO + HO_2 \rightarrow HOCl + O_2$	JPL-06
84	$ClO + NO \rightarrow NO_2 + Cl$	JPL-06
85	$ClO + NO_2 + M \rightarrow ClONO_2 + M$	JPL-06

Table 5.2: (continued) WACCM4.0 Gas-phase Reactions.

no.	Reactions	Comments
	Chlorine Radicals Continued	
86	$ClO + ClO \rightarrow 2\ Cl + O_2$	JPL-06
87	$ClO + ClO \rightarrow Cl2 + O_2$	JPL-06
88	$ClO + ClO \rightarrow Cl + OClO$	JPL-06
89	$ClO + ClO + M \rightarrow Cl_2O_2 + M$	JPL-06
90	$Cl_2O_2 + M \rightarrow 2\ ClO + M$	JPL-06
91	$HCl + OH \rightarrow H_2O + Cl$	JPL-06
92	$HCl + O \rightarrow Cl + OH$	JPL-06
93	$HOCl + O \rightarrow ClO + OH$	JPL-06
94	$HOCl + Cl \rightarrow HCl + ClO$	JPL-06
95	$HOCl + OH \rightarrow ClO + H_2O$	JPL-06
96	$ClONO_2 + O \rightarrow ClO + NO_3$	JPL-06
97	$ClONO_2 + OH \rightarrow HOCl + NO_3$	JPL-06
98	$ClONO_2 + Cl \rightarrow Cl_2 + NO_3$	JPL-06
no.	Reactions	Comments
	Bromine Radicals	
99	$Br + O_3 \rightarrow BrO + O_2$	JPL-06
100	$Br + HO_2 \rightarrow HBr + O_2$	JPL-06
101	$Br + CH_2O \rightarrow HBr + HO_2 + CO$	JPL-06
102	$BrO + O \rightarrow Br + O_2$	JPL-06
103	$BrO + OH \rightarrow Br + HO_2$	JPL-06
104	$BrO + HO_2 \rightarrow HOBr + O_2$	JPL-06
105	$BrO + NO \rightarrow Br + NO_2$	JPL-06
106	$BrO + NO_2 + M \rightarrow BrONO_2 + M$	JPL-06
107	$BrO + ClO \rightarrow Br + OClO$	JPL-06
108	$BrO + ClO \rightarrow Br + Cl + O_2$	JPL-06
109	$BrO + ClO \rightarrow BrCl + O_2$	JPL-06
110	$BrO + BrO \rightarrow 2\ Br + O_2$	JPL-06
111	$HBr + OH \rightarrow Br + H_2O$	JPL-06
112	$HBr + O \rightarrow Br + OH$	JPL-06
113	$HOBr + O \rightarrow BrO + OH$	JPL-06
114	$BrONO_2 + O \rightarrow BrO + NO_3$	JPL-06

Table 5.2: (continued) WACCM4.0 Gas-phase Reactions.

no.	Reactions	Comments
	Halogen Radicals	
115	$CH_3Cl + Cl \rightarrow HO_2 + CO + 2HCl$	JPL-06
116	$CH_3Cl + OH \rightarrow Cl + H_2O + HO_2$	JPL-06
117	$CH_3CCl_3 + OH \rightarrow 3\ Cl + H_2O$	JPL-06
118	$HCFC22 + OH \rightarrow Cl + H_2O + HO_2$	JPL-06
119	$CH_3Br + OH \rightarrow Br + H_2O + HO_2$	JPL-06
	CH_4 and Derivatives	
120	$CH_4 + OH \rightarrow CH_3O_2 + H_2O$	JPL-06
121	$CH_3O_2 + NO \rightarrow CH_2O + NO_2 + HO_2$	JPL-06
122	$CH_3O_2 + HO_2 \rightarrow CH_3OOH + O_2$	JPL-06
123	$CH_3OOH + OH \rightarrow 0.7\ CH_3O_2 + 0.3\ OH + 0.3\ CH_2O + H_2O$	JPL-06
124	$CH_2O + NO_3 \rightarrow CO + HO_2 + HNO_3$	JPL-06
125	$CH_2O + OH \rightarrow CO + H_2O + H$	JPL-06
126	$CH_2O + O \rightarrow OH + HO_2 + CO$	JPL-06
127	$CO + OH \rightarrow H + CO_2$	JPL-06

Table 5.3: WACCM4.0 Heterogeneous Reactions on liquid and solid aerosols.

no.	Reaction	Comments
	Sulfate Aerosol	
1	$N_2O_5 + H_2O \rightarrow 2\ HNO_3$	JPL-06; f (sulfuric acid wt %)
2	$ClONO_2 + H_2O \rightarrow HOCl + HNO_3$	JPL-06; f (T, P, HCl, H_2O, r)
3	$BrONO_2 + H_2O \rightarrow HOBr + HNO_3$	JPL-06; f (T, P, H_2O, r)
4	$ClONO_2 + HCl \rightarrow Cl_2 + HNO_3$	JPL-06; f (T, P, HCl, H_2O, r)
5	$HOCl + HCl \rightarrow Cl_2 + H_2O$	JPL-06; f (T, P, HCl, HCl, H_2O, r)
6	$HOBr + HCl \rightarrow BrCl + H_2O$	JPL-06; f (T, P, HCl, HOBr, H_2O, r)
	NAT Aerosol	
7	$N_2O_5 + H_2O \rightarrow 2\ HNO_3$	JPL-06; $\gamma = 4 \times 10^{-4}$
8	$ClONO_2 + H_2O \rightarrow HOCl + HNO_3$	JPL-06; $\gamma = 4 \times 10^{-3}$
9	$ClONO_2 + HCl \rightarrow Cl_2 + HNO_3$	JPL-06; $\gamma = 0.2$
10	$HCl + HCl \rightarrow Cl_2 + H_2O$	JPL-06; $\gamma = 0.1$
11	$BrONO_2 + H_2O \rightarrow HOBr + HNO_3$	JPL-06; $\gamma = 0.3$
	Water-Ice Aerosol	
12	$N_2O_5 + H_2O \rightarrow 2\ HNO_3$	JPL-06; $\gamma = 0.02$
13	$ClONO_2 + H_2O \rightarrow HOCl + HNO_3$	JPL-06; $\gamma = 0.3$
14	$BrONO_2 + H_2O \rightarrow HOBr + HNO_3$	JPL-06; $\gamma = 0.3$
15	$ClONO_2 + HCl \rightarrow Cl_2 + HNO_3$	JPL-06; $\gamma = 0.3$
16	$HOCl + HCl \rightarrow Cl_2 + H_2O$	JPL-06; $\gamma = 0.2$
17	$HOBr + HCl \rightarrow BrCl + H_2O$	JPL-06; $\gamma = 0.3$

Table 5.4: WACCM4.0 Photolytic Reactions.

no.	Reactants	Products	Comments
1	$O_2 + h\nu$	$O + O(^1D)$	Ly-α: Chabrillat and Kockarts (1997, 1998) ϕ(Ly-α): Lacoursiere et al. (1999) SRB: Koppers and Murtaugh (1996) For wavelengthν regions not Ly-α or SRB, σ (120-205nm): Brasseur and Solomon (1986); σ (205-240 nm): Yoshino et al. (1988)
2	$O_2 + h\nu$	2 O	see above
3	$O_3 + h\nu$	$O(^1D) + O_2$	σ (120-136.5nm): Tanaka et al. (1953); σ (136.5-175nm): Ackerman (1971); σ (175-847nm): WMO (1985); except for σ (185-350nm): Molina and Molina (1986) ϕ (<280nm): Marsh (1999) ϕ (>280nm): JPL-06.
4	$O_3 + h\nu$	$O + O_2$	see above
5	$N_2O + h\nu$	$O(^1D) + N_2$	JPL-06
6	$NO + h\nu$	N + O	Minschwaner et al. (1993)
7	$NO + h\nu$	$NO^+ + e$	
8	$NO_2 + h\nu$	NO + O	JPL-06
9	$N_2O_5 + h\nu$	$NO_2 + NO_3$	JPL-06
10	$N_2O5 + h\nu$	$NO + O + NO_3$	JPL-06
11	$HNO_3 + h\nu$	$OH + NO_2$	JPL-06
12	$NO_3 + h\nu$	$NO_2 + O$	JPL-06
13	$NO_3 + h\nu$	$NO + O_2$	JPL-06
14	$HO_2NO_2 + h\nu$	$OH + NO_3$	JPL-06
15	$HO_2NO_2 + h\nu$	$NO_2 + HO_2$	JPL-06
16	$CH_3OOH + h\nu$	$CH_2O + H + OH$	JPL-06
17	$CH_2O + h\nu$	CO + 2 H	JPL-06
18	$CH_2O + h\nu$	$CO + H_2$	JPL-06
19	$H_2O + h\nu$	H + OH	ϕ (Ly-α): Slanger et al. (1982); ϕ (105-145nm): Stief et al. (1975); ϕ (>145): JPL-06 ϕ (120-182nm): Yoshino et al. (1996); ϕ (183-194nm): Cantrell et al. (1997)

Table 5.4: (continued) WACCM4.0 Photolytic Reactions.

no.	Reactants	Products	Comments
20	H_2O + hν	H_2 + O(^{1}D)	(see above)
21	H_2O + hν	H + 2 O	(see above)
22	H_2O_2 + hν	2 OH	JPL-06
23	Cl_2 + hν	2 Cl	JPL-06
24	ClO + hν	Cl + O	JPL-06
25	OClO + hν	O + ClO	JPL-06
26	Cl_2O_2 + hν	Cl + ClOO	Burkholder et al. (1990); Stimpfle et al. (2004)
27	HOCl + hν	Cl + OH	JPL-06
28	HCl + hν	Cl + H	JPL-06
29	$ClONO_2$ + hν	Cl + NO_3	JPL-06
30	$ClONO_2$ + hν	ClO + NO_2	JPL-06
31	BrCl + hν	Br + Cl	JPL-06
32	BrO + hν	Br + O	JPL-06
33	HOBr + hν	Br + OH	JPL-06
34	$BrONO_2$ + hν	Br + NO_3	JPL-06
35	$BrONO_2$ + hν	BrO + NO_2	JPL-06
36	CH_3Cl + hν	Cl + CH_3O_2	JPL-06
37	CCl_4 + hν	4 Cl	JPL-06
38	CH_3CCl3 + hν	3 Cl	JPL-06
39	CFC11 + hν	3 Cl	JPL-06
40	CFC12 + hν	2 Cl	JPL-06
41	CFC113 + hν	3 Cl	JPL-06
42	HCFC22 + hν	Cl	JPL-06
43	CH_3Br + hν	Br + CH_3O_2	JPL-06
44	CF_3Br + hν	Br	JPL-06
45	CF_2ClBr + hν	Br + Cl	JPL-06
46	CO_2 + hν	CO + O	σ (120-167): Nakata, et al. (1965); σ (167-199): Huffman (1971)
47	CH_4 + hν	H + CH_3O_2	σ: JPL-06; based on Brownsword et al. (1997)
48	CH_4 + hν	H_2 + 0.18 CH_2O + 0.18 O + 0.44 CO_2 + 0.44 H_2 + 0.38 CO + 0.05 H_2O	see above

Table 5.5: Ion-neutral and recombination reactions and exothermicities.

Reaction	ΔH (kJ mol^{-1})
$O^+ + O_2 \rightarrow O_2^+ + O$	150.11
$O^+ + N_2 \rightarrow NO^+ + N$	105.04
$N_2^+ + O \rightarrow NO^+ + N(^2D)$	67.53
$O_2^+ + N \rightarrow NO^+ + O$	406.16
$O_2^+ + NO \rightarrow NO^+ + O_2$	271.38
$N^+ + O_2 \rightarrow O_2^+ + N$	239.84
$N^+ + O_2 \rightarrow NO^+ + O$	646.28
$N^+ + O \rightarrow O^+ + N$	95.55
$N_2^+ + O_2 \rightarrow O_2^+ + N_2$	339.59
$O_2^+ + N_2 \rightarrow NO^+ + NO$	–
$N_2^+ + O \rightarrow O^+ + N_2$	–
$NO^+ + e \rightarrow 0.2N + 0.8N(^2D) + O$	82.389
$O_2^+ + e \rightarrow 1.15O + 0.85O(^1D)$	508.95
$N_2^+ + e \rightarrow 1.1N + 0.9N(^2D)$	354.83

5.6.8 Electric Field

The global electric field is based on a composite of two empirical models for the different latitude regions: at high latitude the Weimer95 model [Weimer, 1995], and at low- and midlatitude the Scherliess model [Scherliess et al., 2002]. In the following the different models are described since the model is not published to date.

Low- and midlatitude electric potential model

The low- and mid latitude electric field model was developed by Lűdger Scherliess [Scherliess et al., 2002]. It's based on Incoherent Scatter Radar data (ISR) from Jicamarca, Arecibo, Saint Santin, Millstone Hill, and the MU radar in Shigaraki. The electric field is calculated for a given year, season, UT, S_a, local time, and with longitudinal/latitudinal variation. The empirical model is constructed from a model for low solar flux ($S_a = 90$) and a high solar flux model ($S_a = 180$). The global electric potential is expressed according to Richmond et al. [1980] by

$$\Phi(d,T,t,\lambda) = \sum_{k=0}^{2}\sum_{l=-2}^{2}\sum_{m=-n}^{n}\sum_{n=1}^{12} A_{klmn} P_n^m(sin\lambda) f_m(\frac{2\Pi t}{24}) f_l(\frac{2\Pi T}{24}) f_{-k}(\frac{2\Pi(d+9)}{365.24}) \tag{5.88}$$

Table 5.6: Ionization reactions.

$O + h\nu \rightarrow O^+ + e$
$O + e^* \rightarrow O^+ + e + e^*$
$N + hv \rightarrow N^+ + e$
$O_2 + h\nu \rightarrow O_2^+ + e$
$O_2 + e^* \rightarrow O_2^+ + e + e^*$
$O_2 + h\nu \rightarrow O + O^+ + e$
$O_2 + e^* \rightarrow O + O^+ + e + e^*$
$N_2 + h\nu \rightarrow N_2^+ + e$
$N_2 + e^* \rightarrow N_2^+ + e + e^*$
$N_2 + h\nu \rightarrow N + N^+ + e$
$N_2 + e^* \rightarrow N + N^+ + e + e^*$
$N_2 + h\nu \rightarrow N(^2D) + N^+ + e$
$N_2 + e^* \rightarrow N(^2D) + N^+ + e + e^*$

Table 5.7: EUVAC model parameters.

wavelength interval nm	F_i^0 ph cm^{-2}s^{-1}	R_i
0.05 - 0.4	5.010e+01	6.240e-01
0.4 - 0.8	1.000e+04	3.710e-01
0.8 - 1.8	2.000e+06	2.000e-01
1.8 - 3.2	2.850e+07	6.247e-02
3.2 - 7.0	5.326e+08	1.343e-02
7.0 - 15.5	1.270e+09	9.182e-03
15.5 - 22.4	5.612e+09	1.433e-02
22.4 - 29.0	4.342e+09	2.575e-02
29.0 - 32.0	8.380e+09	7.059e-03
32.0 - 54.0	2.861e+09	1.458e-02
54.0 - 65.0	4.830e+09	5.857e-03
65.0 - 79.8	1.459e+09	5.719e-03
65.0 - 79.8	1.142e+09	3.680e-03
79.8 - 91.3	2.364e+09	5.310e-03
79.8 - 91.3	3.655e+09	5.261e-03
79.8 - 91.3	8.448e+08	5.437e-03
91.3 - 97.5	3.818e+08	4.915e-03
91.3 - 97.5	1.028e+09	4.955e-03
91.3 - 97.5	7.156e+08	4.422e-03
97.5 - 98.7	4.482e+09	3.950e-03
98.7 - 102.7	4.419e+09	5.021e-03
102.7 - 105.0	4.235e+09	4.825e-03
105.0 - 121.0	2.273e+10	3.383e-03

with

$$f_m(\phi) = \sqrt{2}\sin(m\phi) \qquad m > 0 \tag{5.89}$$
$$f_m(\phi) = 1 \qquad m = 0 \tag{5.90}$$
$$f_m(\phi) = \sqrt{2}\cos(m\phi) \qquad m < 0 \tag{5.91}$$

the day of the year is denoted by d, universal time by T, magnetic local time by t, and geomagnetic latitude λ. The values of d, T, and t are expressed as angles between 0 and 2Π. P_n^m are fully normalized Legendre polynomials. Due to the assumption that the geomagnetic field lines are highly conducting, the $n + m$ odd coefficients are set to zero to get a symmetrical electric potential about the magnetic equator. The coefficients A_{klmn} are found by a least–square fit for low and high solar flux. The solar cycle dependence is introduced by inter- and extrapolation of the sets of coefficients A_{klmn}^{low} for $S_a = 90$ and A_{klmn}^{high} for $S_a = 180$.

$$A_{klmn} = A_{klmn}^{low} + S_{aM}[A_{klmn}^{high} - A_{klmn}^{low}] \tag{5.92}$$

with

$$S_{aM} = \frac{arctan[(S_a - 65)^2/90^2] - a_{90}}{a_{180} - a_{90}} \tag{5.93}$$
$$a_{90} = arctan[(90 - 65)^2/90^2] \tag{5.94}$$
$$a_{180} = arctan[(180 - 65)^2/90^2] \tag{5.95}$$

We are using the daily $F_{10.7}$ number for S_a. S_{aM} levels off at high and low solar flux numbers, and therefore the model does not predict unrealistic high or low electric potential values.

The geomagnetic field is described by modified apex coordinates [Richmond, 1995] which already take into account the distortion of the magnetic field. Modified apex coordinates have a reference height associated with them, which in our case is set to 130 km. The electric field $\mathbf{E}$ and the electromagnetic drift velocity $\mathbf{v}_E$ can be expressed by quantities mapped to the reference height, e.g. by E_{d1}, E_{d2} and v_{e1}, v_{e2}. These quantities are not actual electric field or electromagnetic drift velocity components, but rather the representation of the electric field or electromagnetic drift velocities by being constant along the geomagnetic field line. The fields in an arbitrary direction $\mathbf{I}$ can be expressed by

$$\mathbf{I} \cdot \mathbf{E} = \mathbf{I} \cdot \mathbf{d}_1 E_{d1} + \mathbf{I} \cdot \mathbf{d}_2 E_{d2} \tag{5.96}$$
$$\mathbf{I} \cdot \mathbf{v}_E = \mathbf{I} \cdot \mathbf{e}_1 v_{e1} + \mathbf{I} \cdot \mathbf{e}_2 v_{e2} \tag{5.97}$$

The basis vector $\mathbf{d}_1$ and $\mathbf{e}_1$ are in more–or–less magnetic eastward direction and $\mathbf{d}_2$ and $\mathbf{e}_2$ in downward/ equatorward direction. The base vectors vary with height, $\mathbf{d}_i$ is decreasing and $\mathbf{e}_i$ increasing with altitude. Therefore when the base vectors are applied to the mapped field at the reference height, e.g. E_{d1}, E_{d2} and v_{e1}, v_{e2}, they already take into account the height and directional variation of the corresponding quantity. Note that the modified apex coordinates are using the International Geomagnetic Reference Field (IGRF), and in the WACCM4 code the IGRF is only defined between the years 1900 and 2000. The description of the IGRF can be updated every 5 years to be extended in time.

High–latitude electric potential model

The high–latitude electric potential model from Weimer [Weimer, 1995] is used. The model is based on spherical harmonic coefficients that were derived by least square fitting of measurements from the Dynamics Explorer 2 (DE2) satellite. The variation of the spherical harmonic coefficients with the interplanetary magnetic field (IMF) clock angle, IMF strength, solar wind velocity and season can be reproduced by a combination of Fourier series and multiple linear regression formula. The final model varies with magnetic latitude, magnetic local time, season, IMF strength and direction, and solar wind velocity. For our purpose we have set the solar wind speed to a constant value of 400 km/s and only consider the effects of IMF B_z ($B_y = 0$). Since the IMF conditions are not known all the time, we developed an empirical relation between B_z and the K_p index and the solar flux number S_a. Both, the K_p index and the daily solar flux number $F_{10.7}$, are known in the WACCM4 model.

$$\begin{aligned} B_z(K_p, F_{10.7}) = &- 0.085K_p^2 - 0.08104K_p + 0.4337 + \\ &0.00794F_{10.7} - 0.00219K_pF_{10.7} \end{aligned} \tag{5.98}$$

Note that the Weimer model uses an average year of 365.24 days/year and an average month of 30.6001 days/month. The boundary of the Weimer model is at 46^o magnetic latitude. The model was developed for an averaged northern and southern hemisphere. The B_y value and the season are reversed to get the values for the other hemisphere.

Combing low–/ mid–latitude with the high latitude electric potential

After the low/mid–latitude electric potential Φ_{mid} and the high latitude potential Φ_{hgh} are calculated, both patterns are combined to be smooth at the boundary. The boundary between high and mid latitude λ_{bnd} is defined to lie where the electric field magnitude E from Φ_{hgh} equals 15 mV/m. After finding the longitudinal variation of the high latitude boundary λ_{bnd}, it's shifted halfway towards 54^o magnetic latitude. The width of the transition zone $2\Delta\lambda_{trs}$ from high to mid latitude varies with magnetic local time. First, the high and mid latitude electric potential are adjusted by a constant factor such that the average for the high and mid latitude electric potential along the boundary λ_{bnd} are the same. The combined electric potential Φ is defined by

$$\Phi = \begin{cases} \Phi_{mid} & |\lambda| < \lambda_{bnd} - \Delta\lambda_{trs} \\ \Phi_{hgh} & |\lambda| > \lambda_{bnd} + \Delta\lambda_{trs} \\ F_{int}(\Phi_{mid}, \Phi_{hgh}) & \lambda_{bnd} - \Delta\lambda_{trs} \le |\lambda| \le \lambda_{bnd} + \Delta\lambda_{trs} \end{cases} \tag{5.99}$$

with

$$\begin{aligned} F_{int}(\Phi_{mid}, \Phi_{hgh}) = \frac{1}{3}\frac{1}{2\Delta\lambda_{trs}}[&\{\Phi_{mid}(\phi, \lambda_{bnd} - \Delta\lambda_{trs}) + 2\Phi_{mid}(\phi, \lambda)\} \\ &\{\lambda_{bnd} - |\lambda| + \Delta\lambda_{trs}\} + (\Phi_{hgh}(\phi, \lambda_{bnd} + \Delta\lambda_{trs}) + \\ &2\Phi_{hgh}(\phi, \lambda))\{-\lambda_{bnd} + |\lambda| + \Delta\lambda_{trs}\}] \end{aligned} \tag{5.100}$$

4616 **Calculation of electric field**

The electric field can be derived from the electric potential by

$$\mathbf{E} = -\nabla\Phi \tag{5.101}$$

The more-or-less magnetic eastward electric field component E_{d1} and the in general downward/ equatorward E_{d2} component are calculated. These components are constant along the magnetic field line. They are calculated at a reference height $h_r =$ 130 km with $R = R_{earth} + h_r$. The electric field does not vary much with altitude, and therefore we assume in the code that the electric field is constant in height.

$$E_{d1} = -\frac{1}{Rcos\lambda}\frac{\partial\Phi}{\partial\phi} \tag{5.102}$$

$$E_{d2} = \frac{1}{R\sin I}\frac{\partial\Phi}{\partial\lambda} \tag{5.103}$$

4617 with $\sin I = 2\sin\lambda[4 - 3\cos^2\lambda]^{0.5}$.

4618 **Calculation of electrodynamic drift velocity**

The electric field is calculated on a $2^o \times 2^o$ degree geomagnetic grid with the magnetic longitude represented by the magnetic local time (MLT) from 0 MLT to 24 MLT. Therefore, the magnetic local time of the geographic longitudes of the WACCM4 grid has to be determined first to map from the geomagnetic to the geographic WACCM4 grid. The magnetic local time is calculated by using the location of the geomagnetic dipole North pole, the location of the subsolar point, and the apex longitude of the geographic WACCM4 grid point. A bilinear interpolation is used for the mapping. Note that every processor calculates the global electric field, which is computationally inexpensive. Otherwise, to calculate the electric field some communication between the different processors would be necessary to get the spatial derivatives.
The mapped electric field is rotated into the geographic direction by

$$\mathbf{E} = \mathbf{d}_1 E_{d1} + \mathbf{d}_2 E_{d2} \tag{5.104}$$

with the components of $\mathbf{E}$ being the geographic eastward, westward and upward electric field.
At high altitudes the ion–neutral collision frequency ν_{in} is small in relation to the angular gyrofrequency of the ions Ω_i ($\nu_{in} \ll \Omega_i$), and the electron–neutral collision frequency ν_{en} is much smaller than the angular gyrofrequency of the electrons Ω_e ($\nu_{en} \ll \Omega_e$), due to the decrease in neutral density with increasing altitude. Therefore, the ion drift $\mathbf{v}_{i\perp}$ perpendicular to the geomagnetic field can be simplified by the electrodynamic drift velocity $\mathbf{v}_E$

$$\mathbf{v}_{i\perp} \approx \mathbf{v}_E = \frac{\mathbf{E} \times \mathbf{B}_o}{\mathbf{B}_o^2} \tag{5.105}$$

4619 with $\mathbf{B}_o$ the geomagnetic main field from IGRF.

Ion drag calculation

The following is written according to the source code. Two subroutines iondrag_calc exist in the code, one uses the calculated ion drag coefficients if WACCM_MOZART is used, and the other one uses look-up tables for the ion drag coefficients λ_1 and λ_2.
It is assumed that the electron T_e and ion T_i temperature is equal to the neutral temperature T_n.

$$T_i = T_e = T_n \tag{5.106}$$

The dip angle I of the geomagnetic field is calculated by

$$I = \arctan \frac{B_z}{\sqrt{B_{north}^2 + B_{east}^2}} \tag{5.107}$$

with a minimum dip angle $|I| \geq 0.17$. The declination is

$$D = \arctan \frac{B_{east}}{B_{north}} \tag{5.108}$$

The magnetic field component B_z, B_{east}, B_{north} are determined from the International Geomagnetic Reference Field (IGRF).
The collision frequencies ν in units of s^{-1} are determined by, e.g. Schunk and Nagy [2000]

$$\frac{1}{N_{O_2}}\nu_{O_2^+-O_2} = 2.59 \times 10^{-11}\sqrt{\frac{T_i+T_e}{2}}\left[1 - 0.73 log_{10}\sqrt{\frac{T_i+T_e}{2}}\right]^2 \tag{5.109}$$

$$\frac{1}{N_{O_2}}\nu_{O^+-O_2} = 6.64 \times 10^{-10} \tag{5.110}$$

$$\frac{1}{N_{O_2}}\nu_{NO^+-O_2} = 4.27 \times 10^{-10} \tag{5.111}$$

$$\frac{1}{N_O}\nu_{O^+-O} = 3.67 \times 10^{-11}\sqrt{\frac{T_i+T_e}{2}}\left[1 - 0.064 log_{10}\sqrt{\frac{T_i+T_e}{2}}\right]^2 f_{cor} \tag{5.112}$$

$$\frac{1}{N_O}\nu_{NO^+-O} = 2.44 \times 10^{-10} \tag{5.113}$$

$$\frac{1}{N_O}\nu_{O_2^+-O} = 2.31 \times 10^{-10} \tag{5.114}$$

$$\frac{1}{N_{N_2}}\nu_{O_2^+-N_2} = 4.13 \times 10^{-10} \tag{5.115}$$

$$\frac{1}{N_{N_2}}\nu_{NO^+-N_2} = 4.34 \times 10^{-10} \tag{5.116}$$

$$\frac{1}{N_{N_2}}\nu_{O^+-N_2} = 6.82 \times 10^{-10} \tag{5.117}$$

with N_n the number density for the neutral n in units of $1/cm^3$, and the temperature in Kelvins. The collisions frequencies for $\nu_{O_2^+-O_2}$ and ν_{O^+-O} are resonant, all other are nonresonant. The

arbitrary correction factor f_{cor} multiplies the ν_{O^+-O} collision frequency and is set to $f_{cor} = 1.5$ which has been found to improve agreement between calculated and observed winds and electron densities in the upper thermosphere in other models. The mean mass $\overline{m}_{mid}$ [g/mole] at the midpoints of the height level is calculated in the Mozart module. The number densities $[1/cm^3]$ are

$$N_{O_2} = \frac{N\overline{m}_{mid} mmr_{O_2}}{m_{O_2}} \tag{5.118}$$

$$N_O = \frac{N\overline{m}_{mid} mmr_O}{m_O} \tag{5.119}$$

$$N_{N_2} = \frac{N\overline{m}_{mid} mmr_{N_2}}{m_{N_2}} \tag{5.120}$$

$$N_{O_2^+} = \frac{N\overline{m}_{mid} mmr_{O_2^+}}{m_{O_2^+}} \tag{5.121}$$

$$N_{O^+} = \frac{N\overline{m}_{mid} mmr_{O^+}}{m_{O^+}} \tag{5.122}$$

$$N_e = \frac{N\overline{m}_{mid} mmr_e}{m_e} \tag{5.123}$$

with mmr the mass mixing ratio, and N the total number density in units of $1/cm^3$. The pressure $[dyne/cm^2]$ and the mean mass at the midpoint $\overline{m}_{mid}$ in units of $g/mole$ are

$$p = 10\, p_{mid} \tag{5.124}$$

$$N\overline{m}_{mid} = \frac{p\,\overline{m}}{k_B T_n} \tag{5.125}$$

with the factor 10 to convert from [Pa] to $[dyne/cm^2]$, and k_B the Boltzmann constant. The collision frequencies are

$$\nu_{O_2^+} = \nu_{O_2^+-O_2} + \nu_{O_2^+-O} + \nu_{O_2^+-N_2} \tag{5.126}$$

$$\nu_{O^+} = \nu_{O^+-O_2} + \nu_{O^+-O} + \nu_{O^+-N_2} \tag{5.127}$$

$$\nu_{NO^+} = \nu_{NO^+-O_2} + \nu_{NO^+-O} + \nu_{NO^+-N_2} \tag{5.128}$$

$$\begin{aligned} \nu_{en} = {} & 2.33 \times 10^{-11} N_{N_2} T_e (1 - 1.21 \times 10^{-4} T_e) + \\ & 1.82 \times 10^{-10} N_{O_2} \sqrt{T_e} (1 + 3.6 \times 10^{-2} \sqrt{T_e}) + \\ & 8.9 \times 10^{-11} N_O \sqrt{T_e} (1 + 5.7 \times 10^{-4} T_e) \end{aligned} \tag{5.129}$$

The ratios r between collision frequency ν and gyro frequency Ω are

$$r_{O_2^+} = \frac{\nu_{O_2^+}}{\Omega_{O_2^+}} \tag{5.130}$$

$$r_{O^+} = \frac{\nu_{O^+}}{\Omega_{O^+}} \tag{5.131}$$

$$r_{NO^+} = \frac{\nu_{NO^+}}{\Omega_{NO^+}} \tag{5.132}$$

$$r_e = \frac{\nu_{en}}{\Omega_e} \tag{5.133}$$

with the gyro frequency for ions $\Omega_i = eB/m_i$ and for electrons $\Omega_e = eB/m_e$. The Pedersen conductivity [S/m] is

$$\begin{aligned}\sigma_P =&\frac{e}{B}[N_{O^+}\frac{r_{O^+}}{1+r_{O^+}^2} + N_{O_2^+}\frac{r_{O_2^+}}{1+r_{O_2^+}^2}+\\ &N_{NO^+}\frac{r_{NO^+}}{1+r_{NO^+}^2} + N_e\frac{r_e}{1+r_e^2}]\end{aligned} \tag{5.134}$$

The Hall conductivity [S/m] is

$$\begin{aligned}\sigma_H =&\frac{e}{B}[-N_{O^+}\frac{1}{1+r_{O^+}^2} - N_{O_2^+}\frac{1}{1+r_{O_2^+}^2}-\\ &N_{NO^+}\frac{1}{1+r_{NO^+}^2} + N_e\frac{1}{1+r_e^2}]\end{aligned} \tag{5.135}$$

The ion drag coefficients are

$$\lambda_1 = \frac{\sigma_P B^2}{\rho} \tag{5.136}$$

$$\lambda_2 = \frac{\sigma_H B^2}{\rho} \tag{5.137}$$

with $\rho = N\frac{\overline{m}}{N_A}$, and N_A the Avagadro number. The ion drag tensor in magnetic direction $\underline{\lambda}^{mag}$ is

$$\underline{\lambda}^{mag} = \begin{pmatrix}\lambda_{xx}^{mag} & \lambda_{xy}^{mag}\\ \lambda_{yx}^{mag} & \lambda_{yy}^{mag}\end{pmatrix} = \begin{pmatrix}\lambda_1 & \lambda_2 sinI\\ -\lambda_2 sinI & \lambda_1 sin^2 I\end{pmatrix} \tag{5.138}$$

with the x–direction in magnetic east, and y–direction magnetic north in the both hemispheres. The ion drag tensor can be rotated in geographic direction by using the rotation matrix $\mathbf{R}$

$$\mathbf{R} = \begin{pmatrix}\cos D & \sin D\\ -\sin D & \cos D\end{pmatrix} \tag{5.139}$$

Applying the rotation to the ion drag tensor $\mathbf{R}\underline{\lambda}^{mag}\mathbf{R}^{-1}$ leads to

$$\Lambda = \begin{pmatrix}\lambda_{xx} & \lambda_{xy}\\ \lambda_{yx} & \lambda_{yy}\end{pmatrix} = \tag{5.140}$$

$$\begin{pmatrix}\lambda_{xx}^{mag}cos^2 D + \lambda_{yy}^{mag}sin^2 D & \lambda_{xy}^{mag} + (\lambda_{yy}^{mag} - \lambda_{xx}^{mag})\sin D\cos D\\ \lambda_{yx}^{mag} + (\lambda_{yy}^{mag} - \lambda_{xx}^{mag})\sin D\cos D & \lambda_{yy}^{mag}\cos^2 D + \lambda_{xx}^{mag}\sin^2 D\end{pmatrix} \tag{5.141}$$

The ion drag acceleration $\mathbf{a}_i$ due to the Ampère force is

$$\mathbf{a}_i = \frac{\mathbf{J}\times\mathbf{B}}{\rho} = \lambda_1(\mathbf{v}_E - \mathbf{u}_{n\perp}) + \lambda_2\hat{\mathbf{b}}\times(\mathbf{v}_E - \mathbf{u}_{n\perp}) \tag{5.142}$$

with $\mathbf{u}_{n\perp}$ the neutral wind velocity perpendicular to the geomagnetic field and $\hat{\mathbf{b}}$ the unit vector of the geomagnetic field. The tendencies on the neutral wind are calculated by

$$\frac{\partial \mathbf{v}_{En}}{\partial t} = -\Lambda\mathbf{v}_{En} \tag{5.143}$$

For stability an implicit scheme is used with

$$\frac{\mathbf{v}_{En}(t+\Delta t)-\mathbf{v}_{En}(t)}{\Delta t}=-\Lambda\mathbf{v}_{En}(t+\Delta t) \tag{5.144}$$

which leads to

$$(\frac{1}{\Delta t}I+\Lambda)\mathbf{v}_{En}(t+\Delta t)=\frac{1}{\Delta t}\mathbf{v}_{En}(t) \tag{5.145}$$

with I the unit matrix. Solving for $\mathbf{v}_{En}(t+\Delta t)$ gives

$$\mathbf{v}_{En}(t+\Delta t)=\frac{1}{\Delta t}(\frac{1}{\Delta t}I+\Lambda)^{-1}\mathbf{v}_{En}(t) \tag{5.146}$$

The tendencies are determined by

$$\frac{\partial\mathbf{v}_{En}}{\partial t}=\frac{\mathbf{v}_{En}(t+\Delta t)-\mathbf{v}_{En}(t)}{\Delta t}=\frac{1}{\Delta t}[\frac{1}{\Delta t}(\frac{1}{\Delta t}I+\Lambda)^{-1}-1]\mathbf{v}_{En}(t) \tag{5.147}$$

The tensor $\frac{1}{\Delta t}I+\Lambda$ is

$$\begin{pmatrix}\lambda^*_{11} & \lambda^*_{12}\\ \lambda^*_{21} & \lambda^*_{22}\end{pmatrix}=\begin{pmatrix}\frac{1}{\Delta t}+\lambda_{xx} & \lambda_{xy}\\ \lambda_{yx} & \frac{1}{\Delta t}+\lambda_{yy}\end{pmatrix} \tag{5.148}$$

$$\frac{Det}{\Delta t}=\frac{1}{\Delta t}\frac{1}{\lambda^*_{11}\lambda^*_{22}-\lambda^*_{12}\lambda^*_{21}} \tag{5.149}$$

The tendencies applied to the neutral winds with $\mathbf{v}_{En}=(u_E-u_n,v_E-v_n)$ gives

$$d_t u_i=\frac{1}{\Delta t}\left[\frac{Det}{\Delta t}\left(\lambda^*_{12}(v_E-v_n)-\lambda^*_{22}(u_E-u_n)\right)+u_E-u_n\right] \tag{5.150}$$

$$d_t v_i=\frac{1}{\Delta t}\left[\frac{Det}{\Delta t}\left(\lambda^*_{21}(u_E-u_n)-\lambda^*_{11}(v_E-v_n)\right)+v_E-v_n\right] \tag{5.151}$$

4621

4622

The electromagnetic energy transfer to the ionosphere is

$$\mathbf{J}\cdot\mathbf{E}=\mathbf{J}\cdot\mathbf{E}'+\mathbf{u}_n\cdot\mathbf{J}\times\mathbf{B} \tag{5.152}$$

The first term on the right hand side denotes the Joule heating, which is the electromagnetic energy transfer rate in the frame of reference of the neutral wind. The second term represents the generation of kinetic energy due to the Ampère force. Since the electric field is small along the magnetic field line, we consider only the perpendicular component to the magnetic field of the Joule heating $\mathbf{J}_\perp\cdot\mathbf{E}'$. The electric field in the frame of the neutral wind $\mathbf{u}$ can be written as

$$\mathbf{E}'=\mathbf{E}+\mathbf{u}\times\mathbf{B} \tag{5.153}$$

The Joule heating can be expressed by

$$\mathbf{J}_\perp \cdot \mathbf{E}' = \sigma_P \mathbf{E}'^2 \tag{5.154}$$

with

$$\mathbf{E}'^2 = B^2 (\frac{\mathbf{E} \times \mathbf{B}}{B^2} - \mathbf{u}_\perp)^2 \tag{5.155}$$

and $\frac{\mathbf{E}\times\mathbf{B}}{B^2}$ the electromagnetic drift velocity $\mathbf{v}_E$ with the components u_E and v_E. The Joule heating Q_J is

$$Q_J = (u_E - u_n)^2 \lambda_{xx} + (u_E - u_n)(v_E - v_n)(\lambda_{xy} - \lambda_{yx})_+ (v_E - v_n)^2 \lambda_{yy} \tag{5.156}$$

Note, that the vertical velocity components are not taken into account here.

5.6.9 Boundary Conditions

The upper boundary conditions for momentum and for most constituents are the usual zero flux conditions used in CAM4. However, in the energy budget of the thermosphere, much of the SW radiation at wavelengths <120 nm is absorbed above 145 km (the upper boundary of the model), where LW radiation is very inefficient. This energy is transported downward by molecular diffusion to below 120 km, where it can be dissipated more efficiently by LW emission. Imposing a zero flux upper boundary condition on heat omits a major term in the heat budget and causes the lower thermosphere to be much too cold. Instead, we use the Mass Spectrometer-Incoherent Scatter (MSIS) model [Hedin, 1987, 1991] to specify the temperature at the top boundary as a function of season and phase of the solar cycle. The version of the MSIS model used in WACCM4.0is NRLMSISE-00 [see http://uap-www.nrl.navy.mil/models_web/msis/msis_home.htm].

For chemical constituents, surface mixing ratios of CH_4, N_2O, CO_2, H_2, CFC-11, CFC-12, CFC-113, HCFC-22, H-1211, H-1301, CCl_4, CH_3CCH_3, CH_3Cl, and CH_3Br are specified from observations. The model accounts for surface emissions of NO_X and CO based on the emission inventories described in Horowitz et al. [2003]. The NO_X source from lightning is distributed according to the location of convective clouds based on Price et al. [1997*a*] and Price et al. [1997*b*], with a vertical profile following Pickering et al. [1998]. Aircraft emissions of NO_X and CO are included in the model and based on Friedl [1997].

At the upper boundary, a zero-flux upper boundary condition is used for most species whose mixing ratio is negligible in the lower thermosphere, while mixing ratios of other species are specified from a variety of sources. The MSIS model is used to specify the mixing ratios of O, O_2, H, and N; as in the case of temperature, the MSIS model returns values of these constituents as functions of season and phase of the solar cycle. CO and CO_2 are specified at the upper boundary using output from the TIME-GCM [Roble and Ridley, 1994]. NO is specified using data from the Student Nitric Oxide Explorer (SNOE) satellite [Barth et al., 2003], which has been parameterized as a function of latitude, season, and phase of the solar cycle in the Nitric Oxide Empirical Model (NOEM) of Marsh et al. [2004]. Finally, a global-mean value (typical of the sunlit lower thermosphere) is specified for species such as H_2O, whose abundance near the top of the model is very small under sunlit conditions, but which can be rapidly transported upward

by diffusive separation in polar night (since they are lighter than the background atmosphere). In these cases, a zero-flux boundary condition leads to unrealistically large mixing ratios at the model top in polar night.

Chapter 6

Initial and Boundary Data

6.1 Initial Data

In this section, we describe how the time integration is started from data consistent with the spectral truncation. The land surface model requires its own initial data, as described by Bonan [1996]. The basic initial data for the model consist of values of u, v, T, q, Π, and Φ_s on the Gaussian grid at time $t = 0$. From these, U, V, T', and Π are computed on the grid using (3.139), and (3.177). The Fourier coefficients of these variables U^m, V^m, T'^m, Π^m, and Φ_s^m are determined via an FFT subroutine (3.277), and the spherical harmonic coefficients $T_n'^m, \Pi_n^m$, and $(\Phi_s)_n^m$ are determined by Gaussian quadrature (3.278). The relative vorticity ζ and divergence δ spherical harmonic coefficients are determined directly from the Fourier coefficients U^m and V^m using the relations,

$$\zeta = \frac{1}{a(1-\mu^2)}\frac{\partial V}{\partial \lambda} - \frac{1}{a}\frac{\partial U}{\partial \mu}, \tag{6.1}$$

$$\delta = \frac{1}{a(1-\mu^2)}\frac{\partial U}{\partial \lambda} + \frac{1}{a}\frac{\partial V}{\partial \mu}. \tag{6.2}$$

The relative vorticity and divergence coefficients are obtained by Gaussian quadrature directly, using (3.282) for the λ–derivative terms and (3.285) for the μ–derivatives.

Once the spectral coefficients of the prognostic variables are available, the grid–point values of ζ, δ, T', Π, and Φ_s may be calculated from (3.308), the gradient $\nabla\Pi$ from (3.311) and (3.312), and U and V from (3.317) and (3.318). The absolute vorticity η is determined from the relative vorticity ζ by adding the appropriate associated Legendre function for f (3.245). This process gives grid–point fields for all variables, including the surface geopotential, that are consistent with the spectral truncation even if the original grid–point data were not. These grid–point values are then convectively adjusted (including the mass and negative moisture corrections).

The first time step of the model is forward semi–implicit rather than centered semi–implicit, so only variables at $t = 0$ are needed. The model performs this forward step by setting the variables at time $t = -\Delta t$ equal to those at $t = 0$ and by temporarily dividing $2\Delta t$ by 2 for this time step only. This is done so that formally the code and the centered prognostic equations of chapter 3 also describe this first forward step and no additional code is needed for this special step. The model loops through as indicated sequentially in chapter 3. The time step $2\Delta t$ is set to its original value before beginning the second time step.

6.2 Boundary Data

In addition to the initial grid–point values described in the previous section, the model also requires lower boundary conditions. The required data are surface temperature (T_s) at each ocean point, the surface geopotential at each point, and a flag at each point to indicate whether the point is land, ocean, or sea ice. The land surface model requires its own boundary data, as described by Bonan [1996]. A surface temperature and three subsurface temperatures must also be provided at non-ocean points.

For the uncoupled configuration of the model, a seasonally varying sea–surface temperature, and sea–ice concentration dataset is used to prescribe the time evolution of these surface quantities. This dataset prescribes analyzed monthly mid-point mean values of SST and ice concentration for the period 1950 through 2001. The dataset is a blended product, using the global HadISST OI dataset prior to 1981 and the Smith/Reynolds EOF dataset post-1981 (see Hurrell, 2002). In addition to the analyzed time series, a composite of the annual cycle for the period 1981-2001 is also available in the form of a mean "climatological" dataset. The sea–surface temperature and sea ice concentrations are updated every time step by the model at each grid point using linear interpolation in time. The mid-month values have been evaluated in such a way that this linear time interpolation reproduces the mid-month values.

Earlier versions of the global atmospheric model (the CCM series) included a simple land-ocean-sea ice mask to define the underlying surface of the model. It is well known that fluxes of fresh water, heat, and momentum between the atmosphere and underlying surface are strongly affected by surface type. The CAM 5.0 provides a much more accurate representation of flux exchanges from coastal boundaries, island regions, and ice edges by including a fractional specification for land, ice, and ocean. That is, the area occupied by these surface types is described as a fractional portion of the atmospheric grid box. This fractional specification provides a mechanism to account for flux differences due to sub-grid inhomogeneity of surface types.

In CAM 5.0 each atmospheric grid box is partitioned into three surface types: land, sea ice, and ocean. Land fraction is assigned at model initialization and is considered fixed throughout the model run. Ice concentration data is provided by the external time varying dataset described above, with new values determined by linear interpolation at the beginning of every time-step. Any remaining fraction of a grid box not already partitioned into land or ice is regarded as ocean.

Surface fluxes are then calculated separately for each surface type, weighted by the appropriate fractional area, and then summed to provide a mean value for a grid box:

$$F_{\psi_T} = a_i \, F_{\psi_i} + a_o \, F_{\psi_o} + a_l \, F_{\psi_l} \ , \tag{6.3}$$

where F denotes the surface flux of the arbitrary scalar quantity ψ, a denotes fractional area, and the subscripts T, i, o, and l respectively denote the total, ice, ocean, and land components of the fluxes. For each time-step the aggregated grid box fluxes are passed to the atmosphere and all flux arrays which have been used for the accumulations are reset to zero in preparation for the next time-step. The fractional land values for CAM 5.0 were calculated from Navy 10-Min Global Elevation Data. An area preserving binning algorithm was used to interpolate from the high-resolution Navy dataset to standard model resolutions.

The radiation parameterization requires monthly mean ozone volume mixing ratios to be specified as a function of the latitude grid, 23 vertical pressure levels, and time. The ozone path

lengths are evaluated from the mixing–ratio data. The path lengths are interpolated to the model η–layer interfaces for use in the radiation calculation. As with the sea–surface temperatures, the seasonal version assigns the monthly averages to the mid–month date and updates them every 12 hours via linear interpolation. The actual mixing ratios used in the standard version were derived by Chervin [1986] from analysis of Dütsch [1986].

The sub-grid scale standard deviation of surface orography is specified in the following manner. The variance is first evaluated from the global Navy $10'$ topographic height data over an intermediate grid (*e.g.* $2^\circ \times 2^\circ$ grid for T42 and lower resolutions, $1.67^\circ \times 1.67^\circ$ for T63, and $1.0^\circ \times 1.0^\circ$ for T106 resolution) and is assumed to be isotropic. Once computed on the appropriate grid, the standard deviations are binned to the CAM 5.0 grid (*i.e.,* all values whose latitude and longitude centers fall within each grid box are averaged together). Finally, the standard deviation is smoothed twice with a 1–2–1 spatial filter. Values over ocean are set to zero.

Appendix A

Physical Constants

Following the American Meteorological Society convention, the model uses the International System of Units (SI) (see August 1974 *Bulletin of the American Meteorological Society*, **Vol. 55**, No. 8, pp. 926-930).

a	=	6.37122×10^6 m	Radius of earth
g	=	9.80616 m s^{-2}	Acceleration due to gravity
π	=	3.14159265358979323846	Pi
t_s	=	86164.0 s	Earth′s sidereal day
Ω	=	$2 * \pi / t_s$ [s^{-1}]	Earth′s angular velocity
σ_B	=	5.67×10^{-8} W m^{-2} K^{-4}	Stefan − Boltzmann constant
k	=	1.38065×10^{-23} JK^{-1}	Boltzmann constant
N	=	6.02214×10^{26}	Avogadro′s number
R^*	=	$k\,N$ [JK^{-1}]	Universal gas constant
m_{air}	=	28.966 kg	Molecular weight of dry air
R	=	R^*/m_{air} [J kg^{-1} K^{-1}]	Gas constant for dry air
m_v	=	18.016 kg	Molecular weight of water vapor
R_v	=	R^*/m_v [J kg^{-1} K^{-1}]	Gas constant for water vapor
c_p	=	1.00464×10^3 J kg^{-1} K^{-1}	Specific heat of dry air at constant pressure
κ	=	2/5	Von Karman constant
z_{vir}	=	$R_v/R - 1$	Ratio of gas constants for water vapor and dry air
L_v	=	2.501×10^6 J kg^{-1}	Latent heat of vaporization
L_i	=	3.337×10^5 J kg^{-1}	Latent heat of fusion
ρ_{H_2O}	=	1.0×10^3 kg m^{-3}	Density of liquid water
c_{pv}	=	1.81×10^3 J kg^{-1} K^{-1}	Specific heat of water vapor at constant pressure
T_{melt}	=	273.16 °K	Melting point of ice
p_{std}	=	1.01325×10^5 Pa	Standard pressure
ρ_{air}	=	$p_{std}/(R\,T_{melt})$ [kgm^{-3}]	Density of dry air at standard pressure/temperature

The model code defines these constants to the stated accuracy. We do not mean to imply that these constants are known to this accuracy nor that the low-order digits are significant to the physical approximations employed.

Appendix B

Acronyms

ABL	Atmospheric Boundary Layer
AMIP	Atmospheric Model Intercomparison Project
AMWG	Atmospheric Model Working Group
BATS	Biosphere-Atmosphere Transfer Scheme
CAM	Community Atmosphere Model
CAPE	Convectively Available Potential Energy
CCM	Community Climate Model
CCN	Cloud Condensation Nucleus
CCSM	Community Climate System Model
CFC	Chloro-Fluoro Carbon
CFL	Courant-Friedrichs-Levy Condition
CGD	NCAR Climate and Global Dynamics Division
CGS	Centimeters/grams/seconds
CKD	Clough-Kneizys-Davies
CLM	Community Land Model
CMS	(NCAR) Climate Modeling Section
CSIM	Community Sea-Ice Model
CWP	Condensed Water Path
DAO	(NASA Goddard) Data Assimilation Office
DAS	Data Assimilation System
DISORT	DIScrete-Ordinate method Radiative Transfer
ECMWF	European Centre for Medium Range Forecasts
EOF	Empirical Orthogonal Function
FASCODE	FASt atmosphere Signature Code
FFSL	Flux-Form Semi-Lagrangian Transport
FFT	Fast Fourier Transform
FV/fv	Finite Volume
GCM	General Circulation Model
GENLN	General Line-by-line Atmospheric Transmittance and Radiance Model
GEOS	Goddard Earth Observing System
GFDL	Geophysical Fluid Dynamics Laboratory
GSFC	Goddard Space Flight Center
GMT	Greenwich Mean Time

HadISST	Hadley Centre for Climate Prediction and Research SST
HITRAN	High-resolution Transmission Molecular Absorption Database
ICA	Independent Column Approximation
IPCC	International Panel on Climate Change
KNMI	Royal Netherlands Meteorological Institute
LBL	Line by line
LCL	Lifting condensation level
LSM	Land Surface Model
MATCH	Model for Atmospheric Transport and Chemistry
M/R	Maximum/Random overlap
NASA	National Space Administration
NCAR	National Center for Atmospheric Research
NCEP	National Center for Environmental Prediction
NOAA	National Oceanographic and Atmospheric Administration
NWP	Numerical Weather Prediction
OI	Optimal Interpolation
OPAC	Optical Properties of Aerosols and Clouds
PBL	Planetary Boundary Layer
PCMDI	Program for Climate Model Diagnosis and Intercomparison
PPM	Piece-wise Parabolic Method
RHS	Right Hand Side
RMS	Root-mean Square
SCMO	Sufficient Condition for Monotonicity
SI	International System of Units
SOM	Slab Ocean Model
SST	Sea-surface temperature
TOA	Top Of Atmosphere
TOM	Top Of Model
UCAR	University Corporation for Atmospheric Research
WKB	Wentzel-Kramer-Brillouin approximation

Appendix C

Resolution and dycore-dependent parameters

The following adjustable parameters differ between various finite volume resolutions in the CAM 5.0. Refer to the model code for parameters relevant to alternative dynamical cores.

Table C.1: Resolution-dependent parameters

Parameter	FV 1 deg	FV 2 deg	Description
$q_{ic,warm}$	2.e-4	2.e-4	threshold for autoconversion of warm ice
$q_{ic,cold}$	18.e-6	9.5e-6	threshold for autoconversion of cold ice
$k_{e,strat}$	5.e-6	5.e-6	stratiform precipitation evaporation efficiency parameter
$RH^{low}_{\min}$	.92	.91	minimum RH threshold for low stable clouds
$RH^{high}_{\min}$	.77	.80	minimum RH threshold for high stable clouds
$k_{1,deep}$	0.10	0.10	parameter for deep convection cloud fraction
p_{mid}	750.e2	750.e2	top of area defined to be mid-level cloud
$c_{0,shallow}$	1.0e-4	1.0e-4	shallow convection precip production efficiency parameter
$c_{0,deep}$	3.5E-3	3.5E-3	deep convection precipitation production efficiency parameter
$k_{e,conv}$	1.0E-6	1.0E-6	convective precipitation evaporation efficiency parameter
v_i	1.0	0.5	Stokes ice sedimentation fall speed (m/s)

Bibliography

Abdul-Razzak, H., and S. J. Ghan, A parameterization of aerosol activation 2. multiple aerosol types, *J. Geophys. Res.*, *105* **(D5)**, 6837–6844, 2000*a*.

Abdul-Razzak, H., and S. J. Ghan, A parameterization of aerosol activation 2. multiple aerosol types, *Journal of Geophysical Research-Atmospheres*, *105* **(D5)**, 6837–6844, 2000*b*, 294KT Times Cited:82 Cited References Count:27.

Alcamo, J., A. Bouwman, J. Edmonds, A. Grubler, T. Morita, and A. Sugandhy, An evaluation of the ipcc is92 emission scenarios, in *Climate Change 1994: Radiative Forcing of Climate Change and an Evaluation of the IPCC IS92 Emission Scenarios*, edited by J. Houghton, 247–304, Cambridge University Press, 1995.

Andrews, D. G., J. R. Holton, and C. B. Leovy, *Middle Atmosphere Dynamics*. Academic Press, 1987.

Ansmann, A. et al., Influence of Saharan dust on cloud glaciation in southern Morocco during the Saharan Mineral Dust Experiment, *J. Geophys. Res.*, *113* **(D04210)**, 2008.

Ansmann, A., M. Tesche, P. Seifert, D. Althausen, R. Engelmann, J. Furntke, U. Wandinger, I. Mattis, and D. Müller, Evolution of the ice phase in tropical altocumulus: SAMUM lidar observations over Cape Verde, *J. Geophys. Res.*, *114* **(D17208)**, 2009.

Anthes, R. A., Summary of workshop on the NCAR Community Climate/forecast Models 14–26 July 1985, Boulder, Colorado, *Bull. Am. Meteorol. Soc.*, *67*, 94–198, 1986.

Arakawa, A., and V. R. Lamb, A potential enstrophy and energy conserving scheme for the shallow-water equations, *Mon. Wea. Rev.*, *109*, 18–36, 1981.

Asselin, R., Frequency filter for time integrations, *Mon. Wea. Rev.*, *100*, 487–490, 1972.

Baede, A. P. M., M. Jarraud, and U. Cubasch, Adiabatic formulation and organization of ECMWF's model, Technical Report 15, ECMWF, Reading, U.K., 1979.

Balachandran, N., and D. Rind, Modeling the effects of uv variability and the qbo on the troposphere-stratosphere system. part i: The middle atmosphere, *J. Climate*, *8*, 2058–2079, 1995.

Banks, P. M., and G. Kockarts, *Aeronomy, Part B*. Academic Press, San Diego, Calif., 1973, 355 pp.

Barker, H., A parameterization for computing grid-averaged solar fluxes for inhomogenous marine boundary layer clouds. part I: Methodology and homgenous biases, *J. Atmos. Sci.*, *53*, 2289–2303, 1996.

Barker, H., B. A. Weilicki, and L. Parker, A parameterization for computing grid-averaged solar fluxes for inhomogenous marine boundary layer clouds. part II: Validation using satellite data, *J. Atmos. Sci.*, *53*, 2304–2316, 1996.

Barth, C. A., K. D. Mankoff, S. M. Bailey, and S. Solomon, Global observations of nitric oxide in the thermosphere, *J. Geophys. Res.*, *108*, doi:10.1029/2002JA009458, 2003.

Barth, M. C., P. J. Rasch, J. T. Kiehl, C. M. Benkovitz, and S. E. Schwartz, Sulfur chemistry in the National Center for Atmospheric Research Community Climate Model: Description, evaluation, features and sensitivity to aqueous chemistry, *J. Geophys. Res.*, *105*, 1387–1415, 2000.

Bates, J. R., F. H. M. Semazzi, R. W. Higgins, and S. R. Barros, Integration of the shallow water equations on the sphere using a vector semi-Lagrangian scheme with a multigrid solver, *Mon. Wea. Rev.*, *118*, 1615–1627, 1990.

Bath, L., J. Rosinski, and J. Olson, User's Guide to NCAR CCM2, Technical Report NCAR/TN-379+IA, National Center for Atmospheric Research, Boulder, CO, 156 pp., 1992.

Bath, L. M., M. A. Dias, D. L. Williamson, G. S. Williamson, and R. J. Wolski, User's Guide to NCAR CCM1, Technical Report NCAR/TN-286+IA, National Center for Atmospheric Research, Boulder, CO, 173 pp., 1987.

Beheng, K. D., A parameterization of warm cloud microphysical conversion processes, *Atmos. Res.*, *33*, 193–206, 1994.

Beres, J. H., R. R.Garcia, B. A. Boville, and F. Sassi, Implementation of a gravity wave source spectrum parameterization dependent on the properties of convection in the whole atmosphere community climate model (waccm), *J. Geophys. Res.*, *110*, doi:10.1029/2004JD005504, 2005.

Berger, A. L., Long-term variations of daily insolation and quaternary climatic changes, *J. Atmos. Sci.*, *35*, 2362–2367, 1978.

Biermann, U. M., B. P. Luo, and T. Peter, Absorption spectra and optical constants of binary and ternary solutions of h2so4, hno3, and h2o in the mid infrared at atmospheric temperatures, *The Journal of Physical Chemistry A*, *104* **(4)**, 783–793, 01, 2000.

Bigg, E. K., The supercooling of water, *Proc. Phys. Soc. B*, *66*, 688–694, 1953.

Binkowski, F. S., and S. J. Roselle, Models-3 community multiscale air quality (CMAQ) model aerosol component 1. model description, *Journal of Geophysical Research-Atmospheres*, *108*, 4183, 2003.

Binkowski, F. S., and U. Shankar, The regional particulate matter model .1. model description and preliminary results, *Journal of Geophysical Research-Atmospheres*, *100*, 26191–26209, 1995.

Blackadar, A. K., The vertical distribution of wind and turbulent exchange in a neutral atmosphere, *J. Geophys. Res.*, *67*, 3095–3102, 1962.

Bloomfield, P., Inferred lifetimes, in *NASA Report on Concentrations, Lifetimes and Trends of CFCs, Halons and Related Species*, edited by J. Kaye, S. Penkett,, and F. Osmond, NASA, Washington, D.C., 1994.

Bonan, G. B., A land surface model (LSM version 1.0) for ecological, hydrological, and atmospheric studies: Technical description and user's guide, Technical Report NCAR/TN-417+STR, National Center for Atmospheric Research, Boulder, CO, 150 pp., 1996.

Bonan, G. B., K. W. Oleson, M. Vertenstein, S. Levis, X. Zeng, Y. Dai, R. E. Dickinson, , and Z.-L. Yang, The land surface climatology of the Community Land Model coupled to the NCAR Community Climate Model, *J. Climate*, *15*, 3123–3149, 2002.

Bond, T., D. G. Streets, K. F. Yarber, S. M. Nelson, J.-H. Woo, and Z. Klimont, A technology-based global inventory of black and organic carbon emissions from combustion, *J. Geophys. Res.*, *109*, 2004.

Bond, T. C., and R. W. Bergstrom, Light absorption by carbonaceous particles: An investigative review, *Aerosol. Sci. Technol.*, *40*, 27–67, 2006.

Bond, T. C., E. Bhardwaj, R. Dong, R. Jogani, S. K. Jung, C. Roden, D. G. Streets, and N. M. Trautmann, Historical emissions of black and organic carbon aerosol from energy-related combustion, 1850-2000, *Global Biogeochemical Cycles*, *21* **(2)**, –, 2007, 174KO Times Cited:24 Cited References Count:98.

Bourke, W., B. McAvaney, K. Puri, and R. Thurling, Global modeling of atmospheric flow by spectral methods, in *Methods in Computational Physics*, Vol. 17, 267–324, Academic Press, New York, 1977.

Boville, B. A., and C. S. Bretherton, Heating and dissipation in the NCAR community atmosphere model, *J. Climate*, *16*, 3877–3887, 2003*a*.

Boville, B. A., and C. S. Bretherton, Heating and kinetic energy dissipation in the ncar community atmosphere model, *J. Climate*, *16*, 3877–3887, 2003*b*.

Boville, B. A., J. T. Kiehl, P. J. Rasch, and F. O. Bryan, Improvements to the ncar csm-1 for transient climate simulations, *J. Climate*, *14*, 164–179, 2001.

Brasseur, G. P., J. J. Orlando, and G. S. Tyndall, *Atmospheric Chemistry and Global Change*. Oxford University Press, 1999.

Bretherton, C. S., J. R. McCaa, and H. Grenier, A new parameterization for shallow cumulus convection and its application to marine subtropical cloud-topped boundary layer. part i: Description and 1d results, *Mon. Wea. Rev.*, *132*, 864–882, 2004.

Bretherton, C. S., and S. Park, A new moist turbulence parameterization in the community atmosphere model, *J. Climate*, *22*, 3422–3448, 2009*a*.

Bretherton, C. S., and S. Park, A new moist turbulence parameterization in the Community Atmosphere Model, *J. Clim.*, *22*, 3422–3448, 2009*b*.

Briegleb, B. P., Delta-Eddington approximation for solar radiation in the NCAR Community Climate Model, *J. Geophys. Res.*, *97*, 7603–7612, 1992.

Bryan, F. O., B. G. Kauffman, W. G. Large, and P. R. Gent, The NCAR CSM Flux Coupler, Technical Report NCAR/TN-424+STR, National Center for Atmospheric Research, Boulder, Colorado, 58 pp., 1996.

Bryant, F. D., and P. Latimer, Optical efficiencies of large particles of arbitrary shape and orientation, *J. Colloid Interface Sci.*, *30*, 291–304, 1969.

Cariolle, D., A. Lasserre-Bigorry, J.-F. Royer, and J.-F. Geleyn, A general circulation model simulation of the springtime antarctic ozone decrease and its impact on mid-latitudes., *J. Geophys. Res.*, *95*, 1883–1898, 1990.

Chabrillat, S., and G. Kockarts, Simple parameterization of the absorption of the solar lyman-alpha line, *Geophys. Res. Lett.*, *24*, 2659–2662, 1997.

Chervin, R. M., Interannual variability and seasonal climate predictability, *J. Atmos. Sci.*, *43*, 233–251, 1986.

Clough, S. A., M. W. Shephard, E. H. Mlawer, J. S. Delamere, M. J. Iacono, K. Cady-Pereira, S. Boukabara, and P. D. Brown, Atmospheric radiative transfer modeling: a summary of the aer codes, *J. Quant. Spectrosc. Radiat. Transfer*, *91*, 233–244, 2005.

Clough, S., and M. Iacono, Line-by-line calculation of atmospheric fluxes and cooling rates 2. application to carbon dioxide, ozone, methane, nitrous oxide and the halocarbons., *J. Geophys. Res.*, *100*, 16519–16535, 1995.

Colella, P., and P. R. Woodward, The piecewise parabolic method (ppm) for gas-dynamical simulations, *J. Comp. Phys.*, *54*, 174–201, 1984.

Collins, W. D., A global signature of enhanced shortwave absorption by clouds, *J. Geophys. Res.*, *103(D24)*, 31,669–31,680, 1998.

Collins, W. D., P. J. Rasch, B. A. Boville, J. J. Hack, J. R. MaCaa, D. L. Williamson, J. T. Kiehl, B. P. Briegleb, C. Bitz, S. J. Lin, M. Zhang, and Y. Dai, Description of the ncar community atmosphere model (cam 3.0), Technical report, National Center for Atmospheric Research, 2004*a*.

Collins, W. D., P. J. Rasch, B. A. Boville, J. J. Hack, J. R. McCaa, D. L. Williamson, J. T. Kiehl, B. P. Briegleb, C. Bitz, S.-J. Lin, M. Zhang, and Y. Dai, *Description of the NCAR Community Atmosphere Model (CAM3)*. Nat. Cent. for Atmos. Res., Boulder, Colo., 2004*b*.

Collins, W., J. Hackney, and D. Edwards, A new parameterization for infrared emission and absorption of water vapor in the national center for atmospheric research community atmospheric model, *J. Geophys. Res.*, *107*, doi: 10.1029/2001JD001365, 2002.

Considine, D. B., A. R. Douglass, D. E. Kinnison, P. S. Connell, and D. A. Rotman, A polar stratospheric cloud parameterization for the three dimensional model of the global modeling initiative and its response to stratospheric aircraft emissions, *J. Geophys. Res.*, *105*, 3955–3975, 2000.

Considine, D. B., P. S. Connell, D. Bergmann, D. A. Rotman, and S. Strahan, Sensitivity of Global Modeling Initiative CTM predictions of Antarctic ozone recovery to GCM and DAS generated meteorological fields, *J. Geophys. Res.*, *109*, doi:10.1029/20003JD004487, 2004.

Cooke, W. F., C. Liousse, H. Cachier, and J. Feichter, Construction of a 1x1 fossil fuel emission data set for carbonaceous aerosol and implementation and radiative impact in the ECHAM4 model, *J. Geophys. Res.*, *104*, 22137 – 22162, 1999.

Cooke, W. F., and J. J. N. Wilson, A global black carbon aerosol model, *J. Geophys. Res.*, *101*, 19395–19409, 1996.

Côté, J., and A. Staniforth, A two-time-level semi-Lagrangian semi-implicit scheme for spectral models, *Mon. Wea. Rev.*, *116*, 2003–2012, 1988.

Cotton, W. R., G. J. Tripoli, R. M. Rauber, and E. A. Mulvihill, Numerical simulation of the effects of varying ice crystal nucleation rates and aggregation processes on orographic snowfall, *J. Appl. Meteor.*, *25*, 1658–1680, 1986.

Dai, Y., X. Zeng, R. E. Dickinson, and coauthors, The Common Land Model: Documentation and User's Guide, `http://climate.eas.gatech.edu/dai/clmdoc.pdf`, 2001.

Daley, R., C. Girard, J. Henderson, and I. Simmonds, Short-term forecasting with a multi-level spectral primitive equation model. Part I—model formulation, *Atmosphere*, *14*, 98–116, 1976.

DeCaria, A. J., K. E. Pickering, G. L. Stenchikov, and L. E. Ott, Lightning-generated nox and its impact on tropospheric ozone production: A three-dimensional modeling study of a stratosphere-troposphere experiment: Radiation, aerosols and ozone (sterao-a) thunderstorm, *J. Geophys. Res.*, *110*, D14303, 2006.

Dennis, J., A. Fournier, W. F. Spotz, A. St.-Cyr, M. A. Taylor, S. J. Thomas, and H. Tufo, High resolution mesh convergence properties and parallel efficiency of a spectral element atmospheric dynamical core, *Int. J. High Perf. Comput. Appl.*, *19*, 225–235, 2005.

Dentener, F., S. Kinne, T. Bond, O. Boucher, J. Cofala, S. Generoso, P. Ginoux, S. Gong, J. J. Hoelzemann, A. Ito, L. Marelli, J. E. Penner, J. P. Putaud, C. Textor, M. Schulz, G. R. van derWerf, and J. Wilson, Emissions of primary aerosol and precursor gases in the years 2000 and 1750 prescribed data-sets for aerocom, *Atmospheric Chemistry and Physics*, *6*, 4321–4344, 2006*a*, 087YG Times Cited:81 Cited References Count:52.

Dentener, F., D. Stevenson, K. Ellingsen et al., Global atmospheric environment for the next generation, *Environmental Science and Technology*, *40*, 3586–3594, 2006*b*.

Deville, M. O., P. F. Fischer, and E. H. Mund, *High Order Methods for Incompressible Fluid Flow*. Cambridge University Press, 1 edition, 8, 2002.

Dickinson, R. E., A. Henderson-Sellers, P. J. Kennedy, and M. F. Wilson, Biosphere-atmosphere transfer scheme (BATS) for the NCAR Community Climate Model, Technical Report NCAR/TN-275+STR, National Center for Atmospheric Research, Boulder, Colorado, 69 pp., 1987.

Dütsch, H. U., Vertical ozone distribution on a global scale, *Pure Appl. Geophys.*, *116*, 511–529, 1986.

Dye, J. E., D.Baumgardner, B. W. Gandrun, S. R. Kawa, K. K. Kelly, M. Loewenstein, G. V. Ferry, K. R. Chan, and B. L. Gary, Particle size distributions in arctic polar stratospheric clouds, growth and freezing of sulfuring acid droplets, and implications for cloud formation, *J. Geophys. Res.*, *97*, 8015–8034, 1992.

Easter, R. C., S. J. Ghan, Y. Zhang, R. D. Saylor, E. G. Chapman, N. S. Laulainen, H. Abdul-Razzak, L. R. Leung, X. D. Bian, and R. A. Zaveri, Mirage: Model description and evaluation of aerosols and trace gases, *Journal of Geophysical Research-Atmospheres*, *109* **(D20)**, –, 2004, 867ZR Times Cited:37 Cited References Count:280.

Eaton, B. E., User's Guide to the Community Atmosphere Model AM4.0, Technical report, National Center for Atmospheric Research, Boulder, Colorado, http://www.ccsm.ucar.edu/models/ccsm4.0/cam/docs/users_guide/book1.html, 2010.

Emmons, e. a., L. K., Description and evaluation of the model for ozone and related chemical tracers, version 4 (mozart-4), *Geosci. Model Dev*, *3*, 43–67, 2010.

Emmons, L. K., S. Walters, P. G. Hess, J.-F. Lamarque, G. G. Pfister, D. Fillmore, C. Granier, A. Guenther, D. Kinnison, T. Laepple, J. Orlando, X. Tie, G. Tyndall, C. Wiedinmyer, S. L. Baughcum, and S. Kloster, Description and evaluation of the Model for Ozone and Related chemical Tracers, version 4 (MOZART-4), *Geosci. Model Dev.*, *3*, 43–67, 2010.

Ferrier, B., A double-moment multiple-phase four-class bulk ice scheme. part I: Description, *J. Atmos. Sci.*, *51*, 249–280, 1994.

Fiedler, F., and H. A. Panofsky, The geostrophic drag coefficient and the "effective roughness length, *Quart. J. Roy. Meteor. Soc.*, *98*, 213–220, 1972.

Field, P. R., O. Möhler, P. Connolly, M. Krmer, R. Cotton, A. J. Heymsfield, H. Saathoff, and M. Schnaiter, Some ice nucleation characteristics of Asian and Saharan desert dust, *Atmospheric Chemistry and Physics*, *6* **(10)**, 2991–3006, 2006.

Field, P. R., A. J. Heymsfield, and A. Bansemer, Shattering and particle inter-arrival times measured by optical array probes in ice clouds, *J. Atmos. Oceanic Technol.*, *23*, 1357–1371, 2007.

Fomichev, V. I., J. P. Blanchet, and D. S. Turner, Matrix parameterization of the 15 μm co_2 band cooling in the middle and upper atmosphere for variable co_2 concentration, *J. Geophys. Res.*, *103*, 11505–11528, 1998.

Fomichev, V. I., V. P. Ogibalov, and S. R. Beagley, Solar heating by the near-IR co_2 bands in the mesosphere, *Geophys. Res. Lett.*, *31*, L21102, 2004.

Fournier, A., M. A. Taylor, and J. Tribbia, The spectral element atmosphere model (SEAM): High-resolution parallel computation and localized resolution of regional dynamics, *Mon. Wea. Rev.*, *132*, 726–748, 2004.

Friedl, R., editor, *Atmospheric effects of subsonic aircraft: Interim assessment report of the advanced subsonic technology program*. 1997.

Fritts, D. C., and T. J. Dunkerton, Fluxes of heat and constituents due to convectively unstable gravity waves, *jas*, *42*, 549–556, 1985.

Fu, Q., P. Yang, and W. B. Sun, An accurate parameterization of the infrared radiative properties of cirrus clouds for climate models, *J. Climate*, *11*, 2223–2237, 1998.

Fuch, N. A., *The Mechanics of Aerosols*. Pergamon, Oxford, 1964.

Galperin, B., L. H. Kanta, S. Hassid, and A. Rosati, A quasi-equilibrium turbulent energy model for geophysical flows, *J. Atmos. Sci.*, *45*, 55–62, 1988.

Garcia, R. R., Parameterization of planetary wave breaking in the middle atmosphere, *jas*, 2001.

Garcia, R. R., D. R. Marsh, D. E. Kinnison, B. A. Boville, and F. Sassi, Simulation of secular trends in the middle atmosphere, 1950-2003, *J. Geophys. Res.*, *112*, doi:10.1029/2006JD007485, 2007.

Garcia, R. R., and S. Solomon, The effect of breaking gravity waves on the dynamical and chemical composition of the mesosphere and lower thermosphere, *J. Geophys. Res.*, *90*, 3850–3868, 1985.

Garcia, R. R., and S. Solomon, A new numerical model of the middle atmosphere. part ii: Ozone and related species, *J. Geophys. Res.*, *99*, 12937–12951, 1994.

Gent, P. R., S. Yeager, R. B. Neale, S. Levis, and D. Bailey, Improvements in a half degree atmopshere/land version of the CCSM., *Climate Dynamics*, *79*, 25–58, 2009.

Gettelman, A., H. Morrison, and S. J. Ghan, A new two-moment bulk stratiform cloud microphysics scheme in the NCAR Community Atmosphere Model (CAM3), Part II: Single-column and global results, *J. Clim.*, *21* **(15)**, 3660–3679, 2008.

Gettelman, A., A. X. Liu, S. J. Ghan, H. Morrison, S. Park, A. J. Conley, S. A. Klein, J. Boyle, D. L. Mitchell, and J. L. F. Li, Global simulations of ice nucleation and ice supersaturation with an improved cloud scheme in the community atmosphere model, *J. Geophys. Res.*, *108*, ????–????, 2010*a*.

Gettelman, A. et al., Multi-model assessment of the upper troposphere and lower stratosphere: Tropics and trends, *in press J. Geophys. Res.*, 2010*b*.

Ghan, S. J., and R. C. Easter, Computationally efficient approximations to stratiform cloud microphysics parameterization, *Mon. Weather Rev.*, *120* **(1572-1582)**, 1992.

Ghan, S. J., and R. C. Easter, Impact of cloud-borne aerosol representation on aerosol direct and indirect effects, *Atmospheric Chemistry and Physics*, *6*, 4163–4174, 2006, 086FO Times Cited:5 Cited References Count:47.

Ghan, S. J., L. R. Leung, R. C. EasterEaster, and K. AbdulRazzak, Prediction of cloud droplet number in a general circulation model, *J. Geophys Res-Atmos*, *102*, 21777–21794, 1997.

Ghan, S. J., and R. A. Zaveri, Parameterization of optical properties for hydrated internally-mixed aerosol, *J. Geophys. Res.*, *112*, DOI 10.1029/2006JD007927, 2007.

Giraldo, F. X., Trajectory calculations for spherical geodesic grids in cartesian space, *Mon. Wea. Rev.*, *127*, 1651–1662, 1999.

Granier, C., A. Guenther, J. Lamarque, A. Mieville, J. Muller, J. Olivier, J. Orlando, J. Peters, G. Petron, G. Tyndall, and S. Wallens, POET, a database of surface emissions ofozone precursors, 2005, last access: August 2008.

Gregory, D., R. Kershaw, and P. M. Inness, Parameterization of momentum transport by convection. ii: Tests in single column and general circulation models, *Q. J. R. Meteorol. Soc.*, *123*, 1153–1184, 1997*a*.

Gregory, D., R. Kershaw, and P. M. Inness, Parametrization of momentum transport by convection. II: Tests in single-column and general circulation models, *Q. J. R. Meteorol. Soc.*, *123*, 1153–1183, 1997*b*.

Grenier, H., and C. S. Bretherton, A moist pbl parameterization for large-scale models and its application to subtropical cloud-topped marine boundary layer, *Mon. Wea. Rev.*, *129*, 357–377, 2001.

Griffin, R. J., D. R. Cocker, R. C. Flagan, and J. H. Seinfeld, Organic aerosol formation from the oxidation of biogenic hydrocarbons, *J. Geophys. Res.*, *104*, 3555 – 3567, 1999.

Guenther, A. B., X. Jiang, C. L. Heald, T. Sakulyanontvittaya, T. Duhl, L. K. Emmons, and X. Wang, The model of emissions of gases and aerosols from nature version 2.1 (megan2.1): an extended and updated framework for modeling biogenic emissions, *Geoscientific Model Development Discussions*, *5* **(2)**, 1503–1560, 2012.

Hack, J. J., Parameterization of moist convection in the National Center for Atmospheric Research Community Climate Model (CCM2), *J. Geophys. Res.*, *99*, 5551–5568, 1994*a*.

Hack, J. J., Parameterization of moist convection in the national center for atmospheric research community climate model (ccm2), *J. Geophys. Res.*, *99*, 5551–5568, 1994*b*.

Hack, J. J., L. M. Bath, G. W. Williamson, and B. A. Boville, Modifications and enhancements to the NCAR Community Climate Model (CCM1), Technical Report NCAR/TN-336+STR, National Center for Atmospheric Research, Boulder, Colorado, 97 pp., 1989.

Hack, J. J., B. A. Boville, B. P. Briegleb, J. T. Kiehl, P. J. Rasch, and D. L. Williamson, Description of the NCAR Community Climate Model (CCM2), Technical Report NCAR/TN-382+STR, National Center for Atmospheric Research, 120 pp., 1993.

Heald, C. L., D. K. Henze, L. W. Horowitz, J. Feddema, J.-F. Lamarque, A. Guenther, P. G. Hess, F. Vitt, J. H. Seinfeld, A. H. Goldstein, and I. Fung, Predicted change in global secondary organic aerosol concentrations in response to future climate, emissions, and land-use change, *J. Geophys. Res.*, *113*, 2008.

Heald, C. L., M. J. Wilkinson, R. K. Monson, C. A. Alo, G. Wang, and A. Guenther, Response of isoprene emission to ambient co2 changes and implications for global budgets, *Glob. Change Biol.*, *15*, 1127 – 1140, 2009.

Hedin, A. E., Extension of the MSIS thermosphere model into the middle and lower atmosphere, *J. Geophys. Res.*, *96*, 1159, 1991.

Hedin, A., MSIS-86 thermospheric model, *J. Geophys. Res.*, *92*, 4649, 1987.

Heinbockel, J. H., *Introduction to Tensor Calculus and Continuum Mechanics*. Trafford Publishing, Victoria, B.C., 12, 2001.

Held, I. M., and M. J. Suarez, A proposal for the intercomparison of the dynamical cores of atmospheric general circulation models, *Bull. Am. Meteorol. Soc.*, *75*, 1825–1830, 1994.

Henze, D. K., J. H. Seinfeld, N. L. Ng, J. H. Kroll, T.-M. Fu, D. J. Jacob, and C. L. Heald, Global modeling of secondary organic aerosol formation from aromatic hydrocarbons: high- vs. low-yield pathways, *Atmospheric Chemistry and Physics*, *8* **(9)**, 2405–2420, 2008.

Hildebrand, F. B., *Introduction to Numerical Analysis*. McGraw-Hill, New York, New York, 1956, 511 pp.

Holstlag, A. M., and B. A. Boville, Local versus nonlocal boundary layer diffusion in a global climate model, *J. Climate*, *6*, 1825–1842, 1993.

Holton, J. R., The role of gravity wave induced drag and diffusion in the momentum budget of the mesosphere, *J. Atmos. Sci.*, *39*, 791–799, 1982.

Holtslag, A. A. M., and B. A. Boville, Local versus nonlocal boundary-layer diffusion in a global climate model, *J. Climate*, *6*, 1825–1842, 1993*a*.

Holtslag, A. A. M., and B. A. Boville, Local versus nonlocal boundary layer diffusion in a global model, *J. Climate*, *6*, 1825–1842, 1993*b*.

Holtslag, A. A. M., E. I. F. deBruijn, and H.-L. Pan, A high resolution air mass transformation model for short-range weather forecasting, *Mon. Wea. Rev.*, *118*, 1561–1575, 1990.

Hoose, C., and J. E. Kristjansson, A classical-theory-based parameterization of heterogeneous ice nucleation by mineral dust, soot and biological particles in a global climate model, *in press, J. Atmos. Sci.*, 2010.

Horowitz, e. a., L., A global simulation of tropospheric ozone and related tracers: Description and evaluation of mozart, version 2, *Journal of Geophysical Research-Atmospheres*, *108*, 4784,, 2003.

Horowitz, L., S. Walters, D. Mauzerall, L. Emmons, P. Rasch, C. Granier, X. Tie, J.-F. Lamarque, M. Schultz, G. Tyndall, J. Orlando, and G. Brasseur, A global simulation of tropospheric ozone and related tracers: Description and evaluation of mozart, version 2, *J. Geophys. Res.*, *108*, 4784, 2003.

Hortal, M. 1999. Aspects of the numerics of the ECMWF model. in *Proceedings of ECMWF Seminar: Recent developments in numerical methods for atmospheric modelling, 7–11 September 1998*, 127–143, .

Hoskins, B. J., The mathematical theory of frontogenesis, *Ann. Rev. Fluid Mech.*, *14*, 131–151, 1982.

Hsu, Y.-J. G., and A. Arakawa, Numerical modeling of the atmosphere with an isentropic vertical coordinate, *Mon. Wea. Rev.*, *118*, 1933–1959, 1990.

Iacono, M., E. Mlawer, S. Clough, and J.-J. Morcrette, Impact of an improved longwave radiation model, rrtm, on the energy budget and thermodynamic properties of the ncar community climate model, ccm3, *J. Geophys. Res.*, *105*, 14873–14890, 2000.

Iacono, M., J. Delamere, E. Mlawer, and S. Clough, Evaluation of upper tropospheric water vapor in the ncar community climate model (ccm3) using modeled and observed hirs radiances, *J. Geophys. Res.*, *108(D2), 4037*, 2003.

Iacono, M., J. Delamere, E. Mlawer, M. Shephard, S. Clough, and W. Collins, Radiative forcing by long-lived greenhouse gases: Calculations with the aer radiative transfer models, *J. Geophys. Res.*, 2008.

Ikawa, M., and K. Saito, description of the nonhydrostatic model developed at the forecast research department of the mri, Technical Report 28, Meteorological Institute MRI, 1990.

Jablonowski, C., and D. L. Williamson, A baroclinic instability test case for atmospheric model dynamical cores, *Q. J. R. Meteorol. Soc.*, *132*, 2943–2975, 2006.

Jakob, C., and S. A. Klein, A parametrization of cloud and precipitation overlap effects for use in general circulation models, *Q. J. Roy. Meteorol. Soc.*, *126*, 2525 – 2544, 2000.

Junker, C., and C. Liousse, A global emission inventory of carbonaceous aerosol from historic records of fossil fuel and biofuel consumption for the period 1860-1997, *Atmospheric Chemistry and Physics*, *8* **(5)**, 1195–1207, 2008, 273CS Times Cited:8 Cited References Count:52.

Kader, B. A., and A. M. Yaglom, Mean fields and fluctuation moments in unstably stratified turbulent boundary layers, *J. Fluid Mech.*, *212*, 637–662, 1990.

Kain, J. S., and J. M. Fritsch, A one-dimensional entraining/detraining plume model and its application in convective parameterization, *J. Atmos. Sci.*, *47*, 2784–2802, 1990.

Kärcher, B., O. Möhler, P. J. DeMott, S. Pechtl, and F. Yu, Insights into the role of soot aerosols in cirrus cloud formation, *Atmos. Chem. Phys.*, *7*, 4203–4227, 2007.

Kärcher, B., and C. Voigt, Formation of nitric acid/water ice particles in cirrus clouds, *Geophys. Res. Lett.*, *33*, 2006.

Karniadakis, G. E., and S. J. Sherwin, *Spectral/hp Element Methods for Computational Fluid Dynamics (Numerical Mathematics and Scientific Computation)*. Oxford University Press, USA, 2 edition, 8, 2005.

Kasahara, A., Various vertical coordinate systems used for numerical weather prediction, *Mon. Wea. Rev.*, *102*, 509–522, 1974.

Kasten, F., Falling speed of aerosol particles, *J. Appl. Meteorol.*, *7*, 944–947, 1968.

Kerminen, V. M., and M. Kulmala, Analytical formulae connecting the "real" and the "apparent" nucleation rate and the nuclei number concentration for atmospheric nucleation events, *Journal of Aerosol Science*, *33* **(4)**, 609–622, 2002, 535VC Times Cited:67 Cited References Count:26.

Kershaw, R., and D. Gregory, Parametrization of momentum transport by convection. I: Theory and cloud modelling results, *Q. J. R. Meteorol. Soc.*, *123*, 1133–1151, 1997.

Khairoutdinov, M. F., and Y. Kogan, A new cloud physics parameterization in a large-eddy simulation model of marine stratocumulus, *Mon. Weather Rev.*, *128*, 229–243, 2000.

Kiehl, J. T., and B. P. Briegleb, A new parameterization of the absorbance due to the 15 micron band system of carbon dioxide, *J. Geophys. Res.*, , 9013–9019, 1991.

Kiehl, J. T., J. J. Hack, and B. P. Briegleb, The simulated Earth radiation budget of the National Center for Atmospheric Research Community Climate Model CCM2 and comparisons with the Earth Radiation Budget Experiment (ERBE), *J. Geophys. Res.*, *99*, 20815–20827, 1994.

Kiehl, J. T., J. Hack, G. Bonan, B. Boville, B. Briegleb, D. Williamson, and P. Rasch, Description of the NCAR Community Climate Model (CCM3), Technical Report NCAR/TN-420+STR, National Center for Atmospheric Research, Boulder, Colorado, 152 pp., 1996.

Kiehl, J. T., J. J. Hack, G. B. Bonan, B. B. Boville, D. L. Williamson, and P. J. Rasch, The National Center for Atmospheric Research Community Climate Model: CCM3, *J. Climate*, *11*, 1131–1149, 1998.

Kinnison, D. E., G. P. Brasseur, S. Walters, R. R. Garcia, D. A. Marsch, F. Sassi, B. A. Boville, V. L. Harvey, C. E. Randall, L. Emmons, J. F. Lamarque, P. Hess, J. J. Orlando, X. X. Tie, W. Randel, L. L. Pan, A. Gettelman, C. Granier, T. Diehl, U. Niemaier, and A. J. Simmons, Sensitivity of chemical tracers to meteorological parameters in the MOZART-3 chemical transport model, *J. Geophys. Res.*, *112*, D20302, 2007.

Kloster, S., J. Feichter, E. Maier-Reimer, K. D. Six, P. Stier, and P. Wetzel, Dms cycle in the marine ocean-atmosphere system a global model study, *Biogeosciences*, *3*, 29 – 51, 2006.

Kockarts, G., Nitric oxide cooling in the terrestrial thermosphere, *Geophys. Res. Lett.*, *7*, 137–140, 1980.

Koehler, K. A., S. M. Kreidenweis, P. J. DeMott, M. D. Petters, A. J. Prenni, and C. M. Carrico, Hygroscopicity and cloud droplet activation of mineral dust aerosol, *Geophysical Research Letters*, *36*, –, 2009*a*, 435FB Times Cited:4 Cited References Count:25.

Koehler, K. A., S. M. Kreidenweis, P. J. DeMott, M. D. Petters, A. J. Prenni, and C. M. Carrico, Hygroscopicity and cloud droplet activation of mineral dust aerosol., *Geophys. Res. Lett.*, *36*, 2009*b*.

Koepke, M. H. P., and I. Schult, Optical properties of aerosols and clouds: The software package opac, *Bull. Am. Meteorol. Soc.*, *79*, 831–844, 1998.

Koppers, G. A. A., and D. P. Murtagh, Model studies of the influence of O_2 photodissociation parameterizations in the schumann-runge bands on ozone related photolysis in the upper atmosphere, *Ann. Geophys.*, *14*, 68–79, 1996.

Kroll, J. H., N. L. Ng, S. M. Murphy, R. C. Flagan, and J. H. Seinfeld, Secondary organic aerosol formation from isoprene photooxidation, *Environmental Science and Technology*, *40* **(6)**, 1869–1877, 2006, 024RN Times Cited:121 Cited References Count:62.

Lack, D. A., X. X. Tie, N. D. Bofinger, A. N. Wiegand, and S. Madronich, Seasonal variability of secondary organic aerosol: A global modeling study, *J. Geophys. Res.*, *109*, 2004.

Lamarque, J.-F., P. Hess, L. Emmons, L. Buja, W. Washington, and C. Granier, Tropospheric ozone evolution between 1890 and 1990, *J. Geophys. Res.*, *110*, D08304, 2005.

Lamarque, J. F., T. C. Bond, V. Eyring, C. Granier, A. Heil, Z. Klimont, D. Lee, C. Liousse, A. Mieville, B. Owen, M. G. Schultz, D. Shindell, S. J. Smith, E. Stehfest, J. vanAardenne, O. R. Cooper, M. Kainuma, N. Mahowald, J. R. McConnell, V. Naik, K. Riahi, and D. P. vanVuuren, Historical (18502000) gridded anthropogenic and biomass burning emissions of reactive gases and aerosols: methodology and application, *Atmospheric Chemistry and Physics Discussion*, *10*, 49635019, 2010*a*.

Lamarque, J., T. C. Bond, V. Eyring, C. Granier, A. Heil, Z. Klimont, D. Lee, C. Liousse, A. Mieville, B. Owen, M. G. Schultz, D. Shindell, S. J. Smith, E. Stehfest, J. van Aardenne, O. R. Cooper, M. Kainuma, N. Mahowald, J. R. McConnell, V. Naik, K. Riahi, and D. P. van Vuuren, Historical (1850-2000) gridded anthropogenic and biomass burning emissions of reactive gases and aerosols: methodology and application, *Atmospheric Chemistry & Physics Discussions*, *10*, 4963–5019, Feb., 2010*b*.

Lamarque, J.-F., L. K. Emmons, P. G. Hess, D. E. Kinnison, S. Tilmes, F. Vitt, C. L. Heald, E. A. Holland, P. H. Lauritzen, J. Neu, J. J. Orlando, P. J. Rasch, and G. K. Tyndall, CAM-chem: Description and evaluation of interactive atmospheric chemistry in the Community Earth System Model, *Geoscientific Model Development*, *5* **(2)**, 369–411, 2012.

Large, W. G., J. C. McWilliams, and S. C. Doney, Oceanic vertical mixing: A review and a model with a nonlocal boundary layer parameterization, *Rev. Geophys.*, *32*, 363–403, 1994.

5172 Large, W. G., and S. Pond, Sensible and latent heat flux measurements over the ocean, *J. Phys.*
5173 *Oceanogr.*, *12*, 464–482, 1982.

5174 Lauritzen, P., C. Jablonowski, M. Taylor, and R. Nair, Rotated versions of the jablonowski
5175 steady-state and baroclinic wave test cases: A dynamical core intercomparison, *Journal of*
5176 *Advances in Modeling Earth Systems*, *In Press*, 2010.

5177 Lauritzen, P. H., A stability analysis of finite-volume advection schemes permitting long time
5178 steps, *Mon. Wea. Rev.*, *135*, 2658–2673, 2007.

5179 Lauritzen, P. H., P. A. Ullrich, and R. D. Nair, Atmospheric transport schemes: Desirable
5180 properties and a semi-lagrangian view on finite-volume discretizations, in: P.H. Lauritzen,
5181 R.D. nair, C. Jablonowski, M. Taylor (Eds.), Numerical techniques for global atmospheric
5182 models, *Lecture Notes in Computational Science and Engineering, Springer*, 2010, to appear.

5183 Lawrence, P. J., and T. N. Chase, Representing a new modis consistent land surface in the
5184 community land model (CLM 3.0), *J. Geophys. Res.*, *112*, 2007.

5185 Lawson, R. P., B. Barker, B. Pilson, and Q. Mo, In situ observations of the microphysical
5186 properties of wave, cirrus and anvil clouds. Part 2: Cirrus cloud, *J. Atmos. Sci.*, *63*, 3186–
5187 3203, 2006.

5188 Le Texier, H., S. Solomon, and R. R. Garcia, Role of molecular hydrogen and methane oxidation
5189 in the water vapor budget of the stratosphere, *Q. J. R. Meteorol. Soc.*, *114*, 281–295, 1988.

5190 Lean, J., Evolution of the sun's spectral irradiance since the maunder minimum, *Geophys. Res.*
5191 *Lett.*, *27* **(16)**, 2425–2428, 2000.

5192 Liao, H., P. J. Adams, S. H. Chung, J. H. Seinfeld, L. J. Mickley, and D. J. Jacob, Interac-
5193 tions between tropospheric chemistry and aerosols in a unified general circulation model, *J.*
5194 *Geophys. Res.*, *108*, 4001, 2003.

5195 Lim, Y. B., and P. J. Ziemann, Products and mechanism of secondary organic aerosol formation
5196 from reactions of n-alkanes with oh radicals in the presence of nox, *Environmental Science*
5197 *and Technology*, *39* **(23)**, 9229–9236, 2005, 989ZK Times Cited:53 Cited References Count:48.

5198 Lin, S.-J., W. C. Chao, Y. C. Sud, and G. K. Walker, A class of the van leer-type transport
5199 schemes and its applications to the moisture transport in a general circulation model, *Mon.*
5200 *Wea. Rev.*, *122*, 1575–1593, 1994.

5201 Lin, S.-J., and R. B. Rood, Multidimensional flux form semi-lagrangian transport schemes, *Mon.*
5202 *Wea. Rev.*, *124*, 2046–2070, 1996.

5203 Lin, S.-J., and R. B. Rood, An explicit flux-form semi-lagrangian shallow water model on the
5204 sphere, *Q. J. R. Meteorol. Soc.*, *123*, 2531–2533, 1997.

5205 Lin, S.-J., A vertically lagrangian finite-volume dynamical core for global models, *Mon. Wea.*
5206 *Rev.*, *132*, 2293–2397, 2004.

Lin, Y.-L., R. R. Farley, and H. D. Orville, Bulk parameterization of the snow field in a cloud model, *J. Clim. Appl. Meteorol.*, *22*, 1065–1092, 1983.

Lindzen, R. S., Turbulence and stress due to gravity wave and tidal breakdown, *J. Geophys. Res.*, *86*, 9701–9714, 1981.

Liu, X., J. E. Penner, S. J. Ghan, and M. Wang, Inclusion of ice microphysics in the NCAR Community Atmosphere Model version 3 (CAM3), *J. Clim.*, *20*, 4526–4547, 2007.

Liu, X., R. C. Easter, S. J. Ghan, R. Zaveri, P. J. Rasch, X. Shi, J. F. Lamarque, A. Gettelman, H. M. F. Vitt, A. Conley, S. P. R. B. Neale, C. Hannay, A. M. L. Ekman, P. Hess, N. Mahowald, W. D. Collins, M. J. Iacono, C. S. Bretherton, M. G. Flanner, D., and Mitchell, Toward a minimal representation of aerosols in climate models: description and evaluation in the community atmosphere model CAM5, *Geosci. Model Dev.*, *5*, 709–739, 2012*a*.

Liu, X., R. C. Easter, S. J. Ghan, R. Zaveri, P. Rasch, X. Shi, J.-F. Lamarque, A. Gettelman, H. Morrison, F. Vitt, A. Conley, S. Park, R. Neale, C. Hannay, A. M. L. Ekman, P. Hess, N. Mahowald, W. Collins, M. J. Iacono, C. S. Bretherton, M. G. Flanner, and D. Mitchell, Toward a minimal representation of aerosols in climate models: description and evaluation in the community atmosphere model cam5, *Geoscientific Model Development*, *5* **(3)**, 709–739, 2012*b*.

Liu, X., and S. Ghan, A modal aerosol model implementation in the Community Atmosphere Model, version 5 (CAM5), *J. Atmos. Sci.*, 2010.

Liu, X., and J. E. Penner, Ice nucleation parameterization for global models, *Meteor. Z.*, *14* **(499-514)**, 2005.

Liu, X. H., J. E. Penner, and M. Herzog, Global modeling of aerosol dynamics: Model description, evaluation, and interactions between sulfate and nonsulfate aerosols, *Journal of Geophysical Research-Atmospheres*, *110* **(D18)**, –, 2005, 968RL Times Cited:39 Cited References Count:207.

Lohmann, U., J. Feichter, C. C. Chuang, and J. Penner, Prediction of the number of cloud droplets in the echam gcm, *J. Geophys. Res.*, *104* **(D8)**, 9169–9198, 1999.

Lord, S. J., W. C. Chao, and A. Arakawa, Interaction of a cumulus cloud ensemble with the large-scale environment. part iv: The discrete model, *J. Atmos. Sci.*, *39*, 104–113, 1982.

Machenhauer, B., The spectral method, in *Numerical Methods Used in Atmospheric Models*, World Meteorological Organization, Geneva, Switzerland, 1979.

Machenhauer, B. 1998. MPI workshop on conservative transport schemes. in *Report No. 265,* . Max-planck-Institute for Meteorology.

Machenhauer, B., E. Kaas, and P. H. Lauritzen, Finite volume methods in meteorology, in: R. Temam, J. Tribbia, P. Ciarlet (Eds.), Computational methods for the atmosphere and the oceans, *Handbook of Numerical Analysis*, *14*, 2009, Elsevier, 2009, pp.3-120.

Maday, Y., and A. T. Patera, Spectral element methods for the incompressible Navier Stokes equations, in *State of the Art Surveys on Computational Mechanics*, edited by A. K. Noor, and J. T. Oden, 71–143, ASME, New York, 1987.

Madronich, S., Photodissociation in the atmosphere: 1. Actinic flux and the effects of ground reflections and clouds, *J. Geophys. Res.*, *92(D8)*, 9740 – 9752, 1987.

Mahowald, N., J.-F. Lamarque, X. X. Tie, and E. Wolff, Seasalt aerosol response to climate change: Last glacial maximum, preindustrial, and doubled carbon dioxide climates, *J. Geophys. Res.*, *111*, 2006*a*.

Mahowald, N. M., D. R. Muhs, S. Levis, P. J. Rasch, M. Yoshioka, C. S. Zender, and C. Luo, Change in atmospheric mineral aerosols in response to climate: Last glacial period, preindustrial, modern, and doubled carbon dioxide climates, *Journal of Geophysical Research-Atmospheres*, *111* **(D10)**, –, 2006*b*, 050EP Times Cited:68 Cited References Count:123.

Mahowald, N. M., D. R. Muhs, S. Levis, P. J. Rasch, M. Yoshioka, C. S. Zender, and C. Luo, Change in atmospheric mineral aerosols in response to climate: Last glacial period, preindustrial, modern, and doubled carbon dioxide climates, *J. Geophys. Res.*, *111*, 2006*c*.

Mahowald, N. M., M. Yoshioka, W. D. Collins, A. J. Conley, D. W. Fillmore, and D. B. Coleman, Climate response and radiative forcing from mineral aerosols during the last glacial maximum, pre-industrial, current and doubled-carbon dioxide climates, *Geophysical Research Letters*, *33* **(20)**, –, 2006*d*, 100WD Times Cited:16 Cited References Count:21.

Manabe, S., Climate and the ocean circulation: 1. The atmospheric circulation and the hydrology of the earth's surface, *Mon. Wea. Rev.*, *97*, 739–774, 1969.

Marsh, D., S. Solomon, and A. Reynolds, Empirical model of nitric oxide in the lower thermosphere, *J. Geophys. Res.*, *109*, doi:10.1029/2003JA010199, 2004.

Martensson, E. M., E. D. Nilsson, G. deLeeuw, L. H. Cohen, and H. C. Hansson, Laboratory simulations and parameterization of the primary marine aerosol production, *Journal of Geophysical Research-Atmospheres*, *108* **(D9)**, –, 2003, 682QU Times Cited:51 Cited References Count:32.

Marti, J., and K. Mauersberger, A survey and new measurements of ice vapor pressure at temperatures between 170 and 250 K, *Geophys. Res. Lett.*, *20*, 363–366, 1993.

Martin, G. M., D. W. Johnson, and A. Spice, The measurement and parameterization of effective radius of droplets in warm stratocumulus clouds, *J. Atmos. Sci.*, *51*, 1823–1842, 1994.

Matthes, K., D. R. Marsh, R. R. Garcia, D. E. Kinnison, F. Sassi, and S. Walters, The role of the qbo in modulating the influence of the 11-year solar cycle on the atmosphere using constant forcings, *J. Geophys. Res.*, *??*, doi:10.1029/2009JD013020, 2010.

McAvaney, B. J., W. Bourke, and K. Puri, A global spectral model for simulation of the general circulation, *J. Atmos. Sci.*, *35*, 1557–1583, 1978.

McFarlane, N. A., The effect of orographically excited gravity wave drag on the general circulation of the lower stratosphere and troposphere, *J. Atmos. Sci.*, *44*, 1775–1800, 1987.

McFarlane, R. P. S. A., and S. A. Klein, Albedo bias and the horizontal variability of clouds in subtropical marine boundary layers: Observations from ships and satellite, *J. Geophys. Res.*, *104*, 6138–6191, 1999.

McIntyre, M. E., On dynamics and transport near the polar mesopause in summer, *J. Geophys. Res.*, *94*, 14,617–14,628, 1989.

McLinden, C., S. Olsen, B. Hannegan, O. Wild, and M. Prather, Stratospheric ozone in 3-d models: A simple chemistry and the cross-tropopause flux, *J. Geophys. Res.*, *105*, 14,653–14,665, 2000.

Meinshausen, M., S. J. Smith, K. Calvin, J. S. Daniel, M. L. T. Kainuma, J.-F. Lamarque, K. Matsumoto, S. Montzka, R. S., K. Riahi, A. Thomson, G. J. M. Velders, and D. P. vanVuuren, The rcp greenhouse gas concentrations and their extensions from 1765 to 2300, *Climatic Change*, *109*, 213 – 241, 2011.

Merikanto, J., I. Napari, H. Vehkamaki, T. Anttila, and M. Kulmala, New parameterization of sulfuric acid-ammonia-water ternary nucleation rates at tropospheric conditions, *Journal of Geophysical Research-Atmospheres*, *112* **(D15)**, –, 2007, 202AA Times Cited:16 Cited References Count:39.

Metzger, S., F. Dentener, S. Pandis, and J. Lelieveld, Gas/aerosol partitioning: 1. A computationally efficient model, *J. Geophys. Res.*, *107*, 4323, 2002.

Meyers, M. P., P. J. DeMott, and W. R. Cotton, New primary ice-nucleation parameterizations in an explicit cloud model, *J. Applied Met.*, *31*, 708–721, 1992.

Minschwaner, K., and D. E. Siskind, A new calculation of nitric oxide photolysis in the stratosphere, mesosphere, and lower thermosphere, *J. Geophys. Res.*, *98*, 20401–20412, 1993.

Mitchell, D. L., Parameterization of the Mie extinction and absorption coefficients for water clouds, *J. Atmos. Sci.*, *57*, 1311–1326, 2000.

Mitchell, D. L., Effective diameter in radiation transfer: General definition, applications and limitations, *J. Atmos. Sci.*, *59*, 2330–2346, 2002.

Mitchell, D. L., and W. P. Arnott, A model predicting the evolution of ice particle size spectra and radiative properties of cirrus clouds. part ii: Dependence of absorption and extinction on ice crystal morphology, *J. Atmos. Sci.*, , 817–832, 1994.

Mitchell, D. L., A. Macke, and Y. Liu, Modeling cirrus clouds. Part II: Treatment of radiative properties, *J. Atmos. Sci.*, *53*, 2697–2988, 1996*a*.

Mitchell, D. L., A. Macke, and Y. Liu, Modeling cirrus clouds. part ii: Treatment of radiative properties, *J. Atmos. Sci.*, *53*, 2967–2988, 1996*b*.

Mitchell, D. L., W. P. Arnott, C. Schmitt, A. J.Baran, S. Havemann, and Q. Fu, Contributions of photon tunneling to extinction in laboratory grown hexagonal columns, *J. Quant. Spectrosc. Radiat. Transfer*, *70*, 761–776, 2001.

Mitchell, D. L., A. J. Baran, W. P. Arnott, and C. Schmitt, Testing and comparing the modified anomalous diffraction approximation, *J. Atmos. Sci.*, *59*, 2330–2346, 2006*a*.

Mitchell, D. L., R. P. d'Entremont, and R. P. Lawson, Passive thermal retrievals of ice and liquid water path, effective size and optical depth and their dependence on particle and size distribution shape, 12th AMS Conference on Atmospheric Radiation, July, 2006*b*.

Mlawer, E., S. Taubman, P. Brown, M. Iacono, and S. Clough, Radiative transfer for inhomogeneous atmospheres: Rrtm, a validated correlated-k model for the longwave, *J. Geophys. Res.*, *102*, 16663–16682, 1997.

Mlynczak, M. G., and S. Solomon, A detailed evaluation of the heating efficiency in the middle atmosphere, *J. Geophys. Res.*, *98*, 10,517–10,541, 1993.

Monahan, E. C., D. E. Spiel, and K. L. Davidson, A model of marine aerosol generation via whitecaps and wave disruption, in *Oceanic Whitecaps*, edited by E. C. Monahan, G. M. Niocaill,, and D. Reidel, Norwell, Mass., 1986.

Moncet, J.-L., and S. Clough, Accelerated monochromatic radiative transfer for scattering atmospheres: Application of a new model to spectral radiance observations, *J. Geophys. Res.*, *102* **(21)**, 853–866, 1997.

Morrison, H., J. A. Curry, and V. I. Khvorostyanov, A new double-moment microphysics parameterization for application in cloud and climate models. part i: Description, *J. Atmos. Sci.*, *62*, 1665–1677, 2005.

Morrison, H., and A. Gettelman, A new two-moment bulk stratiform cloud microphysics scheme in the NCAR Community Atmosphere Model (CAM3), Part I: Description and numerical tests, *J. Clim.*, *21* **(15)**, 3642–3659, 2008.

Morrison, H., and J. O. Pinto, Mesoscale modeling of springtime arctic mixed-phase stratiform clouds using a new two-moment bulk microphysics scheme, *J. Atmos. Sci.*, *62*, 3683–3704, 2005.

Mote, P. W., J. R. Holton, J. M. Russell, and B. A. Boville, A comparison of observed (haloe) and modeled (ccm2) methane and stratospheric water vapor, *grl*, *20*, 1419—1422, 1993.

Neale, R. B., J. H. Richter, and M. Jochum, The impact of convection on ENSO: From a delayed oscillator to a series of events, *J. Climate*, *21*, 5904–5924, 2008.

Neale, R. B., and B. J. Hoskins, A standard test case for AGCMs including their physical parametrizations: I: The proposal, *Atmos. Sci. Lett.*, *1*, 101–107, 2001*a*.

Neale, R. B., and B. J. Hoskins, A standard test case for AGCMs including their physical parametrizations: II: Results for the Met Office Model, *Atmos. Sci. Lett.*, *1*, 108–114, 2001*b*.

Neu, J. L., and M. J. Prather, Toward a more physical representation of precipitation scavenging in global chemistry models: cloud overlap and ice physics and their impact on tropospheric ozone, *Atmospheric Chemistry and Physics*, *12* **(7)**, 3289–3310, 2012.

Newman, P. A., J. S. Daniel, D. W. Waugh, and E. R. Nash, A new formulation of equivalent effective stratospheric chlorine (EESC), *Atmos. Chem. Phys.*, *7* **(17)**, 4537–4552, 2007.

Ng, N. L., P. S. Chhabra, A. W. H. Chan, J. D. Surratt, J. H. Kroll, A. J. Kwan, D. C. McCabe, P. O. Wennberg, A. Sorooshian, S. M. Murphy, N. F. Dalleska, R. C. Flagan, and J. H. Seinfeld, Effect of nox level on secondary organic aerosol (soa) formation from the photooxidation of terpenes, *Atmospheric Chemistry and Physics*, *7* **(19)**, 5159–5174, 2007*a*, 235MS Times Cited:42 Cited References Count:63.

Ng, N. L., J. H. Kroll, A. W. H. Chan, P. S. Chhabra, R. C. Flagan, and J. H. Seinfeld, Secondary organic aerosol formation from m-xylene, toluene, and benzene, *Atmospheric Chemistry and Physics*, *7* **(14)**, 3909–3922, 2007*b*.

Nousiainen, T., and G. M. McFarquhar, Light scattering by quasi-spherical ice crystals, *J. Atmos. Sci.*, *61*, 2229–2248, 2004.

Odum, J. R., T. P. W. Jungkamp, R. J. Griffin, H. J. L. Forstner, R. C. Flagan, and J. H. Seinfeld, Aromatics, reformulated gasoline, and atmospheric organic aerosol formation, *Environmental Science and Technology*, *31* **(7)**, 1890–1897, 1997*a*, Xh483 Times Cited:168 Cited References Count:29.

Odum, J. R., T. P. W. Jungkamp, R. J. Griffin, H. J. L. Forstner, R. C. Flagan, and J. H. Seinfeld, Aromatics, reformulated gasoline, and atmospheric organic aerosol formation, *Environ. Sci. Technol.*, *31*, 1890–1897, 1997*b*.

Ogibalov, V. P., and V. I. Fomichev, Parameterization of solar heating by the near IR co_2 bands in the mesosphere, *Adv. Space Res.*, *32*, 759–764, 2003.

Ohara, T., H. Akimoto, J. Kurokawa, N. Horii, K. Yamaji, X. Yan, and T. Hayasaka, An asian emission inventory of anthropogenic emission sources for the period 1980 – 2020, *Atmos. Chem. Phys.*, *7* **(16)**, 4419–4444, 2007.

Okin, G. S., A new model of wind erosion in the presence of vegetation, *Journal of Geophysical Research-Earth Surface*, *113* **(F2)**, –, 2008, 276QS Times Cited:5 Cited References Count:41.

Orszag, S. A., Fourier series on spheres, *Mon. Wea. Rev.*, *102*, 56–75, 1974.

Ovtchinnikov, M., and S. J. Ghan, Parallel simulations of aerosol influence on clouds using cloud-resolving and single-column models, *Journal of Geophysical Research-Atmospheres*, *110* **(D15)**, –, 2005, 916EG Times Cited:9 Cited References Count:45.

Pankow, J. F., An absorption model of the gas aerosol partitioning involved in the formation of secondary organic aerosol, *Atmos. Environ.*, *28*, 189 – 193, 1994.

Park, S., and C. S. Bretherton, The university of washington shallow convection and moist turbulence schemes and their impact on climate simulations with the community atmosphere model, *J. Climate*, *22*, 3449–3469, 2009.

Park, S., C. S. Bretherton, and P. J. Rasch, The revised cloud macrophysics in the community atmosphere model, *J. Climate*, *000*, 0000–0000, 2010.

Peter, T., C. Bruhl, and P. J. Crutzen, Increase in the PSC formation probability caused by high-flying aircraft, *J. Geophys. Res.*, *18*, 1465–1468, 1991.

Petters, M., and S. Kreidenweis, A single parameter representation of hygroscopic growth and ccn activity, *Atmos. Chem. Phys.*, *7*, 1961–1971, 2007.

Pickering, K., Y. Wang, W.-K. Tao, C. Price, and J. Mueller, Vertical distributions of lightning NO_x for use in regional and global chemical transport models, *J. Geophys. Res.*, *103*, 31,203–31,216, 1998.

Pincus, R. H. W. B., and J.-J. Morcrette, A fast, flexible, approximation technique for computing radiative transfer in inhomogeneous cloud fields, *J. Geophys. Res.*, *108(D13)*, 4376, 2003.

Poschl, U., M. Canagaratna, J. T. Jayne, L. T. Molina, D. R. Worsnop, C. E. Kolb, and M. J. Molina, Mass accommodation coefficient of h2so4 vapor on aqueous sulfuric acid surfaces and gaseous diffusion coefficient of h2so4 in n-2/h2o, *Journal of Physical Chemistry A*, *102* **(49)**, 10082–10089, 1998, 146ZX Times Cited:40 Cited References Count:41.

Prather, M. J., Tropospheric o3 from photolysis of o2, *Geophys. Res. Lett.*, *36*, 2009.

Prather, M., Catastrophic loss of stratospheric ozone in dense volcanic clouds, *J. Geophys. Res.*, *97*, 187–10,191, 1992.

Prenni, A. J., J. Y. Harrington, M. Tjernstrom, P. J. DeMott, A. Avramov, C. N. Long, S. M. Kreidenweis, P. Q. Olsson, and J. Verlinde, Can ice-nucleating aerosols effect Arctic seasonal climate?, *Bull. Am. Meteorol. Soc.*, *88*, 541–550, 2007.

Price, C., J. Penner, and M. Prather, NO_x from lightning. Part 1: Global distribution based on lightning physics, *J. Geophys. Res.*, *102*, 5929–5941, 1997*a*.

Price, C., J. Penner, and M. Prather, NO_x from lightning. Part 2: Constraints from the global atmospheric electric circuit, *J. Geophys. Res.*, *102*, 5943–5952, 1997*b*.

Price, C., and D. Rind, A simple lightning parameterization for calculating global lightning distributions, *J. Geophys. Res.*, *97*, 9919–9933, 1992.

Pruppacher, H. R., and J. D. Klett, *Microphysics of Clouds and Precipitation*. Kluwer Academic, 1997.

Rančić, M., R. Purser, and F. Mesinger, A global shallow-water model using an expanded spherical cube: Gnomonic versus conformal coordinates, *Q. J. R. Meteorol. Soc.*, *122*, 959–982, 1996.

Rasch, P. J., B. A. Boville, and G. P. Brasseur, A three-dimensional general circulation model with coupled chemistry for the middle atmosphere, *J. Geophys. Res.*, *100*, 9041–9071, 1995.

Rasch, P. J., M. C. Barth, J. T. Kiehl, S. E. Schwartz, and C. M. Benkovitz, A description of the global sulfur cycle and its controlling processes in the National Center for Atmospheric Research Community Climate Model, Version 3, *J. Geophys. Res.*, *105*, 1367–1385, 2000.

Rasch, P. J., and J. E. Kristjánsson, A comparison of the CCM3 model climate using diagnosed and predicted condensate parameterizations, *J. Climate*, *11*, 1587–1614, 1998*a*.

Rasch, P. J., and J. E. Kristjansson, A comparison of the ccm3 model climate using diagnosed and predicted condensate parameterizations, *J. Climate*, *11*, 1587–1614, 1998*b*.

Rasch, P. J., and D. L. Williamson, On shape-preserving interpolation and semi-Lagrangian transport, *SIAM J. Sci. Stat. Comput.*, *11*, 656–687, 1990.

Raymond, D. J., and A. M. Blyth, A stochastic mixing model for non-precipitating cumulus clouds, *J. Atmos. Sci.*, *43*, 2708–2718, 1986.

Raymond, D. J., and A. M. Blyth, Extension of the stochastic mixing model to cumulonimbus clouds, *J. Atmos. Sci.*, *49*, 1968–1983, 1992.

Reisner, J., R. Rasmussen, and R. T. Bruintjes, Explicit forecasting of supercooled liquid water in winter storms using the mm5 forecast model, *Q. J. R. Meteorol. Soc.*, *124*, 1071–1107, 1998.

R.G.Roble, Energetics of the mesosphere and thermosphere, in *The upper mesosphere and lower thermosphere : a review of experiment and theory*, edited by R. Johnson, and T. Killeen, *Geophys. Monogr., 87*, 1–21, 1995.

Richmond, A., Ionospheric electrodynamics using magnetic apex coordinates, *J. Geomag. Geoelectric.*, *47*, 191, 1995.

Richmond, A., M. Blanc, B. Emery, R. Wand, B. Fejer, R. Woodman, S. Ganguly, P. Amayenc, R. Behnke, C. Calderon, and J. Evans, An empirical model of quiet-day ionospheric electric fields at middle and low latitudes, *J. Geophy. Res*, *85*, 4658, 1980.

Richter, J. H., F. Sassi, and R. R. Garcia, Towards a physically-based wave source parameterization in a general circulation model, *J. Atmos. Sci.*, *67*, 136–156, 2010.

Richter, J. H., and P. J. Rasch, Effects of convective momentum transport on the atmospheric circulation in the community atmosphere model, version 3, *J. Climate*, *21*, 1487–1499, 2008.

Ridley, B., K. Pickering, and J. Dye, Comments on the parameterization of lightning-produced no in global chemistry-transport models, *Atmos. Environ.*, *39*, 6184–6187, 2005.

Riemer, N., H. Vogel, B. Vogel, and F. Fiedler, Modeling aerosols on the mesoscale-gamma: Treatment of soot aerosol and its radiative effects, *Journal of Geophysical Research-Atmospheres*, *108* **(D19)**, –, 2003, 732EM Times Cited:17 Cited References Count:90.

Ringler, T. D., R. P. Heikes, , and D. A. Randall, Modeling the atmospheric general circulation using a spherical geodesic grid: A new class of dynamical cores, *Mon. Wea. Rev.*, *128*, 2471–2490, 2000.

Ritchie, H., and M. Tanguay, A comparison of spatially averaged Eulerian and semi-Lagrangian treatments of mountains, *Mon. Wea. Rev.*, *124*, 167–181, 1996.

Robert, A. J., The integration of a low order spectral form of the primitive meteorological equations, *J. Meteorol. Soc. Japan*, *44*, 237–245, 1966.

Roble, R., and E. Ridley, An auroral model for the ncar thermospheric general circulation model (TGCM), *Ann. Geophys.*, *87*, 369, 1987.

Roble, R., and E. Ridley, A thermosphere-ionosphere-mesosphere-electrodynamics general circulation model (TIME-GCM): Equinox solar cycle minimum simulations (30-500 km), *Geophys. Res. Lett.*, *21*, 417–420, 1994.

Rothman, L. S., A. Barbe, D. C. Benner, L. R. Brown, C. Camy-Peyret, M. R. Carleer, K. Chance, C. Clerbaux, V. Dana, V. M. Devi, A. Fayt, J.-M. Flaud, R. R. Gamache, A. Goldman, D. Jacquemart, K. W. Jucks, W. J. Lafferty, J.-Y. Mandin, S. T. Massie, V. Nemtchinov, D. A. Newnham, A. Perrin, C. P. Rinsland, J. Schroeder, K. M. Smith, M. A. H. Smith, K. Tang, R. A. Toth, J. V. Auwera, P. Varanasi, and K. Yoshino, The HITRAN molecular spectroscopic database: Edition of 2000 including updates of 2001, *J. Quant. Spectrosc. Radiat. Transfer*, *82*, 2003.

Rothman, L., I. Gordon, A. Barbe, D. Benner, P. Bernath, M. Birk, V. Boudon, L. Brown, A. Campargue, J.-P. Champion, K. Chance, L. Coudert, V. Dana, V. Devi, S. Fally, J.-M. Flaud, R. Gamache, A. Goldman, D. Jacquemart, I. Kleiner, N. Lacome, W. Lafferty, J.-Y. Mandin, S. Massie, S. Mikhailenko, C. Miller, N. Moazzen-Ahmadi, O. Naumenko, A. Nikitin, J. Orphal, V. Perevalov, A. Perrin, A. Predoi-Cross, C. Rinsland, M. Rotger, M. Simeckov, M. Smith, K. Sung, S. Tashkun, J. Tennyson, R. Toth, A. Vandaele, and J. V. Auwera, The hitran 2008 molecular spectroscopic database, *Journal of Quantitative Spectroscopy and Radiative Transfer*, *110* **(9-10)**, 533 – 572, 2009, HITRAN.

Rotstayn, L. D., B. F. Ryan, and J. J. Katzfey, A scheme for calculation of the liquid fraction in mixed-phase stratiform clouds in large-scale models, *Mon. Weather Rev.*, *128* **(4)**, 1070–1088, 2000.

Rotstayn, L. D., and U. Lohmann, Tropical rainfall trends and the indirect aerosol effect, *J. Climate*, *15*, 2103 – 2116, 2002.

Sadourny, R., Conservative finite-difference approximations of the primitive equations on quasi-uniform spherical grids, *Mon. Wea. Rev.*, *100* **(2)**, 136–144, 1972.

Sander, S. P., et al., Chemical kinetics and photochemical data for use in atmospheric studies. Evaluation number 15, Technical Report Publication 06-02, Jet Propulsion Laboratory, Pasadena, CA, 2006.

Sanderson, M., W. Collins, R. Derwent, and C. Johnson, Simulation of global hydrogen levels using a lagrangian three-dimensional model, *J. Atmos. Chem.*, *46* **(1)**, 15–28, SEP, 2003.

Sandu, A., F. A. Potra, V. Damian-Iordache, and G. R. Carmichael, Efficient implementation of fully implicit methods for atmospheric chemistry, *J. Comp. Phys.*, *129*, 101–110, 1996.

Sandu, A., J. Verwer, M. vanLoon, G. Carmichael, F. Potra, D. Dabdub, and J. Seinfeld, Benchmarking stiff ODE solvers for atmospheric chemistry problems I: Implicit versus explicit, *Atmospheric Environment*, *31*, 3151–3166, 1997.

Sangster, W. E., A meteorological coordinate system in which the Earth's surface is a coordinate surface, Ph.D. thesis, University of Chicago, Department of Geophysical Sciences, 1960.

Sato, R. K., L. M. Bath, D. L. Williamson, and G. S. Williamson, User's guide to NCAR CCMOB, Technical Report NCAR/TN-211+IA, National Center for Atmospheric Research, Boulder, Colorado, 133 pp., 1983.

Satoh, M., *Atmospheric Circulation Dynamics and Circulation Models (Springer Praxis Books / Environmental Sciences)*. Springer, 1 edition, 6, 2004.

Scherliess, L., A. Richmond, and B. Fejer. 2002. Global empirical ionospheric electric field model. draft, Center for Atmospheric and Space Science, Utah State University, Logan.

Schubert, W. H., J. S. Wakefield, E. J. Steiner, and S. K. Cox, Marine stratocumulus convection. part i: Governing equations and horizontally homogeneous solutions, *J. Atmos. Sci.*, *36*, 1286–1307, 1979.

Schunk, R., and A. Nagy, *Ionospheres: Physics, Plasma Physics, and Chemistry*. Cambridge, University Press, 2000.

Seinfeld, J. H., and S. N. Pandis, *Atmospheric Chemistry and Physics: From Air Pollution to Climate Change*. John Wiley, Hoboken, N. J, 1998.

Sihto, S. L., M. Kulmala, V. M. Kerminen, M. D. Maso, T. Petaja, I. Riipinen, H. Korhonen, F. Arnold, R. Janson, M. Boy, A. Laaksonen, and K. E. J. Lehtinen, Atmospheric sulphuric acid and aerosol formation: implications from atmospheric measurements for nucleation and early growth mechanisms, *Atmospheric Chemistry and Physics*, *6*, 4079–4091, 2006.

Simmons, A. J., and D. M. Burridge, An energy and angular momentum conserving vertical finite-difference scheme and hybrid vertical coordinates, *Mon. Wea. Rev.*, *109*, 758–766, 1981.

Simmons, A. J., and R. Strüfing, An energy and angular-momentum conserving finite-difference scheme, hybrid coordinates and medium-range weather prediction, Technical Report ECMWF Report No. 28, European Centre for Medium–Range Weather Forecasts, Reading, U.K., 68 pp., 1981.

Simmons, A. J., and R. Strüfing, Numerical forecasts of stratospheric warming events using a model with hybrid vertical coordinate, *Q. J. R. Meteorol. Soc.*, *109*, 81–111, 1983.

Skamarock, W., Kinetic energy spectra and model filters, in: P.H. Lauritzen, R.D. nair, C. Jablonowski, M. Taylor (Eds.), Numerical techniques for global atmospheric models, *Lecture Notes in Computational Science and Engineering, Springer, 2010*, 2010, to appear.

Slingo, J. M., The development and verification of a cloud prediction scheme for the ECMWF model, *Q. J. R. Meteorol. Soc.*, *113*, 899–927, 1987*a*.

Slingo, J. M., The development and verification of a cloud prediction scheme for the ecmwf model, *Q. J. R. Meteorol. Soc.*, *113*, 899–927, 1987*b*.

Smith, R. N. B., A scheme for predicting layer clouds and their water content in a general circulation model, *Q. J. R. Meteorol. Soc.*, *116*, 435–460, 1990.

Smith, S. J., H. Pitcher, and T. M. L. Wigley, Global and regional anthropogenic sulfur dioxide emissions, *Glob. Biogeochem. Cycles*, *29*, 99–119, 2001.

Smith, S. J., R. Andres, E. Conception, and J. Lurz, Historical sulfur dioxide emissions 18502000: Methods and results, Technical report, Pacific Northwest National Laboratory, Joint Global Change Research Institute, 2004.

Solomon, S., and L. Qiang, Solar extreme-ultraviolet irradiance for general circulation models, *J. Geophys. Res.*, *110*, A10306, doi:10.1029/2005JA011160, 2005.

Sparks, J. P., J. M. Roberts, and R. K. Monson, The uptake of gaseous organic nitrogen by leaves: A significant global nitrogen transfer process, *Geophys. Res. Lett.*, *30*, 2003.

Spiteri, R. J., and S. J. Ruuth, A new class of optimal high-order strong-stability-preserving time discretization methods, *SIAM J. Numer. Anal.*, *40* **(2)**, 469–491, 2002.

Staniforth, A., N. Wood, and C. Girard, Energy and energy-like invariants for deep non-hydrostatic atmospheres, *Q. J. R. Meteorol. Soc.*, *129*, 3495–3499, 2003.

Starr, V. P., A quasi-lagrangian system of hydrodynamical equations, *J. Meteor.*, *2*, 227–237, 1945.

Stier, P., J. Feichter, S. Kinne, S. Kloster, E. Vignati, J. Wilson, L. Ganzeveld, I. Tegen, M. Werner, Y. Balkanski, M. Schulz, O. Boucher, A. Minikin, and A. Petzold, The aerosol-climate model echam5-ham, *Atmospheric Chemistry and Physics*, *5*, 1125–1156, 2005, 912EM Times Cited:156 Cited References Count:125.

Suarez, M. J., and L. L. Takacs, Documentation of the aries/geos dynamical core: Version 2, Technical Report Technical Memorandum 104 606 Vol. 5, NASA, 1995.

Sundqvist, H., Parameterization of condensation and associated clouds in models for weather prediction and general circulation simulation, in *Physically-based Modeling and Simulation of Climate and Climate Change*, Vol. 1, edited by M. E. Schlesinger, 433–461, Kluwer Academic, 1988.

Tabazadeh, A., R. P. Turco, and M. Z. Jacobson, A model for studying the composition and chemical effects of stratospheric aerosols, *J. Geophys. Res.*, *99*, 12,897–12,914, 1994.

Tabazadeh, A., M. L. Santee, M. Y. Danilin, H. C. Pumphrey, P. A. Newman, P. J. Hamill, and J. L. Mergenthaler, Quantifying denitrification and its effect on ozone recovery, *Science*, *288*, 1407–1411, 2000.

Taylor, M. A., J. Edwards, and A. St.Cyr, Petascale atmospheric models for the community climate system model: New developments and evaluation of scalable dynamical cores, *J. Phys. Conf. Ser.*, *125* **(012023)**, 2008.

Taylor, M. 2010. Conservation of mass and energy for the moist atmospheric primitive equations on unstructured grids. in *Numerical Techniques for Global Atmospheric Models, Springer Lecture Notes in Computational Science and Engineering,* . Springer.

Taylor, M., J. Tribbia, and M. Iskandarani, The spectral element method for the shallow water equations on the sphere, *J. Comp. Phys.*, *130*, 92–108, 1997.

Taylor, M. A., A. St.Cyr, and A. Fournier. 2009. A non-oscillatory advection operator for the compatible spectral element method. in *Computational Science ICCS 2009 Part II, Lecture Notes in Computer Science 5545*, 273–282*,* , Berlin / Heidelberg. Springer.

Taylor, M. A., and A. Fournier, A compatible and conservative spectral element method on unstructured grids, *J. Comp. Phys.*, *In Press*, –, 2010.

Temperton, C., Treatment of the Coriolis terms in semi-Lagrangian spectral models, in *Atmospheric and Ocean Modelling. The André J. Robert Memorial Volume*, edited by C. Lin, R. Laprise,, and H. Ritchie, 293–302, Canadian Meteorological and Oceanographic Society, Ottawa, Canada, 1997.

Temperton, C., M. Hortal, and A. Simmons, A two-time-level semi-Lagrangian global spectral model, *Q. J. R. Meteorol. Soc.*, *127*, 111–127, 2001.

Thomas, S., and R. Loft, Parallel semi-implicit spectral element methods for atmospheric general circulation models, *J. Sci. Comput.*, *15*, 499–518, 2000.

Thomas, S., and R. Loft, The NCAR spectral element climate dynamical core: Semi-implicit Eulerian formulation, *J. Sci. Comput.*, *25*, 307–322, 2005.

Thomason, L. W., L. R. Poole, and T. Deshler, A global climatology of stratospheric aerosol surface area density measurements: 1984-1994, *J. Geophys. Res.*, *102*, 8967–8976, 1997.

Thompson, G. M., R. M. Rasmussen, and K. Manning, Explicit forecasts of winter precipitation using and improved bulk microphysics scheme. part I: Description and sensitivity analysis, *Mon. Weather Rev.*, *132*, 519–542, 2004.

Thompson, G., P. R. Field, R. M. Rasmussen, and W. D. Hall, Explicit forecasts of winter precipitation using an improved bulk microphysics scheme. part ii: Implementation of a new snow parameterization, *Monthly Weather Review*, *136* **(12)**, 5095–5115, 2008.

Tie, X., G. Brasseur, L. Emmons, L. Horowitz, and D. Kinnison, Effects of aerosols on tropospheric oxidants: A global model study, *Journal of Geophysical Research-Atmospheres*, *106* **(D19)**, 22931–22964, 2001, 481UJ Times Cited:64 Cited References Count:92.

Tie, X., G. Brasseur, and W. Lei, Global NOx production by lightning, *J. Atmos. Chem.*, *43*, 61–74, 2002.

Tie, X., S. Madronich, S. Walters, D. P. Edwards, P. Ginoux, N. Mahowald, R. Zhang, C. Lou, and G. Brasseur, Assessment of the global impact of aerosols on tropospheric oxidants, *J. Geophys. Res.*, *110*, D03204, 2005*a*.

Tie, X. X., S. Madronich, S. Walters, D. P. Edwards, P. Ginoux, N. Mahowald, R. Y. Zhang, C. Lou, and G. Brasseur, Assessment of the global impact of aerosols on tropopshic ozidants, *J. Geophys. Res.*, *110* **(D03204)**, 2005*b*.

Tilmes, S., R. Garcia, D. Kinnisen, A. Gettelman, and P. J. Rasch, Impact of geoengineered aerosols on the troposphere and stratosphere, *J. Geophys. Res.*, *114*, 2009.

van de Hulst, H. C., *Light Scattering by Small Particles*. Dover, 1957.

Vavrus, S., and D. Waliser, An improved parameterization for simulating arctic cloud amount in the CCSM3 climate model, *J. Climate*, *21*, 5673–5687, 2008.

Vehkamaki, H., M. Kulmala, I. Napari, K. E. J. Lehtinen, T. T., N. Noppel, and A. Laaksonen, an improved parameterization for sulfuric acid-water nucleation rates for tropospheric and stratospheric conditions, *Journal of Geophysical Research-Atmospheres*, *107*, 4622, 2002.

Walcek, C. J., R. A. Brost, J. S. Chang, and M. L. Wesely, So2, sulfate and hno3 deposition velocities computed using regional landuse and meteorological data, *Atmos. Environ.*, *20*, 946 – 964, 1986.

Walmsley, J., and M. Wesely, Modification of coded parametrizations of surface resistances to gaseous dry deposition, *Atmos. Environ.*, *30* **(7)**, 1181–1188, APR, 1996.

Wang, H., J. J. Tribbia, F. Baer, A. Fournier, and M. A. Taylor, A spectral element version of CAM2, *Mon. Wea. Rev.*, *135*, 38253840, 2007.

Wang, M. H., J. E. Penner, and X. H. Liu, Coupled impact aerosol and NCAR CAM3 model: Evaluation of predicted aerosol number and size distribution, *Journal of Geophysical Research-Atmospheres*, *114*, D06302, 2009.

Wang, Y.-M., J. Lean, and N. Sheeley, Modeling the sun's magnetic field and irradiance since 1713, *The Astrophysical Journal*, *625* **(1)**, 2005.

Warren, S., and R. E. Brandt, Optical constants of ice from the ultraviolet to the microwave: A revised compilation, *J. Geophys. Res.*, *113*, 2008.

Washington, W. M., Documentation for the Community Climate Model (CCM), Version $\emptyset$, Technical Report NTIS No. PB82 194192, National Center for Atmospheric Research, Boulder, Colorado, 1982.

Webster, S., A. R. Brown, D. R. Cameron, and P. Jones, Improvements to the representation of orography in the met office unified model, *Quart. J. Roy. Meteor. Soc.*, *129*, 1989–2010, 2003.

Weimer, D., Models of high-latitude electric potentials derived with the least error fit of spherical harmonic coefficients, *J. Geophy. Res*, *100*, 19,595, 1995.

van der Werf, G. R., J. T. Randerson, L. Giglio, G. J. Collatz, P. S. Kasibhatla, and A. F. Arellano Jr., Interannual variability in global biomass burning emissions from 1997 to 2004, *Atmospheric Chemistry and Physics*, *6* **(11)**, 3423–3441, 2006.

Wesely, M., Parameterization of surface resistances to gaseous dry deposition in regional-scale numerical models, *Atmos. Environ.*, *23*, 1293–1304, 1989.

Wesely, M., and B. Hicks, A review of the current status of knowledge on dry deposition, *Atmos. Environ.*, *34* **(12-14)**, 2261–2282, 2000.

Wiacek, A., and T. Peter, On the availability of uncoated mineral dust ice nuclei in cold cloud regions, *Geophys. Res. Lett.*, *36* **(L17801)**, 2009.

Wiedinmyer, C., S. K. Akagi, R. J. Yokelson, L. K. Emmons, J. A. Al-Saadi, J. J. Orlando, and A. J. Soja, The fire inventory from ncar (finn): a high resolution global model to estimate the emissions from open burning, *Geoscientific Model Development*, *4* **(3)**, 625–641, 2011.

Williamson, D. L., Description of NCAR Community Climate Model (CCM0B), Technical Report NCAR/TN-210+STR, National Center for Atmospheric Research, Boulder, Colorado, NTIS No. PB83 23106888, 88 pp., 1983.

Williamson, D. L., Time-split versus process-split coupling of parameterizations and dynamical core, *Mon. Wea. Rev.*, *130*, 2024–2041, 2002.

Williamson, D. L., L. M. Bath, R. K. Sato, T. A. Mayer, and M. L. Kuhn, Documentation of NCAR CCM0B program modules, Technical Report NCAR/TN-212+IA, National Center for Atmospheric Research, Boulder, Colorado, NTIS No. PB83 263996, 198 pp., 1983.

Williamson, D. L., J. T. Kiehl, V. Ramanathan, R. E. Dickinson, and J. J. Hack, Description of NCAR Community Climate Model (CCM1), Technical Report NCAR/TN-285+STR, National Center for Atmospheric Research, Boulder, Colorado, 112 pp., 1987.

Williamson, D. L., and J. G. Olson, Climate simulations with a semi-Lagrangian version of the NCAR Community Climate Model, *Mon. Wea. Rev.*, *122*, 1594–1610, 1994*a*.

Williamson, D. L., and J. G. Olson, Climate simulations with a semi-lagrangian version of the NCAR community climate model, *Mon. Wea. Rev.*, *122*, 1594–1610, 1994*b*.

Williamson, D. L., and P. J. Rasch, Two-dimensional semi-Lagrangian transport with shape-preserving interpolation, *Mon. Wea. Rev.*, *117*, 102–129, 1989.

Williamson, D. L., and J. M. Rosinski, Accuracy of reduced grid calculations, *Q. J. R. Meteorol. Soc.*, *126*, 1619–1640, 2000.

Williamson, D. L., and G. S. Williamson, Circulation statistics from January and July simulations with the NCAR Community Climate Model (CCM0B), Technical Report NCAR/TN-224+STR,, National Center for Atmospheric Research, Boulder, Colorado, NTIS No. PB85 165637/AS, 112 pp., 1984.

Williamson, G. S., CCM2 datasets and circulation statistics, Technical Report NCAR/TN-391+STR, National Center for Atmospheric Research, Boulder, Colorado, 85 pp., 1993.

Williamson, G. S., and D. L. Williamson, Circulation statistics from seasonal and perpetual January and July simulations with the NCAR Community Climate Model (CCM1): R15, Technical Report NCAR/TN-302+STR, National Center for Atmospheric Research, Boulder, Colorado, 199 pp., 1987.

Wilson, J., C. Cuvelier, and F. Raes, A modeling study of global mixed aerosol fields, *Journal of Geophysical Research-Atmospheres*, *106* **(D24)**, 34,08134,108, 2001.

Wilson, J. D., Representing drag on unresolved terrain as a distributed momentum sink, *J. Atmos. Sci.*, *59*, 1629–1637, 2002.

Wiscombe, W. J., Mie scattering calculations: Advances in technique and fast, vector-speed computer codes., Technical Report Tech. Note. NCAR/TN-140+STR, NCAR, 1996.

World Meteorological Organization, Scientific Assessment of Ozone Depletion: 2002 Global Ozone Research and Monitoring Project, Report no. 47, 498 pp., Geneva, 2003.

Wu, T. T., High frequency scattering, *Phys. Rev.*, *104*, 1201–1212, 1956.

Yang, P., H. Wei, H. L. Huang, B. A. Baum, Y. X. Hu, G. W. Kattawar, M. I. Mishchenko, and Q. Fu, Scattering and absorption property database for nonspherical ice particles in the near- through far-infrared spectral region, *Appl. Opt.*, *44*, 5512–5523, 2005.

Yonemura, S., S. Kawashima, and H. Tsuruta, Carbon monoxide, hydrogen, and methane uptake by soils in a temperate arable field and a forest, *J. Geophys. Res.*, *105* **(D11)**, 14,347–14,362, JUN 16, 2000.

Yoshioka, M., N. M. Mahowald, A. J. Conley, W. D. Collins, D. W. Fillmore, C. S. Zender, and D. B. Coleman, Impact of desert dust radiative forcing on sahel precipitation: Relative importance of dust compared to sea surface temperature variations, vegetation changes, and greenhouse gas warming, *Journal of Climate*, *20* **(8)**, 1445–1467, 2007, 157SY Times Cited:33 Cited References Count:80.

Young, K. C., The role of contact nucleation in ice phase initiation of clouds, *J. Atmos. Sci.*, *31*, 768–776, 1974.

Zeng, X., and R. E. Dickinson, Effect of surface sublayer on surface skin temperature and fluxes, *J. Climate*, *11*, 537–550, 1998.

Zeng, X., M. Zhao, and R. E. Dickinson, Intercomparison of bulk aerodynamic algorithms for the computation of sea surface fluxes using TOGA COARE and TAO data, *J. Climate*, *11*, 2628–2644, 1998.

Zerroukat, M., N. Wood, and A. Staniforth, A monotonic and positive-definite filter for a semi-lagrangian inherently conserving and efficient (slice) scheme, *Q. J. R. Meteorol. Soc.*, *131* **(611)**, 2923–2936, 2005.

Zhang, G. J., and N. A. McFarlane, Sensitivity of climate simulations to the parameterization of cumulus convection in the Canadian Climate Centre general circulation model, *Atmosphere-Ocean*, *33*, 407–446, 1995.

Zhang, L. M., S. L. Gong, J. Padro, and L. Barrie, A size-segregated particle dry deposition scheme for an atmospheric aerosol module, *Atmospheric Environment*, *35* **(3)**, 549–560, 2001, 395TK Times Cited:136 Cited References Count:49.

Zhang, M., W. Lyn, C. S. Bretherton, J. J. Hack, and P. J. Rasch, A modified formulation of fractional stratiform condensation rate in the ncar community atmosphere model (cam2), *J. Geophys. Res.*, *000*, 1000–0000, 2003*a*.

Zhang, M., W. Lin, C. S. Bretherton, J. J. Hack, and P. J. Rasch, A modified formulation of fractional stratiform condensation rate in the NCAR community atmospheric model CAM2, *J. Geophys. Res.*, *108* **(D1)**, 2003*b*.

Zhang, Y., and L. Paxton, An empirical kp-dependent global auroral model based on timed/guvi fuv data, *Journal of Atmospheric and Solar-Terrestrial Physics*, *70* **(8-9)**, 1231 – 1242, 2008.

Zilitinkevich, S. S., *Dynamics of the Atmospheric Boundary Layer*. Gidrometeoizdat, Leningrad, 1970, 292 pp.